

Supercritical Fluid Engineering Science

July 22, 2012 | <http://pubs.acs.org>
Publication Date: December 17, 1992 | doi: 10.1021/bk-1992-0514.fw001

ACS SYMPOSIUM SERIES **514**

Supercritical Fluid Engineering Science

Fundamentals and Applications

Erdogan Kiran, EDITOR
University of Maine

Joan F. Brennecke, EDITOR
University of Notre Dame

Developed from a symposium sponsored
by the American Institute of Chemical Engineers
at their 1991 Annual Meeting,
Los Angeles, California,
November 17–22, 1991



American Chemical Society, Washington, DC 1993

In Supercritical Fluid Engineering Science; Kiran, E., et al.;
ACS Symposium Series; American Chemical Society: Washington, DC, 1992.



Library of Congress Cataloging-in-Publication Data

Supercritical fluid engineering science: fundamentals and applications
/ Erdogan Kiran, editor, Joan F. Brennecke, editor.

p. cm.—(ACS symposium series, ISSN 0097-6156; 514)

“Developed from a symposium sponsored by the American Institute of Chemical Engineers at their 1991 Annual Meeting, Los Angeles, California, November 17–22, 1991.”

Includes bibliographical references and indexes.

ISBN 0-8412-2513-3

1. Supercritical fluid extraction—Congresses.

I. Kiran, Erdogan, 1946— . II. Brennecke, Joan F., 1962—
III. American Institute of Chemical Engineers. Meeting (1991: Los Angeles, Calif.) IV. Series.

TP156.E8S83 1992
660'.284248—dc20

92-33287
CIP

The paper used in this publication meets the minimum requirements of American National Standard for Information Sciences—Permanence of Paper for Printed Library Materials, ANSI Z39.48-1984.

Copyright © 1993

American Chemical Society

All Rights Reserved. The appearance of the code at the bottom of the first page of each chapter in this volume indicates the copyright owner's consent that reprographic copies of the chapter may be made for personal or internal use or for the personal or internal use of specific clients. This consent is given on the condition, however, that the copier pay the stated per-copy fee through the Copyright Clearance Center, Inc., 27 Congress Street, Salem, MA 01970, for copying beyond that permitted by Sections 107 or 108 of the U.S. Copyright Law. This consent does not extend to copying or transmission by any means—graphic or electronic—for any other purpose, such as for general distribution, for advertising or promotional purposes, for creating a new collective work, for resale, or for information storage and retrieval systems. The copying fee for each chapter is indicated in the code at the bottom of the first page of the chapter.

The citation of trade names and/or names of manufacturers in this publication is not to be construed as an endorsement or as approval by ACS of the commercial products or services referenced herein; nor should the mere reference herein to any drawing, specification, chemical process, or other data be regarded as a license or as a conveyance of any right or permission to the holder, reader, or any other person or corporation, to manufacture, reproduce, use, or sell any patented invention or copyrighted work that may in any way be related thereto. Registered names, trademarks, etc., used in this publication, even without specific indication thereof, are not to be considered unprotected by law.

PRINTED IN THE UNITED STATES OF AMERICA

American Chemical Society
Library

1155 16th St., N.W.

In Supercritical Fluid Engineering Science, Kiran, E., et al.;
ACS Symposium Series; American Chemical Society: Washington, DC, 1992.

1993 Advisory Board

ACS Symposium Series

M. Joan Comstock, *Series Editor*

V. Dean Adams
Tennessee Technological
University

Robert J. Alaimo
Procter & Gamble
Pharmaceuticals, Inc.

Mark Arnold
University of Iowa

David Baker
University of Tennessee

Arindam Bose
Pfizer Central Research

Robert F. Brady, Jr.
Naval Research Laboratory

Margaret A. Cavanaugh
National Science Foundation

Dennis W. Hess
Lehigh University

Hiroshi Ito
IBM Almaden Research Center

Madeleine M. Joullie
University of Pennsylvania

Gretchen S. Kohl
Dow-Corning Corporation

Bonnie Lawlor
Institute for Scientific Information

Douglas R. Lloyd
The University of Texas at Austin

Robert McGorin
Kraft General Foods

Julius J. Menn
Plant Sciences Institute,
U.S. Department of Agriculture

Vincent Pecoraro
University of Michigan

Marshall Phillips
Delmont Laboratories

George W. Roberts
North Carolina State University

A. Truman Schwartz
Macalaster College

John R. Shapley
University of Illinois
at Urbana–Champaign

Peter Willett
University of Sheffield (England)

Foreword

THE ACS SYMPOSIUM SERIES was first published in 1974 to provide a mechanism for publishing symposia quickly in book form. The purpose of this series is to publish comprehensive books developed from symposia, which are usually “snapshots in time” of the current research being done on a topic, plus some review material on the topic. For this reason, it is necessary that the papers be published as quickly as possible.

Before a symposium-based book is put under contract, the proposed table of contents is reviewed for appropriateness to the topic and for comprehensiveness of the collection. Some papers are excluded at this point, and others are added to round out the scope of the volume. In addition, a draft of each paper is peer-reviewed prior to final acceptance or rejection. This anonymous review process is supervised by the organizer(s) of the symposium, who become the editor(s) of the book. The authors then revise their papers according to the recommendations of both the reviewers and the editors, prepare camera-ready copy, and submit the final papers to the editors, who check that all necessary revisions have been made.

As a rule, only original research papers and original review papers are included in the volumes. Verbatim reproductions of previously published papers are not accepted.

M. Joan Comstock
Series Editor

Preface

THIS BOOK WAS DEVELOPED FROM SELECTED PAPERS presented at the "Symposium on Supercritical Fluids" held at the American Institute of Chemical Engineers Annual Meeting in Los Angeles, California, in November 1991. The book was designed to report on recent developments and to reflect the diversity and expanding scope of applications of supercritical fluids. The chapters in the first part of the book are devoted to phase behavior, thermodynamics, and transport properties. The second part reports on recent research on molecular interactions, modeling, and computer simulations. The third part covers more specific applications, including polymers, pharmaceuticals, coal and petroleum products, environmental remediation, and chromatography.

The first chapter of the book reports on the current state of supercritical fluid science and technology and in doing so provides an overview of the book itself. In contrast to earlier years when most of the attention was on single fluids, such as carbon dioxide, and on extractions as the primary mode of application, in recent years emphasis has been shifting to binary and multicomponent fluids and processes with greater complexity. As reflected by the chapters in this book, recent research is focused more on the generation and prediction of property values needed for design and on the understanding of the molecular interactions and the physical and chemical processes encountered in diverse applications.

We thank the authors for their contributions and the numerous reviewers for their valuable suggestions. We also thank M. A. Abraham, A. Akgerman, H. R. Cochran, J. L. Fulton, K. P. Johnston, M. A. Matthews, B. J. McCoy, M. Radosz, and A. S. Teja for cochairing the sessions at the symposium.

ERDOGAN KIRAN
University of Maine
Orono, ME 04469

JOAN F. BRENNECKE
University of Notre Dame
Notre Dame, IN 46556

July 10, 1992

Chapter 1

Current State of Supercritical Fluid Science and Technology

Erdogan Kiran¹ and Joan F. Brennecke²

¹Department of Chemical Engineering, University of Maine,
Orono, ME 04469

²Department of Chemical Engineering, University of Notre Dame,
Notre Dame, IN 46556

This chapter is an overview of the current state of the supercritical fluids science and technology. It gives the new directions in research and applications which involve both physical and chemical transformations. Among the new trends are the greater research and use of binary and multicomponent fluids to optimize and facilitate these transformations. Applications have expanded beyond extractions and separations to include reactions, polymer processing, pharmaceuticals, food processing and environmental remediation.

Interest in supercritical fluids and their applications is continuing with an expanding scope and sophistication. This monograph contains selected papers from the Symposium on Supercritical Fluids at the Annual AIChE meeting held in Los Angeles, California, in November 1991 and purposely reflects the diversity and expanding scope of supercritical fluids research. The basic philosophy of utilization is centered around the fact that the properties of supercritical fluids can be varied from gas-like to liquid-like values by simply adjusting the pressure. These fluids are therefore very attractive as tunable process solvents or reaction media.

Even though in earlier years most of the attention was on single processing fluids such as carbon dioxide and extractions as the primary mode of application, in recent years emphasis has been shifting to binary and multi-component fluids and processes with a greater degree of complexity which may include either physical or chemical transformations. As a result, recent research is focused more on the generation and prediction of fundamental property values needed for design, and understanding of the molecular interactions and physicochemical processes in such complex systems. In addition to a broadening of activities related to

0097-6156/93/0514-0001\$06.00/0
© 1993 American Chemical Society

applications involving physical transformations, a marked increase is noted in explorations related to chemical transformations. Among these, oxidation reactions in supercritical water for waste destruction has been most visible. Organic substances and oxygen are soluble in supercritical water which permits oxidation to occur in a single phase. Inorganic salts are only sparingly soluble in supercritical water and can be separated from the reaction medium. Currently, supercritical water oxidation is at an advanced stage of evaluation for treatment of industrial wastes, and NASA is considering the technology for implementation in long duration extraterrestrial human exploration missions. It is being considered as an advanced life support technology for processing of solid waste and reclamation of water in space stations.

The use of binary and multicomponent fluids is driven by a desire to either manipulate the critical temperature of the mixture, or to introduce polar or non-polar features to regulate interactions of the fluid with a specific compound. Binary mixtures of carbon dioxide with polar compounds such as alcohols and with non-polar compounds such as alkanes have therefore been of special interest. In binary mixtures, critical temperatures assume values between the critical temperatures of the components. The critical pressures, however, often take values higher than the critical pressures of the pure components. For example, addition of about 7 mole % ethanol to carbon dioxide results in a mixture with a critical temperature of about 52 °C, but a critical pressure of 97 bar, compared to 31.1 °C and 73.8 bar for carbon dioxide and 240.9 °C and 61.4 bar for ethanol. Such a mixture offers the desirable features of having polar character in the fluid at a much lower temperature than would be possible by using pure alcohols. Ability to adjust and lower the operational temperature becomes important for many applications involving thermally labile compounds such as biomaterials. Similar intermediate critical temperatures with a modest increase in the critical pressures are achieved also in binary mixtures of carbon dioxide with alkanes which would have desirable features of alkanes at lower operational temperatures.

The following overview is divided into four sections: (1) measurement and prediction of the phase behavior, (2) determination of transport properties, (3) understanding and using the local structure of fluid solutions, and (4) applications. The emphasis is on the use of supercritical fluid mixtures and their application for both physical and chemical processes.

Measurement and Prediction of Phase Behavior

Since there is a growing interest in the use of binary and multicomponent supercritical fluid mixtures to tailor separations, modify physical properties and influence reactions, there is a corresponding interest in the phase behavior of these mixtures. Experimentally determined critical data are however not available for all binary mixtures of interest, and the available data for some systems are limited only to a narrow concentration range. To fill this gap, there is continual research activity on the phase behavior and critical properties of binary mixtures. The first

two chapters of the present book indeed deal with binary mixtures of carbon dioxide with alcohols, and alkanes. To ensure operation in the supercritical region of binary solvent mixtures of defined compositions, knowledge of the gas-liquid critical point is essential. Such information, in addition to being of great value in designing binary process fluids, are equally important to operations in which carbon dioxide may be used to separate the other component from more complex mixtures. Carbon dioxide can, for example, be used to remove alcohols from aqueous solutions.

If pressure and temperature conditions are not above the critical temperature and pressure for the mixture, unlike pure fluids, binary fluid mixtures may display multiphase equilibrium behavior such as the liquid-liquid-vapor (llg) phase behavior. Multiphase equilibria of binary and ternary mixtures composed of both polar and non-polar species are important especially with respect to separability of solutes between the liquid phases. Two chapters in the book (Chapters 4 and 5) are concerned with multiphase equilibria encountered in mixtures of carbon dioxide with alcohols or hydrocarbons, and in mixtures of propane with triglycerides. The latter is of significance in processing of natural products such as edible oils. Another chapter (Chapter 7) discusses the four-phase, liquid-liquid-liquid-gas equilibrium observed for ternary mixtures of carbon dioxide, water, and 2-butoxyethanol at conditions near the critical point of carbon dioxide. These mixture are important for understanding process applications involving microemulsions.

Estimation of the solubility of a substance in supercritical fluids or in mixtures containing a component at supercritical conditions is key to the evaluation of many applications of supercritical fluids. Research on predictive procedures are continuing. For these predictions, the physical properties of the solvent and the solute and an equation of state are required. Simpler forms of equations of state such as the ideal gas, truncated virial equation of state, and the basic form of the cubic equation of state, the van der Waals equation, are not very effective in describing fluids at high pressures. Modified cubic equation of states such as the Redlich-Kwong or the Peng-Robinson equations of state which incorporate temperature dependent attractive terms are found to be more successful and are, therefore, used most frequently. These equations of state are used to describe not only single fluids but multicomponent fluid mixtures as well. For mixtures, the success of the equation depends on the use of proper mixing rules and assignment of interaction parameters. Interaction parameters are normally determined from experimental data. Recently, a group contribution method has been developed to allow estimation of the interaction parameter for some systems in the absence of experimental data (Chapter 6). Even with modified cubic equations, for systems containing polar components, predictions become poorer. One of the more recent approaches to model associating systems is the use of the SAFT (Statistical Associating Fluid Theory) equation of state. The use of various equations of state are illustrated in Chapter 2 for carbon dioxide-alcohol systems, and in Chapter 7 for carbon dioxide-water-surfactant mixtures, and in Chapter 6 for estimation of solubility of hydrocarbons and cholesterol in supercritical carbon

dioxide. Solubility of cholesterol is, of course, of significance in applications related to food industry.

Determination and Correlation of Transport Properties

Even though phase equilibria and solubility information is essential for effective use of supercritical fluids, for many applications such as extractions, reactions, or impregnation processes, information on transport properties such as diffusivity, viscosity, and thermal conductivity become equally important. These questions are particularly important for processing of materials such as coal, biomass, or polymers. A well known advantage of supercritical fluids compared to ordinary liquid solvents is that diffusion coefficients in supercritical fluids are higher than in liquid, leading to more favorable mass transfer rates. The available data is, however, very limited even for self diffusion coefficients. Nonetheless, recent research is expanding the data base for binary diffusion coefficients and exploring the influence on solute diffusivities the addition of a second component to the process fluid. Chapter 8 provides an account of the limitations of the existing methods such as the hydrodynamic Wilke-Chang correlation, Batchinski-Hildebrand free-volume theories, or the dense gas Enskog relationships based on the hard-sphere theory and its modifications. Data are reported for the diffusivity of selected organic compounds (benzoic acid, phenanthrene and acridine) in carbon dioxide and in carbon dioxide/ methanol and carbon dioxide/acetone mixed solvents. The results show that both the increased local density of the solvent around the solute in the pure solvent case and the preferential attraction of the cosolvent (acetone or methanol) around the solute in the mixed solvent systems significantly influence the diffusion of the solute. These transport measurements corroborate some of the investigations of local intermolecular interactions discussed in the next section.

At present understanding and modeling of the diffusivity in mixed solvents is severely limited by the lack of available volumetric and viscosity data on mixed solvents. Experimental data on the viscosity of supercritical fluids and solutions are needed however, not only for modeling diffusivities and prediction of mass transfer rates, but also for (1) modeling and prediction of viscosities themselves, (2) proper design of process equipment such as pumps, mixers, and heat exchangers, and (3) for establishment of improved processing conditions. Polymer solutions constitute an important case and data is needed over a wide range of concentrations since supercritical fluids can be used in fairly diverse polymer applications-- dissolution and fractionation at one end, and lowering the viscosity of polymer melts for easier processing at the other.

Recent work on the viscosity of normal alkanes and polymer solutions has shown that density is an excellent scaling factor and viscosities can be described as an exponential function of density. The exponential dependence on density points to greater applicability of the Doolittle type free volume theories in describing viscosity at high pressures. Chapter 9 provides an account of various methods of

correlation of viscosity and presents data for solutions of polystyrene in supercritical n-butane. Investigation of pressure or density dependence of viscosity of polymer solutions can provide information on the change of "goodness" of the solvent and solvent/polymer interactions. The concept of Theta Pressure or Theta Density as opposed to conventional Theta Temperature introduced in that chapter has significant theoretical and practical implications for polymer solutions.

Investigation and Modeling of Molecular Interactions and Local Fluid Structure

A considerable amount of recent research is directed to develop an improved understanding of local fluid structure and the molecular interactions between solutes and other components in supercritical fluid mixtures. Theoretical studies based on molecular dynamic simulations, Monte Carlo calculations, and integral equation theories, as well as experimental studies using absorbance and fluorescence spectroscopy point to local density enhancement of the solvent around the solute in near critical fluids. Energetic and entropic contributions to this enhancement are discussed in Chapter 11. Description of local fluid structure in fluid mixtures containing a co-solvent, and systems involving polar solutes has been of particular interest. This is because with addition of cosolvents, solute interactions with the solvent mixture can be varied dramatically. Two main questions arise regarding cosolvent addition to supercritical fluids: (1) what is the nature and the mechanism of the increased solubility of solutes, and (2) how does pressure, and temperature and the nature of the supercritical solvent influence chemical association, especially of common co-solvents that can self-associate through hydrogen bonding? Chapter 12 shows that much of the solute solubility enhancement is due simply to the increase in local and bulk density when the cosolvent is added. In addition, fluorescent probes which are sensitive to the local solvent environment are being used to study the nature of solvent and co-solvent interactions. The reactions of the probe 7-azaindole in methanol/carbon dioxide fluid mixtures reveal that the structure of the hydrogen bonding environment between the solute and the cosolvent is significantly weaker than what one observes in liquids (Chapter 17). This is also true for the self-association of alcohols in supercritical carbon dioxide and ethane, which is significantly less than in liquid organic solutions. However, the results based on molecular dynamic simulations and infrared spectroscopy demonstrate that the cluster sizes in a supercritical fluid depend on the nature of the solvent and there is a distribution of cluster sizes (Chapters 13 and 14). For example, at similar operational conditions, methanol-methanol aggregation is found to be greater in ethane than in carbon dioxide whereas solvent-methanol aggregation is observed to be greater in carbon dioxide than in ethane. These observations are of significance in understanding the function of alcohols as modifiers in enhancing solubility of polar solutes in non-polar supercritical fluids.

Generally, the solubility enhancement when a cosolvent is added to a supercritical fluid is determined by tedious solubility measurements. Chapter 18 in this book presents a fast way, using supercritical fluid chromatography, that requires very small amounts of modifier to determine the cosolvent effect, thus yielding information on the strength of solute/cosolvent interactions.

Some of the same methods, i.e., integral equation theory calculations, used to describe the interaction between species in supercritical fluid mixtures can be used to analyze the structure of these mixtures in the vicinity of a solid surface (Chapter 15). These studies are aimed at providing an understanding of adsorption-desorption equilibria between a solid surface and a fluid media. Such analyses are important for many processes involving adsorption from a supercritical fluids solution or desorption into a supercritical fluid solution. Examples include regeneration of sorbents with supercritical fluids, supercritical fluid chromatography and supercritical fluid extraction of contaminated solids.

The fact that the local densities and local compositions around solutes or solid surfaces in supercritical fluids are different than in bulk have consequences not only for solubility, or adsorption-desorption processes, but also for reactions in supercritical fluids. Information on molecular interactions and solvent effects on reactions is of great significance. A review chapter in the book (Chapter 16) provides an overview of a broad range of spectroscopic investigations of reactions in supercritical fluids. While the solvent can act in a variety of manners to affect reaction rates including (1) increased reactant solubilities and reduced mass transfer resistances, (2) facilitated separation of products from the reaction medium, (3) catalyst life extension through minimization of fouling and deactivation, (4) pressure effect on the rate constant, (5) changes in selectivities, and (6) increased diffusion rates, there is growing realization of the importance of the effect of local densities and local compositions. Understanding the local molecular phenomena may be the key to future developments for better description of reaction rates in supercritical fluids.

Applications

As already stated, the application areas of supercritical fluids are expanding very rapidly. A number of chapters in the book have been devoted to specific application areas. These are related to pharmaceuticals, polymers, chromatography, extractions, coal and petroleum processing, and environmental remediation. They involve both physical and chemical transformations and the use of multicomponent supercritical fluid mixtures.

An interesting example of pharmaceutical applications is the use of supercritical fluids in production of controlled release drugs. Chapter 19 describes co-dissolution of a biocompatible polymer such as poly(D,L-lactic acid) and a pharmaceutical compound (such as lovastatin) in supercritical carbon dioxide followed by rapid expansion to form polymer-drug microspheres of controllable

size. Carbon dioxide, being non-toxic and a gas at normal temperatures and pressures, is ideal for such applications.

Use of supercritical fluids in polymer processing encompasses a wide range of applications from polymerization to fractionation, or impregnations and morphological modifications. Chapter 21 describes use of supercritical fluids in forming microcellular foams (polymer aerogels) which display small pore sizes and low densities. Formation of microporous structures from polymerization of methacrylate based co-monomers in supercritical Freon-22 is described. In this particular application, using supercritical fluids as the polymerization medium helps form the polymer network which can then be supercritically dried in the same vessel without the need to exchange the solvent.

Perhaps one of the most successful application areas of supercritical fluids is Supercritical Fluid Chromatography. It has become a widely used analytical technique for separation and analysis. As already indicated above, the technique is also used to generate fundamental information on molecular interactions and thermodynamics of solvent-solute interactions. It is used alone or coupled with supercritical fluid extraction or with post characterization techniques such as IR or MS. Various modes of operation include pressure, temperature, or density programming, or solvent gradient methods in which a second component is added to the eluent fluid. Proper selection of the pressure, temperature, density or solvent gradients with time are important for improved separations and optimization. Chapter 22 describes the recent methodology of optimization.

Extractions and reactions using supercritical fluids still constitute the major mode of operation in many application areas. Extractions are carried out either to isolate a desired compound of higher value, or remove undesirable components from a raw material to obtain a product with improved properties. Extraction of caffeine from coffee is a well known example. Removal of impurities from polymers, cleaning of electronic parts, binder removal from ceramics, separation of buckminsterfullerenes, and environmental remediation are among more specific applications. Chapter 28 describes an interesting application in which isotropic petroleum pitch, a waste material produced from crude oil refining, has been extracted with supercritical toluene to produce a valuable product, mesophase pitch, which can be used to make high performance carbon-fibers. Chapter 30 illustrates a different use for supercritical toluene. It has been used as a reaction medium to carry out cracking of cis-polyisoprene while suppressing the formation of polycondensates. Such reactions have significance in disposing of used tires, a major source of solid waste. Supercritical toluene has in the past been used to conduct cracking reactions of coal for liquefaction. With respect to coal extraction, recent research is exploring effectiveness of polar solvents. Chapter 29 describes the kinetics of extraction of coal with t-butanol. Supercritical water is being evaluated for removal of N, S, and O containing organic compounds from coal to produce cleaner burning fuels (Chapter 26).

At present, an application area of much activity is the environmental remediation and removal of toxic contaminants from soils and industrial waste using supercritical fluids. These also involve either extractions or reactions.

Several specific applications are covered in the book. Chapter 23 is related to extraction of organics from contaminated soils with near-critical carbon dioxide. Model studies have been conducted using soil, activated carbon and alumina loaded with known amounts of naphthalene or phenol. Slurrying the soil with water is introduced to facilitate the handling and processing of solids at high pressures. Presence of water affects system dynamics and the solutes are distributed in three phases, i.e., carbon dioxide, water and the solid. How the differences in solid-solute and solvent-solute interactions affect the extractability of the organic solutes into the critical fluid phase are discussed in terms of the different behaviors displayed by phenol and naphthalene.

For total treatment of wastewaters and sludges, reactive remediation using supercritical water oxidation is rapidly expanding. Complete miscibility of oxygen and organic compounds in supercritical water creates a single-fluid phase and favorable reaction environments. In supercritical water greater than 99.99% destruction of many of the EPA priority pollutants are achievable with short residence times. However, salts which are soluble in subcritical water become insoluble at supercritical conditions. Therefore, one of the current practical issues related to implementation of the technology is the removal of solids from the process. Chapter 24 discusses the kinetics of oxidation of organic compounds in supercritical water, and Chapter 28 reports on model studies on the engineering aspects of removal of sodium chloride, sodium sulfate, sodium nitrate from supercritical oxidation process streams. Reactions of some model compound in supercritical water are discussed in Chapter 26.

This review is by no means inclusive of all the developments and applications related to supercritical fluids. Those that have been covered are the ones that were discussed during the AIChE symposium in Los Angeles, in November 1991. The breadth and the growth in the field can be further appreciated through examination of some of the recent monographs and conference proceedings. The most recent ones are

(1) *Supercritical Fluid Technology. Theoretical and Applied Approaches in Analytical Chemistry*; Bright, F.V.; McNally, M. E. P., Eds; ACS Symposium Series 488, American Chemical Society: Washington, DC; 1992.

(2) *Supercritical Fluid Technology. Reviews in Modern Theory and Applications*; Bruno, T.J.; Ely, J. F., Eds.; CRC Press: Boston, MA; 1991.

(3) *Abstracts of the 4th International Symposium on Supercritical Fluid Chromatography and Extraction*, Cincinnati, Ohio, May 20-22, 1992.

(4) *Proceedings of the 2nd International Symposium on Supercritical Fluids*, Boston, Massachusetts, 20-22 May, 1991.

The Journal of Supercritical Fluids routinely provides accounts of the most recent research.

RECEIVED July 23, 1992

Chapter 2

High-Pressure Vapor–Liquid Equilibria in Carbon Dioxide and 1-Alkanol Mixtures

David W. Jennings, Michael T. Gude, and Aryn S. Teja¹

School of Chemical Engineering, Georgia Institute of Technology,
Atlanta, GA 30332–0100

CO₂ + 1-alkanol systems are of interest as solvent/co-solvent pairs in the supercritical extraction of biomaterials, in alkanol dehydration processes, in the processing of syngas, and in supercritical drying. In spite of these interests, however, only the CO₂ + methanol and CO₂ + ethanol systems have received much attention in the literature. Moreover, there appears to be some disagreement between the different sets of published data even for these systems. In order to compile a reliable set of data for modelling processes which involve CO₂ + 1-alkanol mixtures, we have measured vapor - liquid equilibria in CO₂ + ethanol, CO₂ + 1-butanol, and CO₂ + 1-pentanol mixtures at temperatures ranging from 314 to 337 K and pressures from 4.63 to 11.98 MPa. In this paper, we compare our data with data reported in the literature, and note trends as the 1-alkanol increases in size. The correlation of the data with a simple equation of state and an equation of state based on Statistical Associating Fluid Theory is also discussed.

High pressure vapor - liquid equilibria in CO₂ + 1-alkanol systems are of interest in a number of applications. These applications include the extraction of biomaterials with supercritical CO₂ + 1-alkanol mixtures, the separation of 1-alkanols from aqueous solutions using supercritical carbon dioxide [1-8], the production of alkanols from syngas [9-11], and the supercritical drying of aerogels [12]. Thermodynamic modelling of these processes requires a knowledge of binary vapor - liquid equilibria (VLE). In spite of this need, however, only the CO₂ + methanol and CO₂ + ethanol systems have received much attention in the literature. This is evident from the summary of vapor - liquid equilibrium measurements given in Tables I and II. Critical properties of CO₂ + methanol mixtures have been measured by Brunner [13]; those of CO₂ + ethanol mixtures have been measured

¹Corresponding author

0097-6156/93/0514-0010\$07.00/0
© 1993 American Chemical Society

Table I: Vapor - Liquid Equilibrium Measurements in CO₂ + 1-Alkanol Systems

System	Temperature Range (K)	Pressure Range (MPa)	Reference
CO ₂ /Methanol	288.15-333.15	1.6-4.3	Hemmaplardh and King, Jr. [16] ¹
	298.15	0.22-6.13	Katayama <i>et al.</i> [17]
	298.15-313.15	0.58-8.06	Ohgaki and Katayama [18]
	213.15-273.15	0.01-1.69	Schneider [19]
	323.15-398.15	0.5-18.50	Semenova <i>et al.</i> [20]
	263.15-273.15	1.72-1.78	Lazalde-Crabtree <i>et al.</i> [21] ¹
	298.15-473.15	0.41-15.06	Brunner <i>et al.</i> [22] ²
	230.0-330.0	0.69-10.65	Hong and Kobayashi [23]
	313.4	0.68-7.71	Suzuki <i>et al.</i> [9]
CO ₂ /Ethanol	298.15-348.15		Gupta <i>et al.</i> [24] ¹
	304.2-308.2	3.75-7.67	Takishima <i>et al.</i> [4]
	307.85-337.85	1.25-10.95	Panagiotopoulos [25]
	304.6-323.1	2.22-9.17	Yao <i>et al.</i> [26]
	304.2-323.4	3.31-7.96	Feng <i>et al.</i> [5]
	313.46-333.27	0.53-10.63	Nagahama <i>et al.</i> [6]
	313.4-333.4	0.51-10.65	Suzuki <i>et al.</i> [9]
	314.2-337.2	5.55-10.85	Jennings <i>et al.</i> [27]
CO ₂ /1-Propanol	305.6-313.1	2.10-8.04	Yao <i>et al.</i> [26]
	313.4-333.4	0.52-10.82	Suzuki <i>et al.</i> [9]
CO ₂ /1-Butanol	298.15		Massoudi and King, Jr. [28] ¹
	313.15-383.15	2.02-16.45	King <i>et al.</i> [29]
	314.6-337.4	4.63-11.78	Jennings <i>et al.</i> [27]
	313.15	≈0.2-8.2	Winkler and Stephan [30] ³
CO ₂ /1-Pentanol	314.3-337.5	5.18-11.98	Jennings <i>et al.</i> [31]
CO ₂ /1-Hexanol	323.4-401.8	9.10-19.50	Nickel and Schneider [32] ⁴
CO ₂ /1-Decanol	343.3-402.0	13.0-24.80	Nickel and Schneider [32] ⁴
CO ₂ /1-Dodecanol			Katzenski-Ohling [33] ⁴
CO ₂ /1-Hexadecanol			Hölscher [34] ⁴
CO ₂ /1-Octadecanol	323.4-402.0	10.0-53.20	Friedrich and Schneider [35] ⁴
1 = Vapor Phase Only 2 = Bubble/Dew Point Measurements 3 = Graphical Results Only 4 = Phase Compositions Reported in Concentrations. No Phase Densities Given			

Table II: Measurements of Carbon Dioxide Solubility in 1-Alkanols

System	Temperature Range (K)	Pressure Range (MPa)	Reference
CO ₂ /Methanol	291.15-307.15	≈0.1	Kunrath [36]
	298.15-348.15	5.1-8.6	Krichevsky and Koroleva [37]
	273.15-348.15	0.69-6.97	Krichevsky and Lebedewa [38]
	223.15-348.15	0.1-3.04	Bezedel and Teodorovich [39]
	194.45-273.15	0.01-0.10	Shenderei <i>et al.</i> [40]
	213.15-247.15	0.1-1.62	Shenderei <i>et al.</i> [41]
	228.15-247.15		Shenderei <i>et al.</i> [42]
	223.65-328.15	≈0.1	Otsuka and Takada [43]
	243.15-273.15	0.20-3.33	Yorizane <i>et al.</i> [44]
	283.15-313.15	0.10	Tokunaga <i>et al.</i> [45]
	258.0	0.51-1.65	Ferrell and Rousseau [46]
	298.15	0.10	Won <i>et al.</i> [47]
	247.15	≈1.0-1.5	Takeuchi <i>et al.</i> [48] ¹
	248.15-273.15	to 3.5	Zeck and Knapp [49]
	233.15-298.15	0.30-5.08	Weber <i>et al.</i> [50]
243.2-298.1	0.19-5.45	Chang and Rousseau [51]	
CO ₂ /Ethanol	293.15-373.15	3.04-14.19	Sander [52]
	291.15-307.15	≈0.1	Kunrath [36]
	212.65-247.95	0.10-0.10	Shenderei <i>et al.</i> [40]
CO ₂ /1-Propanol	293.15-373.15	2.03-12.16	Sander [52]
	283.15-313.15	≈0.1	Tokunaga [53]
	212.65-247.95	0.10-0.10	Shenderei <i>et al.</i> [40]
CO ₂ /1-Butanol	212.65-247.95	0.10-0.10	Shenderei <i>et al.</i> [40]
CO ₂ /1-Octanol	282.66-313.64	≈0.1	Wilcock <i>et al.</i> [54]
CO ₂ /1-Decanol	284.01-313.49	≈0.1	Wilcock <i>et al.</i> [54]
1 = Graphical Results Only			

by Baker and Anderson [14]; and Gurdial *et al.* [15] have measured critical pressures and temperatures in CO₂ + methanol through 1-hexanol mixtures.

The present study was undertaken as part of a continuing effort on the measurement and correlation of phase equilibria in CO₂ + 1-alkanol systems in our laboratory. A flow apparatus was constructed for the measurement of high pressure vapor - liquid equilibria in binary and multicomponent systems of interest. Vapor - liquid equilibria for the CO₂ + ethanol, CO₂ + 1-butanol, and CO₂ + 1-pentanol systems were measured at temperatures ranging from 314 to 337 K and pressures from 4.63 MPa to 11.98 MPa. In this paper, we summarize our experimental results, compare these with data reported in the literature, and examine trends exhibited by CO₂ + 1-alkanol systems. In addition, we compare the ability of a simple cubic equation of state as well as an equation of state based on Statistical Associating Fluid Theory to correlate the data.

Experimental

A schematic diagram of the apparatus used in our studies is shown in Figure 1. Since the apparatus and experimental procedure have been described in detail previously [27,55], only a brief outline is given here. Carbon dioxide from a cylinder and 1-alkanol from a liquid reservoir were pumped through a series of coils and static mixers placed inside a constant temperature air bath. Vapor - liquid equilibrium was attained during the pumping process. After equilibration, the phases were separated in a high pressure view cell and each phase was depressurized across a micrometering valve. The 1-alkanol from each phase was condensed and collected in a cold trap, while the carbon dioxide was allowed to pass through a wet test meter. Equilibrium phase compositions were calculated from the weight of 1-alkanol collected and the measured volume of carbon dioxide from the wet test meters. Small corrections were made for the residual 1-alkanol not condensed and for the carbon dioxide dissolved in the condensed 1-alkanol. Typically, 4 - 6 liquid samples and 3 - 5 vapor samples were collected at one pressure and temperature. The reported compositions represent an average of all the samples equilibrated at the desired conditions. To verify that equilibrium conditions had been attained during the pumping process, some experiments at a given temperature and pressure were repeated at different flowrates.

Additionally, in order to verify the validity of the measurements from our apparatus, vapor - liquid equilibria in CO₂ + water and CO₂ + ethanol systems were measured and compared with literature data. The results of the CO₂ + water measurements are shown in Figures 2 and 3 for the liquid and vapor phases, respectively. The data of Weibe [56] (verified by several investigators) and Briones *et al.* [57] are included for comparison. Although the temperatures are not exactly the same, good agreement between the data sets was obtained for both the liquid and vapor phases. Comparisons of the measurements on the CO₂ + ethanol system with those of other investigators are discussed below.

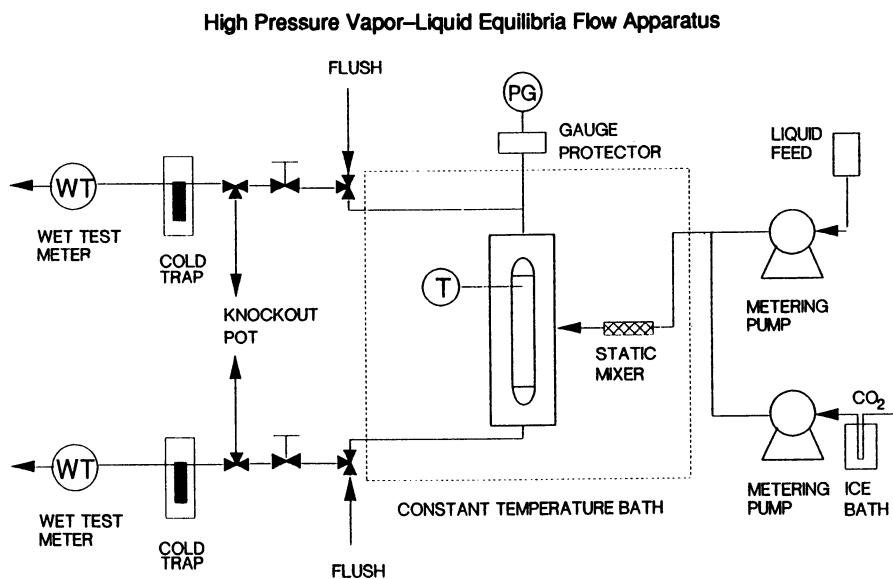


Figure 1. Schematic diagram of experimental apparatus.

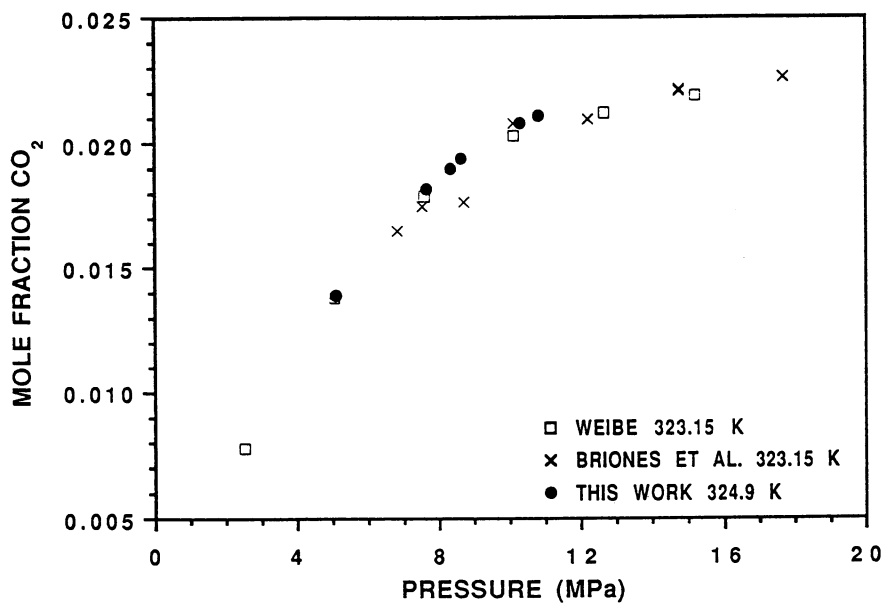


Figure 2. CO₂ + water liquid phase measurements.

Results and Discussion

CO₂ + Methanol System. As is evident from Tables I and II, the largest number of investigations have been of the CO₂ + methanol system. However, many of these measurements do not report coexisting phase compositions, but only the composition of one phase. The measurements have been reviewed by Weber *et al.* [50] and by Brunner *et al.* [22]. Brunner *et al.* have also commented on the quality of various data sets. Chang and Rousseau [51] showed comparisons between their solubility measurements and those of six different groups of investigators. Subsequently, measurements by Hong and Kobayashi [23] filled some of the gaps noted by these comparisons.

CO₂ + Ethanol System. Vapor - liquid equilibrium data for CO₂ + ethanol mixtures were measured in our apparatus at 314.5 K, 325.2 K, and 337.2 K [27]. The data at 314.5 K are compared with measurements by Suzuki *et al.* [9] (313.4 K), Yao *et al.* [26] (313.1 K), Feng *et al.* [5] (313.2 K), and Nagahama *et al.* [6] (313.5 K) in Figure 4. The data at 325.2 K are compared with the measurements of Panagiotopoulos (323.2 K) [25], Yao *et al.* (323.1 K), and Feng *et al.* (323.4) in Figure 5. The critical pressures and compositions reported for the CO₂ + ethanol system by Gurdial *et al.* [15] (obtained by interpolation of their data at various temperatures) are included in Figures 4 and 5. The vapor - liquid equilibrium data at 337.2 K are compared with the measurements of Panagiotopoulos at 337.8 K in Figure 6. Note that although the temperatures are not identical in these comparisons, the isotherms show good agreement with the data of Suzuki *et al.* and Panagiotopoulos. The data by Yao *et al.* are not in agreement with measurements of this study or with the data of any other investigator. Their data also exhibit a significant amount of scatter and therefore must be considered suspect. The data of Feng *et al.* at pressures below 6 MPa show fair agreement with the liquid phase compositions of Suzuki *et al.*, Panagiotopoulos, and of this work. However, the liquid phase compositions at higher pressures show incorrect behavior. Also, even with the scale of Figures 4 and 5, the vapor phase compositions of Feng *et al.* can be seen to be lower in ethanol composition than the data of any other investigator. On the other hand, the data of Nagahama *et al.* are seen to be slightly high in carbon dioxide compositions for the liquid phase. The critical points of Gurdial *et al.* are higher in pressure than is indicated by the vapor - liquid phase equilibrium data of any of the investigators. More discussion on the critical behavior of the CO₂ + 1-alkanol systems is given in a following section.

CO₂ + 1-Propanol System. The only reported vapor - liquid equilibrium measurements for the CO₂ + 1-propanol system are those by Suzuki *et al.* [9] and Yao *et al.* [26]. Results at 313 K are shown in Figure 7 along with the critical point measurement of Gurdial *et al.* [15]. The data of Yao *et al.* for the CO₂ + 1-propanol system do not exhibit the same amount of scatter as do their CO₂ + ethanol measurements. However, their liquid phase data show higher carbon

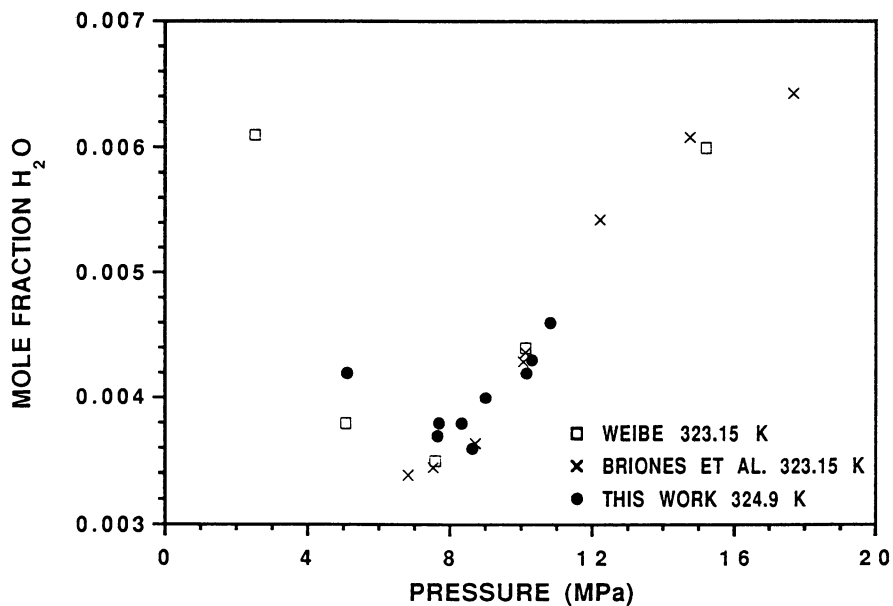


Figure 3. CO_2 + water vapor phase measurements.

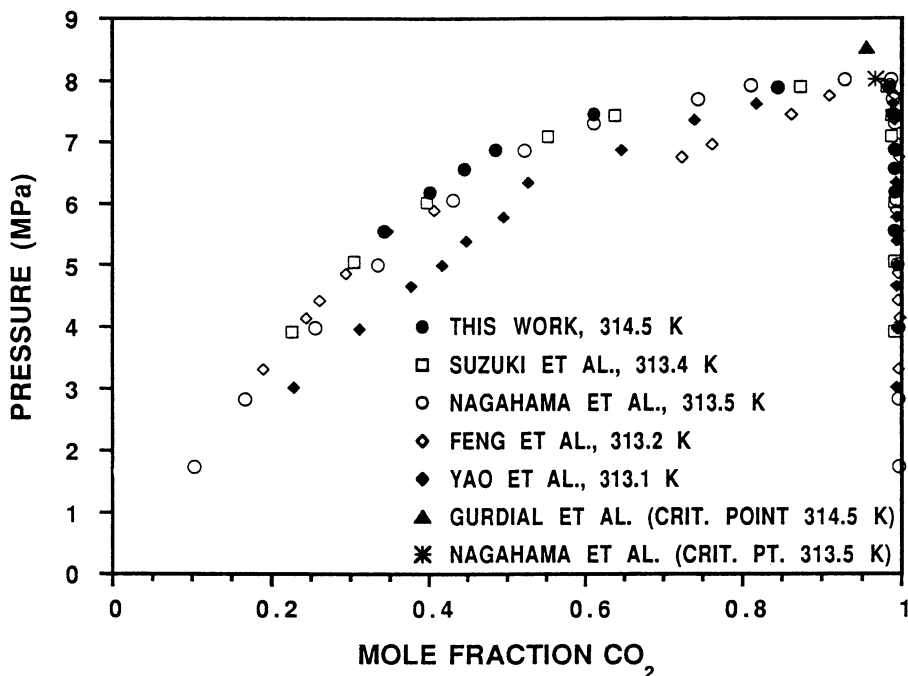


Figure 4. CO_2 + ethanol vapor-liquid equilibria at 314.5 K.

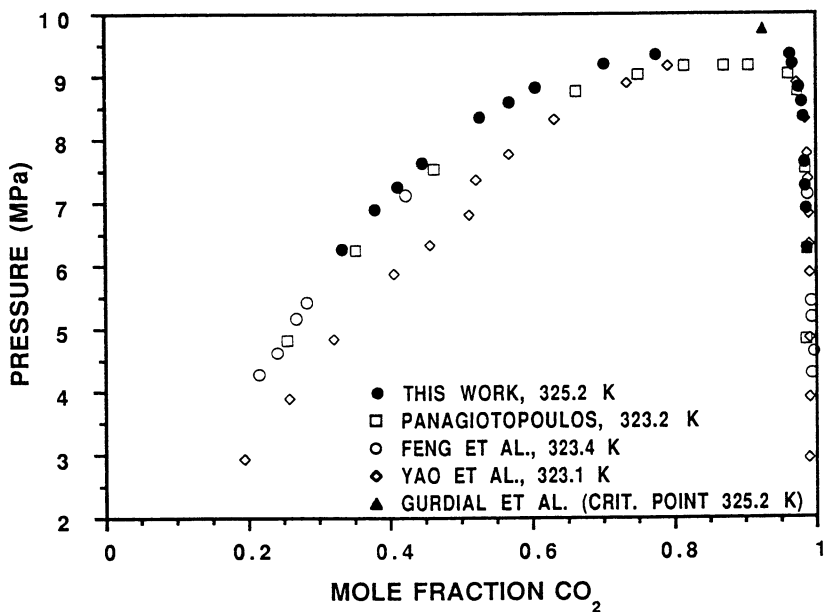


Figure 5. CO₂ + ethanol vapor-liquid equilibria at 325.2 K.

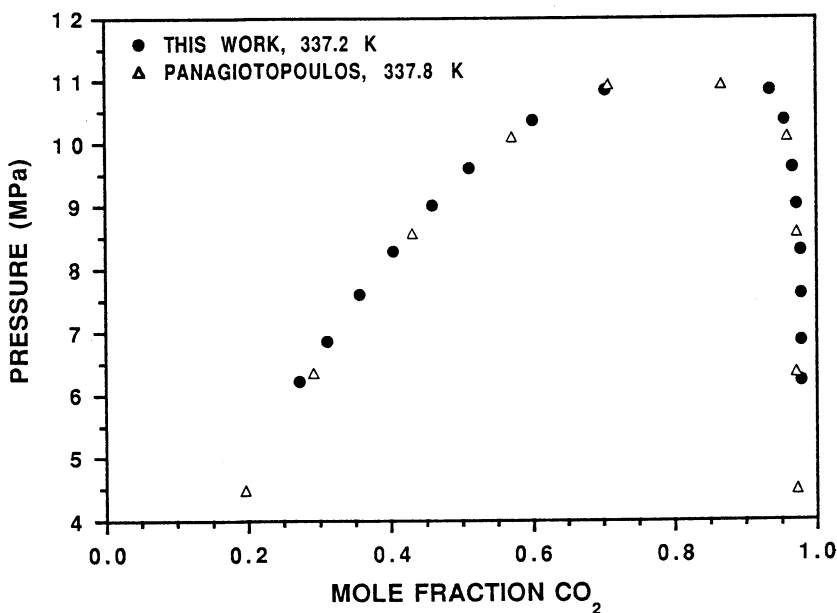


Figure 6. CO₂ + ethanol vapor-liquid equilibria at 337.2 K.

dioxide compositions than the data of Suzuki *et al.*. It will be shown below that the liquid phase data of Suzuki *et al.* are higher in carbon dioxide composition than is justified by measurements of CO₂ + ethanol, CO₂ + 1-butanol, and CO₂ + 1-pentanol mixtures. The critical point of Gurdial *et al.* appears to be in agreement with the measurements presented in Figure 7.

CO₂ + 1-Butanol System. Vapor - liquid equilibrium data in CO₂ + 1-butanol mixtures were measured in our apparatus at 314.8 K, 325.3 K, and 337.2 K [27]. The measurements at 314.8 K are compared with those of King *et al.* at 313.15 K [29] and with the liquid phase data of Winkler and Stephan at 313.15 [30] in Figure 8. The critical point of Gurdial *et al.* [15] is also included in Figure 8. The data of Winkler and Stephan were obtained by digitizing the graphical results presented in their paper. However, due to the small 1-butanol compositions in the vapor phase and the scale of the graph of Winkler and Stephan, the vapor phase compositions could not be determined by digitization. As is obvious, the results obtained by us are in considerable disagreement with the data of King *et al.* even after allowance is made for the temperature differences in the two sets of measurements. However, there is good agreement with the liquid phase measurements of Winkler and Stephan. We have noted elsewhere [27] that measurements by King *et al.* [58] for the system CO₂ + n-hexadecane at 333.15 K also showed higher carbon dioxide compositions in the liquid phase than measurements of Charoensombut-amon *et al.* [59] and D'Souza *et al.* [60] at the same temperature. Additionally, the measurements of King *et al.* were made in a blind cell and, because of the odd shape of the isotherm in the critical region, King *et al.* hypothesized that the data points at the highest two pressures were indicative of two liquid phases. No liquid - liquid equilibria were observed in this work or in the work of Winkler and Stephan. This is further supported by the recent work of Lam *et al.* [61], who report that the liquid - liquid - vapor locus in the CO₂ + 1-butanol system terminates at an upper critical end point of 22.99 bar and 259.25 K. Liquid - liquid phase separation is therefore unlikely at the conditions studied by King *et al.* and their measurements must be considered erroneous. As with the CO₂ + ethanol systems, the critical point of Gurdial *et al.* again appears to be too high in pressure.

CO₂ + 1-Pentanol System. Vapor - liquid equilibrium data were measured in our apparatus for CO₂ + 1-pentanol mixtures at 314.6, 325.9, and 337.4 K [31]. No other literature data are available for this system. The data at 314.6 K are shown in Figure 9 along with the critical point measured by Gurdial *et al.* [15]. The phase behavior is similar to that exhibited by other CO₂ + 1-alkanol systems discussed above and the critical point of Gurdial *et al.* appears to be slightly higher than is justified by the vapor - liquid equilibrium measurements.

CO₂ + Higher 1-Alkanol Systems. Vapor - liquid equilibria for CO₂ + higher 1-alkanol systems has been measured by Schneider and coworkers for the mixtures CO₂ + 1-hexanol [32], CO₂ + 1-decanol [32], CO₂ + 1-dodecanol [33],

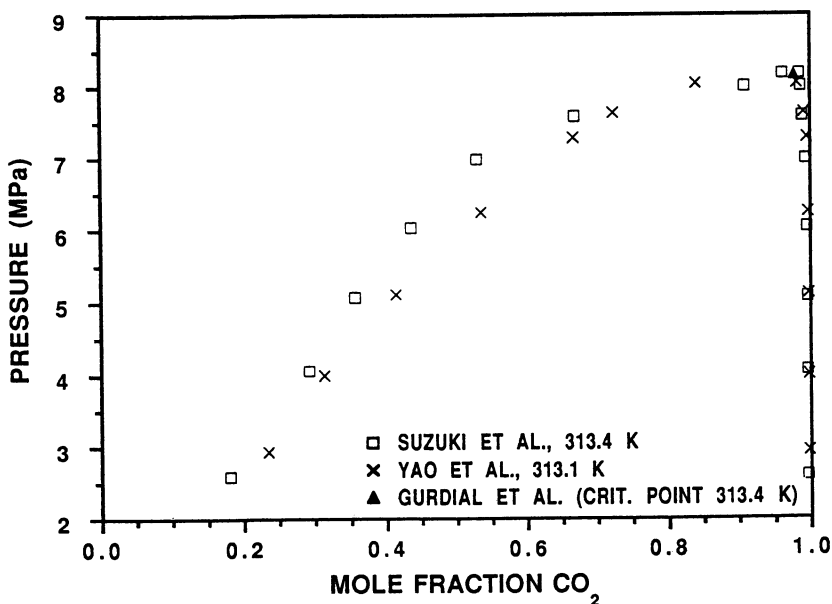


Figure 7. CO₂ + 1-propanol vapor-liquid equilibria at ≈313 K.

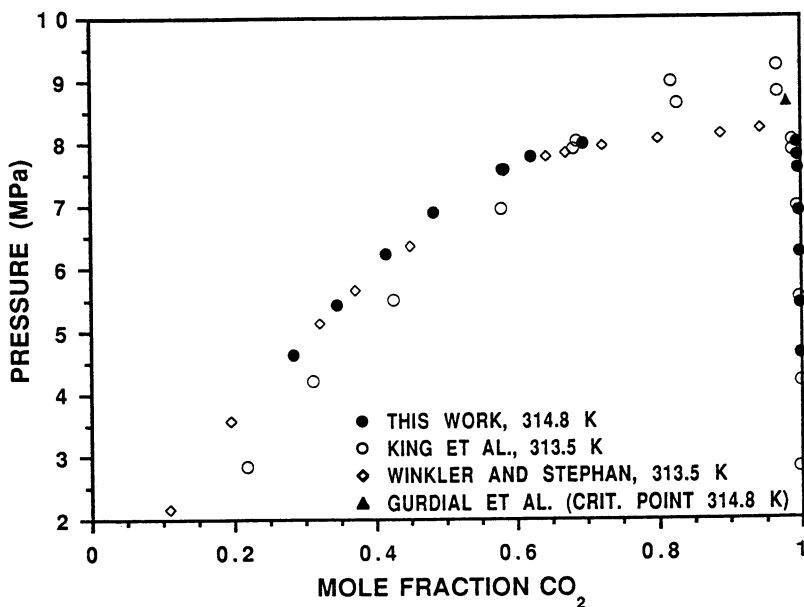


Figure 8. CO₂ + 1-butanol vapor-liquid equilibria at 314.8 K.

CO₂ + 1-hexadecanol [34], and CO₂ + 1-octadecanol [35] using a near-infrared spectroscopic technique. However, the phase compositions are reported in units of (g/cm³) and no phase densities are reported. Solubilities of carbon dioxide in 1-octanol and 1-decanol at atmospheric pressure have also been reported by Wilcock *et al.* [54].

Discussion of CO₂ + 1-Alkanol Systems. In order to check the consistency of the data sets, the CO₂ + 1-alkanol measurements were plotted together. The data of some of the other investigators were also included for comparison. The liquid phase compositions at about 314 K are presented in Figure 10. The data obtained in this study show regular trends with the size of the 1-alkanol (also seen in the estimated critical pressures and phase compositions). The critical pressures of the mixtures show a consistent increase as the size of the 1-alkanol increases from ethanol to 1-pentanol. The liquid phase compositions show a consistent crossover behavior. At the lower pressures, the systems with the larger 1-alkanol also contain higher amounts of carbon dioxide. However, as the systems approach their respective critical regions, a crossover occurs. When the data of the other investigators are examined, it can be seen that there are inconsistencies in some of their measurements. It was previously shown that good agreement was obtained with the CO₂ + ethanol measurements of Suzuki *et al.*. This is seen again in Figure 10, which also shows that the CO₂ + 1-propanol measurements of Suzuki *et al.* are in disagreement with the trends exhibited by the CO₂ + 1-alkanol systems in this study. The inconsistency in the trends exhibited by the CO₂ + 1-propanol data of Suzuki *et al.* is surprising, since good agreement was obtained with their CO₂ + ethanol measurements. The liquid composition measurements of CO₂ + 1-alkanol systems near 337 K are shown in Figure 11. The data of Suzuki *et al.* at 333.4 K are also included. Again, the data of this study show the same regular trends as noted previously at 314 K. Due to the temperature differences in the various data sets, it is not possible to directly compare the results of this study with the data of Suzuki *et al.*. However, the CO₂ + ethanol and CO₂ + 1-propanol data of Suzuki *et al.* at 333.4 K appear to exhibit slightly different behavior from that at 313.4 K (different crossover behavior and less difference in phase compositions at lower pressures). This would indicate that the CO₂ + 1-propanol data may be suspect. As shown earlier, fairly good agreement is obtained between the CO₂ + ethanol measurements of Panagiotopoulos and those of this study.

The vapor phase compositions for the measurements of CO₂ + 1-alkanol systems near 314 K are shown in Figure 12. With the exception of the data of King *et al.*, the measurements in general appear to exhibit expected trends. The same is true for the vapor phase compositions of CO₂ + 1-alkanol systems near 337 K (Figure 13), although on this expanded scale slight differences can be seen between the CO₂ + ethanol measurements of Panagiotopoulos and those of this study.

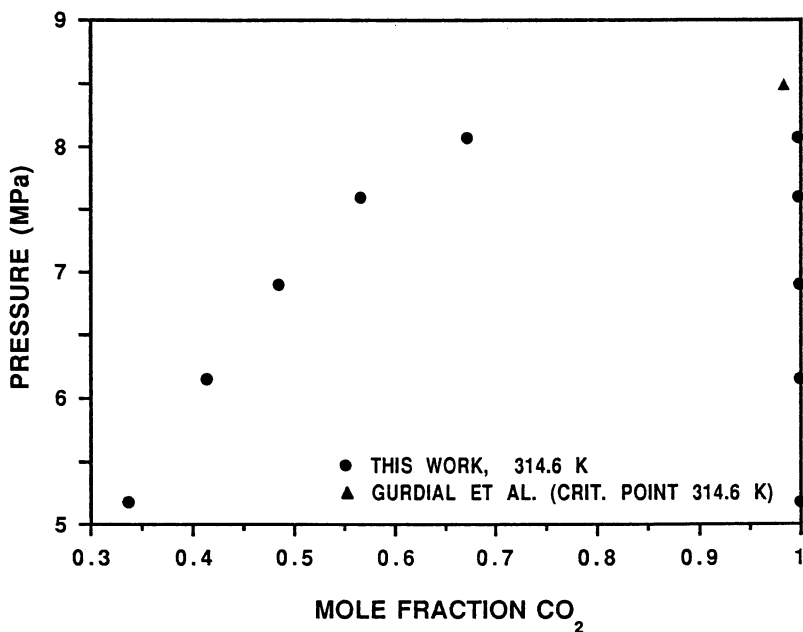


Figure 9. CO₂ + 1-pentanol vapor-liquid equilibria at 314.6 K.

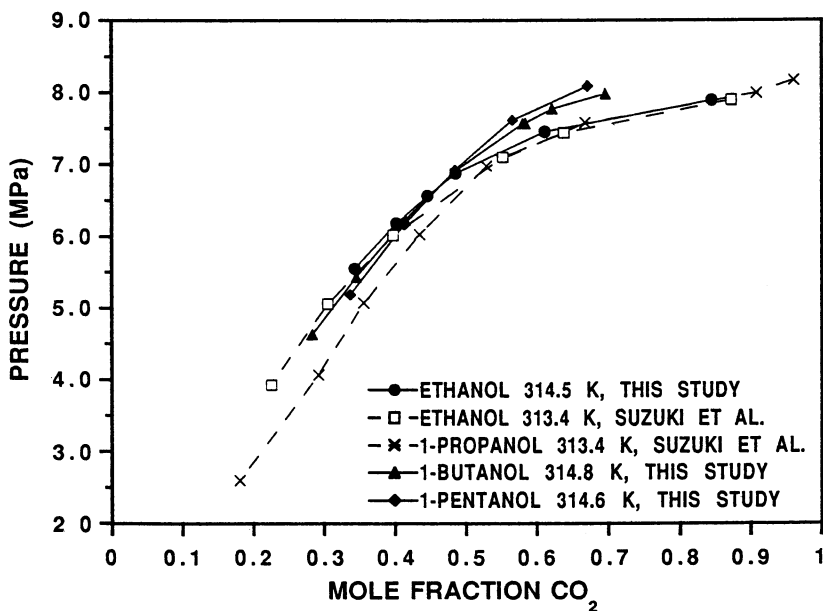


Figure 10. CO₂ + 1-alkanol liquid phase compositions at ~314 K.

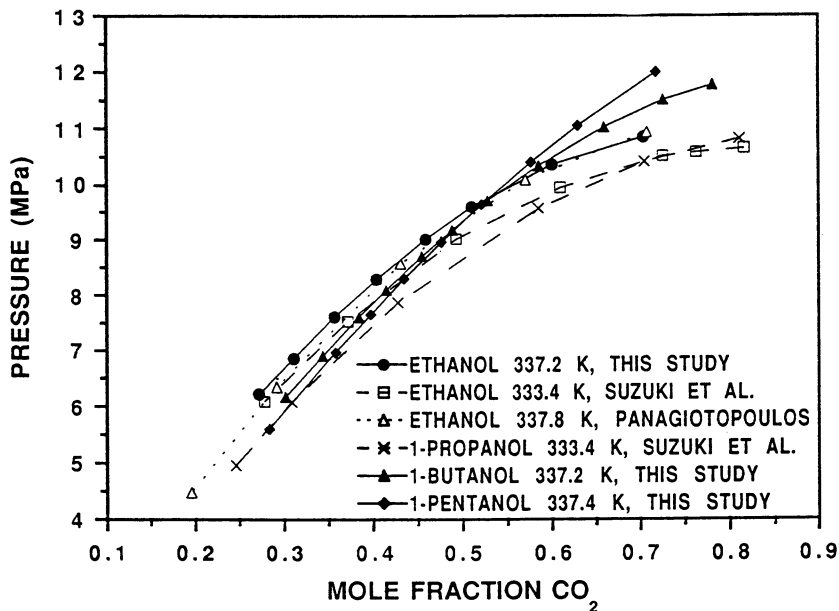


Figure 11. CO₂ + 1-alkanol liquid phase compositions at ≈ 337 K.

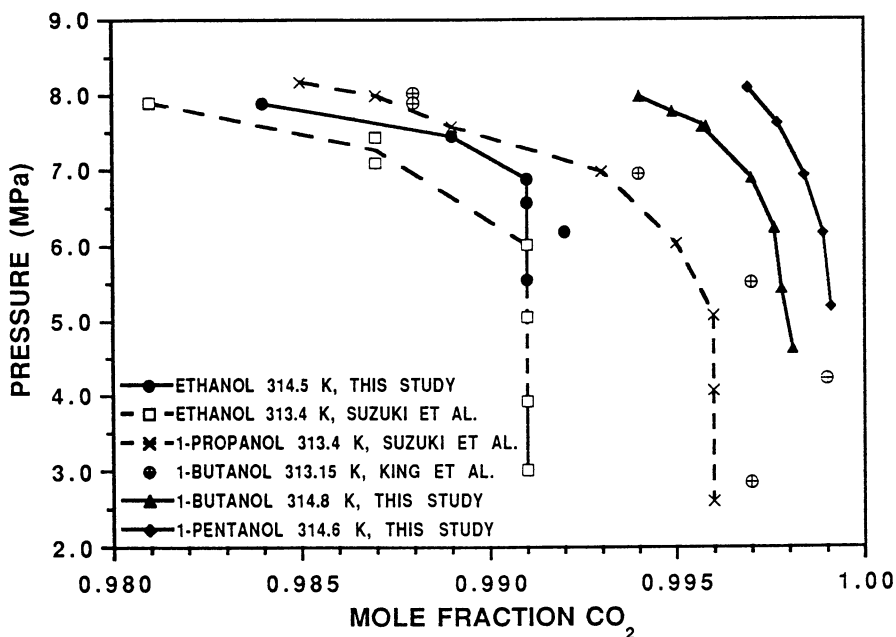


Figure 12. CO₂ + 1-alkanol vapor phase compositions at ≈ 314 K.

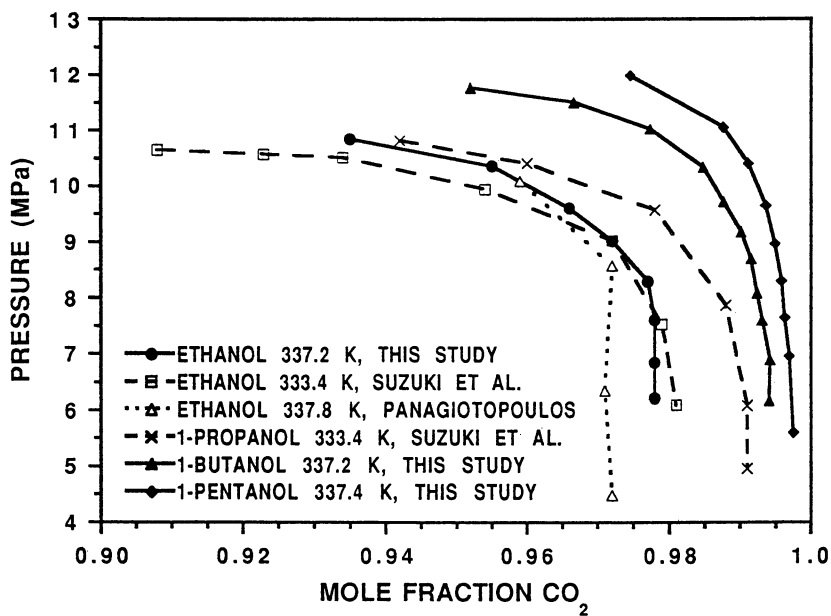


Figure 13. CO₂ + 1-alkanol vapor phase compositions at ≈337 K.

Critical Behavior

A knowledge of the critical locus facilitates the extrapolation of vapor - liquid equilibrium data in the critical region and allows a closure of the bubble and dew point surfaces. However, measurement techniques for vapor - liquid equilibria are least accurate in the critical region, since even small pressure disturbances result in large density fluctuations due to the large compressibility of a near critical fluid.

As shown previously (Figures 4 - 9), the critical pressures reported by Gurdial *et al.* [15] in general appear to be high in relation to the phase envelopes measured by us or by other workers. A possible cause could be that the experimental technique used by Gurdial *et al.* did not allow them to ascertain that the total density in the view cell corresponded to the critical density of the mixture. This is necessary for the measurement of the true critical point, since opalescence can be observed not only at the critical point, but also in its immediate vicinity. Measured "critical" (or phase transition) temperatures at densities higher or lower than the critical density would be lower than the true critical temperatures. This is only true for pure and dilute mixtures, where the phase boundary in $T - \rho$ coordinates in the critical region is symmetric with the critical point at the top. Critical pressures corresponding to given critical temperatures would therefore be too high, as is the case with the data of Gurdial *et al.*. Further, the data reported by Gurdial do not show the expected trend as the carbon number of the solute increases in the 1-alkanol series. The critical pressures of $\text{CO}_2 + 1$ -pentanol mixtures appear to be almost identical with those of 1-butanol, whereas the solute influence on the critical properties is strongly noticeable as the solute is changed from ethanol to 1-propanol or from 1-pentanol to 1-hexanol.

We have also compared the slopes $\left(\frac{dT_c}{dx}\right)$ and $\left(\frac{dP_c}{dx}\right)$ of the critical lines at infinite dilution (where x is the mole fraction of carbon dioxide) obtained from the data of Gurdial *et al.* with those estimated from the vapor - liquid equilibrium data of this work. The slopes of the Gurdial *et al.* data do not exhibit regular trends with increasing carbon number as exhibited by the slopes obtained from the vapor - liquid equilibrium data. It should, however, be noted that there is greater uncertainty in the slopes estimated from the vapor - liquid equilibrium data. The slopes of the critical lines were also correlated using the Patel - Teja equation of state (PT EOS) [62]. The slopes of the critical lines are given by:

$$\begin{aligned} \left(\frac{dT_c}{dx}\right)^\infty &= \frac{\left(\frac{dP}{dx}\right)_{v,T}^2 - \left(\frac{d^2P}{dV dx}\right)_T}{\left(\frac{d^2P}{dT dV}\right)_x} \\ \left(\frac{dP_c}{dx}\right)^\infty &= \left(\frac{dP}{dx}\right)_{v,T} + \left(\frac{dP}{dT}\right)_{v,x} \left(\frac{dT_c}{dx}\right)^\infty \end{aligned}$$

The equation of state could be used to correlate either set of slopes provided a binary interaction parameter k_{ij} is used in the calculations. The experimental

Table III: Slopes of critical lines at infinite dilution. Experiment and prediction. Optimal k_{ij} values in parentheses

System	$\left(\frac{dT_c}{dx}\right)_c^\infty$ (K)		$\left(\frac{dP_c}{dx}\right)_c^\infty$ (bar)	
	T _c - x ¹	VLE ²	P _c - x ¹	VLE ²
CO ₂ - Ethanol	-210 (0.23)	-220 (0.22)	-230 (0.17)	-200 (0.18)
CO ₂ - 1-Butanol	-550 (0.17)	-340 (0.23)	-650 (0.12)	-300 (0.20)
CO ₂ - 1-Pentanol	-590 (0.19)	-420 (0.23)	-590 (0.17)	-450 (0.20)

1: Using the data of Gurdial *et al.*
2: Using the data of this work

slopes could be correlated with reasonably small k_{ij} values which are, however, different from the optimal k_{ij} values obtained in the vapor - liquid equilibrium correlations discussed below. The results are shown in Table III where the optimal k_{ij} values are given in parentheses. Note that the k_{ij} values for correlating the vapor - liquid equilibrium slopes show regular behavior with carbon number of the 1-alkanol.

In Figures 14 - 16 the critical line from the data of Gurdial *et al.* projected in $P - x$ space is shown together with phase envelopes measured in this work at the different temperatures. The critical lines do not seem to correctly represent the composition dependence of the critical behavior indicated by the vapor - liquid equilibrium data.

Modelling of Vapor - Liquid Equilibria

The CO₂ + ethanol, CO₂ + 1-butanol, and CO₂ + 1-pentanol data were correlated with the Patel - Teja equation of state (PT EOS) using classical mixing rules and with an equations of state based on Statistical Associating Fluid Theory (SAFT EOS). The correlation results with the PT EOS with classical mixing rules were not completely satisfactory, as shown below. This is not surprising, since cubic equations of state generally do not provide good results for systems containing polar components. Other mixing rules can be used to provide improved correlations but generally require an additional adjustable constant. As an alternative, the SAFT EOS was examined for correlating CO₂ + 1-alkanol data. The SAFT EOS was developed by Chapman *et al.* [63,64] and by Haung and Radosz [65,66]

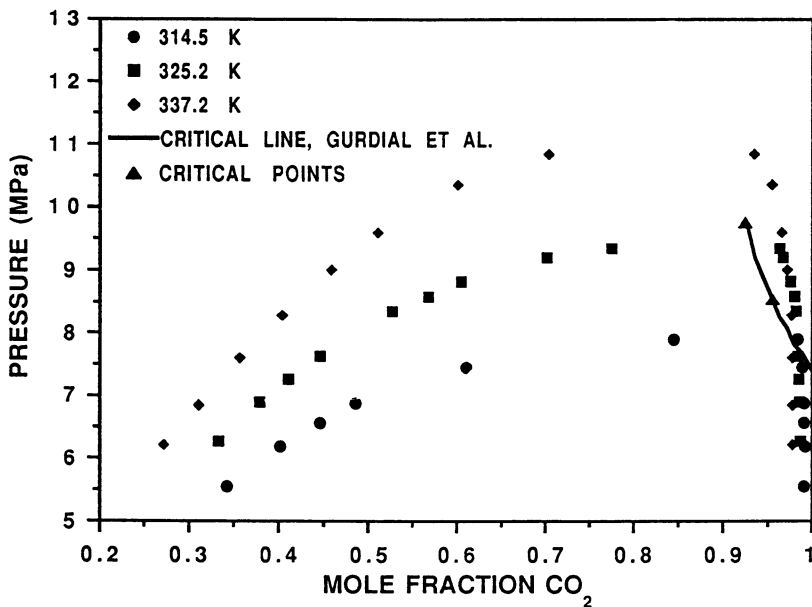


Figure 14. Critical locus/phase envelope for CO_2 + ethanol.

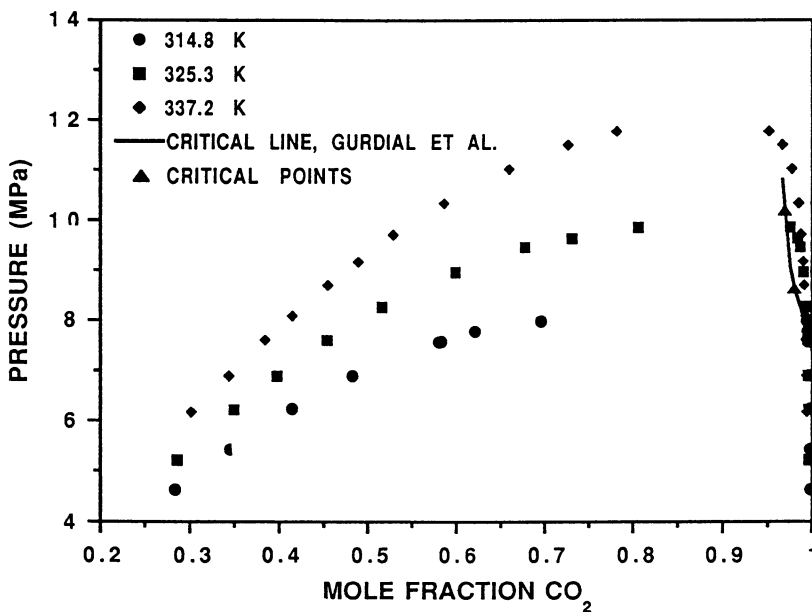


Figure 15. Critical locus/phase envelope for CO_2 + 1-butanol.

Table IV: Equation of State Modelling for CO₂ + 1-Alkanol Systems

System	Temperature (K)	Equation of State	Mixing Rule	Optimized k_{ij}	Objective Function
CO ₂ + Ethanol	314.5	SAFT	VDW1	0.048	508.17
		SAFT	VF	0.058	478.18
		PT	-	0.088	166.12
	325.2	SAFT	VDW1	-	-
		SAFT	VF	0.052	712.52
		PT	-	0.083	168.08
	337.2	SAFT	VDW1	0.052	585.50
		SAFT	VF	0.057	565.35
		PT	-	0.085	175.37
CO ₂ + 1-Butanol	314.8	SAFT	VDW1	0.070	599.41
		SAFT	VF	0.074	570.27
		PT	-	0.093	198.81
	325.3	SAFT	VDW1	0.059	707.17
		SAFT	VF	0.064	648.06
		PT	-	0.080	320.83
	337.2	SAFT	VDW1	0.071	886.81
		SAFT	VF	0.074	841.30
		PT	-	0.086	425.00
CO ₂ + 1-Pentanol	314.6	SAFT	VDW1	0.087	370.50
		SAFT	VF	0.088	351.35
		PT	-	0.102	162.37
	325.9	SAFT	VDW1	0.073	697.33
		SAFT	VF	0.077	651.96
		PT	-	0.089	338.96
	337.4	SAFT	VDW1	0.083	613.79
		SAFT	VF	0.085	574.83
		PT	-	0.100	239.80

for associating systems and was considered promising for the systems of interest in this work. The results of the calculations using the SAFT EOS and the PT EOS are discussed below.

The critical properties and acentric factors required in the PT EOS were taken from Reid *et al.* [67] and the EOS parameters used were those recommended by Patel and Teja [62]. The SAFT EOS parameters were taken from Huang and Radosz [65]. Both a volume fraction (VF) and van der Waals one fluid (VDW1) mixing rule were used in the SAFT EOS.

The binary interaction coefficients, k_{ij} , were obtained by optimizing the following objective function:

$$obj.func. = \sum_{k=1}^{NPs} \sum_{i=1}^{NComp} \left(\left| \frac{x_i^{calc} - x_i^{exp}}{x_i^{exp}} \right| 100 + \left| \frac{y_i^{calc} - y_i^{exp}}{y_i^{exp}} \right| 100 \right)$$

The experimental pressures and temperatures were used in the calculations. The results of the correlation are presented in Table IV. The cubic EOS consis-

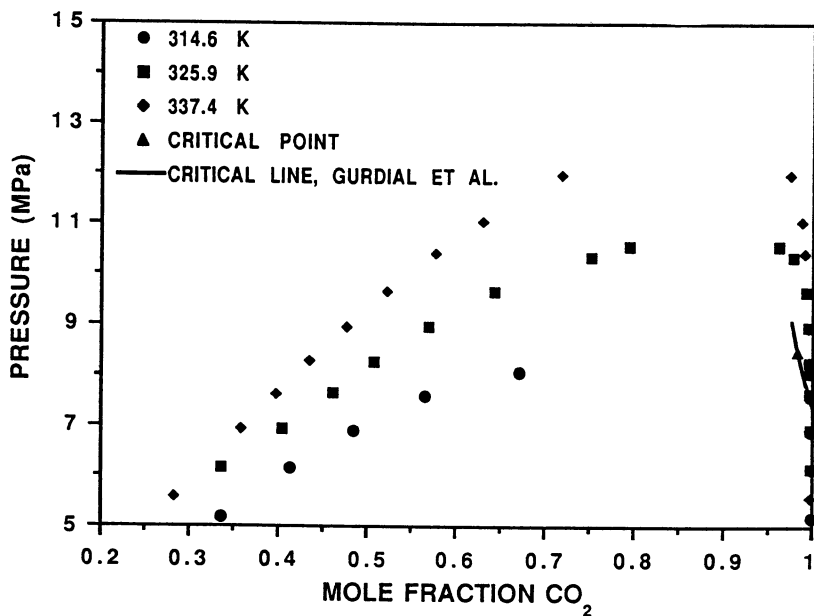


Figure 16. Critical locus/phase envelope for CO_2 + 1-pentanol.

tently gave better results than the SAFT EOS regardless of the mixing rule used with the SAFT EOS. This appears to be largely due to a better fit of the vapor phase. The volume fraction mixing rule gave better results than the van der Waals one fluid mixing rule for the SAFT EOS. This agrees with the conclusions of Huang and Radosz that the volume fraction mixing rule gives better results in the critical region. It should be added here that many of the measured data points in these systems are in the near-critical region.

Figures 17 - 19 show our calculations at the highest measured isotherm for the CO_2 + ethanol, CO_2 + 1-butanol, and CO_2 + 1-pentanol systems, respectively. The volume fraction mixing rule is shown for the SAFT EOS. It is seen that neither EOS is able to correlate the data within the accuracy of the experiment. It would therefore appear that more work is still necessary to obtain a satisfactory thermodynamic model for systems containing associating components.

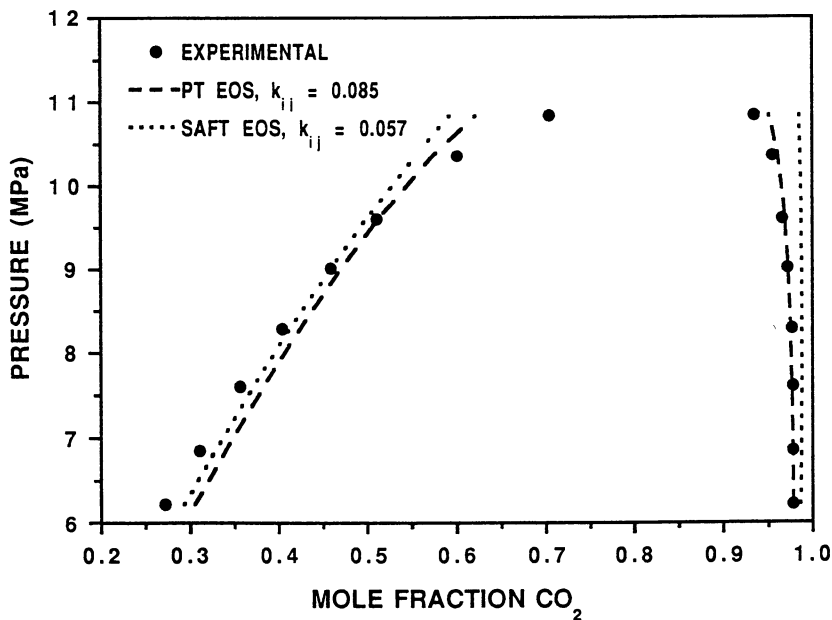


Figure 17. Correlation of CO₂ + ethanol vapor-liquid equilibria at 337.2 K.

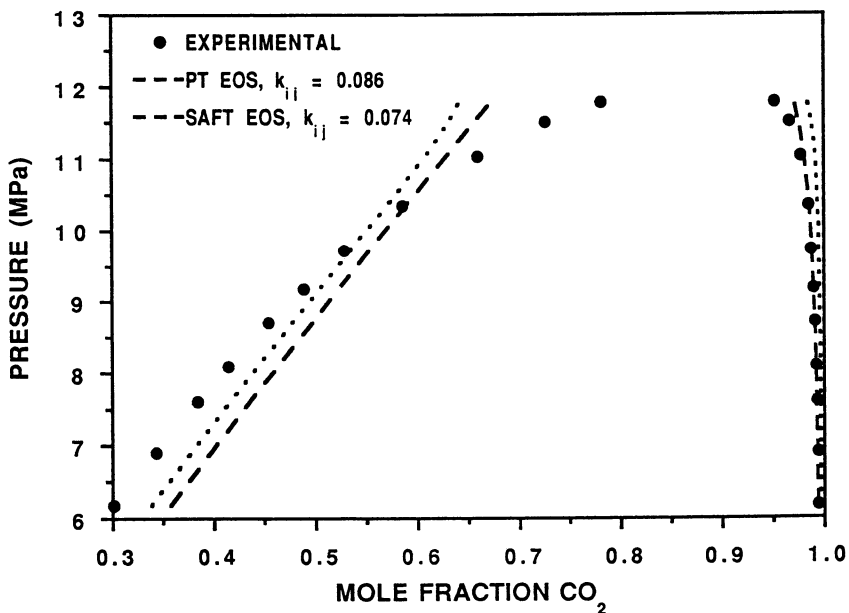


Figure 18. Correlation of CO₂ + 1-butanol vapor-liquid equilibria at 337.2 K.

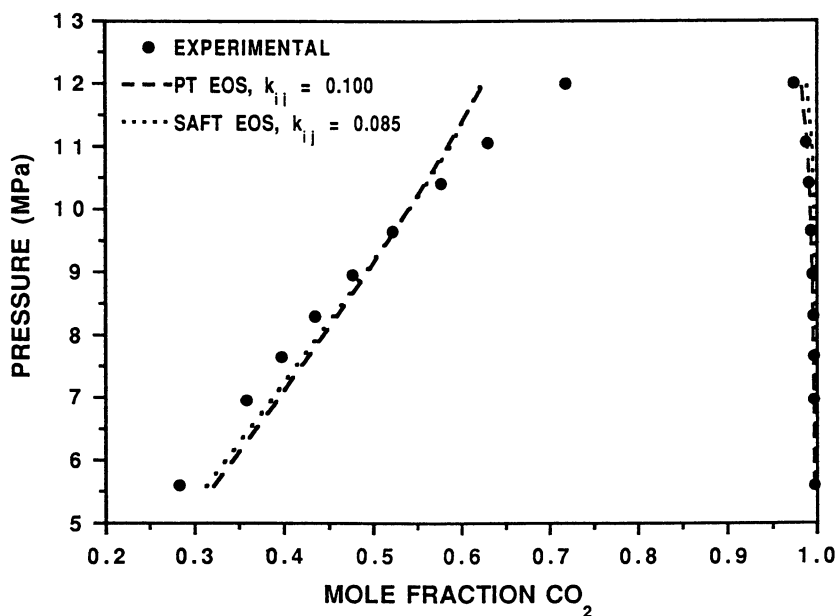


Figure 19. Correlation of CO₂ + 1-pentanol vapor-liquid equilibria at 337.4 K.

Acknowledgments

The authors would like to thank Dr. Maciej Radosz and the Exxon Research and Engineering Company for the use of their SAFT EOS software. Acknowledgment is also made to the Donors of the Petroleum Research Fund, administered by the American Chemical Society, for partial support of this research.

Literature Cited

- [1] DeFillippi, R. P.; Moses, J. M. *Biotech. and Bioeng. Symp.* **1982**, 12, 205.
- [2] Kuk, M. S.; Montagna, J. C. In *Chemical Engineering at Supercritical Fluid Conditions*; Editors, Paulaitis, M. E.; Penninger, J. M. L.; Gray, R. D.; Davidson, P. Ann Arbor Science: Ann Arbor, MI, 1983; chapter 4.
- [3] Gilbert, M. L.; Paulaitis, M. E. *J. Chem. Eng. Data* **1986**, 31, 296.
- [4] Takishima, S.; Saiki, K.; Arai, K.; Saito, S. *J. Chem. Eng. Jap.* **1986**, 19, 48.
- [5] Feng, Y. S.; Du, X. Y.; Li, C. F.; Hou, Y. J. In *Proc. of the First Inter. Symp. on Supercritical Fluids*; Chairman, Perrut, M.; Nice, France, 1988, 75.
- [6] Nagahama, K.; Suzuki, J.; Suzuki, T. In *Proc. of the First Inter. Symp. on Supercritical Fluids*; Chairman, Perrut, M.; Nice, France, 1988, 143.
- [7] Inomata, H.; Arai, K.; Saito, S.; Ohba, S.; Takeuchi, K. *Fluid Phase Equilib.* **1989**, 53, 23.
- [8] de la Ossa, E. M.; Brandani, V.; Del Re, G.; Di Giacomo, G.; Ferri, E. *Fluid Phase Equilib.* **1990**, 56, 325.
- [9] Suzuki, K.; Sue, H.; Itou, M., Smith, R. L.; Inomata, H.; Arai, K.; Saito, S. *J. Chem. Eng. Data* **1990**, 35, 63.
- [10] Suzuki, K.; Sue, H.; Itou, M., Smith, R. L.; Inomata, H.; Arai, K.; Saito, S. *J. Chem. Eng. Data* **1990**, 35, 67.
- [11] Suzuki, K.; Sue, H.; Arai, K.; Saito, S. *Fluid Phase Equilib.* **1990**, 59, 115.
- [12] Ayen, R. J.; Iacobucci, P. A. *Rev. Chem. Eng.* **1988**, 5, 157.
- [13] Brunner, E. *J. Chem. Thermodynamics* **1985**, 17, 671.
- [14] Baker, L. C. W.; Anderson, T. F. *J. Am. Chem. Soc.* **1957**, 79, 2071.
- [15] Gurdial, G. S.; Foster, N. R.; Yun, J. S. In *Proc. of the Second Inter. Symp. on Supercritical Fluids*; Chairman, McHugh, M. A.; Boston, MA, 1991, 66.
- [16] Hemmaplardh, B.; King Jr., A. D. *J. Phys. Chem.* **1972**, 76, 2170.
- [17] Katayama, T.; Ohgaki, K.; Maekawa, G.; Goto, M.; Nagano, T. *J. Chem. Eng. Jap.* **1975**, 8, 89.
- [18] Ohgaki, K.; Katayama, T. *J. Chem. Eng. Data* **1976**, 21, 53.
- [19] Schneider, R. Ph.D. thesis, Technical University, Berlin, 1978.
- [20] Semenova, A. I.; Emel'yanova, E. A.; Tsimmerman, S. S.; Tsiklis, D. S. *Russian J. Phys. Chem.* **1979**, 53, 1428.
- [21] Lalalde-Crabtree, H.; Breedveld, G. J. F.; Prausnitz, J. M. *AIChE J.* **1980**, 26, 462.
- [22] Brunner, E.; Hültenschmidt, W.; Schlichthärle *J. Chem. Thermodynamics* **1987**, 19, 273.
- [23] Hong, J.; Kobayashi, R. *Fluid Phase Equilib.* **1988**, 41, 269.
- [24] Gupta, S. K.; Leslie, R. D.; King Jr., A. D. *J. Phys. Chem.* **1973**, 77, 2011.

- [25] Pangiotopoulos, A. Z. Ph.D. thesis, Massachusetts Institute of Technology, 1986.
- [26] Yao, S.; Liu, F.; Han, Z.; Zhu, Z. In *Proc. of the Inter. Symp. of Thermodynamics in Chem. Eng. Ind.*; China, 1988, 688.
- [27] Jennings, D. W.; Lee, R. J.; Teja, A. S. *J. Chem. Eng. Data* **1991**, *36*, 303.
- [28] Massoudi, R.; King Jr., A. D. *J. Phys. Chem.* **1973**, *77*, 2016.
- [29] King, M. B.; Alderson, D. A.; Fallah, F. H.; Kassim, D. M.; Kassim, K. M.; Sheldon, J. R.; Mahmud, R. S. In *Chemical Engineering at Supercritical Fluid Conditions*; Editors, Paulaitis, M. E.; Penninger, J. M. L.; Gray, R. D.; Davidson, P. Ann Arbor Science: Ann Arbor, MI, 1983; chapter 2.
- [30] Winkler, S.; Stephan, K. In *Proc. of the Second Inter. Symp. on Supercritical Fluids*; Chairman, McHugh, M. A.; Boston, MA, 1991, 59.
- [31] Jennings, D. W.; Chang, F.; Bazaan, V.; Teja, A. S. *J. Chem. Eng. Data submitted*
- [32] Nickel, D.; Schneider, G. M. *J. Chem. Thermodynamics* **1989**, *21*, 293.
- [33] Katzenski-Ohling, G. Ph.D. thesis, University of Bochum, 1986.
- [34] Hölscher, I. F. Ph.D. thesis, University of Bochum, 1986.
- [35] Friedrich, J.; Schneider, G. M. *J. Chem. Thermodynamics* **1989**, *21*, 307.
- [36] Kunerth, W. *Phys. Rev.* **1922**, *19*, 512.
- [37] Krichevskii, I. R.; Koroleva, M. *Acta. Physicochim. URSS* **1941**, *15*, 327.
- [38] Krichevskii, I. R.; Lebedewa, E. S. *Zh. Fiz. Khim.* **1947**, *21*, 715.
- [39] Bezdell, L. S.; Teodovich, V. P. *Gazov. Prom.* **1958**, *3(8)*, 38.
- [40] Shenderei, E. R.; Zelvenskii, YA. D.; Ivanovskii, F. P. *Gazov. Prom.* **1958**, *3(12)*, 36.
- [41] Shenderei, E. R.; Zelvenskii, YA. D.; Ivanovskii, F. P. *Khim. Prom.* **1959**, *4*, 328.
- [42] Shenderei, E. R.; Zelvenskii, YA. D.; Ivanovskii, F. P. *Khim. Prom.* **1961**, *5*, 309.
- [43] Otsuka, E.; Takada, M.; *J. Fuel Soc. Jap.* **1963**, *42*, 229.
- [44] Yorizane, M.; Sadamoto, S.; Masuoka, H.; Eto, Y. *Kogyo Kagaku Zasshi* **1969**, *72*, 2174.
- [45] Tokunga, J.; Nitta, T.; Katayama, T. *Kagaku Kogaku Zasshi* **1969**, *33*, 775.
- [46] Ferrell, J. K.; Rousseau, R. W. *EPA Interagency Energy Environ. Progr. Rep.* **1979**, EPA-600/7-79-097.
- [47] Won, Y. S.; Chung, D. K.; Mills, A. F. *J. Chem. Eng. Data* **1981**, *26*, 140.
- [48] Takeuchi, K.; Matsumura, K.; Yaginuma, K. *Fluid Phase Equilib.* **1983**, *14*, 255.
- [49] Zeck, S.; Knapp, H. In *Proc. Inter. Congress of Chem. Eng. Chem. Equip. Design and Automation*; Prague, 1984.
- [50] Weber, W.; Zeck, S.; Knapp, H. *Fluid Phase Equilib.* **1984**, *18*, 253.
- [51] Chang, T.; Rousseau, R. W.; *Fluid Phase Equilib.* **1985**, *23*, 243.
- [52] Sander, W. *Z. Physik. Chem.* **1912**, *78*, 513.
- [53] Tokunga, J. *J. Chem. Eng. Data* **1975**, *20*, 41.
- [54] Wilcock, R. J.; Battino, R.; Danforth, W. F.; Wilhem, E. *J. Chem. Thermodynamics* **1978**, *10*, 817.

- [55] Jennings, D. W. Ph.D. thesis, Georgia Institute of Technology, 1991.
- [56] Weibe, R. *Chem. Revs.* **1941**, 29, 475.
- [57] Briones, J. A.; Mullins, J. C.; Thies, M. C.; Kim, B. U. *Fluid Phase Equilib.* **1987**, 36, 235.
- [58] King, M. B.; Kassim, K.; Bott, T. R.; Sheldon, J. R. *Ber. Bunsen-Ges. Phys. Chem.* **1984**, 88, 820.
- [59] Charoensombut-amon, T.; Martin, R. J.; Kobayashi, R. *Fluid Phase Equilib.* **1986**, 31, 89.
- [60] D'Souza, R.; Patrick, J. R.; Teja, A.S. *Can. J. Chem. Eng.* **1988**, 66, 319.
- [61] Lam, D. H.; Jangkamolkulchai, A.; Luks, K. D. *Fluid Phase Equilib.* **1990**, 60, 131.
- [62] Patel, N. C.; Teja, A. S. *Chem. Eng. Sci.* **1982**, 37, 463.
- [63] Chapman, W. G.; Gubbins, K. E.; Jackson, G.; Radosz, M. *Fluid Phase Equilib.* **1989**, 52, 31.
- [64] Chapman, W. G.; Gubbins, K. E.; Jackson, G.; Radosz, M. *Ind. Eng. Chem. Res.* **1990**, 29, 1709.
- [65] Huang, S. H.; Radosz, M. *Ind. Eng. Chem. Res.* **1990**, 29, 2284.
- [66] Huang, S. H.; Radosz, M. *Ind. Eng. Chem. Res.* *submitted*
- [67] Reid, R. C.; Prausnitz, J. M.; Poling, B. E. *The Properties of Gases and Liquids*; 4th ed.; McGraw-Hill, New York, 1987.

RECEIVED April 27, 1992

Chapter 3

Phase Behavior of Supercritical Fluid–Entrainer Systems

Gurdev S. Gurdial, Neil R. Foster¹, S. L. Jimmy Yun, and Kevin D. Tilly

School of Chemical Engineering and Industrial Chemistry, University of New South Wales, P.O. Box 1, Kensington 2033, Australia

The critical loci for binary mixtures of CO₂-oxygenated hydrocarbons and CO₂-alkanes have been experimentally determined for solute concentrations up to 7 mol%. The binary systems studied were CO₂-acetone, CO₂-isopropanol, CO₂-(C₁-C₆) n-alcohols and CO₂-(C₅-C₁₀) n-alkanes.

The apparatus used to obtain the data consisted primarily of a high pressure sight gauge fitted with a thermocouple and a pressure transducer. The overall error for each temperature and pressure measurement was ±0.2 K and ±0.5 bar, respectively, with an estimated error of ±1.5% for the determination of the organic compound composition.

The results obtained are of relevance to SCF-entrainer studies where it is necessary to ensure the existence of a single homogenous fluid phase.

The critical point of pure substances and mixtures of defined composition is a property of considerable importance from both theoretical and practical considerations. Accurate determination of the critical point is of theoretical interest as it defines the temperature and pressure at which the vapour and liquid phases existing in equilibrium have identical properties. Therefore, the critical point is the key parameter in the construction of phase diagrams as it represents the upper boundary of the vapour-liquid region (*I*). The locus of the critical points represents the boundary between the regions of homogenous and heterogenous phase behaviour of phase diagrams for mixtures. Determination of these phase boundaries allows one to estimate retrograde regions and appropriate operating conditions for supercritical fluid extraction (SCFE). The critical loci of mixtures is of theoretical interest since it may be argued that in the light of the complex nature of the

¹Corresponding author

0097-6156/93/0514-0034\$06.00/0
© 1993 American Chemical Society

topology of the critical lines in the PVT_x space, the calculation of these points can be used to provide a stringent test of any theory (2).

While the true critical properties of mixtures (critical temperature, critical pressure and critical volume) are not usually used directly as correlating parameters, knowledge of the true gas-liquid critical region of the mixtures is necessary for the development of correlations for predicting the thermodynamic and physical properties of process fluids (3,4).

From practical considerations, a knowledge of the true critical properties of mixtures is of great importance in petroleum and natural gas engineering, and for rational design of chemical reactors and high pressure extraction and separation equipment. Indeed, the PVT properties of mixtures in the critical region is necessary for the economic assessment of processes involving SCFs.

SCFE is a relatively new technology for commercial separation processes. In the past few years research has been increasingly directed to studying the solubility of solid solutes (5,6,7,8) and liquid solutes (9,10) in chemically diverse SCFs.

Small amounts of co-solvents, which are referred to as modifiers or entrainers, may be added to modify the polarity and solvent strength of the primary supercritical fluid to increase the solute solubility (and/or selectivity) and to minimize operating costs in a continuous extraction process (11,12,13,14). The co-solvents used are commonly polar or non-polar organic compounds which are miscible with the supercritical fluid solvent. The addition of a small amount of co-solvent into a primary SCF tends to increase both the critical temperature and pressure of the resulting solvent mixture.

To ensure operation in the critical region of a binary solvent mixture of defined composition, knowledge of the gas-liquid critical point for the mixture is essential. The objective of this study was to experimentally determine the gas-liquid critical loci (i.e. pressure-temperature-composition, P_c - T_c - x) for binary polar and non-polar organic compound-CO₂ systems at solute concentrations up to 7 mole %. The binary systems studied were all based on CO₂ with additions of acetone, isopropanol, C₁-C₆ n-alcohols and C₅-C₁₀ n-alkanes. The results obtained are of relevance to SCF-entrainer studies where small amounts of co-solvents, typically lower than 10 mole %, are used.

Experimental

Materials The source and purity of the CO₂ and the organic solvents used for the determination of gas-liquid critical loci of binary mixtures are given in Table I together with other physical properties (15). These samples were used without further purification.

Apparatus The gas-liquid critical temperatures, T_c , and pressures, P_c , of mixtures of known composition were determined using a specially designed high

pressure Reflex Jerguson sight gauge (Model 13R32). The apparatus is shown schematically in Figure 1. The sight gauge, rated to 265 bar at 363 K, consisted of a stainless steel chamber with a thick borosilicate glass window on one face to provide visual observation of the phases present. The sight gauge was fitted with a type K thermocouple which was connected to a microcomputer thermometer (JENCO Model 7000CH). The temperature of the sight gauge was controlled by immersion in an agitated water bath with a Thermoline Unistat heater/circulator.

The pressure at equilibrium was determined by a pressure transducer (DRUCK Model DPI 260). A needle valve was used to seal off the the volume inside the sight gauge, thus enabling the volume to be held constant throughout each experiment. A three-way valve mounted externally to the apparatus provided access to a wet test gas meter or CO₂ supply.

The sample was agitated mechanically using a special stirrer consisting of 1/16 in. tubing. A short length of steel rod was connected to the upper end of the tubing whilst washers were attached at regular intervals at the lower end. By means of magnets, the stirrer was moved up and down to provide the agitation required.

Preparation of Mixtures The binary mixtures of CO₂ with acetone, C₁-C₆ n-alcohols and C₅-C₇, and C₁₀ n-alkanes were prepared by loading the Jerguson sight gauge with a known volume of the organic solvent and then adding the liquid CO₂ to approximately 2/3 of the viewing length of the Jerguson gauge. The mass of the organic solvent injected was calculated from the measured volume and density whilst the mass of CO₂ present in the Jerguson gauge was determined by venting the gas through a wet test meter after the critical values were determined. From this information the mixture composition was evaluated.

Measurement Procedure Once the binary mixture was prepared, the Jerguson sight gauge was introduced into the water bath and the temperature raised slowly until the gas-liquid critical point was reached. During the heating, the sample was agitated intermittently with the stirrer to ensure homogeneity of the vessel contents, thus eliminating variations in density along the length of the sight gauge.

The critical point was determined visually by observing the temperature and pressure at which the meniscus reappeared upon cooling. The reappearance of the gas-liquid meniscus was rapid and was usually accompanied by cloudiness or opalescence. For each binary mixture, the critical points were measured at six or eight compositions. The reappearance of the gas-liquid meniscus was taken as the criterion to establish the critical point since it is a sharper phenomena compared with the disappearance of the gas-liquid interface upon heating.

The accuracy of the method for determining the critical points was evaluated in a test conducted with food grade CO₂ which yielded critical values of T_c = 304 K and P_c = 74 bar. This represented a relative deviation of less than 0.1% and 0.3%, respectively, from the literature values of 304.2 K and 73.8 bar (16). For all the

TABLE I. Sources, purity and properties of the organic solvents used

Compound	Source	Purity	MW*	T _c (K)*	P _c (Bar)*
CO ₂	Liquid-Air	99.8	44.01	304.2	73.8
Acetone	BDH	99.5	58.08	508.1	47.0
Methanol	BDH	99.8	32.04	512.6	80.9
Ethanol	BDH	99.8	46.07	513.9	61.4
Propan-1-ol	BDH	99.5	60.09	536.8	51.7
Propan-2-ol	BDH	99.8	60.09	508.3	47.6
n-Butanol	BDH	99.5	74.12	563.1	44.2
n-Pentanol	BDH	99.0	88.15	588.2	39.1
n-Hexanol	BDH	98.0	102.18	611.0	40.5
n-Pentane	BDH	99.5	72.15	469.7	33.7
n-Hexane	BDH	99.5	86.18	507.5	30.1
n-Heptane	BDH	99.5	100.2	540.3	27.4
n-Octane	SIGMA	99.0	114.2	568.8	24.8
n-Nonane	BDH	99.0	128.26	594.6	23.1
n-Decane	BDH	99.5	142.29	617.7	21.2

* Data obtained from ref. 15

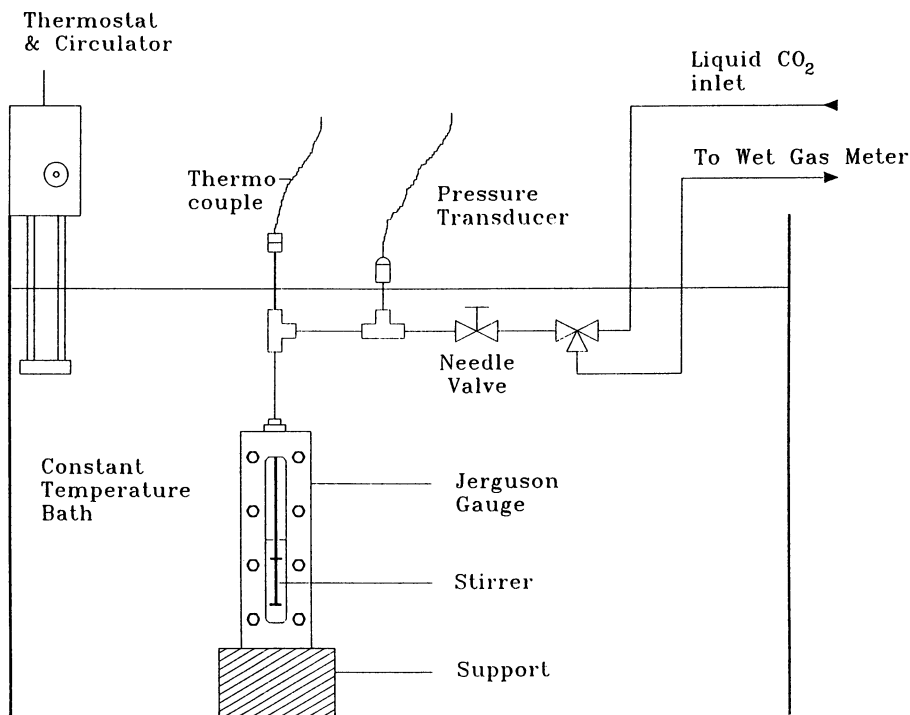


Figure 1. Apparatus for critical locus determination

binary systems investigated, the uncertainties in the accuracy of the P_c - T_c - x measurements are estimated to be ± 0.5 bar, ± 0.2 K, respectively, with an estimated error of $\pm 1.5\%$ for the determination of the organic compound composition.

Results and Discussion

The experimental P_c - T_c - x results for the fourteen binary mixtures of CO_2 with acetone, C_1 - C_6 n -alcohols, iso-propanol and C_5 - C_{10} n -alkanes are given in Table II. The projected critical loci on the P - T plane for the binary CO_2 -alcohols and CO_2 - n -alkanes are illustrated in Figures 2 and 3 respectively. The critical loci for binary CO_2 -alcohols, and CO_2 - n -alkanes mixtures are almost straight lines for the composition range investigated.

It is important to note that the critical loci curve across the entire composition range for the binary mixtures of CO_2 with n -butane and n -pentane studied by Poettman and Katz (17) exhibited a maximum-pressure point. Systems which form positive azeotropes, such as binary mixtures of CO_2 with ethane and propane, tend to exhibit a minimum-temperature point in the critical loci curve. As no azeotrope is expected to form in the systems studied, since the critical temperatures of all the components investigated (see Table I) differ greatly from that of CO_2 , the critical loci curve would be expected to display a point of maximum-pressure.

The relationships between the critical temperature and the composition for the binary CO_2 -alcohols and CO_2 - n -alkanes are depicted in Figures 4 and 5 respectively. The variation of the critical pressure with the composition for the binary CO_2 -alcohols and CO_2 - n -alkanes mixtures is shown in Figures 6 and 7.

When components belonging to different chemical families and of varying degree of relative size are mixed, great diversity in the values of the critical temperatures and pressures of the resultant binary mixtures are observed. This is clearly demonstrated in Figures 4-7. For example, at 1.0 mole% methanol in CO_2 , the critical temperature and pressure were altered by 0.7% and 3.2% respectively. The critical temperature and pressure increased by 2.7% and 14.0%, respectively, for 1.0 mole% n -hexanol in CO_2 . These data indicate that as the relative size of the molecules increases (i.e. the ratio of the molecular weight of the less volatile to that of the more volatile compound), the critical temperature and pressure also increase significantly for a given composition. In addition, the n -hexanol in CO_2 system also exhibits more complicated phase behaviour. At compositions higher than 0.99 mole% hexanol (ie. $T_c > 312.4\text{K}$, $P_c > 85.1$ bar), small amounts of condensation have been observed. This observation is consistent with the findings of Lam et al. (18), who found that the critical locus terminates at 312.93 K and 84.07 bar. Consequently, it would appear that at higher concentrations the system exhibits a separate critical locus branch.

The critical temperatures and pressures are also affected by the chemical nature of the components. This is illustrated by comparing, for example, the binary system of

Table II. Experimental P_c - T_c - x of Binary Mixtures

CO ₂ -Acetone System			CO ₂ -Methanol System			CO ₂ -Ethanol System		
Mole % Acetone	T_c (K)	P_c (Bar)	Mole % Methanol	T_c (K)	P_c (Bar)	Mole% Ethanol	T_c (K)	P_c (Bar)
0	304.0	74.0	0.76	305.0	76.2	0.95	305.8	76.5
0.76	307.4	77.2	1.26	306.2	76.6	2.14	308.4	78.3
1.50	308.3	78.6	1.89	307.2	77.4	2.78	310.3	80.7
2.25	310.7	80.2	3.07	309.1	79.7	3.66	312.1	82.5
3.03	312.5	82.6	4.38	311.7	82.7	4.64	315.2	86.1
3.78	316.0	85.4	5.68	314.9	86.5	6.38	320.1	91.9
4.46	317.6	86.0	6.93	320.5	93.5	7.32	325.1	97.4
5.86	322.2	90.0	6.93	320.5	93.5	7.32	325.1	97.4
6.48	323.5	90.4						
CO ₂ -n-Propanol System			CO ₂ -i-Propanol System			CO ₂ -n-Butanol System		
Mole % n-Propanol	T_c (K)	P_c (Bar)	Mole % i-Propanol	T_c (K)	P_c (Bar)	Mole % n-Butanol	T_c (K)	P_c (Bar)
0.70	307.6	75.8	0.70	306.6	75.3	0.28	305.5	75.8
1.29	309.6	77.8	1.39	308.6	77.1	0.54	307.2	77.8
1.94	312.2	80.5	2.15	310.7	79.5	0.82	308.4	78.6
2.54	314.9	83.3	2.80	312.9	81.4	1.10	310.3	81.1
3.17	316.4	85.2	3.45	314.9	83.1	1.36	311.6	82.9
3.77	320.3	90.0	4.17	317.0	85.5	1.89	314.5	85.9
			4.98	319.8	88.4	2.46	317.8	90.7
			5.74	322.0	90.9	3.34	329.2	108.1
CO ₂ -n-Pentanol System			CO ₂ -n-Hexanol System			CO ₂ -Pentane System		
Mole% n-Pentanol	T_c (K)	P_c (Bar)	Mole % n-Hexanol	T_c (K)	P_c (Bar)	Mole % n-Pentane	T_c (K)	P_c (Bar)
0.45	307.5	76.6	0.20	306.1	77.1	1.16	306.7	74.3
0.84	309.7	78.9	0.40	307.5	77.8	2.20	308.9	74.9
1.28	312.0	81.5	0.57	308.2	79.2	3.37	311.9	76.2
1.82	315.0	85.5	0.81	310.6	81.8	4.80	316.3	78.5
2.37	318.5	90.8	0.99	312.4	84.4	5.69	318.1	79.4
						7.03	322.7	81.9

Continued on next page

Table II. Experimental P_c - T_c - x of Binary Mixtures (cont...)

CO ₂ -Hexane System			CO ₂ -n-Heptane System			CO ₂ -n-Octane System		
Mole%	T _c	P _c	Mole %	T _c	P _c	Mole %	T _c	P _c
n-Hexane	(K)	(Bar)	n-Heptane	(K)	(Bar)	n-Octane	(K)	(Bar)
0.42	305.0	75.4	0.36	305.5	75.8	0.69	307.7	76.5
1.06	306.4	76.5	0.69	307.3	77.1	1.37	310.4	78.9
1.74	308.0	77.7	1.03	308.7	78.5	2.16	315.5	83.8
2.36	309.8	78.6	1.38	309.8	79.7	2.90	319.9	88.5
3.00	311.3	80.3	1.76	311.4	81.0	3.64	325.2	94.0
3.74	313.6	81.4	2.04	312.2	81.3			
4.91	316.8	84.9	2.47	314.8	84.4			
5.86	319.1	87.1	3.26	317.8	86.5			
7.27	322.3	89.5	3.81	320.8	89.4			
			4.54	323.2	92.1			
CO ₂ -n-Nonane System			CO ₂ -n-Decane System					
Mole %	T _c	P _c	Mole %	T _c	P _c			
n-Nonane	(K)	(Bar)	n-Decane	(K)	(Bar)			
0.38	306.6	75.7	0.29	305.9	77.0			
0.75	308.6	77.6	0.59	307.8	79.4			
1.20	312.5	81.6	1.20	310.0	82.1			
1.61	315.4	84.8	1.55	315.2	88.0			
1.96	317.6	87.3	1.91	319.5	94.3			
			2.27	324.2	100.3			

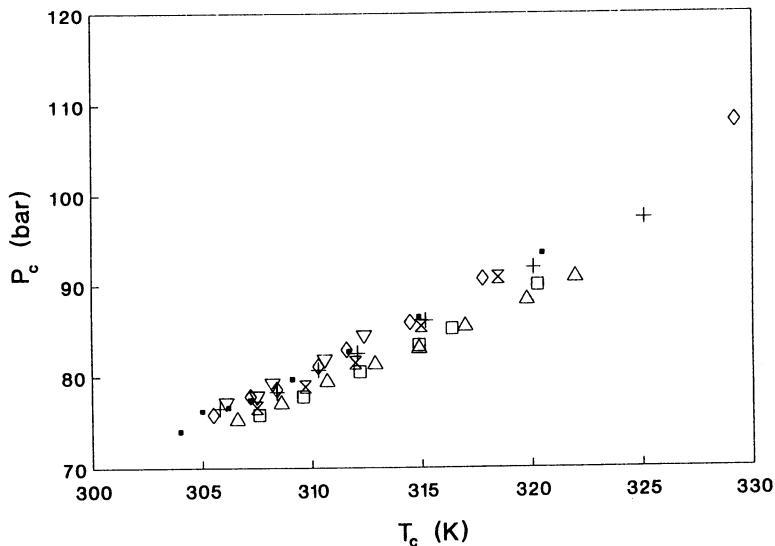


Figure 2. Experimental gas-liquid critical temperatures and pressures for CO₂-alcohol systems. (⊕) methanol; (+) ethanol; (□) n-propanol; (◇) n-butanol; (⊗) n-pentanol; (▽) n-hexanol; (Δ) i-propanol

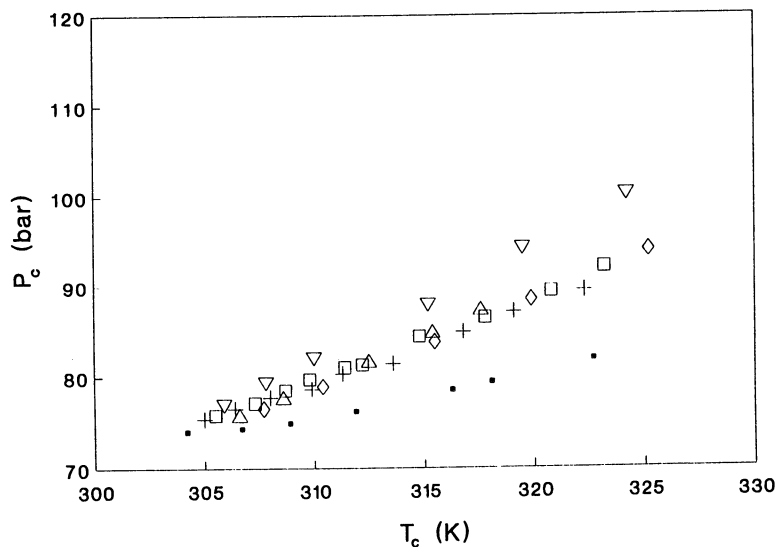


Figure 3. Experimental gas-liquid critical temperatures and pressures for CO₂-n-alkane systems. (⊕) n-pentane; (+) n-hexane; (□) n-heptane; (◇) n-octane; (Δ) n-nonane; (▽) n-decane

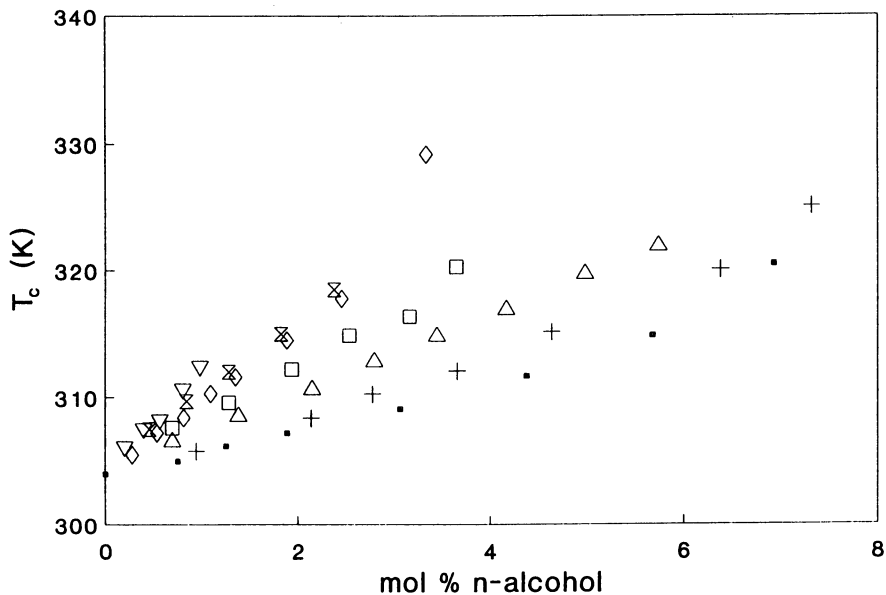


Figure 4. Experimental T_c - x curve for CO_2 -alcohol systems. (\odot) methanol; ($+$) ethanol; (\square) n-propanol; (\diamond) n-butanol; (\otimes) n-pentanol; (∇) n-hexanol; (Δ) i-propanol

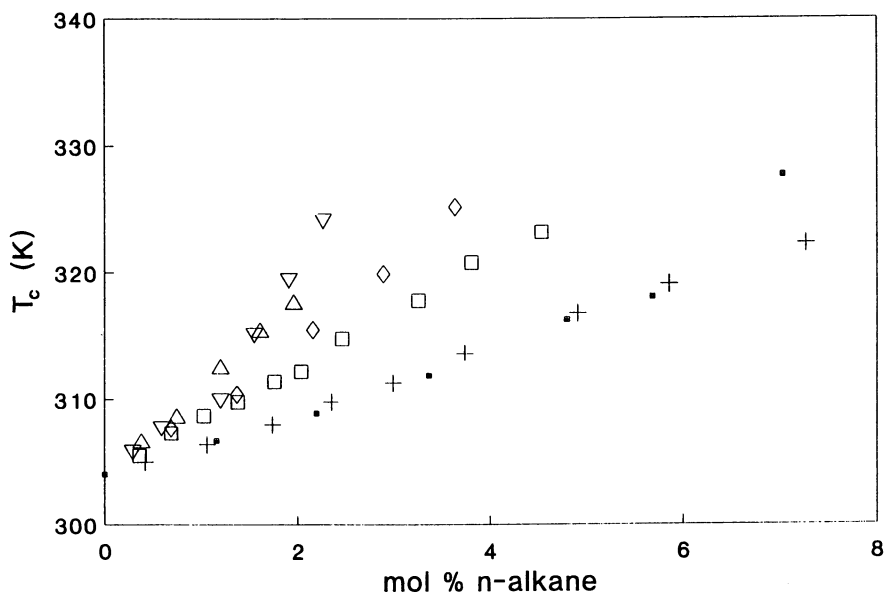


Figure 5. Experimental T_c - x curve for CO_2 -n-alkane systems. (\odot) n-pentane; ($+$) n-hexane; (\square) n-heptane; (\diamond) n-octane; (Δ) n-nonane; (∇) n-decane

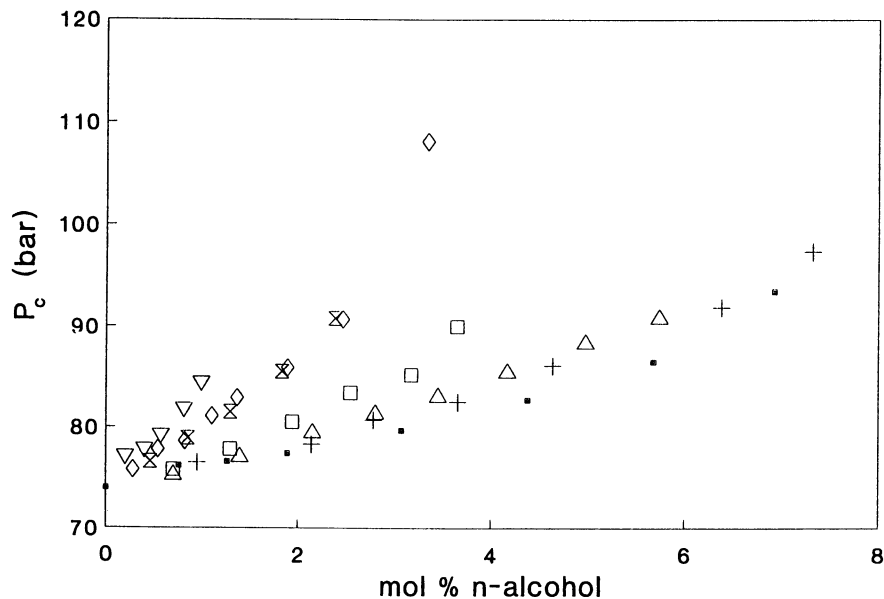


Figure 6. Experimental P_c - x curve for CO_2 -alcohol systems. (◻) methanol; (+) ethanol; (◻) n-propanol; (◊) n-butanol; (⊗) n-pentanol; (▽) n-hexanol; (Δ) i-propanol

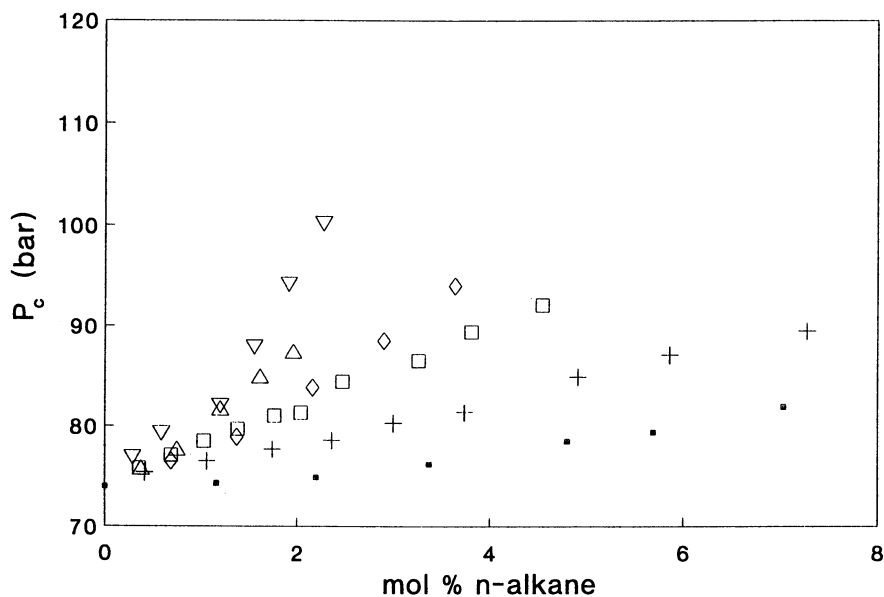


Figure 7. Experimental P_c - x curve for CO_2 -n-alkane systems. (◻) n-pentane; (+) n-hexane; (◻) n-heptane; (◊) n-octane; (Δ) n-nonane; (▽) n-decane

CO₂-n-hexane and CO₂-n-hexanol. For 1.0 mole% n-hexane in CO₂, the critical temperature and pressure was increased by 0.7% and 3.4% respectively, compared with a value of 2.7% for the critical temperature and 14.0% for the critical pressure for the same composition of n-hexanol in CO₂.

Comparison of the critical loci for mixtures containing n-propanol and i-propanol show the effect of structure on compounds with identical molecular weight and similar polarity. It is shown in Figure 2 that the P_c-T_c projection of these two compounds are very similar, but examination of the P_c-x and T_c-x projections, in Figure 6 and Figure 4 respectively, show that the primary alcohol increases the critical properties of the mixture to a greater degree, at constant composition than does the secondary alcohol. The dependence of critical pressure on composition for CO₂-i-propanol mixtures is similar to that of ethanol, which tends to indicate that the maximum linear length of the molecule is more influential on the critical point of the mixture than the molecular weight.

The results obtained in the present study indicate qualitatively that the critical properties of a binary mixture depend on both the relative size of the molecules and on their chemical nature. The more polar cosolvents affect the critical properties to a greater degree than do the non-polar cosolvents, and the larger cosolvent molecules have more influence on the critical properties compared to smaller molecules.

The data presented define the conditions at which a cosolvent-CO₂ system can be operated as a single supercritical phase, and provide the basis to choose meaningful system conditions for supercritical CO₂-entrainer solubility determinations.

Acknowledgement

The authors gratefully acknowledge the valuable and constructive comments made by Professor K. D. Luks regarding this work. Financial support from the Australian Research Council and the Australian Government under the auspices of the GIRD programme is also gratefully acknowledged.

Literature Cited

1. Kay, W. B. *Acc. Chem. Res.*, **1968**, *1*, pp 344.
2. Teja, A. S.; Smith, R. L. In *Chemical Engineering at Supercritical Conditions*; Paulaitis, M. E., Penninger, J. M. L., Gray, R. D., Davidson, P., Eds.; Ann Arbor Science: Ann Arbor, MI, **1983**, pp 341-357.
3. Joshi, D. K. and Prausnitz, J. M. *AIChE J.*, **1984**, *30*, pp 522.
4. Leland, T. W. and Chappellear, P. S. *Ind. Eng. Chem.*, **1968**, *60*, pp 15.
5. McHgh M. A.; Paulaitis, M. E. *J. Chem. Eng. Data* **1980**, *25*, pp 326.
6. Kurnik, R. T.; Holla, S. M.; Reid, R. C. *J. Chem. Eng. Data* **1981**, *26*, pp 47.
7. Johnston, K. P.; Ziger, D. H.; Eckert, C. A. *Ind. Eng. Chem. Fundam.* **1982**, *21*, pp 191.

8. Schmitt, W. J.; Reid, R. C. *J. Chem. Eng. Data* **1986**, *31*, pp 204.
9. King, M. B.; Alderson, D. L.; Fallah, F. H.; Kassin, D. M.; Kassim, K. M.; Sheldon, J. R.; Mahmud, R. S. In *Chemical Engineering at Supercritical Conditions*, Paulaitis, M. E.; Penninger, J. M. L.; Gray, R. D., Jr.; Davidson, P. A. Eds., Ann Arbor Science, Ann Arbor, MI., **1983**, pp 31-80.
10. McHugh, M. A.; Mallett, M. W.; Kohn, J. P. In *Chemical Engineering at Supercritical Conditions*, Paulaitis, M. E.; Penninger, J. M. L.; Gray, R. D., Jr.; Davidson, P. A. Eds., Ann Arbor Science, Ann Arbor, MI., **1983**, pp 113-137.
11. Schmitt, W. J.; Reid, R. C. *Fluid Phase Equilib.* **1986**, *32*, pp 77.
12. Dobbs, J. M.; Wong, J. M.; Johnston, K. P. *J. Chem. Eng. Data* **1986**, *31*, pp 303.
13. Dobbs, J. M.; Wong, J. M.; Lahiere, R. J.; Johnston, K. P. *Ind. Eng. Chem. Res.* **1987**, *26*, pp 56.
14. Dobbs, J. M.; Johnston, K. P. *Ind. Eng. Chem. Res.* **1987**, *26*, pp 1476.
15. *The Properties of Gases and Liquids*; Reid, R. C.; Prausnitz, J. M. Pauling, B. E., Eds.; McGraw-Hill: NY, **1987**.
16. *IUPAC International Thermodynamics of the Fluid State-Carbon Dioxide*; Angus, S.; Armstrong, B., deReuck, K. M. Eds.; Pergamon: Oxford, **1976**.
17. Poettmann, F. H.; Katz, D. L. *Ind. Eng. Chem.* **1945**, *37*, pp 847.
18. Lam, D. H.; Jangkamolkulchai, A.; Luks, K. D. *Fluid Phase Equil.*, **1990**, *60*, pp 131.

RECEIVED April 27, 1992

Chapter 4

Three-Phase Behavior in Binary Mixtures of Near-Critical Propane and Triglycerides

E. J. M. Straver, J. L. de Roo, C. J. Peters, and J. de Swaan Arons

Department of Chemical Engineering and Materials Science, Laboratory of Applied Thermodynamics and Phase Equilibria, Delft University of Technology, Julianalaan 136, 2628 BL Delft, Netherlands

This contribution reports on the three-phase behavior liquid-liquid-vapor (l_1l_2g) in binary mixtures of near-critical propane and triglycerides. The triglycerides, investigated in this work, range in carbon number from 51 (tripalmitin) up to 57 (tristearin). Using a Cailletet apparatus the three-phase equilibria, including the lower and upper critical endpoints (LCEP and UCEP), were measured. A comparison of the experimental results with earlier measurements of three-phase equilibria l_1l_2g in near-critical propane and heavy normal paraffins lead to some interesting conclusions. It was established that the length of the three-phase region

$\Delta T = T(\text{UCEP}) - T(\text{LCEP})$ in binaries of triglycerides and normal paraffins with the same carbon number is identical. This suggests that the three-phase behavior in the binaries of triglycerides is no longer influenced by the presence of functional groups and branching of the triglyceride molecules.

Carbon dioxide and propane both have been studied as near-critical solvents for the recovery, purification and fractionation of vegetable oils, animal fats and fish oils; see for example McHugh and Krukonis (1), Lee et al. (2), Eggers et al. (3) and del Valle and Aguilera (4). The interest stems of course from the special features of near-critical solvents: both product and residue can be obtained in a highly pure state due to the very high volatility of the solvent at reduced pressures. A significant advantage of the use of highly volatile solvents, in comparison with solvents like liquid hexane, is the strongly reduced presence of minute amounts of the solvent in the product. Although carbon dioxide is attractive for its relative inertness, propane is of special interest as a solvent for various reasons:

0097-6156/93/0514-0046\$06.00/0
© 1993 American Chemical Society

- its critical point is at conditions where most oils are liquids with an appreciable volatility;
- oils mainly have a paraffinic nature and consequently are more related to propane than to carbon dioxide.

In addition to the latter point it is known that (Peters et al. (5)) binary mixtures of near-critical propane and normal paraffins with a carbon number higher than 29, show liquid-liquid immiscibility, whereas binary mixtures of carbon dioxide and normal paraffins already show this phenomenon at a carbon number higher than 6. For details on the behavior of propane as a near-critical solvent for paraffinic and polyaromatic hydrocarbons one is referred to Peters et al. (5,6).

Similarly as mineral oils, edible oils are natural products also with a complex composition. From techniques used in the mineral oil industry it is known that broad ranges of components can be characterized in their behavior by selecting a limited number of key components. For example Cotterman et al. (7,8) discussed how from a selection of a limited number of key components predictions for multicomponent mixtures can be obtained. It is to be expected that for the prediction of the behavior of edible oils a similar approach will be applicable. Therefore, the current research also contributes to the knowledge of the selection of suitable key components for edible oils. Some details on this aspect of the current study were already discussed by Straver et al. (9). Previously Coorens et al. (10) reported on the phase behavior of the binary propane + tripalmitin (PPP). Recently Peters et al. (11) and Straver et al. (12) determined experimentally the phase behavior of the binary propane + triolein (OOO) and propane + tristearin (SSS) respectively.

In this study we will focus on the three-phase behavior liquid-liquid-vapor (l_1l_2g) of binaries of near-critical propane and pure triglycerides. In particular it will be investigated how this three-phase behavior compares with similar phase behavior, reported earlier by Peters et al. (5), in binaries of near-critical propane and normal paraffins with a comparable number of carbon atoms. For that purpose this three-phase behavior was determined experimentally in the propane binaries of tripalmitin (PPP), α -stearodipalmitin (SPP), α -palmitodistearin (PSS) and tristearin (SSS).

Phase Behavior

The fluid phase behavior occurring in binaries of propane and triglycerides is of type V in the classification of Van Konynenburg and Scott (13). This type of phase behavior was first recognized by Kuenen (14). More recently, detailed discussions on this type of phase behavior were given by Diepen (15), Luks (16), Peters (17) and Peters et al. (18). The characteristics of this type of phase behavior will be recalled here only briefly. Figure 1 shows a schematical p,T,x-projection for propane binaries of triglycerides, including the presence of the solid phase of the triglyceride. From Figure 1 it can be seen that in this type of phase behavior partial miscibility in the liquid phase occurs, i.e. in the near-critical region of propane a three-phase equilibrium l_1l_2g exists. This three-phase equilibrium starts in the lower critical endpoint (LCEP) and

American Chemical Society
Library

In Supercritical Fluid Engineering Science: Kiran, E., et al.;
ACS Symposium Series 500, American Chemical Society: Washington, DC, 1992.

terminates in the upper critical endpoint (UCEP). Figure 1 also shows that the critical locus is separated into two branches. One branch originates in the LCEP of the 1_11_2g -equilibrium and, via a maximum in pressure, terminates in the critical point of the pure triglyceride. The other branch originates in the critical point of propane and ends in the UCEP of the 1_11_2g -equilibrium. For a detailed discussion on this type of phase behavior one is also referred to Peters et al. (19,20).

Experimental

The experimental work was carried out in a high pressure Cailletet equipment. In this equipment pressures up to approximately 15 MPa can be achieved and temperatures from 250 K up to 450 K can be attained. This equipment was discussed in the literature by Van der Kooi (21) and De Loos et al. (22). The experimental procedures used were quite similar as discussed previously by Peters et al. (23,24) in their studies on the binaries ethane + pentacosane and ethane + tetracosane, respectively. In addition detailed information on the experimental procedures was also given by Van der Kooi (21), Peters (17) and Coorens et al. (10).

The temperature in the experimental work could be measured with an accuracy of 0.02 K and the pressure could be determined within 0.002 MPa. The purity of the propane used was 99.95 mole % and was checked by measuring its saturated vapor pressure curve. Excellent agreement with data of Goodwin and Haynes (25) was obtained. All other chemicals had a minimum purity of at least 99.0 mole % and were used without further purification.

Experimental Results

In Table I the experimental data of the three-phase equilibria 1_11_2g of the four binaries, investigated in this work, are summarized.

Table II summarizes the data of the critical endpoints separately. In general it appeared to be possible to determine the complete three-phase region on samples with an overall composition of approximately 2 mole %. Because it was not possible to sample the coexisting phases, the composition of these phases could not be determined.

Discussion and Conclusions

As a result of earlier work, Peters et al. (5), the conjectures of Rowlinson and Freeman (26) and Rowlinson and Swinton (27), that mixtures of propane and n-alkanes will not demix for carbon numbers less than 37 or 39, were found to be incorrect. Experimentally a three-phase equilibrium was already established in the propane binary of dotriacontane, i.e. a normal paraffin with a carbon number as low as 32. This finding was also in disagreement with that of Leder

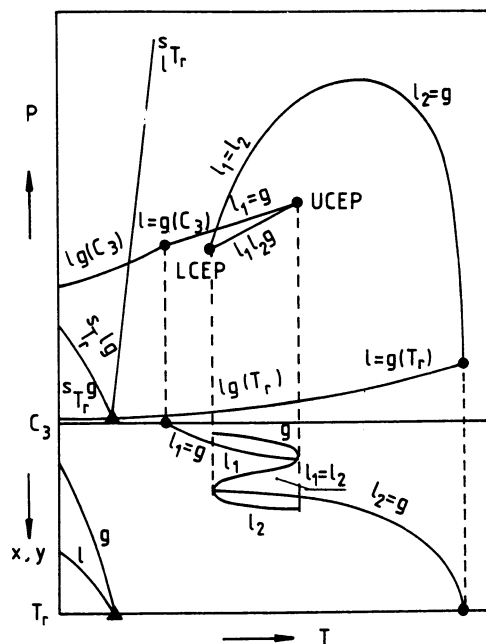


Figure 1. Schematical p,T,x -projection of the phase behavior of binary mixtures of propane and triglycerides.

Table I. Experimental results of the three-phase behavior l_1l_2g in binary systems of near-critical propane and triglycerides

PPP		SPP		PSS		SSS	
T/K	p/MPa	T/K	p/MPa	T/K	p/MPa	T/K	p/MPa
348.99	2.876	346.72	2.770	344.93	2.660	343.10	2.574
349.48	2.900	347.25	2.797	345.00	2.665	343.20	2.579
350.11	2.940	350.22	2.959	345.95	2.709	343.52	2.594
352.07	3.036	354.21	3.191	348.80	2.870	345.48	2.693
357.04	3.336	358.21	3.443	350.81	2.977	346.03	2.733
359.39	3.481	362.21	3.701	353.69	3.150	348.01	2.843
360.78	3.590	366.22	3.988	355.67	3.266	350.44	2.965
361.01	3.610	370.20	4.277	358.58	3.460	352.91	3.126
362.33	3.676			360.52	3.574	355.42	3.259
364.46	3.831			363.45	3.780	357.88	3.422
368.77	4.147			365.37	3.908	360.41	3.574
369.23	4.182			368.32	4.131	362.85	3.750
369.75	4.217			369.76	4.240	365.20	3.902
369.91	4.249			370.14	4.264	367.84	4.105
370.03	4.251					369.82	4.253
370.31	4.258					370.11	4.268

Table II. LCEP'S and UCEP'S of the three-phase equilibria l_1l_2g in binary systems of near-critical propane and triglycerides

TRIGLYCERIDE	LCEP		UCEP	
	T/K	p/MPa	T/K	p/MPa
PPP	348.99	2.876	370.31	4.258
SPP	346.72	2.770	370.20	4.277
PSS	344.93	2.660	370.14	4.264
SSS	343.10	2.574	370.11	4.268

et al. (28), who found no liquid-liquid immiscibility in the propane binary of a normal paraffin with a carbon number of 36. For the propane + normal paraffin systems Figure 2 shows the temperatures of the UCEP's and LCEP's as a function of the carbon number. The experimental data of the three-phase equilibria, including the critical endpoints, can be found elsewhere (Peters et al. (5)).

It is known from the classical theory of tricritical points, as discussed by Griffiths (29) and Scott (30), that the $2/3$ power of the temperature region $\Delta T = T(\text{UCEP}) - T(\text{LCEP})$ of the three-phase region is proportional to the carbon number. The group of Scott, Knobler and collaborators found no departures from linearity in the ethane systems, but their range of carbon numbers was restricted. However, Figure 3 shows that in the propane systems for carbon numbers less than 40 also linearity is observed, but nonlinear behavior is observed for carbon numbers beyond 40.

Figure 4 is similar to Figure 2, but now the LCEP's and UCEP's (open triangles) of the three-phase equilibria l_1l_2g of the propane binaries of the triglycerides have been included. The open circles represent the critical endpoints of the propane systems with the normal paraffins, whereas the open triangles are the critical endpoints of the propane systems with the triglycerides. The black triangles are LCEP's measured by Hixson and Bockelmann (31). Figure 5 is similar to Figure 3, but now the ΔT -data of the propane systems of the triglycerides (open triangles) have been included.

From both Figure 4 and 5 it can be seen that the open triangles (data of the triglyceride systems) are a continuous extension of the loci connecting the open circles (data of the normal paraffin systems). This suggests that the three-phase behavior l_1l_2g of the propane systems of the triglycerides is identical to that of the propane systems of the normal paraffins with the same carbon number. Due to the presence of long aliphatic chains in the triglyceride molecules, the influence of the functional groups of these molecules no longer plays a role in the occurrence of the three-phase equilibrium l_1l_2g . Also it should be recognized that a triglyceride molecule can be considered as a branched paraffin and that this fact apparently does not cause deviation from the three-phase behavior in comparison to that of the normal paraffins. Hence, in conclusion, it can be established that triglyceride molecules with carbon numbers beyond 50 have similar three-phase behavior l_1l_2g in near-critical propane as normal paraffins with the same carbon number.

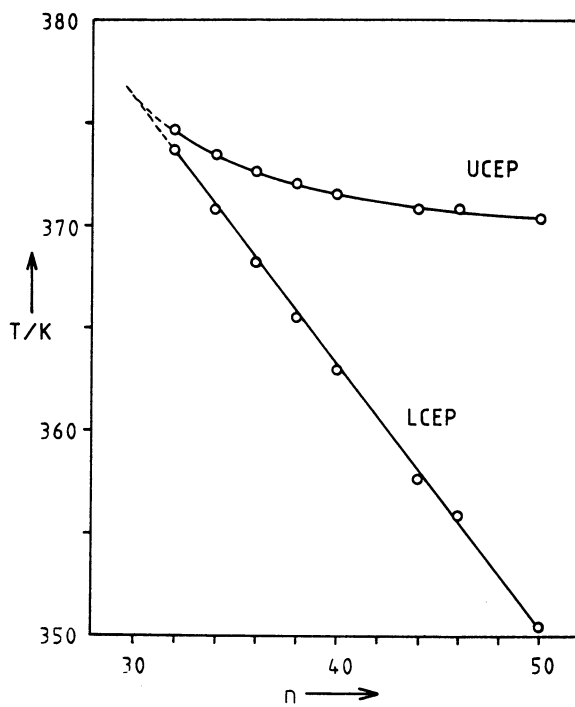


Figure 2. Experimental data of the LCEP's and UCEP's of propane binaries with normal paraffins. Full curves are best fits to the experimental data.

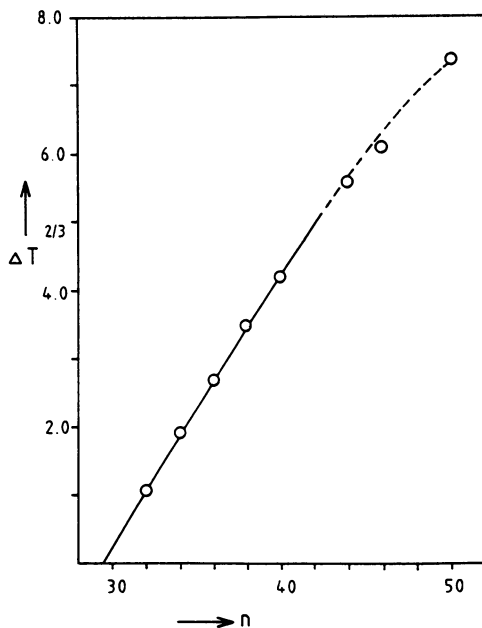


Figure 3. Plot of $\Delta T^{2/3}$ versus carbon number n of the three-phase region of propane binaries of normal paraffins.

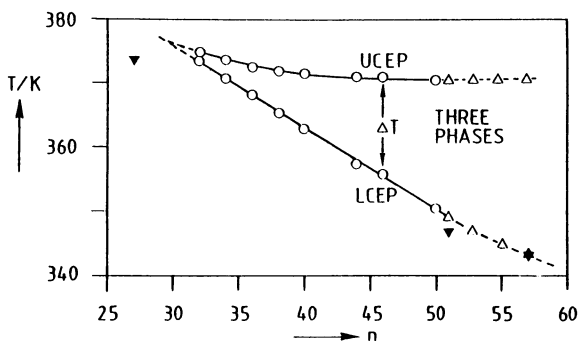


Figure 4. Experimental data of the LCEP's and UCEP's of propane binaries with normal paraffins (open circles) and triglycerides (open triangles). Black triangles are LCEP's taken from Hixson and Bockelmann (31). Full curves are best fits to the experimental data.

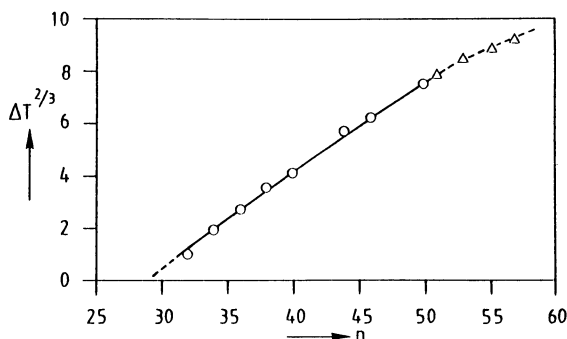


Figure 5. Plot of $\Delta T^{2/3}$ versus carbon number n of the three-phase region of propane binaries of normal paraffins (open circles) and triglycerides (open triangles).

Acknowledgement

The authors gratefully acknowledge the supply of the pure triglycerides by Unilever Research, Vlaardingen (The Netherlands).

Literature Cited

1. McHugh, M.; Krukoni, V.; *Supercritical fluid extraction*. Butterworth, London, England, 1986.
2. Lee, A.K.K.; Bulley, N.R.; Fattori, M.; Meisen, A.; *J. Am. Chem. Soc.* **1986**, *63*, 921.
3. Eggers, E.; Sievers, U.; Stein, W.; *J. Am. Chem. Soc.* **1985**, *62*, 1222.
4. Valle, J.M. del; Aguilera, J.M.; *Ind. Eng. Chem. Res.* **1988**, *27*, 1551.
5. Peters, C.J.; Kooi, H.J. van der; Roo, J.L. de; Swaan Arons, J. de; Gallagher, J.S.; Levelt Sengers, J.M.H.; *Fluid Phase Equilibria* **1989**, *51*, 339.
6. Peters, C.J.; Rijkers, M.P.W.M.; Roo, J.L. de; Swaan Arons, J. de; *Fluid Phase Equilibria* **1989**, *52*, 373.
7. Cotterman, R.L.; Dimitrelis, D.; Prausnitz, J.M.; *Ber. Bunsen Physik. Chem.* **1984**, *87*, no 9.
8. Cotterman, R.L.; Bender, R.; Prausnitz, J.M.; *Ind. & Eng. Chem. Fund.* **1985**, *24*, 194.
9. Straver, E.J.M.; Roo J.L. de; Peters, C.J.; Swaan Arons, J. de; *Proceedings 2nd International Symposium on Supercritical Fluids*, Boston, Massachusetts, U.S.A., **1991**, 482.
10. Coorens, H.G.A.; Peters, C.J.; Swaan Arons, J. de; *Fluid Phase Equilibria* **1988**, *40*, 135.
11. Peters, C.J.; Roo, J.L. de; Swaan Arons, J. de; *Fluid Phase Equilibria* **1993**, in preparation.
12. Straver, E.J.M.; Peters, C.J.; Swaan Arons, J. de; *Fluid Phase Equilibria*, **1993**, in preparation.

13. Konynenburg, P.H. van; Scott, R.L.; *Phil. Trans. of the Roy. Soc. (London)* **1980**, 298, 495.
14. Kuehnen, J.P.; *Theorie der Verdampfung und Verflüssigung von Gemischen und der fraktionierten Destillation*. Verlag von Johann Ambrosius Barth, Leipzig, Germany, **1906**.
15. Diepen, G.A.M.; *De oplosbaarheid van vaste stoffen in superkritische gassen*. Ph. D. Thesis: Delft University of Technology, The Netherlands, **1947**.
16. Luks, K.D.; *Proc. 2nd Int. Conf. on Phase Equilibria and Fluid Properties in the Chemical Industry*, West-Berlin, **1980**.
17. Peters, C.J.; *Phase behavior of binary mixtures of ethane + n-eicosane and statistical mechanical treatment of fluid phases*. Ph. D. Thesis: Delft University of Technology, The Netherlands, **1986**.
18. Peters, C.J.; Lichtenthaler, R.N.; Swaan Arons, J. de; *Fluid Phase Equilibria* **1986**, 29, 495.
19. Peters, C.J.; Roo, J.L. de; Lichtenthaler, R.N.; *Fluid Phase Equilibria* **1987**, 34, 287.
20. Peters, C.J.; Spiegelaar, J.; Swaan Arons, J. de; *Fluid Phase Equilibria* **1988**, 41, 245.
21. Kooi, H.J. van der; *Metingen en berekeningen aan het systeem methaan - n-eicosaan*. Ph. D. Thesis: Delft University of Technology, The Netherlands, **1981**.
22. Loos, Th. W. de; Kooi, H.J. van der; Poot, W.; Ott, P.L.; *Delft Progr. Rep.* **1983**, 8, 200.
23. Peters, C.J.; Roo, J.L. de; Swaan Arons, J. de; *J. Chem. Therm.* **1987**, 19, 265.
24. Peters, C.J.; Kooi, H.J. van der; Swaan Arons, J. de; *J. Chem. Therm.* **1987**, 19, 395.
25. Goodwin, R.D.; Haynes, W.M.; *Thermodynamic properties of propane from 85 to 700 K at pressures to 70 MPa*: NBS Monograph 170, US Department of Commerce, NBS, **1982**.
26. Rowlinson, J.S.; Freeman, P.I.; *Pure Appl. Chem.* **1961**, 2, 329.
27. Rowlinson, J.S.; Swinton, F.L.; *Liquids and liquid mixtures*. **1982**, London, England.
28. Leder, F.; Irani, C.A.; McHenry, J.A.; *AIChE J.* **1976**, 22, 199.
29. Griffiths, R.B.; *J. Chem. Phys.* **1974**, 60, 195.
30. Scott, R.L.; *J. Chem. Phys.* **1987**, 86, 4106.
31. Hixson, A.W.; Bockelman, J.B.; *Trans. Am. Chem. Eng.* **1942**, 38, 891.

RECEIVED May 14, 1992

Chapter 5

Multiphase Equilibrium Behavior of a Mixture of Carbon Dioxide, 1-Decanol, and *n*-Tetradecane

C. L. Patton, S. H. Kisler, and K. D. Luks

Department of Chemical Engineering, The University of Tulsa,
Tulsa, OK 74104-3189

The liquid-liquid-vapor (llg) phase equilibrium behavior of the mixture CO₂ + 1-decanol + *n*-tetradecane was experimentally studied using a visual cell (stoichiometric) technique with pressure discrimination of ± 0.01 bar, achieved by coupling a dead weight gauge to the cell pressure transducer. The portion of the three-phase surface of the ternary system examined is bounded by the llg loci of the binary mixtures CO₂ + 1-decanol and CO₂ + *n*-tetradecane and from above by an upper critical end point (1-1-g) locus. Phase compositions and molar volumes are reported for the two liquid phases along the 298.15 K isotherm. This three-phase llg surface is unusual in that it has a two-phase (lg) "hole" in it which is completely bounded by 1-1-g critical end points. A rationale for the occurrence of this hole in the llg surface is offered.

During the past several years, our group has been engaged in the study of liquid-liquid-vapor (llg) phase equilibria in well-defined systems such as CO₂ + hydrocarbon, ethane + hydrocarbon and nitrous oxide + hydrocarbon binary mixtures, where the hydrocarbon has frequently been one of the members of the homologous series of *n*-paraffins or *n*-alkylbenzenes. The goals of these studies were to map out the patterns of the multiphase equilibria of these prototype mixtures in thermodynamic phase space and to generate phase equilibrium data that would support the prediction of phase equilibria within and near regions of llg immiscibility.

With the studies of these essentially nonpolar systems as a point of reference, we have undertaken a series of studies of the multiphase equilibria of binary mixtures composed of both polar and nonpolar species. Studies were performed on the llg immiscibility behavior of certain members of the homologous series of ethane + 1-alkanol, CO₂ + 1-alkanol, and nitrous oxide + 1-alkanol binary mixtures (1-3). More

0097-6156/93/0514-0055\$06.00/0
© 1993 American Chemical Society

recently, boundaries and liquid phase properties of the llg surface for the ternary mixture ethane + methanol + 1-decanol were reported (4). This system has a "fold" in its llg surface when projected onto pressure-temperature coordinates. The presence of a fold in such ternary systems where the solutes are relatively nonvolatile in the gas solvent has implications with respect to the separability function of the solutes between the two liquid phases, often marking a shift in that function across the value of unity at the fold (5,6).

In this present study, the goals are to map out the three-phase llg region for a system composed of the gas solvent CO₂ and the solutes 1-decanol and n-tetradecane and examine the separability of the solutes between the two liquid phases. The solutes are respectively polar and nonpolar in nature, although the size of the paraffinic part of 1-decanol diminishes to some degree the influence of its dipole moment [This decrease in influence of the hydroxyl group with chain length in 1-alkanols has been discussed by Teja et al. (7)]. The solutes are similarly llg-immiscible with CO₂, with their respective llg loci located just below the CO₂ vapor pressure curve in pressure-temperature space and extending from a sllg point upwards to an UCEP (l-l=g) point.

For CO₂ + 1-decanol, the sllg point is at 32.14 bar, 270.54 K (2), and the UCEP is at 77.48 bar, 307.15 K. For CO₂ + n-tetradecane, the sllg point is at 30.82 bar, 269.10 K (8), and the UCEP is at 82.54 bar, 311.15 K. The binary UCEP's cited here were measured in this present study and are close to the values reported by Lam et al. (2) and Hottovy et al (8). Studies of the binary llg system CO₂ + n-tetradecane have also been performed by van der Steen et al. (9) and Laugier et al. (10). The n-tetradecane appears to exhibit higher volatility than 1-decanol in the configuration of a CO₂-rich llg binary system. At a given temperature, the llg pressure for CO₂ + n-tetradecane is less than that of CO₂ + 1-decanol, as much as 1.5 bar less at about 307 K. The ternary llg surface has a fold when projected onto pressure-temperature coordinates.

Reported in this study are the P-T loci of the ternary UCEP's and the critical end points l=l-g that bound the two-phase lg hole in the llg surface. Also reported is the barotropic inversion locus where the ρ_1 and ρ_2 mass densities are identical. At temperatures below this locus, the CO₂-rich ρ_1 phase is denser than the solute-rich ρ_2 phase. Compositions and molar volumes for the two liquid phases are reported at T = 298.15 K.

Experimental

A detailed description of the apparatus is given in Fall and Luks (11) and is updated in Jangkamolkulchai and Luks (12). The experimental procedure employs a volumetrically calibrated visual glass equilibrium cell with a typical total volume of 8 to 9 cm³. Known amounts of 1-decanol and n-tetradecane are loaded in the cell, at which time the vapor space is thoroughly flushed with CO₂. Measured amounts of CO₂ are added to the cell from a high-pressure bomb. The cell contents are then brought to equilibrium by a magnetically actuated steel ball stirrer.

Mass balances for conjugate measurements at a given temperature and pressure are used to calculate the compositions and molar volumes. The conjugate measurements herein are respectively dominant (volumetrically) in each of the liquid phases ρ_1 and ρ_2 . (Since n-tetradecane and 1-decanol are relatively non-volatile, the vapor phase

is assumed to be pure CO₂; thus, only l₁- and l₁-dominant measurements are employed.) The cell temperature was measured with a Pt-resistance thermometer to an estimated accuracy of ± 0.02 K. Pressures were measured with a precision of ± 0.01 bar using pressure transducers calibrated with a dead-weight gauge after each experiment. Phase volumes in the visual cell were determined using a cathetometer to an accuracy of ± 0.005 cm³.

The 1-decanol and n-tetradecane were obtained from Aldrich Chemical Co. with a stated purity of 99+ mol %. Chromatographic analyses of these solutes were consistent with the stated purity. No further purification was performed.

The CO₂ was purchased from Air Products and Chemicals, Inc. as "Coleman Grade" with a stated purity of 99.99 mol %. The CO₂ was first transferred to an evacuated storage bomb immersed in an ice bath. The vapor phase was vented to remove any light gas impurities. The purity was verified by liquefying the CO₂ at 298.15 K. The vapor pressure at this temperature was within 0.03 bar of that reported by Vargaftik (13). In addition, the critical temperature and pressure were within 0.06 K and 0.03 bar of those reported by Vargaftik (13). Single-phase CO₂ data were obtained from Angus et al. (14) for performing necessary stoichiometric computations.

Results

Figure 1 is a projection of the ternary llg surface onto pressure-temperature space. The pressure coordinate is represented by the difference between the actual pressure and the pure CO₂ vapor pressure (extrapolated above the critical temperature, if necessary). Experimental data corresponding to (1) the l-l=g boundary, (2) a lg hole bounded by l-l-g points, and (3) a locus of barotropic inversion points (i.p.) in Figure 1 are presented in Table I. The llg surface is bounded compositionally by the two binary llg loci for CO₂, n-tetradecane and CO₂ + 1-decanol, and from above (temperature-wise) by the ternary l-l-g locus. No data were taken on the sllg-type boundaries that would terminate the llg surface from below. The temperatures and pressures of the critical end points l-l=g and l-l-g are estimated (by our experience) to be precise to ± 0.05 K and ± 0.03 bar respectively. Figure 2 is a plot of the lg hole in terms of temperature and the mole fraction X of n-tetradecane on a CO₂-free basis. Since the two solutes are essentially nonvolatile at the temperatures of the lg hole and l₁=l₁-g is the nature of the critical end points bounding the lg hole, the values of X will be virtually identical with the loadings of the solutes, which are performed outside the experimental bath using a scale sensitive to ± 0.00001 g and reliable to at least ± 0.0001 g. Thus the values of X in Table I and Figure 2 should be precise to at least ± 0.001 for the unstable liquid phase at the boundary of the lg hole.

The barotropic inversion points in Table I and Figure 1 for the ternary system extend from about 283 to 293 K. Temperatures and pressures for these points are difficult to determine accurately since the equal densities of the two liquid phases naturally prevents these phases from settling out separately. Thus, the data in Table I for this locus should be considered as rough estimates. The locus is in two parts, being interrupted by the lg hole presented above. A barotropic inversion of the liquid phases had been reported earlier at about 283 K for the binary llg system CO₂ + 1-decanol (3) and at 293 K for the

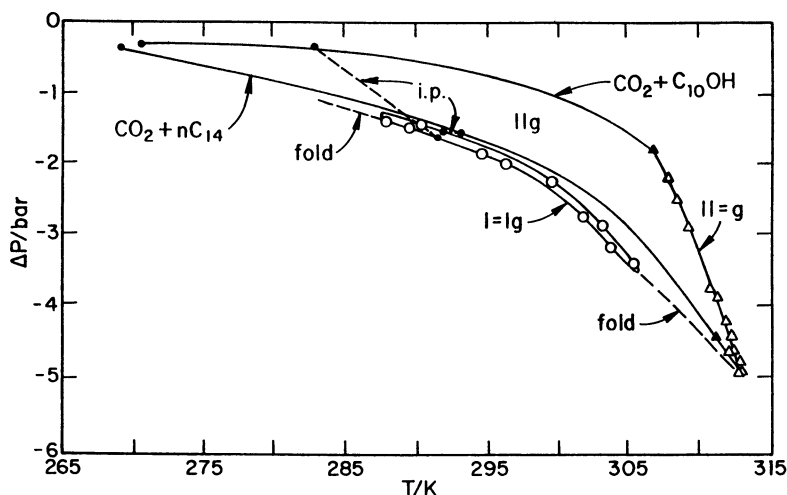


Figure 1. A projection in pressure-temperature space of the ternary llg surface for the mixture CO_2 + n-tetradecane (nC_{14}) + 1-decanol (C_{10}OH). The pressure coordinate is expressed as the difference between the pure CO_2 vapor pressure (extrapolated if necessary) and the actual pressure. Triangles denote the l-1=g points (filled for the binary mixtures). Open circles denote the l=1-g points bounding the two-phase lg hole in the surface. The dashed lines labeled i.p. denote the two parts of the barotropic inversion locus.

Table I. Temperature T and Pressure P Raw Data for the Liquid-Liquid-Vapor Barotropic Inversion and Critical End Point Boundary Loci for the Ternary Mixture CO_2 + Tetradecane + 1-Decanol

Barotropic Inversion		l=1-g			l-1=g	
T/K	P/bar	T/K	P/bar	X(C_{14})	T/K	P/bar
283.60	45.02	296.46	59.60	.7360	307.15	77.48 ^a
284.43	45.87	294.71	57.25	.7576	308.11	78.77
285.30	46.39	289.84	51.26	.8099	308.45	79.14
285.46	46.82	288.26	49.44	.8758	309.34	80.32
285.89	47.21	290.42	52.01	.9099	310.83	82.47
286.80	48.18	299.46	63.84	.9099	311.34	83.32
287.65	49.03	303.47	69.68	.8758	311.82	84.00
289.06	50.63	305.51	72.71	.8099	312.15	84.50
289.14	50.61	303.89	70.13	.7576	312.46	84.96
290.40	52.12	302.24	67.73	.7360	312.58	85.05
290.78	52.43				312.89	85.60
291.56	53.32				312.91	85.59
292.01	53.83				312.86	85.49
293.24	55.52				312.05	84.09
293.48	55.98				311.15	82.54 ^b

^a binary system CO_2 + 1-decanol

^b binary system CO_2 + n-tetradecane

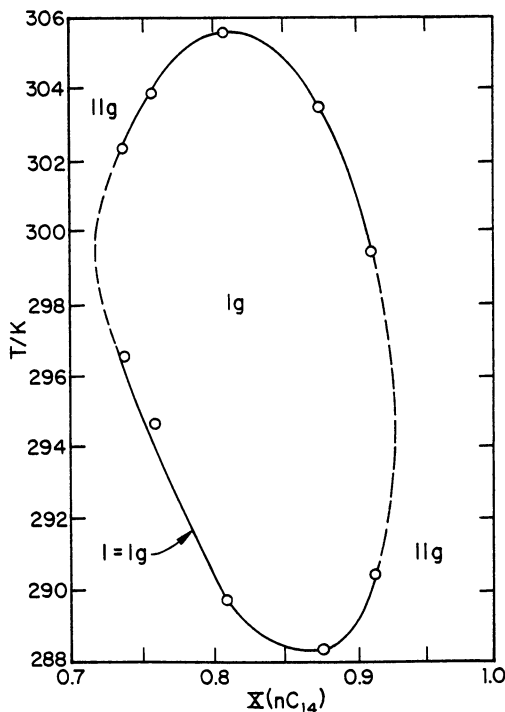


Figure 2. Temperature versus n-tetradecane mole fraction (on a CO_2 -free basis) for the l_1 - l - g points bounding the lg hole in the ternary llg surface.

binary system CO_2 + n-tetradecane (9); the existence of the latter inversion point can also be inferred from the data of Hottovy et al. (8) and Laugier et al. (10).

Table II reports the compositions and molar volumes of the two liquid phases along the 298.15 K isotherm. Figures 3-5 are graphical representations of the same data. This isotherm is in two parts, since it crosses the lg hole, with each piece extending from a binary llg boundary to a l_1 - l - g critical end point. The mole fractions of CO_2 reported for the l_1 and l phases are considered good to ± 0.004 and ± 0.002 respectively. The mole fractions X for the liquid phases are considered good to ± 0.01 . The molar volumes for the l_1 and l phases are considered good to ± 0.4 $cm^3 \cdot g^{-1}$. These estimates are conservative, being based on the average absolute deviations (AAD's) of the raw data from the smoothed curves shown in Figures 3-5. The AAD's are typically 2/3 the magnitude of the above stated uncertainties.

Remarks

A unique feature of this ternary llg surface is that it has a lg hole enclosed by l_1 - l - g critical end points. Given the plot in Figure 2, one can identify CO_2 -free compositions of the solutes with accompanying

Table II. Liquid Phase l_1 and l_2 Compositions and Molar Volumes as a Function of Pressure for the Liquid-Liquid-Vapor Region of CO_2 + n-Tetradecane + 1-Decanol at 293.15 K

P/bar	l_1 Phase			l_2 Phase			
	X(c_{11})	x(CO_2)	v/(cm ³ /g-mol)	P/bar	X(c_{11})	x(CO_2)	v/(cm ³ /g-mol)
63.41	.0000	.6153	100.4	63.41	.0000	.9902	58.3
63.16	.0647	.6315	100.5	63.36	.0207	.9919	58.9
62.97	.0978	.6321	103.0	63.24	.0801	.9905	58.3
62.80	.1475	.6281	108.6	63.12	.1767	.9886	58.9
62.63	.2033	.6416	113.7	62.97	.2522	.9834	58.4
62.61	.2102	.6408	112.9	62.91	.3181	.9885	58.2
62.48	.2753	.6533	118.3	62.72	.4156	.9850	57.8
62.36	.3238	.6540	118.6	62.64	.4303	.9841	58.3
62.25	.3795	.6803	114.6	62.47	.4749	.9794	57.9
62.22	.4058	.7021	110.5	62.30	.5130	.9758	57.3
62.14	.4576	.7463	97.1	62.19	.5861	.9749	57.2
62.08	.5022	.7813	90.4	62.17	.5688	.9742	56.1
62.02	.5703	.7958	88.2	62.05	.6009	.9661	58.4
61.94	.6024	.8179	83.2	61.97	.6611	.9590	60.4
61.92	.6379	.8476	80.9	61.93	.6691	.9544	61.1
61.90	.6795	.8486	80.2	62.16	.9545	.9595	61.8
62.05	.9404	.8808	74.7	62.20	.9649	.9622	61.5
62.14	.9643	.8614	79.3	62.26	.9814	.9646	60.7
62.30	1.0000	.8351	83.5	62.30	1.0000	.9681	60.3

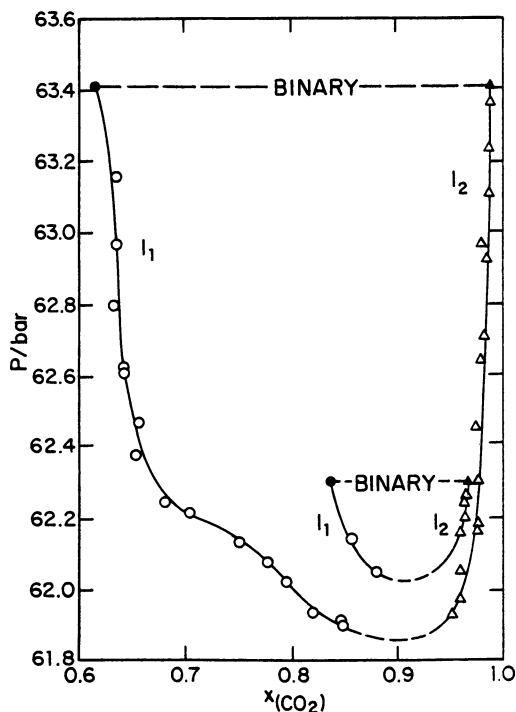


Figure 3. Pressure versus CO_2 mole fraction for the l_1 and l_2 phases at 298.15 K.

temperatures (or pressures) as states that are double critical end points (DCEP). These compositions are $X = 0.717$ at 299.5 K (61.9 bar) and $X = 0.951$ at 295.2 K (62.0 bar). We offer the following explanation, from a van der Waals viewpoint, for the occurrence of this lg hole.

Figure 6 is a schematic diagram of the occurrence of llg behavior for a solvent + a homologous series of solutes, such as n-paraffins or 1-alkanols. The diagram is based on the study of van Konynenburg and Scott (15) as interpreted by Miller and Luks (5). van Konynenburg and Scott's ordinate would be the van der Waals a-parameter. Herein, in this schematic, we simply use "size", assuming that the a-parameter would increase with molecular size in a homologous series. Also we have added the truncation of the llg region by the formation of a solid phase (as a slg locus), which does occur in reality, but is not directly obtainable from van der Waals' equation-of-state. Such pictures based on experimental data have been presented for the homologous series of mixtures CO_2 + n-paraffins by Miller and Luks (5) and for CO_2 + 1-alkanols by Lam et al. (3). Using these two references, we have placed on the schematic diagram, Figure 6, the relative locations of the binary systems CO_2 + n-tetradecane (" nC_{14} ") and CO_2 + 1-decanol (" $C_{10}OH$ ") as members of their respective homologous series of mixtures. The llg surface of a ternary mixture of CO_2 + n-tetradecane + 1-decanol would be expected to span between these two binary llg loci.

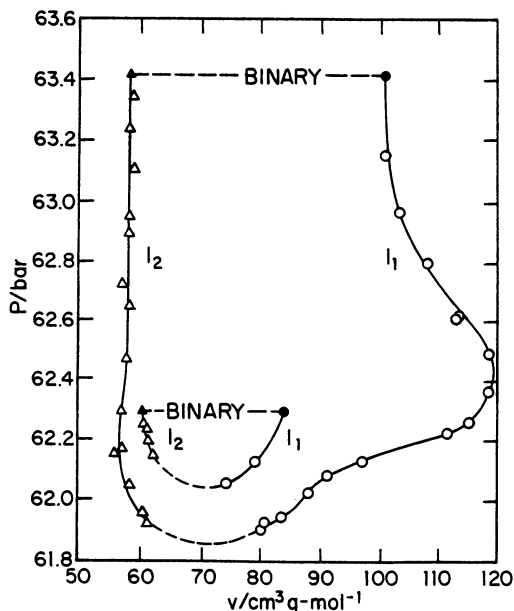


Figure 4. Pressure versus molar volume for the l_1 and l_2 phases at 298.15 K.

The dashed line labeled $T = T_c$ is meant to represent the nature of an isotherm in terms of apparent solute size as we understand it for, say, 298.15 K for a ternary mixture with two solutes. We have a minimum (fold) in the surface; at 298.15 K, it occurs in the two-phase lg region, or hole. There is enough hydrogen bonding in 1-decanol to make it llg -immiscible with CO_2 , even more llg -immiscible than CO_2 + n-tetradecane, given that CO_2 + n-tridecane has a llg locus in two parts (16,17). As 1-decanol solute is added to the n-tetradecane solute, the hydrogen bonding that can take place when the 1-decanol is dilute is more than countered by the decrease in the average chain length of the solute mixture. The solute mixture begins to look essentially like n-tridecane with its two llg branches, thereby creating a hole in the llg surface. The lg hole grows as 1-decanol is added, but then decreases as the concentration of the 1-decanol becomes sufficient for the hydrogen bonding to dominate the decrease in the average solute chain length. The increase in hydrogen bonding has the effect of making the solvent-solute system more llg immiscible, thereby causing the hole to close. The CO_2 -free compositions at which the lg hole opens and closes are given above. The lg hole in this study is completely enclosed in the llg surface. One could envision systems in which the lg hole would overlap the $l-l=g$ locus, thereby creating a gap in that locus terminated by two tricritical points.

The separabilities of the two hydrocarbons in the liquid phases along the 298.15 K isotherm range from about 0.6 to 3.6 where the separability is defined by

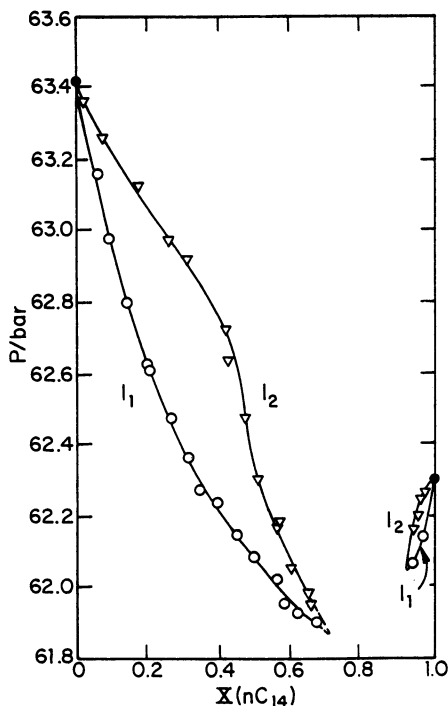


Figure 5. Pressure versus n-tetradecane mole fraction (on a CO₂-free basis) for the l₁ and l₂ phases at 298.15 K.

$$\left[\frac{(X_{nC_{14}}^{l_2}/X_{nC_{14}}^{l_1})}{[(X_{C_{1000}}^{l_2}/X_{C_{1000}}^{l_1})]} \right]$$

For the left branch of the 298.15 K isotherm shown in Figure 3, the l₁ phase is 1-decanol-rich, and the separabilities vary from a limiting value of about 2.0 as X(nC₁₄) approaches zero (the CO₂ + 1-decanol llg point) to a maximum value of about 3.6 to a minimum of 1.0 at the critical end point. The right branch has a n-tetradecane-rich l₁ phase, and the separabilities range from a maximum of 1.0 at the critical end point to a limiting minimum value of about 0.6 as it approaches the binary CO₂ + n-tetradecane llg point. Since this ternary system has a vapor phase that is virtually pure CO₂, the separabilities will switch from greater than one to less than one at (or very near to) the fold where it exists. Miller et al. (18) identified a similar such fold for the CO₂ + n-butylbenzene + n-eicosane llg system but did not detail it. Another similar llg system is ethane + methanol + 1-decanol (4), in which the vapor phase is virtually pure ethane. The first system is discussed in some detail in Miller and Luks (5). Neither system had a lg hole or gap in its llg surface. Folds, in general, are points of compositional collinearity (5,6).

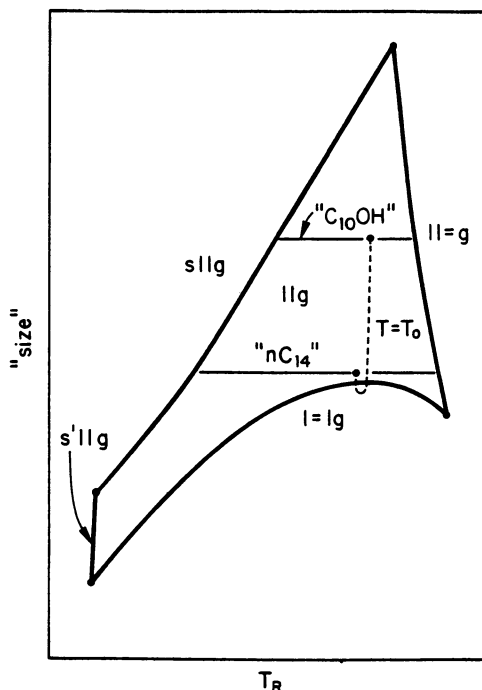


Figure 6. Schematic diagram of the llg domain for solute molecular size versus reduced temperature according to van der Waals for a typical homologous series of solvent + solute mixtures. Indicated is the relative position of n -tetradecane (nC_{14}) and 1-decanol ($C_{10}OH$) in their respective homologous series with solvent CO_2 . The dashed line hypothesizes the position of CO_2 + solute mixtures of n -tetradecane + 1-decanol on such a diagram at temperature $T_1 = 298.15$ K.

Legend of Symbols

AAD	average absolute deviation
i.p.	barotropic inversion point
$C_{10}OH$	1-decanol
DCEP	double critical end point
g	vapor phase
l, l_1, l_2	liquid phases
$l-l=g$	three-phase critical end point where the less dense l -phase and the g -phase are critically identical. (also referred herein as the UCEP)
$l=l-g$	three-phase critical end point where the liquid phases are critically identical.
nC_{14}	n -tetradecane
P	pressure
T	temperature
UCEP	upper critical end point ($l-l=g$)
v	molar volume of a phase
x	mole fraction
X	mole fraction on a CO_2 -free basis

Acknowledgments

Support of this research was provided by the National Science Foundation (Grant No. CTS-8914725). The apparatus used is a part of the PVTx Laboratory at the University of Tulsa and was purchased with funds provided by several industries, the University of Tulsa, and a National Science Foundation specialized equipment grant (No. CPE-8104650).

Literature Cited

1. Lam, D. H.; Jangkamolkulchai, A.; Luks, K. D. *Fluid Phase Equil.* 1990, *59*, pp 263-277.
2. Lam, D. H.; Jangkamolkulchai, A.; Luks, K. D. *Fluid Phase Equil.* 1990, *60*, pp 119-130.
3. Lam, D. H.; Jangkamolkulchai, A.; Luks, K. D. *Fluid Phase Equil.* 1990, *60*, pp 131-141.
4. Lam, D. H.; Luks, K. D. *J. Chem. Eng. Data* 1991, *36*, pp 307-311.
5. Miller, M. M.; Luks, K. D. *Fluid Phase Equil.* 1989, *44*, pp 295-304.
6. Patton, C. L.; Green, K. A.; Luks, K. D. *Fluid Phase Equil.* 1992, (in press).
7. Teja, A. S.; Lee, R. J.; Rosenthal, D.; Anselme, M. *Fluid Phase Equil.* 1990, *56*, pp 153-169.
8. Hottovy, J. D.; Luks, K. D.; Kohn, J. P. *J. Chem. Eng. Data* 1981, *26*, pp 256-258.
9. van der Steen, J.; de Loos, Th. W.; de Swaan Arons J. *Fluid Phase Equil.* 1989, *51*, pp 353-367.
10. Laugier, S.; Richon, D.; Renon, H. *Fluid Phase Equil.* 1990, *54*, pp 19-34.
11. Fall, D. J.; Luks, K. D. *J. Chem. Eng. Data* 1984, *29*, pp 413-417.
12. Jangkamolkulchai, A.; Luks, K. D. *J. Chem. Eng. Data* 1989, *34*, pp 92-99.
13. Vargaftik, N. B. *Tables on the Thermophysical Properties of Liquids and Gases*; Second edition; John Wiley and Sons: New York, NY, 1975, pp 167-168.
14. Angus, S.; Armstrong, B.; de Reuck, K. M. *International Thermodynamic Tables of the Fluid State Carbon Dioxide*; Pergamon Press: Oxford, 1976.
15. van Konynenburg, P. H.; Scott, R. L. *Philos. Trans. R. Soc. London, Ser. A.* 1980, *298*, pp 495-540.
16. Fall, D. J.; Luks, K. D. *J. Chem. Eng. Data* 1985, *30*, pp 276-279.
17. Enick, R.; Holder, G. D.; Morsi, B. I. *Fluid Phase Equil.* 1985, *22*, pp 209-224.
18. Miller, M. M.; Jangkamolkulchai, A.; Luks, K. D. *Fluid Phase Equil.* 1989, *50*, pp 189-199.

RECEIVED April 27, 1992

Chapter 6

Group Contribution Method for Estimating the Solubility of Selected Hydrocarbon Solutes in Supercritical Carbon Dioxide

Thomas E. Carleson¹, Sirish Chandra¹, Chien Wai², Larry Wai²,
and Shawn S. Huang³

¹Department of Chemical Engineering and ²Department of Chemistry,
University of Idaho, Moscow, ID 83843

The Peng Robinson equation of state with van der Waals type mixing rules was used to correlate the solubilities of a range of hydrocarbon solutes in carbon dioxide. Interaction parameters determined from the fitting of the data were calculated. A multivariable linear fit routine was used to determine the chemical group contributions to the interaction parameters. Predicted values of the interaction parameters generally agreed with those calculated from experimental data within 10%. The prediction of the effect of pressure on the solubility of phenanthrene in supercritical carbon dioxide shows an increase in the effect of the value of the interaction parameter upon the predicted solubility as the pressure approaches and exceeds the critical point.

Supercritical solvents exhibit properties intermediate between gases and liquids. They exhibit viscosities and diffusivities comparable to those of gases, yet densities comparable to liquids. Consequently, mass transfer rates may approach those of gases and solubilities those of liquids. Recent interest in supercritical extraction has resulted in many articles in the literature on such topics as extraction of food materials, hazardous organics, and pharmaceuticals (*1-4*).

In order to evaluate applications for supercritical extraction, one must be able to estimate the solubility of the material extracted in the supercritical solvent. In order to do this an equation of state is required as well as physical properties for the solvent and solute. The interaction between the solvent and solute is often

³Current address: Exxon Oil Company, 3319 Mercer, Room 349, Houston, TX 77027-6019

0097-6156/93/0514-0066\$06.00/0
© 1993 American Chemical Society

included as an interaction term which is determined from experiment. In this paper, a group contribution method is developed to allow the estimation of the interaction parameter in the absence of experiments.

Theory

To determine the fugacity coefficient of a solute in a supercritical solvent, an equation of state must be used with appropriate mixing rules. The literature is replete with various equations of state including the van der Waals, Redlich Kwong, Peng Robinson, Redlich Kwong Soave, Schmitt-Reid equations, among others (5-7). In recent reviews, the Peng Robinson equation of state appears as good as the other more complicated equations (5).

For a pure fluid, a and b parameters in the Peng Robinson equation can be determined from the critical constants and acentric factor for the fluid. If the fluid is a mixture, these constants are determined from mixing rules. The simple classical Van der Waals mixing rules are often used where the pure component constants are weighted with mole fraction as indicated below.

$$a = \sum_{i=1}^n \sum_{j=1}^n x_i x_j a_{ij}$$

$$b = \sum_{i=1}^n x_i b_i$$

$$a_{ij} = (1 - k_{ij})(a_i a_j)^{1/2}, \quad i \neq j$$

$$a_{ii} = a_i$$

where x_i are the mole fraction of the components, a_i are the pure component constants, and k_{ij} is the interaction parameter.

From thermodynamics (δ) the following equation can be derived for determining the fugacity coefficient.

$$RT \ln \phi_i = - \int_{\infty}^V \left[\left(\frac{\partial P}{\partial N_i} \right)_{T,V,N_{ij}} - \frac{RT}{V} \right] dV - RT \ln Z$$

$$\ln\phi_i = \frac{b_i}{b_m} (Z - 1) - \ln(Z - B) +$$

$$\frac{A}{2^{3/2} B} \left(\frac{\sum_{j=1}^n x_j a_{ij}}{a_m} - \frac{b_i}{b_m} \right) \ln \left[\frac{Z - B(1-2^{1/2})}{Z + B(1+2^{1/2})} \right]$$

where N_i is the moles of component i and Z is the compressibility. From relating pressure and volume to Z by the Peng Robinson equation of state and using the mixing rules above, one is able to determine the fugacity coefficient in the last two equations above. The compressibility is related to constants A and B as

$$Z^3 - (1 - B)Z^2 + (A - 3B^2 - 2B)Z - (AB - B^2 - B^3) = 0$$

$$A = \frac{aP}{R^2 T^2}$$

$$B = \frac{bP}{RT}$$

where A and B are constants defined as above.

In the absence of critical property data, one may use a variety of predictive methods (9-19). For example, for critical temperature prediction one can use the group contribution method of Lydersen (14) while the critical pressure may be estimated by a similar group contribution method (15) which may also be used to estimate the critical volume. In addition, the vapor pressure may be estimated by the method of Riedel (20) or others (21-22).

Applications and Discussion

The above equations (Theory section) were incorporated in a computer program in BASIC. The program was used to predict the effect of pressure on the solubility of phenanthrene depicted in Figure 1. The solid curve in this figure is the curve for the predicted solubility based upon the experimental measurement of the interaction parameter. The program was also prepared to determine interaction parameters based upon solubility measurements.

A multivariable linear regression was used to take experimentally measured values of the interaction parameter and prepare chemical group contributions similar to those in the methods described above for the prediction of the critical

properties. Literature values for the interaction parameters were obtained from the work by Haselow (23) who correlated experimental measurements of solubilities of a variety of compounds with the Peng Robinson equation of state and standard mixing rules. These values were used to determine the group contributions in the simple model below.

$$k_{12} = c + \sum_{i=1}^k \Delta_i$$

The estimated group contributions, Δ_i , are tabulated in Table I. These values are for the Peng Robinson equation of state where carbon dioxide is the solvent. Due to the limited data set and no variation of temperature incorporated in the model, the contributions for several chemical groups are grouped together as one and the calculated interaction parameters are assumed independent of temperature. The parameter c , the intercept, was found to be 0.03155.

Table I. Group Contributions to Interaction Parameter

<i>Increments</i>	Δ_i
-C6H6 Phenyl	0.02539
-H (replaced from phenyl groups)	0.01139
>C=, -CH<, -CH=, >CH2	0.00888
-CH3	0.00131
-COOH (carboxyl)	-0.01885
>C=O	-0.01024
>CH-OH	0.04135
Intercept	0.03155

Note: This table is for the Peng-Robinson equation of state with conventional mixing rules for data for compounds listed in Table II.

Table II shows a comparison between the calculated values of the interaction parameter based upon the group contribution method and those listed in the literature. The differences are all less than 10% for the compounds that were used in the data set to determine the group contributions (i.e. benzoic acid through pyrene). Three additional compounds, phenanthrene, cholesterol, and toluene, are listed which were not included in the data set used to determine the group contributions. The calculated value of the interaction parameter for phenanthrene agrees fairly well with the experimental. The error is comparable to those for the compounds included in the data set. The calculated value for toluene, however, is about 30% below the experimental value. This may be due

to the higher volatility of toluene relative to the other compounds and the fact that it is a liquid at room temperature and pressure.

Table II. Comparison of k_{12} values for Peng-Robinson Equation of State for CO₂ solvent

<i>Solute</i>	<i>MW</i>	<i>k₁₂ (exp)</i>	<i>k₁₂ (calc)</i>	<i>% diff.</i>
Benzoic Acid	122.13	0.0381	0.0381	0.0
1,4-Napthoquinone	158.16	0.0834	0.0834	0.0
Phenol	94.11	0.0983	0.0983	0.0
Fluorene	166.23	0.1059	0.1140	7.6
2,6-dimethylnapthalene	156.23	0.1108	0.1179	6.4
2,3-dimethylnapthalene	156.23	0.1132	0.1179	4.2
Napthalene	128.19	0.1146	0.1039	-9.3
Triphenylmethane	244.34	0.1195	0.1166	-2.4
Hexamethylbenzene	246.44	0.1257	0.1218	-3.1
Pyrene	202.26	0.1658	0.1634	-1.4
Phenanthrene	178.24	0.1284	0.1229	-4.3
Toluene	92.15	0.0810	0.0582	-28.2
<u>Cholesterol</u>	<u>386.67</u>	<u>0.2061</u>		

Data for compounds benzoic acid through pyrene were used to estimate group contributions in Table I. Reference is (23).

For illustration of the effect of the interaction parameter on the predicted solubility, Figure 2 depicts the predicted value of the solubility of phenanthrene based upon +/- 20% of the calculated value of the interaction parameter (0.123).

Experimental data and the predicted values (solid line) for the experimental value of the interaction parameter (0.128) are also depicted. Figure 2 shows that the effect of the interaction parameter increases with pressure. At low pressures, the effect is slight. Above the critical point of carbon dioxide (304 K and 72.9 atm), at 310 K and 80 bars, the predicted solubility rises from 8×10^{-4} to 8×10^{-3} when k_{ij} changes from 0.098 to 0.147. This illustrates the importance of accurate k_{ij} values for predicting solubilities.

Table II also shows the calculated value of the interaction parameter for cholesterol and Figure 3 the predicted solubilities. The methods discussed in the above Property Predictive Methods section were used to determine the critical temperature (586.94 K), critical pressure (12.476 bars), acentric factor (0.8913) and the vapor pressure dependence on temperature. Figure 3 also indicates the effect of varying the interaction parameter on the predicted solubility. These

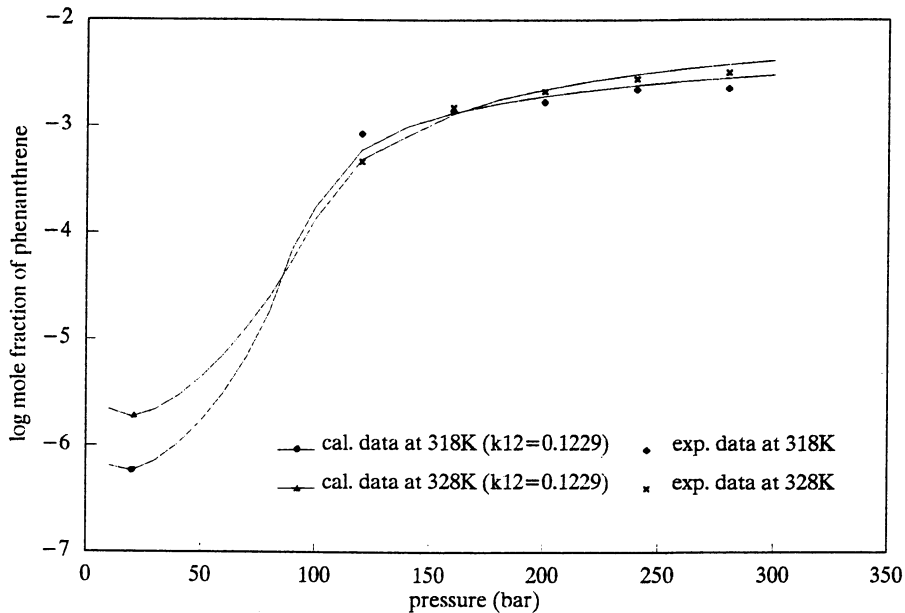


Figure 1. Measured and predicted values of the solubility of phenanthrene in supercritical CO_2 .

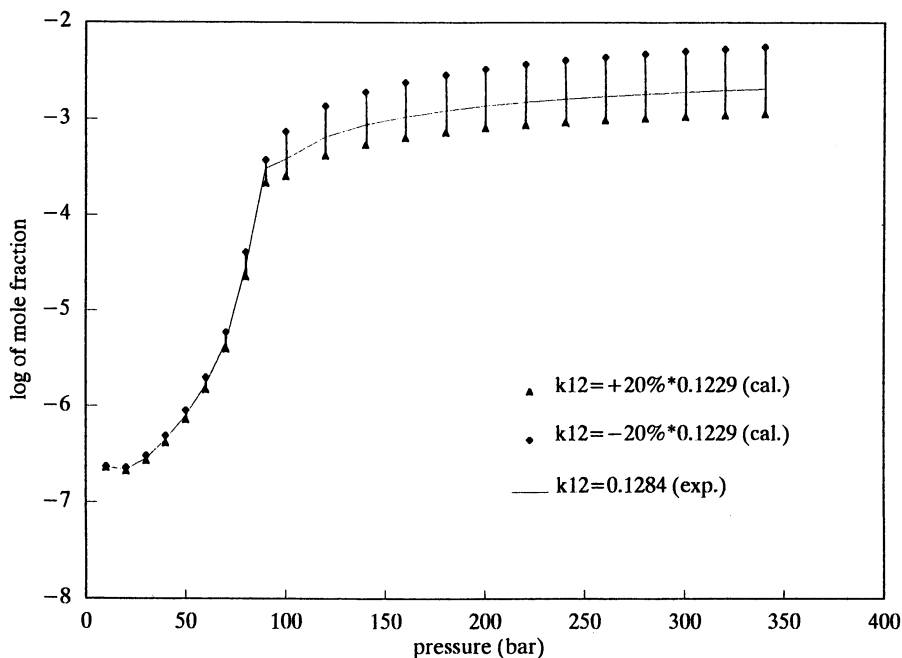


Figure 2. Measured and predicted values of the solubility of phenanthrene in supercritical CO_2 (310 K).

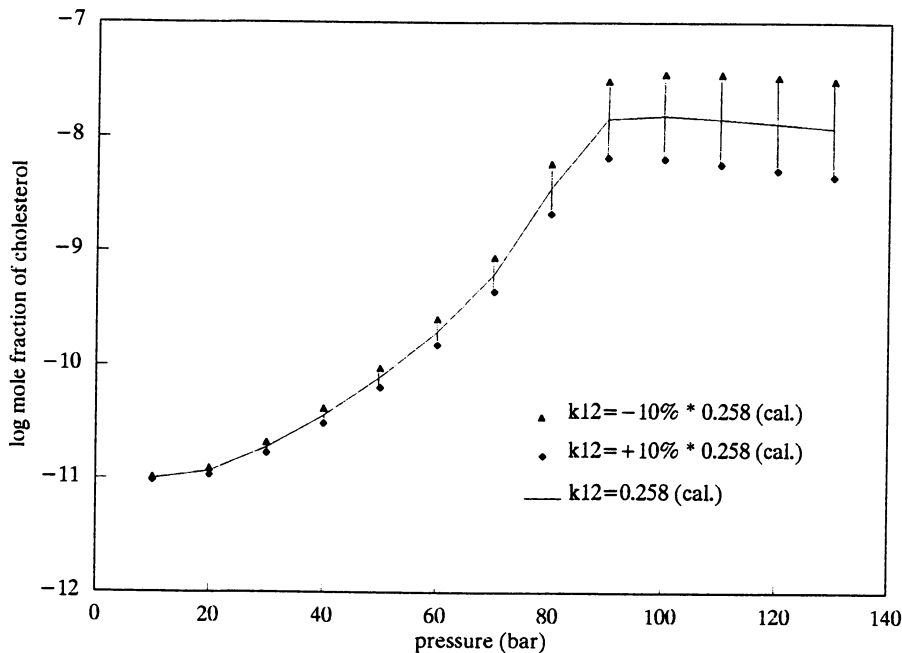


Figure 3. The effect of pressure on the solubility of cholesterol.

results indicate that group correlations may be used to estimate critical constants as well as values of the interaction parameter for solids where such data is lacking.

Conclusions

The Peng Robinson equation of state is a fairly accurate yet simple equation for the correlation of solute solubilities in supercritical solvents. Coupled with simple van der Waals mixing rules and an adjustable interaction parameter, the equation can be used to correlate a wide variety of solutes (23). In this paper, a group contribution method was developed which allows estimation of the interaction parameters based upon chemical structure. With limited data and with no variation of the parameter with temperature, good agreement was found between the predicted interaction parameters and those measured. The effect of the interaction parameter on solute solubility increases with pressure. Consequently, accurate interaction parameters are required for accurate solubility predictions as the solvent critical point is approached.

Acknowledgments

Support for this work was provided by grants from the U.S. Bureau of Mines; EG&G, Idaho; and the National Science Foundation under the EPSCOR program. The support of these organizations is gratefully acknowledged.

Literature Cited

1. Williams, D.F. *Chem Engr Sci.* **1981**, *36*, 1769.
2. Paulaitis, M.E.; Krukonis, V.J.; DiAndreth, J.R.; Reid, R.C. *Rev. Chem Engr.* **1982**, *1(2)*, 179.
3. Eckert, C.A.; King, M.L. *Biotech. Prog.* **1986**, *2(2)*, 73.
4. McHugh, M.A.; Krukonis, V.J. *Supercritical Fluid Extraction: Principles and Practice*, Butterworths: Boston, MA, 1986.
5. Brennecke, J.F.; Eckert, C.A. *AIChE J.* **1989**, *35(9)*, 1409.
6. Modell, M.; Reid, R.C. *Thermodynamics and Its Applications*, Prentice-Hall: Englewood Cliffs, NJ, 1983.
7. Schmitt, W.J.; Reid, R.C. *J. Chem. Engr. Data.* **1986**, *31*, 204.
8. Walas, Stanley M. *Phase Equilibria in Chemical Engineering*, Butterworth: Boston, MA, 1985.
9. American Petroleum Institute; *Technical Data Book-Petroleum Refining*, API: Washington, DC, 1981.
10. Klinecicz, K.M.; Reid, R.C. *AIChE J.* **1984**, *30(1)*, 137.
11. Ambrose, D. National Physical Laboratory: Teddington, 1978, NPL Report Chem 92.
12. Ambrose, D. National Physical Laboratory: Teddington, 1978, NPL Report Chem 98.
13. Ambrose, D. National Physical Laboratory: Teddington, 1980, NPL Report Chem 107.
14. Lyderson, A.L; Estimation of Critical Properties of Organic Compounds, Univ. Wisconsin, Coll. Eng., Eng. Exp. Stn. Rep. 3, Madison, WI, 1955.
15. Fedors, R.F. *AIChE J.* **1979**, *25*, 202.
16. Vetere, A. *AIChE J.* **1976**, *22*, 950.
17. Pitzer, K.S.; Lippman, D.Z.; Curl, R.F., Jr.; Huggins, C.M.; Patersen, D.E. *J. Am. Chem. Soc.* **1955**, *77*, 3427.
18. Edmister, W.C. *Petroleum Refiner* **1958**, *37(4)*, 173.
19. Lin, H.-M.; Chao, K.-C. *AIChE J.* **1984**, *30(6)*, 981.
20. Riedel, L. *Chem. Ing. Tech.* **1954**, *26*, 83.
21. Othmer, D.F.; Maurer, P.W.; Molinary, C.J.; Kowalaski, R.C.; *Ind. Eng. Chem.* **1957**, *49*, 125.
22. Othmer, D.F.; Yu, E.-S. *Ind. Engr. Chem.* **1968**, *60*, 22.
23. Haselow, J.S.; Han, S.J.; Greenkorn, R.A.; Chao, K.C. In *Equations of State-Theories and Applications*, Chao, K.C.; Robinson, R.L., Jr., Eds.; ACS Symposium Series 300; American Chemical Society: 1986, 156.

RECEIVED March 23, 1992

Chapter 7

Equation-of-State Analysis of Phase Behavior for Water–Surfactant–Supercritical Fluid Mixtures

C.-P. Chai Kao, M. E. Pozo de Fernandez, and M. E. Paulaitis

Department of Chemical Engineering, Center for Molecular and Engineering Thermodynamics, University of Delaware, Newark, DE 19716

Four-phase, liquid-liquid-liquid-gas equilibrium observed for ternary mixtures of CO₂, H₂O, and 2-butoxyethanol (C₄E₁) at conditions near the critical point of CO₂ is modeled using the Peng-Robinson equation of state (PR EOS). A detailed analysis of phase behavior for the three constituent binary mixtures and three related CO₂/alcohol and H₂O/alcohol binary mixtures are also described. Vapor pressures and saturated liquid densities for pure C₄E₁ and isothermal pressure-liquid composition data for vapor-liquid equilibrium for CO₂/C₄E₁ and H₂O/C₄E₁ binary mixtures are also reported. Comparisons of the experimentally determined and predicted phase behavior for H₂O/CO₂/C₄E₁ ternary mixtures show that this simple cubic equation of state with new combining rules is capable of predicting the complex multiphase behavior in the vicinity of the critical point of CO₂, but that these predictions can be sensitive to the regressed values of the PR EOS parameters.

Microemulsions exhibit a panoply of phase equilibria in addition to rich structural diversity. Kahlweit *et al.* (1) and Kilpatrick *et al.* (2) have described the phase behavior of multicomponent structureless fluid mixtures and microemulsions in terms of the effect of thermodynamic variables (temperature, pressure, and chemical potential) on the extent and interaction of the binary and ternary miscibility gaps. These phenomenological models provide a basis for understanding the phase behavior of microemulsion-forming mixtures despite taking no account of microstructure(s) in microemulsions. The relationship between the structure and phase behavior of microemulsions -- the two outstanding characteristics of microemulsions -- remains unclear, and indeed there need be no such relation. Experimental data establishes that

0097-6156/93/0514-0074\$06.00/0
© 1993 American Chemical Society

there are general patterns of phase behavior exhibited by microemulsions, and these patterns are universal (3,4). Kahlweit *et al.* (5) have also shown experimentally that the intrinsic phase behavior is independent of any underlying microstructure for H₂O/decane/C_iE_j ternary mixtures where (i,j) = (4,1), (8,3), and (12,5).

For ternary mixtures containing water, C_iE_j amphiphiles, and liquid alkanes, the characteristic progression in temperature of three-phase, liquid-liquid-liquid (LLL) equilibrium, represented by the ubiquitous "fish" on a temperature-composition phase diagram, is the widely accepted benchmark for this phase behavior. The three-phase behavior has also been studied as a function of the chemical nature of both the amphiphile and the alkane, and the addition of salts or ionic surfactants (6). The effect of pressure on the phase behavior of microemulsions has not been studied as extensively. Sassen *et al.* (7) measured compositions for three-phase LLL equilibrium for H₂O/decane/C₄E₁ ternary mixtures as a function of pressure up to 300 atm, and found the characteristic transition from a surfactant-rich hydrocarbon phase to a surfactant-rich water phase with increasing pressure. Kahlweit *et al.* (1) described the effect of pressure on this three-phase equilibrium for ternary mixtures of H₂O and C₄E₂ with two phenylalkanes, and established the existence of a tricritical point at elevated pressures for ternary mixtures containing lower molecular weight alkanes. The phase behavior observed for H₂O/alkane/C_iE_j ternary mixtures is believed to result from a delicate balance of critical phenomena intrinsic to the binary mixtures; namely, the upper critical solution temperature (UCST) for the alkane/C_iE_j mixture and the lower critical solution temperature (LCST) for the H₂O/C_iE_j mixture. Although this balance can be sensitive to changes in, for example, the hydrophobic/hydrophilic nature of the amphiphile or to changes in a field variable, such as temperature, the effect of pressure is not large, and pressure changes on the order of hundreds of atmospheres are typically required to observe phase behavior obtained with much smaller changes in temperature.

Pressure can have a significant impact, however, on the phase behavior for H₂O/C_iE_j mixtures with highly compressible supercritical fluids (SCF). The phase behavior for even simple mixtures containing supercritical fluids at conditions near the critical point of the SCF can also be rich in diversity and complexity, with three or more coexisting phases and a multitude of higher order critical phenomena frequently observed. In this paper, we present an analysis of the phase behavior for ternary mixtures of water, 2-butoxyethanol (C₄E₁), and CO₂ at conditions near the critical point of CO₂. This analysis is based on Peng-Robinson equation of state (PR EOS) calculations of fugacities for the three components in all coexisting fluid phases. New mixing rules are also proposed which improve the simultaneous description of VLE and LLE. Measurements of vapor pressures and liquid densities for pure C₄E₁, and isothermal P_x data for vapor-liquid equilibrium for CO₂/C₄E₁ and H₂O/C₄E₁ binary mixtures are also reported.

A key element in calculating the correct phase behavior for H₂O/C₄E₁/CO₂ ternary mixtures at conditions near the critical point of CO₂ is to predict the observed four-phase, liquid-liquid-liquid-gas (LLLG) equilibrium, from which the three-phase, LLG and LLL equilibria and all two-phase, LL and LG equilibria are derived. Therefore, in assessing the capabilities of our modified PR EOS to describe the phase behavior for this ternary mixture, and for general application to other water/nonionic surfactant/SCF mixtures, we have concentrated on predicting the observed four-phase, LLLG equilibrium. Ritter and Paulaitis (8) measured H₂O/C₄E₁/CO₂ phase

compositions for LLLG equilibrium at conditions near the critical point of CO₂. Four-phase, LLLG equilibrium has also been observed for similar ternary mixtures at these conditions: H₂O/CO₂/C₈E₃ (8), H₂O/CO₂/isopropanol (9), and H₂O/CO₂/1-butanol (10). DiAndreth and Paulaitis (11) also predicted the global multiphase behavior for H₂O/CO₂/isopropanol ternary mixtures using the original PR EOS with the conventional quadratic mixing rules and one binary interaction parameter for each pair of mixture constituents. Panagiotopoulos and Reid (9) modified the geometric mean combining rule in these mixing rules to calculate LLLG equilibrium for H₂O/CO₂/1-butanol ternary mixtures. The new combining rule proposed here represents a more general formulation of their modification which reduces to either the conventional quadratic combining rule in the original PR EOS or the modified combining rule of Panagiotopoulos and Reid when appropriate simplifying approximations are made.

Thermodynamic Model

Previous work has shown that relatively simple thermodynamic models, based on excess Gibbs free energy expressions, can capture the essential features of the phase behavior for ternary liquid mixtures consisting of water, hydrocarbons, and nonionic surfactants. Foremost among these features are the three-phase, liquid-liquid-liquid equilibrium behavior and related critical phenomena (*i.e.*, critical endpoints and tricritical points). Kahlweit *et al.* (1) described this three-phase behavior using a two-suffix Margules expression to characterize the solution thermodynamics for each pair of mixture constituents. By adjusting Margules parameters, a tricritical point could be obtained by converging L₁L₂ and L₂L₃ critical endpoints. Although this model will not provide quantitative representations of the phase behavior for H₂O/hydrocarbon/C_iE_j mixtures, the calculations do show that qualitatively correct patterns can be obtained with the simplest of Gibbs free energy expressions. Kilpatrick *et al.* (2) considered a free energy expression based on the Flory-Huggins equation which was modified to include "exponential screening" of water-hydrocarbon interactions. This model gave a reasonable quantitative representation of the phase behavior for H₂O/alkane/C₄E₁ mixtures at 25°C as the *n*-alkane was varied from *n*-hexane to *n*-tetradecane. However, a second exponential screening factor was required for H₂O/alkane/C₈E₃ mixtures, and the resulting calculations for these ternary mixtures were still much less quantitative. Schick and coworkers (12, 13) developed a more sophisticated lattice model that incorporates three-particle interactions and energetically favors lattice configurations with the surfactant located on sites between water and hydrocarbon. Water-surfactant hydrogen bonding was also treated. The model describes the temperature progression of the three-phase equilibrium, the effect of salt on this three-phase behavior and yields qualitative information about microstructure.

None of the Gibbs free energy models described above include a volumetric dependence, and hence the effect of pressure on phase behavior can not be addressed. In contrast, our interests in supercritical fluids have influenced our selection of an equation of state to calculate fluid-phase equilibria. This equation based on the equation of state originally proposed by Peng and Robinson (14),

$$P = \frac{RT}{v-b} - \frac{a}{v(v+b)+b(v-b)} \quad (1)$$

where the conventional quadratic mixing rules for the PR EOS parameters are

$$a = \sum_i \sum_j a_{ij} x_i x_j \quad (2)$$

$$b = \sum_i \sum_j b_{ij} x_i x_j \quad (3)$$

We propose the following modification to the geometric mean combining rule for the PR EOS parameter for the interaction energy,

$$a_{ij} = \sqrt{a_{ii} a_{jj}} \left(1 - \frac{x_i K A_{jj} + x_j K A_{ii}}{x_i + x_j} \right) \quad (4)$$

and retain the standard arithmetic mean combining rule for the PR EOS parameter for the excluded volume,

$$b_{ij} = \frac{(b_{ii} + b_{jj})}{2} (1 - K B_{ij}) \quad (5)$$

These modified combining rules now contain three adjustable parameters for each pair of mixture constituents: $K A_{ij}$, $K A_{ji}$, and $K B_{ij}$. When $K A_{ij} = K A_{ji}$ in equation (4), the original geometric mean combining rule is recovered. The physical significance of different $K A_{ij}$ and $K A_{ji}$ values is seen by taking the infinite dilution limit for each component,

$$a_{ij} = (1 - K A_{ji}) \sqrt{a_{ii} a_{jj}} \text{ as } x_i \rightarrow 0 \quad (6)$$

$$a_{ij} = (1 - K A_{ij}) \sqrt{a_{ii} a_{jj}} \text{ as } x_j \rightarrow 1 \quad (7)$$

which implies that intermolecular interactions between components i and j in a solution infinitely dilute in component i is different from intermolecular interactions between the same two components in a solution infinitely dilute in component j . One could expect this behavior if, for example, one component is strongly associating and thus interacts differently when it is present in excess, as an associated species, compared to when it is present at infinite dilution. Water would be a prime example of such an associating component.

Data Reduction

The PR EOS parameters for pure supercritical CO_2 were calculated from the correlations proposed by Peng and Robinson (14). For pure C_4E_1 , these parameters were determined by simultaneously fitting vapor pressures and saturated liquid densities. Vapor pressures for C_4E_1 were measured over a temperature range from 64.8° to 90.3°C, and the saturated liquid density was measured at 64.3°C. The

results are given in Table I in addition to selected literature data. The measured vapor pressures were first fit to the equation proposed by Gomez-Nieto and Thodos (15) from which the critical temperature and pressure of C_4E_1 can be estimated: $T_c = 636.5$ K and $P_c = 32$ atm. Initial guesses for the critical temperature and pressure in this data regression were obtained using Lydersen's method (16). The temperature dependence of the saturated liquid molar volume of C_4E_1 was calculated from a modified Rackett equation (17). These correlations were then used to derive the following expressions for the PR EOS parameters for pure C_4E_1 as a function of reduced temperature,

Table I. Vapor Pressure and Liquid Densities for C_4E_1

$T(^{\circ}C)$	P^s (psia)	ρ^l (g/cc)
64.8	0.2546	
72.3	0.3715	
80.4	0.5572	
90.3	0.8828	
171.2 †	14.696	
20.0 †		0.903
64.3		0.865

† - Chemical Engineers' Handbook, Perry & Chilton, 5th ed.

$$a_{C_4E_1} = (10.71422 - 10.48165 T_r + 3.814832 T_r^2) * 10^7 \quad (8)$$

$$b_{C_4E_1} = 97.52816 + 63.49862 T_r - 38.63925 T_r^2 \quad (9)$$

The same approach was applied to obtain PR EOS parameters for pure water. Regression of vapor pressures and saturated liquid densities from 25° to 150°C gave the following expressions,

$$a_{H_2O} = (13.64733 - 15.08321 T_r + 7.301165 T_r^2) * 10^6 \quad (10)$$

$$b_{H_2O} = 18.55704 - 7.976691 T_r + 5.847549 T_r^2 \quad (11)$$

where the critical temperature of water is 647.3 K.

For H_2O/CO_2 binary mixtures, KB_{ij} was set equal to zero, and KA_{ij} and KA_{ji} were fit to VLE and LLE data at elevated pressures and temperatures of 25°, 31.04°, and 50°C (18-21). These KA_{ij} and KA_{ji} values are also given in Table II, and the measured and calculated phase compositions at 50°C are shown in Figure 1. The agreement at 50°C is representative of that obtained at all three temperatures, and is notably very good over the entire range of pressures up to nearly one kilobar and for two phases that have very different compositions. The negative and slightly temperature dependent value of KA_{21} would not be expected based on London dispersion forces and may reflect water association in the H_2O -rich phase. In contrast, the value of KA_{12} is positive and independent of temperature.

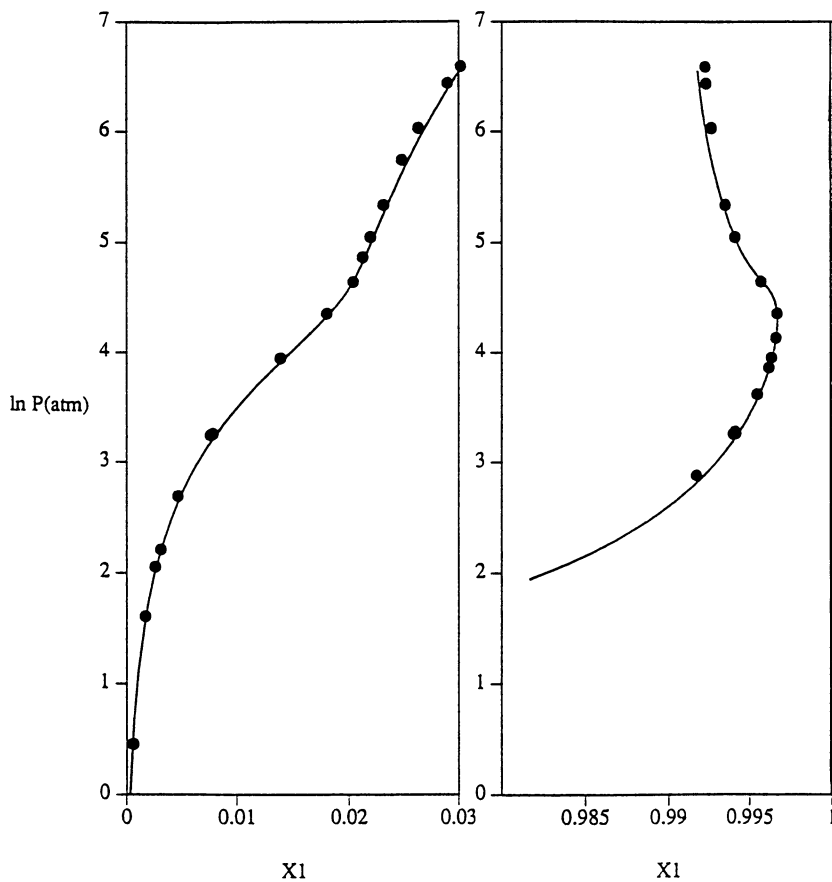


Figure 1. Comparison of measured and calculated phase compositions for $\text{H}_2\text{O}/\text{CO}_2$ binary mixtures at 50°C (x_1 is the mole fraction of CO_2).

Table II. Regressed PR EOS Parameters for Binary Mixtures Containing CO₂

SYSTEM	T (°C)	KA ₁₂	KA ₂₁	KB ₁₂
CO ₂ (1)/H ₂ O(2)	25.	0.16	- 0.218	0
	31.04	0.16	- 0.213	0
	50.	0.16	- 0.198	0
CO ₂ (1)/C ₄ E ₁	48.15	0.045	0	0
CO ₂ (1)/Isopropanol(2)	61.8	0.085	0.12	0
CO ₂ (1)/ 1-Butanol (2)	52.15	0.088	0.15	0

For CO₂/C₄E₁ binary mixtures, VLE pressures and liquid compositions were measured at 48.15°C. The experimental results are given in Table III and shown in Figure 2. The calculated isotherm in this figure is based on the KA_{ij} and KB_{ij} values in Table II. Since vapor compositions were not measured, additional regressions of experimental data for similar mixtures were performed to determine whether the CO₂/C₄E₁ PR EOS parameters are reasonable. Isothermal Pxy measurements for VLE were regressed for CO₂/isopropanol at 61.8°C (22) and CO₂/1-butanol at 52.15°C (23). The measured and calculated phase envelopes are compared in Figures 3 and 4, and the resulting PR EOS parameters are given in Table II. For all three systems, accurate phase diagrams are obtained with KB₁₂ set equal to zero and small non-negative values of KA₁₂ and KA₂₁. The somewhat smaller KA_{ij} values obtained for CO₂/C₄E₁ binary mixtures reflect the higher solubility of CO₂ in C₄E₁.

For H₂O/C₄E₁ binary mixtures, VLE pressures and liquid phase compositions were measured at 64.3°C. These results are given in Table IV. Equally good fits of the data were obtained with two different sets of PR EOS parameters: (1) KA₁₂=0.004, KA₂₁=-0.154, and KB₁₂=0.15; and (2) KA₁₂=-0.175, KA₂₁=-0.31, and KB₁₂=0.02. Although measured liquid compositions can be represented with reasonable accuracy, both sets of parameters significantly underpredict the solubility of H₂O in the C₄E₁-rich liquid phase for three-phase, LLG equilibrium measured at higher pressures (24, 25). An independent fit of the measured phase compositions for LLG equilibrium was also accomplished, and these parameters were used to predict the measured liquid compositions for VLE. Poor agreement was obtained over a substantial range of pressures and C₄E₁ mole fractions, suggesting that either the equation of state is unable to describe simultaneously VLE and LLE for this system or the measured phase compositions for LLE are not consistent with those measured for VLE. An independent test of the PR EOS to simultaneously fit both VLE and LLE was carried out for H₂O/1-butanol binary mixtures at 60°C. The calculated and measured phase compositions are compared in Figure 5 and show that good agreement is obtained for both VLE and LLE when only two PR EOS parameters are used. Based on these results, accurate representations of both VLE and LLE are expected for H₂O/C₄E₁ binary mixtures using the modified PR EOS proposed here, and a closer examination of the LLG equilibrium data for H₂O/C₄E₁ mixtures is also warranted.

At atmospheric pressure, H₂O/C₄E₁ binary mixtures exhibit liquid-liquid equilibrium with a LCST at 44.5°C and an UCST at 135.5°C (26). We examined the ability of our modified PR EOS to describe this solubility behavior by searching for a set of KA_{ij} and KB_{ij} values that would give the characteristic closed loop liquid-liquid

Table III. Measured VLE Pressures and Liquid Compositions for CO₂/C₄E₁ Mixtures at 48.15 °C

xCO ₂	P (atm)
0.0613	3.743
0.1281	9.322
0.2232	17.284
0.3076	24.224
0.4457	45.250
0.5034	53.348
0.5875	64.507
0.6742	74.510
0.7418	81.111
0.7405	85.193
0.8205	89.140

Table IV. Measured VLE Pressures and Liquid Compositions for C₄E₁/H₂O Mixtures at 64.3 °C

xC ₄ E ₁	P (atm)
0.8953	0.0782
0.8632	0.1027
0.8144	0.1157
0.7129	0.1528
0.6498	0.1884
0.6148	0.1877
0.5537	0.2046
0.5396	0.2166
0.4780	0.2181
0.4621	0.2211
0.3761	0.2386
0.3586	0.2380
0.2435	0.2478
0.2305	0.2479
0.1491	0.2481

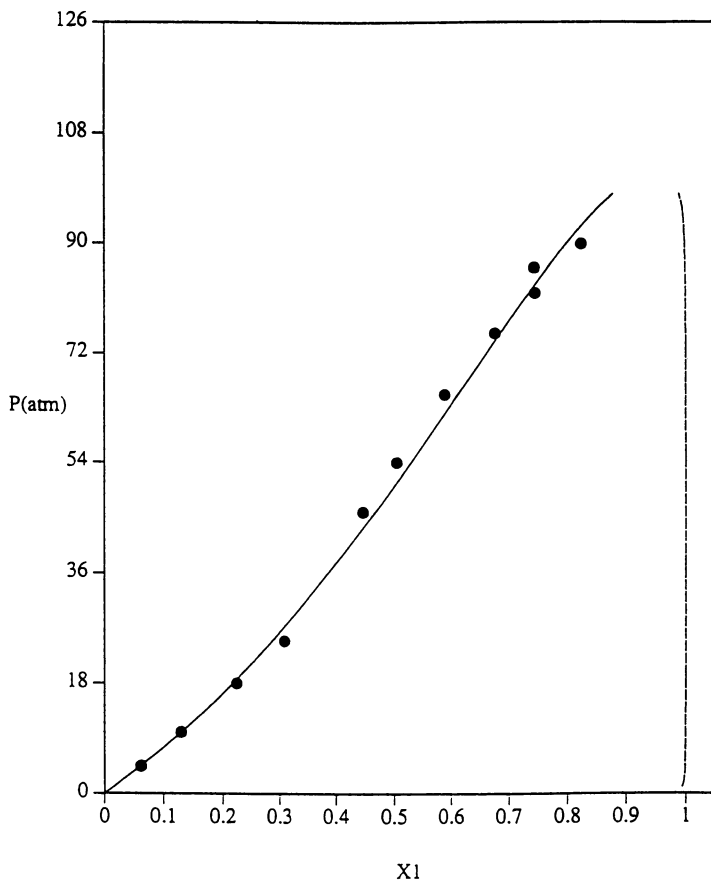


Figure 2. Measured vapor-liquid equilibrium pressures and liquid compositions for CO₂/C₄E₁ binary mixtures at 48.15°C (x_1 is the mole fraction of CO₂).

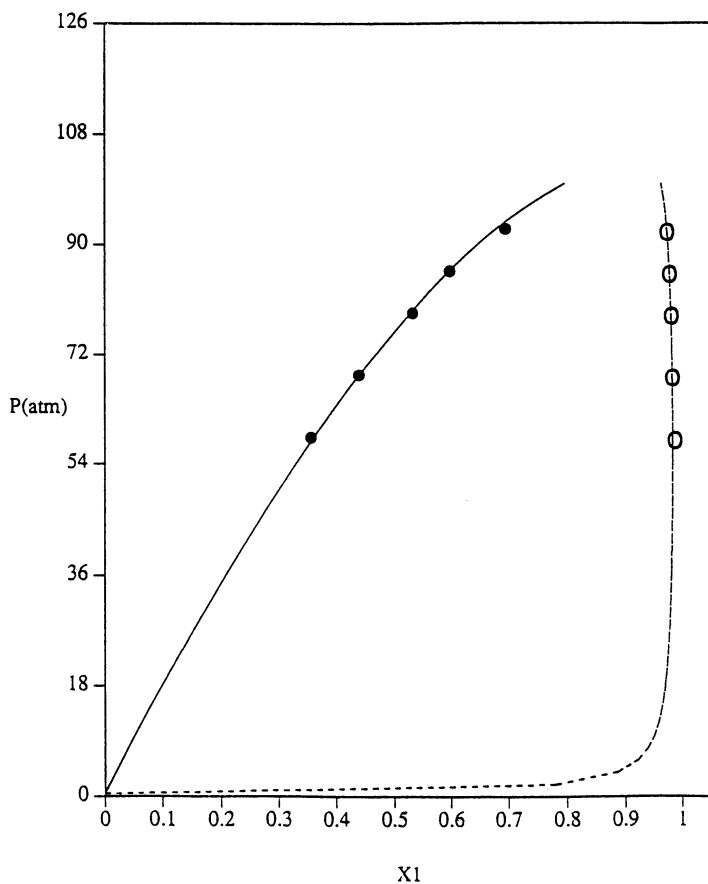


Figure 3. Comparison of the measured [Radosz, 1984] and calculated isothermal VLE pressure-composition diagrams for CO_2 /isopropanol binary mixtures at 61.8°C (x_1 is the mole fraction of CO_2).

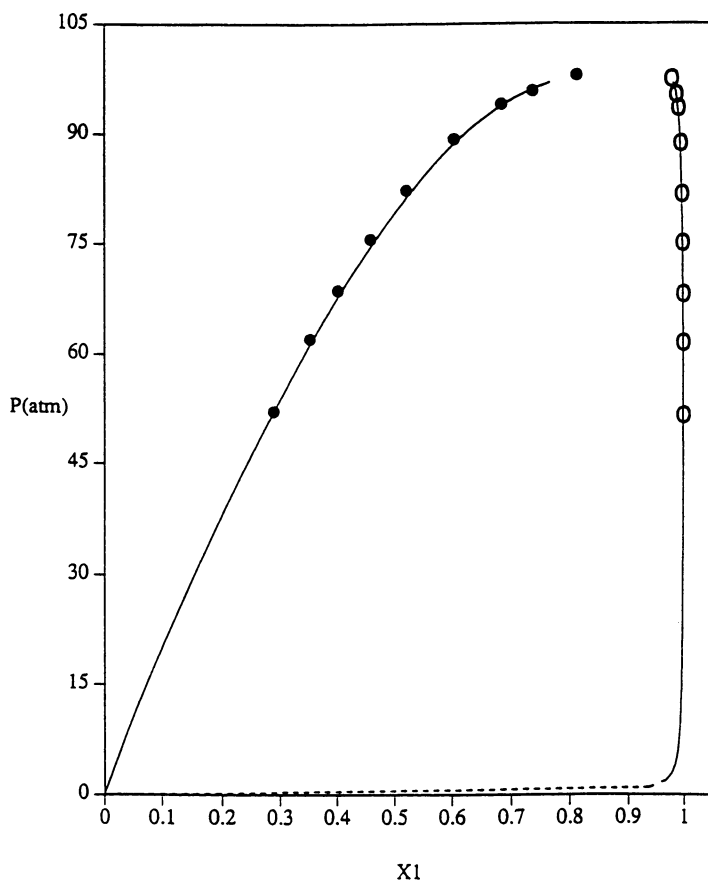


Figure 4. Comparison of the measured [Jennings *et al.*, 1991] and calculated isothermal VLE pressure-composition diagrams for $\text{CO}_2/1$ -butanol binary mixtures at 52.15°C (x_1 is the mole fraction of CO_2).

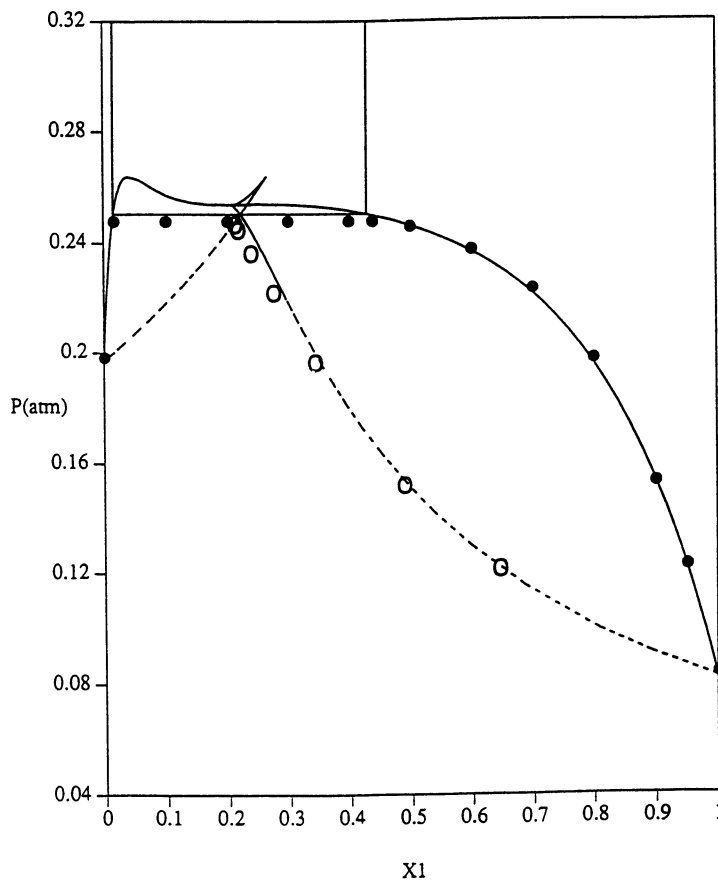


Figure 5. Comparison of the measured and calculated isothermal pressure-composition diagrams for VLE and LLE for $\text{CO}_2/1\text{-butanol}$ binary mixtures at 60°C (x_1 is the mole fraction of CO_2).

miscibility gap as a function of temperature. A set of temperature-independent parameters could not be found; however, a quantitative fit of the measured phase compositions could be obtained with constant values for KA_{12} and KA_{21} , and a slightly temperature-dependent value for KB_{12} . The calculated results are compared to measured phase compositions in Figure 6, and the temperature dependence of the KB_{12} parameter is shown in Figure 7. The results in Figure 6 support recent calculations of van Pelt *et al.* (27) showing that equations of state can, in fact, predict closed loop liquid-liquid miscibility gaps characteristic of type VI pressure-temperature projections.

Predicted Phase Diagrams for $H_2O/C_4E_1/CO_2$ Ternary Mixtures

Phase diagrams for $H_2O/C_4E_1/CO_2$ ternary mixtures at 50°C were predicted using the values of KA_{ij} and KB_{ij} in Table II and the two different sets of KA_{ij} and KB_{ij} values for H_2O/C_4E_1 binary mixtures reported above. These phase diagrams are shown in Figures 8 and 9. In Figure 8, two different regions of three-phase, LLG equilibrium are predicted at 50°C and 118 atm based on the second set of H_2O/C_4E_1 parameters. Four-phase, LLLG equilibrium would be obtained at higher pressures if these two three-phase triangles merge to form a single four-phase quadrilateral. However, additional calculations at higher pressures show that the CO_2 -rich three-phase triangle reaches a gas-liquid critical endpoint before it can merge with the second LLG triangle. Thus, only LLG equilibrium is observed at higher pressures, and no four-phase equilibrium is predicted with this set of H_2O/C_4E_1 parameters.

Four-phase, LLLG equilibrium is predicted, however, based on the first set of H_2O/C_4E_1 parameters. The predicted phase diagram at 50°C and 80 atm (Figure 9) again shows the two separate three-phase, LLG equilibrium triangles. As pressure is increased, these triangles now merge to form the four-phase quadrilateral corresponding to LLLG equilibrium. At a slightly higher pressure, this four-phase quadrilateral will split along its other diagonal to form a second pair of three-phase triangles, as shown in Figure 10 at 50°C and 96.285 atm. Thus, four-phase, LLLG equilibrium is obtained at 50°C and a pressure between 80 and 96.285 atm. It is interesting to note that the correct LLLG equilibrium behavior is obtained with the set of H_2O/C_4E_1 parameters containing an unusually large KB_{ij} value, which suggests that the excluded volume for H_2O/C_4E_1 intermolecular interactions must be small. In contrast, DiAndreth and Paulaitis (11) calculated the correct LLLG equilibrium behavior for H_2O/CO_2 /isopropanol ternary mixtures using only one $KA_{ij}=KA_{ji}$ parameter for H_2O /isopropanol.

Conclusions

The measured four-phase, LLLG equilibrium for ternary mixtures of H_2O , C_4E_1 , and CO_2 at conditions near the critical point of CO_2 can be modeled using the PR EOS with the combining rules given in equations (4) and (5) and parameters obtained from fits of VLE and LLE data for the three constituent binary mixtures.

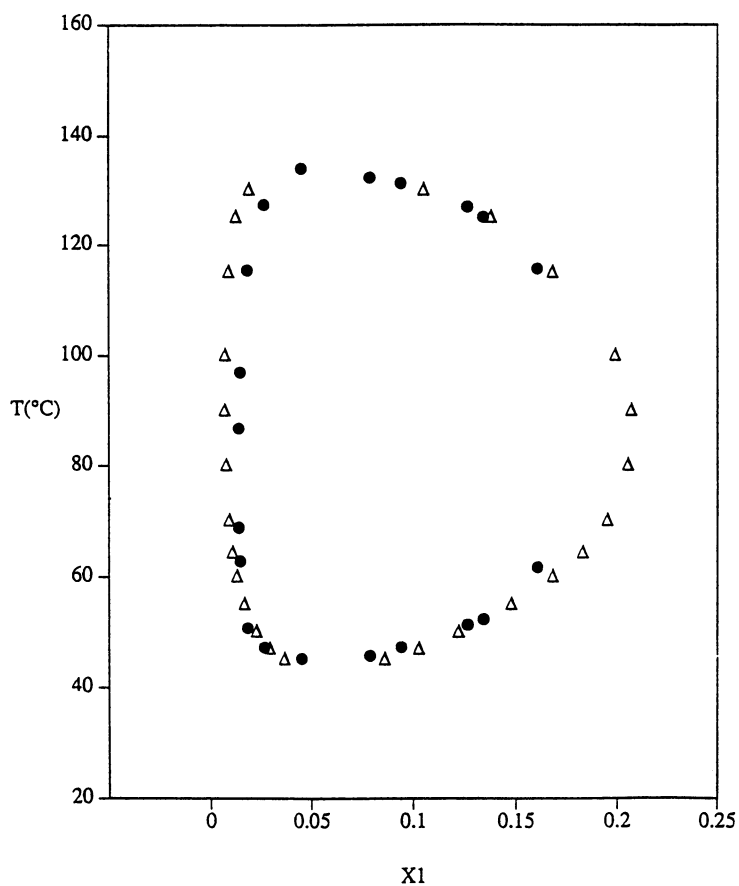


Figure 6. Comparison of the measured (open triangles) and calculated (closed circles) closed loop liquid-liquid miscibility gap for H₂O/C₄E₁ binary mixtures (x_1 is the mole fraction of C₄E₁).

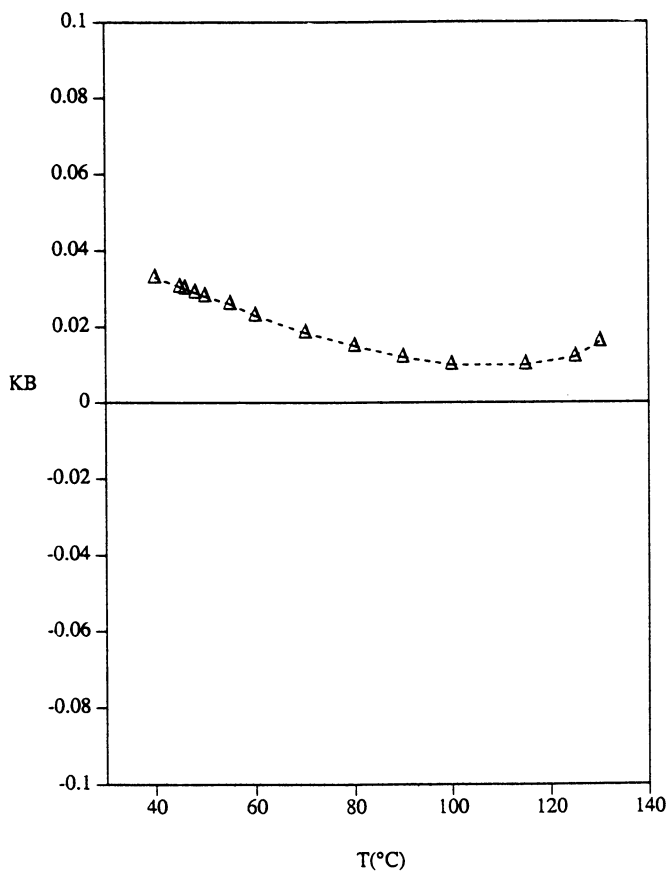


Figure 7. Temperature dependence of the KB_{12} parameter fit to the closed loop liquid-liquid miscibility gap for H_2O/C_4E_1 binary mixtures in Figure 6.

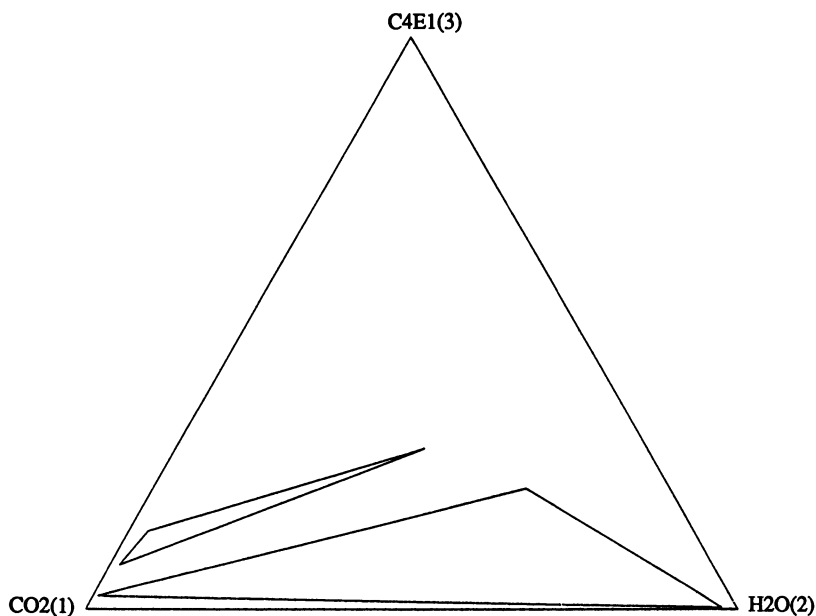


Figure 8. Phase diagram for H₂O/C₄E₁/CO₂ ternary mixtures at 50°C and 118 atm ($KA_{32}=-0.175$, $KA_{23}=-0.31$, and $KB_{23}=0.02$).

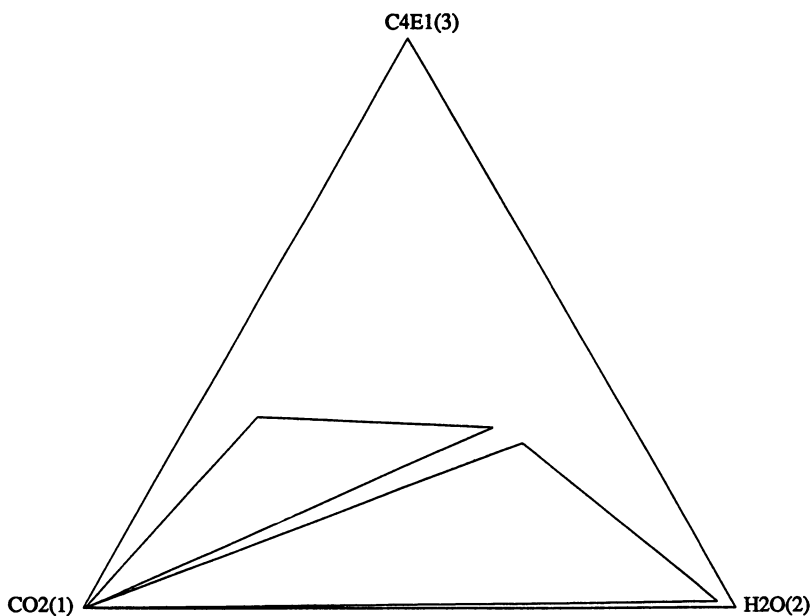


Figure 9. Phase diagram for H₂O/C₄E₁/CO₂ ternary mixtures at 50°C and 80 atm ($KA_{32}=-0.154$, $KA_{23}=-0.004$, and $KB_{23}=0.154$).

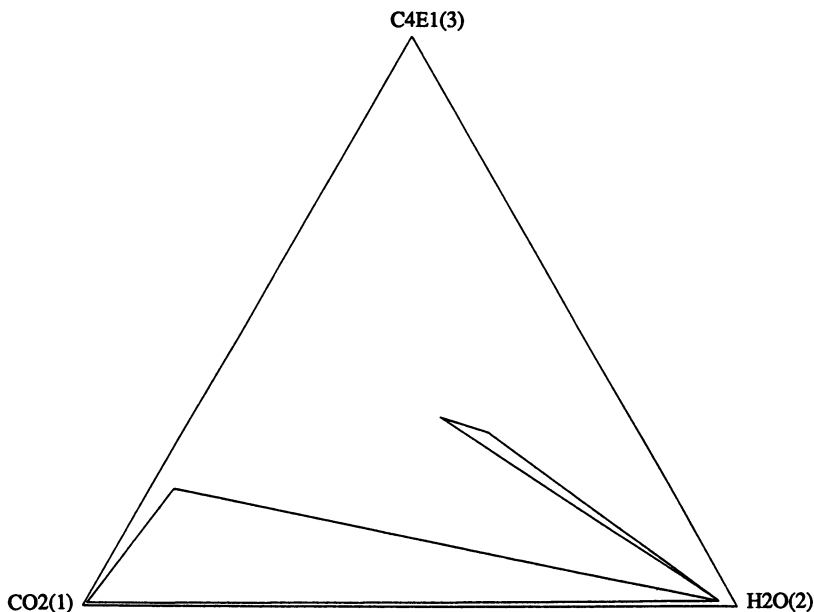


Figure 10. Phase diagram for H₂O/C₄E₁/CO₂ ternary mixtures at 50°C and 96.285 atm ($KA_{32}=-0.154$, $KA_{23}=-0.004$, and $KB_{23}=0.154$).

Data regressions for the CO₂/H₂O and CO₂/C₄E₁ binary mixtures were straightforward and required at most only two PR EOS parameters. The CO₂/C₄E₁ parameters were also found to be consistent with those obtained from fits of VLE data for binary mixtures of CO₂ with isopropanol and CO₂ with 1-butanol. The H₂O/C₄E₁ parameters proved more difficult to obtain. The analysis of phase equilibria observed for this mixture also demonstrated the importance of the KB_{ij} parameter. Three different sets of KA_{ij} and KB_{ij} values were regressed from the experimental data. However, it was found that only one of these parameter sets predicted the observed four-phase, LLLG equilibrium for CO₂/H₂O/C₄E₁ ternary mixtures. The closed loop liquid-liquid miscibility gap characteristic of the phase behavior for this binary mixture could also be described in quantitative agreement with experimental results, but a temperature-dependent KB_{ij} parameter was required, thereby suggesting that the LLE calculations may be sensitive to this KB_{ij} parameter. Nevertheless, the results presented here encourage the application of the PR EOS with the proposed combining rules to calculate phase equilibria for mixtures containing H₂O, supercritical fluids, and other nonionic surfactants.

Literature Cited

1. Kahlweit, M., Strey, R., Firman, P., Haase, D., for Jen, J. and Schomäcker, R. *Langmuir*. 1988, 4, 499.

2. Kilpatrick, P. K., Gorman, C. A., Davis, H. T., Scriven, L. E., and Miller, W. G. *J. Phys. Chem.* **1986**, *90*, 5292.
3. Prince, A. *Alloy Phase Equilibria*; Elsevier: Amsterdam, 1966.
4. Knickerbocker, B. M.; Pesheck, C. V.; Davis, H. T.; Scriven, L. E. *J. Phys. Chem.* **1982**, *86*, 393.
5. Kahlweit, M., Strey, R., Firman, P., and Haase, D. *Langmuir.* **1985**, *1*, 281.
6. Kahlweit, M.; Strey, R., Schomacker, R., Hasse, D. *Langmuir.* **1989**, *5*, 305.
7. Sassen, C. I., de Loos, Th. W., and de Swaan Arons, J. *J. Phys. Chem.* **1991**, *95*, 10760.
8. Ritter, J. M. and Paulaitis, M. E. *Langmuir.* **1990**, *6*, 934.
9. DiAndreth, J. R., and Paulaitis, M.E., *Fluid Phase Equilibria* **1987**, *32*, 261.
10. Panagiotopoulos, A. Z. and Reid, R. C. *Fluid Phase Equilibria.* **1986**, *29*, 525.
11. DiAndreth, J. R., and Paulaitis, M.E., *Chem. Eng. Sci.* **1989**, *44*, 1061.
12. Gompper, G. and Schick, M. *J. Phys. Rev.B.* **1990**, *41*, 9148.
13. Carneiro, G. M. and Schick, M. *J. Chem. Phys.* **1988**, *89*, 4368.
14. Peng, D.-Y. and Robinson, D. B. *IEC Fundam.* **1976**, *15* (1), 59.
15. Gomez-Nieto, M. and Thodos, G. *AIChE Journal* . **1977**, *23*, 904.
16. Reid, R. C., Prausnitz, J. M. and Poling, B. E. *The Properties of Gases and Liquid*; 4th ed.; McGraw-Hill Book Co.: New York, NY, 1987.
17. Spencer, C. F. and Adler, S. B. *J. Chem. Eng. Data* **1978**, *23*, 82.
18. Wiebe, R. *Chem. Rev.* **1941**, *29*, 475.
19. Wiebe, R. and Gaddy, V. L. *J. Am. Chem. Soc.* **1941**, *63*, 475.
20. Coan, C. R. and King, A. D. Jr. *J. Am. Chem. Soc.* **1971**, *93*, 1357.
21. Zawisza, A. and Malesinska, B. *J. Uiem Emp. Data* . **1981**, *26*, 388.
22. Radosz, M. *J. Chem. Engr. Data* . **1986**, *31* (1), 43-5.
23. Jennings, D. W., Lee, R.-J., and Teja, A. S. *J. Chem. Engr. Data* . **1991**, *36*, 303.
24. Cox H. L. and Cretcher, L. H. *J. Am. Chem. Soc.* **1926**, *48*, 451.
25. Poppe, G. *Bull. Soc. Chim. Belg.* **1935**, *44*, 640
26. Chakhovskoy, N. *Bull Soc. Chim. Belg.* **1956**, *65*, 474.
27. van Pelt, A., Peters, C. J., and de Swaan Arons, J. *J. Chem. Phys.* **1991**, *95*, 7569.

RECEIVED May 14, 1992

Chapter 8

Diffusion in Liquid and Supercritical Fluid Mixtures

V. M. Shenai, B. L. Hamilton, and M. A. Matthews

Department of Chemical Engineering, University of Wyoming,
Laramie, WY 82071-3295

The unusual thermodynamic behavior of near-critical solvents and the chemical effects of entrainers can have strong influence in diffusion coefficients in supercritical solvent mixtures. Precise experimental data are reported for diffusion of various solutes in supercritical CO₂, and in an ordinary liquid solvent, acetone. In addition, 5 mole percent methanol (a common entrainer used in supercritical fluid chromatography) was added to each of these solvents and the effect of this entrainer was observed. These data were examined in light of the behavior predicted by the hard-sphere and hydrodynamic theories. Local clustering of the solvent and/or entrainer about the solute is shown to affect the diffusion coefficients measurably. Neither hydrodynamic nor hard-sphere theories can account for local composition effects.

One of the oft-stated advantages of supercritical solvents compared to ordinary liquid solvents is that diffusion coefficients in supercritical solvents are higher than in liquids, hence mass transfer rates should be more favorable. For this reason there have been several recent experimental and theoretical studies of diffusion in supercritical solvents (1-5). The data base is still severely limiting for testing theoretical predictions and developing generalized correlations for diffusivity in supercritical fluids, particularly when small amounts of an entrainer are added to the supercritical solvent.

In this work the Taylor dispersion technique is used to obtain diffusion coefficients for three solutes: benzoic acid, acridine, and phenanthrene. The solvents used were: supercritical carbon dioxide; carbon dioxide with 5 mole percent methanol added as an entrainer; acetone; and acetone plus five mole percent methanol added as an entrainer. It is well known that the addition of methanol as an entrainer has a strong influence on the solubility of acridine and benzoic acid in supercritical carbon dioxide. These data allow observation of the

0097-6156/93/0514-0092\$06.00/0
© 1993 American Chemical Society

effects of the entrainer on the diffusion coefficient, and allow comparison of the ordinary liquid solvent, acetone, with the supercritical solvent carbon dioxide.

In the supercritical systems we expect that solvent/solute clustering may influence the diffusion coefficients noticeably. In the supercritical solvent + entrainer systems, we expect at least one additional mechanism, namely chemical clustering between methanol and some of the solutes, to be important in the diffusion process. Because methanol can demonstrate both acidic and basic character, strong acid/base association is expected when either benzoic acid or acridine are the solutes. Using either acetone or acetone + methanol as the liquid solvent allows one to distinguish the influence of the thermodynamic region upon the diffusion coefficient. For instance, the effect of the entrainer methanol upon the diffusion coefficient may be much more noticeable when the solvent is in the supercritical state, as opposed to the subcooled liquid state.

The methods commonly used to correlate diffusion measurements are based on theories that do not account for local phenomena like clustering. The data reported herein can be used to examine the validity of commonly used correlations.

Methods for correlating diffusivities

It is common to correlate diffusivities in ordinary liquids by using some variant of hydrodynamic theory or hard-sphere theory, particularly when the solute is dilute and strong compositional effects can be ignored. These two approaches are frequently applied when correlating diffusion coefficients in supercritical solvents (e.g., 1). These theories are based on physical models that inadequately describe the complex thermodynamic behavior of supercritical solute/solvent systems.

In hydrodynamic theory, the essential parameters needed for prediction and correlation are the solvent bulk viscosity and some measure of the solute size. For example, the Stokes-Einstein equation (6, 7) predicts that diffusivity is inversely proportional to the solvent viscosity μ :

$$D_{12} = \frac{kT}{6\pi\mu r} \quad (1)$$

where r is the hydrodynamic radius of the solute molecule, and k is the Boltzmann constant. This equation regards the solute molecule as moving in a continuum of solvent, with no "slip" between the solute and solvent.

Hydrodynamic theory has provided the basis for many correlations, the most well-known of which is probably the Wilke-Chang equation (8):

$$\frac{D_{12}}{T} = 7.4 \times 10^{-8} (\beta M_1)^{1/2} (v_2)^{0.6} \quad (2)$$

In this dimensional equation, the diffusivity must be in cm^2/s , the viscosity in centipoise, the temperature T in kelvins, and the solute molar volume v_2 in cm^3/mole . The empirical constant β corrects for solvent self-association. Many other correlations of this form have been proposed. The main feature of this

and similar equations is that the required physical properties are the solvent bulk viscosity and some measure of the pure solute size.

In hard-sphere theory, the essential parameters needed for prediction and correlation are the solvent bulk molar volume and the size of the solute. A concise representation of hard-sphere diffusivity is given by (9):

$$D_{12} = A \cdot C \cdot D_{12}^E \quad (3)$$

D_{12}^E is the Enskog-Thorne diffusion coefficient, applicable up to the moderately dense gas region. C is a correction term which accounts for "backscattering" and "vortex formation" in very dense liquids. This correction term is available only from molecular dynamics simulations of the diffusion process. A is a second correction term, proposed by Chandler (9), called the "roughness factor." It was intended to correct for the exchange of angular momentum when solute and solvent molecules collide. In some instances, workers have used molecular dynamics values for C and the Enskog-Thorne D_{12}^E with experimental data to back out the roughness parameter A , which becomes the adjustable parameter in a correlation. It has been found in some cases that the roughness factor appears to be a function of temperature, contrary to the original proposal of Chandler.

Molecular dynamics simulations have been performed over a fairly limited range of solute/solvent size and mass ratios. Frequently in supercritical fluid processing applications, the solute is much larger and heavier than the solvent and molecular dynamics simulations in the desired region are unavailable. When this is the case, some have resorted to a different correlation approach. When available simulations are correlated with temperature and solvent molar volume, the following approximate form is observed:

$$\frac{D_{12}}{\sqrt{T}} = M(V - V_0)^{2/3} \quad (4)$$

V is the solvent molar volume, V_0 is the limiting solvent volume at which diffusion ceases, and M is a parameter presumably accounting for solute and solvent size and mass, "roughness," and any other factors. This equation is similar in spirit to Batchinski/Hildebrand free volume approach (10,11), and is attractive due to its simplicity. The term V_0 has been determined from experiment and is very close to the molar volume of the solvent at the liquid-solid phase transition (12), which is a pleasing agreement with physical expectations. The required physical property data are solvent molar volume, and the "sizes" (e.g. molecular masses, hard-core volumes) of the solute and solvent.

In the supercritical state, it has been established by a variety of experimental (13,14) and theoretical (15,16) means that the local environment around a dilute solvent molecule may be substantially more dense than the bulk fluid. This clustering has a substantial effect on phase equilibria; all successful commercial applications of supercritical fluid processing demonstrate strongly attractive behavior between solute and solvent (17). In addition, use of a cosolvent as an

entrainer to promote specific cosolvent/solute chemical interactions also leads to clustering. Thus it stands to reason that the diffusion process should also be strongly affected by the clustering phenomenon, and that this should be taken into account in correlation of experimental data. However, hydrodynamic theory and hard-sphere theory, which use bulk-solvent thermophysical properties, have no theoretical provision to take local phenomena into account. In addition, it is significant to note that the hard sphere potential function, which is the basis of hard-sphere theory, has no attractive component and is therefore incapable of predicting the liquid-vapor phase transition, critical point, or the strongly attractive forces which cause the clustering phenomena.

Experimental

Previous work has indicated that the clustering phenomena, particularly chemical clustering, will decrease the diffusion coefficients. Here we report accurate experimental data for the binary systems CO₂ (solvent) plus solutes acridine or phenanthrene or benzoic acid, and for the ternary systems CO₂ plus methanol (solvent) plus solutes acridine or phenanthrene or benzoic acid. Data for the same solutes in the subcritical solvent acetone, or acetone/methanol mixtures, are also reported. Acetone is in some respects chemically analogous to CO₂ (18), so these data allow one to make comparison between diffusion in ordinary and supercritical solvents. The goal is to examine the applicability of "traditional" methods of correlation to the supercritical state.

The experimental apparatus and procedure have been described (19). The data reported herein for diffusion in supercritical CO₂ and CO₂ + methanol at 170 atm (2500 psia) supersede those data reported previously. We have improved our experimental apparatus to eliminate a small extraneous variance in the response curves introduced by the injection valve; consequently, the accuracy of the reported values has now been improved. The experimental results reported for the supercritical solvents at 272 atm (4000 psia) are new data, as are the results for diffusion in acetone + methanol solvent. All experimental data are reported in Tables I and II.

In the rest of this section we make some general comments related to the precision and accuracy of the reported data. The standard deviations of the measurements are reported in Tables I and II; these are based on 10 or more repeat measurements for each point. The maximum standard deviation observed when using supercritical solvents was 4.2%, and the maximum standard deviation in the ordinary liquid solvents was 3.5%, therefore the reproducibility is quite good.

It is noted that diffusivities in the ternary systems have been interpreted using the "pseudo-binary" assumption, which is not exact. However, at the extremely low solute concentrations experienced in supercritical systems, this assumption should not introduce serious errors.

When the Taylor dispersion method is used to measure diffusion in ordinary liquid solvents, the main sources of experimental error are due to extraneous variance associated with the sample injection and detection hardware, as well as

Table I. Diffusion Coefficients in supercritical CO₂ and CO₂ + 5 mole percent methanol ($10^9 D_{12}$, m²/s)

Solute	T (K)	CO ₂		CO ₂ + CH ₃ OH	
		170 atm	272 atm	170 atm	272 atm
Benzoic acid	308	9.7 ± 0.4	8.9 ± 0.2	7.2 ± 0.2	6.0 ± 0.1
	318	11.9 ± 0.3	10.4 ± 0.2	8.4 ± 0.3	6.8 ± 0.2
	328	12.9 ± 0.4	12.1 ± 0.3	9.7 ± 0.3	8.0 ± 0.3
Phenanthrene	308	9.6 ± 0.4	8.4 ± 0.2	8.8 ± 0.2	7.4 ± 0.1
	318	11.4 ± 0.4	9.2 ± 0.2	10.1 ± 0.3	8.4 ± 0.2
	328	12.6 ± 0.3	10.3 ± 0.2	11.9 ± 0.5	9.4 ± 0.2
Acridine	308	7.7 ± 0.3	6.7 ± 0.1	7.1 ± 0.1	6.3 ± 0.1
	318	8.9 ± 0.3	7.7 ± 0.1	8.2 ± 0.2	7.2 ± 0.1
	328	10.3 ± 0.1	8.9 ± 0.2	9.2 ± 0.2	8.2 ± 0.2

to secondary flow effects (20). It is possible to eliminate these almost completely with careful design; one will then observe an experimental response which is a (nearly perfect) Gaussian curve. The diffusion coefficient is calculated by fitting the response curve to a Gaussian model and obtaining the variance by non-linear least squares regression (21). We then plot the experimental response curve against the best-fit Gaussian response; any significant deviation from Gaussian behavior can easily be observed and indicates qualitatively a departure of the experiment from the ideal Taylor dispersion model. This visual check is one of our main criteria for accepting or rejecting an experiment.

When the Taylor dispersion technique is used with near-critical solvents, additional experimental difficulties may be introduced (3). We have determined that solute adsorption occurs for the acridine/CO₂ system, as indicated by substandard conformance of the measured response to a Gaussian curve (Figure 1). Although a deactivated fused silica tube was used (and several different tubes were used over the course of the study), it seems that there are still a few active siloxyl groups present, and that the basic molecule acridine tends to adsorb on these sites. This additional peak tailing was not observed in any other system, not even in the CO₂/methanol/acridine system. In this latter case the methanol appeared to have a passivating effect on the surface of the diffusion tube. Solute adsorption has been previously observed when using stainless steel diffusion columns (22).

For all other systems except CO₂/acridine, the confidence limits on the experimental values may be judged from the standard deviations, and we believe that systematic error has been reduced to as low a level as possible. For the system CO₂/acridine, the accuracy of the measurements is impaired to an unknown degree by the systematic additional variance due to adsorption; consequently,

Table II. Diffusion Coefficients in acetone and acetone + 5 mole percent methanol ($10^9 D_{12}$, m^2/s)

Solute	T (K)	Acetone	Acetone + CH ₃ OH
Benzoic acid	308	3.14 ± 0.08	3.07 ± 0.06
	318	3.42 ± 0.07	3.37 ± 0.07
	328	3.84 ± 0.07	3.86 ± 0.08
Phenanthrene	308	3.24 ± 0.05	3.25 ± 0.03
	318	3.56 ± 0.07	3.66 ± 0.07
	328	4.04 ± 0.06	4.10 ± 0.08
Acridine	308	3.16 ± 0.04	3.18 ± 0.05
	318	3.62 ± 0.06	3.54 ± 0.03
	328	3.95 ± 0.07	4.07 ± 0.06

the values for this binary pair must be used with more caution. The effect of adsorption (increased peak tailing) is to increase the variance of the response curve and consequently to decrease the calculated value of the diffusion coefficient. This can be understood by considering the simplest solution to the Taylor dispersion experiment, which indicates that the effective dispersion coefficient K is given by (23):

$$K = \frac{R^2 u^2}{48 D_{12}} \quad (5)$$

In this equation R is the radius of the diffusion tube and u is the average velocity of the solvent flowing in the tube. Thus, as the variance of the observed response curve increases (increased dispersion coefficient), the diffusion coefficient calculated from that variance must decrease. We can thus say qualitatively that the "true" diffusion coefficients for CO₂/acridine should be somewhat higher than the values reported in Table I.

Discussion

From the data in Table I, the diffusivities of phenanthrene are slightly lower than those of benzoic acid when the solvent is pure CO₂. The diffusivities of acridine in pure CO₂ are considerably lower than those of phenanthrene, but this is likely an artifact introduced by the adsorption effect observed for acridine, as discussed above. Because both acridine and phenanthrene are 3-ring aromatics, with nearly equal molecular weights, one might expect the diffusivities to be more nearly the same in pure CO₂. Because of the greater uncertainty associated with the acridine/CO₂ data, further discussion of this system is limited.

The addition of methanol at a given temperature and pressure reduces the observed diffusivities in all cases. The effect is partly due to an increase in bulk solvent density due to the presence of methanol, and it is more revealing to look at the temperature/density dependence of the diffusion coefficient, rather than

temperature/pressure dependence. However, Table I does give some insight. The relative effect of methanol on benzoic acid is greater than the effect on phenanthrene. This suggests that for benzoic acid the chemical association with methanol is an additional mechanism which acts to decrease the diffusion coefficient. Phenanthrene does not undergo acid/base association as benzoic acid does, and therefore this mechanism is not acting to slow the diffusion of phenanthrene.

It is observed from Table II that the addition of methanol to acetone has an almost negligible effect on the diffusion coefficients at a given temperature and pressure. Therefore the chemical association effect which can clearly be seen for benzoic acid and acridine in the supercritical environment is not seen in the environment of an ordinary liquid solvent.

To examine the suitability of hard sphere theory for correlating diffusivities in supercritical fluids, we prepared the plots suggested by equation 4. There are two features associated with hard sphere theory that one would observe if the theoretical framework is suitable. First, the quantity D_{12}/\sqrt{T} should be correlated with solvent molar volume, equation 4. Earlier treatments suggested a linear dependence of this group with molar volume, but more recent molecular dynamics simulations have suggested that D_{12}/\sqrt{T} is linear with $V^{2/3}$ (24). Second, regardless of the exact functionality, constant density experiments should show no pressure dependence of D_{12}/\sqrt{T} .

For self-diffusion coefficients, both the linearity and the equality of constant density experiments have been observed, in both sub-critical and supercritical fluids (24). Similarly, for binary diffusion in sub-critical solvents, involving non-associating species, the theory holds reasonably well (12). Chemical clustering does not occur in any of these systems, and the theory appears to provide a reasonable basis for correlation.

The binary diffusion coefficients for benzoic acid and phenanthrene in supercritical solvent are plotted in Figures 2-3 according to the form suggested by RHS theory (units are kelvins, m^2/s , and cm^3/mol). For reference, near the right-hand side of each figure appears a $\pm 5\%$ error bar, which is larger than any experimentally-observed standard deviation. Molar volumes of pure CO_2 were calculated from the IUPAC equation of state, while molar volumes of the CO_2 + methanol solvent were estimated using the Lee-Kesler corresponding states approach (25). There is a scarcity of experimental data regarding volumetric behavior of CO_2 /cosolvent mixtures, and this introduces additional uncertainty into the subsequent analysis; however, the Lee-Kesler approach did give acceptable agreement ($\pm 1.5\%$ or less error) with the few data reported by Dobbs et al. (26) for densities of CO_2 + 3.5 mole percent methanol.

Benzoic acid (Figure 2) shows a statistically significant (based on the t -test) pressure dependence in pure CO_2 (examine the open and closed circles at $V^{2/3}$ of about 14). In addition, the low-pressure data points (open circles) show a significant non-linearity, while the three high-pressure points appear more linear. Linear regression of the three high pressure data points (according to equation 4) gives an intercept corresponding to $V_0 = 34 \text{ cm}^3/\text{mol}$, which is close

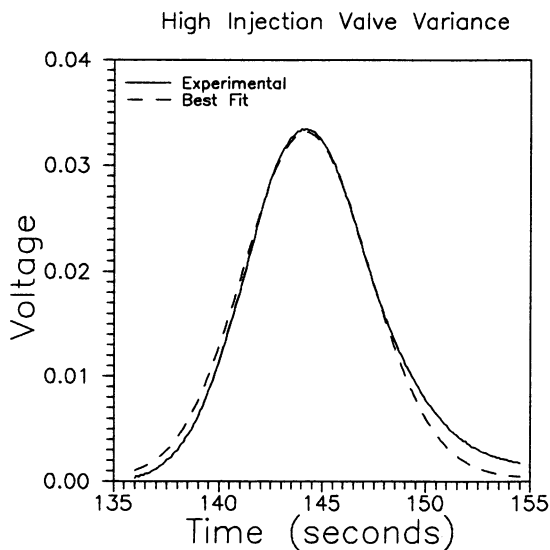


Figure 1. Experimental and best-fit response curves for a Taylor dispersion experiment showing peak asymmetry due to adsorption.

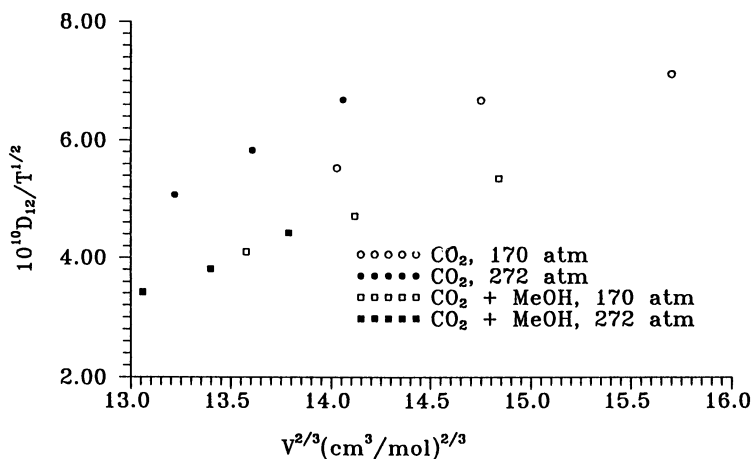


Figure 2. Diffusion coefficients for benzoic acid plotted according to rough hard sphere theory.

to the molar volume of compressed liquid CO₂ near its triple point. This intercept value is in accordance with the studies cited above where diffusion in ordinary liquids was studied (e.g., 12). When methanol is added (open and closed squares), the pressure dependence disappears, and in addition the apparent curvature lessens. We now propose an interpretation of these features of Figure 2 which considers clustering to occur between the solute and solvent, or between solute and entrainer. Additional local interactions peculiar to supercritical fluids, such as solvent/cosolvent and solute/solute interactions, are not considered.

First, consider the effect of pressure on the pure solvent. At the lower pressures, the solvent is nearer its critical point, the fluid compressibility is more sensitive to temperature, and the tendency of the pure solvent to cluster around the solute is stronger. Therefore at lower pressure, the solute molecule "sees" a higher local density than at higher pressure, for a given solvent bulk density. This explains why the diffusion coefficient would be lower at low pressure and a given bulk density: the solvent is moving through a locally more dense fluid. In addition, at the lower pressure the local density is more sensitive to temperature, which could explain why the low pressure data are non-linear in $V^{2/3}$, while the higher pressure data appear linear.

When methanol is added, the pressure dependence of diffusivity disappears, and linearity is observed. This suggests that chemical clustering of methanol around benzoic acid is persistent over the range of temperatures and pressures studied. Other studies have also indicated the presence of chemical association between methanol and benzoic acid. The fact that diffusivities are lower in CO₂/methanol mixtures than in pure CO₂ is also evidence of the existence of a methanol/solute cluster.

While the analysis above seems to explain the behavior of benzoic acid very neatly, it does not explain the behavior of phenanthrene. The phenanthrene data (Figure 3) also show effects of pressure and entrainer addition, but for this solute the behavior is the opposite of that observed for benzoic acid. Once again there is a pressure dependence of D_{12}/\sqrt{T} in pure CO₂, but for this solute the higher-pressure data fall below the lower pressure measurements, which is the reverse of benzoic acid behavior. In the mixed solvent, the pressure dependence again nearly disappears, but D_{12}/\sqrt{T} is now higher than in the pure solvent. Clearly, accounting for this behavior using local molecular phenomena is now a much more complicated situation. It will be necessary to take into account both the differences in size and chemical interactions between the solute and the surrounding solvent/cosolvent molecules.

Olesik and Woodruff (1) also note deviations from RHS theory for their measurements on *m*-cresol in CO₂, and CO₂ + entrainer mixtures. Rather than using the approach suggested by equation 3, they used equation 2 to back-calculate the RHS theory "translational-rotational coupling factor" from their data. These factors, originally intended to be density-independent and constant for a given binary, were found to be functions of both density and composition. With this approach, local density enhancements whether due to

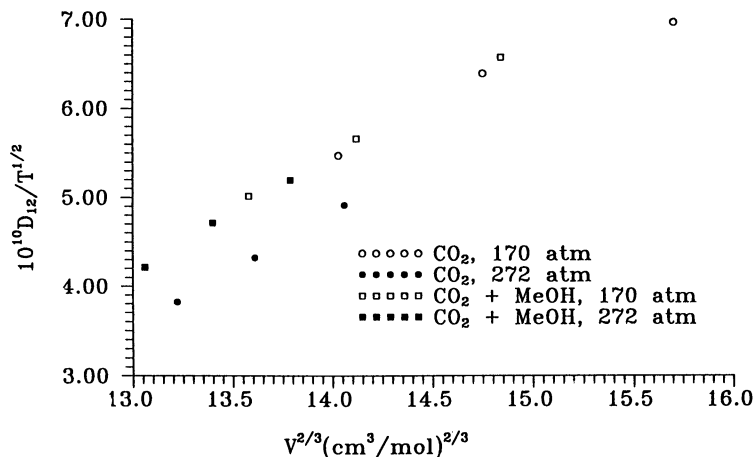


Figure 3. Diffusion coefficients for phenanthrene plotted according to rough hard sphere theory.

binary clustering or chemical association, are all lumped into the roughness factor.

Figures 4 and 5 show the diffusivities for benzoic acid and phenanthrene plotted according to hydrodynamic theory; D_{12} should be linear with T/μ , with μ being the solvent viscosity. In these plots the viscosity of pure CO_2 was taken from the IUPAC tables, while the mixture viscosities were estimated using the procedure of Lucas, outlined by Reid et al. (27). Units of viscosity are Pa·s.

Figure 4, benzoic acid, again demonstrates a significant pressure/density dependence in pure CO_2 , while diffusivities in the mixed solvent are more nearly on the same straight line. Figure 5, phenanthrene, now shows that the data fall more nearly on a straight line. There is still discernible pressure dependence in the mixed solvent, however.

Conclusions

These results show some of the effects of density and cosolvent upon diffusion coefficients. In particular, the frequently-used RHS theory and hydrodynamic theory show significant shortcomings upon closer inspection. Additional quantitative interpretation is at present inhibited by lack of accurate volumetric and viscosity data on the mixed solvents, and by lack of PVT information on the dilute solutes in these solvents. In addition, significant advances in modeling specific interactions between solute/solvent/cosolvent will be required.

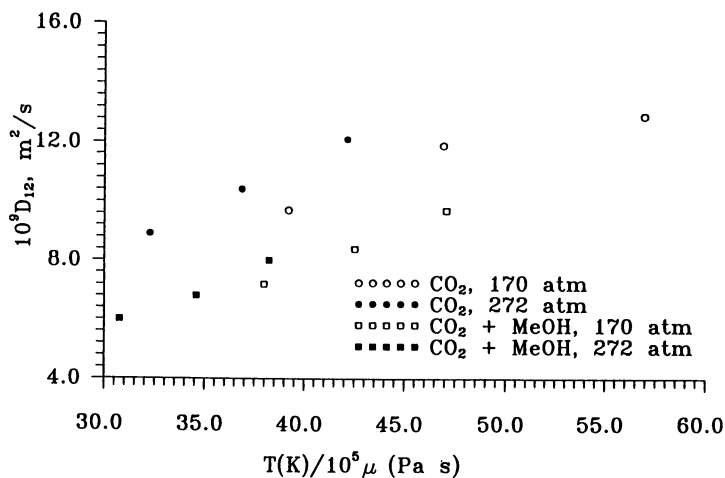


Figure 4. Diffusion coefficients for benzoic acid plotted according to hydrodynamic theory.

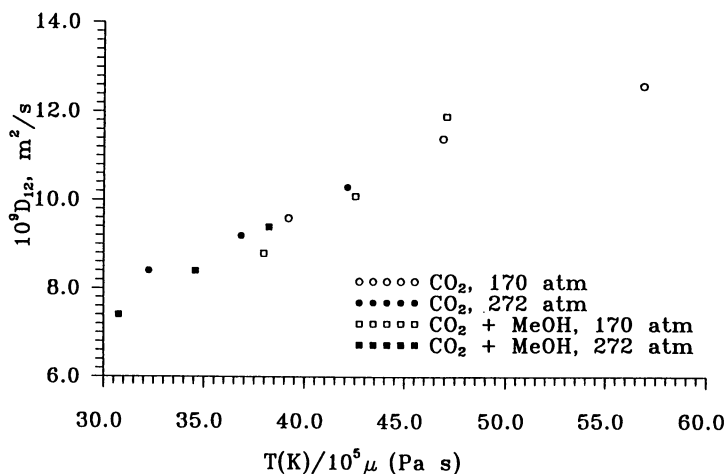


Figure 5. Diffusion coefficients for phenanthrene plotted according to hydrodynamic theory.

Literature Cited

1. Olesik, S. V.; Woodruff, J. L. *Anal. Chem.* **1991**, *63*, 670.
2. Funazukuri, T.; Hachisu, S.; Wakao, N. *Ind. Eng. Chem. Res.* **1991**, *30*, 1323.
3. Clifford, A. A.; Coleby, S. E. *Proc. R. Soc. Lond. A.* **1991**, *433*, 63.
4. Dahmen, N.; Kordikowski, A.; Schneider, G. M. *J. Chromat.* **1990**, *505*, 169.
5. Sassiati, P. R.; Mourier, P.; Caude, M. H.; Rosset, R. H. *Anal. Chem.*, **1987**, *59*, 1164.
6. Sutherland, W. *Phil. Magazine* **1905**, *9*, 781.
7. Tyrrell, H. J. V.; Harris, K. R. *Diffusion in Liquids*. Butterworths Press: London, 1984.
8. Wilke, C. R.; Chang, P. *AIChE Journal* **1955**, *1*, 264.
9. Chandler, D. *J. Chem. Phys.* **1975**, *62*, 1358.
10. Batchinski, A. J. *Z. Physik. Chem.* **1913**, *84*, 643.
11. Hildebrand, J. H. *Science* **1971**, *174*, 490.
12. M. A. Matthews; A. Akgerman. *J. Chem. Phys.* **1987**, *87*, 2285.
13. Eckert, C. A.; Ziger, D. H.; Johnston, K. P.; Kim, S. *J. Phys. Chem.* **1986**, *90*, 2738.
14. Johnston, K. P.; McFann, G. J.; Lemert, R. M. *Fluid Phase Equilib.* **1989**, *52*, 337.
15. Petsche, I. B.; Debenedetti, P. G. *J. Chem. Phys.* **1989**, *91*, 7075.
16. Wu, R.-S.; Lee, L. L.; Cochran, H. D. *Ind. Eng. Chem. Res.* **1990**, *29*, 977.
17. Debenedetti, P. G.; Mohamed, R. S. *J. Chem. Phys.* **1988**, *90*, 4528.
18. Walsh, J. M.; Ikonomou, G. D.; Donohue, M. D. *Fluid Phase Equilib.* **1987**, *33*, 295.
19. Smith, S. A.; Shenai, V. M.; Matthews, M. A. *J. Supercritical Fluids* **1990**, *3*, 175.
20. Alizadeh, A.; Nieto de Castro, C. A.; Wakeham, W. A. *Int. J. Thermo-phys.* **1980**, *1*, 243.
21. Akgerman, A. Final Report of Project DE-AC22-70032 to the U. S. Department of Energy, 1988.
22. Feist, R.; Schneider, G. M. *Sep. Sci. Tech.* **1982**, *17*, 261.
23. Taylor, G. I. *Proc. Roy. Soc.* **1953**, *A219*, 186.
24. Erkey, C.; Gadalla, H.; Akgerman, A. *J. Supercritical Fluids* **1990**, *3*, 180.
25. Lee, B. I.; Kesler, M. G. *AIChE Journal* **1975**, *21*, 510.
26. J. M. Dobbs; J. M. Wong; R. J. Lahiere; K. P. Johnston. *Ind. Eng. Chem. Res.* **1987**, *26*, 56.
27. Reid, R. C.; Prausnitz, J. M.; Poling, B. E. *The Properties of Gases and Liquids*; 4th ed.; McGraw-Hill: New York, NY, 1987.

RECEIVED April 27, 1992

Chapter 9

Viscosity of Polymer Solutions in Near-Critical and Supercritical Fluids

Polystyrene and *n*-Butane

Erdogan Kiran and Yasar L. Sen¹

Department of Chemical Engineering, University of Maine,
Orono, ME 04469

Viscosity and density of polystyrene solutions in *n*-butane have been measured as a function of pressure up to 70 MPa in the temperature range 395 to 445 K using a specially designed falling cylinder viscometer. Results are presented for molecular weights 4,000 and 9,000 at 4 and 12 % by wt concentrations. It is shown that viscosities increase with increasing pressure, polymer concentration or molecular weight but decrease with increasing temperature. At a given pressure, the temperature dependence of viscosity follows the usual Arrhenius type variation with $\eta = A \exp(B/T)$. Both the temperature and pressure dependence are correlated with density and for each polymer solution, viscosity data merge to a single curve when plotted as a function of density. This dependence on density is described by an equation of the form $\eta = C_1 + C_2 \exp(C_3\rho)$. Concentration dependence of viscosity and the significance of intrinsic viscosity and its pressure and temperature dependence in terms of hydrodynamic volume of the polymer and solvent-polymer interactions are also discussed.

In the past decade, a significant amount of research effort has been devoted to the properties of fluids and fluid mixtures under pressure, especially at near- and supercritical conditions (1,2,3). These fluids are finding increasing use as *tunable process solvents or tunable reaction media* in the chemical process industries. Their tunable nature stems from the fact that the properties of these fluids are easily adjusted by manipulations of pressure and can be customized for a given process, which may involve either *physical transformations* (such as separation by selective or sequential dissolutions) or *chemical transformations* (such as reactions or reactive extractions).

¹Current address: SEKA, Izmit, Turkey

0097-6156/93/0514-0104\$06.00/0
© 1993 American Chemical Society

Processing with near- and supercritical fluids is particularly important to the polymer industry. These fluids can be used in polymer formation (4, 5), fractionation and purification (3, 6, 7), or other modifications (8). Since equilibrium solubility and reactivity are the key parameters needed for the initial assessment of the feasibility of a given process, a majority of the research has so far been concentrated on the thermodynamics and phase behavior of these systems (3, 9, 10, 11, 12, 13). There has been relatively little research on the rates of momentum, mass, and energy transfer and the related transport coefficients, namely, viscosity, diffusivity, and thermal conductivity in these fluids. Transport coefficients are needed for the ultimate optimal process design, and among these, viscosity is especially important since it also influences the mass and heat transfer characteristic.

Open literature on the viscosity of polymers solutions at high pressures is very limited and are often reported at temperatures far below the critical temperature of the solvent involved (14-20). Most of the available literature is on polystyrenes in solvents such as trans decalin (19), trans-decahydronaphthalene (14), t-butyl acetate (15, 17, 18), and a series of other solvents including cyclohexane, cyclopentane, diethylmalonate, and 1-phenyldecane(16). One other publication reports on the viscosity of poly (dimethyl siloxane) in cyclohexyl bromide (21).

A number of these earlier studies on polymer solutions have been conducted with a different practical objective such as understanding high pressure lubrication and the consequences of phase separation under shear flow, and the use of polymers as additives in motor oils and in oil recovery (18, 20, 22). Studies on the viscosity of polymer-fluid systems in which the fluid is a non-solvent under ordinary conditions, but becomes a solvent at high pressures is a relatively new activity (23).

In addition to its practical importance in processing applications, investigation of the viscosities of polymer solutions in supercritical fluids is of theoretical interest. Since the solvent power is related to the density, a supercritical fluid can be changed from a *good* to a *poor* solvent or vice versa by manipulating the density of the fluid. In particular, at a given temperature, pressure manipulations may permit obtaining a θ - solvent which would be characterized by a θ - pressure in which polymer chains would assume their unperturbed dimensions. This notion of θ - pressure or θ - density as opposed to conventional θ - temperature is currently being explored (24). Measurement of viscosity as a function of fluid density, in particular evaluation of the intrinsic viscosities would provide crucial information on the changes of hydrodynamic volume as θ conditions are approached.

In our previous publications we have reported on the solubility of polystyrene standards of known molecular weights (4,000 and 9,000) and polydispersities (≤ 1.06) in n-butane and n-pentane (9, 25, 26). Preliminary results on their viscosities were also presented (23). Recently we reported on the complete viscosity data for these and higher alkanes (27). We now report on the viscosities of solutions of these polymers in n-butane at pressures up to 70 MPa in the temperature range of 395-445 K. For n-butane this corresponds to a reduced temperature (T/T_c) range from 0.93 to 1.04 and a reduced pressure (P/P_c) range from 7.9 to 18.5. Pressures are all above critical, and temperatures cover below and above critical conditions. The results are presented in terms of the effect of

pressure, temperature, density and the molecular weight and concentration of the polymer.

Experimental

Viscometer. The viscometer used in this study has been especially designed for investigation of supercritical fluids and polymer solutions (27, 28). It is a high-pressure high-temperature viscometer which permits the measurement of viscosity, density and phase behavior all in the same instrument over a wide range of temperatures (up to 200 °C) and pressures (up to 70 MPa). A schematic diagram of the system is shown in Figure 1. The viscometer unit consists of a view cell (VC) with a fall tube (FT) and variable-volume part (VVP) all enclosed in an air-heated oven. Viscosity measurements are based on the measurement of the fall time of a cylindrical sinker using three LVDT (linear variable differential transformer) coils (C1) positioned along the fall tube. Density measurements are based on the measurement of viscometer volume at any time during an experiment by monitoring the movement of the piston in the variable-volume part with the help of another LVDT coil (C2). There are two sapphire windows (SW) which permit the visual inspection of the phase state of the system under investigation. The cell content is mixed with the aid of either an external electromagnetic stirrer (MS) or a magnetic recirculation pump (MRP).

Viscometer temperature is measured with an accuracy of ± 1.5 K using a J-type thermocouple and read with a resolution of 0.1 K. Pressures are measured with an accuracy of ± 0.06 MPa using a Dynisco pressure transducer and read with a resolution of 0.007 MPa. Fall times are recorded with a computer with an accuracy of ± 2 ms. Volume displacements are determined with $\pm 0.2\%$ accuracy.

The inlet ports SP and SI are used to load the solute (polymer) and the solvent to the viscometer. Once the thermal equilibrium is reached, temperature, pressure and piston position are all recorded whenever a fall time measurement is taken. At each temperature and pressure, allowing sufficient time between consecutive measurements, several fall time measurements are recorded. A pull-up electromagnet (PM) is used to reposition the sinker after each measurement. At any given temperature, pressure changes are accomplished by changing the position of the piston in the variable volume part of the cell using the pressure generator (PGN).

In case of polymer solutions, the cell is first loaded with known amount of the polymer and the solvent to give a selected concentration, and then the temperature and pressure are adjusted to achieve complete solubility. The solvation process is facilitated with the action of the recirculation pump. Fall time measurements are taken at temperatures and pressures corresponding to the complete miscibility range.

From measurement of the fall time and the density, viscosities are determined using the relationship

$$\eta = K(\rho_s - \rho)t \quad (1)$$

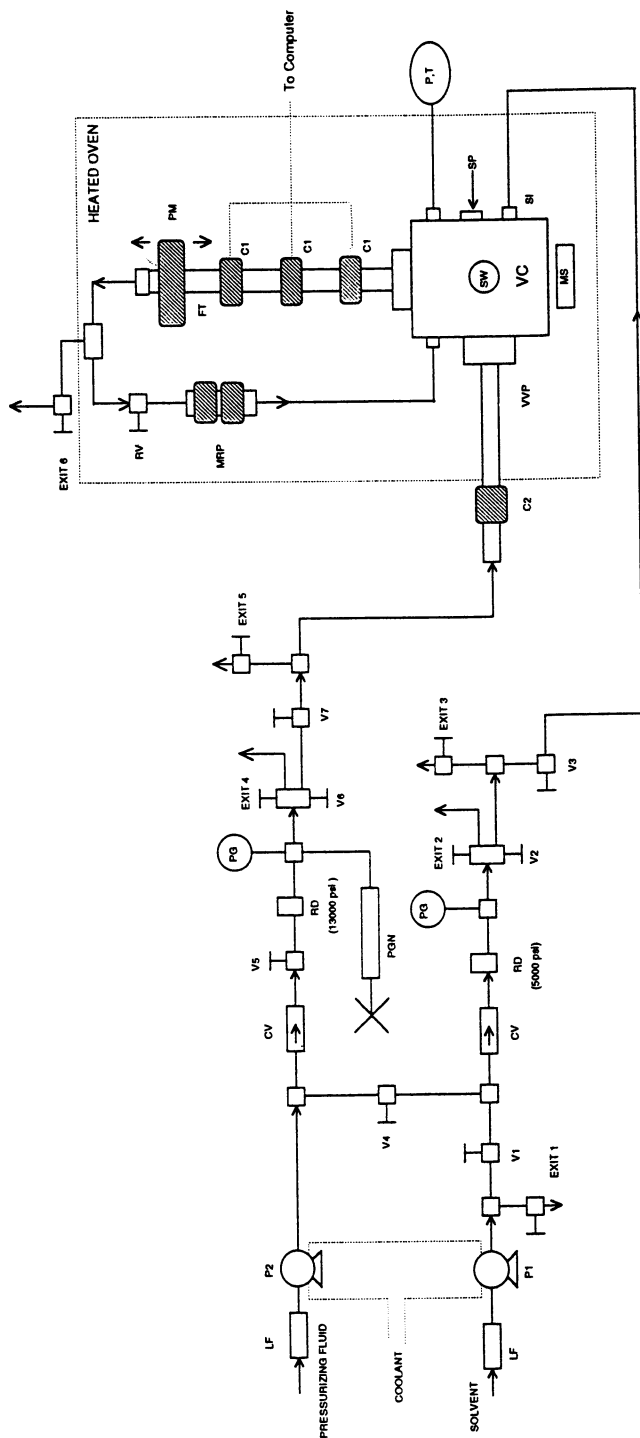


Figure 1. Schematic diagram of the viscometer system. [LF = line filter; P1, P2 = high pressure pumps; V = valve; CV = check valve; RD = rupture disc; PG = pressure gauge; PGN = pressure generator; C1; C2 = LVDT coils; VVP = variable volume piston; MS = magnetic stirrer; VC = view cell; SW = sapphire window; SI = solvent inlet; SP= solute port; P, T = pressure / temperature sensor; FT = fall tube; PM = pull-up magnet; MRP = magnetic recirculation pump].

where ρ_s and ρ are the densities of the sinker and the fluid, t is the fall time for the sinker and K is the instrument calibration constant which is determined by measuring the fall time of fluids of known viscosity and density.

Procedure for calibration and other operational details of the viscometer have been described in our previous publications (27, 28). Using this systems, viscosities and densities are determined with 3% and 1% accuracy, respectively.

Materials. Polystyrene standards with nominal molecular weights of 4,000 ($M_w/M_n = 1.06$) and 9,000 ($M_w/M_n = 1.09$) were obtained from Pressure Chemical Co. The solvent *n*-butane (purity 99.9%) was obtained from Matheson. It was used without further purification. The critical properties of *n*-butane are $T_c = 425.2$ K, $P_c = 3.80$ MPa, and $\rho_c = 0.2279$ g/cm³

Results and Discussion

Demixing Pressures. Figure 2 shows the demixing pressures, as determined through visual observations of the view-cell of the viscometer, as a function of temperature at 4 and 12 % by wt polymer concentrations. The region above each curve represents the one-phase homogeneous solutions. At these concentrations, the behavior is UCST type, that is at a given pressure, one-phase regions are entered upon increasing the temperature. At a fixed temperature, two-phase regions are entered with a decrease in pressure. Temperature sensitivity of the demixing pressures (dP/dT) shows a marked increase at temperatures below the critical temperature of the solvent (425 K). These demixing pressures are higher for the higher molecular weight sample for a given concentration. For each polymer sample, in going from 4 to 12 % concentration, demixing pressures are also observed to increase. This is as expected since the critical polymer concentration for these systems occur at a higher concentration, at 25 wt % (for MW = 9,000) and 32 wt % (for MW = 4,000) (25). Complete solubility envelopes for polystyrene-butane system have been described in our previous publications (25).

Viscosities. The viscosity measurements in the present study have all been carried out in the temperature and pressure range corresponding to the one-phase solutions shown in Figure 2.

Effect of Temperature and Pressure. Figures 3 to 6 show the variation of viscosity with pressure as a function of temperature. The results are shown for the 4 and 12% by wt polymer concentrations. The general observations are that viscosities increase with increasing pressure but decrease with increasing temperature. The sensitivity to a change in pressure, $(d\eta/dP)_T$, is observed to be greater at temperatures lower than the critical temperature of the solvent. As pressures are decreased, viscosities tend to approach each other. Even though viscosities were not measured through the phase transition regions in the present study, should phase separation be permitted to take place, viscosities would eventually approach that for the pure solvent, *n*-butane. In fact viscosity measurements are used in the literature as a method for determination of the demixing conditions for polymer solutions (14, 15, 16).

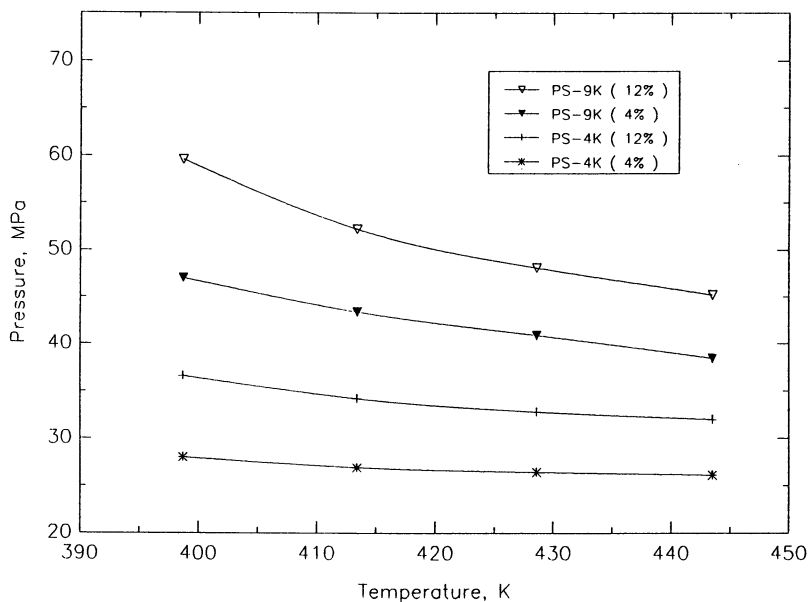


Figure 2. Demixing pressures for polystyrene standards of molecular weight 4,000 and 9,000 at 4 and 12% by wt concentrations in n-Butane. The regions above each curve correspond to the one-phase regions.

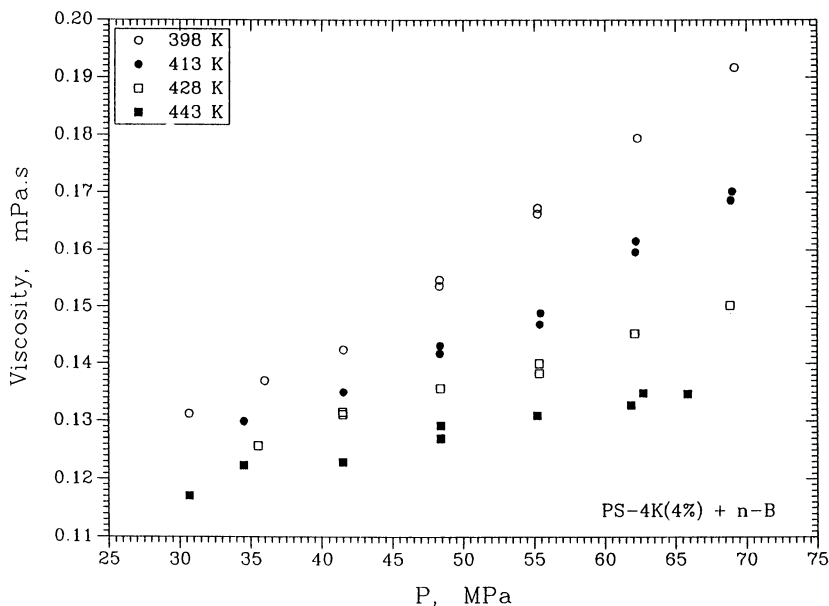


Figure 3. Variation of viscosity of polystyrene solutions in n-Butane with pressure at selected temperatures. Molecular weight = 4,000. Concentration = 4% by wt.

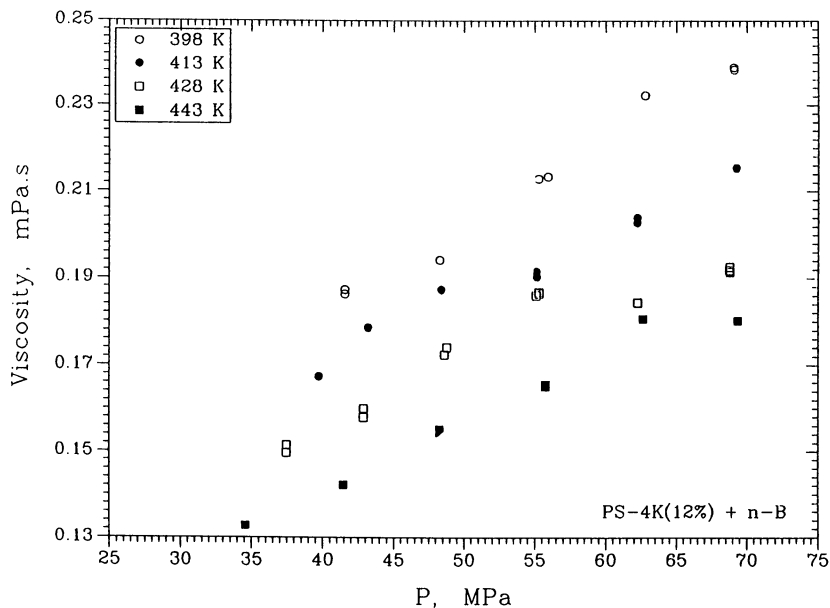


Figure 4. Variation of viscosity of polystyrene solutions in n-Butane with pressure at selected temperatures. Molecular weight = 4,000. Concentration = 12 % by wt.

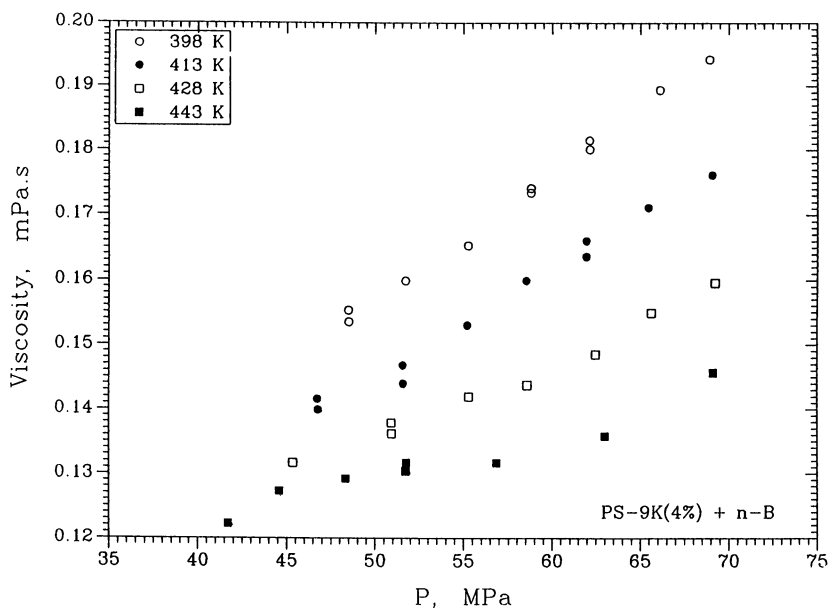


Figure 5. Variation of viscosity of polystyrene solutions in n-Butane with pressure at selected temperatures. Molecular weight = 9,000. Concentration = 4 % by wt.

The temperature dependence of viscosity is often described by Arrhenius type exponential expressions such as the Andrade Equation (29, 30)

$$\eta = A \exp (B/T) \quad (2)$$

or

$$\ln \eta = \text{Constant} + B/T \quad (3)$$

where B is related to the flow activation energy and A is a term of entropic significance. Temperature dependence of viscosity in the present study is also represented well with such a relationship. Figure 7 is an example showing the variation of $\ln \eta$ with $1/T$ for the 12 % solutions at 69MPa.

For correlation of the pressure dependence of viscosity at a given temperature, a range of empirical relationships have been proposed in the literature (22, 29, 30). Some recent correlations used to describe polymeric systems are of the form

$$\ln \eta = f (M) + f(T) + f(T,P) \quad (4)$$

which incorporates functions which depend on molecular weight, temperature and temperature and pressure (31).

In the present study, data were not tested to find suitable correlations to describe the pressure dependence of viscosity. Instead, density correlations which combine the effects of both temperature and pressure have been developed.

Effect of Density. A special advantage offered by the present experimental system is the ability to measure the densities under actual experimental temperature and pressure conditions. Density is known to be a good scaling parameter for viscosity. For example the Enskog relationship expresses viscosity as

$$\eta = \eta_0 \{ 1/\chi + 0.800 (b\rho) + 0.761(b\rho)^2 \} \quad (5)$$

where η is the viscosity, η_0 is the low pressure viscosity, b is the excluded volume (related to the hard sphere diameter), and ρ is the mol density, and χ is the radial distribution function (29, 30, 32)

Relationships based on the free volume theories such as the Batschinski equation

$$1/\eta = B (V-V_0) \quad (6)$$

or the Doolittle equation

$$\eta = A \exp \{ C V_0 / (V-V_0) \} \quad (7)$$

in which $(V-V_0)$ is the free volume and A, B, and C are constants, also predict density dependent variations since free volume is inversely related to the density (33, 34, 35). In fact, the free volume theories suggest that viscosities may perhaps be expressed as polynomial or exponential functions of density of the form

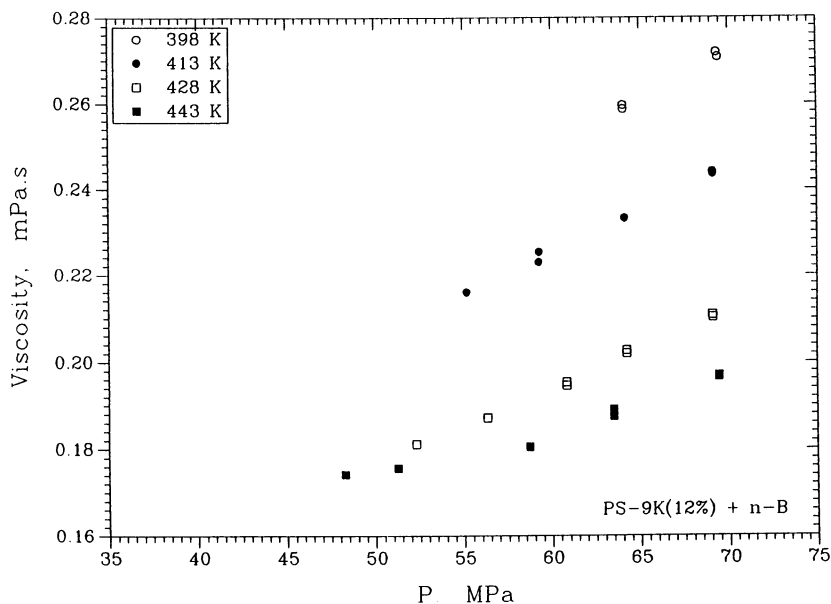


Figure 6. Variation of viscosity of polystyrene solutions in n-Butane with pressure at selected temperatures. Molecular weight = 9,000. Concentration = 12 % by wt.

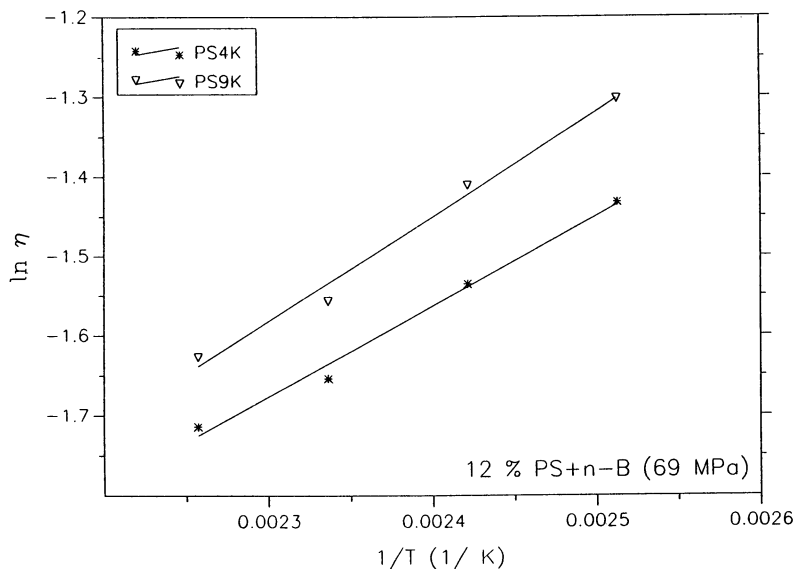


Figure 7. Variation of \ln viscosity with $1/T$ for polystyrene solutions in n-Butane at a constant pressure of 69 MPa. Molecular weights 4,000 and 9,000. Concentration = 12 % by wt.

$$\eta = A_1\rho + A_2\rho^2 + A_3\rho^3 \quad (8)$$

or

$$\eta = B_1 \exp(B_2\rho) \quad (9)$$

We have recently shown that density can indeed be used to correlate the viscosities of alkanes over a wide range of temperatures and pressures (27). The viscosity versus pressure plots obtained at different temperatures all merge to a single curve when plotted against density for n-butane, n-pentane, n-hexane, and n-octane. The dependence of viscosity on density for these alkanes has been represented by an exponential function of the form

$$\eta = C_1 + C_2 \exp(C_3\rho). \quad (10)$$

Figures 8-11 show the viscosity data presented in Figures 3-6 in the density domain. All data reduce to a single curve which again is found to be correlated well with the exponential equation (Equation 10) used to correlate the alkanes. The solid curves shown in the figures represent the correlation curves. Table 1 shows the parameters for the correlations for the pure solvent and each polymer-solvent system.

Effect of Concentration and Molecular Weight of Polymer. Figure 12 is a comparison of the viscosities of n-butane and the polymer solutions as a function of pressure at 443 K. As would be expected, viscosities increase with an increase in the concentration or the molecular weight of the polymer. The sensitivity to pressure change appears to be greater for the more concentrated solutions. The influence of the molecular weight is also greater in the more concentrated solutions. Molecular weight effects are augmented at higher pressures.

In order to separate the contributions to the viscosity change over that of the solvent as pressure is increased, relative viscosities η/η_0 have been evaluated. Here η_0 represent the viscosity of pure n-butane at the same temperature and pressure conditions. They are shown in Figures 13 and 14 at 443 K at two different pressures (55 and 69 MPa) for 4, 8, and 12 wt % concentrations. The change in relative viscosity shows more clearly that the viscosity is affected more as polymer concentration or molecular weight is increased.

The variation of relative viscosity with concentration shown in Figures 13 and 14 can be described by parabolic expressions of the form

$$\eta_r = 1.0 + Ac + Bc^2 \quad (11)$$

the coefficients of which may be related to the intrinsic viscosity. Intrinsic viscosity is defined as the limit of $\{(\eta_r - 1)/c\}$ as concentration c goes to zero. It is also related to η_r according to

$$\eta_r = 1.0 + [\eta]c + k[\eta]c^2 \quad (12)$$

where k is known as the Huggins constant (36, 37). Both the intrinsic viscosity and

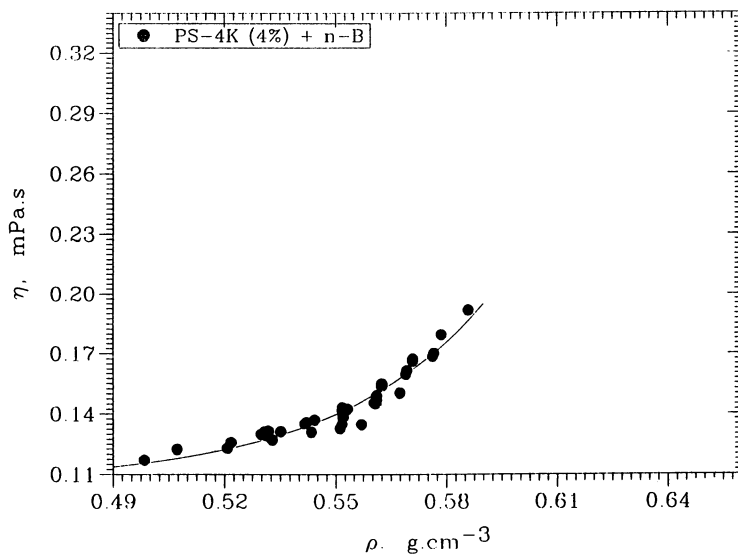


Figure 8. Variation of viscosity of polystyrene solutions in n-Butane with density of the solution. Molecular weight = 4,000. Concentration = 4 % by wt.

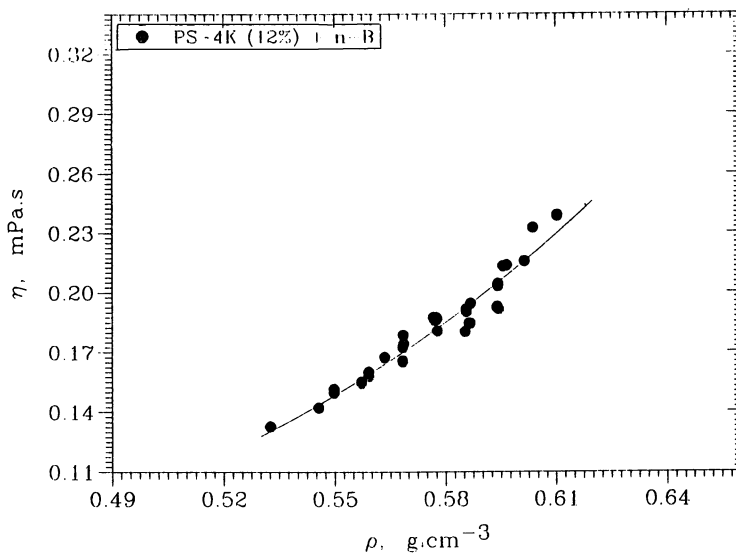


Figure 9. Variation of viscosity of polystyrene solutions in n-Butane with density of the solution. Molecular weight = 4,000. Concentration = 12 % by wt.

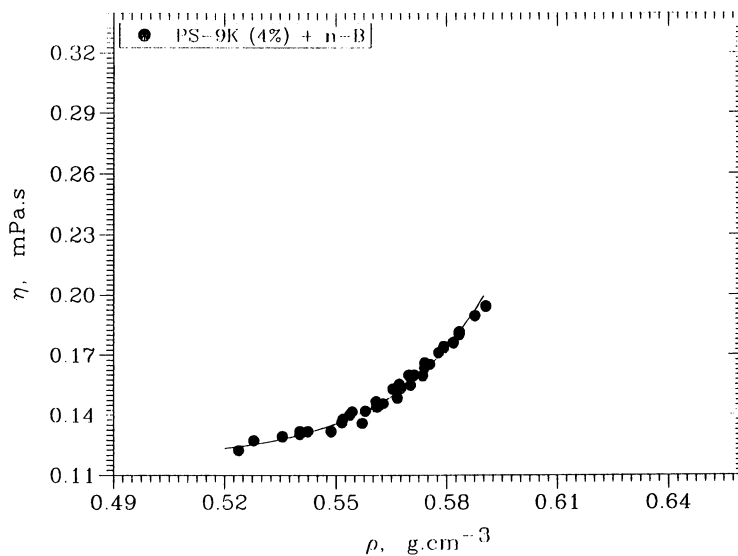


Figure 10. Variation of viscosity of polystyrene solutions in n-Butane with density of the solution. Molecular weight = 9,000. Concentration = 4 % by wt.

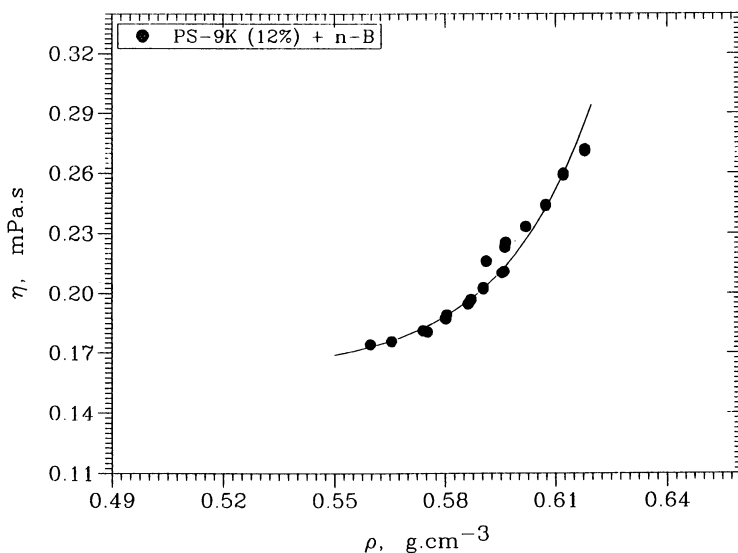


Figure 11. Variation of viscosity of polystyrene solutions in n-Butane with density of the solution. Molecular weight = 9,000. Concentration = 12 % by wt.

Table 1. Parameters for the Density Correlations of Viscosity

System	C_1	C_2	C_3	S_e^*
<i>N- Butane</i>	0.0261	0.75207×10^{-3}	8.98439	0.0050
<i>Polystyrene + n-Butane</i>				
<i>Molecular weight 4,000</i>				
Concentration: 4 wt%	0.1057	0.6127×10^{-7}	24.052	0.0041
12 wt%	-0.0160	0.4218×10^{-2}	6.661	0.0066
<i>Molecular weight 9,000</i>				
Concentration: 4 wt%	0.1175	0.169×10^{-10}	37.799	0.0050
12 wt%	0.1605	0.285×10^{-11}	39.661	0.0050

* S_e Standard error of estimating η values using the given coefficients

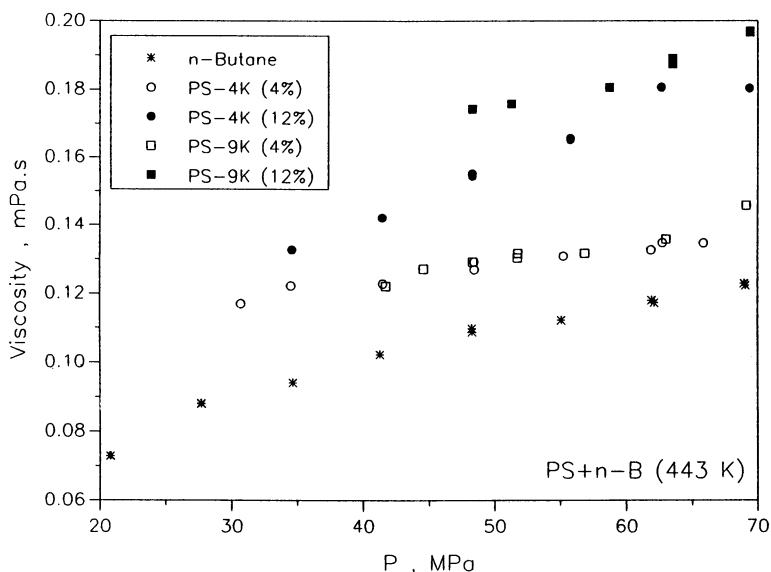


Figure 12. Comparison of the viscosities of n-Butane with polystyrene solutions in n-Butane at 443 K. Molecular weights 4,000 and 9,000. Concentrations = 4 % and 12 % by wt.

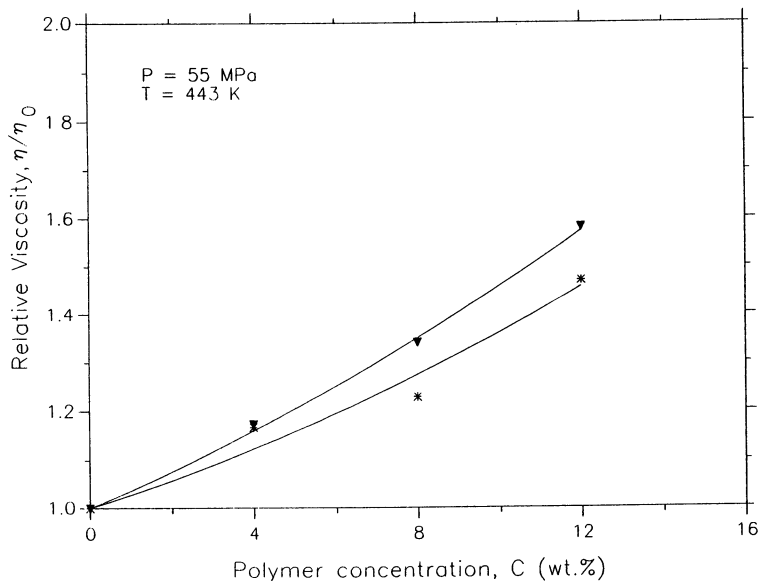


Figure 13. Variation of relative viscosity of polystyrene solutions in n-Butane with concentration at 55 MPa and 443K. (\blacktriangledown = molecular weight 9,000; * = molecular weight 4,000).

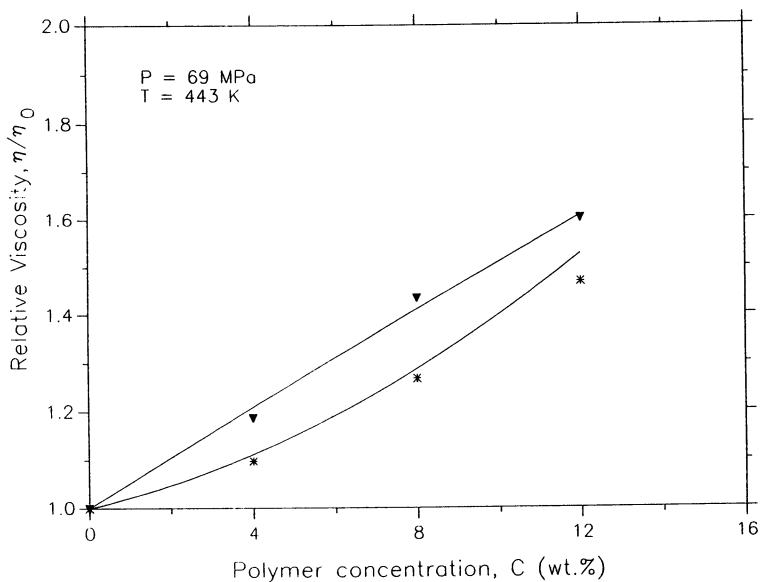


Figure 14. Variation of relative viscosity of polystyrene solutions in n-Butane with concentration at 69 MPa and 443K. (\blacktriangledown = molecular weight 9,000; * = molecular weight 4,000).

the Huggins constants depend on the the nature of the polymer-solvent system and the polymer-solvent interactions. The pressure and temperature dependence of the intrinsic viscosity and the Huggins constant are therefore of particular interest since they can be used as a probe of the changes in the polymer-solvent interactions. (17, 18, 19, 21). Changes in intrinsic viscosity with temperature also provides information on the nature of the heat of mixing. For example, a rise in intrinsic viscosity with temperature is interpreted as an indication of endothermic heat of mixing (38).

Because the present data is limited to only a few concentrations, extrapolation to zero concentration to determine the intrinsic viscosity in the systems studied is not easy. The alternative approach is to analyze the concentration dependence of the relative viscosity and compare the coefficients of the parabolic correlations of the relative viscosity data shown in Figures such as 12 and 13. Using the values of the coefficient A which should in principle be equal to $[\eta]$, estimates of the order of the magnitudes of the intrinsic viscosities can be deduced. At 55 MPa, the intrinsic viscosities are in the order of 2.0 and 3.5, and at 69 MPa, they are 2.0 and 5.5 for the 4,000 and 9,000 molecular weight samples, respectively. The intrinsic viscosity increases with pressure (in going from 55 MPa to 69 MPa) and the molecular weight (from 4,000 to 9,000). The pressure effect is more significant for the higher molecular weight sample. The increase in intrinsic viscosity with molecular weight is in accord with the usual expectation from the Mark-Houwink type relationship, i.e.,

$$[\eta] = KM^a \quad (13)$$

where K and a are characteristic parameters for a given polymer-solvent system. In θ -solvents $a = 0.5$ and becomes higher with improvement of the polymer-solvent interactions.

According to the Flory-Fox formulations (37, 39), intrinsic viscosities, in particular the product of the intrinsic viscosity and the molecular weight are related to the hydrodynamic volume

$$[\eta] M = 2.5 N \{ 4/3\pi R^3 \} \alpha^3 \quad (14)$$

where N is the Avagadro's number, R is the equivalent radius of the hydrodynamic sphere in a Flory θ -solvent, and α is the expansion of the coil in a good solvent over that of the Flory θ -solvent. The present data which indicates an increase in the intrinsic viscosity suggest that upon increase in the pressure at a fixed temperature the solvent has become a better solvent for the polymer. The dependence of the intrinsic viscosity on pressure, temperature and the polymer weight is being currently explored in greater detail (24).

Conclusions

This study has shown that temperature dependence of the viscosity of polystyrene solutions in near and supercritical n-butane can be described by the usual Arrhenius

type expressions. Density is shown to be an excellent scaling factor for these solutions. Measurement of viscosity and in particular examination of the pressure and temperature dependence of the intrinsic viscosity can be used to assess the changes in the characteristics of the solvent and the solvent-solute interactions in supercritical fluids.

Literature Cited

1. *Supercritical Fluid Technology. Reviews in Modern Theory and Applications*; Bruno, T.J.; Ely, J. F., Eds.; CRC Press: Boston, MA, 1991.
2. *Supercritical Fluid Science and Technology*; Johnston, K. P.; Penninger, J. M. L., Eds.; ACS Symposium Series 406; American Chemical Society: Washington, DC, 1989.
3. McHugh, M. A.; Krukonis, V.J. *Supercritical Fluid Extraction: Principles and Practice*; Butterworths: Boston, MA, 1986.
4. Kiran, E.; Saraf, V. P. *J. Supercrit. Fluid*, **1990**, 3, 198.
5. Kumar, S. K.; Suter, U. W. *Polym. Prepr., Am. Chem. Soc., Div. Polym. Chem.* **1987**, 28, 286.
6. Watkins, J. J.; Krukonis, V. J.; Condo, P.T.; Pradhan, D.; Ehrlich, P. J. *Supercrit. Fluids*, **1991**, 4, 24.
7. Schmitz, F. P.; Klesper, E. *J. Supercrit. Fluids*, **1990**, 3, 29.
8. Matson, D. W.; Fulton, J. L.; Peterson, R.C.; Smith, R. D.; *Ind. Eng. Chem. Res.* **1987**, 26, 2298.
9. Kiran, E.; Saraf, V. P.; Sen, Y. L. *Int. J. Thermophysics* **1989**, 10(2), 437.
10. Kiran, E.; Zhuang, W.; Sen, Y.L. *J. Appl. Polym. Sci.*, accepted for publication.
11. Kiran, E.; Zhuang, W. *Polymer*, accepted for publication.
12. Seckner, A. J.; McClelland, A. K.; McHugh, M. A. *AIChE J.* **1988**, 34(1), 9.
13. Chen, S. J.; Radosz, M. *Proc. 2nd. Int. Symp. on Supercritical Fluids*, Boston, MA, 20-22 May, 1991; p.225.
14. Wolf, B. A.; Jend, R. *Macromolecule*, **1979**, 12(4), 732.
15. Schmidt, J. R.; Wolf, B.A.; *Colloid & Polymer Sci.*, **1979**, 257, 1188.
16. Wolf, B. A.; Geerissen, H. *Colloid & Polymer Sci.*, **1981**, 259, 1214.
17. Schmidt, J. R.; Wolf, B. A. *Macromolecules*, **1982**, 15(4), 1192.
18. Wolf, B. A.; Geerissen, H.; Jend, R.; Schmidt, J. R. *Rheol. Acta*, **1982**, 21, 505.
19. Kubota, K.; Ogino, K. *Polymer*, **1979**, 20, 175.
20. Wolf, B. A. in *Chemistry and Physics of Macromolecules*; Fischer, E. W.; Schulz, R. C.; Sillescu, H., Eds.; VCH Publishers: New York, NY, 1991; pp. 273-294.
21. Kubota, K.; Ogino, K. *Macromolecules*, **1979**, 12(1), 74.
22. Berthe, D.; Vergne, Ph. *J. Rheol.* **1990**, 34(8), 1387.
23. Sen, Y. L.; Kiran, E. in *Proc. 2nd. Int. Symp. on Supercritical Fluids*, Boston, MA, 20-22 May, 1991; p. 29.
24. Kiran, E. research in progress.
25. Saraf, V. P.; Kiran, E. *Polymer*, **1988**, 29, 2061.

26. Saraf, V. P.; Kiran, E. *J. Supercrit. Fluids*, **1988**, *1*, 37.
27. Kiran, E.; Sen, Y. L. *Int. J. Thermophysics*, **1992**, *13*(3), 411.
28. Sen, Y. L.; Kiran, E. *J. Supercrit. Fluids*, **1990**, *3*, 91.
29. Reid, R. C.; Prausnitz, J. M.; Poling, B. E. *Properties of Gases and Liquids, 4th Edition*, McGraw-Hill: New York, NY, 1987; pp. 388-490.
30. Vesovic, V.; Wakeham, W. A. in *Supercritical Fluid Technology*; Bruno, J. J.; Ely, J. F., Eds.; CRC Press: Boston, MA, 1991; pp. 245-289.
31. Saeki, S.; Tsubokawa, M.; Yamaguchi, T. *Polymer*, **1989**, *60*, 1895.
32. Starling, K. E.; Ellington, R. T. *AIChE J.* **1964**, *10*(1), 11.
33. Stefan, K.; Lucas, K. *Viscosity of Dense Fluids*; Plenum Press: New York, NY, 1979.
34. Hogenboom, D. L.; Webb, W.; Dixon, J. A. *J. Chem. Phys.* **1967**, *46*(7), 2586.
35. Hildebrand, J. H. *Science*, **1971**, *174*, 490.
36. Flory, P. J. *Principles of Polymer Chemistry*; Cornell University Press: Ithaca, NY, 1953.
37. Huggins, M. L. *J. Am. Chem. Soc.* **1942**, *64*, 2716.
38. Sen, A.; Rubin, I. D. *Macromolecules*, **1990**, *23*, 2519.
39. Flory, P. J.; Fox, T. G. *J. Am. Chem. Soc.* **1951**, *23*, 1904.

RECEIVED July 23, 1992

Chapter 10

Thermophysical Properties of Natural Gas Mixtures Derived from Acoustic Cavity Measurements

S. O. Colgate and A. Sivaraman

Department of Chemistry, University of Florida,
Gainesville, FL 32611-2046

Acoustic resonance measurements on a simulated natural gas mixture (13 components) confined to a cavity have been used to obtain sonic speeds, ideal gas heat capacities and second acoustic and density virial coefficients for the mixture between 298 K and 450 K. The results are also compared with two model predictions (AGA 8 and NIST DDMIX). Comparison of experimental sonic speeds in normal-butane with earlier measurements (4) show good agreement. Sonic speed measurements on n-butane have been extended to elevated temperatures.

Accurate determination of the thermodynamic properties of a multicomponent gas mixture is generally not possible using only information about the properties of the pure components. Data on some mixtures are inevitably required. The number and variety of mixtures of interest precludes detailed measurements on each of them and speaks to the need for predictive models. The art of property prediction for gas mixtures has advanced as the speed and power of numerical techniques and the availability of property measurements on select mixtures has grown. Although most models consider only pair-wise interactions, data on multicomponent mixtures are useful for testing the reliability of model predictions. Because of the importance of knowledge of gas mixture behavior to the natural gas and petroleum industries, experimental measurements on specific natural gases or simulated natural gases are particularly useful.

In this work, an automated spherical acoustic resonator assembly developed for acquiring data on the thermodynamic sonic speed in gases was used to study n-butane and a thirteen component simulated natural gas.

Experimental

The sample gaseous mixture was prepared by Scott Specialty Gases Co., Plumsteadville, PA (U.S.A.) from thirteen 99.99 mol per cent pure components

0097-6156/93/0514-0121\$06.00/0

© 1993 American Chemical Society

blended together in specific proportions. The mixture was composed of nonhydrocarbons, light hydrocarbons and heavy hydrocarbons. Its composition is given in Table I. During the operations of transferring the gas mixture to the apparatus, the gas storage tank, connecting lines, valves and other accessories were heated, and temperature was controlled to maintain the pressure above 14 MPa which assures the homogeneity of the mixture as a single phase.

Table I. Composition of the Simulated Natural Gas Mixture

Component	Mole % (± 0.001)
Nitrogen	1.810
Carbon Dioxide	1.410
Methane	83.479
Ethane	6.990
Propane	3.780
N-Butane	1.140
Iso-Butane	0.479
N-Pentane	0.304
Iso-Pentane	0.306
N-Hexane	0.229
N-Heptane	0.051
N-Octane	0.017
N-Nonane	0.005

The heart of the experimental apparatus is a spherical acoustic resonator of diameter 0.305 m (12") equipped with high temperature PZT-bimorph transducers. The design and construction of the system and the basic experimental procedures have been described elsewhere (*1*). The temperature and pressure were measured using a four wire platinum resistance thermometer and a digital absolute pressure gauge, respectively. These were calibrated against NIST Standards and are accurate to ± 0.001 mK and ± 10 Pa, respectively. The system under study was continuously stirred and blended by action of the in-line circulation pump operating at 3 L min^{-1} . At this rate the perturbations in resonance frequency generated by the pumping action were well below 0.01 Hz. After reaching a level of stability for which the resonance being tracked by the data acquisition system remained centered within a 0.01 Hz wide window, a minimum of forty measurements were made. The median of these was independent of pumping action for the rates used in this work.

A programmable signal synthesizer (HP3325A) and a lock-in amplifier (SR510) were programmed to scan, detect, isolate and track the first radial mode resonance under control of a Compaq AT computer. The temperature of the resonator was controlled to ± 0.005 K at selected temperatures in the range 298 K to 450 K. The resonator was first maintained at a temperature of 300 K and evacuated thoroughly. The apparatus was then charged with n-butane to a pressure 59.71 kPa, and the first radial mode resonance frequency was located and locked onto by the computer. The first radial mode was

selected because of its sharpness and relatively low frequency. When using the spherical cavity resonator as an absolute sonic meter it is common to measure several radial modes, compute a value of the sonic speed for each one and determine an average. When using the apparatus as a relative sonic meter the sonic speed is inferred from the resonance response of system gas to that of a reference gas (argon). Experience has shown that the results are insensitive to which radial mode is used for comparison so long as the resonance frequency is well below the level where relaxation effects are important. Resonance frequency was measured at 14 kPa intervals up to 104.39 kPa. The system was then evacuated and the experiment repeated at a higher temperature. In this manner isothermal runs were performed on n-butane at 300.00 K, 348.15 K, 373.15 K, 423.15 K and 448.15 K. The experimental results are listed in Table II.

Following collection of the n-butane data, similar experiments were performed on the gas mixture of Table I. First radial mode resonance frequencies were measured against system pressure over the range 101.36 kPa → 620.56 kPa for isotherms at 298.15 K, 323.15 K, 373.15 K and 423.15 K. The results are listed in Table III.

Sonic Speed Calculation

The sonic speed through a lossless fluid confined to a rigid spherical cavity can be deduced from the sphere radius r and the frequency $f_{n,\ell}$ of an acoustic resonance associated with the normal mode of eigenvalue $v_{n,\ell}$

$$c_{\text{gas}} = 2\pi r(f_{n,\ell}/v_{n,\ell}) \quad (1)$$

Ferris (1) has listed values of $v_{n,\ell}$ for the first 84 resonance modes, and values for higher modes are easily calculated if needed. Although we have found for this apparatus the thermal and viscous boundary effects and losses due to precondensation (2-3) or adsorption and compliance of the resonator walls are small (4-5), they can be reasonably accounted for by operating the system in a relative rather than absolute mode. This was done by comparing the respective resonance frequency as measured above with that observed when the apparatus was filled with a reference gas of well known behavior. Argon is such a gas and was used as a standard in these measurements. The sonic speed in argon has been carefully measured in this laboratory and the results have been shown to be in close agreement with other reported values (2,5). Using this method, the sonic speed in the gas mixture was taken to be

$$c_{\text{gas}} = c_{\text{Ar}} (f_{\text{gas}}/f_{\text{Ar}}) \quad (2)$$

where f_{gas} and f_{Ar} are the measured resonance frequencies for the same vibration mode of the system gas and of pure argon; c_{Ar} is the sonic speed of argon under the conditions of pressure and temperature for which the frequency measurements are made.

Table II. Sonic speeds in normal butane

T/K	p/kPa (± 0.01 kPa)	f/Hz (± 0.005 Hz)	c/(m/sec) (± 0.01 m/sec)
300.00	59.71	1001.35	213.51
	70.95	998.67	212.94
	82.46	995.84	212.33
	91.84	993.74	211.89
	104.39	990.61	211.22
348.15	51.92	1078.91	230.02
	61.99	1077.23	229.67
	71.50	1075.85	229.37
	82.67	1073.82	228.94
	92.39	1072.23	228.60
373.15	101.77	1070.85	228.31
	51.51	1115.51	238.15
	61.64	1114.11	237.85
	71.85	1112.87	237.58
	82.12	1111.23	237.23
423.15	91.70	1110.02	236.98
	101.77	1108.70	236.69
	51.71	1185.00	252.61
	61.99	1184.06	252.41
	70.81	1183.17	252.22
448.15	82.74	1182.09	251.99
	91.91	1181.20	251.80
	102.05	1180.27	251.60
	51.02	1217.29	259.49
	61.99	1216.29	259.28
	71.50	1215.43	259.10
	82.74	1214.46	258.89
	92.26	1213.61	258.71
	102.12	1212.98	258.57

Table III. Sonic speeds in a simulated natural gas mixture

T/K	p/kPa (± 0.01 kPa)	f/Hz (± 0.005 Hz)	c/(m/sec) (± 0.01 m/sec)
298.15	101.36	1853.08	395.10
	207.88	1850.54	394.56
	315.79	1847.70	393.95
	414.39	1845.14	393.40
	517.26	1842.33	392.81
	620.96	1839.91	392.29
323.15	101.36	1919.95	409.60
	217.12	1917.59	409.10
	311.45	1915.70	408.70
	415.29	1913.55	408.24
	521.40	1911.42	407.79
	620.96	1909.55	407.39
373.15	101.01	2043.68	436.30
	207.40	2042.54	436.06
	312.07	2041.39	435.81
	416.73	2040.24	435.57
	522.78	2039.19	435.34
	620.96	2037.95	435.08
423.15	101.31	2156.06	459.61
	211.88	2155.59	459.51
	310.34	2155.16	459.42
	413.91	2154.67	459.31
	518.16	2154.13	459.20
	620.62	2153.60	459.09

Results and Discussion

n-Butane. The principal purpose of this work was to generate experimental data on a well defined gas mixture with the characteristics of natural gas to help support the evaluation and development of predictive models. Although the reliability of the present spherical acoustic resonator apparatus for sonic speed measurements had been demonstrated in earlier publications (2-4), the recent report of sonic speed measurements on n-butane in another spherical resonator by Ewing and co-workers (5) provided the opportunity for a comparison of the performance of two similar units. The present measurements on n-butane were made with this in mind, and care was taken to ensure that the low temperature states of this study overlapped the

higher temperature states of Ewing, et al. The present work also extended the temperature range of sonic speed measurements in n-butane to 450 K.

Figure 1 shows the variation in sonic speed with pressure for the five isotherms of n-butane. The results of Ewing, et al. at 300 K are shown in the figure as solid squares. The general agreement is clearly indicated. The average deviation of the Ewing values from the present ones is 0.01%. The actual deviations are shown in Figure 2.

Simulated Natural Gas Mixture. The acoustic resonance measurements for the simulated natural gas mixture have been analyzed using a pressure series expansion:

$$c^2 = A_0 [1 + (\beta_a/RT) p + \dots], \quad (3)$$

where c is the sonic speed,

$$A_0 = \gamma^\circ RT/\bar{M}, \quad (4)$$

in which $\gamma^\circ = C_{p,m}^\circ/C_{v,m}^\circ$, R = gas constant and \bar{M} = mole fraction mean of the molar mass. β_a is the second acoustic virial coefficient.

The variations in c^2 with system pressure for the four isotherms of the gas mixture are shown graphically in Figure 3. The prediction of two popular correlations, AGA 8 and DDMIX, are shown for comparison. Both models predict sonic speeds somewhat higher than the present measurements, and the disparity increases with increasing temperature. Over the range of pressures studied here and at 298.15 K the AGA 8 and DDMIX models give values about 0.09% and 0.18% higher than the measured sonic speeds, respectively. Deviations of the measured sonic speeds from the model values for this case are shown in Figure 4. The deviations increase to about 0.5% at the highest temperature of this study. The plots of c^2 versus p in Figure 2 are quite linear suggesting that for these data Equation (3) may reasonably be truncated after the second term. Linear fits were typically good ($r^2 > 0.999$). Higher order approximations did not improve the fits, and for this limited pressure range there was no need to keep terms in the expansion beyond the first two. Linear regressions of the results thus yield experimental values of the expansion coefficients in Equation (3). Values of A_0 and β_a are listed in Table IV.

The ratio of reference state heat capacities γ° can be calculated using Equation 4, and the ideal gas heat capacity $C_{p,m}^\circ$ may be calculated from γ° as

$$C_{p,m}^\circ = R [\gamma^\circ/(\gamma^\circ - 1)] \quad (5)$$

The resulting values of γ° and $C_{p,m}^\circ$ are also listed in Table IV.

Results for $C_{p,m}^\circ$ of the gas mixture are shown graphically in Figure 5. The reference state heat capacities ($C_{p,m}^\circ$) were fitted to a polynomial function and the resultant parameters along with the standard deviation (s) of the experimental points from the analytical function are:

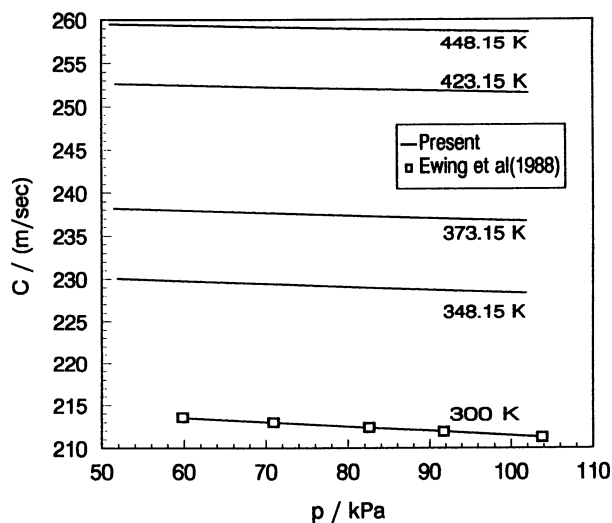


Figure 1. Sonic speeds in n-butane at elevated temperatures and compared with Ewing, et al. at 300 K.

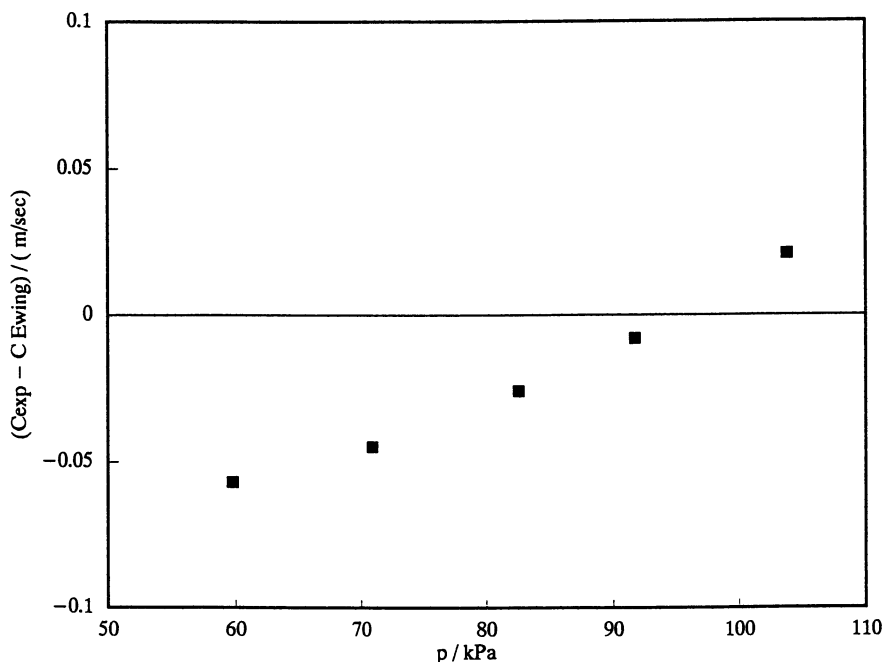


Figure 2. Deviation plot of present sonic data with that of Ewing, et al. at 300 K for butane.

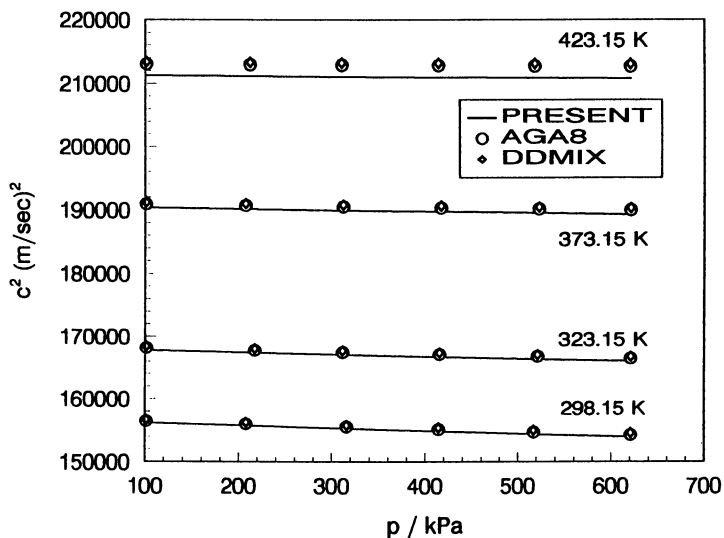


Figure 3. Square of the experimental sonic speed vs pressure for the simulated natural gas mixture at elevated temperatures and compared with the predictions of the AGA8 and DDMIX models at 298.15 K.

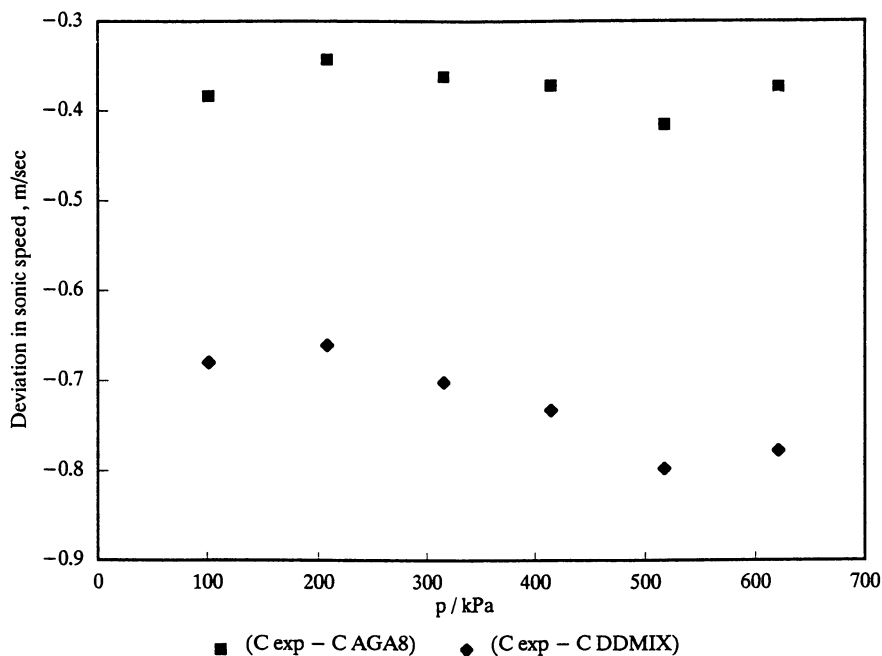


Figure 4. Deviation plot of present sonic data with that of the models AGA8 and DDMIX at 298.15 K for the natural gas mixture.

Table IV. Values of A_0 , β_a , γ° and $C_{p,m}^\circ$ for the simulated natural gas mixture

T/K	$A_0/(\text{m/sec})^2$	$\beta_a(\text{cc/mol})$	γ°	$C_{p,m}^\circ(\text{kJ/kgm mol K})$
298.15	156552.9	-68.2	1.2596	40.35
323.15	168125.0	-55.9	1.2480	41.84
373.15	190566.7	-33.1	1.2251	45.26
423.15	211346.8	-15.5	1.1981	50.28

$$C_{p,m}^\circ = 50.06589 - 1.10750 \times 10^{-1} (T/K) + 2.62806 \times 10^{-4} (T/K)^2 \quad (6)$$

(298 \leq T/K \leq 450); s = 0.16

Figure 6 shows the variation of the second acoustic virial coefficient (β_a) with temperature. The acoustic virial is related to the amount-of-substance density virial B(T) as follows:

$$\beta_a = 2B + 2(\gamma^\circ - 1) T \left(\frac{dB}{dT} \right) + \frac{(\gamma^\circ - 1)^2}{\gamma^\circ} T^2 \left(\frac{d^2B}{dT^2} \right) \quad (7)$$

This equation is difficult to solve for B(T) without some knowledge of the temperature derivatives. It is known that the second virial coefficient is not very sensitive to the details of the intermolecular potential and that even simple models can often fit experimental B(T) data well (6,7). The temperature functionalities of B(T) for a number of intermolecular potential models are well known (6). Of these the second virial coefficient for a square well potential is particularly simple and has been used before to fit virial coefficients inferred from acoustic measurements (5). The square well potential has three adjustable parameters: the effective hard sphere diameter σ , the well depth ϵ and the well width R-1 in units of σ . The model is known to represent second acoustic virials well for many molecules, including small alkanes, when R is fixed at 1.8 (6). In this case the analytical expression for the second virial coefficient is

$$B(T) = b_0(5.832 - 4.832 e^{\epsilon/KT}) \quad (8)$$

where $b_0 = 2/3 \pi \tilde{N}\sigma^3$ and \tilde{N} s Avogadro's number. A nonlinear regression of the present data to this model gives

$$B(T)/(\text{cc/mol}) = 337.638 - 279.743 \exp \left(\frac{107.089 \text{ K}}{T} \right) \quad (9)$$

The resulting values of B(T) are listed in Table V.

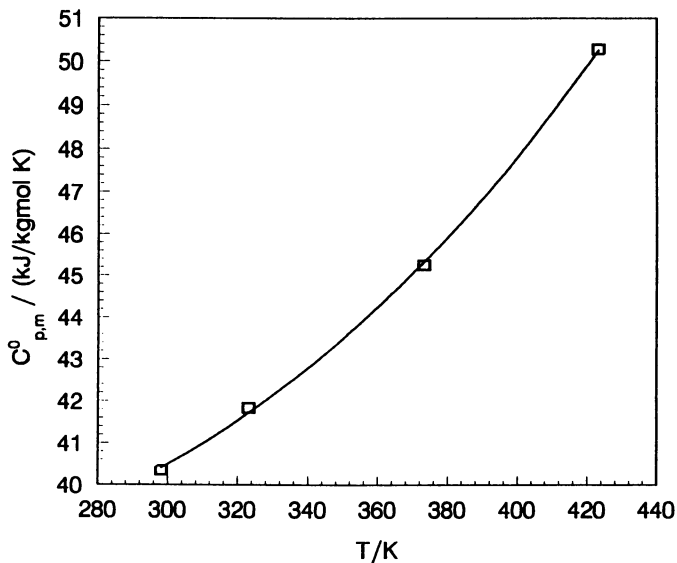


Figure 5. Reference state isobaric heat capacity vs temperature of the simulated natural gas mixture.

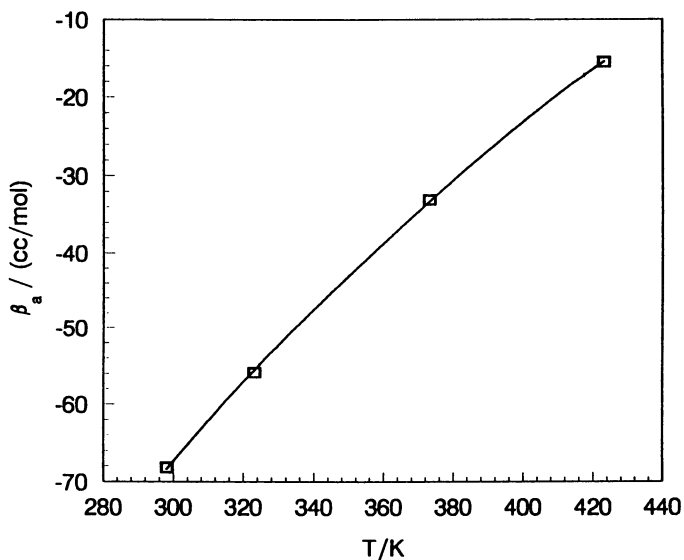


Figure 6. Second acoustic virial coefficient β_a vs temperature for the simulated natural gas mixture.

Table V. Second virial coefficients of the stimulated natural gas mixture determined for square well potential

T/K	B(T)/(cc/mol)
298.15	-63.0
323.15	-52.0
373.15	-35.1
423.15	-22.7

Figure 7 shows this function and the values corresponding to the four experimental temperatures. The square well parameters determined for this gas mixture are: $\sigma = 3.5805 \times 10^{-10}$ m, $b_0 = 57.894$ cc/mol and $\epsilon = 1.4785 \times 10^{-21}$ J.

Conclusions

The measurement of spherically symmetric resonance mode frequencies of a gas confined to a rigid walled spherical acoustic resonator can yield accurate values of the sonic speed at frequencies sufficiently low to avoid significant losses due to molecular vibrational relaxation. These speeds are related to certain thermophysical properties which may be inferred from the resonance measurements. The present apparatus operates at elevated temperatures and thus extends the range of possible acoustic measurements. The method is applicable to both pure and mixed gases. Results on the latter can benefit the evaluation and development of predictive models. While the temperature limit of the present acoustic resonance apparatus is about 450 K, a new system recently fabricated in this laboratory has operated at temperatures to 800 K. It will be used to acquire sonic speed measurements on systems at high temperatures.

Legend of Symbols

B	=	Second virial coefficient
β_a	=	Second acoustic virial
$C_{p,m}^\circ$	=	Ideal gas heat capacity at constant pressure, kJ/kgm mol-K.
c	=	Sonic speed, m/sec
γ	=	Ratio of specific heats
M	=	Mole fraction mean of the molar mass.
p	=	Pressure, kPa
R	=	Universal gas constant
T	=	Temperature, K

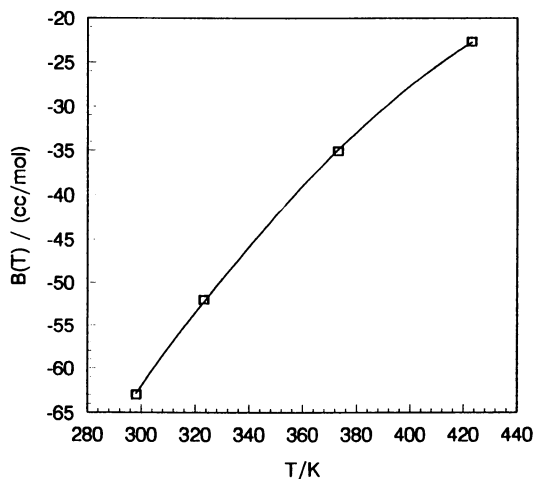


Figure 7. Second virial coefficient $B(T)$ vs temperature for the simulated natural gas mixture.

Acknowledgments

The authors thank Dr. E. Jones and Dr. J. Shen of Chevron Oil & Field Co., LaHabra, California and Dr. Jeff Savidge of G.R.I., Chicago for continued support and encouragement. We also acknowledge the financial support of the Gas Processors Association, Tulsa, Oklahoma; the Gas Research Institute, Chicago, Illinois; and the Chevron Oil Field Company, LaHabra, California.

Literature Cited

1. Ferris, H.g. *J. Acoust. Soc. Am.* **1952**, *24*, 57.
2. Colgate, S.O.; Sivaraman, A.; Reed, K., *J. Chem. Thermody.* **1990**, *22*, 245.
3. Colgate, S.O.; Sivaraman, A.; Reed, K., *Fluid Phase Equilibria*, **1990**, *60*, 191.
4. Colgate, S.O.; Sona, C.F.; Reed, K.; Sivaraman, A. *J. Chem. Eng. Data*, **1990**, *35*, 1.
5. Ewing, M.B.; Goodwin, A.R.H.; McGlashan, M.L.; Trusler, J.P.M. *J. Chem. Thermody.*, **1988**, *20*, 243.
6. Hirschfelder, J.O.; Curtiss, C.F.; Bird, R.B. "*Molecular Theory of Gases and Liquids*", John Wiley and Sons: New York, NY, 1954.
7. Boyd, M.E. and Mountain, R.D., *Phys. Rev. A* **1970**, *2*, 2164.

RECEIVED April 27, 1992

Chapter 11

Competitive Energetic and Entropic Effects Describing Solvation in Near-Critical Solutions

F. Munoz and E. H. Chimowitz

Department of Chemical Engineering, University of Rochester,
Rochester, NY 14627

This work addresses the issue of local fluid structure adaptations in near-critical fluid mixtures, and its role on determining the behavior of solubilities in these systems. Applying the Kirkwood coupling approach we show that the solute chemical potential can be characterized as a short-range function determined by contributions arising from a small local neighborhood around the solute. Using the Percus-Yevick equation and the Buff and Brout theory the interrelationship between the solute chemical potential, the solute average potential energy and local density enhancements is discussed revealing an interesting energetic and entropic competing effect in these systems. This effect appears to play a central role in determining solubility behavior. Finally this analysis is extended to ternary and higher order systems.

The behavior of supercritical fluid mixtures has been the subject of much interest in recent years. Research in this area has led to the formulation of a number of practical applications such as separations using retrograde phenomena (1–3), supercritical fluid chromatography applications (4–7), techniques for the formation of fine powders for pharmacology applications (8,9) and in the regeneration of activated carbon beds (10). Several review articles and volumes are available discussing the recent developments in the field (11–14).

In addition an improved molecular understanding of the properties and behavior of these systems has emerged. Several studies based on first principles have been reported within the last few years advancing insightful interpretations into the role of molecular interactions in determining the behavior in these systems. Several approaches and techniques have been applied to study the molecular fluid structure in the near-critical region, among them Molecular Dynamics (15,16), Monte Carlo methods (17,18), integral equation theories (19–23), classical–nonclassical descriptions (24–29).

0097–6156/93/0514–0134\$06.00/0

© 1993 American Chemical Society

Several works, both theoretical and experimental, have addressed the question of relating local density enhancements to observed macroscopic thermodynamic properties, and the uncommon behavior of solvation of low volatility solutes in supercritical fluid solvents. Within this context we mention the fluorescence spectroscopy studies by Kim and Johnston (30,31) and Brennecke and Eckert (32), which provided experimental evidence of local density enhancements in near-critical fluids. Petsche and Debenedetti (16) used molecular dynamics to investigate the structure and dynamics of the local environment surrounding an infinitely dilute solute in a near-critical solvent modeled with the Lennard-Jones potential for both attractive and repulsive mixtures. The authors concluded that for attractive mixtures, pronounced solvent enrichment was exhibited in the vicinity of the solvent's critical point with local densities up to 3.86 times higher than the bulk. This increase in local solvent density buildup has often been referred to as clustering, but near the CEP, as stated by Cochran and Lee (21) it is also evident that the cluster consists mainly of a diffuse, long-range buildup of solvent density about the solute which extends 10–14 solvent diameters from the solute. McGuigan and Monson (20) showed that the physical effects associated with near-critical phenomena, like the observed divergence of the solute partial molar volume, are principally due to the long range correlations in the solvent and not to drastic changes in the local structure about the solute as implied by clustering ideas.

In this contribution we present an alternative approach for addressing the issue of local structure changes about a solute and their effect on macroscopic thermodynamic properties. First we show that the solute residual chemical potential μ_i^r is uncorrelated to the diverging partial molar properties \bar{V}_i , \bar{H}_i^f and \bar{S}_i^f , in the infinite dilution limit as the solvent's critical point is approached; thus the residual chemical potential μ_i^r appears to be a better candidate to study the effect of short-range structural changes upon solubility. Then we show that the residual chemical potential μ_i^r depends on contributions arising from its direct local environment confined to about 3 to 5 solvation shells. We proceed to partition the residual chemical potential μ_i^r into energetic and entropic short-range contributions confined to the same local region. We discuss the competitive energetic and entropic effects that emerge from our analysis as playing a central role in determining the behavior of solubility in these systems. Finally the formal analysis is extended to ternary mixtures.

Development of local properties to describe solvation

Our approach is based on the observation that the chemical potential of the dilute solute 1 (dissolved in a solvent 2), μ_1 is a short range function. This can be seen from the following reasoning. The residual chemical potential of the species in solution can be obtained using the Kirkwood equation (33). In particular, in the limit $x_1 \rightarrow 0$ we have

$$\mu_i^r = \rho \int_0^1 \int_0^\infty u_{i2}(r) g_{i2}(r, \xi) 4\pi r^2 dr d\xi \quad (1)$$

where u_{ij} is the intermolecular potential, ξ is the Kirkwood coupling parameter, ρ the

phase density and $g(r, \xi)$ the pair correlation function with the system coupled to the extent ξ . The residual chemical potential is formally defined by equation (2) below

$$\mu_1^r = \mu_1(T, V, N_1, N_2) - \mu_1^*(T, V, N_1, N_2) = \bar{H}_1^r - T\bar{S}_1^r \quad (2)$$

where

$$\bar{H}_1^r = \bar{H}_1(T, V, N_1, N_2) - \bar{H}_1^*(T, V, N_1, N_2) \quad (3)$$

$$\bar{S}_1^r = \bar{S}_1(T, V, N_1, N_2) - \bar{S}_1^*(T, V, N_1, N_2) \quad (4)$$

where superscript r refers to a residual property, $*$ the ideal gas state, \bar{M} is a partial molar property (M denotes any extensive property), H the system enthalpy, S the entropy, V the volume, T the temperature, N_1 the number of solute molecules, and N_2 the number of solvent molecules. The residual partial molar enthalpy and entropy are given by equations

$$\bar{H}_1^r = \left(\frac{\partial H^r}{\partial N_1} \right)_{T, V, N_2} + \bar{V}_1 \left(\frac{\partial H}{\partial V} \right)_{T, N_1, N_2} \quad (5)$$

$$\bar{S}_1^r = \left(\frac{\partial S^r}{\partial N_1} \right)_{T, V, N_2} + \bar{V}_1 \left(\frac{\partial S}{\partial V} \right)_{T, N_1, N_2} - k \quad (6)$$

where k is Boltzmann's constant. Notice that since \bar{V}_1 , at infinite dilution diverges as the critical point is approached so will \bar{H}_1^r and \bar{S}_1^r . Now using $H = \frac{3}{2}NkT + U + PV$ in equation (5) where U is the system's potential energy we get

$$\bar{H}_1^r = \left(\frac{\partial U}{\partial N_1} \right)_{T, V, N_2} + \bar{V}_1 \left[P + \left(\frac{\partial U}{\partial V} \right)_{T, N_1, N_2} \right] - kT \quad (7)$$

The term in square brackets in equation (7) is equal to $T(\partial S/\partial V)_{T, N_1, N_2}$. Thus equation (7) can be written as

$$\bar{H}_1^r = \left(\frac{\partial U}{\partial N_1} \right)_{T, V, N_2} + T\bar{V}_1 \left(\frac{\partial S}{\partial V} \right)_{T, N_1, N_2} - kT \quad (8)$$

Thus from equations (6) and (8) we have that the diverging part of the residual partial molar entropy \bar{S}_1^r , which we call ΔS_1^D , and the diverging part of the residual partial molar enthalpy \bar{H}_1^r , which we call ΔH_1^D are given by equations (9) and (10) below,

$$\Delta S_1^D = \bar{V}_1 \left(\frac{\partial S}{\partial V} \right)_{T, N_1, N_2} = \bar{V}_1 \left(\frac{\partial P}{\partial T} \right)_{V, N_1, N_2} \quad (9)$$

$$\Delta H_1^D = T \bar{V}_1 \left(\frac{\partial S}{\partial V} \right)_{T, N_1, N_2} = T \bar{V}_1 \left(\frac{\partial P}{\partial T} \right)_{V, N_1, N_2} = T \Delta S_1^D \quad (10)$$

Using equations (6) through (10) we can write

$$\bar{S}_1^r = \left(\frac{\partial S^r}{\partial N_1} \right)_{T, V, N_2} - k + \Delta S_1^D \quad (11)$$

$$\bar{H}_1^r = \left(\frac{\partial U}{\partial N_1} \right)_{T, V, N_2} - kT + T \Delta S_1^D \quad (12)$$

Thus using equations (11) and (12) in equation (2) we have that the diverging parts of the residual partial molar entropy and energy cancel exactly and they do not contribute in determining the value of μ_1^r .

This argument allows us to infer that μ_1^r is uncorrelated with the diverging partial molar properties \bar{V}_1 , \bar{H}_1^r , and \bar{S}_1^r , and that the nature of μ_1^r will really depend on the nature of both $(\partial S^r/\partial N_1)_{T, V, N_2}$ and $(\partial U/\partial N_1)_{T, V, N_2}$. These three latter properties can be calculated from first principles using a statistical mechanical approach which will also provide molecular structure details in terms of the pair correlation functions $g_{ij}(r)$. This approach will allow us to elucidate the role of local density inhomogeneities in determining μ_1^r , $(\partial S^r/\partial N_1)_{T, V, N_2}$ and $(\partial U/\partial N_1)_{T, V, N_2}$.

Toward this end we chose to look at the chemical potential function

$$\mu_1^r/\rho = 4\pi \int_0^1 \int_0^\infty u_{12}(r) g_{12}(r, \xi, \rho) r^2 dr d\xi \quad (13)$$

and its configurational energy counterpart

$$u_1/\rho = 4\pi \int_0^\infty u_{12}(r) g_{12}(r, \xi=1, \rho) r^2 dr \quad (14)$$

where the average density dependence in the pair correlation function is explicitly shown. The short range nature of these functions is ensured by the inclusion of the intermolecular potential in the integrand. These integrals would be constants according to the van der Waals equation for example. The radial distribution functions needed in equations (13) and (14) were calculated with the Percus and Yevick (34) equation.

To perform the calculations a novel numerical method of solving the Percus-Yevick equation (this method is also applicable to other integral equations such as the

hypernetted-chain equation) was developed and comparisons with literature values were performed (35). In our calculations we used the usual reduced density $\rho^* = \rho\sigma_{22}^3$ and reduced temperature $T^* = kT/\epsilon_{22}$. Our calculations for the reduced critical density gave $\rho_c^* = \rho_c\sigma^3 = 0.28$ and $T_c^* = 1.32$. These results compare very well with other reported values for a Lennard-Jones (LJ) fluid (36).

In order to study the contribution to the chemical potential arising from different regions of space, a function was constructed from equation (13) by replacing the upper limit in the spatial integral by a variable R as shown in equation (15)

$$F_{12}(R)/\rho = 4\pi \int_0^R \int_0^1 u_{12}(r) g_{12}(r, \xi) r^2 d\xi dr \quad (15)$$

Figure 1 shows the radial evolution, at various densities, of the chemical potential function given by equation (15) above. The abscissa is the reduced distance $r^* = r/\sigma_{22}$. Figure 1 is at a temperature $T^* = 1.32$, very close to the pure solvent critical temperature. These results are for an attractive mixture represented by the LJ parameters used by Shing and Chung (17) in their attempt to represent the Naphthalene(1)–CO₂(2) system; these parameters are listed in Table I. Also shown in this figure are dashed lines at each density that show the neighborhood within which at least 90% of the contribution to the solute's chemical potential is to be found. There appears to be a striking invariance to this neighborhood, irrespective of proximity to the critical point or whether or not the solution is attractive or repulsive in character (35). Hence μ_1^* appears to be a truly short range property confirming our previous results. Based upon these results a molecular neighborhood of between 3 to 5 solvation shells can be defined as the region of interest for probing local fluid properties related to solvation. The same short-range nature was observed for the potential energy of the solute by studying the function constructed from equation (14) as follows

$$E_{12}(R)/\rho = 4\pi \int_0^R u_{12}(r) g_{12}(r) r^2 dr \quad (16)$$

Thus we refer to both properties μ_1^* and u_1 as *local* properties. The motivation for defining a *local* entropy s_1^* of the same short-range nature as μ_1^* and u_1 emerges from the following discussion concerning local density enhancements.

Table I. Lennard-Jones potential parameters from Shing and Chung (17)

	1-1	1-2	2-2
(ϵ_{ij}/k) , K	629.49	353.20	204.68
σ_{ij} , Å	5.627	4.7290	3.831

Naphthalene(1)–CO₂(2)

Local Density Enhancements: Calculations for the solute's chemical potential and potential energy were done at various densities as shown in Figure 2 for a temperature $T^*=1.32$ for the mixture defined by the parameters from Table I. Superimposed on those results is the local density buildup function in a neighborhood of 3 solvent molecule diameters around the solute molecule defined as

$$\Delta\rho_{local} \equiv \left(\frac{N-N_v}{N_v} \right) * 100\% \quad (17)$$

where N is the actual number of molecules in this volume and N_v the number that would exist if the local density were the same as the prevailing bulk density. This function shows a distinct maximum as the critical density is approached with a maximum density enhancement of about 70% at the conditions shown. We notice however that the solute chemical potential function in the form given by equation (13) appears to be weakly coupled to the local density changes over a wide average density range. In contrast, the potential energy function in equation (14) shows strongly varying behavior with density, exhibiting, at least in schematic terms, a mirror-image reflection of the local density enhancement function, $\Delta\rho_{local}$.

Definition of a local entropy: The fact that the solute residual chemical potential μ_1^r appears invariant to local solvent density enhancements while the solute average potential energy u_1 shows strong dependence with them, suggests that entropy is an important factor here, and it has been overlooked to this point. This motivated us to study entropic effects associated with $\Delta\rho_{local}$. Since all the variables under consideration (μ_1^r , u_1 and $\Delta\rho_{local}$) are dependent on a small local neighborhood around the solute then the entropic variable of interest here must also be confined to the same local neighborhood. Consequently in order to arrive at the proper definition of the relevant entropic property it is clear that we first must be able to partition energetic and entropic effects in a clear-cut way into short-range contributions (related to local structure) and long-range contributions (which are apparently less relevant for a short range property such as μ_1^r). We accomplish this as follows; the residual chemical potential μ_1^r can be written as

$$\mu_1^r = \left(\frac{\partial U}{\partial N_1} \right)_{T,V,N_2} - T \left(\frac{\partial S^r}{\partial N_1} \right)_{T,V,N_2} \quad (18)$$

Using Euler's theorem we obtain,

$$\left(\frac{\partial U}{\partial N_1} \right)_{T,V,N_2} = \tilde{U} - \tilde{V} \left(\frac{\partial U}{\partial V} \right)_{T,N} + x_2 \left(\frac{\partial \tilde{U}}{\partial x_1} \right)_{T,\tilde{V}} \quad (19)$$

where $\tilde{U}=U/N$, and $\tilde{V}=V/N$. The following relationships have been simplified to the case of an infinitely dilute solute ($x_1 \rightarrow 0$); the detailed derivations are published elsewhere (35). The average potential energy per molecule is given by equation (20) below,

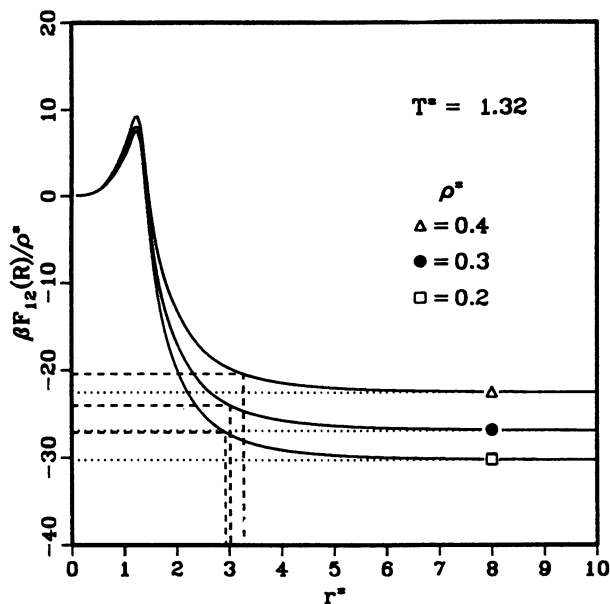


Figure 1. $\beta F_{12}(R)/\rho^*$ in the limit $x_1 \rightarrow 0$, at $T^* = 1.32$ and $\rho^* = 0.2, 0.3, 0.4$. (Reproduced with permission from ref. 35. Copyright 1992 Elsevier Science Publishers B.V.)

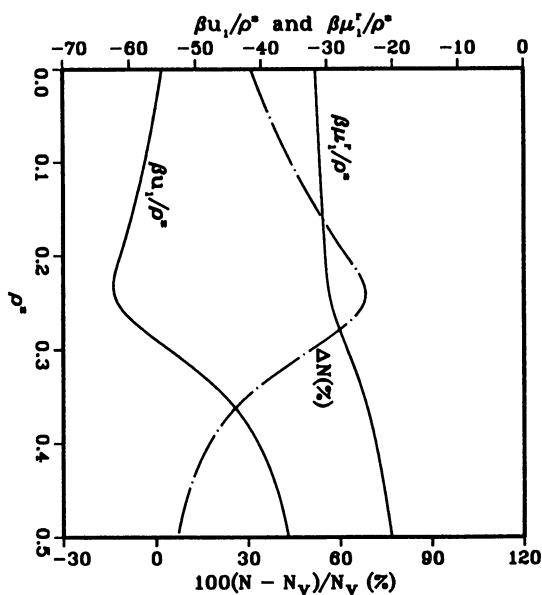


Figure 2. $\beta u_1/\rho^*$, $\beta \mu_1/\rho^*$ and local density deviation around the solute molecule. (Reproduced with permission from ref. 35. Copyright 1992 Elsevier Science Publishers B.V.)

$$\tilde{U} = 2\pi\rho \int u_{22}(r)g_{22}(r)r^2 dr \quad (20)$$

and

$$\tilde{V} \left(\frac{\partial U}{\partial V} \right)_{T,N} = -\rho \left(\frac{\partial \tilde{U}}{\partial \rho} \right)_T = -(\tilde{U} + \Lambda) \quad (21)$$

with

$$\Lambda = 2\pi\rho \int u_{22}(r) \left(\frac{\partial g_{22}(r)}{\partial \ln \rho} \right)_T r^2 dr \quad (22)$$

The last derivative in equation (19) is given by

$$\left(\frac{\partial \tilde{U}}{\partial x_1} \right)_{T,\tilde{V}}^{\infty} = u_1 - 2\tilde{U} + \Phi \quad (23)$$

with

$$\Phi = 2\pi\rho \int u_{22}(r) \left(\frac{\partial g_{22}(r)}{\partial x_1} \right)_{T,\tilde{V}}^{\infty} r^2 dr \quad (24)$$

Using equations (21) and (23) in (19) the following expression is obtained

$$\left(\frac{\partial U}{\partial N_1} \right)_{T,V,N_2}^{\infty} = u_1 + \Lambda + \Phi \quad (25)$$

where u_1 is the average potential energy of the solute (equation (14)) and as discussed earlier can be characterized as a *local* or *short-range* function similarly to μ_1^f . The term Λ was studied extensively by Buff and Brout (37) and Hildebrand and Scott (38) showing that Λ is very small compared to \tilde{U} and can be neglected in equation (21). The term Φ however contains long-range contributions, as discussed in our recent work (35). Thus the Φ term in equation (25) cannot be characterized as *local* or *short range* in the near critical region, clearly in contrast to the case of u_1 and μ_1^f . Therefore equation (25) provides a clear-cut partitioning of $(\partial U/\partial N_1)_{T,V,N_2}^{\infty}$ into *local* and *long-range* contributions. A similar partitioning of the entropic term in equation (18) would permit a definition of a *local* entropy. We propose the following definition for this purpose:

$$\left(\frac{\partial S^r}{\partial N_1} \right)_{T,V,N_2} \equiv s_1^r + \Delta S_{envir}^r \quad (26)$$

where s_1^r is a *local* entropic change associated with a solute molecule going into solution, and ΔS_{envir}^r is the balance of the entropic change experienced by the system outside this local neighborhood.

Now using equations (25) and (26) in (18)

$$\mu_1^r = u_1 - Ts_1^r + [\Lambda + \Phi - T\Delta S_{envir}^r] \quad (27)$$

As of now the definitions of the terms s_1^r and ΔS_{envir}^r are still open. From our discussion above both μ_1^r and u_1 are considered to be *local* properties with their main contribution arising from a region of about 3 to 5 solvation shells. The property s_1^r is being defined as their entropic counterpart confined to the same local environment. Thus the local properties u_1 and s_1^r contain all the factors contributing to μ_1^r (which is local as well). This requires setting the term between brackets to zero. This in turn is equivalent to the statement that long range contributions (taken into account by the term in brackets) have no net effect on μ_1^r . Doing so then, the definitions of s_1^r and ΔS_{envir}^r in equation (26) follow immediately, with

$$s_1^r \equiv \frac{u_1 - \mu_1^r}{T} \quad (28)$$

which of necessity is short ranged, and is in fact confined to the same length scales as both μ_1^r and u_1 (eqs. (13) and (14)) as intended. And

$$\Delta S_{envir}^r \equiv \frac{\Lambda + \Phi}{T} \quad (29)$$

which is necessarily long ranged through the quantity Φ .

Linearity of Solubility Data and Local Properties s_1^r and u_1

The competition between the energetic and entropic effects alluded to earlier is demonstrated in Figure 3 where $s_1^r/k\rho$ and $\beta u_1/\rho$ are shown at various densities at a temperature of $T^* = 1.32$, very close to the solvent's critical temperature. These local entropic and energetic contributions tend to cancel, at least for the molecular parameters used here, resulting in a chemical potential variation that, as mentioned earlier, is weakly coupled with local density enhancements (see Figure 2). It is possible to show that this weak coupling implies that the derivative $(\partial \ln x_1 / \partial \rho)_{T,\sigma}$ should be approximately constant. This follows from the equation derived in (35) and shown below

$$\left(\frac{\partial \ln x_1}{\partial \rho} \right)_{T,\sigma} \approx \left(\frac{\partial \ln \rho_1}{\partial \rho} \right)_{T,\mu_1} = - \left(\frac{\partial \beta \mu_1^r}{\partial \rho} \right)_{T,\mu_1} \quad (30)$$

where x_1 is the mole fraction of component 1, ρ is the fluid phase density, $\rho_1 = x_1 \rho$, σ denotes a derivative taken along the saturation envelope and μ_1 denotes a derivative taken along a path of constant solute chemical potential. Equation (30) is a very good

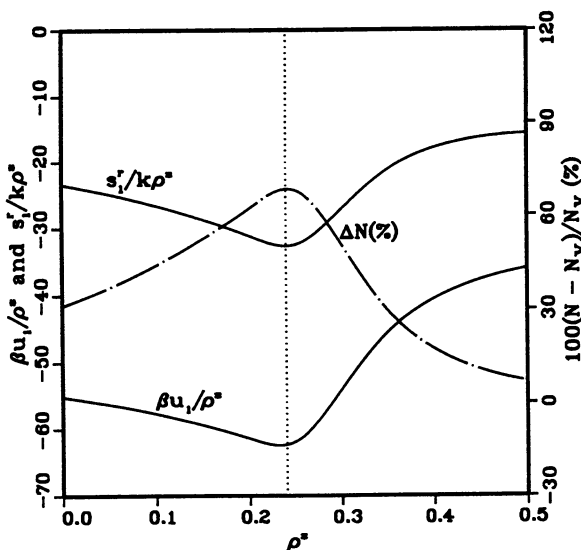


Figure 3. $\beta u_1/\rho^*$, $s_1^r/k\rho^*$ and local density deviation around the solute molecule. The maximum of $\Delta N(\%)$ correlates with the minimum of u_1 and s_1^r . (Reproduced with permission from ref. 35. Copyright 1992 Elsevier Science Publishers B.V.)

approximation for the systems of interest here since the incompressible solid solute chemical potential is nearly independent of pressure. The fact that the function in equation (13) is a weak function of density implies that the derivatives in equation (30) are approximately constant and hence the logarithm of the solubility is a nearly linear function of density. The constancy of this derivative has been observed and analyzed in many diverse sets of data (39–42). Here we have established a connection between these experimental observations and the dependency of the solute molecule's chemical potential on the density of the fluid in its immediate neighborhood.

Local properties for ternary and higher order systems at finite compositions

The systems more typically found in practical applications involve at least two or more components at finite composition. For this reason we are extending the formalism of the previously described results for ternary and higher order systems.

The chemical potential and the potential energy of a ternary system are given in equations (31) and (32) below

$$\mu_1^r = \left(\frac{\partial U}{\partial N_1} \right)_{T,V,N_2,N_3} - T \left(\frac{\partial S^r}{\partial N_1} \right)_{T,V,N_2,N_3} \quad (31)$$

$$\tilde{U} = 2\pi\rho \sum \sum x_i x_j \int u_{ij}(r) g_{ij}(r) r^2 dr \quad (32)$$

The extensions of equations (19) and (21) to higher order systems are given by equations (33) and (34) below

$$\left(\frac{\partial U}{\partial N_1}\right)_{T,V,N_2,N_3} = \tilde{U} - \tilde{V} \left(\frac{\partial U}{\partial V}\right)_{T,N} + x_2 \left(\frac{\partial \tilde{U}}{\partial x_1}\right)_{T,\tilde{V},x_3} + x_3 \left(\frac{\partial \tilde{U}}{\partial x_1}\right)_{T,\tilde{V},x_2} \quad (33)$$

$$\tilde{V} \left(\frac{\partial U}{\partial V}\right)_{T,N} = -\rho \left(\frac{\partial \tilde{U}}{\partial \rho}\right)_T = -(\tilde{U} + \sum \sum x_i x_j \Lambda_{ij}) \quad (34)$$

where

$$\Lambda_{ij} = 2\pi\rho \int u_{ij}(r) \left(\frac{\partial g_{ij}(r)}{\partial \ln \rho}\right)_T r^2 dr \quad (35)$$

The remainder of equation (33) can be written as

$$x_2 \left(\frac{\partial \tilde{U}}{\partial x_1}\right)_{T,\tilde{V},x_3} + x_3 \left(\frac{\partial \tilde{U}}{\partial x_1}\right)_{T,\tilde{V},x_2} = u_1 - 2\tilde{U} + \sum \sum x_i x_j \Phi_{ij} \quad (36)$$

with

$$\Phi_{ij} = 2\pi\rho \int u_{ij}(r) \left[x_2 \left(\frac{\partial g_{ij}(r)}{\partial x_1}\right)_{T,\tilde{V},x_3} + x_3 \left(\frac{\partial g_{ii}(r)}{\partial x_1}\right)_{T,\tilde{V},x_2} \right] r^2 dr \quad (37)$$

The solute average potential energy is given by

$$u_1 = 4\pi\rho \sum x_i \int u_{1i}(r) g_{1i}(r) r^2 dr \quad (38)$$

Using equations (33), (34) and (36),

$$\left(\frac{\partial U}{\partial N_1}\right)_{T,V,N_2,N_3} = u_1 + \sum \sum x_i x_j \Lambda_{ij} + \sum \sum x_i x_j \Phi_{ij} \quad (39)$$

Equation (39) is the extension of equation (25) to multicomponent systems. The considerations regarding the short-range and long-range contributions in equation (39) are entirely analogous to those regarding equation (25). Similarly the extension of equation (26) is given by

$$\left(\frac{\partial S^r}{\partial N_1}\right)_{T,V,N_2,N_3} \equiv s_1^r + \Delta S_{env}^r \quad (40)$$

Considering that long-range contributions have no net effect on μ_1^r , permits one to define s_1^r and ΔS_{envir}^r as follows

$$s_1^r \equiv \frac{u_1 - \mu_1^r}{T} \quad (41)$$

$$\Delta S_{envir}^r \equiv \frac{\sum \sum x_i x_j \Lambda_{ij} + \sum \sum x_i x_j \Phi_{ij}}{T} \quad (42)$$

A study using the Percus-Yevick equation and the generalized multicomponent relationships presented here is currently in progress, with a view to increasing our understanding of local solvent density effects in supercritical fluid mixtures.

Concluding Remarks

In this work using model fluid potentials we have shown that both the solute chemical potential and the solute average potential energy depend on contributions arising from a local neighborhood around the solute of about three to five solvation shells. Examination of the effects of local solvent density enhancements on these two properties have revealed the existence of an interesting competing effect between energetic and entropic contributions to the chemical potential. A partitioning of the energetic and entropic terms into short-range and long-range contributions has been proposed leading to the definition of a local entropy. The results presented here show local solvent density enhancements around a solute molecule as the critical density is approached. However it appears that competitive energetic and entropic contributions can occur as a result of those density enhancements, leading to a solute chemical potential that remains relatively invariant with respect to density inhomogeneities.

Notation:

$g_{ij}(r)$ = molecular pair distribution function

k = Boltzmann's constant

N = number of molecules

r = intermolecular distance

$r^* = r/\sigma_{22}$ = reduced distance

P = pressure

S = entropy

T = temperature

$T^* = kT/\epsilon_{22}$ = reduced temperature

$u(r)$ = intermolecular potential

$U = 2\pi N\rho \int u(r)g(r)r^2dr$ = average potential energy of the system

u_1 = average potential energy of the solute molecule

$s_1^r \equiv (u_1 - \mu_1^r)/T$ = residual (*local*) entropy of the solute molecule

$\Delta S_{envir}^r \equiv (\Lambda + \Phi)/T$ = balance entropy of solute molecule environment

V = volume

x_i = mole fraction

$$E_{12}(R) \equiv 4\pi\rho \int u_{12}(r)g_{12}(r)r^2dr$$

$$F_{12}(R) \equiv 4\pi\rho \int \int u_{12}(r)g_{12}(r,\xi)r^2d\xi dr$$

$$\mu_1^r = \mu_1(T, V, N_1, N_2) - \mu_1^*(T, V, N_1, N_2) = \text{solute residual chemical potential}$$

$$\bar{H}_1^r = \bar{H}_1(T, V, N_1, N_2) - \bar{H}_1^*(T, V, N_1, N_2) = \text{solute residual partial molar enthalpy}$$

$$\bar{S}_1^r = \bar{S}_1(T, V, N_1, N_2) - \bar{S}_1^*(T, V, N_1, N_2) = \text{solute residual partial molar entropy}$$

$$\Delta S_1^D = \bar{V}_1(\partial S/\partial V)_T = \bar{V}_1(\partial P/\partial T)_V$$

$$\Delta H_1^D = T\bar{V}_1(\partial S/\partial V)_T = T\bar{V}_1(\partial P/\partial T)_V = T\Delta S_1^D$$

Greek letters:

$$\beta = 1/kT$$

ξ = Kirkwood coupling parameter

μ_i = chemical potential

$\rho = N/V$ = number density

$\rho^* = N\sigma_{22}^3/V$ = reduced density

$$\Lambda = 2\pi\rho \int u_{22}(r)(\partial g_{22}(r)/\partial \ln \int)_{T,x_1}^\infty r^2dr$$

$$\Phi = 2\pi\rho \int u_{22}(r)(\partial g_{22}(r)/\partial x_1)_{T,\bar{v}}^\infty r^2dr$$

Subscripts:

₁ = solute

₂ = solvent

Superscripts:

^r = residual property

^{*} = reduced property

^D = diverging part of thermodynamic property

Acknowledgment

The authors would like to acknowledge the National Science Foundation which supported this work through grant #CTS-8908828, and the Donors of the Petroleum Research Fund administered by the American Chemical Society for financial support.

Literature Cited

1. Chimowitz, E.H.; Pennisi, K.P. *AIChE J.* **1986**, *32*, 1665.
2. Johnston, K.P.; Barry, S.E.; Read, N.K.; Holcomb, T.R. *Ind. Eng. Chem. Res.* **1987**, *26*, 2372.
3. Kelley, F.D.; Chimowitz, E.H. *J. Supercrit. Fluids.* **1989**, *2*, 106.
4. Yonker, C.R.; Wright, R.W.; Frye, S.L.; Smith, R.D. In *Supercritical Fluids, Chemical and Engineering Principles and Applications*; Squire, T.G.; Paulaitis, M.E. Eds.; ACS Symposium Series 329; 1987, Chap. 14.
5. Klesper, E.; Schmitz, F.P. *J. Supercrit. Fluids.* **1988**, *1*, 45.
6. Hütz, A.; Schmitz, F.P.; Leyendercker, D.; Klesper, E. *J. Supercrit. Fluids.* **1990**, *3*, 1.

7. Kelley, F.D.; Chimowitz, E.H. *AIChE J.* **1990**, *36*, 1163.
8. Matson, D.W.; Fulton, J.L.; Petersen, R.C.; Smith, R.D. *Ind. Eng. Chem. Res.* **1987**, *26*, 2298.
9. Debenedetti P.G., *AIChE J.* **1990**, *36*, 1289.
10. Recasens, F.; McCoy, B.J.; Smith, J.M. *AIChE J.* **1989**, *35*, 951.
11. Paulaitis, M.E.; Krukonis, V.J.; Kurnik, R.T.; Reid, R.C. *Rev. in Chem. Eng.* **1983**, *1*, 181.
12. *Supercritical Fluid Technology*; Penninger, J.M.L. Radosz, M.; McHugh, M.A.; Krukonis, V.J., Eds.; Elsevier Science: 1985.
13. Brennecke, J.F.; Eckert, C.A. *AIChE J.* **1989**, *35*, 1409.
14. Johnston, K.P.; Penninger, J.M.L. *Supercritical Fluid Science and Technology*; Johnston, K.P.; Penninger, J.M.L., Eds.; ACS Symposium Series 406; 1989.
15. Debenedetti, P.G.; *J. Chem. Phys.* **1988**, *88*, 2681.
16. Petsche, I.B.; Debenedetti, P.G.; *J. Chem. Phys.* **1989**, *91*, 7075.
17. Shing, K.S.; Chung, S.T. *J. Phys. Chem.* **1987**, *91*, 1674.
18. Shing, K.S.; Chung, S.T. *AIChE J.* **1988**, *34*, 1973.
19. McGuigan, D.B.; Monson, P.A. *Mol. Phys.* **1987**, *26*, 3.
20. McGuigan, D.B.; Monson, P.A. *Fluid Phase Equilibria.* **1990**, *57*, 227.
21. Cochran, H.D.; Lee, L.L. *AIChE J.* **1988**, *34*, 170.
22. Cochran, H.D.; Lee, L.L. In *Supercritical Fluid Science and Technology*; Johnston, K.P.; Penninger, J.M.L., Eds.; ACS Symposium Series 406; 1989.
23. Wu, R.; Lee, L.L.; Cochran, H.D. *Ind. Eng. Chem. Res.* **1990**, *29*, 977.
24. Griffiths, R.B.; Wheeler, J.C. *Phys. Rev. A.* **1970**, *2*, 1047.
25. Wheeler, J.C. *Ber. Bunsenges. Phys. Chem.* **1972**, *76*, 308.
26. Levelt Sengers, J.M.H.; Morrison, G.; Chang, R.F. *Fluid Phase Equil.* **1983**, *14*, 19.
27. Levelt Sengers, J.M.H.; Chang, R.F.; Morrison, G. In *Equations of State: Theories and Applications*; Chao, K.C.; Robinson, R.L., Eds., Am. Chem. Soc. Symp. Ser. 300; 1986; p 110.
28. Chang, R.F.; Morrison, G.; Levelt Sengers, J.M.H. *J. Phys. Chem.* **1984**, *88*, 3389.
29. Chang, R.F.; Levelt Sengers, J.M.H. *J. Phys. Chem.* **1986**, *90*, 5921.
30. Kim, S.W.; Johnston, K.P. *Ind. Eng. Chem. Res.* **1987**, *26*, 1206.
31. Kim, S.W.; Johnston, K.P. *AIChE J.* **1987**, *33*, 1603.
32. Brennecke, J.F.; Eckert, C.A.; *Ind. Eng. Chem. Res.* **1990**, *29*, 1682.
33. Hill, T.L. *Statistical Mechanics*; McGraw-Hill: New York, NY, 1956.
34. Percus, J.K.; Yevick, G.K. *Phys. Rev.* **1958**, *110*, 1.
35. Munoz, F.; Chimowitz, E.H. *Fluid Phase Equilibria.* **1992**, *71*, 237.
36. Rowlinson, J.S.; Swinton, F.L. *Liquids and Liquid Mixtures*; Butterworths: Boston, 1982; p 254.
37. Buff, F.P.; Brout, R. *J. Chem. Phys.* **1955**, *23*, 458.
38. Hildebrand, J.H.; Scott, R.L. 1950. *The Solubility of Nonelectrolytes*; 3rd edn. Reinhold Publishing Corporation: New York, NY, 1950.

American Chemical Society
Library

In Supercritical Fluid Engineering Science: Kiran, E., et al.;
ACS Symposium Series 406; Washington, DC, 1992.
Washington, D.C. 20036

39. Johnston, K.P.; Eckert, C.A. *AIChE J.* **1981**, *27*, 773.
40. Schmitt, W.J.; Reid, R.C. In *Supercritical Fluid Technology*; Penninger, J.M.L.; Radosz, M.; McHugh, M.A.; Krukonis, V.J., Eds.; Elsevier Science: 1985; p 123.
41. Kumar, S.K.; Johnston, K.P. *J. Supr. Fluids.* **1988**, *1*, 15.
42. Jonah, D. *Chem. Eng. Comm.* **1989**, *79*, 1.

RECEIVED June 23, 1992

Chapter 12

Chemical Potentials in Ternary Supercritical Fluid Mixtures

David M. Pfund¹ and Henry D. Cochran²

¹Chemical Sciences Department, Pacific Northwest Laboratory,
Richland, WA 99352

²Chemical Technology Division, Oak Ridge National Laboratory,
Oak Ridge, TN 37831

The solubility of a solute in a supercritical fluid can be greatly enhanced by adding an appropriate co-solvent or entrainer. We have explored this solubility enhancement at a molecular level using integral equation theory. With a method we developed previously, based on scaled particle theory (SPT), we are able to estimate the chemical potential of a solute from molecular distribution functions calculated from the hybrid mean spherical approximation. A multistep charging process permits a separate determination of the effects of short-ranged repulsive and long-ranged attractive interactions on the chemical potential. The SPT-based method provides a means of explaining how a small concentration of a third component can greatly alter the chemical potential, and therefore the solubility, of a solute in a supercritical solvent.

Theoretical studies of supercritical fluid extraction have focused their attention on the structure and properties of binary mixtures (1-7). Attention needs to be turned to ternary mixtures since the presence of a third component can significantly affect the solubility of a solute in a supercritical solvent (8-11). The third component can also affect the selectivity of a supercritical solvent for one solute or another (12,13). The Peng-Robinson equation of state can sometimes provide a correlation of these effects, however the values of the binary interaction parameters obtained in such correlations can not be interpreted in terms of the properties of the molecules (12). In previous work (14) we presented an interpretation of these effects in terms of fluctuation theory. The authors developed expressions relating the solubility to the Kirkwood-Buff affinities of the solute for the solvent and of the solute for the third component. In other work (15,16) we developed and tested a technique for estimating chemical potentials in supercritical fluid mixtures. The technique described how large solvent-solute attractions act to reduce the chemical potential, and therefore increase the solubility of a solute. In the present paper we extend the chemical potential prediction technique to ternary mixtures.

Only recently have theoretical methods been devised for and applied to the calculation of chemical potentials. Methods based on molecular simulation techniques have been

0097-6156/93/0514-0149\$06.00/0
© 1993 American Chemical Society

used to estimate chemical potentials in fluids using realistic fluid models such as the Lennard-Jones model (17-25). These techniques can provide rigorous estimates of chemical potentials in the chosen model for mixtures of gases or liquids that are not too strongly non-ideal.

Simulations are less useful in the study of supercritical solutions (which tend to be dilute mixtures of unlike species and to have very long-ranged correlation functions). Lotfi and Fischer (19) have found that large system sizes and long run times are required in order to obtain reproducible results from the Widom test particle method (17) for large solutes in mixtures at infinite dilution. Approximate theories can provide a fast way of estimating chemical potentials in such asymmetric mixtures. Simulations provide the means for verifying the accuracy of theories.

Theory

Integral equation theories can be used to estimate potentially long-ranged correlation functions in dilute mixtures of unlike species (2). The hybrid mean spherical approximation (HMSA) integral equation theory is a theory for the correlation functions in fluids modeled with spherical particles. It provides accurate estimates of the pressures and internal energies of such fluids (26). In this theory the Ornstein - Zernike (OZ) equation,

$$\begin{aligned} h_{ij}(r) - C_{ij}(r) = & \rho_1 \int_V C_{i1}(\mathbf{r}_i, \mathbf{r}_1) h_{1j}(\mathbf{r}_1, \mathbf{r}_j) d\mathbf{r}_1 \\ & + \rho_2 \int_V C_{i2}(\mathbf{r}_i, \mathbf{r}_2) h_{2j}(\mathbf{r}_2, \mathbf{r}_j) d\mathbf{r}_2 \\ & + \rho_3 \int_V C_{i3}(\mathbf{r}_i, \mathbf{r}_3) h_{3j}(\mathbf{r}_3, \mathbf{r}_j) d\mathbf{r}_3 \end{aligned} \quad (1)$$

(written for a ternary mixture) is solved simultaneously with the closure equation (26),

$$C_{ij} = h_{ij} - \left(\frac{1}{s}\right) \ln \left[s g_{ij} e^{\beta u_{ij}^0} (s-1) \right] - \beta u_{ij}^1 \quad (2)$$

to yield the direct and total correlation functions, C_{ij} and h_{ij} respectively, in the fluid. u_{ij}^0 and u_{ij}^1 are the repulsive and attractive parts of the intermolecular pair potential according to the division of Weeks, Chandler, and Anderson (27). The adjustable switching function s is varied to achieve thermodynamic consistency between the bulk moduli obtained from the virial and compressibility equations. The reliability of integral equation theories (including the HMSA) for states very near to the liquid-vapor critical point has not been extensively studied. Numerical schemes for solving Equations (1) and (2) which require $h_{ij}(r) = 0$ for $r > R_{\max}$ are unable to approach the critical point closely and the results will deviate from known analytic solutions for simple models and theories (28). The conditions for which the HMSA theory will be applied in the present work will be sufficiently removed from the critical point so that the theory will supply accurate estimates of structures, pressures, and internal energies (16). The estimated correlation functions for the near critical states of Reference (5) are consistent with simulation results

but lack the statistical noise characteristic of such simulations. In this work we investigate the chemical potentials calculated from the HMSA theory using a Kirkwood charging process based on scaled particle theory.

In the Kirkwood charging process, the residual chemical potential of a solute species j equals the change in Helmholtz free energy (or work) at constant temperature and volume which occurs on moving a molecule of j (referred to as a test particle) from a fixed position in an ideal gas to a fixed position in the fluid of interest (29). This free energy change will be referred to as the work of insertion. The new (or test) particle may be inserted in an arbitrary number of steps over an arbitrary path. The insertion process is equivalent to switching on a field source at that position; for a given path the switching on is accomplished by varying a coupling parameter λ' . The resulting free energy change is (30),

(3)

$$A(1) - A(0) = \int_{\lambda_i}^{\lambda_f} \left\{ \left[\rho_1 \int g_{1t}(r_{1t}; \lambda') \frac{\partial}{\partial \lambda} [u_{1t}(r_{1t}; \lambda')] dr_{1t} \right] + \left[\rho_2 \int g_{2t}(r_{2t}; \lambda') \frac{\partial}{\partial \lambda} [u_{2t}(r_{2t}; \lambda')] dr_{2t} \right] + \left[\rho_3 \int g_{3t}(r_{3t}; \lambda') \frac{\partial}{\partial \lambda} [u_{3t}(r_{3t}; \lambda')] dr_{3t} \right] \right\} d\lambda'$$

where the pair correlation function of molecules of species i surrounding the test particle is denoted by g_i and the pair potential between the test particle and molecules of species i is u_{it} .

As is shown in Equation (3), the work of insertion is a function of the correlation functions for fluid particles surrounding a test particle. These functions will be determined from the HMSA theory. The OZ equations which are used are those for a mixture consisting of a test particle species which is at infinite dilution in the fluid of interest (which may contain the solute at finite concentrations). The components of the test particle pair potentials u_i^0 and u_i^1 which appear in Equations (2) and (3) vary with the coupling parameter for each step in the charging process.

In applying Kirkwood charging one must first specify a charging path by which the test particle is inserted into the fluid. If Kirkwood charging is used with integral equation theories (which are inherently inexact) then different charging paths can yield different chemical potentials (31). It is possible that results obtained from different charging paths differ in their accuracy. In this work a multi-step charging process is used to divide the

work of insertion into positive repulsive and negative attractive contributions. These contributions result from the short-ranged WCA repulsive potentials u_{ij}^0 and long-ranged WCA attractive potentials u_{ij}^1 , respectively. The free energy change for each step is determined from Equation (3) and the results are summed to give the residual chemical potential.

The charging path followed in this work is a traditional one used in solvation theory (32). This traditional approach views interphase transfers as occurring in two steps, the first being the formation of a cavity big enough to hold the repulsive core of a test solute molecule (which defines the molecular size) and the second being the placement of such a molecule within the cavity and allowing it to interact with the surrounding molecules. Inserting a hard sphere test particle into the fluid is a process equivalent to forming a cavity. The hard sphere is inserted into the fluid using the particle scaling technique originally developed for scaled particle theory (SPT) (33-35). Associated with this step is a free energy change or work of cavity formation.

Effective hard sphere diameters must be defined for the softly repulsive species in the fluid. These diameters determine the cavity radii at the end of the hard sphere insertion process. They are obtained during the process of switching-on the softly repulsive interactions between the test particle and the surrounding particles. The hard sphere test particle of species j is softened until it becomes the WCA repulsive particle. The WCA repulsive test particle of species j interacts with surrounding particles of species i according to the pair potential u_{ij}^0 . Associated with this step is a free energy change or work of softening. The total repulsive contribution to the residual chemical potential equals the work of cavity formation plus the work of softening. The effective hard sphere diameters for interactions with the hard sphere test particle are chosen so that the work of softening is approximately zero. The work of softening is estimated using a technique adapted from liquid state perturbation theory (36).

In the last step the attractive components u_{ij}^1 of the pair potentials for interactions of species i with the test particle of species j are switched-on; the repulsive components u_{ij}^0 being fully charged after the hard sphere insertion and softening steps. Associated with this step is a free energy change or work of binding. After completing this step the test particle is equivalent to an ordinary particle of species j , interacting with species i according to the potential $u_{ij} = u_{ij}^0 + u_{ij}^1$.

In a previous work (15), we described the development of the SPT-based method and its application to the HMSA theory. Extension of the method to ternary mixtures of Lennard-Jones particles or to a similar model of fluids is straightforward. The complete charging process is illustrated in Figure 1. In the first step (proceeding counter clockwise from the upper left) a free mass-point is replaced by a hard point test particle. The hard point can approach the center of a particle of species j to within a distance $d_{ij}/2$, where d_{ij} is the effective diameter of species j . In the second particle scaling step the hard sphere test particle of species i grows to a diameter of d_{ij} . In the third softening step the hard sphere is replaced by a soft WCA repulsive test particle. The effective diameters are chosen so that the free energy change for the third step is zero. In the fourth step the WCA attractive potentials are added to the test particle and it becomes a new molecule of species i . The work of cavity formation is the sum of free energy changes for the first two steps. The work of solvent-solute binding equals the free energy change for the fourth.

The assumptions made in the development of the method were presented previously (15). These assumptions were found to introduce a negligible error in predicted chemical potentials. The principle source of error was determined to be the predicted test particle correlation functions obtained from the HMSA theory (16). The SPT-based charging path minimizes this error under certain conditions. The error was found to be small at low pressures, in compressed liquids, and at supercritical temperatures. It was found that the method presented here is useful in the study of chemical potentials in those supercritical fluids that can be described with spherically symmetric potential models.

Potential Parameters

Ternary mixtures were constructed of the following Lennard-Jones species:

<u>Species</u>	<u>Type</u>	<u>$\sigma, \text{\AA}$</u>	<u>$\epsilon/k, \text{Kelvin}$</u>
1	Solvent	3.753	246.1
2	Co-solvent	3.626	481.8
3	Solute	5.883	674.1

The solvent parameters (taken from Reference 37) were developed from virial coefficient data for carbon dioxide. The co-solvent parameters (taken from Reference 38) were developed from dilute gas viscosity data of methanol. The solute parameters were calculated from an equation in Reference 38 using the critical temperature, critical pressure, and acentric factor of benzoic acid. The parameters are not intended to provide a quantitative description of these components. They are merely intended to be a set of Lennard-Jones parameters likely to yield co-solvent effects.

Results

Solute chemical potentials are a function of both the bulk density of the fluid and the local environment of the solute. Solute residual chemical potentials at infinite dilution were calculated in the following mixtures at a temperature of 344.54 K ($kT/\epsilon_{11} = 1.4$):

<u>Density</u> <u>gmol./cm³</u>	<u>Mole Fraction</u> <u>Co-solvent</u>	<u>Pressure,</u> <u>atm.</u>	<u>Contributions</u>		<u>$(\mu_3 - \mu_3^*)/kT$</u>
			<u>Repulsive</u>	<u>Attractive</u>	
0.01099	0.035	92.4	4.01	-12.10	-8.09
0.01099	0.0	108.02	4.08	-11.88	-7.80
0.00599	0.0	92.4	1.86	-7.08	-5.22
0.01571	0.035	134.1	7.92	-16.92	-9.05
0.01443	0.0	134.1	6.72	-15.34	-8.62

where the pressures have been calculated using the HMSA theory. Since the critical temperature of a pure Lennard-Jones fluid occurs at approximately $kT/\epsilon_{11} = 1.35$ (or 332.24 K), the mixtures are at a reduced temperature T_r of approximately 1.037. The critical density of a pure Lennard-Jones fluid occurs at approximately $\rho\sigma_{11}^3 = 0.35$ (or 0.01099 gmol./cm³). Since the mixtures were relatively close to the critical point at a pressure of 92.4 atmospheres, the addition of a small amount of co-solvent resulted in nearly a doubling of the density. The increase in density was the principle cause of the reduction in the residual chemical potential from -5.22 to -8.09. To obtain lower residual chemical potentials for the solute in a binary mixture requires increasing the pressure. At the higher pressure of 134.1 atmospheres the density of the mixture containing the co-solvent was more nearly equal to the density of pure carbon dioxide at the same pressure. Under such conditions the effect of co-solvent addition was to change the local environment of the solute resulting in a reduction of the residual chemical potential from -8.62 to -9.05.

Figure 2 displays the pair correlation functions of solvent and co-solvent molecules with the solute in the first three mixtures listed above. The corresponding aggregation numbers for species with the solute are:

Density gmol./cm ³	Mole Fraction Co-solvent	Pressure, atm.	Number of Solvent Molecules	Number of Cosolvent Molecules
0.01099	0.035	92.4	60.8	6.0
0.01099	0.0	108.02	27.7	-
0.00599	0.0	92.4	44.5	-

The aggregation numbers were obtained from the Kirkwood-Buff fluctuation integrals as discussed in a previous work (2). The aggregation numbers are sensitive to long-ranged correlations. The solute/solvent correlation functions are similar in the binary and ternary mixtures when examined at equal densities. The co-solvent has a very small effect on the first and second maxima of the solute/solvent pair correlation function at constant density. The co-solvent appears to enhance the long-range correlation of solvent molecules around solute molecules. The co-solvent exhibits very strong short-range and long-range correlations with solute molecules.

The predicted effect of co-solvent addition on the solute chemical potential yields solubility enhancements in qualitative agreement with experiment. The solubility of a solid solute in a supercritical fluid depends inversely on the bulk density and inversely on the exponential of the residual chemical potential of the solute:

$$y_3 \propto \frac{1}{\rho} \exp\left(-\frac{\mu_3 - \mu_3^*}{kT}\right) \quad (18)$$

The left hand side of Equation 18 is plotted versus pressure in Figure 3. The solubility was enhanced by a factor of 9.6 at 92.4 atmospheres and by a factor of 1.4 at 134.1 atmospheres by the addition of co-solvent. Experimental enhancements of benzoic acid solubility due to methanol addition into carbon dioxide range from approximately 6.0 at low pressures to approximately 3.5 at high pressures at a reduced temperature of 1.013 (11).

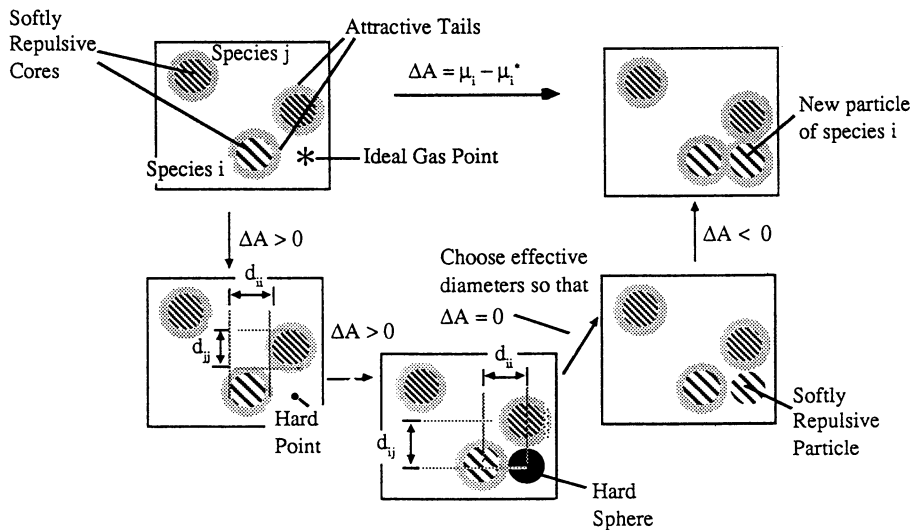


Figure 1: The residual chemical potential of species i equals the sum of Helmholtz free energy changes for four steps.

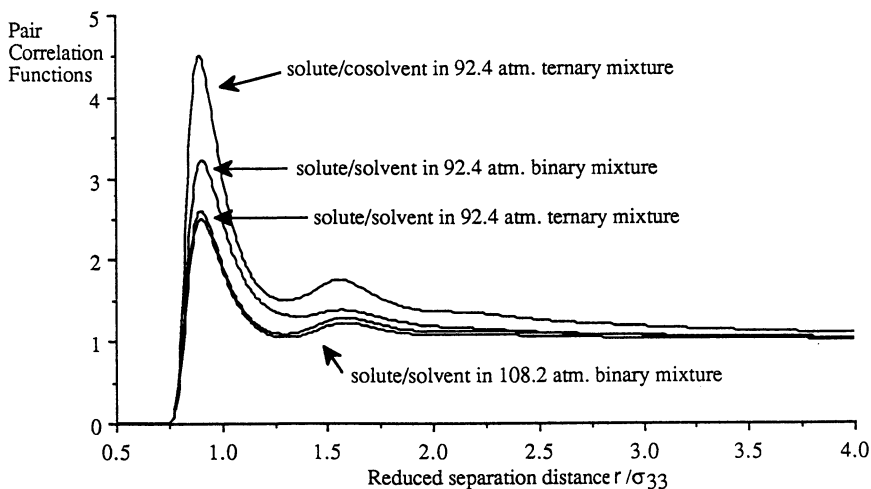


Figure 2: Pair correlation functions for fluid species interacting with solute molecules. Conditions are given in the text.

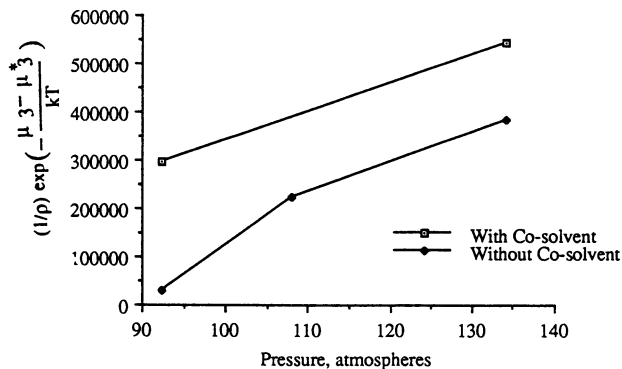


Figure 3: Solute solubility is proportional to the quantity plotted on the ordinate. Conditions are given in the text.

Conclusions

In summary, the residual chemical potential of a solute in a pairwise additive, spherically symmetric, ternary fluid model has been expressed as the sum of an approximately determined work of inserting a hard point plus formally exact contributions due to particle scaling, softening the hard sphere, and adding attractive potentials.

The method has been used qualitatively to predict the solubility enhancement of a solid in a supercritical fluid due to addition of a co-solvent. Near the critical point of the solvent the solubility was greatly enhanced because of an increase in the density of the fluid upon co-solvent addition. At higher pressures the bulk density remained essentially constant upon co-solvent addition. The observed solubility enhancement was therefore due to an alteration of the local environment of the solute molecule.

This work shows that simple fluids (spherically symmetric, non-polar fluids) are capable of exhibiting enhanced supercritical solubility upon addition of a co-solvent and that appeals to “special” or “chemical” interactions (though such interactions may exist in a given system) are not necessary to explain the phenomenon.

Acknowledgments

This research was supported by the Director, Office of Energy Research, Office of Basic Energy Sciences, Chemical Sciences Division of the U.S. Department of Energy (DOE) under contract DE-AC06-76-RLO1830 with Pacific Northwest Laboratory and under contract DE-AC05-84OR21400 with Martin Marietta Energy Systems, Inc. Pacific Northwest Laboratory is operated for DOE by Battelle Memorial Institute.

Literature Cited

1. Debenedetti, P.G. *Chem. Eng. Sci.* **1987**, *42*, 2203.
2. Cochran, H.D.; Pfund, D.M.; Lee, L.L. In *Proc. Int. Symp. on Supercritical Fluids (Nice, France)*; Perrut, M. Ed.; Institut National Polytechnique de Lorraine: 1988; p. 245.

3. Debenedetti, P.G.; Mohamed, R.S. *J. Chem. Phys.* **1989**, *90*, 4528.
4. Cochran, H.D.; Pfund, D.M.; Lee, L.L. *Sep. Sci. Technol.* **1988**, *23*, 2031.
5. Petsche, I.B.; Debenedetti, P.G. *J. Chem. Phys.* **1989**, *91*, 7075.
6. Cochran, H.D.; Pfund, D.M.; Lee, L.L. *Fluid Phase Equil.* **1988**, *39*, 161.
7. Peter, S.; Brunner, G.; Rhia R. In *Zur Trennung Schwerfluchtiger Stoffe mit Hilfe Fluider Phasen*; Monograph 73; DECHEMA: 1974.
8. Yonker, C.R.; Frye, S.L.; Kalkwarf, D.R.; Smith, R.D. *J. Phys. Chem* **1986**, *90*, 3022.
9. Schmitt, W.J.; Reid, R.C. *Fluid Phase Equil.* **1986**, *32*, 77.
10. van Alsten, J.D. *Ph.D. Dissertation, University of Illinois, Urbana-Champaign*: 1986.
11. Dobbs, J.M.; Wong, J.M.; Lahiere, R.J.; Johnston, K.P. *I&EC Res.* **1987**, *26*, 56.
12. Kurnik, R.T.; Reid, R.C. *Fluid Phase Equil.* **1982**, *8*, 93.
13. Kwiatkowski, J.; Lisicki, Z.; Majewski, W. *Ber. Berbunsenges. Phys. Chem.* **1984**, *88*, 865.
14. Cochran, H.D.; Johnson, E.; Lee, L.L. *J. Supercrit. Fluids* **1990**, *3*, 157.
15. Cochran, H.D.; Pfund, D.M.; Lee, L.L. *J. Chem. Phys.* **1991**, *94*, 3107.
16. Cochran, H.D.; Pfund, D.M.; Lee, L.L. *J. Chem. Phys.* **1991**, *94*, 3114.
17. Widom, B. *J. Chem. Phys.* **1963**, *39*, 2808.
18. Heinbuch, U.; Fischer, J. *Mol. Sim.* **1987**, *1*, 109.
19. Lotfi, A.; Fischer, J. *Mol. Phys.* **1989**, *66*, 199.
20. Shing, K.S.; Gubbins, K.E.; Lucas, K. *Mol. Phys.* **1988**, *65*, 1235.
21. Shing, K.S.; Gubbins, K.E. *Mol. Phys.* **1982**, *46*, 1109.
22. Powles, J.G.; Evans, W.A.; Quirke, N. *Mol. Phys.* **1982**, *46*, 1347.
23. Panagiotopoulos, A.; Suter, U.W.; Reid, R.C. *Ind. Eng. Chem. Fundam.* **1986**, *25*, 525.
24. Haile, J.M. *Fluid Phase Eq.* **1986**, *26*, 103.
25. Shukla, K.P.; Haile, J.M. *Mol. Phys.* **1987**, *62*, 617.
26. Zerah, G.; Hansen, J. *J. Chem. Phys.* **1986**, *84*, 2336.
27. Weeks, J.D.; Chandler, D.; Andersen, H.C. *J. Chem. Phys.* **1971**, *54*, 5237.
28. Cummings, P.T.; Monson, P.A. *J. Chem. Phys.* **1985**, *82*, 4303.
29. Ben-Naim, A. *Solvation Thermodynamics*; Plenum Press: New York, 1987.
30. Kirkwood, J.G. *J. Chem. Phys.* **1935**, *3*, 300.
31. Kjellander, R.; Sarmen, S. *J. Chem. Phys.* **1989**, *90*, 2768.
32. Eley, D.D. *Trans. Faraday Soc.* **1938**, *35*, 1281.
33. Reiss, H.; Frisch, H.L.; Lebowitz, J.L. *J. Chem. Phys.* **1959**, *31*, 369.
34. Lebowitz, J.L.; Helfand, E.; Praestgaard, E. *J. Chem. Phys.* **1963**, *43*, 774.
35. Reiss, H.; Frisch, H.L.; Helfand, E.; Lebowitz, J.L. *J. Chem. Phys.* **1960**, *32*, 119.
36. Lado, F. *Phys. Rev. A* **1973**, *8*, 2548.
37. Maitland, G.C.; Rigby, M.; Smith, E.B.; Wakeham, W.A. *Intermolecular Forces, Their Origin and Determination*; Clarendon Press: Oxford, 1981.
38. Reid, R.C.; Prausnitz, J.M.; Sherwood, T.K. *The Properties of Gases and Liquids*; third edition; McGraw-Hill: New York, 1977.

RECEIVED April 27, 1992

Chapter 13

Aggregation of Methanol in Supercritical Fluids

A Molecular Dynamics Study

David M. Pfund, John L. Fulton, and Richard D. Smith

Chemical Methods and Separations Group, Chemical Sciences Department,
Pacific Northwest Laboratory, Richland, WA 99352

Variations in solvent properties greatly alter the equilibrium between non-hydrogen bonded monomer and various hydrogen bonded species. Molecular dynamics simulations were performed for model supercritical binary mixtures of methanol in ethane and carbon dioxide. The effects of variations in solvent type, density, and concentration on methanol aggregation and *n*-mer equilibria were examined. A closed ring pentamer was found to be a favored structure in carbon dioxide. Increasing the density of the solvent resulted in a shift in the equilibrium towards the pentamer. At constant pressure, methanol aggregates were larger in ethane than in carbon dioxide, aggregates of six or more methanol molecules being common in ethane. Results from the simulations to determine the fraction of methanol in monomer form were found to be in qualitative agreement with experimental results.

Hydrogen bonding compounds can form aggregates in supercritical fluids at high solute concentrations. A complete description of the nature of these clusters would be an important step towards understanding the behavior of polar solutes such as simple alcohols or large, nonionic surfactants in supercritical fluids. Some understanding of the clusters formed in gas and liquid phases has already been achieved. *Ab initio* studies have estimated the methanol-methanol potential surface and have determined the binding energies of clusters of various sizes and geometries formed in the gas phase (1,2). Thermal conductivity measurements of methanol vapor have shown that aggregates of four or more methanols were present (3). Molecular dynamics simulations of liquid methanol found that chains of methanol occurred with those consisting of five or six methanol molecules being the most prevalent (4). Some polymer rings were found in liquid methanol, though they were present at low concentrations. Infra-red spectroscopic studies have been performed on solutions of methanol in organic liquids (5-7). The results from these latter experiments have been colored by assumptions about the nature of the aggregates which were assumed to be present and by the limited use made of the available spectrum.

0097-6156/93/0514-0158\$06.00/0
© 1993 American Chemical Society

Recent research has suggested the importance of solvent effects on the aggregation of hydrogen bonding solute molecules in supercritical fluids. Infra-red studies of the O-H stretching band of methanol in supercritical fluids have shown that the frequency in hydrocarbon solvents is simply related to the dielectric constant with a continuum model (8). The O-H stretch in carbon dioxide (a quadrupolar solvent) deviates from the continuum model, suggesting that short-ranged solvent ordering about solute monomer is influencing the extent of hydrogen bonding. The effective number of solvent molecules participating in these multi-body interactions and their relative positions remains inaccessible to experiment, and is therefore a valid target for theoretical study. In this paper we examine the effect of the solvent on methanol aggregates in supercritical fluids with the aid of molecular dynamics. We compare the aggregates of methanol molecules formed in supercritical carbon dioxide with those formed in supercritical ethane to study the effect of the solvent on the distribution of cluster sizes, the most probable geometries of the clusters, and their mutual potential energies.

Molecular simulations provide a means of testing our intuitive pictures of microscopic fluid structure. Petsche and Debenedetti have studied the formation of solvent-solute aggregates in Lennard-Jones models of dilute supercritical mixtures (9). Molecular dynamics simulations were used to obtain the solvent structure around solutes in attractive and repulsive mixtures. They found that in attractive mixtures, solutes were surrounded by chains of indirectly bound solvent particles (exterior solvent particles which were connected to the solute through intermediate solvent particles). Shing and Chung (10) have studied Lennard-Jones + quadrupole models of naphthalene and carbon dioxide using Monte-Carlo simulations in the NPT ensemble. Naphthalene solubilities were predicted from calculated chemical potentials and were found to be in qualitative agreement with experiment. Recently, Cummings et al. (11) have studied aggregation around ions in the Simple Point Charge model of supercritical water using molecular dynamics calculations performed in the NVT ensemble. The reaction field technique was used to handle the long-ranged Coulomb forces. They found that the short-ranged H-bonding structure of the fluid was little different from that of ambient water. The long-ranged structure resembled that in simple supercritical fluids. In addition, they determined that supercritical aqueous solutions were in some cases easier to simulate than liquid solutions because long-lived orientational correlations do not occur frequently in the former case. Simulations cannot be used to study structures in every mixture of interest. Long-ranged correlations occur in systems close to the critical point. Such systems can not be studied using simulations involving a limited number of particles (9). Similarly, simulations provide little information about the structure of solute-solute aggregates in very dilute supercritical mixtures.

Structures in molecular fluids can be studied by applying interaction site models of the intermolecular pair potential. In such models the pair potential between molecules m and m' is assumed to be the sum of site-site interactions (12,13):

$$U_{mm'}(\mathbf{r}_m, \mathbf{r}_{m'}) = \sum_{\alpha_m} \sum_{\beta_{m'}} U_{\alpha_m \beta_{m'}} |\mathbf{r}_{\alpha_m} - \mathbf{r}_{\beta_{m'}}| \quad (1)$$

The site-site pair correlation functions (SSPCF) $g_{\alpha\beta}(r)$ obtained from interaction site models provide a convenient means of describing structures in molecular fluids. If $r = |\mathbf{r}_{\alpha} - \mathbf{r}_{\beta}|$ is the distance between sites, then $\rho_{\alpha}\rho_{\beta}g(r)_{\alpha\beta}$ is the probability density that site α

of a molecule is positioned a distance r from site β of another molecule. These functions can be obtained from simulated configurations using the same method of constructing histograms used in simulations of monatomic fluids (14). The site-site functions do not convey as much information as the full angle dependent correlation functions. However, many thermodynamic and structural properties can be expressed in terms of the site-site functions (15). The number of solvent nearest neighbors surrounding a solute is given by,

$$N_{\alpha\beta} = \rho_{\alpha} \int_0^R g_{\alpha\beta} 4\pi r^2 dr \quad (2)$$

where site α lies on the solvent, site β lies on the solute, and ρ_{α} is the number density of the solvent. When determining the number of molecules in the first solvation shell, the upper limit of integration R is the distance to the first minimum in $g_{\alpha\beta}$. The excess number of solvent molecules (above the bulk average) which surround a solute is given by the Kirkwood-Buff fluctuation integral (16),

$$\Gamma_{\alpha\beta} = \rho_{\alpha} \int_0^{L/2} (g_{\alpha\beta} - 1) 4\pi r^2 dr \quad (3)$$

where L is the length of the simulation box and all coordinates lie in the interval $(-0.5L, +0.5L)$. The integral provides a measure of the extent to which solvent molecules tend to cluster around the solute. Positive values are the result of a local solvent excess, whereas negative values are the result of a local deficit of solvent (17). Kirkwood-Buff solution theory (18) relates the fluctuation integral to the partial molar volume of the solute and to the rate of change of solubility with pressure. Dilute mixtures for which the solvent-solute fluctuation integral is negative have been referred to as repulsive. In such cases the solute exhibits a positive partial molar volume near the critical point (17). Similarly, dilute mixtures for which this integral is positive have been referred to as attractive. Solutes in attractive mixtures exhibit large negative partial molar volumes near the critical point.

Potential Models

Lennard-Jones + Coulomb site-site potentials were used in this work. The form of the potential is,

$$u_{\alpha\beta} = 4\epsilon_{\alpha\beta} \left[\left(\frac{\sigma_{\alpha\beta}}{r} \right)^{12} - \left(\frac{\sigma_{\alpha\beta}}{r} \right)^6 \right] + \frac{q_{\alpha} q_{\beta} e^2}{4\pi\epsilon_0 r} \quad (4)$$

where the subscripts m and m' of Equation (1) are not shown.

Interactions between methanol molecules were described using the transferable intermolecular potential (TIP) model of Jorgensen (19):

Site Pair	ϵ/k (K)	σ (Å)
CH ₃ - CH ₃	91.15	3.861
O-O	87.94	3.083

together with electric charges of $q_o = -0.685$ on the oxygen site, $q_H = +0.4$ on the hydrogen site and $q_{CH_3} = +0.285$ on the methyl group. In the TIP model hydroxyl hydrogens are taken to be point charges and the methyl group is treated as a single site (19). The geometric combining rules specified by Jorgensen were used to obtain Lennard - Jones parameters for the cross interactions. Each methanol molecule was taken to be rigid with a methyl - oxygen bond length of 1.427 Å, a oxygen - hydroxyl hydrogen bond length of 0.956 Å, and a methyl - hydroxyl hydrogen distance of 1.958 Å.

For the study of mixtures of methanol in carbon dioxide, the carbon dioxide model of Murthy, Singer, and McDonald was used (20,21),

Site Pair	ϵ/k (K)	σ (Å)
O - O	83.1	3.014
C - C	29.0	2.785
C - O	49.091	2.8995

together with electric charges of $q_o = -0.298$ on each of the oxygen sites and $q_c = +0.596$ on the carbon site. The carbon - oxygen bond length used was 1.16 Å. For the study of mixtures of methanol in ethane, the TIP model parameters were used to describe the methyl groups on the ethane molecule. The methyl - methyl distance was fixed at 1.535 Å.

Parameters for solvent-solute interactions were estimated using Jorgensen's geometric combining rules.

Simulation Method

Systems of 500 molecules in a cubic box were simulated in the N-V-isokinetic ensemble. The technique of Fincham, Quirke, and Tildesley was used to simultaneously constrain the bond lengths and the translational and rotational temperatures of the linear carbon dioxide or ethane molecules (14,22). The equations of motion were solved using the "leap-frog" method. A constraint dynamics algorithm was developed (using the techniques of Reference 14) for maintaining the geometry and temperature of the non-linear methanol molecules using the leap-frog method. Preliminary tests of energy and linear momentum conservation in the absence of the temperature constraint were performed using Lennard - Jones sites. Simulations began with the molecules positioned on a face-centered cubic lattice. For the solvent molecules initial translational velocities were chosen from a Gaussian distribution, and squares of the magnitudes of the angular velocities were chosen from an exponential distribution. The initial motion of the methanol molecules was purely translational with a kinetic energy equal to the necessary combined rotational and translational energies, uniformly divided among all of the molecules. In this work the potentials were spherically truncated at distances greater than one half of the box length. As in the original simulations of liquid methanol using the TIP model, Ewald sums were not taken (23,24). This simplification is justified due to the approximate nature of the TIP dipole moment and hydrogen bond energy and to the fact that simple thermodynamics are not sensitive to the truncation. Relatively long truncation distances were used in this work.

Equilibration periods of at least 20,000 time steps (1.2 fs each) were used. Runs lasted for an additional 20,000 time steps. Solute positions were saved and statistics for computing site-site pair correlation functions were accumulated every 50 time steps after equilibration. Cluster sizes and energies were calculated later from the saved positions using a modified version of the standard cluster counting algorithm (14). The algorithm partitions the solute molecules into mutually exclusive hydrogen bonded clusters. A pair of molecules was considered to be hydrogen bonded when the distance between an oxygen and a hydrogen on two hydroxyl groups was less than the separation distance at the first minimum of the SSPCF g_{OH} . The first minimum in g_{OH} occurs at a separation distance of about 2.62 Å. This criterion is of course arbitrary, and may be more or less stringent than that implicit in a given type of experiment for detecting hydrogen bonded clusters. After a cluster was identified, its mutual potential (or binding) energy was calculated from the TIP model. Histograms of frequency of appearance versus binding energy were obtained for each size cluster in each mixture. The positions of sites were saved for randomly selected clusters with energies near the most probable value. These positions were used in constructing plots of the clusters.

The Cases

Each simulation was performed at a temperature of 313.15 Kelvin. The molecular density of the solvent was set to a value equal to the experimental density of pure solvent at the pressure of interest. The conditions simulated were:

<u>Solvent</u>	<u>Pressure, bar</u>	<u>Solvent density used, molecules/Å³</u>
carbon dioxide	200	0.01151
carbon dioxide	400	0.01309
ethane	200	0.00804

These conditions were chosen in an attempt to approximate the micro-structures and therefore necessarily the (unknown) densities of experimental mixtures discussed elsewhere in this volume (25). At pressures of 200 and 400 Bar the real fluids are sufficiently compressed so that the experimental molar volumes are expected to be approximately equal to those of the pure solvent plus those of the solute. No attempt was made to reproduce the experimental PVT relationship with the approximate potential models used in this work. Reference will be made to the experimental pressures when discussing the simulations as a matter of convenience. The simulations of methanol in carbon dioxide and in ethane were made at concentrations of 6.4 mole percent solute (using 32 methanol molecules in the simulation cell). Methanol in concentrations of five to ten percent is commonly used as an entrainer in supercritical fluids (26). Extensive solute-solute aggregation was observed in the ethane solvent. A simulation was also made of a dilute mixture of 3.2% methanol in ethane (using 16 methanol molecules in the simulation cell) in order to confirm that phase separation had not taken place in the more concentrated solution. The site-site correlation functions obtained at the two concentrations were nearly the same (except for decreases in the long-ranged portion of the solute-solute functions with decreasing concentration), indicating that phase separation did not occur.

The solute molecules were very mobile and the cluster size distributions converged rapidly. In all cases the monomer concentrations converged after 120 configurations were

sampled (the accuracy of calculated concentrations of larger n-mers is given in the Results section below). Totals of 367 and 400 samples were taken in the low and high density carbon dioxide mixtures, respectively. 397 and 563 samples were taken in the high and low solute concentration mixtures in ethane, respectively. The RMS displacements of solute molecules during the entire sampling period (after melting the initial lattice) were 0.30 and 0.26 box lengths in the low density and high density carbon dioxide mixtures, respectively. These figures include numerous crossings of the periodic box boundaries - the RMS lengths of the trajectories of solute molecules for the same mixtures were 3.49 and 3.97 box lengths, respectively. The solute molecules were slightly more mobile in the ethane solvent. In the high and low concentration mixtures in ethane the RMS solute displacements were 0.31 and 0.49 box lengths and the RMS trajectory lengths were 4.1 and 4.8 box lengths, respectively.

Results And Discussion

It is frequently assumed that the predominant cluster which appears in a solution of an alcohol in a fluid is that which has some special stability in the gas phase. It is also frequently assumed that the properties of the solvent act only to shift the equilibrium between polymer species which are the same in every solvent. The results that follow demonstrate that there is in fact a distribution of cluster sizes in a supercritical fluid and that the nature of the solvent influences the type of species which compete in the equilibrium.

At equal temperatures, pressures and compositions methanol-methanol aggregation was significantly greater in ethane than in carbon dioxide. Plotted in Figure 1 are the site-site pair correlation functions for oxygen-hydrogen interactions for a 6.4 mole percent solution of methanol in the two solvents at 40°C and approximately 200 bar. The higher first peak in the ethane solvent indicates that a greater percentage of the methanol molecules were hydrogen bonded than in carbon dioxide. The longer ranged tail of the correlation function in ethane indicates that aggregate sizes are larger in ethane than in carbon dioxide. Plotted in Figure 2 are the solute-solute aggregation numbers determined from Equation 3. In carbon dioxide the average number of excess (above the bulk average) methanol molecules surrounding each methanol molecule was approximately two, whereas in ethane the average excess was approximately eight. The presence of a maximum in the curve for the ethane solvent case indicates that the size of the system used in the NVT simulation was too small (11). Thus, the differences between aggregation numbers obtained in ethane and carbon dioxide should be considered as only a qualitative reflection of the differences between the two solvents. Plotted in Figure 3 are the solute-solute neighbor numbers determined from Equation 2 as a function of radius R about a hydroxyl hydrogen atom. On average, approximately 0.7 methanol molecules were contained within the first coordination shell surrounding a methanol molecule in the ethane solvent, and approximately 0.35 methanol molecules were contained within the first shell in carbon dioxide.

Solvent-solute aggregation was greater in carbon dioxide than in ethane. Also plotted in Figure 2 are the solvent-solute aggregation numbers in the two solvents. In carbon dioxide there is a net deficit (below the bulk average) of two solvent molecules surrounding each methanol molecule, whereas in ethane the deficit was approximately four solvent molecules. As suggested by experimental work done in our laboratory (8,25),

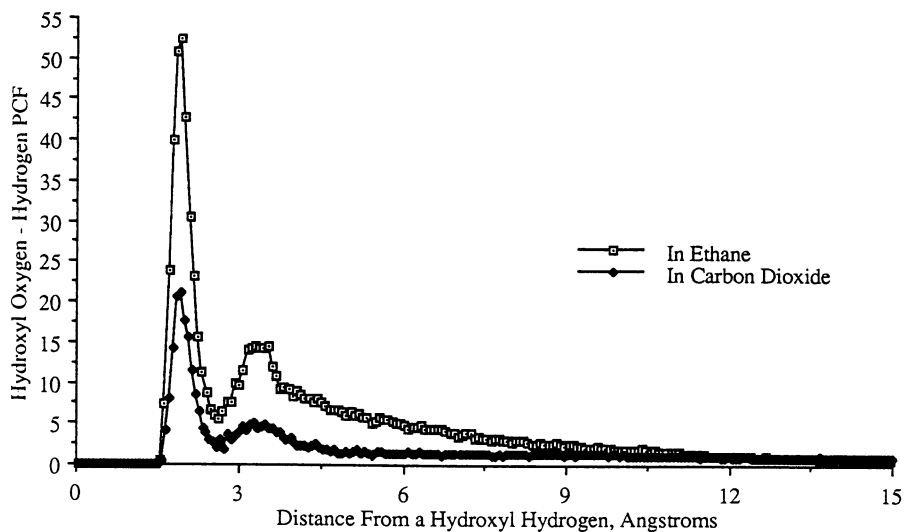


Figure 1: Intermolecular site-site pair correlation functions for methanol hydrogens with methanol oxygens.

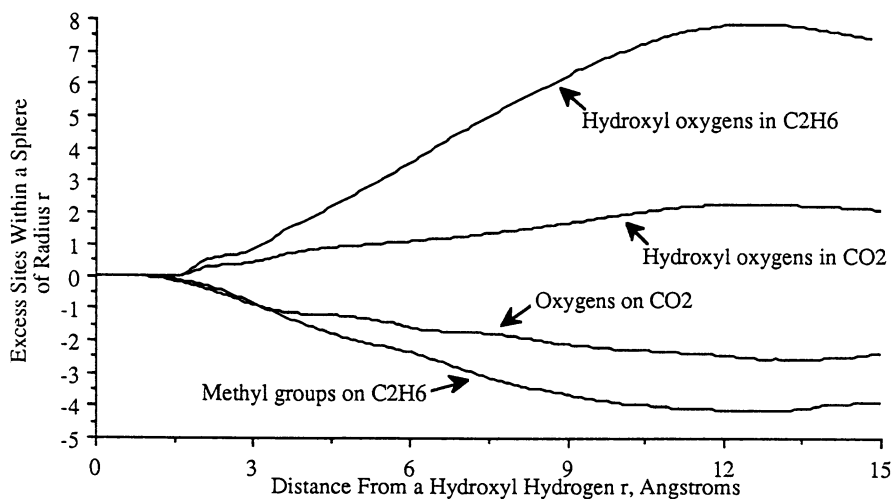


Figure 2: The excess number of various sites within spheres of radius r surrounding a methanol hydrogen.

the carbon dioxide-methanol interaction is shown to be relatively strong. This interaction interferes with hydrogen bond formation. Also plotted in Figure 3 are the solvent-solute neighbor numbers in the two solvents. Approximately 0.2 carbon dioxide molecules were contained within the first solute-solute shell; essentially no ethane molecules were able to get this close to a hydroxyl hydrogen. This was partially due to the lower solvent molecular density in ethane and partially due to the large excluded volume for interactions between the solvent methyl groups and groups on the solute. In Figure 4 solvent neighbor numbers divided by the bulk solvent density are plotted versus distance from the hydrogen divided by the (solvent end group)-hydrogen size parameter. This parameter is equal to one-half of the Lennard-Jones size parameter for the end group on a solvent molecule (an oxygen atom in carbon dioxide and a methyl group in ethane). The (solvent end group)-hydrogen size parameters (1.93Å in ethane and 1.51Å in carbon dioxide) are approximately equal to the distances of closest approach between the end of a solvent molecule and a hydroxyl hydrogen. The scaled solvent-solute neighbor numbers are larger in ethane than in carbon dioxide. Similar results were obtained when considering the number of solvent molecules surrounding a solute methyl group. Carbon dioxide is more dense than ethane and its molecules are smaller, allowing a greater number of them to approach the solute molecules more closely than can ethane.

Figure 5 compares the distribution of cluster sizes which formed in a 6.4 mole percent solution of methanol in carbon dioxide at 40°C and approximately 200 bar with the distribution formed in ethane under the same conditions. The calculated extent of hydrogen bonding in each fluid was in qualitative agreement with experiment. The indicated error bars are the variances from the final values of the time average compositions (excluding the averages over the first 120 samples). 50% of the methanol molecules were found to be in monomer form in carbon dioxide, as compared with a value of 41% \pm 5% obtained experimentally using infra-red spectroscopy (8,25). 34% of the methanol molecules were in monomer form in ethane, as compared with the experimental value of 23% \pm 5%. The difference between percentages obtained from simulation and those obtained from experiment may indicate that the criterion for hydrogen bonding used in analyzing the simulation results is too strict. It may also indicate that the mixture densities differ significantly from the input pure solvent densities at 200 bar. At higher pressures the simulation results for monomer concentration were much closer to the experimental values. Summarized in Table I are the experimental and calculated values for the percentage of monomer in each of the cases examined. The simulation detected high concentrations of dimers through pentamers in carbon dioxide, with the dimers being predominant. The concentration of hexamers and larger clusters was small. In ethane the concentrations of monomer through pentamers was greatly reduced relative to carbon dioxide in favor of clusters larger than the pentamer. IR experiments which use the O-H stretching frequency as a measure of the extent of hydrogen bonding provide some evidence that dimers are less prevalent in ethane than in carbon dioxide (8,25). The broad absorbance band due to the O-H stretch in polymers has high energy shoulder in the carbon dioxide solvent which is not as prominent when ethane is the solvent. This shoulder has been assigned to smaller oligomers, for example dimers or trimers. As will be shown below, the polymers formed in the two solvents differed in geometry as well as in relative abundance.

The geometry of methanol dimers formed in carbon dioxide at approximately 200 bar differed from that of dimers formed in ethane under similar conditions. The dimers formed

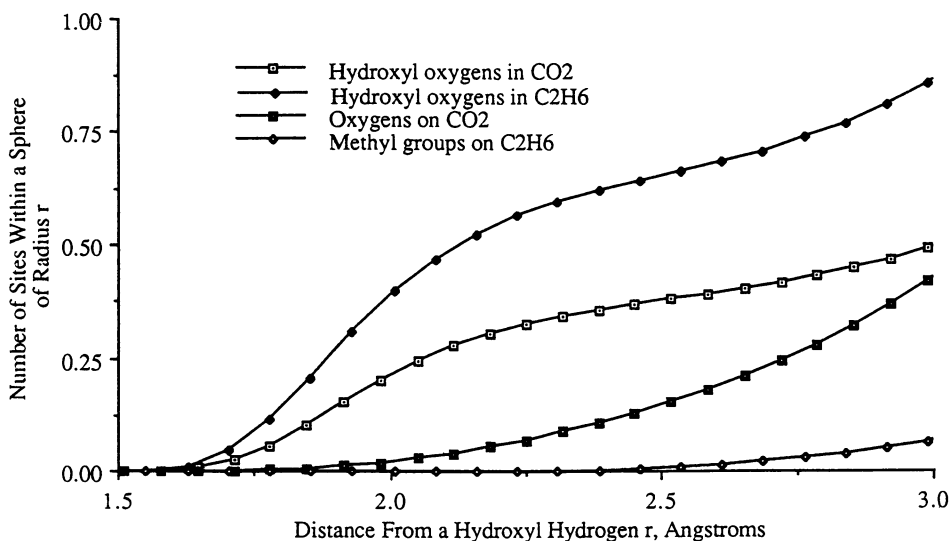


Figure 3: The absolute number of various sites within spheres of radius r surrounding a methanol hydrogen.

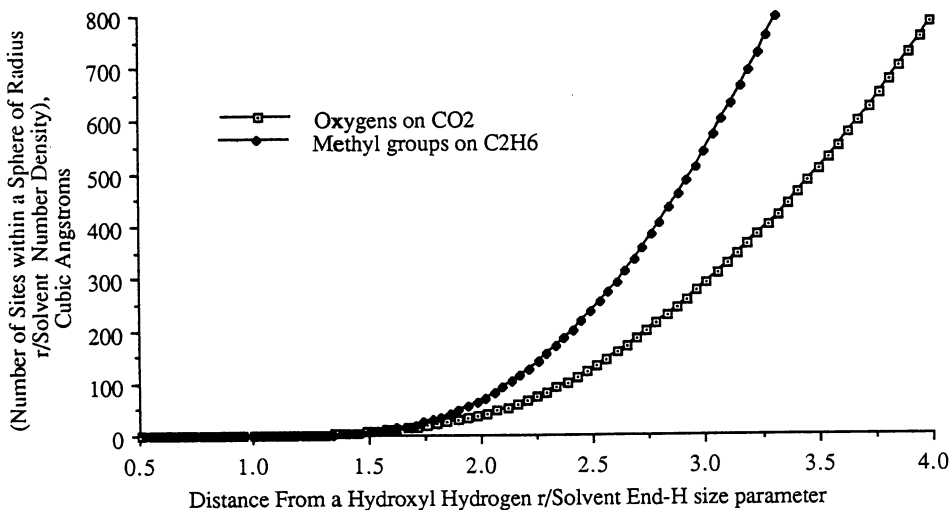


Figure 4: The volume of bulk fluid needed to have the same number of solvent sites in it as does a sphere of radius r about a methanol hydrogen.

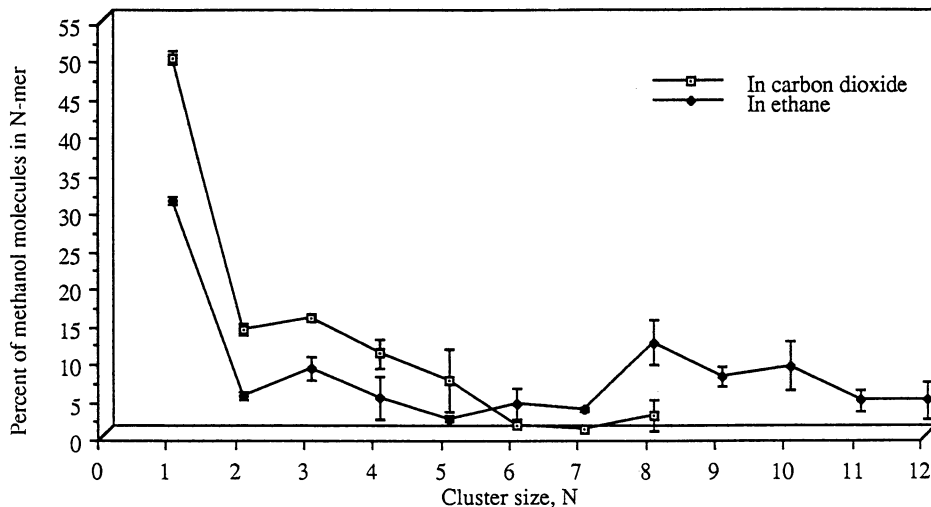


Figure 5: The distribution of methanol polymer sizes in supercritical ethane and carbon dioxide. Conditions given in the text.

Table I. Comparison Between Calculated and Experimental Monomer Concentrations

Solvent	Conditions		Mole Percent Methanol	Percentage of Methanol Molecules in Monomer Form	
	Approx. P, Bar	T, °C		Experimental	Calculated
CO ₂	200	40	6.4	41 ± 5	51 ± 0.9
CO ₂	400	40	6.4	36 ± 5	42 ± 1.6
C ₂ H ₆	200	40	6.4	23 ± 5	31 ± 0.6
C ₂ H ₆	200	40	3.2	40 ± 5	34 ± 3.3

in carbon dioxide tended to have anti-parallel orientations of the C-O bonds which present the methyl groups to the bulk fluid. The dimers observed in ethane tended to adopt a parallel orientation of methyl and oxygen groups. Figure 6 shows stereoplots of typical dimers in carbon dioxide and ethane which have mutual potential energies (excluding the solvent) of -4.5 kcal/mol and -4.0 kcal/mol, respectively. The hydrogen atoms are not drawn to scale. The dimers shown were randomly selected from the dimers with energies approximately equal to the most probable dimerization energies in the two solvents. In the dimer shown for the carbon dioxide system, one O-H distance was 1.80Å and the other was 3.40Å. Another species with anti-parallel C-O bonds found in carbon dioxide was a linear dimer with a binding energy of -5.7 kcal/mol. In spite of being tightly bound, dimers with energies this low appeared infrequently in the simulation due to interactions with other species in the system. The dimer shown for the ethane system is a V-dimer. The V-dimer found in ethane had a relatively high energy due to the large hydrogen bond distance (2.18Å) and the strained structure of the dimer. The dimers of this type found in ethane ranged from a nearly T-dimer (with the O-H bonds of the molecules perpendicular to each other) with a binding energy of -5.0 kcal/mol to a highly strained V-dimer with weak binding of -3.0 kcal/mol. The latter dimer had short O-H distances of 1.79Å and 3.09Å indicating strong hydrogen bonding but placed the methyl groups in very close proximity to each other.

The trimers and tetramers which formed in carbon dioxide tended to be more loosely bound than those found in ethane. In both solvents a variety of structures formed including both linear and cyclic tetramers. Figure 7 shows typical trimers which formed in carbon dioxide and ethane with mutual potential energies of -10.0 kcal/mol and -10.6 kcal/mol, respectively. These energies are the most probable trimerization energies in the two solvents. The trimer shown for the carbon dioxide system was bent into a partial ring. A tetramer structure with the most probable energy (-15.4 kcal/mol) was found to be linear, though one with a similar energy (-16.0 kcal/mol) was loosely cyclic. The trimer formed in ethane shown in Figure 7 is not part of an obvious pattern. The distribution of tetramer binding energies in ethane was broad, a result of the presence of both linear and tightly bound cyclic tetramers. There may also be cyclic trimers present in ethane as well - the distribution of binding energies indicates the presence of trimers with an energy of approximately -13 kcal/mol which may be cyclic. The trimer shown in Figure 7 may be described as loosely cyclic, with O-H distances of 1.79Å, 2.59Å and 2.73Å.

The most striking difference in N-mer geometries in the two solvents occurred for the pentamers. In carbon dioxide, the most probable pentameric species was cyclic. Linear and branched pentamers were prevalent in ethane. Cyclic pentamers appeared infrequently in the simulation using ethane solvent. Figure 8 shows stereoplots of such clusters formed in carbon dioxide and ethane which have a mutual potential energy of -26.7 kcal/mol and -20.0 kcal/mol, respectively. The results of ab initio calculations by Curtiss (1) have demonstrated that cyclic forms are more tightly bound than are linear forms due to a cooperative effect. He has postulated that the added stability of cyclic forms is due to the presence of multi-body terms in the potential energy. In this work, the cooperative effect was observed using only pairwise additive potentials. The cyclic structure allows the formation of an extra hydrogen bond not found in linear pentamers. Increased stabilization of the cyclic pentamer may also occur due to a small amount of hydrogen bonding between non-adjacent hydroxyl groups. Not only are the five hydrogen bonds which form the ring extremely short (three of them are shorter than 1.9Å) but the remaining

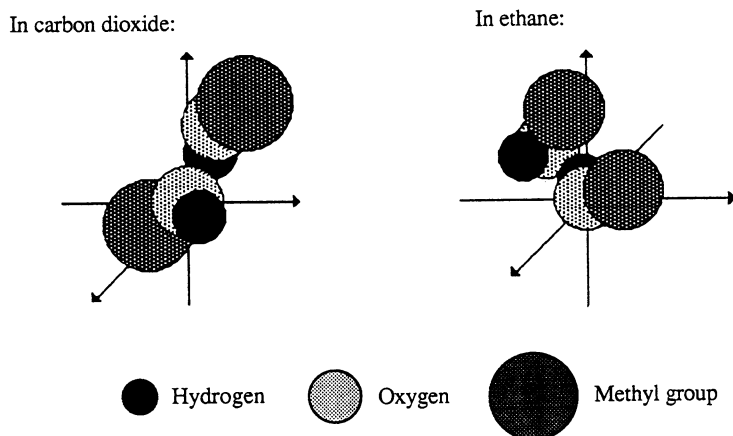


Figure 6: The dimers formed at the most probable binding energies in carbon dioxide and in ethane. Hydrogen atoms are not drawn to scale.

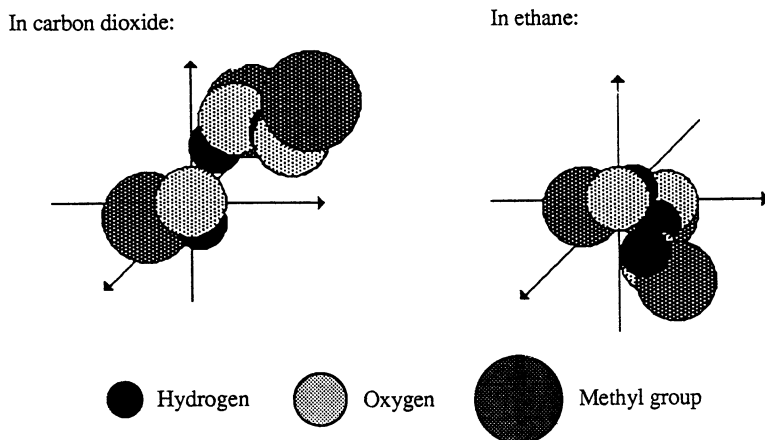


Figure 7: The trimers formed at the most probable binding energies in carbon dioxide and in ethane. Hydrogen atoms are not drawn to scale.

O-H distances are also short (four of them are shorter than 3.1 Å). The resulting ring was slightly squashed.

As was shown in Figure 5, only small concentrations of species larger than the pentamer were found in the carbon dioxide solvent. The fall-off in the concentration of large aggregates may stem from an energetically unfavorable structural re-arrangement which occurs when the hexamer is formed from the pentamer in the carbon dioxide solvent. The most probable hexamer in carbon dioxide was a broken ring with a linear tail attached to it. Figure 9 shows a plot of such a hexamer, a species which has a mutual potential energy of -26.2 kcal/mol. This energy (approximately equal to the potential energy of a trimer plus that of a tetramer) is slightly higher than that for the most probable (cyclic) pentamer. This similarity of binding energies occurs because both the hexamer and the cyclic pentamer contain five hydrogen bonds. The hexamer does not benefit from the cooperative effect to the same degree as does the cyclic pentamer. Hexamers of even higher energy also appeared frequently in the simulation. On average, the reduction in binding energy obtained from forming a hexamer from a pentamer and a monomer in carbon dioxide was very small and may not have been significantly different from zero. Also shown in Figure 9 is a typical hexamer formed in ethane solvent, with a mutual potential energy of -25.0 kcal/mol (the most probable hexamerization energy in ethane). It was a linear (in this case, a branched) form, as were the larger polymers observed in the ethane solvent.

No energetically unfavorable structural rearrangements were necessary to form large polymers in ethane. In carbon dioxide, the greatest incremental reduction in binding energy occurred when forming the pentamer from the tetramer. The incremental reduction on forming the average hexamer from the average pentamer was small - only 1.2 kcal/mol. In ethane the incremental reduction in binding energy is large when forming a polymer of any size. Plotted in Figure 10 is the reduction in average binding energy for forming N-mer from (N-1)-mer versus polymer size N in the two solvents. As discussed above, the cyclic pentamer formed in carbon dioxide is particularly stable; a large reduction in binding energy occurs upon forming it from tetramers and a very small reduction on average occurs upon forming hexamers from it. The large polymers in ethane were very tightly bound. The average heptamerization and octamerization energies in ethane were -36.07 kcal/mol. and -42.85 kcal/mol., respectively. The corresponding values in carbon dioxide were -29.6 kcal/mol. and -34.28 kcal/mol. (based on the small available sample of seven heptamers and 33 octamers).

Increasing the pressure results in an increase in the size of methanol aggregates. Plotted in Figure 11 are the percentages of the methanol molecules in each size cluster in carbon dioxide at 200 bar and at 400 bar. Both mixtures contained 6.4 mole percent methanol and were at a temperature of 40°C. Forty two percent of the methanol molecules were found to be in monomer form at approximately 400 bar as compared with a value of 36% ± 5% obtained experimentally. Increasing the carbon dioxide pressure leads to shift in the equilibrium towards the stable cyclic pentamer at the expense of monomer and trimer.

Conclusions

The results of this work were shown to be in qualitative agreement with experiment. At equal temperatures, pressures and compositions methanol-methanol aggregation was

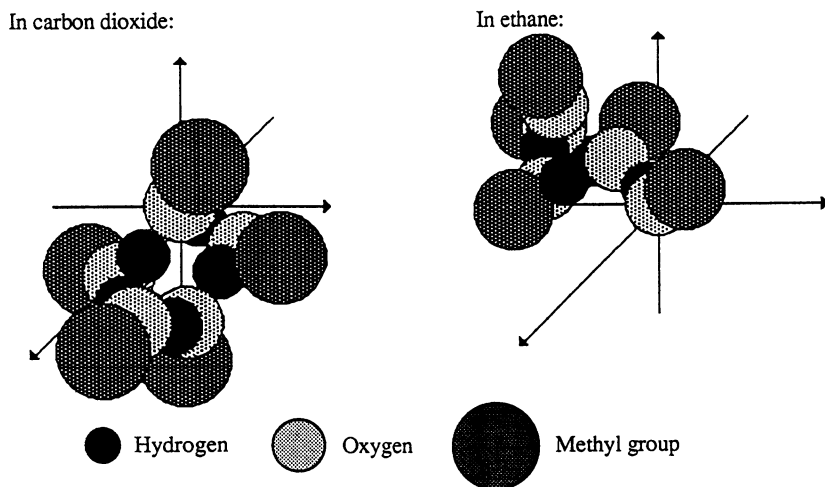


Figure 8: The pentamers formed at the most probable binding energies in carbon dioxide and in ethane. Hydrogen atoms are not drawn to scale.

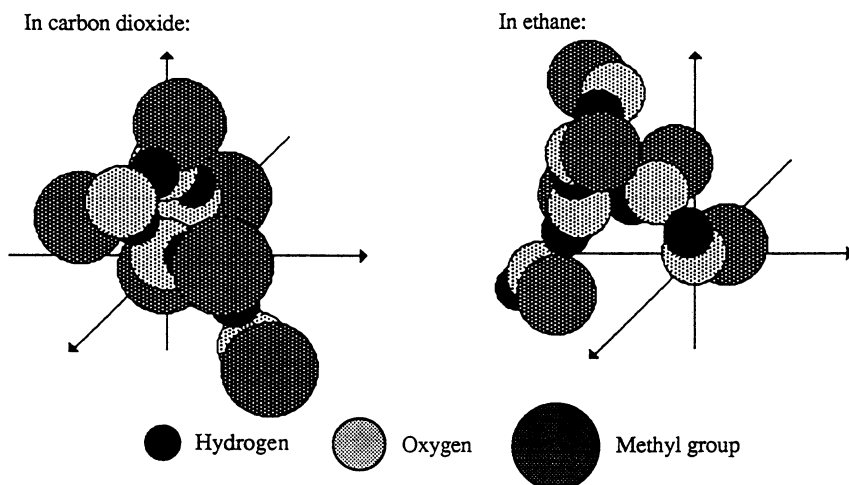


Figure 9: The hexamers formed at the most probable binding energies in carbon dioxide and in ethane. Hydrogen atoms are not drawn to scale.

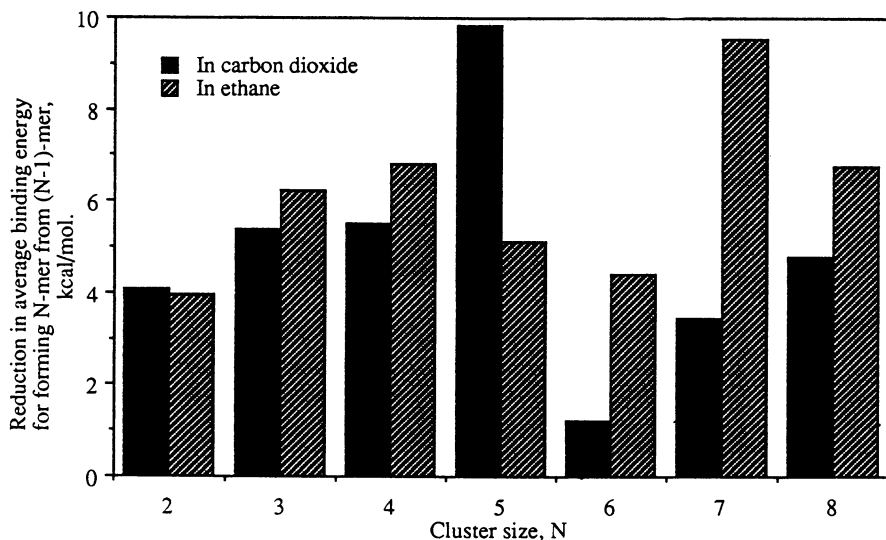


Figure 10: Average increment in binding energy for forming an N-mer from a (N-1)-mer in carbon dioxide and ethane. Conditions given in the text.

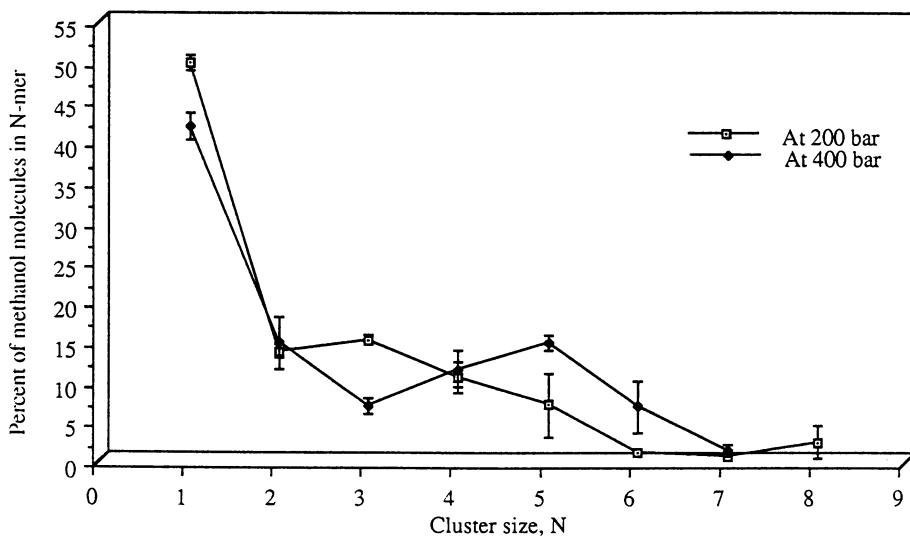


Figure 11: The effect of pressure on the distribution of methanol polymer sizes in supercritical carbon dioxide.

significantly greater in ethane than in carbon dioxide. Increasing carbon dioxide pressure led to increasing solute-solute aggregation as did increasing the concentration of the solute in the ethane solvent. At 200 bar and 40°C there were more dimers and trimers present in carbon dioxide than in ethane. The results of the simulations also supported the supposition made previously by us that solvent-solute aggregation is greater in carbon dioxide than in ethane. This greater degree of solvation of methanol molecules in carbon dioxide leads to higher concentrations of monomer in that solvent than in ethane. These positive results suggest that the qualitative conclusions made about the type and nature of solute clusters in supercritical carbon dioxide and ethane are correct.

Both the distribution of methanol polymer sizes and the geometries of the polymers differed in the two solvents. In carbon dioxide the cyclic pentamer exhibited enhanced stability. In carbon dioxide only small concentrations of polymers larger than the pentamer were formed. This fall-off in the concentration of large aggregates may have stemmed from an energetically unfavorable structural re-arrangement which occurred when the hexamer was formed from the cyclic pentamer. Increasing the carbon dioxide pressure lead to a shift in the equilibrium towards the stable pentamer at the expense of monomer and trimer. In ethane a variety of linear, branched, and ring structures formed. The most probable pentamer in ethane was linear. No energetically unfavorable structural rearrangements were necessary to form large polymers in ethane. In ethane, large polymers are much more tightly bound than the corresponding polymers in carbon dioxide.

These results suggest that the solvent species influences the distribution of N-mers not only by influencing the solubility of the monomer but also by influencing the geometries and stabilities of large N-mers.

Acknowledgments

This research was supported by the Director, Office of Energy Research, Office of Basic Energy Sciences, Chemical Sciences Division of the U.S. Department of Energy (DOE) under contract DE-AC06-76-RLO1830 Pacific Northwest Laboratory is operated for DOE by Battelle Memorial Institute.

Literature Cited

- (1) Curtiss, L.A. *J. Chem Phys.* **1977**, *67*, 1144.
- (2) Jorgensen, W.L. *J. Chem Phys.* **1979**, *71*, 5034.
- (3) Renner, T.A.; Kucera, G.H.; Blander, M. *J. Chem Phys.* **1977**, *66*, 17.
- (4) Jorgensen, W.L. *J. Am. Chem. Soc.* **1981**, *103*, 341.
- (5) Van Ness, H.C.; Van Winkle, J.V.; Richtol, H.H.; Hollinger, H.B. *J. Phys. Chem.* **1967**, *71*, 1483.
- (6) Fletcher, A.N.; Heller, C.A. *J. Phys. Chem.* **1967**, *71*, 3742.
- (7) Symons, M.C.; Thomas, V.K. *J. Chem. Soc., Faraday Trans.* **1981**, *77*, 1883.
- (8) Fulton, J.L.; Yee, G.G.; Smith, R.D. *J. Am. Chem. Soc.* **1991**, *113*, 8327.
- (9) Petsche, I.B.; Debenedetti, P.G. *J. Chem Phys.* **1989**, *91*, 7075.
- (10) Shing, K.S.; Chung, S.T. *J. Phys. Chem.* **1987**, *91*, 1674.

- (11) Cummings, P.T.; Cochran, H.D.; Simonson, J.M.; Mesmer, R.E.; Karaborni, S. *J. Chem. Phys.* **1991**, *94*, 5606.
- (12) Lee, L.L. *Molecular Thermodynamics of Non-Ideal Fluids*; Butterworths: Boston, 1988.
- (13) Rossky, P.J., and Chiles, R.A., *Mol. Phys.* **51** (3), p. 661 (1984).
- (14) Allen, M.P.; Tildesley, D.J. *Computer Simulation of Liquids*; Oxford University Press: New York, 1987.
- (15) Cummings, P.T.; Stell, G. *Mol. Phys.* **1982**, *46*, 383.
- (16) Kirkwood, J.G.; Buff, F.P. *J. Phys. Chem.* **1951**, *19*, 774.
- (17) Debenedetti, P.G.; Mohamed, R.S. *J. Chem. Phys.* **1989**, *90*, 4528.
- (18) Cochran, H.D.; Pfund, D.M.; Lee, L.L. *Sep. Sci. and Tech.* **1988**, *23*, 2031.
- (19) Jorgensen, W.L. *J. Am. Chem. Soc.* **1981**, *103*, 335.
- (20) Murthy, C.S.; Singer, K.; McDonald, I.R. *Mol. Phys.* **1981**, *44*, 135.
- (21) Geiger, L.C.; Ladanyi, B.M.; Chapin, M.E. *J. Chem. Phys.* **1990**, *93*, 4533.
- (22) Fincham, D.; Quirke, N.; Tildesley, D.J. *J. Chem. Phys.* **1986**, *84*, 4535.
- (23) Jorgensen, W.L. *J. Am. Chem. Soc.* **1981**, *103*, 341.
- (24) Jorgensen, W.L. *J. Am. Chem. Soc.* **1980**, *102*, 543.
- (25) Fulton, J.L.; Yee, G.G.; Smith, R.D. in *Supercritical Engineering Science Fundamentals and Applications*; Brennecke, J.F.; Kiran, E., Eds.; ACS Symposium Series; American Chemical Society: Washington D.C.
- (26) Walsh, J.M.; Ikononou, G.D.; Donohue, M.D. *Fluid Phase Equilibria*, **1987**, *33*, 295.

RECEIVED April 27, 1992

Chapter 14

Hydrogen Bonding of Simple Alcohols in Supercritical Fluids

An FTIR Study

John L. Fulton, Geary G. Yee, and Richard D. Smith

Chemical Methods and Separations Group, Chemical Sciences Department,
Pacific Northwest Laboratory, Richland, WA 99352

FT-IR spectroscopy has been used to measure the degree of intermolecular hydrogen bonding between solute molecules of simple alcohols (methanol to dodecanol) in supercritical carbon dioxide and supercritical ethane. In these fluids an equilibrium is established between the free nonhydrogen bonded monomer and the various hydrogen bonded species, of which the tetrameric and pentameric species are believed to predominate at lower mole fractions of the alcohol. The fluid pressure, temperature, and the alcohol concentration significantly affect the equilibrium distribution of the monomer and oligomeric species. Both supercritical and subcritical binary solutions containing up to 0.10 mole fraction alcohol were examined under conditions ranging from 200 to 400 bar and 40°C. The spectral data support the existence of a weak complex between the alcohol monomer and carbon dioxide.

Simple alcohols such as methanol and 2-propanol are widely used as modifiers to enhance the solubility of polar solutes in the supercritical fluid phase. Such modifiers increase the solvent strength of the fluid by increasing the overall dielectric constant of the binary supercritical solution. The alcohol modifier can also readily hydrogen bond with other alcohol molecules or other polar solutes to form new bimolecular or multimolecular species. These intermolecularly hydrogen-bonded species have a greatly reduced dipole moment or polarity compared to the parent solute species. This reduction in turn improves the solubility of these species in nonpolar supercritical fluids.

A hydrogen-bonded aggregate represents just one of a range of different molecular assemblies that are known to form in supercritical fluids. The simplest aggregate is the van der Waals-driven solvent clusters that form around solutes when the solution is near the critical point. At the other end of the spectrum of

0097-6156/93/0514-0175\$06.00/0

© 1993 American Chemical Society

molecular aggregates are the large multimolecular structures that form upon addition of certain surfactants to apolar supercritical fluids (1,2,3). This aggregation process is driven mainly by strong ionic interaction of the surfactant head groups within the aqueous cores as well as a host of different secondary effects. The magnitude of the forces that drive aggregation of alcohol clusters is intermediate between those that form the solvent clusters and those that form the surfactant cluster. Spectroscopic studies of hydrogen bonding of alcohols in apolar liquid solvents extend back 50 years (4,5,6). Such studies have suggested that alcohol molecules form hydrogen-bonded "clusters" in apolar liquid solvents consisting of from two to six molecules per cluster. The extent of hydrogen bonding of alcohols in apolar liquid solvents is consistent with a multiple equilibria model. At low concentrations (7) (mole fraction alcohol, $x_{\text{alcohol}} < 0.003$) the alcohol exists in the monomer form. Upon increasing the concentration, the aggregation progresses through dimer, trimer to tetramer, and higher oligomers at higher concentrations of the alcohol.

In supercritical fluids the size of the alcohol aggregate is similar to that found for liquid solvents. We have reported aggregation numbers in the range of 3 to 5 for dodecanol-*d* in CO₂ and ethane (8). This study confirmed the expectation that generally the size of an alcohol aggregate formed in supercritical fluids such as CO₂ is little different from that observed in liquid and gas phases. There is, however, believed to be specific interaction between CO₂ and an alcohol that is not found in the alkane/alcohol system (9). This interaction has been ascribed to an attractive CO₂-quadrupole/alcohol dipole interaction that greatly increases the solubility of the alcohol in CO₂. This interaction also perturbs the monomer-aggregate equilibria towards the monomer form of the alcohol. Recently, Yee et al. (10) reported aggregation numbers for *n*-butanol and a fluorinated butanol in CO₂ and ethane and found that for lower concentrations of the alcohol ($0.05 < x_{\text{alcohol}} < 0.2$) the typical aggregate contains about four molecules. This study also noted higher than expected alcohol solubility in CO₂. Using a near-infrared spectroscopic technique, Schneider et al. (11) measured the degree of association of octanol and hexanol in supercritical CO₂ near phase boundaries.

In this paper we use Fourier transform infrared (FT-IR) spectroscopy to study the aggregation of a series of small alcohols in supercritical CO₂ and supercritical ethane. These alcohols include several of the straight chain alcohols from C₁ to C₁₀, as well as a secondary (2-propanol), and a tertiary alcohol (2-methyl-2-propanol). The IR technique allows one to measure the degree of intermolecular hydrogen bonding between alcohol solute molecules in supercritical solvents. The effects of the alcohol concentration and the alcohol type on the equilibrium distribution of the monomeric and oligomeric species are determined.

Experimental

The anhydrous solutes, methanol-*d* (99.5%), ethanol-*d* (99.5%), 2-propanol(*ol-d*) (98%), 1-butan(*ol-d*) (98%), 2-methyl-2-propanol(*ol-d*) (98%), were used as received from Aldrich. The method for preparation of dodecanol-*d* has been previously reported (8). "SFC" grade CO₂ from Scott Specialty Gases had a reported purity of >99.98% and water content of <3 ppm(V/V). The ethane was

"CP" grade from Alphagaz. Since trace amounts of water can significantly alter the aggregation of alcohol molecules, both the ethane and the CO₂ were further dried by passing the saturated vapor through a large bed of molecular sieve.

A Nicolet 740 FT-IR spectrometer (Nicolet Analytical Instruments) purged with dry nitrogen was used to obtain all infrared spectra. The spectrometer was equipped with a germanium-on-KBr beam splitter and a mercury-cadmium-telluride detector. We co-added 128 scans at 4-cm⁻¹ wavenumber resolution to obtain the desired signal-to-noise ratio. The details of the design of the high pressure cell and background subtraction technique are discussed in an earlier paper (12). Briefly, the reflectance-type IR sample cell had a total volume of 10.0 mL. The contents could be stirred with a Teflon-coated, magnetically coupled stir bar. Two optical windows were used: a single ZnSe window provided for transmission of both the incident and the reflected IR beam, a sapphire window provided for visual observation of the solution to determine the number of phases that were present. Because many of the systems in this study having higher mole fractions of the alcohol were subcritical (13,14), it is helpful to visually ensure that only one phase is present before measuring the sample. Experimental methods were developed to obtain reliable spectra from the present reflectance cell arrangement. Since a primary reflection from the first surface of the IR window cannot be isolated optically from the reflection from the mirror within the IR cell, a subtraction method was used to remove the unwanted reflection component from the sample spectrum (12).

Fluid pressure was monitored to ± 1 bar with an electronic transducer (Precise Sensors, Inc., No. C451), which was calibrated against a bourdon-tube type pressure gauge (Heise ± 0.3 bar accuracy). The temperature of the IR reflectance cell was controlled using a three-mode controller with a platinum resistance probe (Omega, No. N2001). The temperature was also monitored with a platinum resistive thermometer (Fluka, No. 2108A). The sample preparation procedure was as follows. Ethane or CO₂ at 3 to 6 bar were used to purge air from the sample cell prior to introduction of the sample. Known quantities of an alcohol were introduced into the IR cell. The system was then filled with ethane, or CO₂ to the desired pressure using a high-pressure syringe pump (Varian 8500). The contents of the spectroscopy cell were vigorously stirred with a magnetic stir bar for 15 min prior to each measurement. The amount of solvent (either CO₂, or ethane) for any condition of temperature and pressure could be measured within $\pm 5\%$ (after calibration) by integration of vibrational bands for each component. The specific absorbance of these solvent bands (three combination bands near 5000 cm⁻¹ for CO₂ and bands near 4300 cm⁻¹ for ethane) was determined from the known pathlength and from the density of the pure solvents given in published data for CO₂ (15) and ethane (16).

The concentration of alcohol monomer in solution was measured by first determining the specific absorbance of the monomer species at a given temperature and pressure. In dilute solutions, (alcohol mole fractions, $x_{\text{alcohol}} < 5 \times 10^{-3}$) the alcohol was found only in the monomeric, nonhydrogen-bonded form. In this dilute region, the specific absorbance was found to follow a Beer-Lambert-type of relationship with changes in alcohol concentration. The specific absorbance of the alcohol monomer was determined at each pressure studied. For the ethane, there

was little or no change in the intensity of the ν_1^{OD} band with pressure. However, there was a significant change in the intensity of the ν_1^{OD} band in CO_2 solutions. Hence, it was important to determine the specific absorbance of the monomer at each pressure in order to determine the monomer concentration in the more concentrated solutions where significant hydrogen bonding occurs.

The interference of a pair of overtone and combination bands of CO_2 (at ~ 3600 and 3750 cm^{-1}) with the O-H stretch ($\nu_1^{\text{OH}} = 3682 \text{ cm}^{-1}$) of the nonhydrogen-bonded alcohol, required using deuterated alcohols over the normal alcohols in this study (9). The hydrogen bonding properties of the deuterated alcohol in supercritical fluids should not differ greatly from those of the normal alcohol. We know of no previous studies of deuterated alcohols in supercritical fluids, but the measured physical properties of these two isotopes show little difference. We determined the dew point pressure of a 0.030 mole fraction solution of methanol in CO_2 at 40°C and found a pressure of 79.1 ± 1.0 bar for methanol and 78.9 ± 1.0 bar for methanol-*d*. Recently reported values (17) for the isotopic effect on the enthalpy of hydrogen bonding in the liquid phase are -2.70 ± 0.02 kcal/mole for methanol and -2.72 ± 0.02 kcal/mole for methanol-*d*. The difference in the thermodynamic behavior between the normal and deuterated forms of the alcohol in supercritical fluids is expected to be small. Similarly, the size distribution of intermolecularly hydrogen-bonded species is not expected to be significantly different between normal and deuterated forms of the alcohol.

Results

Increasing the mole fraction of methanol-*d* increases the amount of hydrogen bonding in the solution. As shown in Figure 1, with increasing mole fraction of methanol-*d* in CO_2 , the peak at $\sim 2550 \text{ cm}^{-1}$, which is due to the ν_1^{OD} of the hydrogen-bonded alcohol, grows considerably relative to the monomeric ν_1^{OD} at $\sim 2700 \text{ cm}^{-1}$. It is well established in liquid phase studies that hydrogen bonding results in a large red shift of the ν_1^{OD} (18) and of the ν_1^{OH} bands (6,7,19,20). The broad peak centered at $\sim 2550 \text{ cm}^{-1}$ is attributed to the various intermolecular hydrogen bonded species (dimers, trimers, tetramers, and higher oligomers). The general trends of the concentration's effect on the degree of intermolecular hydrogen bonding in supercritical ethane and CO_2 are similar to the effects observed in liquids.

The choice of the deuterated form of the alcohols used in this study was necessitated by the interference of a pair of intense overtone and combination bands of CO_2 (at ~ 3600 and 3750 cm^{-1}) with the O-H stretch ($\nu_1^{\text{OH}} \sim 3630 \text{ cm}^{-1}$) of the nonhydrogen-bonded alcohol. The ν_1^{OH} band of the normal alcohol is obscured by a CO_2 solvent peak, whereas there is a good "window" for the ν_1^{OD} band of the deuterated alcohol. For ethane, there are no interfering solvent bands in either the ν_1^{OH} or the ν_1^{OD} regions. For the deuterated alcohols, the lower wavenumber tail of the ν_1^{OD} band of the intermolecular hydrogen-bonded alcohol species at wavenumbers below 2500 cm^{-1} is partially obscured by the ν_3 band of CO_2 , centered at 2349 cm^{-1} . However, this CO_2 solvent band does not interfere with the ν_1^{OD} monomer band at $\sim 2680 \text{ cm}^{-1}$, which is used in a later section to determine the amount of nonhydrogen-bonded monomer.

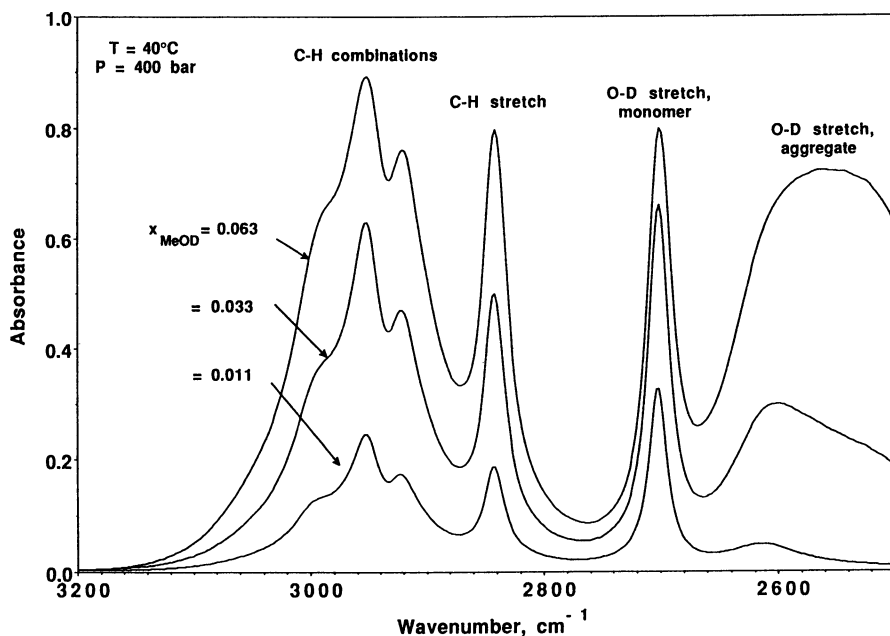


Figure 1. The C-H combination bands, the C-H symmetric stretch, and the O-D stretch of the methanol-*d* monomer in CO₂ at 400 bar and 40°C for three different mole fraction concentrations of the alcohol, $x_{\text{MeOD}} = 0.063$, 0.033 and 0.011. Hydrogen bonding shifts the O-D stretch from 2700 to 2600 cm⁻¹.

The solution in Figure 1 which is at 0.063 mole fraction of methanol is subcritical at 40°C. Gurdial et al. (14) reported critical temperatures and pressures for the *n*-alkanols up to C₁₀ in CO₂. For the methanol/CO₂ system at 40°C, mixtures containing more than $x_{\text{alcohol}} = 0.05$ are subcritical. The transition from a subcritical to a supercritical state does not cause very much change in the solution's properties in this case because at a pressure of 400 bar the system is approaching liquid-like densities.

The spectral data of experiments such as those shown in Figure 1 are summarized in Figure 2, which shows the concentration of the monomer for various total mole fractions of the alcohol at 200 bar and 40°C. Figure 2 also shows the monomer concentration for five other alcohols in CO₂: ethanol-*d*, 2-propanol-*d*, *n*-butanol-*d*, 2-methyl-2-propanol-*d*, and dodecanol-*d*. The dashed line in Figure 2 represents the case where essentially all added alcohol is in the monomer form, i.e., no aggregation. Deviations from this line are due to intermolecular hydrogen bonding. Below a total alcohol concentration of ~0.005 mole fraction, only the monomeric form exists. Upon increasing the alcohol concentration, increasing amounts of hydrogen bonded species are formed.

The data of Figure 2 show the relationship between the equilibrium concentrations of monomer and intermolecularly hydrogen-bonded aggregates. The

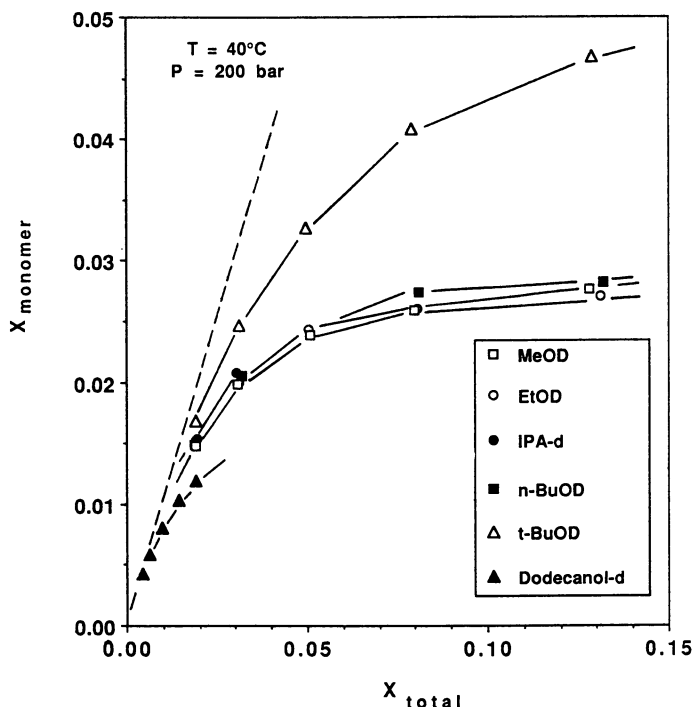


Figure 2. Concentration of monomeric alcohol, x_{monomer} , for various total mole fractions, x_{total} , of the alcohol in CO_2 at 200 bar and 40°C . Data for six different alcohols are shown: methanol-*d*(MeOD), ethanol-*d*(EtOD), 2-propanol-*d*(IPA), 1-butanol-*d*(n-BuOD), 2-methyl-2-propanol-*d*(t-BuOD), dodecanol-*d*.

four small alcohols, methanol, ethanol, 2-propanol and n-butanol show nearly the same equilibrium distribution of monomer and aggregate in CO_2 . For the tertiary alcohol, 2-methyl-2-propanol-*d*, the equilibrium is shifted strongly toward the monomer relative to the other alcohols. For this tertiary alcohol, aggregate formation is strongly sterically hindered for aggregation numbers above two, because of the close proximity of the three CH_3 groups to the OD (or OH). This is the major reason for the high monomer concentrations found in the 2-methyl-2-propanol-*d*/ CO_2 system.

Figure 3 shows the monomer/aggregate equilibria for the six alcohols in ethane under the same conditions of temperature and pressure as in Figure 2. As was observed for CO_2 , the tertiary alcohol monomer concentrations are much higher than the other alcohols because of steric hindrance inhibiting formation of larger aggregates. Since the monomer concentration is so much higher for this alcohol, the solvation effects of this alcohol when used as a fluid modifier for a supercritical fluid should be significantly different from that of the other alcohols. In contrast to alcohols in the CO_2 system, methanol shows the greatest extent of aggregation in ethane.

Figure 4 relates the fraction of alcohol that is in the monomer form for a total alcohol mole fraction of 0.03. The effect of increasing the chain length of the

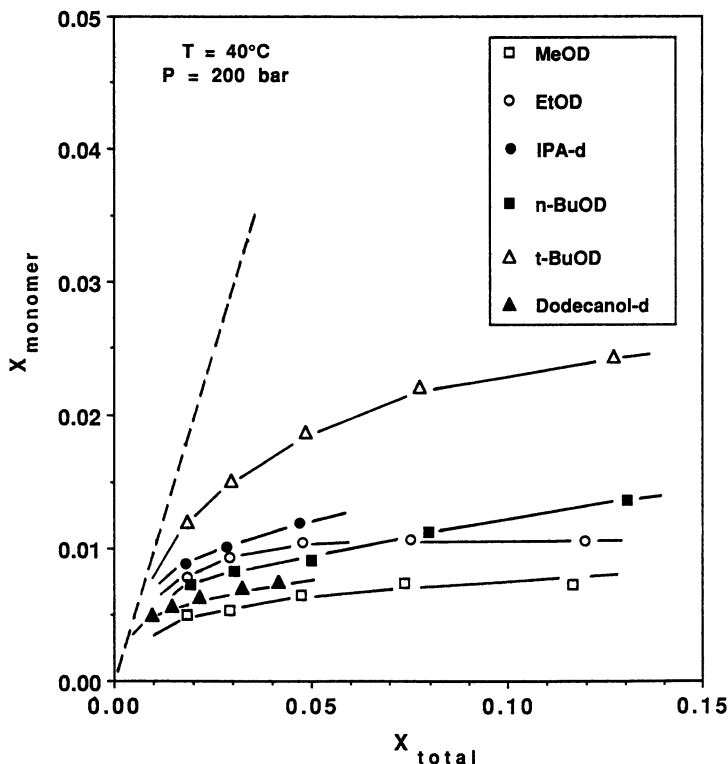


Figure 3. Concentration of monomeric alcohol, x_{monomer} , for various total mole fractions, x_{total} , of the alcohol in ethane at 200 bar and 40°C . Data for six different alcohols are shown: methanol-*d* (MeOD), ethanol-*d* (EtOD), 2-propanol-*d* (IPA), 1-butanol-*d* (n-BuOD), 2-methyl-2-propanol-*d* (t-BuOD), dodecanol-*d*.

alcohol and the differences between the two supercritical solvents, CO_2 and ethane, can be clearly seen. In CO_2 , the monomer/aggregate equilibria of all the alcohols is shifted more towards the monomer relative to the equilibria established in ethane. In a related study (9), we have shown that because of a weak chemical interaction, presumably involving the CO_2 quadrupole and the OH dipole, the free monomer is more soluble in CO_2 . This occurs even though the solvent dielectric constant, of CO_2 ($\epsilon = 1.50$), which is a simple measure of solvent strength, is less than that of ethane ($\epsilon = 1.61$) under these conditions.

As shown in Table I, methanol has a slightly higher dipole moment than that of the other alcohols. Because of the stronger electrostatic effects of the dipole/dipole interactions (or hydrogen bonding), the methanol equilibria should be shifted towards greater aggregation relative to the higher alcohols. This shift is in fact observed for methanol/ethane system, where we see a significantly greater extent of aggregation for this small alcohol. However, for CO_2 , this effect was not observed. In CO_2 , we have the competing "reaction" of the monomer dipole with the CO_2 quadrupole of one or several local CO_2 solvent molecules. The higher dipole moment of the methanol increases the CO_2 /alcohol interaction, which offsets

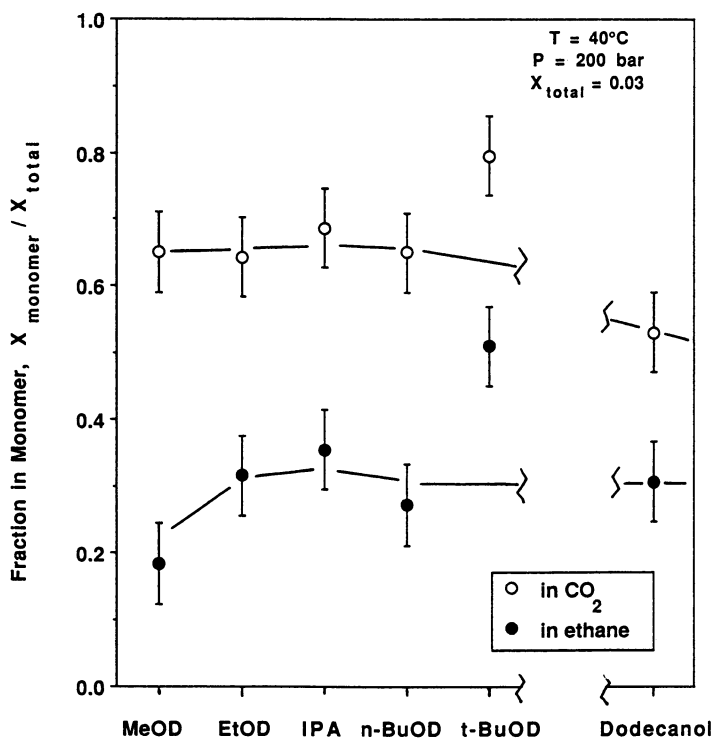


Figure 4. The fraction of the total alcohol that is in the monomer form for the six different alcohols in CO_2 and in ethane. In all cases the total alcohol concentration is $x_{\text{total}} = 0.03$, $T = 40^\circ\text{C}$, and $P = 200 \text{ bar}$. The line connects the n-alkanols data points.

Table I. Properties of alkanols

Alcohol	Boiling Point ($^\circ\text{C}$)	Melting Point ($^\circ\text{C}$)	Dipole Moment ^a (debyes)	Polarizability (10^{-24} cm^3)
methanol	65	-98	1.70	3.3
ethanol	78	-130	1.68	5.4
2-propanol	82	-90	1.66	7.6
2-methyl-2-propanol	83	25		8.9
1-butanol	118	-89	1.66	8.8
dodecanol	260	26	~1.66	~16

^a Gas phase values

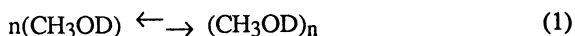
the expected trend of higher aggregation of this alcohol. We also note in Figure 4 an increase in the extent of aggregation of dodecanol in CO₂ relative to the smaller alcohols, but the extent of aggregation of dodecanol in ethane is about the same as that observed for the lower alcohols. The dipole moment of dodecanol is the same as for the lower alcohols, indicating that the hydrogen-bonding energies of the alcohols are about the same. A factor that may be affecting this monomer/aggregate equilibria is the attractive interaction of the long hydrocarbon tails of this alcohol. The polarizability of dodecanol (see Table I) is much larger than that of the lower alcohols. The strong tail-tail interactions will help drive the equilibria towards aggregation in CO₂. Ethane is a much better solvent (it has an appreciably higher dielectric constant) for solvating the long hydrocarbon tail of the alcohol so that the tail-tail attractive interactions are substantially reduced for this alcohol, and the monomer/aggregate equilibria is little perturbed from that of the lower alcohols.

The vapor-liquid equilibria curve for the methanol/CO₂ system in the solvent-rich region of the phase diagram is shown in Figure 5. The dashed line in Figure 5 represents the phase boundaries between a single-phase region above the line and a two-phase region below the line. Schematically illustrated in Figure 5 is the fluid structure at different regions of the vapor-liquid equilibrium curve. These structures have been deduced from FT-IR measurements of hydrogen bonding of single phase systems that are just slightly above the phase boundary. Below an alcohol concentration of $x_{\text{alcohol}} = 0.02$ the alcohol is mostly in the nonintermolecularly hydrogen-bonded monomer form. At a pressure just slightly below the critical pressure (at the critical composition), the two coexisting phases will be structurally and compositionally identical with about 40% of the alcohol molecules in monomer form and about 60% in aggregates. The liquid phase at higher mole fractions of the alcohol will contain a large proportion of intermolecularly hydrogen-bonded aggregates. For two coexisting vapor-liquid phases at about 79 bar (represented by the tie line in Figure 5), the upper vapor phase contains a small percentage of alcohol that is mainly in the monomer form. This upper phase is in equilibrium with an alcohol-rich liquid phase that is mostly in the aggregate form.

How does the fluid structure at the vapor-liquid equilibrium change at different temperatures and, in particular, how does the structure at the mixture critical point change? Previously, we have examined the effects of both pressure and temperature on the monomer/aggregate equilibria of methanol in CO₂ and ethane (9). The main factors that affect the hydrogen-bonding equilibrium are, in order of their importance: (i) the amount of alcohol, (ii) the type of solvent, (iii) the temperature of the system, and finally (iv) the system pressure. For CO₂, increasing the mole fraction of alcohol moves the critical temperature to higher and higher values. At moderate temperatures, ~25° to 75°C, the extent of aggregation at the critical point increases at higher critical temperatures because of the increase in amount of alcohol in the systems. At higher temperatures, >100°C, the monomer may begin to dominate because of the aggregate dissociation at higher temperatures (as related through the van't Hoff relationship (9)).

The formation of intermolecularly hydrogen-bonded alcohol follows a multiple equilibria model of aggregation. At low concentrations, the alcohol exists only as free monomer. Upon increasing the alcohol concentration, aggregation proceeds through dimer, trimer, and finally to higher oligomers. Because of certain structural features, the methanol dimeric and especially the tetrameric species have a

special stability. One expects, then, that above a certain concentration of the alcohol, further additions of alcohol are likely to form mainly the tetrameric aggregate. A representation of the reaction of monomeric species to form an aggregate is shown in Equation 1.



In a solution of an alcohol in an apolar solvent, one finds a relatively narrow distribution of oligomers ($n = 2,3,4$ and higher) that is centered around approximately $n = 4$ (21).

The equilibrium constant, K , for this reaction, Equation 2,

$$K = \left(\frac{x_{n\text{-mer}}}{(x_{\text{monomer}})^n} \right) \quad (2)$$

can be used in a mass action-type of relationship that yields an approximate value for the size of the alcohol aggregate. Equation 3 has been used by Aveyard et al. (7) for simple alcohols and by Pacynko et al. (22) for nonionic surfactants to obtain aggregation numbers.

$$\ln(x_{\text{total}} - x_{\text{monomer}}) = N_A \cdot (\ln x_{\text{monomer}}) + \ln(N_A \cdot K) \quad (3)$$

where N_A = average aggregation number. The value obtained for N_A is only approximate since it is assumed that only two different alcohol species are in solution: monomer and the monodisperse-aggregate species. The actual aggregation process most likely involves a polydisperse system containing dimers, trimer, tetramers and higher oligomers in equilibrium; however, Equation 3 does give an approximate measure of the dominant species in solution.

A plot of $\ln(x_{\text{total}} - x_{\text{monomer}})$ vs. $\ln x_{\text{monomer}}$ yields a line whose slope is equal to the average aggregation number, N_A . Figure 6 shows a typical plot for methanol-*d*, 1-butanol-*d*, and dodecanol-*d* at 40°C and 200 bar. Using this technique, the aggregation numbers for these three alcohols in CO₂ and ethane were determined and are shown in Table II. Aggregation numbers vary from about 3.5 up to 5.0 for the three alcohols, indicating that only small aggregates are forming in these apolar solvents. There is no statistically significant difference in the measured aggregate size between CO₂ and ethane. Similarly, there is little or no difference in the aggregation numbers of the various alcohols. Carbon dioxide does not appear to significantly perturb the *types* of species forming in the fluid, but does alter the monomer-aggregate equilibria. In liquids, Aveyard et al. (7) reported an aggregation number of 4 for dodecanol in *n*-octane at 30°C, whereas Pacynko et al. (22) reported an aggregation number of 5 ± 1 for dodecanol in heptane at 30°C. Aveyard et al. found the aggregation number of dodecanol in *n*-octane increased slightly at higher concentrations of the alcohol. Our measurements of aggregation numbers at slightly higher temperatures, 40°C vs. 30°C, are in general agreement with these previous studies of aggregation of alcohols in liquid alkanes.

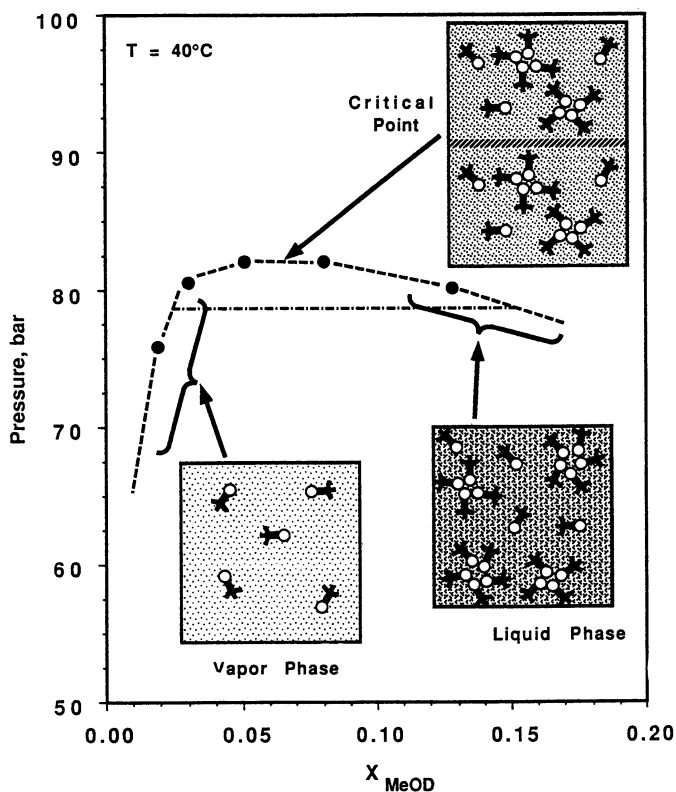


Figure 5. The phase behavior of methanol-*d* in CO₂ at 40°C. In the regions above the solid lines, the systems are single-phase; in the regions below the lines the systems are two-phase. The fluid structure in each region of the vapor-liquid equilibria curve is illustrated.

Table II. Alcohol aggregation numbers, N_A , at 40°C and the range of concentrations, x_{total} (mole fraction), used for the determination of N_A

Alcohol/Fluid	x_{total} Range, $\times 10^{-2}$	$N_A(\pm 1.0)^a$
methanol- <i>d</i> /CO ₂	2.0-12.0	4.9
methanol- <i>d</i> /ethane	2.0-12.0	4.4
n-butanol- <i>d</i> /CO ₂	2.0-12.0	4.9
n-butanol- <i>d</i> /ethane	2.0-12.0	3.6
dodecanol- <i>d</i> /CO ₂	0.5-3.0	4.3
dodecanol- <i>d</i> /ethane	0.5-3.0	3.6

^a Values in parenthesis are two standard deviations, 2σ .

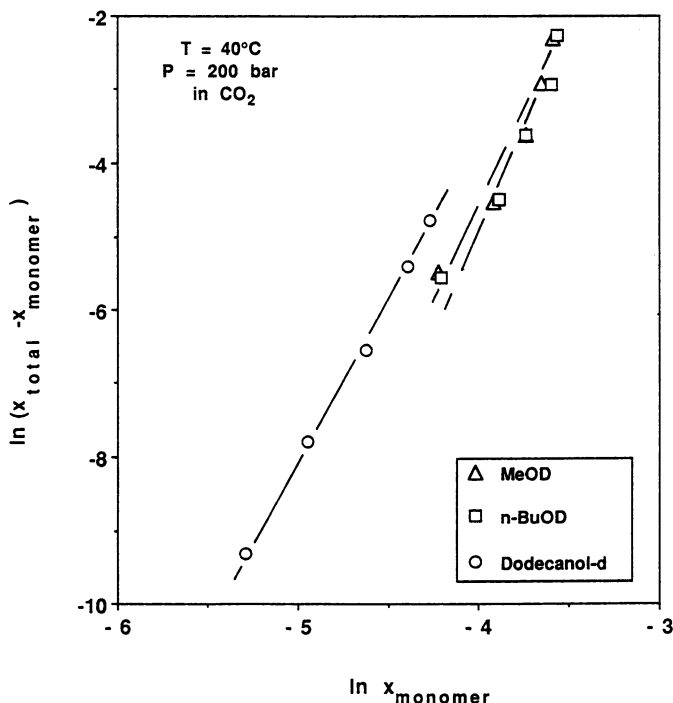


Figure 6. A plot of $\ln(x_{\text{monomer}})$ vs. $\ln(x_{\text{total}} - x_{\text{monomer}})$ for methanol-*d*, 1-butanol-*d*, and dodecanol-*d* in CO_2 at 40°C and 200 bar . The slopes of the lines give the average aggregation number, N_A .

Conclusions

The extent of intermolecular hydrogen bonding of simple alcohols is strongly dependent upon the concentration of the alcohol. Below $x_{\text{alcohol}} = 0.005$ the alcohol is predominantly in the free nonhydrogen-bonded form. Aggregation becomes extensive above alcohol concentrations of $x_{\text{alcohol}} = 0.10$. Because of a specific interaction, possibly involving the CO_2 quadrupole with the OH dipole, the monomer/aggregate equilibria in CO_2 is displaced towards the monomer form of the alcohol.

For the series of alcohols from C_1 up to C_{10} , the extent of intermolecular hydrogen bonding is generally very similar. The small differences in the extent of hydrogen bonding are ascribed to slightly higher dipole moment of the C_1 alcohol and to "tail-tail" attractive interactions of the highly polarizable hydrocarbon portion of the dodecanol. The equilibrium of the tertiary alcohol, 2-methyl-2-propanol, was found to be strongly shifted towards the monomer form, presumably because of steric hindrance. The size of an alcohol aggregate found in supercritical CO_2 or supercritical ethane is generally the same size as the aggregate found in the liquid alkanes at the same alcohol concentrations.

Acknowledgment

This research was supported by the Director, Office of Energy Research, Office of Basic Energy Sciences, Chemical Sciences Division of the U. S. Department of Energy, under contract DE-AC06-76RLO 1830. Pacific Northwest Laboratory is operated for the DOE by Battelle Memorial Institute.

Literature Cited

1. Fulton, J. L.; Smith, R. D. *J. Phys. Chem.* **1988**, *92*, 2903-2907.
2. Smith, R. D.; Fulton, J. L.; Blitz, J. P.; Tingey, J. M. *J. Phys. Chem.* **1990**, *94*, 781-787.
3. Johnston, K. P.; McFann, G. J.; Lemert, R. M. In *Supercritical Fluid Science and Technology*; Johnston, K. P.; Penninger, J. L. M., Eds.; ACS Symposium Series No. 406; Washington, 1989, p. 140.
4. Badger, R. M.; Bauer, S. H. *J. Chem. Phys.* **1937**, *5*, 839-851.
5. Van Ness, H. C.; Winkle, J. V.; Richtol, H. H.; Hollinger, H. B. *J. Phys. Chem.* **1976**, *71*, 1483-1494.
6. Fletcher, A. N.; Heller, C. A. *J. Phys. Chem.* **1967**, *71*, 3742-3756.
7. Aveyard, R.; Briscoe, B. J.; Chapman, J. J. *Chem. Soc. Faraday Trans. I* **1973**, *69*, 1772-1778.
8. Yee, G. G.; Fulton, J. L.; Smith, R. D. *Langmuir*, **1992**, *8*, 337-384.
9. Fulton, J. L.; Yee, G. G.; Smith, R. D. *J. Am. Chem. Soc.* **1991**, *113*, 8327-8334.
10. Yee, G. G.; Fulton, J. L.; Smith, R. D. *J. Phys. Chem.* in press.
11. Friedrich, J.; Schneider, G. M. *J. Chem. Thermodynamics* **1989**, *21*, 307-319.
12. Yee, G. G.; Fulton, J. L.; Blitz, J. P.; Smith, R. D. *J. Phys. Chem.* **1991**, *95*, 1403-1409.
13. Robinson, D. B.; Peng, D.; Chung, S. Y. *Fluid Phase Equilibria* **1985**, *24*, 25-41.
14. Gurdial, G. S.; Foster, N. R.; Yun, J. S. L. In *Proceedings of the 2nd International Symposium on Supercritical Fluids*; McHugh, M. A. Ed.; Johns Hopkins U.: Baltimore, MD, 1991, 66-69.
15. *Gas Encyclopaedia* Elsevier: New York, 1976.
16. Younglove, B. A.; Ely, J. F. *J. Phys. Chem. Ref. Data* **1987**, *16*, 577-798.
17. Edwards, H. G. M.; Farwell, D. W. *J. Molecular Struct.* **1990**, *220*, 217-226.
18. Fletcher, A. N. *J. Phys. Chem.* **1972**, *76*, 2562-2571.
19. Symons, M. C. R.; Thomas, V. *J. Chem. Soc., Faraday Trans. I* **1981**, *77*, 1883-1890.
20. Herndon, W. C.; Vincenti, S. P. *J. Am. Chem. Soc.* **1983**, *105*, 6174-6175.
21. Bartczak, W. M. *Ber. Bunsenges. Phys. Chem.* **1979**, *83*, 987-992.
22. Pacynko, W. F.; Yarwood, J.; Tiddy, G. J. T. *J. Chem. Soc., Faraday Trans. I* **1989**, *85*(6), 1397-1407.

RECEIVED April 27, 1992

Chapter 15

Adsorption from Supercritical Fluids

L. L. Lee¹ and Henry D. Cochran²

¹Department of Chemical Engineering and Materials Science, University of Oklahoma, 100 East Boyd Street, Norman, OK 73019

²Chemical Technology Division, Oak Ridge National Laboratory, P.O. Box 2008, Oak Ridge, TN 37831-6224

Many important processes with supercritical (SC) fluids involve adsorption from SC fluids or desorption into SC fluids; examples include, regeneration of sorbents with SC fluids, SC fluid chromatography, and SC fluid extraction of hazardous chemicals from contaminated soils. In this work we initiate a fundamental, molecular-based study of adsorption from and desorption into SC fluids. Equilibrium properties and fluid structures in the vicinity of the surface (W) are explored using integral equation theory. First, the equilibrium properties of a pure fluid A near W are studied as the fluid state approaches the critical point (CP); both attractive and repulsive A-W interactions are explored. Subsequently, the behavior of a dilute solute B (*i.e.*, system A+B+W) in the vicinity of W will be described under conditions where the solvent A approaches its CP. We examine the degree of preferential adsorption of B *vis-a-vis* attractive or repulsive interactions with A and W. The molecular mechanisms of SC adsorption are determined. The computational challenge of these calculations was considerable, and the necessarily limited range of the calculated correlation functions has resulted in useful qualitative, if not quantitative, information.

Supercritical (SC) fluids are used as solvents in a number of processes in which equilibration is achieved between the SC solvent phase and a condensed phase. In some cases the condensed phase may be a solid surface upon which components may adsorb or from which components may desorb. Examples of such processes involving adsorption from a SC solution or desorption into a SC solution include regeneration of sorbents with SC fluids, SC fluid chromatography, and SC fluid extraction of hazardous chemicals from contaminated soils. The present study was motivated by the importance of adsorption and desorption in these processes with SC fluids. The aim of this work was to improve the fundamental understanding of adsorption-desorption equilibrium between a solid surface and a SC fluid mixture. To our knowledge this problem has not been previously addressed from the perspective of molecular-based theory.

Fundamental, theoretical study of adsorption has employed the techniques of density functional theory (*e.g.* 1,2), integral equation theory (*e.g.* 3-6), or molecular simulation (*e.g.* 7,8). In the present work, techniques based on integral equation

0097-6156/93/0514-0188\$06.00/0
© 1993 American Chemical Society

theory have been employed. In the simplest techniques for application of integral equation theory, due to Henderson, Abraham, and Barker (3), the wall(W)-particle(A) Ornstein-Zernike equation

$$h_{AW}(z) = c_{AW}(z) + 2\pi\rho_A \int_{-\infty}^{\infty} dt c_{AW}(t) \int_{|z-t|}^{\infty} ds s h_{AA}(s) \quad (1)$$

is solved (with an appropriate closure approximation) under the approximation that $h_{AA}(s)$ in equation 1 is taken as equal to the homogeneous total correlation function for the bulk fluid. In equation 1, h_{ij} is the total pair correlation function, c_{ij} is the direct correlation function, and ρ is the number density. The HAB integral equation approach is known (8) to produce results with important qualitative and quantitative failures. In contrast, the Henderson-Plischke-Sokolowski (HPS) approach (4,5) solves the inhomogeneous Ornstein-Zernike equation for the wall-particle system in Fourier space

$$\hat{h}(z_1, z_2, k) = \hat{c}(z_1, z_2, k) + \int dz' \rho(z') \hat{c}(z_1, z', k) \hat{h}(z', z_2, k) \quad (2)$$

where the Hankel transform is defined by

$$\hat{f}(z_1, z_2, k) = \int d^2\mathbf{r} f(z_1, z_2, \mathbf{r}) \exp[i\mathbf{k} \cdot \mathbf{r}] = 2\pi \int dr r f(z_1, z_2, r) J_0(kr) \quad (3)$$

with an appropriate closure approximation plus one of several exact expressions for the inhomogeneous density in terms of the correlation functions. In equations 2 and 3, z_1 is the distance from the wall of particle 1, z_2 is the distance from the wall of particle 2, and r is the projection of the distance between particles 1 and 2 on a plane parallel to the wall. Compared with the HAB approach, solution of the inhomogeneous HPS equation is much more demanding computationally in terms of required memory and CPU cycles but is exact with an exact closure and is much more accurate with an approximate closure.

For an infinitely dilute solute B dissolved in the solvent A, the HPS equation takes the form (A+B/W):

$$\hat{h}_{AA}(z_1, z_2, k) = \hat{c}_{AA}(z_1, z_2, k) + \int dz' \rho_A(z') \hat{h}_{AA}(z_1, z', k) \hat{c}_{AA}(z', z_2, k) \quad (4)$$

and

$$\hat{h}_{AB}(z_1, z_2, k) = \hat{c}_{AB}(z_1, z_2, k) + \int dz' \rho_A(z') \hat{h}_{AA}(z_1, z', k) \hat{c}_{AB}(z', z_2, k) \quad (5)$$

In the present work we have applied the HPS approach to study adsorption equilibrium in systems where the fluid phase is either a pure SC fluid or a dilute solution of a solute in a fluid near the CP of the pure solvent. Previously this approach has not been applied to adsorption in fluid/wall systems with realistic (*i.e.*, Lennard-Jones) potentials when the fluid is a mixture or a near-critical SC fluid. So some development and testing of the calculational technique were prerequisite for this work.

Calculation Method

In numerical calculations it is often desirable to replace the function h by the continuous indirect correlation function $\gamma = h - c$; in this form equations 4 and 5 become

$$\begin{aligned} \hat{\gamma}_{AA}(z_1, z_2, k) &= \int dz' \rho_A(z') \hat{\gamma}_{AA}(z_1, z', k) \hat{c}_{AA}(z', z_2, k) \\ &+ \int dz' \rho_A(z') \hat{c}_{AA}(z_1, z', k) \hat{c}_{AA}(z', z_2, k) \end{aligned} \quad (6)$$

and

$$\begin{aligned} \hat{\gamma}_{AB}(z_1, z_2, k) &= \int dz' \rho_A(z') \hat{\gamma}_{AA}(z_1, z', k) \hat{c}_{AB}(z', z_2, k) \\ &+ \int dz' \rho_A(z') \hat{c}_{AA}(z_1, z', k) \hat{c}_{AB}(z', z_2, k) \end{aligned} \quad (7)$$

There are several possible choices for an exact relation between the inhomogeneous density $\rho(z)$ and the correlation functions. We have chosen the one due to Wertheim (11) and to Lovett, Mou, and Buff (12). The WLMB relation is

$$\frac{\partial \ln \rho(z_1)}{\partial z_1} = -\frac{\partial \beta w(z_1)}{\partial z_1} + \int_0^\infty dz' \frac{\partial \rho(z')}{\partial z'} \hat{c}(z_1, z', 0) \quad (8)$$

For mixtures (A+B/W), WLMB assumes the form:

$$\frac{\partial \ln \rho_A(z_1)}{\partial z_1} = -\frac{\partial \beta w_A(z_1)}{\partial z_1} + \int_0^\infty dz' \frac{\partial \rho_A(z')}{\partial z'} \hat{c}_{AA}(z_1, z', 0) \quad (9)$$

and

$$\frac{\partial \ln \rho_B(z_1)}{\partial z_1} = -\frac{\partial \beta w_B(z_1)}{\partial z_1} + \int_0^\infty dz' \frac{\partial \rho_B(z')}{\partial z'} \hat{c}_{AB}(z_1, z', 0) \quad (10)$$

In our numerical calculations it has proven advantageous to rewrite the WLMB relation in terms of the cavity function y where $g = h + 1 = ye$ and $e = \exp[-u/kT]$ so that equations 9 and 10 become

$$\begin{aligned} \frac{\partial y_{AW}(z_1)}{\partial z_1} &= y_{AW}(z_1) \int_0^\infty dz' \frac{\partial y_{AW}(z')}{\partial z'} e_{AW} \hat{c}_{AA}(z, z', 0) \\ &+ y_{AW}(z_1) \int_0^\infty dz' y_{AW} \frac{\partial e_{AW}(z')}{\partial z'} e_{AW} \hat{c}_{AA}(z, z', 0) \end{aligned} \quad (11)$$

and

$$\begin{aligned} \frac{\partial y_{BW}(z_1)}{\partial z_1} &= y_{BW}(z_1) \int_0^\infty dz' \frac{\partial y_{BW}(z')}{\partial z'} e_{BW} \hat{c}_{AB}(z, z', 0) \\ &+ y_{BW}(z_1) \int_0^\infty dz' y_{BW} \frac{\partial e_{BW}(z')}{\partial z'} e_{BW} \hat{c}_{AB}(z, z', 0) \end{aligned} \quad (12)$$

For the approximate closure relation (to obtain c from γ or h and u) we chose to use the Percus-Yevick (PY) closure (13).

$$g(z_1, z_2, r) \exp[u(z_1, z_2, r)/kT] = g(z_1, z_2, r) - c(z_1, z_2, r) \quad (13)$$

which has proven to have sufficient accuracy for the desired calculations at the densities used in this work (e.g. 14).

The use of different closures with the inhomogeneous OZ relation (coupled with the WLMB equations) is of interest. For hard spheres in contact with a hard wall, Plischke and Henderson (4) have shown that the PY closure is adequate. Similar results have been reported by Attard (15,16) with a spherically symmetric wall. For Lennard-Jones fluids near a hard wall Plischke and Henderson (6) have reported encouraging results with PY. Recently, Kjellander and Sarman (17) studied various closures with a Lennard-Jones fluid in contact with a Lennard-Jones wall in comparison with simulation results. Although the Hybrid Mean Spherical Approximation (HMSA) and the Modified Hypernetted Chain Approximation (MHNC) were somewhat more accurate, the PY closure was found to give reasonably accurate results with much less time-consuming calculations than the HMSA or MHNC closure and was chosen for this work on that basis.

The set of equations 6, 7, 11, 12, and 13 for mixtures is solved by the method of successive substitutions or Picard iterations. The approach, then, is to make an initial guess of the density profile and the pair correlation functions γ ; to transform γ to

Fourier space $\hat{\gamma}$; to solve the inhomogeneous OZ equations 6 and 7 for \hat{c} ; to transform back to real space; to use the closure relation, equation 13, to obtain a new estimate of c ; to iterate equations 6, 7, and 13 to convergence; then, to substitute \hat{c} in equations 11 and 12 obtaining a new estimate of $\rho(z_1)$. The criterion for convergence used is

$$\sum_n \sum_{n < m} \frac{|\gamma_{(n,m,i)}^{new} - \gamma_{(n,m,i)}^{old}|^2}{NZ(NZ+1)/2} \leq 2 \times 10^{-5} \quad (14)$$

Generally, correlation functions and density profiles from a previously converged case were used as initial estimates. For startup, low density limits of the correlation functions were used (essentially, the Boltzmann factors for h and c , as well as $\rho(z)$).

For numerical solution we discretize the three-dimensional equations 6 and 7 for $\hat{\gamma}$ and \hat{c} such that there are L , M , and N grids of Δz_1 , Δz_2 and Δk spacing, respectively.

$$\hat{\gamma}(l,m,n) = \hat{\gamma}(l\Delta z_1, m\Delta z_2, n\Delta k) \quad l = 1, \dots, L; \quad m = 1, \dots, M; \quad n = 1, \dots, N \quad (15)$$

Near the CP of the solvent, the correlation functions γ become long-ranged; this requires $M\Delta z_2$ be large, say $M = 200$ with $\Delta z_2 = 0.03\sigma$. Then, as a reasonable compromise between tractable memory requirements and accuracy of results, we set $L = 80$ with $\Delta z_1 = 0.05\sigma$ and $N = 50$ with $\Delta k = 0.08$ ($L=M$). In order to conserve the use of memory and because both functions of the pairs (c_{AA}, \hat{c}_{AA}) and (c_{AB}, \hat{c}_{AB}) are not required at the same time, these function pairs share the same memory locations (via the EQUIVALENCE statement in FORTRAN). Thus, only six large arrays— γ_{AA} , γ_{AB} , γ_{AB} , c_{AA} , and c_{AB} are required; nevertheless, memory requirements are substantial; for the choices of L , M , and N above, double precision calculations require memory exceeding 15 Mb.

We have accurately calculated and tabulated the Hankel transform for J_0 from 0 to 400, the forward and reverse transformations agreeing to the ninth place.

The bulk fluid molecules interact with the Lennard-Jones potential (LJ:12-6), simulating argon and methane. The wall potentials used are the hard wall (HW) potential simulating, say, Teflon and the LJ:9-3 potential simulating solid CO₂.

Hard Wall

$$\begin{aligned} w(z) &= \infty \quad \text{for } z \leq 0 \\ w(z) &= 0 \quad \text{for } z > 0 \end{aligned} \quad (16)$$

LJ:9-3

$$w(z) = p\epsilon \left[\frac{2}{15} \left(\frac{m\sigma}{z} \right)^9 - \left(\frac{m\sigma}{z} \right)^3 - \right] \quad (17)$$

where p and m are numerical factors to modify the bulk fluid force constants ϵ and σ ; for Ar|CO₂(solid) $p = 2.6427$ and $m = 1.09618$. The parameters of the models are presented in Table 1 and are discussed in greater detail below.

Test Calculations

The first test we performed was reproducing one of the cases by Plischke and Henderson (6) for a pure LJ fluid in contact with a hard wall. For the state $T^* = kT/\epsilon = 1.35$ and $\rho^* = \rho\sigma^3 = 0.40$ our program reproduced Plischke and Henderson's density profile quantitatively. In all of the calculations reported below, we have used finer grid spacing and longer range in the correlation functions than those used by Plischke and Henderson.

The range of the pair correlation function grows without limit upon approach to the CP. This is a significant issue because the value of $f(r)$ in equation 2 must be 0 at

the maximum value of r to perform the Hankel transform. For a state close to the critical point ($T^* = 1.35$ and $\rho^* = 0.35$) we tested the effect of increasing the range by 50%. Figure 1a compares results for the wall-solvent pair correlation function, $g_{WA}(z)$, at this state for arrays of dimension (120,120,50), that is, the number of grid steps in each of the coordinates z_1 , z_2 , and r_{12} is 120, 120, and 50, respectively. This result is compared with the standard for this work (80,80,50). A similar comparison for the wall-solute pair correlation function, $g_{WB}(z)$ is shown in Figure 1b. The increase in the range of the calculation has evidently had a significant quantitative effect (peak maxima are increased by 40-50%), but aside from this amplification of the maxima, no qualitative effect is shown. We suggest that, despite the limited range of the present calculations which compromises the quantitative validity of the results, the qualitative behavior of the results is probably valid. Since these results are the first and only results of their kind and since the range was as long as possible for the present calculational setup, we concluded that the results should be presented for their novel, qualitative value with clear warning to the reader, however, about possible compromise because of the limited range.

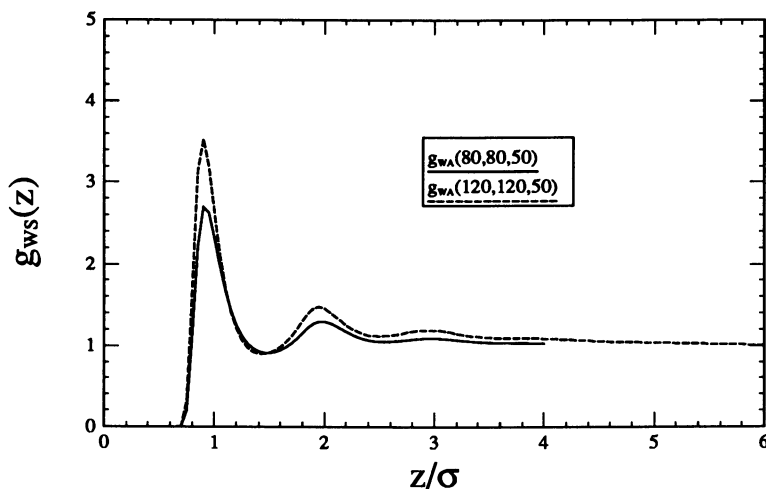


Figure 1a. Effect of range on wall-particle pair correlation function g_{ws} at $T^* = 1.35$ and $\rho^* = 0.35$. Wall-solvent correlation g_{wA} .

We tested the sensitivity of our results to the grid spacing for the systems and states we studied and found that there was no significant effect of grid spacings finer than those used. We were unable to test the method by comparing results with the Monte Carlo results of Finn and Monson (6) because the strong wall forces of the Finn-Monson simulations required grid spacings too fine for calculations by this method with the computer memory available for this work. Figure 2 shows the Boltzmann factor for the wall-particle interactions compared with that for the particle-particle interactions in SC solution. In the discussion of results we address the effects of the strength of the wall attraction on adsorption from SC solutions.

Results and Discussion

We have studied several cases of adsorption from SC solution. We have studied adsorption of the solvent (A) and the attractive solute (B) on a HW for temperatures approaching the bulk CP from above. These results are presented in the following

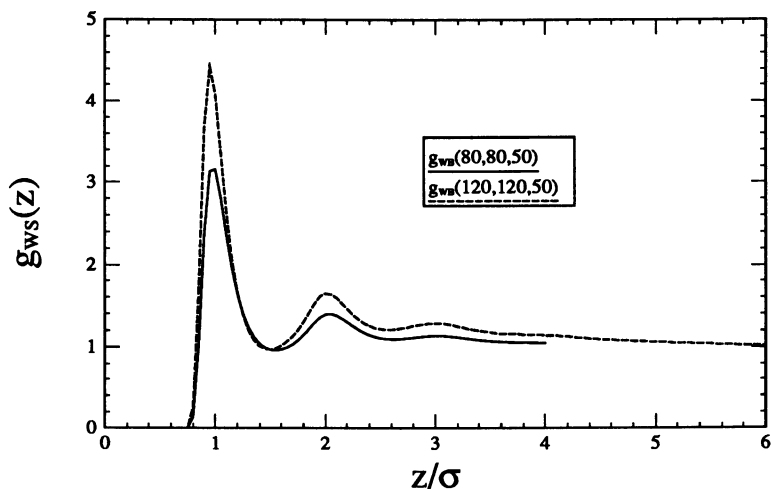


Figure 1b. Effect of range on wall-particle pair correlation function g_{ws} at $T^* = 1.35$ and $\rho^* = 0.35$. Wall-solute (attractive) correlation g_{WB} .

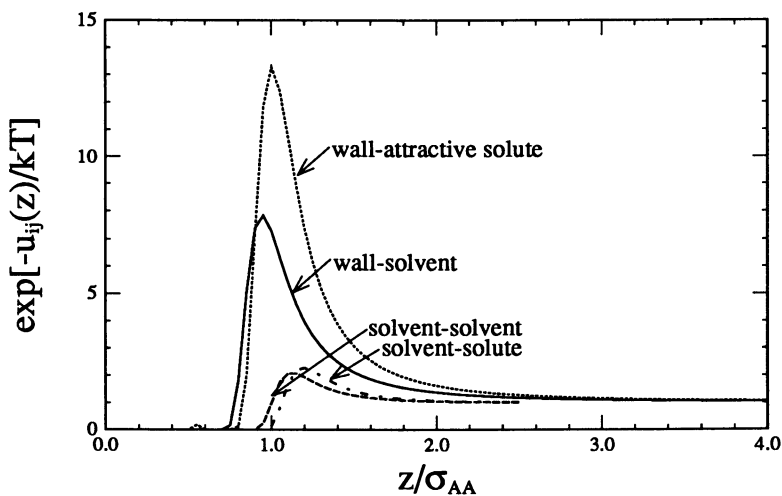


Figure 2 Boltzmann factor at $T^* = 1.35$ for wall-particle and particle-particle interactions.

subsection. We have studied adsorption of the solvent (A) and both the attractive solute (B) and the repulsive solute (also B) on a LJ wall for a near critical state. These results are presented in the second following subsection. Table I presents the parameters of the interaction potentials used in this work. With the hard wall, the solvent (A) parameters model argon; the attractive and repulsive solutes (B) have the same size as A with an arbitrarily greater or smaller interaction energy parameter. With the LJ

wall, again the solvent (A) parameters model argon; the solvent-wall parameters model argon with solid CO₂; the attractive solute (B) models methane; and the repulsive solute (also B) has the same size as the methane model but has interaction energy proportionately smaller than that of argon as methane is larger.

Table I. Parameters of interaction potentials used

pair	$\epsilon/k(K)$	σ (A)	material approximated
<i>Hard Wall</i>			
A-A	119.80	3.400	argon-argon
A-B(repulsive)	100.24	3.400	argon-repulsive solute
A-B(attractive)	143.16	3.400	argon-attractive solute
<i>LJ:9-3 Wall</i>			
A-A	119.80	3.400	argon-argon
A-B(repulsive)	107.82	3.606	argon-repulsive solute
A-B(attractive)	134.45	3.606	argon-methane solute
W-A	153.00	3.727	solid CO ₂ -argon
W-B(repulsive)	297.69	3.957	solid CO ₂ -repulsive solute
W-B(attractive)	297.69	3.957	solid CO ₂ -methane solute

Adsorption at a Hard Wall. Figures 3a and 3b show density profiles near a HW for a SC LJ solvent and an infinitely dilute, repulsive LJ solute, respectively, for density $\rho^* = 0.40$ and temperatures, $T^* = 5.00, 3.00, 2.00,$ and 1.35 . For the HW system, the $z = 0$ intercept of the solvent-wall density profile is a measure of the bulk fluid pressure $P^* = P\sigma^3/\epsilon = g(0)\rho^*T^*$. Of course, the pressure at constant density increases with increasing temperature. It is interesting to note, however that, for the solvent, there is a net deficit at the wall at the near-critical state and for the attractive solute the deficit is substantially greater. The near-critical solvent has a higher affinity for the attractive solute (and even for other solvent molecules) than does the HW.

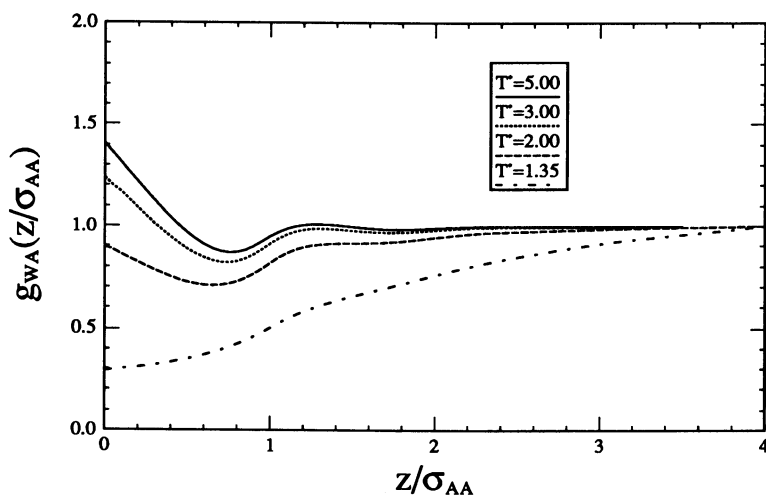


Figure 3a. Effect of temperature on density profiles near a hard wall. Wall-solvent profile g_{WA} .

Adsorption at a Lennard-Jones Wall. Figures 4a, 4b, and 4c show the effect of the wall strength on the density profiles near an attractive LJ:9-3 wall (the HW profiles are also shown for comparison) for the state $\rho^* = 0.35$ and $T^* = 1.35$ for the LJ solvent,

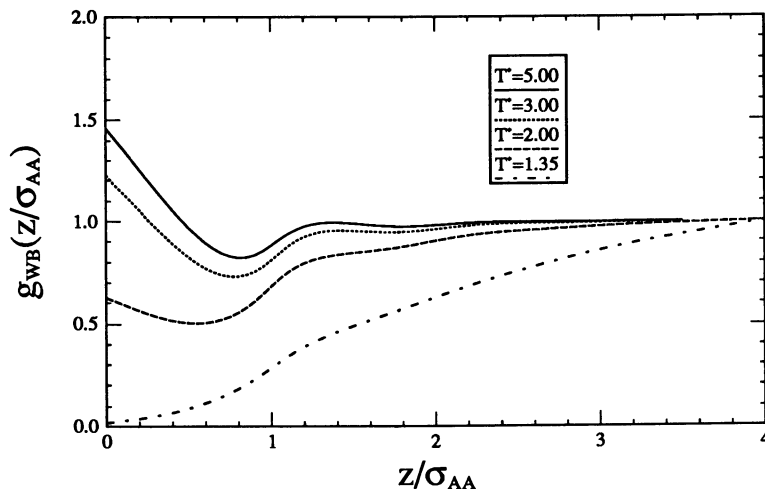


Figure 3b. Effect of temperature on density profiles near a hard wall. Wall-solute (repulsive) profile g_{WB} .

the repulsive solute, and the attractive solute, respectively. The parameter shown for each of the profiles is the percent of the full LJ:9-3 potential used by Finn and Monson (7) to model argon adsorption on solid carbon dioxide. It is evident that, compared to the HW, the LJ:9-3 wall attracts considerable adsorption, the degree of adsorption increasing with the strength of the wall. Accompanying the increased adsorption is an increase in the structure near the wall, showing clear first and second, and even third, maxima in the profile.

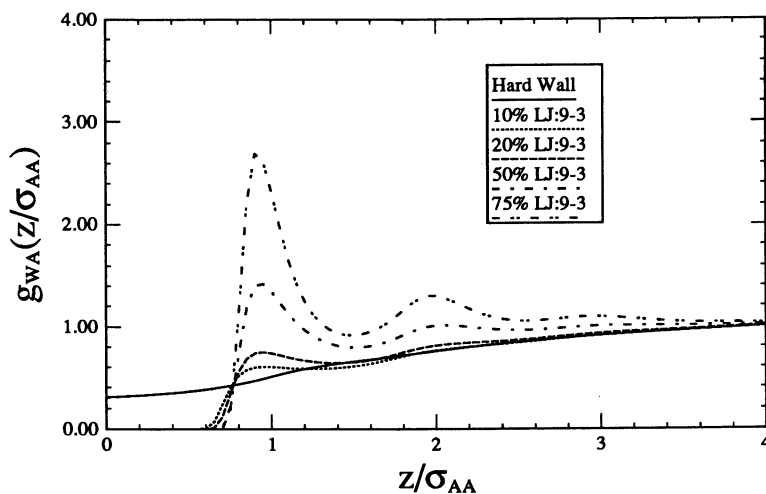


Figure 4a. Effect of wall strength on density profiles near LJ:9-3 wall. Wall-solvent profile g_{WA} .

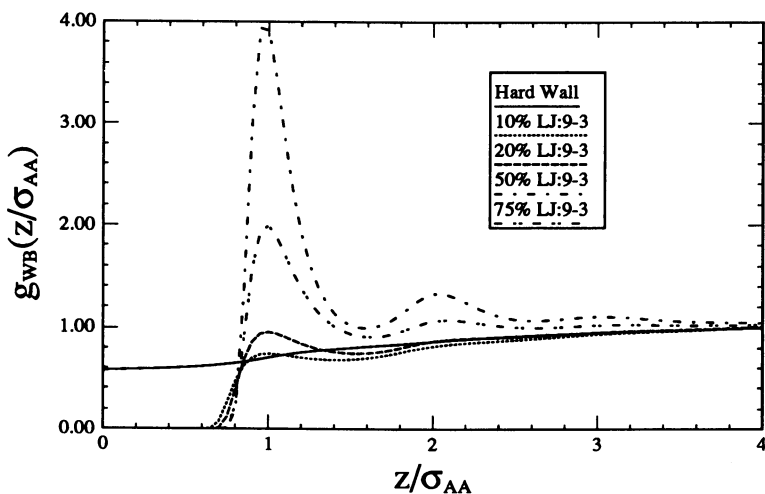


Figure 4b. Effect of wall strength on density profiles near LJ:9-3 wall. Wall-solute (repulsive) profile g_{WB} .

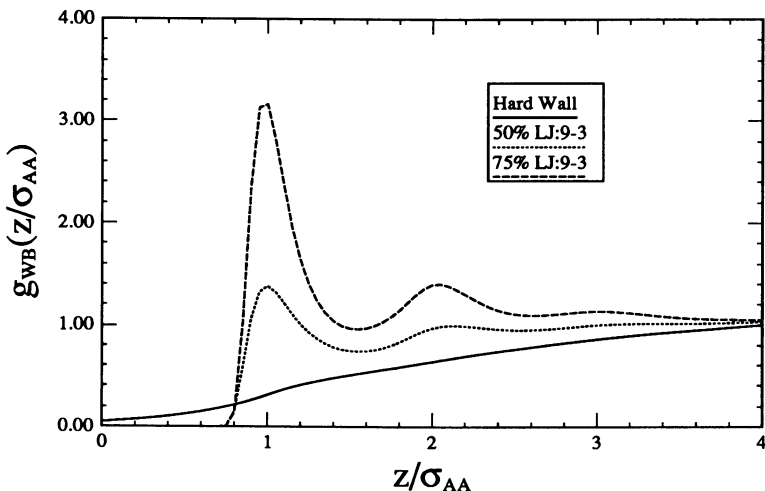


Figure 4c. Effect of wall strength on density profiles near LJ:9-3 wall. Wall-solute (attractive) profile g_{WB} .

Figures 5a, 5b, and 5c replot some of the previous results in such a way as to emphasize the relative adsorption of the solvent, the repulsive solute, and the attractive solute as the strength of the wall interaction increases. The SC solvent draws the attractive solute into solution and away from the wall so that its adsorption on the HW is less than that of the solvent. In contrast, the repulsive solute is expelled from the SC

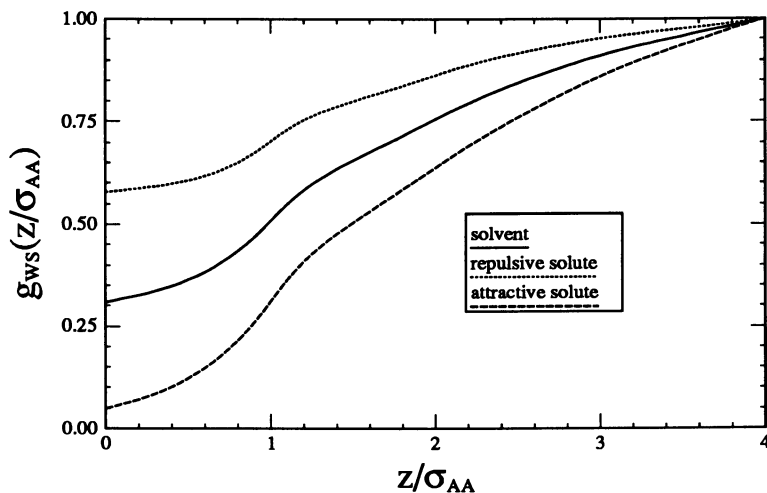


Figure 5a. Competitive adsorption between wall and repulsive or attractive solute. Wall-particle profiles g_{ws} are identified in the legend. Hard wall.

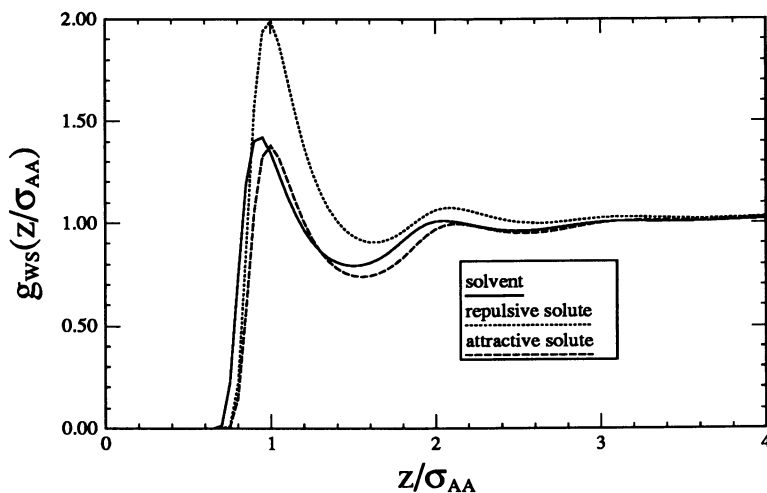


Figure 5b. Competitive adsorption between wall and repulsive or attractive solute. Wall-particle profiles g_{ws} are identified in the legend. 50% LJ:9-3 wall.

solvent so that its adsorption on the HW is relatively greater than that of the solvent. The LJ:9-3 wall with 50% of the wall strength of the Finn-Monson (7) system attracts the solvent, attractive solute, and repulsive solute so that the adsorption of all three is increased. But the adsorption of the attractive solute has increased most so that it has approximately equaled that of the solvent. Here we see competition between the SC

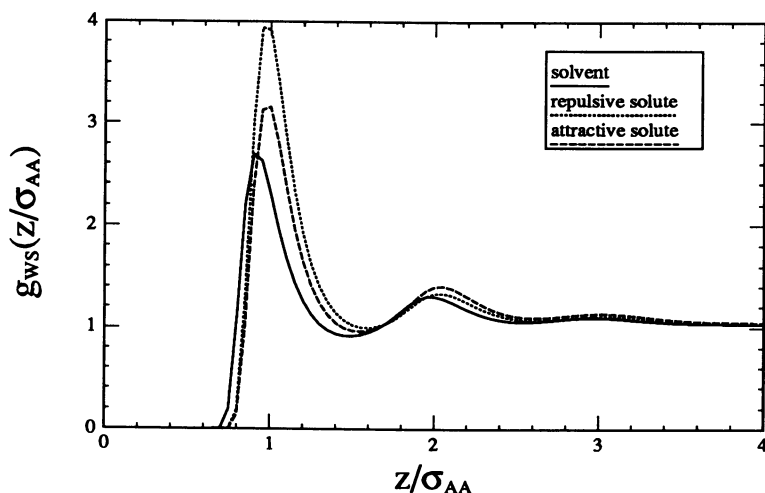


Figure 5c. Competitive adsorption between wall and repulsive or attractive solute. Wall-particle profiles g_{ws} are identified in the legend. 75% LJ:9-3 wall.

solvent and the wall for the attractive solute. At 75% of the Finn-Monson wall strength the adsorption of the attractive solute has overtaken that of the solvent and approaches that of the repulsive solute.

In figure 6a we examine the radial distribution for the solute-solvent correlation $h_{AB}(r)$ for different values of z , the distance from the wall for the attractive solute at the state $\rho^* = 0.35$ and $T^* = 1.35$. The wall-particle profile shown in figure 6b gives a measure of the relative fluid density at the various distances z from the wall. At $z = 0.0\sigma$, $h_{AB}(r)$ shows a single broad peak dropping monotonically to the bulk value; such structure is similar to that of a low density gas. Note in figure 6b that the density at $z = 0.0\sigma$ is low. At $z = 1.0\sigma$, the structure looks more like that of a liquid with a distinct second maximum. In figure 6b, one can see the correspondingly high density at this distance from the wall. The variation in the structure with distance from the wall is qualitatively similar to that seen by Plischke and Henderson (6).

Concluding Remarks

This is the first time, to our knowledge, that a molecular-based study (using the inhomogeneous Ornstein-Zernike equation) has been presented of adsorption equilibrium between a solution (mixture of A and B) and a surface (W) and the first time such study has been focused on SC solutions. This extension of the integral equation method of Plischke, Henderson, and Sokolowski (4-6) has presented significant challenge, and study of interesting problems has aggravated the large (16-52 Mb) memory requirements. Approach to the bulk CP requires long range; approach to surface wetting also requires long range; strong (realistic) wall forces require fine grid spacing; and large solute-solvent asymmetry also requires fine grid spacing. The nested iterations of the inhomogeneous solvent-solvent and solute-solvent Ornstein-Zernike equations and the Wertheim-Lovett-Mou-Buff equations required long runs.

Because of these computational challenges, practical compromises were necessary in the relatively limited range and coarse grids used in the present calculations;

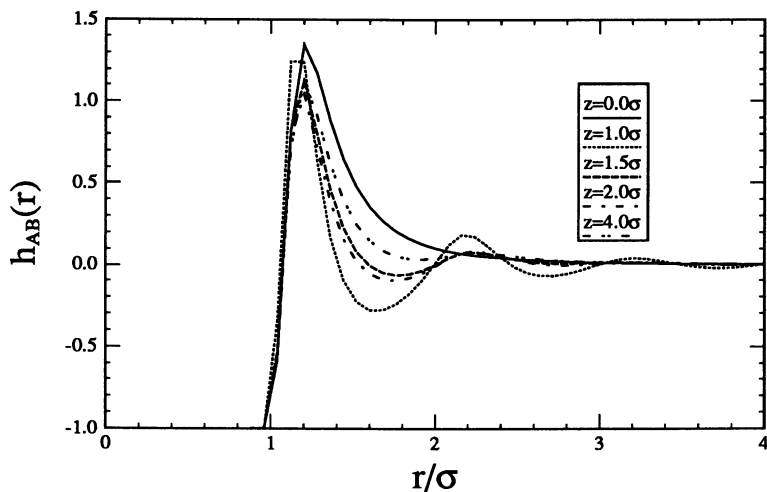


Figure 6a. Effect of distance from wall on radial distribution. Solute-solvent distribution h_{AB}

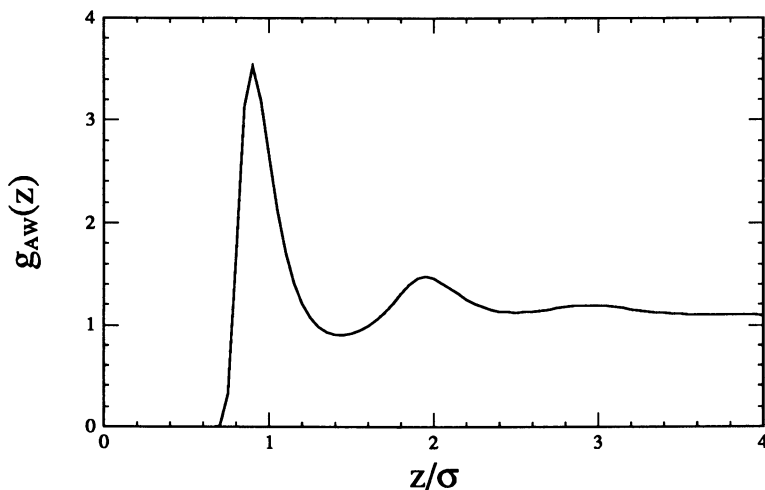


Figure 6b. Effect of distance from wall on radial distribution. Wall-particle profile g_{AW} .

even so, the range was longer and the grid finer than in previous studies by this method (4,6). Likewise, the wall potentials used in this work were relatively weak (7,8). Because of these practical compromises, the results of the present work should be treated with some caution.

Nevertheless, despite the compromises necessary in the computational technique, we believe the results of this study are of qualitative validity and offer new insights into competitive adsorption and adsorption equilibrium between surfaces and SC solutions. Adsorption from SC solutions on a realistic (but weak) wall exhibited expulsion of a repulsive solute from SC solvent to the wall and competition for an attractive solute between the solvent and the wall.

Acknowledgment

We acknowledge the assistance of R.-S. Wu in programming the Hankel transform. This work has been supported in part by the Division of Chemical Sciences of the U. S. Department of Energy through contract number DE-AC05-84OR21400 with Martin Marietta Energy Systems, Inc. and subcontract with the University of Oklahoma.

Literature Cited

1. Ebner, C; Saam, W. F. *Phys. Rev. Lett.*, **1977**, *38*, 1486.
2. Saam, W. F.; Ebner, C. *Phys. Rev. A*, **1978**, *17*, 1768.
3. Henderson, D.; Abraham, F. F.; Barker, J. A. *Mol. Phys.*, **1976**, *31*, 1291.
4. Plischke, M.; Henderson, D. *Proc. Roy. Soc. London A*, **1986**, *404*, 323.
5. Sokolowski, S. *J. Chem. Phys.* **1980**, *73*, 3507.
6. Plischke, M; Henderson, D. *J. Chem. Phys.*, **1986**, *84*, 2846.
7. Finn, J. E.; Monson, P. A. *Phys. Rev. A*, **1989**, *39*, 6402.
8. Finn, J. E.; Monson, P. A. *Mol. Phys.*, **1991**, *72*, 661.
9. Evans, R.; Tarazona, P.; Marconi, U. M. B. *Mol. Phys.*, **1983**, *50*, 993.
10. Debenedetti, P. G.; Mohamed, R. S. *J. Chem. Phys.*, **1989**, *90*, 4528.
11. Wertheim, M. J. *J. Chem. Phys.*, **1976**, *65*, 2377.
12. Lovett, R.; Mou, C. Y.; Buff, F. P. *J. Chem. Phys.*, **1976**, *65*, 570.
13. Percus, J. K.; Yevick, G. J. *Phys. Rev.*, **1958**, *110*, 1.
14. Lee, L. L. *Molecular Thermodynamics of Nonideal Fluids*; Butterworths: Stoneham, MA, **1988**; 164-175.
15. Attard, P. *J. Chem. Phys.*, **1989**, 3072.
16. Attard, P. *J. Chem. Phys.*, **1989**, 3083.
17. Kjellander, R.; Sarman, S. *Mol. Phys.*, **1991**, 665.

RECEIVED May 27, 1992

Chapter 16

Spectroscopic Investigations of Reactions in Supercritical Fluids

A Review

Joan F. Brennecke

Department of Chemical Engineering, University of Notre Dame,
Notre Dame, IN 46556

Supercritical fluids may be attractive as reaction media for a variety of reasons, including increased mass transfer, elimination of the need for multiphase reactions, ease of separation of products or unused reactants, slower deactivation of catalysts, dramatic pressure effects on rate constants and changes in selectivities. However, more recently they have been used as a tool to study the influence of the solvent on the reaction and the solvation of species in supercritical fluid solutions. A number of spectroscopic investigations of reactions have been particularly useful in elucidating information about supercritical solvent effects because they address relatively simple, well-understood reactions on a molecular scale. It has become clear that both bulk transport effects like increased diffusion and microscopic scale thermodynamic properties like increased local densities and local compositions can influence reactions in supercritical fluids. In this paper we review a number of the ways that supercritical fluids can influence reaction rates, and discuss recent studies that probe these influences, paying special attention to spectroscopic investigations.

For many years the focus of supercritical research and development was extractions, separations and the thermodynamic modeling of solubilities and phase behavior. There are a number of excellent reviews and monographs that describe this work (1-3). The last few years have seen a renaissance in the field, as researchers have sought to pursue new applications in crystallizations, polymers, micelles, microemulsions and reactions. Moreover, much attention has been paid to the local environment about dilute species in supercritical fluid solvents (4), the importance of specific chemical interactions like hydrogen bonding, and how these factors affect

0097-6156/93/0514-0201\$06.00/0
© 1993 American Chemical Society

solubilities, reactivities and the nature of the complex molecular structures mentioned above. Reactions, in particular, have attracted attention, due at least in part to interest in the supercritical water oxidation process. In this process, an aqueous stream is raised near or above the critical temperature and pressure of water ($T_c=374^\circ\text{C}$, $P_c=221$ bar), at which conditions oxygen is readily soluble and chlorinated species, or other hydrocarbons and contaminants, are easily oxidized. Unfortunately, reactions in supercritical water are not necessarily the best ones to use in investigating the solvent effect on a fundamental level since it is difficult to observe an uncatalyzed reaction and the operating conditions are very severe. Conversely, studies of elementary or at least well-characterized reactions in supercritical fluids with lower critical temperatures like carbon dioxide, ethane and ethylene, can elucidate much information about the solvent effect on reaction rates and the interactions among species in supercritical solutions.

Therefore, in this paper we will briefly discuss the ways supercritical fluid solvents can affect reactions in general. Besides the effect of increased diffusion on diffusion-controlled reactions, they are all essentially ways that equilibrium thermodynamic properties and structure can influence reaction rates. We will review the spectroscopic, theoretical and computational investigations that lead to the ideas of local densities and local compositions around solutes in supercritical solutions that are different than the bulk. Then we will focus our attention on a number of well-chosen, simple, homogeneous, uncatalyzed reactions that attempt to discern information on molecular interactions and the solvent effect on reactions. Since spectroscopy yields information on the molecular scale, many of these studies involve the use of spectroscopic measurements. Some of the areas not covered in this paper, including heterogeneous, catalyzed reactions can be found in earlier reviews (5,6).

Possible Ways to Affect Reactions in Supercritical Fluids

Supercritical fluid solvents can act in a variety of manners to affect reaction rates. Although not all-inclusive, very roughly, they can be divided into a) increased diffusion rates, b) increased reactant solubilities and elimination of mass transfer resistances, c) facilitated separation, d) catalyst life extension, e) pressure effect on the rate constant, f) changes in selectivities, g) effects of local densities, and h) effects of local compositions. Items b-h are ways in which equilibrium thermodynamics, such as the solubility of a reactant, local molecular structure and reactant partial molar volumes, can affect reaction rates.

a) Increased Diffusion Rates. In the supercritical region diffusivities are greater than they are in liquids since the fluid has a lower density and is more gas-like. In addition, diffusion coefficients are sensitive functions of pressure and temperature in the supercritical region. The rate constant for a diffusion controlled reaction can be modeled with the Stokes-Einstein equation, which states that for a bimolecular reaction the rate constant is given by $8kT/3\eta$, where η is the solution viscosity. As shown in Figure 1, the Stokes-Einstein equation predicts that the bimolecular rate constant of a diffusion controlled reaction in CO_2 should increase by a factor of 2.5 over a small pressure range at 35°C . The effect is even more dramatic

along isotherms closer to the critical temperature, which is 31°C for CO₂. This plot will be used later in the analysis of the charge transfer reaction between benzophenone triplet and tertiary amines in supercritical carbon dioxide (7).

b) Increased Reactant Solubilities and Elimination of Mass Transfer Resistances. Some reactions that would normally take place in a multiphase system can be facilitated by operation in a single phase supercritical solution. For example, in supercritical water oxidation, the reaction is not limited by mass transfer of the oxygen into the water, as it is at ambient conditions, since oxygen and organics can be mixed intimately in a single supercritical water phase. Another excellent example involving photochemistry is the formation of organometallic species in supercritical fluids (8-14). Poliakoff and coworkers have been able to synthesize a variety of previously unknown dinitrogen and dihydrogen organometallic species because the solubility of nitrogen and hydrogen are so high in many supercritical fluids. Moreover, they have developed high pressure Fourier Transform Infrared Spectroscopy (FTIR) and Time-Resolved Infrared Spectroscopy (TRIR) techniques to analyze the products.

c) Facilitated Separation. The solubility of solutes in supercritical fluids are strong functions of temperature in the compressible region near the critical point, as shown in Figure 2 for the classic system of naphthalene in ethylene. This phenomenon is described in detail elsewhere (1, 2). Therefore, careful selection of operating conditions may allow the easy precipitation of the product, if it is less soluble than the reactants. The classic example of this is the polymerization of ethylene, where oligomers will fall out of the supercritical solution when they reach a certain molecular weight, corresponding to the solubility limit. Moreover, in an equilibrium limited reaction, this continuous removal of the product would allow significantly greater conversions. Conversely, if the product is more soluble than the reactants, a slight reduction in pressure after the reactor will precipitate the unused reactants, which can then be reintroduced into the feed mixture. Further reduction in pressure and/or temperature may remove the products, allowing recycle of the supercritical solvent. For example, in the isomerization scheme for paraffinic hydrocarbons proposed by Kramer and Leder (15), the reaction products and Lewis acid catalyst are separated from the SCF phase by carefully adjusting the pressure and/or temperature.

d) Catalyst Life Extension. Since solubilities of heavy organics are much higher in supercritical fluids than in gases, several investigators have observed less coking and deactivation of catalysts when operating in the dense fluid (6). Moreover, diffusivities of solutes in supercritical fluids are close to those in liquids, facilitating the transport of poisons away from the catalyst surface. This is the case in the isomerization of cis- and trans-2-hexene on gamma-Al₂O₃, where C₁₂ to C₃₀ oligomers can be removed from the catalyst surface simply by increasing the pressure to conditions above the critical point (16).

e) Pressure Effect on the Rate Constant. The most pronounced effect of pressure on reactions in the supercritical region has been attributed to the

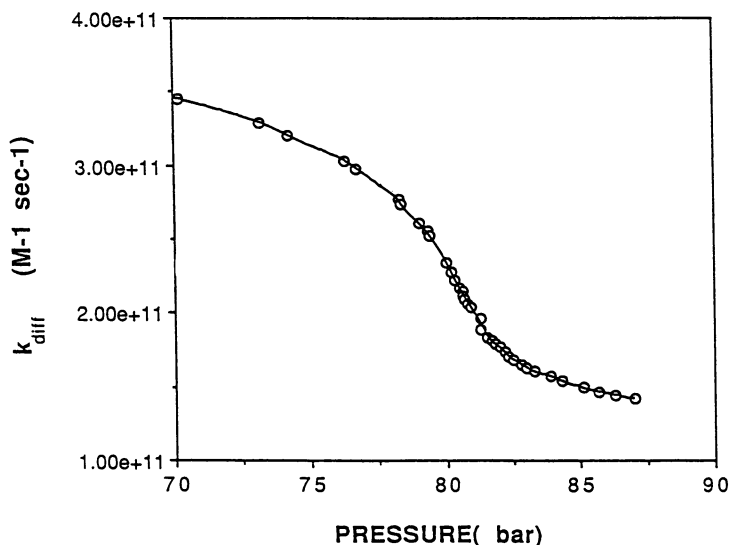


Figure 1. Diffusion controlled bimolecular rate constant for the reaction between benzophenone triplet and triethylamine in carbon dioxide at 35°C as predicted from the Stokes-Einstein equation using experimental viscosity data of Iwasaki and Takahashi (62).

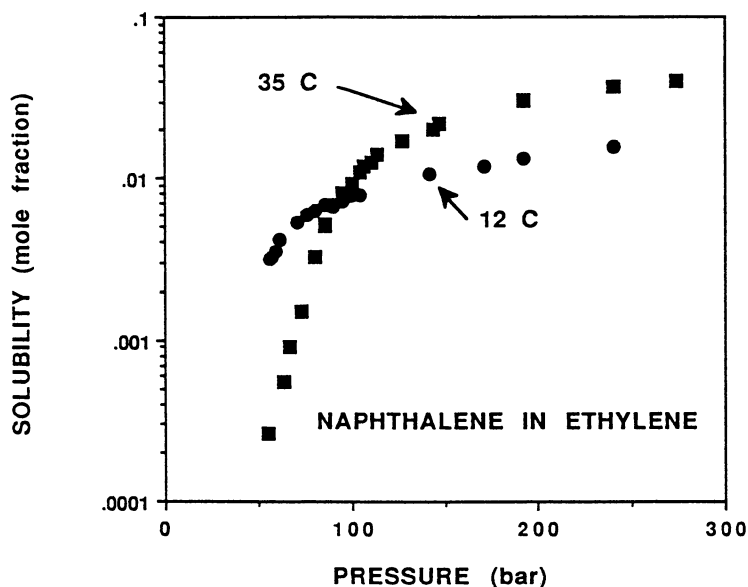


Figure 2. The solubility of naphthalene in supercritical ethylene as a function of pressure, (●) 12°C and (■) 35°C. Data of Diepen and Scheffer (63, 64).

thermodynamic pressure effect on the reaction rate constant. In terms of transition state theory (17), the reactants are in thermodynamic equilibrium with a transition state. Once the transition state complex is formed it proceeds directly to products. With this analysis the pressure effect on the reaction rate constant can be given as follows for a bimolecular reaction:



$$RT \frac{\partial \ln k_{\text{bm}}}{\partial P} = -\Delta v^\ddagger - RT k_T \quad (1)$$

where k_{bm} = bimolecular rate constant ($\text{M}^{-1}\text{s}^{-1}$)

$$\Delta v^\ddagger = \bar{v}_{\text{TS}} - \bar{v}_{\text{A}} - \bar{v}_{\text{B}}$$

\bar{v}_i = partial molar volume

k_T = isothermal compressibility

The last term in the equation is a result of the reactant concentrations changing with pressure. If the rate expressions are written in pressure independent units (i.e., mole fraction) then the last term drops out of the equation. While partial molar volumes in liquids are usually only a few cc/gmol, they can be very large negative values in supercritical fluids, with values as large as -15,000 cc/gmol being reported in the literature (18). As a result, the pressure effect on the reaction rate constant can be very significant. This emphasizes that in supercritical fluids the pressure effect on the reaction rate constant reflects the relative strengths of the intermolecular interactions (both the repulsive size effects and the attractive interactions) between the reactants and the transition state with the SCF solvent, as born out in the experimentally determined partial molar volumes. This is very different than the situation in liquid solvents where partial molar volumes are on the order of 5-10 cc/gmol so that the pressure effect on rate constants can be used to discern information on the size change that occurs in going from the reactants to the transition state. For further discussion see Johnston and Haynes (19).

f) Changes in Selectivities. In a situation where several parallel or competing reactions can take place, the thermodynamic pressure effect on each of the individual rate constants may be different; i.e., the activation volumes are not equal for all the reactions. As a result, increased pressure may favor one reaction over the others. In this way, one may be able to control or enhance selectivities for the desired product by operating at the appropriate temperature and pressure. Reactions demonstrating this idea are discussed below. Moreover, competing reactions may be affected in different ways by the local and specific effects described in sections g and h.

g) Effects of Local Densities. A number of spectroscopic and theoretical studies show that the local density of supercritical fluid solvent around a dilute solute molecule can be significantly greater than the bulk density (20-33). This is especially true in the compressible region near the critical point.

Kim and Johnston (20, 21) used the solvatochromic probe phenol blue to show that the wavelength of maximum absorption in supercritical carbon dioxide

shifted to a greater degree than would be predicted for a fluid with a density equal to the bulk. From this they concluded that the local density around the solute was greater than the bulk. Since the mechanism for the wavelength shift involves stabilization of the excited state by its interaction with the dielectric constant and refractive index of the solvent, one would expect this probe to sense the influence of the solvent over several molecular diameters. Lemert and DeSimone (32) have recently used this same technique with a different probe in a number of supercritical solvents to reach similar conclusions.

Also, Brennecke et al. (25) found that the change in the ratio of two peaks in the steady state fluorescence spectra of pyrene, which is sensitive to the immediate solvent environment, corroborated the idea of local densities greater than the bulk. This probe senses the disruption of symmetry of the solute by interaction with surrounding solvents so its field of influence is much shorter than the solvatochromic probes used by Johnston and coworkers, probably extending only over one or two solvent shells. The enhancements were found in fluoroform and ethylene, as well as carbon dioxide.

Kajimoto and coworkers (30, 31) looked at the fluorescence spectra of the twisted intramolecular charge-transfer states of (N,N-dimethylamino)benzotrile in fluoroform and ethane. The shifts were greater than expected for a homogeneous fluid and could be accurately described by a Langmuir type adsorption model of the solvent aggregation about the solute. Sun et al. (33) found the same trends in a more extensive study of this probe. They also looked at the shifts in the emission of ethyl p-(N,N-dimethylamino)benzoate, another probe that is solvent sensitive and exhibits greater than expected shifts in the spectrum in supercritical fluoroform, carbon dioxide and ethane.

In addition, there are several theoretical studies to support the idea of local densities greater than the bulk around a solute in a supercritical fluid solution. One of these is the molecular dynamics (MD) studies of Petsche and Debenedetti (23), which clearly demonstrate that in an attractive mixture modeled with a simple Lennard-Jones potential the environment around a solute molecule is continuously enriched with solvent relative to bulk conditions. Very importantly, they point out the dynamic nature of the cluster, which loses its identity in a few picoseconds. Also important is the work of Lee and coworkers (26-29), who use integral equation theory to calculate radial distribution functions of the solvent around a solute, compared with the solvent around a solvent. Two important features arise. The first peak in the radial distribution function for the solute/solvent is significantly higher than for the solvent/solvent, suggesting a higher density of solvents within the first coordination sphere. In addition, the tail of the solute/solvent distribution function remains above 1 for a much greater distance. As pointed out by Economou and Donohue (34), this long tail on the radial distribution function can, in itself, account for the large negative partial molar volumes of solutes in supercritical fluids. However, the large body of experimental and theoretical results summarized above suggest that there is also an enrichment in the local density around the solute.

An active area of current research addresses the question of whether and in what cases can density enhancements influence reaction rates. Clearly, the general idea of clustering, which includes the long range correlations which result in the large negative partial molar volumes, influences the reaction rate through the pressure effect

on the rate constant, as described in section d) above. However, there is some evidence to suggest that the local density enhancement can influence reactions, as an interpretation of the reactions presented below. We propose that there are two ways that the locally dense solvent could influence a reaction. First, if the reaction is sensitive to any density-dependent property, such as dielectric constant, the time-averaged locally dense medium, which would have a higher dielectric constant than the bulk, might influence that reaction. Second, the solvents around a solute might be seen as a cage, which could prevent entrance or escape of a species, a concept frequently cited in the chemical literature. In this case, an important consideration is the timescale of the solvent cluster relative to the timescale of the reaction. If the local dense solvent cage is to affect a reaction, then the reaction of the two species must take place within the time that the cage has integrity. According to the MD calculations, this is on the order of picoseconds. Therefore, it is not surprising that reactions that occur on a longer timescale might not see any effects of local density, as will be discussed later.

h) Effects of Local Compositions. Another possible effect on the reaction rate in a SCF is changes in local concentrations of reactants. Kim and Johnston (20, 21) showed that in the compressible region near the critical point the local concentration of a cosolvent around a solute molecule could be as high as seven times that in the bulk. In that study they observed the shift of the solvatochromic dye, phenol blue, in mixtures of carbon dioxide and cosolvents (1 - 5.25 mole % acetone, methanol, ethanol or octane) as a function of pressure. At high pressures, sufficiently removed from the critical point of the solution, the local compositions approached those in the bulk. However, at the low pressures, near the critical point of the solution, the local compositions increased dramatically. The question posed by these studies is whether the reaction rate between a solute and a cosolvent can be enhanced because the equilibrium local composition of one of the reactants is increased. A related situation is the interaction or reaction of a dilute solute with itself. It is, in effect, the limiting case in which the concentration of the cosolvent becomes very dilute and is the same species as the solute. Theoretical calculations of the solute/solute radial distribution function (27) suggests that there should be local areas of higher solute concentration or solute aggregates in supercritical fluids. More recently, Chialvo and Debenedetti (35) have performed molecular dynamics simulations of dilute supercritical Lennard-Jones mixtures. They observe large increases in the first peak of the solute/solute radial distribution function, confirming the integral equation calculations. While the dynamics of the solute interactions are still under study, the preliminary results indicate that the solute molecules undergo an increased collision frequency rather than the formation of a compact solute/solute aggregate. However, using high-pressure EPR spectroscopy, Randolph et al. (36) found that cholesterol does form aggregates in supercritical carbon dioxide. The aggregation was a function of pressure and was even more pronounced with the addition of some cosolvents such as branched butanols and ethanol. That same research group went on to find that stearic acid also forms molecular aggregates in supercritical carbon dioxide (37). In these cases specific chemical interactions, such as hydrogen-bonding, may be contributing to the aggregate formation.

In most reactions it is very difficult to separate the many influences of the supercritical fluid solvent mentioned above since many of them may be operating in concert. Moreover, some of the effects (local compositions, solute attraction, local density enhancement) are influences on the microscopic scale, rather than being based on bulk macroscopic properties. Therefore, to study the influence of the supercritical solvent, one must chose simple, well-characterized reactions. In addition, spectroscopic techniques, that inherently give information on the molecular scale, are particularly useful in studying these reactions. Therefore, below we will discuss a small subset of the supercritical reaction literature, i.e., those reactions studied with spectroscopic techniques, as well as a few seminal works studied by other methods. These are typically studies of simple reactions and the emphasis is on developing a better understanding of the various ways the supercritical solvent can influence the reaction. While many interesting works have been published, this purposely omits those involving heterogeneously catalyzed reactions (for example see (6)), enzymatically catalyzed reactions (for example see (38)) and reactions in supercritical water (for example see (39)). The following discussion is divided into five topical areas: 1) influence of diffusion, 2) the thermodynamic pressure effect on the rate constant, 3) solute/solvent clustering or solvent cage formation, 4) solute/solute interactions, and 5) solute/cosolvent clustering. However, please keep in mind that in many of the examples more than one of these factors may be influencing the reaction.

Example Reactions

1) Influence of Diffusion. The only examples we will give of the influence of transport properties on reactions is the effect of increased diffusion. The diffusion coefficient changes dramatically in the region near the critical point so one would expect a corresponding increase in the rate constant for diffusion controlled reactions. This is, indeed, the case; however, many attempts to demonstrate this increase have been complicated by the thermodynamic influences on the reactions discussed below. One of the clearest examples of the increased diffusion is the work of Bright and coworkers, looking at the formation of pyrene excimer with time-resolved fluorescence spectroscopy (40). In decreasing the pressure from 88 to 75 bar at 32°C, the diffusion controlled rate constant increases from 1.1 to $1.7 \times 10^{-11} \text{ M}^{-1} \text{ s}^{-1}$, which corresponds remarkably well with that predicted from the Stokes-Einstein equation and experimental solvent viscosity data. However, in the work of Randolph and Carlier (41), who examined the Heisenberg spin exchange reaction between nitroxide free radicals with electron paramagnetic resonance (EPR) spectroscopy, they observed rate constants near the critical point greater than one would predict from diffusion control. As discussed in more detail below, they attribute this to the solvent cage around the reactants, increasing the likelihood of reaction per collision. Why this effect was not observed in the excimer formation reaction may be due to the fact that the pyrene molecules must be in a planar or sandwich type arrangement in order to form the dimer. Therefore, entropic as well as energetic effects may be important. Conversely, in the work of Roberts et al. (7), they observed rate constants below the diffusion control limit shown in Figure 2 for reactions that should be at or near diffusion control in liquids. Using laser flash photolysis they examined the reaction between benzophenone triplet and two tertiary

amines, triethylamine and 1,4-Diazobicyclo[2.2.2]octane (DABCO) in both CO₂ at 35°C and ethane at 34°C. These are related to the reactions of benzophenone triplet with 2-propanol or 1,4-cyclohexadiene, discussed below in the section on cosolvent effects, except that the mechanism for the reaction is very different. Unlike the slow kinetically controlled hydrogen abstraction from isopropanol or cyclohexadiene, the reaction of benzophenone triplet with the amines proceeds by charge transfer. In CO₂ it is possible that the amines could be slowed by chemical complexation with the solvent, which is known to form carbamates by reaction with primary and secondary amines. However, since the rates are significantly less than diffusion control in ethane, as well, current investigations are under way to determine if significant back reaction is occurring or other possible reasons for the slowed reaction rates.

Unfortunately, most of the other examples in the literature concerned with diffusion of reactants in supercritical fluids involve heterogeneous catalysis. While these are very interesting studies (for example, see the Fischer-Tropsch reactions studied by Yokota and Fujimoto (42, 43)), they frequently involve other factors, such as the solubilization of waxes and other heavy species that might poison the surface. As a result, it is somewhat more difficult to isolate the influence of diffusion on the reaction.

Finally, another work concerned with diffusion is that of Wu and coworkers (44). They define an activation volume for diffusion, which is the pressure effect on the rate caused by the change in the diffusion coefficients and present a formalism whereby the apparent activation volume can be expressed as the sum of various contributions. The first two contributions, the mechanical pressure effect and the compressibility, are those in equation (1) above. They add an additional term for the activation volume for diffusion; i.e., for a diffusion controlled reaction this would be the dominant term. The next term is one for electrostriction, such as that encountered in the exciplex reaction discussed in the next section. In actuality, the partial molar volume resulting from long-range electrostatic forces, electrostriction, is a part of the true total partial molar volume of that solute. By making it a special term, one is dividing the actual partial molar volume of a solute into that resulting from van der Waals type forces and described by a normal equation of state, and those contributions resulting from the electrostatic attractions. Finally, they add a term for phase behavior effects so that reactions that are taking place in more than one phase can be analyzed. Using this formalism they analyze several reactions, including the pyrolysis of benzyl phenyl ether and dibenzyl ether in toluene and the hydrolysis of dibenzyl ether, phenethyl phenyl ether and guaiacol in water. This method of analysis is particularly useful for these multistep reactions. However, it may miss much of the local, microscopic scale, and specific chemical effects discussed below that we show are very important in influencing reactions in supercritical fluids.

2) The Thermodynamic Pressure Effect on the Rate Constant. Some of the earliest spectroscopic studies of the influence of a supercritical solvent on reactions investigated the pressure effect on the rate constant. Several demonstrated dramatic influences of pressure, with activation volumes of several thousand cc/gmol, resulting in order of magnitude changes in the rate constant with small changes in pressure. This is clearly the predominant effect of pressure in many SCF reactions. Unfortunately, it is difficult to predict this effect with much accuracy since one must

calculate the difference in the partial molar volumes of the transition state and the reactants. Very few experimental values of partial molar volumes in SCF's are available. Calculating partial molar volumes from an equation of state provides a reasonable estimate at best because partial molar volumes are derivative properties and very sensitive to the interaction energy between the solute and the SC solvent.

One of the first works showing a dramatic pressure effect was the Diels-Alder reaction of isoprene and maleic anhydride in supercritical carbon dioxide (45). Paulaitis and Alexander observed a two fold increase in the rate constant at 35°C with a 10 bar increase in pressure. The rate constant continued to increase with increasing pressure until it approached that obtainable in liquid solutions at high pressure, where the fluid is more liquid-like. The pressure effect was significantly less pronounced at higher temperatures, away from the critical temperature of the pure solvent ($T_C = 31^\circ\text{C}$, $P_C = 72.8$ bar for carbon dioxide). Undoubtedly correctly, the authors attributed the dramatic decrease in the rate constant as the pressure was lowered to the critical point to the thermodynamic pressure effect on the rate constant.

Another example of the pressure effect on the rate constant is the work of Johnston and Haynes (19), who used UV-Vis absorption spectroscopy to obtain the kinetics for the unimolecular decomposition of α -chlorobenzyl methyl ether in supercritical 1,1-difluoroethane. They observed an even larger decrease in the rate constant as the pressure was lowered towards the critical point, a change of approximately seven fold with a 14 bar change in pressure, which corresponds to an activation volume of approximately -6000 cc/mol. They were able to correlate the rate constant for this reaction with the absorption transition energy of a solvatochromic probe, which suggests that the aspects of the solvent that are influencing the energy levels of the probe are the same as those influencing the reaction. This could include both short range and longer range interactions. Johnston's group also examined a network of two parallel Diels-Alder reactions and were the first to show that the selectivity, albeit a rather modest increase, in a reaction network could be controlled with pressure (46). In this case, the activation volumes, specifically the partial molar volume of the transition state, must be slightly different for the two reactions.

The first attempt to compare measured values of the pressure effect on a rate constant and calculated values of the activation volume were for the exciplex formation between naphthalene and triethylamine in a study by Eckert and coworkers (47). This is an excited state reaction that takes place only after the naphthalene is irradiated and promoted to the first excited singlet state. Since the exciplex formation was monitored by examining the steady state fluorescence of the exciplex, the absolute rate of the exciplex formation could not be determined directly. However, the pressure effect on that rate constant was found to be very pronounced at pressures and temperatures near the critical. The estimated pressure effect on the rate constant was calculated from the Peng-Robinson equation of state (48) plus an extra term for the electrostriction of the solvent around the transition state, which is believed to have a very large dipole moment of 11.1 Debye. The calculated values of the activation volume, as shown in Figure 3 and reaching an extreme value of -14,000 cc/mol, were dominated by the electrostriction and showed essentially the same trend as the experimental data. Clearly, this is one of the most dramatic pressure effects on a reaction available in the literature.

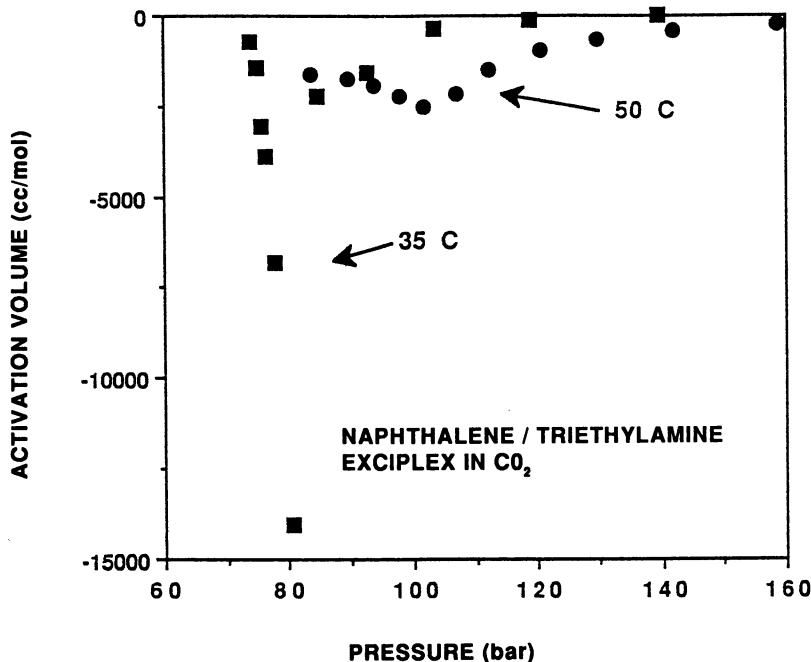


Figure 3. Activation volume for the triethylamine/naphthalene exciplex formation at 35°C (■) and 50°C (●) in supercritical carbon dioxide, as predicted from the Peng-Robinson equation of state and electrostriction. Adapted from reference (47).

The thermodynamic pressure effect can also influence the equilibrium for a reversible reaction since that equilibrium constant is just the ratio of the forward and reverse rate constants. In the dimerization equilibrium of 2-methyl-2-nitrosopropane in carbon dioxide, Yoshimura and Kimura used UV-Vis absorption spectroscopy to show first a decrease and then an increase in the equilibrium constant with increasing pressure (49). This was rationalized as the changing ratio of activation volumes for the two reactions with pressure. To reproduce such a trend they were forced to include three body interactions in their calculation of the activation volume from radial distribution functions. In a later study (50), they examined the kinetics of just the dissociation reaction. For this reaction they observed a slight decrease in the rate constant with increasing pressure, resulting in an activation volume of approximately +300 cc/gmol. They suggest that the activation volume might be calculated using the second virial coefficient; however, additional terms of the virial equation would be necessary to give reasonable estimates of partial molar volumes in the supercritical region.

There have been additional studies of Diels-Alder reactions in supercritical carbon dioxide using IR spectroscopy, including the catalyzed reaction of isoprene and maleic anhydride (51) and the uncatalyzed reaction of isoprene with methyl acrylate (52). Like Paulaitis and Alexander (45), Ikushima and coworkers observed

an increase in the rate constant with increasing pressure, corresponding to an activation volume of approximately -800 cc/gmol and, using a method similar to that of Johnston and Haynes (19), were able to correlate the observed rates with the absorption maxima of a solvatochromic probe. More interestingly, they observe a marked change in the isomer distribution with pressure, changing from over 99% of one product at atmospheric pressure to over 60% of the other isomer near the critical pressure. They suggest that strong solvent/transition state interactions and the aggregation of solvent molecules around the transition state (local density enhancements and solvent cage formation are discussed below) favor one isomer over the other.

In summary, there have been a number of studies that have demonstrated dramatic pressure effects on rate constant for reactions in supercritical fluids. Clearly, in many of the reactions described above the thermodynamic pressure effect on the rate constant is the dominant influence on the reaction rate. These studies show that reaction rates and selectivities in reaction networks can be controlled with small changes in pressure. At present, the main difficulty is prediction of the thermodynamic pressure effect on reactions. This is, in part, because one usually does not know the characteristics of the transition state. However, it is generally difficult to accurately calculate the partial molar volumes in the compressible region near the critical point, that make up the activation volume, with an equation of state.

3) Solute/solvent Clustering or Solvent Cage Formation. The evidence for the influence of increased local solvent density on reactions is very limited and the reported mechanism for that influence varies greatly. We do not know of any examples in which the physical properties of the local dense solvent, such as increased dielectric constant caused by the increased local density, has been shown to directly influence a reaction. However, examples (a) and (b) below are ones in which the influence of the average higher local density is felt. Examples (c) and (d) address the possibility of the formation of solvent cages, that would prevent the entrance or escape of species. In this case, we believe that the important factor in determining whether the solvent cluster will influence the reaction in any way is the timescale of the reaction. If the reaction takes place within the period in which the solvent cluster maintains its integrity, which according to the calculations of Petsche and Debenedetti (23) is on the order of a few picoseconds, one might anticipate some effect of that solvent shell. Even in more asymmetric mixtures than the neon/xenon system they simulated, we do not imagine that the persistence time of the cluster would be more than several hundred picoseconds. We hope to show that the reaction data presented in the literature thusfar is consistent with this view. The studies we will discuss below examine the influence or lack of influence of the solvent shells in terms of a) changing the activation energy of the reaction, b) changing stereoselectivity and regioselectivity by solvent reorganization, c) increasing the probability of reaction per collision, and d) the distribution of recombination products.

(a) Troe and coworkers (53) used picosecond laser flash photolysis to examine the photoisomerization of diphenylbutadiene in liquid and supercritical alkanes, carbon dioxide, sulfur hexafluoride and helium. They observed an increase in the unimolecular rate constant in the region near the critical point where local density augmentations are likely to occur. They attribute the acceleration in the rate

to the solvent lowering the activation energy for the reaction by forming a cluster with the reactant prior to excitation. In other words, the solvent aggregation can move the energy level of the reactants and/or the activated complex to enhance the reaction rate. One would anticipate this to be an effect of the thermodynamically controlled average higher local density and be prevalent even if the reaction were slow. However, the rate constants in this reaction are approximately 10^9 s^{-1} , which is very fast and on the timescale that the cluster would maintain its integrity, so while this reaction demonstrates the influence of the increased local density one cannot draw any information on the importance of timescales from this reaction.

(b) In a study of the photodimerization of isophorone in supercritical trifluoromethane and carbon dioxide by Hrnjez et al. (54), the rate of dimerization was not reported since the study only examined the product distribution. The samples were irradiated with a mercury lamp and the products analyzed by gas chromatography. The results indicate that both the regioselectivity and the stereoselectivity of the products are functions of pressure, especially in the polar solvent. They attribute their results to the need for solvent reorganization around the solutes when the isophorone dimerized to the various configurations. This is an interesting example of not just the energetics of solvent clustering but the entropic considerations as well. Once again, one would expect this effect to be seen even over long timescales, since it involves the equilibrium arrangement of solvent molecules around the more or less polar transition state. Since the rates are not reported, one can only presume this is the case in the reaction.

(c) Like the above study, the Heisenberg spin exchange reaction between nitroxide free radicals in near- and supercritical ethane (41) was undoubtedly undertaken to investigate the possibility of solute/solute aggregation but yielded information on solute/solvent clustering. In this reaction, investigated with electron paramagnetic resonance (EPR) spectroscopy, the bimolecular rate constant for spin exchange should approach diffusion control and the measured rates are in fact on the order of $10^{11} \text{ M}^{-1} \text{ s}^{-1}$. As expected, Randolph and Carlier found that the rates increase at lower pressure, where diffusion coefficients increase. However, in the low pressure region near the critical point, the rate constants are actually greater than those predicted from diffusion control! The authors attribute this phenomenon to solvent cage effects, rather than solute clustering since the rate constants were independent of solute concentration. They suggest that a solvent cage around the two radicals could result in a longer collision time, which would induce a stronger spin exchange and a higher rate of reaction. They clearly point out that the timescale of the collision is on the order of 0.01 ps, well below the several picosecond lifetime of the clusters predicted by Petsche and Debenedetti (23), while the characteristic time for the diffusion is on the order of nanoseconds. As a result, one might expect the solvent cluster to influence the collisions but not the diffusion. This is the first indication that the short-lived solvent cages formed by SCF solvents around solutes can be used to influence reactions.

(d) In the analysis of products from the recombination of fragments from the photofragmentation of two dibenzylketones, O'Shea et al. (55) did not observe any evidence of solvent cage effects. The fragmentation of the parent compound, $\text{B}(\text{CO})\text{X}$, takes place in two steps: first, the formation of radicals $\text{B}(\text{CO})\cdot$ and $\text{X}\cdot$ or $\text{B}\cdot$ and $(\text{CO})\text{X}\cdot$. This takes place very quickly but the next step, the decarbonylation,

where one forms $B\cdot$, CO , and $X\cdot$, is much slower, on the order of hundreds of nanoseconds (56, 57). The O'Shea study looked at the product distribution of the recombination products of benzyl radical ($B\cdot$) and p-xylyl radical ($X\cdot$), i.e., BB , BX or XX , which would be formed most readily after the decarbonylation. The recombination of the radicals formed in the first step ($B(CO)\cdot$ and $X\cdot$ or $B\cdot$ and $(CO)X\cdot$) could be on the order of picoseconds and see the influence of the solvent cage. However, one would not expect to see any solvent cage effects on the $X\cdot$ and $B\cdot$ recombination since the time required to form them, i.e., the decarbonylation rate, is much slower than the persistence time of the solvent clusters. Therefore, it is not surprising that the researchers observe a statistical distribution of the recombination products. This supports our proposition that for a solvent "cage" to influence a reaction in a SCF the reaction must take place before the solvent molecules have time to exchange with other solvent molecules in the bulk.

One other interesting piece of work that yields some information on local solvent densities that is not as easily categorized as those above are the iodine recombination experiments of Troe and coworkers in sub- and supercritical hydrocarbons (58). In the laser photoexcitation of iodine, a caged atomic iodine pair is formed. A simple analysis suggests that either the pair can recombine within the cage or diffuse out of the cage to form free iodine radicals. Therefore, the quantum yield of iodine radicals is a function of the rates of the two possibilities, geminate recombination or diffusion out of the cage. In the original paper, the authors suggested that the excess decrease in the quantum yield at higher densities (over that predicted from diffusion control) was due to stoichiometric complexation of the iodine with solvents, which prevented its dissociation. Later, Combes et al. (59) suggested that the data could be better described by a physical density augmentation that influenced the rate constant of the recombination reaction. It is entirely reasonable that the local density augmentation near the critical point could influence this reaction since the reactions are at or near diffusion control, with bimolecular rate constant on the order of $10^{10}M^{-1}s^{-1}$.

In summary, the reaction rate evidence presented thusfar supports the idea that increased local solvent densities in the compressible region near the critical point can influence reactions by the equilibrium presence of a higher density around the reactant or products, stabilizing a transition state or the formation of a certain product. Conversely, if the solvent cage formed by the locally dense fluid is to affect the reaction it must take place within the time that the solvent cage is believed to maintain its integrity, which is on the order of picoseconds.

4) Solute/cosolvent Clustering. The influence of changing local cosolvent concentrations around a solute in the region near the critical point is addressed in the work of Roberts et al. (60, 61). They examine the reaction between benzophenone triplet and two substrates, isopropanol and cyclohexadiene, using laser flash photolysis. The reactants were chosen to mimic the situation investigated by Kim and Johnston (20, 21); i.e., a dilute solute (benzophenone triplet) and a cosolvent (isopropanol or cyclohexadiene) in supercritical carbon dioxide. The measured bimolecular rate constants increase by a factor of 3 to 5 as the pressure is lowered to conditions near the critical point, as shown in Figure 4. This increase in the rate

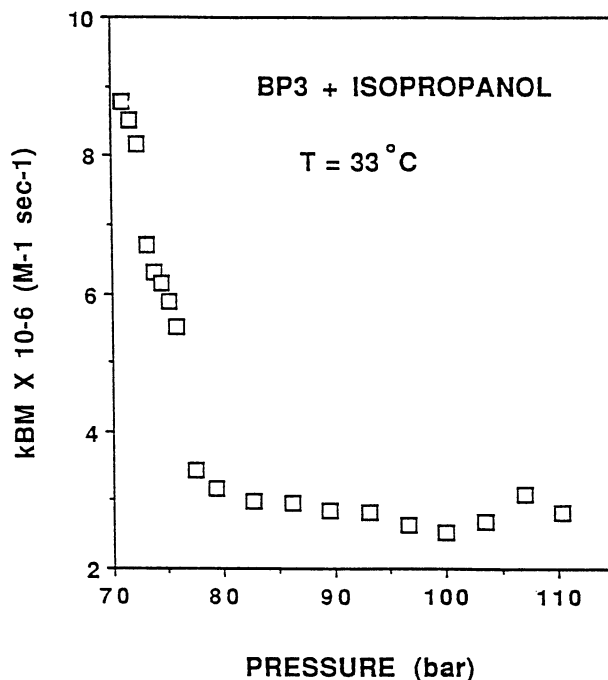


Figure 4. The bimolecular rate constant for the hydrogen atom abstraction reaction between benzophenone triplet and isopropanol at 33°C, as measured by laser flash photolysis. Adapted from reference (60).

constant could not be explained by the pressure effect on the rate constant, which is predicted using the Peng-Robinson equation (48) to be in the opposite direction of the observed results. The authors believe that the most reasonable explanation for the increase in the rate at lower pressure is the increasing local composition of the substrate around the benzophenone triplet, so that the apparent increase in the bimolecular rate constant actually reflects a dramatic increase in the local composition that more than compensates for the inherent decrease in the actual rate constant. To our knowledge, this is the only example in the literature of enhanced reaction rates due to local cosolvent composition increases.

5) Solute/solute Interactions. Solute/solute interactions is the limiting case of cosolvent clustering around solutes, in which the cosolvent becomes very dilute and is the same species as the solute. Beside the local composition measurements of Kim and Johnston (20, 21), direct calculations of the pair distribution function (26-29) and the molecular dynamics results of Chialvo and Debenedetti (35) suggest that the probability of finding another solute in the first shell around a central solute molecule is greater than that calculated based on bulk compositions. Therefore, based on theoretical calculations, one would expect to see some influence of solute aggregation on reactions. Interestingly, at present, the results of dimerization reactions reach conflicting conclusions.

In the photodimerization of cyclohexenone (59) Johnston and coworkers attribute changes in the regioselectivity of the product to solute clusters that increase the local dielectric constant when operating in the region near the phase boundary, i.e., at low pressures near the critical point of the solution. Like the photodimerization of isophorone discussed above, this reaction was initiated with a mercury lamp and the products analyzed by gas chromatograph. The head-to-head dimer (versus head-to-tail) is the more polar species so its formation generally increases with increasing solvent polarity in liquids. In supercritical ethane, as the pressure is lowered to the critical point, it is the head-to-head species that becomes more prevalent, so the authors suggest that even though the bulk dielectric constant is decreasing, the local dielectric constant due to solute aggregation is increasing.

Conversely, in the spin exchange reaction between nitroxide free radicals (41) Randolph and Carlier do not believe that they see any influence of solute/solute interactions because the rate constant is not a function of solute concentration.

Similarly, using time-resolved fluorescence spectroscopy, Bright and coworkers (40) did not see any evidence of solute/solute aggregation in the examination of the rate of formation of pyrene excimers (excited state dimers). The rate exactly followed that predicted by diffusion control, assuming a uniform initial distribution of solute molecules, as discussed above. The prevalence of excimer formation in the steady state fluorescence spectra (47) was attributed solely to a decrease in the reverse reaction relative to liquid solutions. This leads to the conclusion that solute aggregates or clusters either do not exist or do not influence the pyrene excimer formation reaction.

In summary, there have not been any definitive experimental measurements of dimerization rates in supercritical fluids that show the influence of solute aggregation or attraction even though theoretical calculations show that solute/solute interactions are strong in the near critical region. In fact, the results of several of the studies above would lead one to believe that solute/solute interactions in the critical region do not influence reactions. We do not believe that it is a matter of the reactions taking place on a longer timescale than the persistence time of a solute/solute cluster since both the spin exchange reaction and the excimer formation are at or near-diffusion control, having characteristic timescales less than a nanosecond. One might question whether the concentrations used in the dimerization reactions are sufficiently high. This may be important since the MD results (35) suggest that the large first peak in the radial distribution function would lead to increased probability of collision rather than indicate bound solute aggregates. The highest concentration in the excimer studies was 100 μM and in the spin exchange reaction 2 mM. However, in the dimerization of cyclohexenone, which did show solute aggregation effects, the experiments took place at concentrations as high as 100 mM. Therefore, in the examination of dimerization reactions, scanning a wide range of concentrations may be important in observing any influence of solute/solute interactions. More experimental measurements of dimerization rates, static measurements of local concentrations and theoretical calculations are required to bridge the gap between theory and experiment on this subject.

Summary

In this paper we have reviewed the various ways that a supercritical solvent can influence homogeneous uncatalyzed reactions and given examples of a number of reactions studied by spectroscopic techniques. It is possible to enhance and control reactions in SCF's by:

- 1) Taking advantage of the equilibrium phase behavior, such as increased reactant solubility, elimination of mass transfer resistances or ease of product separation.
- 2) The thermodynamic pressure effect on the rate constant, which can be orders of magnitude more dramatic than seen in liquid solvents. However, it is difficult to predict activation volumes in SCF's.
- 3) a) The increased local density of the solvent around a solute, whether due to the time-averaged effect or the formation of short-lived solvent cages, b) the increased local concentration of cosolvents, and c) possibly higher local concentration of solutes, in the compressible region near the critical point.
- 4) Increased diffusion in diffusion-controlled reactions.

In any given reaction more than one of the effects mentioned above may be operative simultaneously so care must be taken in the interpretation of kinetics data. We have emphasized that local molecular phenomenon can influence the reaction rates, so that an understanding of the bulk physical properties of the solvent may not be sufficient to predict the pressure effect on the reaction rate in supercritical fluids. As a result, spectroscopic studies that probe molecular scale interactions and reactivity will continue to be instrumental in developing a detailed understanding of supercritical fluids as reaction media.

Acknowledgments

This work was supported by the National Science Foundation under grants NSF-CTS 90 09562 and NSF-CTS 91-57087 and the American Chemical Society Petroleum Research Fund grant 22947-G5. I would like to thank Dr. John E. Chateaufneuf and Christopher B. Roberts for their helpful discussions.

Literature Cited

1. Paulaitis, M. E.; Krukonis, V. J.; Kurnik, R. T.; Reid, R. C. Rev. Chem. Eng., **1982**, *1*(2), 179.
2. McHugh, M. A.; Krukonis, V. J. Supercritical Fluid Extraction: Principles and Practice, Butterworths, Boston, **1986**.
3. Johnston, K. P.; Peck, D. G.; Kim, S. Ind. Eng. Chem. Res., **1989**, *28*, 1115.
4. Brennecke, J. F.; Eckert, C. A. AIChE J., **1989**, *35*(9), 1409.
5. Subramanian, B.; McHugh, M. A. Ind. Eng. Chem. Process Des. Dev., **1986**, *25*, 1.
6. Tiltscher, H.; Hofmann, H. Chem. Engr. Sci., **1987**, *42*(5), 959.

7. Roberts, C. B.; Chateaufneuf, J. E.; Brennecke, J. F. In Proceedings of the Sixth International Conference on Fluid Properties & Phase Equilibria for Chemical Process Design, Cortina, Italy, July, 1992.
8. Poliakov, M.; Howdle, S. M.; Healy, M. A.; Whalley, J. M. Proc. Internat. Symp. on Supercritical Fluids, ed. M. Perrut, Soc. Chem. Franc., 1988, p. 967.
9. Howdle, S. M.; Poliakov, M. J. Chem. Soc. Chem. Commun., 1989, 1099.
10. Howdle, S. M.; Grebenik, P.; Poliakov, M. J. Chem. Soc. Chem. Commun., 1989, 1517.
11. Howdle, S. M.; Healy, M. A.; Poliakov, M. J. Am. Chem. Soc., 1990, 112, 4804.
12. Jobling, M.; Howdle, S. M.; Healy, M. A.; Poliakov, M. J. Chem. Soc. Chem. Commun., 1990, 1287.
13. Jobling, M.; Howdle, S. M.; Poliakov, M. J. Chem. Soc. Chem. Commun., 1990, 1762.
14. Poliakov, M.; Howdle, S. M.; Jobling, M.; George, M. W. Proc. 2nd Internat. Symp. on Supercritical Fluids, ed. M. McHugh, 1991, p. 189.
15. Kramer, G. M.; Leder, F. U.S. Patent 3 880 945, 1975.
16. Tiltscher, H.; Wolf, H.; Schelchshorn, J. Ber. Bunsenges. Phys. Chem., 1984, 88, 897.
17. Evans, M.G.; Polanyi, M. Trans. Faraday Soc., 1935, 31, 875.
18. Ziger, D. H.; Johnston, K. P.; Kim, S.; Eckert, C. A. J. Phys. Chem., 1986, 86, 2738.
19. Johnston, K. P.; Haynes, C. AIChE J., 1987, 33(12), 2017.
20. Kim, S.; Johnston, K. P. AIChE J., 1987, 33(10), 1603.
21. Kim, S.; Johnston, K. P. Ind. Eng. Chem. Res., 1987, 26, 1206.
22. Debenedetti, P. G. Chem. Engr. Sci., 1987, 42(9), 2203.
23. Petsche, I. B.; Debenedetti, P. G. J. Chem. Phys., 1989, 91(11), 7075.
24. Brennecke, J. F.; Eckert, C. A. In Supercritical Fluid Science and Technology; ACS Symposium Series 406; Johnston, K. P.; Penninger, J., Eds.; American Chemical Society; Washington, DC, 1989.
25. Brennecke, J. F.; Tomasko, D. L.; Peshkin, J.; Eckert, C. A. Ind. Eng. Chem. Res., 1990, 29(8), 1682.
26. Pfund, D. M.; Lee, L. L.; Cochran, H. D. Fluid Phase Equilib., 1988, 39, 161.
27. Wu, R.; Lee, L. L.; Cochran, H. D. Ind. Eng. Chem. Res., 1990, 29, 977.
28. Pfund, D. M.; Lee, L. L.; Cochran, H. D. J. Chem. Phys., 1991, 94(4), 3107.
29. Pfund, D. M.; Lee, L. L.; Cochran, H. D. J. Chem. Phys., 1991, 94(4), 3114.
30. Kajimoto, O.; Futakami, M.; Kobayashi, T.; Yamasaki, K. J. Phys. Chem., 1988, 92, 1347.
31. Morita, A.; Kajimoto, O. J. Phys. Chem., 1990, 94, 6420.
32. Lemert, R. M.; DeSimone, J. M. J. Supercrit. Fluids, 1991, 4, 186.
33. Sun, Y.-P.; Fox, M. A.; Johnston, K. P. J. Am. Chem. Soc., 1992, 114, 1187.
34. Economou, I. G.; Donohue, M. D. AIChE J., 1990, 36(12), 1920.
35. Chialvo, A. A.; Debenedetti, P. G. Ind. Eng. Chem. Res., 1992, 31, 1391.
36. Randolph, T. W.; Clark, D. S.; Blanch, H. W.; Prausnitz, J. M. Science, 1988, 239, 387.
37. Miller, D. A.; Clark, D. S.; Blanch, H. W.; Prausnitz, J. M. J. Supercrit. Fluids, 1991, 4(2), 124.
38. Miller, D. A.; Blanch, H. W.; Prausnitz, J. M. Ind. Eng. Chem. Res., 1991, 30, 939.

39. Shaw, R. W.; Brill, T. B.; Clifford, A. A.; Eckert, C. A.; Franck, E. U. C & EN, **1991**, *69*(51), 26.
40. Zagrobelny, J.; Betts, T. A.; Bright, F. V. J. Am. Chem. Soc., **1992**, in press.
41. Randolph, T. W.; Carlier, C. J. Phys. Chem., **1992**, in press.
42. Yokota, K.; Fujimoto, K. Fuel, **1989**, *68*, 255.
43. Yokota, K.; Fujimoto, K. Ind. Eng. Chem. Res., **1991**, *30*, 95.
44. Wu, B. C.; Klein, M. T.; Sandler, S. I. Ind. Eng. Chem. Res., **1991**, *30*, 822.
45. Paulaitis, M. E.; Alexander, G. C. Pure & Appl. Chem., **1987**, *59*(1), 61.
46. Kim, S.; Johnston, K. P. Chem. Eng. Commun., **1988**, *63*, 49.
47. Brennecke, J. F.; Tomasko, D. L.; Eckert, C.A. J. Phys. Chem., **1990**, *94*, 7692.
48. Peng, D.-Y.; D.B. Robinson Ind. Eng. Chem. Fund., **1976**, *15*(1), 59.
49. Kimura, Y.; Yoshimura, Y.; Nakahara, M. J. Chem. Phys., **1989**, *90*(10), 5679.
50. Yoshimura, Y.; Kimura, Y. Chem. Phys. Lett., **1991**, *181*(9), 517.
51. Ikushima, Y.; Saito, N.; Arai, M. Bull. Chem. Soc. Jpn., **1991**, *64*, 282.
52. Ikushima, Y.; Saito, N.; Arai, M. J. Phys. Chem., **1992**, *96*, 2293.
53. Gehrke, Ch.; Schroeder, J.; Schwarzer, D.; Troe, J.; Voß, F. J. Chem. Phys., **1990**, *92*(8), 4805.
54. Hrnjez, B. J.; Yazdi, P. T.; Fox, M. A.; Johnston, K. P. J. Am. Chem. Soc., **1989**, *111*, 1915.
55. O'Shea K. E.; Combes, J. R.; Fox, M. A.; Johnston, K. P. Photochem. and Photobiol., **1991**, *54*, 571.
56. Lunazzi, L.; Ingold, K. U.; Scaiano, J. C. J. Phys. Chem., **1983**, *87*(4), 529.
57. Turro, N. J.; Gould, I. R.; Baretz, B. H. J. Phys. Chem., **1983**, *87*(4), 531.
58. Otto, B.; Schroeder, J.; Troe, J. J. Chem. Phys., **1984**, *81*(1), 202.
59. Combes, J. R.; Johnston, K. P.; O'Shea, K. E.; Fox, M. A. In Supercritical Fluid Technology; ACS Symposium Series 488; Bright, F. V.; McNally, M. E. P., Eds., American Chemical Society, Washington, D.C., **1992**.
60. Chateaneuf, J. E.; Roberts, C. B.; Brennecke, J. F. In Supercritical Fluid Technology; ACS Symposium Series 488; Bright, F. V.; McNally, M. E. P., Eds., American Chemical Society, Washington, D.C., **1992**.
61. Roberts, C. B.; Chateaneuf, J. E.; Brennecke, J. F. submitted to J. Am. Chem. Soc., **1992**.
62. Iwasaki, H.; Takahashi, M. J. Chem. Phys., **1981**, *74*(3), 1930.
63. Diepen, G. A. M.; Scheffer, F. E. C. J. Am. Chem. Soc., **1948**, *70*, 4085.
64. Diepen, G. A. M.; Scheffer, F. E. C. J. Phys. Chem., **1953**, *57*, 575.

RECEIVED June 15, 1992

Chapter 17

Fluorescence Spectroscopy Study of Alcohol–Solute Interactions in Supercritical Carbon Dioxide

David L. Tomasko¹, Barbara L. Knutson², Joseph M. Coppom²,
Wendy Windsor², Barry West², and Charles A. Eckert²

¹Department of Chemical Engineering, University of Illinois,
Urbana, IL 61801

²School of Chemical Engineering and Specialty Separations Center,
Georgia Institute of Technology, Atlanta, GA 30332–0100

The addition of cosolvent to a supercritical fluid (SCF) can enhance both solubilities and selectivities through specific interactions with the solute of interest. Characterizing the phase behavior in these solutions calls for a molecular level understanding of the local solvent structure and interaction strength around the solute. We describe fluorescence spectroscopy experiments to probe the structure and interaction between methyl alcohol cosolvent and the solute 7-azaindole. The results indicate that the interaction between cosolvent and solute in these systems is quite different than the usual hydrogen bonding observed in liquids. Specifically, there is a clear interaction between solutes and alcohol even at 0.5% alcohol but there is no evidence for stoichiometric hydrogen bonded complexes in supercritical fluid solutions.

Supercritical fluids are currently attracting interest for specialty separations and reactions (1-6). Many of these applications rely on tailored solvents to enhance the specific interactions that increase activities in solution or improve kinetic processes. Cosolvents added to an SCF are a common method of tailoring the solvent and provide an essentially infinite variety of chemical interactions. Before applying SCF technology to a given problem, one runs into several difficulties; foremost is the dearth of reliable experimental data involving cosolvents and also the inability of most phase equilibria models to handle solutions in which strong specific interactions occur.

An important aspect of solution behavior in these highly compressible fluids is the solvent structure about the solute. Several non-thermodynamic techniques (both spectroscopic and computational) have given consistent results showing the local solvent density to be significantly larger than the bulk, an idea that has evoked names such as "clustering," "condensation," and "charisma." (7-12). If the solvent density is enhanced around the solute, it seems reasonable to assume that the cosolvent concentration will be enhanced in the cybotactic region particularly when the cosolvent is capable of participating in a specific interaction (e.g. hydrogen bonding) with the solute. Substantial evidence exists for local composition enhancement in liquid solutions (13-16) along with a few studies in SCF's (17,18).

0097-6156/93/0514-0220\$06.00/0
© 1993 American Chemical Society

Most studies of local composition rely on data over the entire range of solvent/cosolvent composition; however, the range of interest to SCF technology is primarily 0–10% cosolvent. An alternative approach to studying these effects is the use of spectroscopic probes that form charge-transfer complexes or undergo excited state reactions which are more sensitive to the small concentrations of cosolvent. These processes can easily be monitored with fluorescence spectroscopy and may give some insight into specific cosolvent/solute interactions.

Spectroscopy has developed into a particularly useful tool for looking at local interactions in solution primarily because it is non-invasive and it measures the number of interactions rather than the activity of the solute, as in a thermodynamic measurement. The challenge for spectroscopic techniques is two-fold. First, the relationship with thermodynamics is subjective and correlative at present although there is much current activity in this area. Second, in order to interpret spectroscopic results in SCF's one must have some knowledge of the interactions beforehand, i.e. currently one uses the spectroscopic probes to get information about the solvent whereas in liquids the opposite is true. In our work, we have chosen systems that have been fairly well characterized in liquids to indicate the difference in solvent environment when placed in a supercritical fluid.

Experimental

The apparatus for carrying out fluorescence measurements on supercritical solutions has been described elsewhere (11). Cosolvent solutions were prepared in the following manner: A small filter paper was coated with a desired amount of solute from liquid solution and the solvent allowed to evaporate. The filter paper was attached to the top plug of a 1.6 liter pressure vessel and the entire vessel evacuated for thirty minutes down to < 0.15 torr. The solute used in this study has a significantly lower vapor pressure than 0.15 torr so it is unlikely that any sample was lost during this procedure. While evacuating the large vessel, a predetermined amount of cosolvent was weighed into a smaller pressure vessel which was connected in series with the larger vessel. The smaller vessel was sealed and the larger evacuated; then the two were opened to each other and gaseous solvent (CO₂ in this case) was flushed through both at 100 psi in order to remove any air in the cosolvent vessel and connecting tubing. The solvent was flushed through three separate times. While compressing the solvent into the vessels the cosolvent vessel was heated 20–40°C above the boiling point of the cosolvent to ensure vaporization of the cosolvent and complete transfer into the larger mixing vessel. The solvent was compressed to the desired density then the large vessel was isolated from the cosolvent vessel and compressor. Heating tape was placed on one side of the vessel to induce thermal currents and the solution was allowed to mix for a period of 24 hours. The resulting solution was analyzed by gas chromatography to determine the actual mole fraction of cosolvent.

Results and Discussion

7-Azaindole is a sensitive probe of solvent structure in the respect that one can monitor two independent interactions with the cosolvent. First, the tautomer of azaindole resulting from double proton transfer can be observed as a broad structureless emission red-shifted from the monomer by 150–180 nm. Second, an exciplex emission arising from an excited state alcohol-azaindole complex can be observed as a distinct red-shifted peak (20–30 nm) similar in shape and overlapping with the monomer fluorescence band.

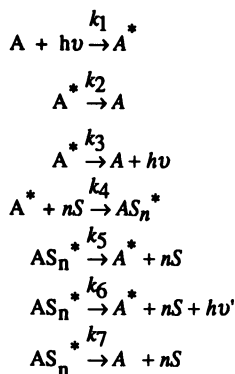
In order to observe tautomer fluorescence, it is proposed that a cyclic hydrogen bonded complex must form in the ground state to prepare for excited state proton transfer (Figure 1). This process was found to require one alcohol molecule per azaindole molecule and the formation of the complex must compete with alcohol association (19,20).

The exciplex between alcohols and 7-azaindole has been studied quite thoroughly. Collins (21) compared alcohol and water solutions with pure hydrocarbon solutions and noted that the position of the azaindole emission shifted sharply with added alcohol at concentrations below 0.1 M. She also noted the initial broadening then narrowing of the overall band width (fwhm) indicative of two species emitting at intermediate alcohol concentrations with complete conversion to exciplex fluorescence at concentrations greater than 0.1 M. Figure 2 shows the proposed mechanism of exciplex formation wherein the non-bonded electrons on the hydroxylic oxygen interact with the vacant π orbital of the excited azaindole. The monomer/exciplex fluorescence band appears to go through a minimum in intensity at 0.5 M alcohol and the greater intensity at higher concentrations is attributed to exciplex formation with aggregated alcohol. Through a kinetic analysis, the exciplex was found to result from a single alcohol complexing with a single azaindole molecule.

Results are presented for 7-azaindole in supercritical CO₂ with 0.5, 1.0, 2.0, and 4.5 mole percent methanol as a cosolvent. Figure 3 shows spectra at all concentrations of cosolvent and at approximately the same mixture density (18 mole/l). The fluorescence intensities do not necessarily correspond to the alcohol concentration due to fluctuations in lamp intensity. Two features are of note: first, the successive addition of alcohol shows a clear transition from monomer emission in pure SCF to exciplex emission in the mixture; second, even at 4.5% alcohol no proton transfer has occurred.

In order to draw conclusions about the solvent environment, we would like to be sure that the photophysical mechanisms are the same as in liquid solvents. The double proton transfer, highly specific and configuration dependent, would most likely result from the ground state hydrogen bonded complex only. However, the exciplex, an electronic interaction, may be influenced mechanistically by the drastic change in solvent environment. To explore this possibility, we have analyzed the exciplex formation using the kinetic model of Walker and coworkers (22) to highlight any discrepancies between the liquid and SCF solutions.

The formation of the exciplex can be modelled with the kinetic scheme shown below.



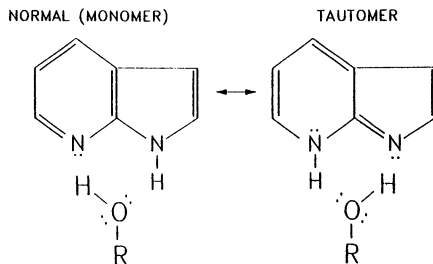


Figure 1. Double proton transfer between alcohol and 7-azaindole to form the azaindole tautomer.

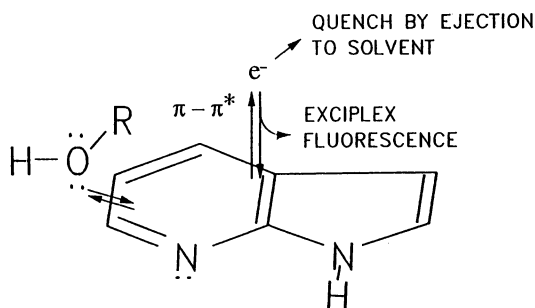


Figure 2. Mechanism of exciplex formation between alcohol and 7-azaindole.

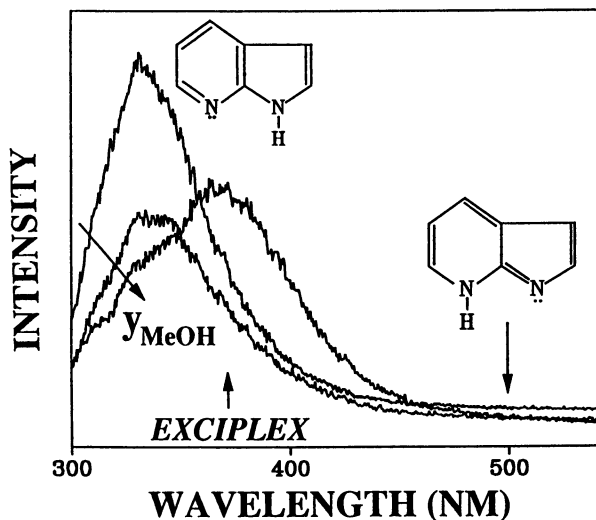


Figure 3. Fluorescence emission from 7-azaindole in supercritical CO₂ with 0, 0.5, 1.0, 2.0 and 4.5 mole % methanol cosolvent.

In a steady state experiment, the concentration of excited solvated species (AS*) will be constant. Since the ratio of intensities of exciplex to monomer is equivalent to the ratio of quantum yields, the steady state condition can be combined with the quantum yields to give the following:

$$I_e / I_m = K[S]^n \quad (1)$$

where,

$$K = \frac{k_4 k_6}{k_3 (k_5 + k_6 + k_7)} \quad (2)$$

and n is the number of solvent molecules in the exciplex. From equation 1, a plot of $\ln(I_e/I_m)$ vs. $\ln([S])$ will give both K and n . In this manner one can observe the dependence of exciplex formation on the cosolvent concentration. The concentration of S (methanol or ethanol in this study) should represent rigorously the monomer concentration. Recent results (23) indicate that alcohols do aggregate in SCF's but to a much lesser extent than in liquids. We have used the total alcohol concentration. If the alcohol does not exist completely as monomer and the azaindole is instead interacting with aggregated alcohol, the plot will turn concave downward or contain a distinct break in slope.

In order to determine the relative amounts of exciplex and monomer species, the spectra were regressed assuming an exciplex and a monomer peak and holding the position and shape (asymmetry) of the monomer fluorescence constant. The monomer position shifts slightly with addition of cosolvent due to changes in the dielectric constant of the solvent but the dielectric constant is linear with density even for mixtures (24). The position of the monomer peak was determined by fitting spectra in pure solvent to a linear function of density. The intensities of the fitted peaks were assumed to represent the relative concentrations of each species. The intensity ratios calculated from different cosolvent concentrations at similar densities have been fit to equation 1 over the complete range of densities studied. The overall correlation shown in Figure 4 yields a slope of 1.0, meaning that the exciplex is formed from one alcohol and one 7-azaindole molecule. This is identical to the results of Collins over the same range of cosolvent concentration. From this we can conclude that the mechanism of exciplex formation is not altered significantly in the SCF.

In liquid solutions, it is not possible to resolve a distinct exciplex peak and the results have been analyzed in terms of the position of the fluorescence. We have taken the overall emission maximum and compared the methanol concentration dependence at several different densities. The shift has been determined relative to the emission maximum in pure CO_2 within $\pm 300 \text{ cm}^{-1}$. Figure 5 shows the dependence of the peak shift on methanol concentration for several different densities and in liquid solvent (21). The steep initial shift with methanol concentration is the formation of the exciplex, while the lesser slope at higher alcohol concentrations in the liquid is the non-specific dielectric shift of the exciplex. In this figure, all the densities from SCF experiments collapse onto a single curve which is less dependent on methanol concentration than the data in liquid 2-methyl butane. The data in SCF solvent rise less steeply than in liquids indicating an environment less enriched in alcohol than a liquid environment. This is not to say the local environment is less concentrated than the bulk, only that the local composition effect, as indicated by exciplex formation, is not as coherent in the SCF. We interpret this to mean that the cosolvent is indeed present in substantial quantities in the local environment about the solute, but the nature of the interaction (i.e. hydrogen bonding) is not the same as in a liquid.

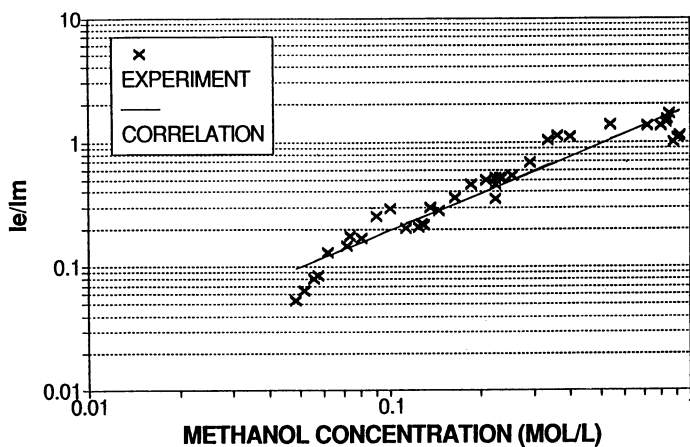


Figure 4. Exciplex to monomer intensity ratio as a function of methanol concentration and correlation with Equation 1.

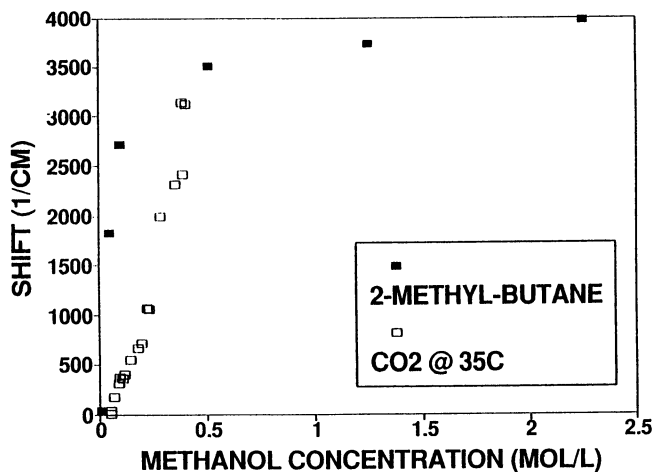


Figure 5. Fluorescence shift from pure solvent for 7-azaindole in 2-methyl butane and CO₂-methanol mixtures.

A recent study on cage effects in supercritical fluids corroborates this finding (25). In the photolysis of two dibenzyl ketones in supercritical ethane and carbon dioxide, there was no evidence for cage recombination of the photogenerated radical pair. The statistically random mixture of combination products led the authors to conclude that cage effects are not supported in the low viscosity SCF even in the region where solvent clustering would be expected. This is another piece of evidence for an unstructured solvent environment about the solute in a supercritical fluid.

We acknowledge the possibility of specific interactions between CO₂ and the methanol cosolvent (23). For this reason, we are currently investigating alcohol-solute interaction in this system in hydrocarbon SCF solutions for future publication.

Conclusions

The addition of cosolvents to SCFs allow the solvent to be specifically tailored to particular components for separation. It is clear through solubility studies that specific interactions between solutes and cosolvents can cause substantial and in some cases extreme enhancements in fluid phase solubility. These interactions are typically short range and directional. Of the available theories for modeling these solutions, those based on physical interactions alone are inadequate to describe such strong interactions. In order to develop the models that will describe these solutions, it is necessary to have a molecular picture of the solution and fundamental thermodynamic data. This study describes spectroscopic experiments to look at the cosolvent/solute interactions on a molecular scale.

In this work, we have studied a fluorescent probe which is sensitive to the local solvent environment. By looking at the behavior of the molecule over a range of cosolvent concentration, we have been able to come to some conclusions regarding the nature of solvent and cosolvent interactions. The results of this work are consistent with previously reported work on naphthols (26). Both 7-azaindole and naphthols have the ability to complex in a specific way with a particular cosolvent when in liquid solution. These complexes need a certain degree of solvent organization for stabilization. The fact that these complexes are not observed in SCF solutions leads us to conclude that the environment is quite dynamic about the solute and is substantially less organized than in liquids. Nonetheless, strong interactions do exist in these solutions as evidenced by the intermediate effects on spectroscopic properties of both probes due to the increased polarity of the solvent. These results are consistent with other studies of reactions in SCFs indicating a lack of cage effects and time-resolved fluorescence studies of pyrene excimer formation in SCF CO₂ (27).

The implication of this work for modeling SCF solutions is that strong interactions do need to be accounted for although the structure of a hydrogen bonding solvent environment is significantly different than what one observes in liquids. Therefore, liquid models which assume certain stoichiometric complexes in solution may be too strong to accurately describe these dynamic solutions.

Acknowledgements

The authors gratefully acknowledge financial support from the Department of Energy (Grants DE-FG22-88PC8922 and DE-FG22-91PC91287) and the E.I. DuPont Nemours Co. The helpful discussions of Prof. Charles L. Liotta are very much appreciated.

Literature Cited

1. Dooley, K.M.; Kao, C-P.; Gambrell, R.P.; Knopf, F.C. *I&EC Res.* **1987**, *26*, 2058.
2. Johnston, K.P.; Haynes, C., *AIChE J.* **1987**, *33*(12), 2017.
3. Ikushima, Y.; Saito, N.; Goto, T. *I&EC Res.* **1989**, *28*, 1364.
4. Tilly, K.D.; Chaplin, R.P.; and Foster, N.R. *Sep. Sci. Tech.* **1990**, *25*(4), 357.
5. Chateaneuf, J.E.; Roberts, C.B.; Brennecke, J.F. In *Recent Advances in Supercritical Fluid Technology: Applications and Fundamental Studies*; Bright, F.V.; McNally, M.E.P., Eds.; ACS Symp. Series; American Chemical Society: Washington, DC, 1992.
6. Eckert, C.A.; Ekart, M.P.; Knutson, B.L.; Payne, K.P.; Tomasko, D.L.; Liotta, C.L.; Foster, N.R. *I&EC Res.* **1991**, *in press*.
7. Kim, S.; Johnston, K.P. *Ind. Eng. Chem. Res.* **1987**, *26*, 1206.
8. Kajimoto, O.; Futakami, M.; Kobayashi, T.; Yamasaki, K. *J. Phys. Chem.* **1988**, *92*, 1347.
9. Petsche, I.B.; Debenedetti, P.G. *J. Chem. Phys.* **1989**, *91*(11), 7075.
10. Cochran, H.D.; Lee, L.L. *ACS Symp. Ser.* **1989**, *406*, 28.
11. Brennecke, J.F.; Tomasko, D.L.; Peshkin, J.; Eckert, C.A. *I&EC Res.* **1990**, *29*, 1682.
12. Knutson, B.L.; Tomasko, D.L.; Eckert, C.A.; Chialvo, A.; Debenedetti, P.G. In *Recent Advances in Supercritical Fluid Technology: Applications and Fundamental Studies*; Bright, F.V.; McNally, M.E.P., Eds.; ACS Symp. Series; American Chemical Society: Washington, DC, 1992.
13. Yurkin, V.G. *Russ. J. Phys. Chem.* **1983**, *57*(2), 314.
14. Hoheisel, C.; Kohler, F. *Fl. Phase Equil.* **1984**, *16*, 13.
15. Rubio, R.G.; Prolongo, M.G.; Cabrerizo, U.; Díaz Peña, M.; Renuncio, J.A.R. *Fl. Phase Equil.* **1986**, *26*, 1.
16. Chatterjee, P.; Bagchi, S. *J. Chem. Soc. Farad. Trans.* **1990**, *86*(10), 1785.
17. Kim, S.; Johnston, K.P. *AIChE J.* **1987**, *33*(10), 1603.
18. Yonker, C.R.; Smith, R.D. *J. Phys. Chem.* **1988**, *92*, 2374.
19. Ingham, K.C.; El-Bayoumi, M.A., *J. Am. Chem. Soc.* **1974**, *96*(6), 1674.
20. Avouris, P.; Yang, L.L.; El-Bayoumi, M.A. *Photochem. Photobiol.* **1976**, *24*, 211.
21. Collins, S.T. *J. Phys. Chem.* **1983**, *87*, 3202.
22. Walker, M.S.; Bednar, T.W.; and Lumry, R. *J. Chem. Phys.* **1967**, *47*(3), 1020.
23. Fulton, J.L.; Smith, R.D. Presented at the AIChE Annual Meeting, Los Angeles, CA, November, **1991**; paper 203g.
24. Dombro, R.A., Jr.; McHugh, M.A.; Prentice, G.A.; Westgate, C.R. *Fl. Phase Equil.* **1991**, *61*, 227.
25. O'Shea, K.E.; Combes, J.R.; Fox, M.A.; Johnston, K.P. *Photochem. and Photobiol.* **1991**, *in press*.
26. Tomasko, D.L.; Knutson, B.L.; Eckert, C.A.; Haubrich, J.E.; Tolbert, L.M. In *Recent Advances in Supercritical Fluid Technology: Applications and Fundamental Studies*; Bright, F.V.; McNally, M.E.P., Eds.; ACS Symp. Series; American Chemical Society: Washington, DC, 1992.
27. Zagrobelny, J.; Betts, T.A.; Bright, F.V. *J. Am. Chem. Soc.* **1991**, *in press*.

RECEIVED July 16, 1992

Chapter 18

Effects of Specific Interactions in Supercritical Fluid Solutions

A Chromatographic Study

Michael P. Ekart¹, Karen L. Bennett², and Charles A. Eckert^{2,3}

¹Department of Chemical Engineering, University of Illinois at Urbana–Champaign, Urbana, IL 61801

²School of Chemical Engineering and Specialty Separations Center, Georgia Institute of Technology, Atlanta, GA 30332–0100

The addition of a small amount of a second component, a cosolvent, to a supercritical fluid can alter phase equilibria dramatically, giving engineers the capability to fine tune the properties of the solvent over a wide range. However, this ability remains largely unexploited in engineering applications due in part to the scarcity of experimental data and lack of accurate models. We have developed a new chromatographic technique to measure these cosolvent effects rapidly. This approach was verified by comparison to literature data obtained by other methods. With this technique, cosolvent effects can be measured in a variety of systems leading to a better understanding of the special intermolecular interactions that occur in supercritical fluid solutions.

Supercritical fluids (SCFs) have many special properties that make them ideal candidates for separation processes (1); however, selectivities in commonly used fluids such as carbon dioxide depend primarily on volatilities (2). One promising approach for manipulating selectivities is the addition of a small amount of cosolvent to the SCF. For example, the solubility of salicylic acid increases by more than an order of magnitude in CO₂ with 3.5 mol% methanol relative to pure CO₂ (3), but the solubility of anthracene increases only slightly (2). Nevertheless, current applications of large-scale cosolvent separations are both sparse and empirical, partly because of a lack of experimental data and accurate models.

One reason that data are scarce is that conventional techniques to measure solubilities in SCFs are time-consuming and require large amounts of pure solute. In this work, we test a new chromatographic technique to measure the effects of cosolvents in SCF solutions on solubilities. This approach is attractive because chromatographic measurements are rapid, require little solute, and inherently separate impurities from the solute.

Several previous researchers have used supercritical fluid chromatography (SFC) to make thermodynamic measurements in pure SCFs. Solubility isotherms for a solute in pure solvents can be measured rapidly using SFC when an independently determined solubility point for the solute is available at the same temperature (4-6). Brown et al. (7) measured stationary phase Henry's constants for several solutes and

³Corresponding author

0097-6156/93/0514-0228\$06.00/0
© 1993 American Chemical Society

correlated them with solute properties. This technique makes possible the measurement of solubilities from retention data where no additional solubility data exist. Shim and Johnston (8) measured the distribution coefficients for naphthalene and phenanthrene between SCF CO₂ and a bonded octadecane liquid phase in addition to solute partial molar volumes and enthalpies in the fluid phase.

Theory

The retention time of a solute depends upon how it is distributed between the mobile phase (in this case, a SCF) and the stationary phase, and is characterized by k_i , the dimensionless capacity factor

$$k_i = \frac{t_i - t_0}{t_0} \quad (1)$$

where t_i is the retention time of solute i and t_0 is the retention time of a solute that does not interact with the stationary phase. Assuming that equilibrium partitioning of the solute between the mobile and stationary phases is the sole mechanism of solute retention, the capacity factor is related to the equilibrium distribution of the solute between the two phases by

$$k_i = \frac{x_i \nu^F V^S}{y_i \nu^S V^F} \quad (2)$$

where x_i and y_i are the mole fractions of component i in the stationary and fluid phases respectively, ν^F and ν^S are the molar volumes of the fluid and stationary phases, and V^F and V^S are the total volumes of the fluid and stationary phases. The validity of this assumption is discussed later.

The fugacity of the solute in the fluid phase, f_i^F , is

$$f_i^F = y_i \varphi_i^\infty P \quad (3)$$

where φ_i^∞ is the fugacity coefficient of solute i at infinite dilution and P is the pressure. Assuming Henry's law is valid in the stationary phase gives

$$f_i^S = x_i H_i \quad (4)$$

where H_i is the Henry's constant for solute i in a given stationary phase. At equilibrium, the fugacities are equal; substituting equations (3) and (4) into (2) then gives

$$\varphi_i^\infty = \frac{k_i H_i V^F \nu^S}{P \nu^F V^S} \quad (5)$$

Bartle et al. (5,6) assumed that the ratio $V^F \nu^S / V^S$ depends on the column and should not vary significantly with pressure. To determine the fugacity of a solute along an

isotherm at a series of pressures in the fluid phase then requires knowledge of Henry's constant at that temperature.

However, this technique has some limitations. Besides equilibrium partitioning, other mechanisms of solute retention must be considered, including adsorption of the solute at the interface between the mobile and stationary phases and interaction with active sites on the stationary phase support. In addition, the amount of fluid absorbed in the stationary phase can vary. These effects are pressure- and temperature-dependent, but because they are very difficult to quantify, previous investigators have ignored them when making thermodynamic measurements with chromatography. The size of the uncertainties is unknown and depends on the stationary phase, but Bartle et al. obtained good results. Our measurements of cosolvent effects eliminate the need for such an assumption by using a comparison technique that may cancel out the effects of retention mechanisms other than bulk absorption.

In our work, we compare the retention of a solute at the same temperature and pressure in the same column, but with different fluids as the mobile phase. Taking the ratio of equation (5) for two different mobile phases (denoted by ' and ") gives

$$\frac{\varphi_i'}{\varphi_i''} = \frac{k_i' H_i' v^{F'} V^{F'} v^{S'} V^{S'}}{k_i'' H_i'' v^{F''} V^{F''} v^{S''} V^{S''}} \quad (6)$$

Several simplifying assumptions may be made. First, because the volume of the mobile phase is much greater than the volume of the stationary phase in the capillary columns that we used, swelling of the stationary phase has negligible effect on V^F , thus it can be considered constant. Second, the ratio v^S/V^S , or the total number of moles of the stationary phase, should not depend greatly upon the mobile phase at constant temperature and pressure.

The third and key assumption is that Henry's constant for a solute is not altered by the changes in composition of the mobile phase. Several researchers have measured significant absorption of solvents and cosolvents into stationary phases (for example, 9-12). It has been proposed that the cosolvent also covers up active sites on the column; this would cause the solute to be retained less thus decreasing the retention time (13). The presence of cosolvent should have some effect on the Henry's constant; however, the magnitude of this effect is unknown and should depend on the stationary phase and the cosolvent. Recent studies have demonstrated that the increase in solvating power of the fluid upon addition of the cosolvent is primarily responsible for the decrease in retention implying that the stationary phase environment around the solute, thus the Henry's constant, is largely unaffected by the cosolvent (14,15). Nevertheless, the assumption of a constant Henry's constant should be checked for each column; the best way to do this is to study systems where the fluid phase thermodynamics are already known.

For the measurements to be meaningful, the pressure drop across the column must be small. In our experiments, we used capillary columns with estimated pressure drops ranging from 0.2 bars, at a column pressure of 90 bars, to 0.9 bars when operating at 350 bars.

After making these assumptions, equation (6) becomes

$$\frac{\varphi_i'}{\varphi_i''} = \frac{k_i' v^{F'}}{k_i'' v^{F''}} \quad (7)$$

The ratio of the molar volumes of the fluid phases should be near unity and can be estimated from an equation of state, from experimental data, or from the t_0 and flow rate measurements. In this work, we used an equation of state to determine this ratio.

Figure 1 demonstrates the meaning of the ratio of infinite dilution activity coefficients. The fugacity coefficient for a solute is shown as a function of composition up to the solubility limit in two different fluids at the same temperature and pressure. At saturation

$$\frac{y_i^{sat''}}{y_i^{sat'}} = \frac{\phi_i^{sat'}}{\phi_i^{sat''}} \quad (8)$$

If the solubilities of the solute in the SCFs are low, as is the case with the solutes studied here, it is reasonable to assume that the ratio of fugacities at the solubility limits is the same as that at infinite dilution. If so, then

$$\Psi = \frac{y_i^{sat''}}{y_i^{sat'}} \approx \frac{\phi_i^{sat'}}{\phi_i^{sat''}} \quad (9)$$

where Ψ is the cosolvent effect; i.e., the relative increase in solubility at some P and T that comes about when the SCF is modified with cosolvent. To obtain the absolute solubility of the solute in the cosolvent solution using this technique, it is necessary to know the solute solubility in the pure SCF.

Infinite dilution fugacity coefficients are a more useful measure of solution thermodynamics than solubilities for theoretical techniques of studying solutions such as statistical mechanics or computer simulations. Solute-solute interactions are eliminated at infinite dilution, thus nonidealities under these conditions are due solely to solute-solvent interactions. This approach separates the problem of determining intermolecular forces from the problem of adding the forces.

Experimental

The supercritical fluid chromatograph used was a Lee Scientific Model 600-D that included a 137 ml syringe pump. Pressure was monitored with a Heise pressure gauge, model 901B, accurate to $\pm 0.035\%$; temperature was measured with a Hart Scientific model 1006 digital thermometer and controlled to $\pm 0.05^\circ \text{C}$. Solutes were detected with a Linear high pressure UV-vis detector (Model 204). The flow rate of the SCF was measured with a soap bubble flowmeter. An SB-Octyl-50 capillary column ($50 \mu\text{m} \times 10 \text{m}$, film thickness $0.25 \mu\text{m}$) from Lee Scientific was used.

SFE grade CO_2 (99.99%) was obtained from Scott Specialty Gases and CP grade ethane (99%) from Matheson Gas Products. HPLC grade methanol was obtained from Aldrich Chemical Co. (99.9+%). Anthracene and 2-naphthol were obtained from Aldrich Chemical Company and used without further purification since the chromatograph separated out the impurities.

The fluid mixtures were prepared in our labs in a 1 liter bomb constructed of 316 stainless steel. A known amount of cosolvent, predetermined to give the desired composition, was loaded into the bomb which had been previously flushed to

eliminate air. The bomb was pressurized to about 415 bars, and the mixture was then stirred for at least a day by a magnetic stir bar inside the bomb. Using this technique, the bomb contained enough fluid to supply the syringe pump with about 150 ml of the mixture without approaching the two phase region. Special care was taken to avoid the two phase region in the mixing bomb, syringe pump, and column at all times; CO₂-methanol phase equilibrium data are available from Hong and Kobayashi (16) and Suzuki et al. (17).

Experiments were carried out at 35° C and 50° C and pressures from 80 to 350 bars. The solutes were injected in *n*-pentane at about 20 µg/ml. We determined that the retention of pentane was the same as that of helium under the conditions of our experiments using a Vorex universal detector (which was unfortunately unable to detect the minute quantity of solutes), so it was assumed that pentane was not retained. Retention time was not sensitive to the concentration of the solute or the identity of the solvent with which it was injected. All solutes were detected at absorption maxima. The retention times were determined from the maxima in the first derivative of the chromatogram.

Results and Discussion

We carried out experiments to check the validity of this technique which involved comparing our results with cosolvent effects reported in the literature. As outlined above, these experiments involved measuring retentions of anthracene and 2-naphthol with pure CO₂ and then a CO₂/methanol mixture as the mobile phase. Figure 2 shows the cosolvent effect for anthracene at 35° C in CO₂ with 3.5 mol% methanol added. Our results agree well with the ratio of the solubility of anthracene in the CO₂/methanol mixture to its solubility in pure CO₂, measured by Dobbs and Johnston (2). As expected, because there are no specific interactions between methanol and anthracene, the cosolvent effect for nonpolar anthracene is modest. Note that in addition to changing the polarity/polarizability characteristics of the fluid, the addition of cosolvent at constant temperature and pressure usually increases the density of the fluid. Both of these changes, in the absence of other factors, will generally tend to increase the solubility of large solute molecules.

Figure 3 shows the cosolvent effect for 2-naphthol under the same conditions; again our results are consistent with those of Dobbs et al. (18). In this case, where 2-naphthol and methanol are capable of hydrogen bonding with each other, the cosolvent effect is much larger. We were not able to measure the cosolvent effect at the higher pressures because the fluid mixture became such a good solvent for 2-naphthol that it was essentially unretained in the column.

A variation of looking at cosolvent effects is measuring the ratio of solubilities of a solute in two different fluids; that is, a solvent effect. In Figure 4, the ratio of 2-naphthol's solubility in ethane to its solubility in CO₂ is plotted versus pressure at 50° C. Our results agree well with the literature (estimated from Schmitt and Reid, 19) despite nearly an order of magnitude change in the ratio. Note that the solvent effect goes from greater than one to less as pressure is increased; this indicates a crossover in the solubility isotherms.

With this technique, cosolvent effects for a variety of solute and cosolvent combinations can be measured, giving us information on specific intermolecular interactions such as hydrogen bonding or charge transfer complex formation. This knowledge will be of use in tailoring solvents to perform specific separations.

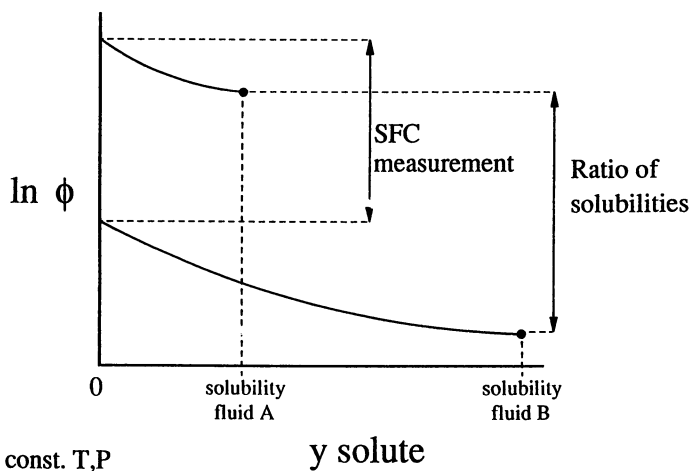


Figure 1. Composition dependence of the fugacity coefficient of a solute in two different fluids at the same temperature and pressure.

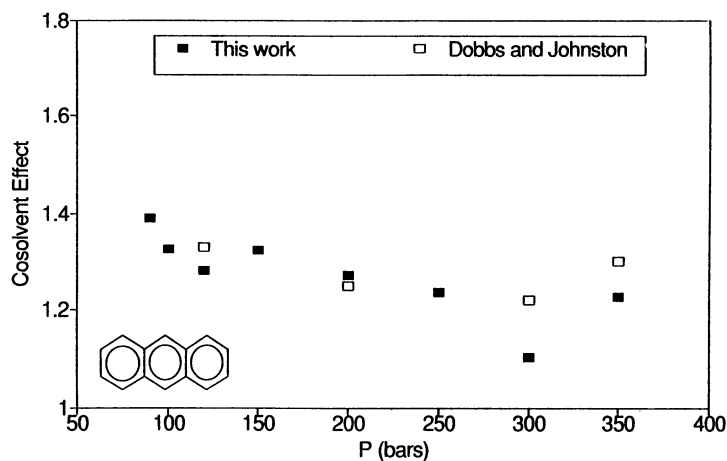


Figure 2. Cosolvent effect for anthracene in CO_2 with 3.5 mol% methanol relative to pure CO_2 at 35°C .

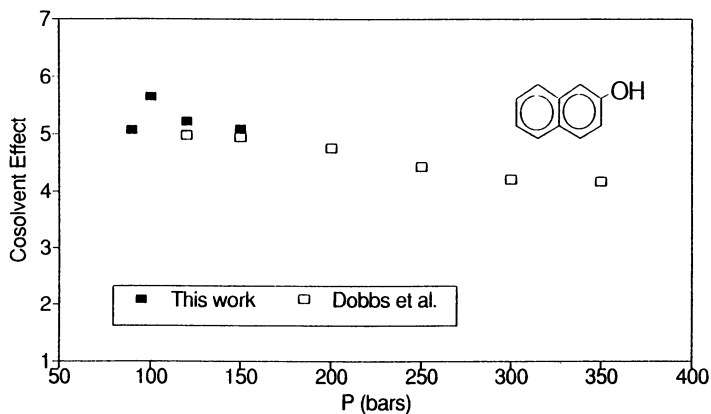


Figure 3. Cosolvent effect for 2-naphthol in CO₂ with 3.5 mol% methanol relative to pure CO₂ at 35° C.

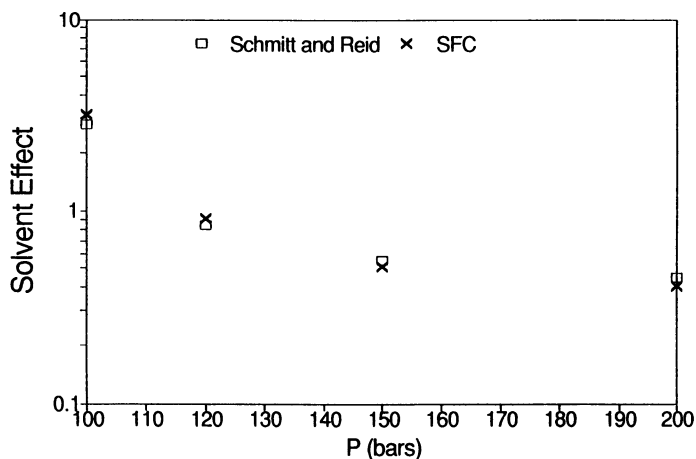


Figure 4. Solvent effect for 2-naphthol in ethane relative to CO₂ at 50° C.

Conclusions

We have developed a SCF chromatographic technique to measure cosolvent effects on solutes in SCF solutions and tested it with nonpolar and polar solutes. Our results agree well with the literature, suggesting that for these solutes and this stationary phase the change in retention due to the presence of cosolvent is attributable to interactions in the fluid phase. This makes possible the rapid measurement of cosolvent effects with minute quantities of solute.

We will extend these studies to solutes and cosolvents representing a wide range of types of specific interactions. This database will aid in the development of better equations of state to allow the prediction of solubilities of solutes in mixed solvents. These tools will provide the design engineer the means to measure or predict cosolvent effects rapidly and inexpensively, allowing the fine tuning of SCF solutions to carry out difficult separations or precise reaction chemistry.

Acknowledgments

The authors gratefully acknowledge funding support for this work from the U.S. Department of Energy under grant numbers DE-FG22-88PC88922 and DE-FG22-91PC91287 as well as support from the E.I. DuPont de Nemours Co. In addition, we would like to acknowledge the helpful advice of Prof. Gunther Holzer.

Literature Cited

1. McHugh, M. A.; Krukonic, V. J. *Supercritical Fluid Extraction: Principles and Practice*; Butterworths: Boston, 1986.
2. Dobbs, J. M.; Johnston, K. P. *Ind. Eng. Chem. Res.* **1987**, *26*, 1476.
3. Foster, N. R., University of New South Wales, personal communication, 1990.
4. Smith, R. D.; Udseth, H. R.; Wright, B. W.; Yonker, C. R. *Sep. Sci. Tech.* **1987**, *22*, 1065.
5. Bartle, K. D.; Clifford, A. A.; Jafar, S. A. *J. Chem. Soc. Faraday Trans.* **1990**, *86*, 855.
6. Bartle, K. D.; Clifford, A. A.; Jafar, S. A. *J. Chem. Eng. Data.* **1990**, *35*, 355.
7. Brown, B. O.; Kishbaugh, A. J.; Paulaitis, M. E. *Fluid Phase Equil.* **1987**, *36*, 247.
8. Shim, J.-J.; Johnston, K. P. *J. Phys. Chem.* **1991**, *95*, 353.
9. Yonker, C. R.; Smith, R. D. *Anal. Chem.* **1989**, *61*, 1348.
10. Yonker, C. R.; Smith, R. D. *J. Chrom.* **1990**, *505*, 139.
11. Strubinger, J. R.; Song, H.; Parcher, J. F. *Anal. Chem.* **1991**, *63*, 98.
12. Strubinger, J. R.; Song, H.; Parcher, J. F. *Anal. Chem.* **1991**, *63*, 104.
13. Levy, J. M.; Ritchey, W. M. *J. High Res. Chrom. Chrom. Comm.* **1985**, *8*, 503.
14. Berger, T. A.; Deye, J. F. *Anal. Chem.* **1990**, *62*, 1181.
15. Crow, J. A.; Foley, J. P. *J. Microcol. Sep.* **1991**, *3*, 47.
16. Hong, J. H.; Kobayashi, R. *Fl. Phase Equil.* **1988**, *41*, 269.
17. Suzuki, K.; Sue, H.; Itou, M.; Smith, R. L.; Inomata, H.; Arai, K.; Saito, S. *J. Chem. Eng. Data.* **1990**, *35*, 63.
18. Dobbs, J. M.; Wong, J. M.; Lahiere, R. J.; Johnston, K. P. *Ind. Eng. Chem. Res.* **1987**, *26*, 56.
19. Schmitt, W. J.; Reid, R. C. *J. Chem. Eng. Data.* **1986**, *31*, 204.

RECEIVED July 16, 1992

Chapter 19

Applications of Supercritical Fluids in the Controlled Release of Drugs

Jean W. Tom, Gio-Bin Lim¹, Pablo G. Debenedetti,
and Robert K. Prud'homme

Department of Chemical Engineering, Princeton University,
Princeton, NJ 08544

Supercritical fluids have been used to form two different types of microparticles intended for controlled drug release applications: drug-loaded polymer microspheres, and small protein particles. A poly(hydroxyacid), poly(D,L-lactic acid) (DL-PLA) and a pharmaceutical (lovastatin) have been dissolved in supercritical CO₂ and coprecipitated by rapid expansion of the resulting supercritical solution (RESS) to form polymer-drug microspheres and microparticles ranging in size from 10 to 100 μm. Variations in the concentration of lovastatin in the precipitate correlated with changes in the precipitate's morphology, ranging from continuous drug-polymer networks, to microparticles, to microspheres. The formation of polymer-drug microparticles by RESS is the first step towards a feasible single-step, low-temperature process that yields solvent and surfactant-free microparticles suitable for controlled drug release. Two model proteins, catalase and insulin, have been dissolved in ethanol/water solution and fed continuously and simultaneously with supercritical CO₂ into a crystallizer to precipitate the proteins. The use of supercritical CO₂ as a gas anti-solvent (GAS) produced catalase and insulin particles ranging from 1 to 5 μm. Particle morphology ranged from microspheres, to rectangular-shaped particles, to needles. Micron-sized protein particles are needed in several controlled release formulations to accommodate the high potency and low dosage of such pharmaceuticals and to achieve a uniform dispersion of the drug in the injectable polymeric microspherical carrier. GAS crystallization is a potentially important process for comminution of proteins since conventional particle reduction methods (spray drying, lyophilization, milling, grinding) cannot produce the micron-sized protein particles needed for controlled release of highly active enzymes.

¹Current address: Department of Chemical Engineering, University of Suwon, Box 77, Suwon, Korea 440-660

Controlled release of drugs or controlled drug delivery is a generic name describing a wide range of systems aimed at providing temporal or spatial control of drug release in the body (1). Of interest here are delivery systems aimed at controlling the rate at which drugs are released (temporal regulation). Conventional means of administering drugs (i.e. pills, tablets) provide a single burst of drug in the blood, followed by a decay in the drug concentration. It is desirable to minimize concentration variations and release the drug at a controlled rate. Controlled release provides improved therapeutic action by enhancing the drug's longevity and effectiveness in the body.

One of the most common methods for the controlled release of drugs is the use of microspheres and microparticles of polymer-drug composites. The drug is distributed uniformly in a polymer carrier. In most applications, the polymer is degraded or eroded by body fluids over time (i.e., it is bioerodible or biodegradable) to non-toxic products (i.e., it is biocompatible), making its removal after drug release unnecessary. The mechanism of drug release from these matrices can involve both diffusion through the matrix and surface erosion of the polymer (2). The microspheres and microparticles are taken orally or injected into the body (<50 μ m for human use) subcutaneously or intramuscularly.

Poly(hydroxyacids) are biocompatible polymers used extensively in studies of polymer-drug matrices. Poly(L-lactic acid) (L-PLA), poly(D,L-lactic acid) (DL-PLA), and poly(glycolic acid) (PGA), as well as copolymers of these hydroxyacids, are approved by the Food and Drug Administration for *in vivo* applications (sutures and bone implants). These polymers are hydrolyzed by body fluids to non-toxic compounds such as lactic and glycolic acid (3). Controlled release systems using these polymers have been studied for release periods ranging from 5 to 90 days (3). The drugs studied in such systems range from steroids (contraceptives) to synthetic organic compounds (anticancer drugs and anesthetics) to polypeptides and proteins (biopharmaceuticals) (3,4). Achieving a uniform dispersion of small pharmaceutical particles throughout the polymer matrix is especially important in applications involving high potency drugs, which require low dosages.

Our interest is in using supercritical fluids both to fabricate polymer-drug microspheres and microparticles, and to process pharmaceuticals for use in controlled drug delivery applications. In this study, rapid expansion of supercritical solutions (RESS) (5) and gas anti-solvent crystallization (GAS crystallization) (6) have been used to produce bioerodible polymer-drug microspheres and micron-sized protein particles, respectively. Our goal is to form polymer-drug microcarriers suitable for human use (<50 μ m) and protein particles (<5 μ m) which can be incorporated into microcarriers.

Background

In recent years, the processing of pharmaceuticals with supercritical fluids has received increased attention. One of the first processes to be studied has been the rapid expansion of supercritical solutions as a route to pharmaceutical particle reduction (7-10). RESS has also been applied to ceramic and polymeric processing. The general area of particle formation using supercritical fluids has recently been reviewed (11). In RESS, a nonvolatile solute is dissolved in a supercritical fluid.

Precipitation of the solute is triggered by reducing the solvent's density, and therefore its solvating capacity (12), through a rapid expansion. Since the solution is highly compressible near the solvent's critical point, large density changes can be obtained with only moderate pressure reductions. The decompression is a mechanical perturbation, which allows rapid establishment of uniform conditions within the solution, minimizing temperature and pressure gradients. Precipitation from a uniform nucleating medium results in particles with a narrow size distribution. Enhancement factors (ratio of actual solubility to the solubility predicted assuming ideal gas behavior at the same pressure and temperature) can be as high as 10^6 for dilute supercritical solutions (13). These high enhancement factors can result in large supersaturations upon rapid expansion, leading to massive nucleation, and hence to very small particles. Since the expansion of a supercritical solution results in large changes in thermophysical properties, and since these properties are extremely sensitive to small changes in temperature and pressure in the highly compressible region, RESS offers, in principle, the ability to control the size and morphology of the resulting particles with modest changes in process conditions (13). The idea, then, is to dissolve a solute at high pressure, exploiting the supercritical fluid's solvent power, and to precipitate it mechanically rather than thermally, exploiting the solvent's high compressibility.

A more recent application of supercritical fluids to particle formation is gas anti-solvent (GAS) crystallization (6,14-15,22). In GAS crystallization, a supercritical fluid is used as an anti-solvent that causes crystallization of solids. The solids are dissolved in a liquid, and a supercritical fluid (having a low solvent power with respect to the solids, but miscible with the liquid) is added to precipitate the solids. The size distribution of the precipitate depends on the rate of addition of the supercritical fluid. The dissolution of supercritical fluids in liquids is often accompanied by a large volume expansion and, consequently, a reduction in the liquid's solvent power. Rapid addition of a supercritical fluid results in a sudden reduction in the liquid's density, a sharp rise in the supersaturation within the liquid mixture, and the consequent formation of small and uniform particles. GAS is useful for processing of solids which are difficult to solubilize in supercritical fluids or sensitive to mechanical handling. Pharmaceutical compounds which fall into this category are polypeptides and proteins.

The advantages that RESS and GAS crystallization have over conventional methods of polymer-drug microsphere formation and particle reduction are numerous. Pharmaceuticals are often prone to degradation or denaturation by heat or oxygen. Their processing often requires mild and inert conditions. Conventional size reduction methods such as milling and grinding can adversely affect the crystallinity and chemical stability of pharmaceuticals (16). The use of low-critical-temperature solvents allows processing at mild temperatures and can lead to the formation of very fine and monodisperse powders. The use of RESS as a means of producing polymer-drug microspheres and microparticles has the potential for eliminating some of the disadvantages of conventional methods. Current techniques for producing polymer-drug microspheres involve dissolution of the polymer and drug in a common organic solvent. Microspheres are formed from such a solution either by addition of an aqueous solution (with dispersing agent) which acts as an anti-solvent, or by evaporation of the solvent (17). A similar technique, spray drying, involves spraying

a solution containing both the polymer and the drug into a hot gas to remove the solvent. Microparticles can also be formed by melt pressing the polymer and the drug, and subsequent grinding. These conventional techniques require the removal of surfactants and organic solvents, and involve the use of high temperatures (spray drying and melt pressing). In the manufacture of microparticles intended for *in vivo* use, the removal of residual surfactants and solvents is a particularly important requirement; however, removal of these residues often requires prolonged vacuum or exposure to high temperatures. In contrast, RESS does not involve surfactants, organic solvents, or high temperatures (if a low-critical-temperature solvent is used), and it yields a solvent-free product (the supercritical solvent is a dilute gas after expansion) in a single processing step.

There are several problems associated with conventional size reduction methods for proteins, and this makes GAS crystallization an attractive alternative. Processes such as spray drying, milling, grinding, lyophilization and sieving either produce particles whose size is often not small enough for incorporation into controlled release microspheres, or have features which can inactivate the protein. Spray drying can reduce particles to less than 5 μm , but exposure to heat and air in the process can deactivate proteins (18). Sieving of lyophilized proteins can reduce particles only to 70 μm (18). Milling and grinding can produce particles of less than 5 μm , but can denature protein compounds. Milling and grinding also require large quantities of material, which makes processing of highly potent and expensive enzymes impractical (18). Gombotz et al. (18) have recently patented a process in which dilute protein solutions are atomized through a nozzle into liquid nitrogen, which freezes the atomized droplets, ranging in size from 10 to 90 μm . The resulting particles are lyophilized, suspended in a non-solvent and exposed to ultrasound to produce protein particles (0.1 to 10 μm) which retain up to 95% of their activity. However, the technique involves multiple steps, requiring several days of processing, and produces a relatively polydisperse sample. As will be explained below, a continuous GAS crystallization process has the potential for completely separating the liquid solvent from the products in a single-step process.

Previous work involving pharmaceuticals and supercritical fluids has focused on RESS as an alternative to milling. Workers have studied the production of phenacetin (9) and lovastatin (8,10) particles using supercritical CO_2 . Larson and King produced lovastatin particles ranging from 10 to 50 μm (8) while Mohamed et al. produced lovastatin aggregates whose elementary units ranged from 0.1 to 1 μm using different process conditions (10). RESS-processed phenacetin particles were on the order of 10 to 15 μm (9). The RESS-processed lovastatin exhibited properties nearly identical to those of the unprocessed material as determined by x-ray diffraction (10) while the phenacetin exhibited differential scanning calorimetry and melting point results similar to jet-milled phenacetin (9). More recent work has addressed the fabrication of bioerodible polymeric microspheres and microparticles (poly(hydroxyacids)) as a first step towards the coprecipitation of polymer-drug microspheres and microparticles (19). In this study, L-PLA, DL-PLA and PGA were found to dissolve in supercritical CO_2 . The starting polymer had molecular weights of 5000-6000 and polydispersities of 2. Initially, low-molecular-weight oligomers were extracted. After sufficient processing (~200 total standard liters of CO_2 per gram polymer loaded in the column, TSLPG), the molecular weight of the extracted polymer rose to about 1500-2000 as

determined by gel permeation chromatography. After removal of low-molecular-weight material, the solubility of L-PLA in supercritical CO₂ and in supercritical CO₂ with 1 wt% acetone ranged from 0.02 wt% (CO₂), and 0.05 wt% (CO₂ + 1 wt% acetone), at 200 bars and 45°C to 0.08 wt% to 0.4 wt%, respectively, at 300 bars 65°C. Proton nuclear magnetic resonance confirmed the chemical identity of the polymer. Product morphologies ranging from irregularly-shaped, to spheroidal particles, to microspheres were obtained. The transition from irregular shape to spheres was effected by increasing the pre-expansion temperature from 80 to 120°C. Degradation (or hydrolysis) experiments on L-PLA showed that the precipitated polymer (after extraction times sufficient to yield non-oligomeric precipitate) had very similar hydrolysis rates to the commercial polymer. Using RESS to produce composite polymer-drug particles by coprecipitation is the logical next step in this work.

Mueller and Fischer (20) have recently patented a process that involves contacting supercritical CO₂ with an organic solution (methylene chloride) of drug (clonidine hydrochloride) and polymer (DL-PLA). Subsequent expansion of the supercritical solution produced microspheres (100µm) containing drug and polymer. *In vitro* measurements showed that more than 50% of the drug was released within the first 24 h. In our work, we avoid the dissolution of drug or polymer in liquid organic solvents. Other cases of RESS coprecipitation reported in the literature involve the inorganic system of SiO₂ and GeO₂ (21) and the polymer/salt system of polyvinylchloride and potassium iodide (5).

GAS crystallization has not been applied to pharmaceuticals. To date, its main applications have been to produce void-free explosives (6,22) and to separate solid mixtures (15,22). The molecular thermodynamics of solubilities in the GAS process have recently been investigated (14). Gallagher and coworkers (22) found that rapid introduction of supercritical CO₂ to cyclohexanone solutions of cyclotrimethylenetrinitramine (RDX), an explosive, resulted in monodisperse and ultrafine 5 µm RDX particles. In the same study, RDX was selectively crystallized from acetone mixtures containing RDX and a related compound (HDX) using supercritical CO₂ as a gas anti-solvent. Chang and Randolph (15) crystallized β-carotenes from mixtures of β-carotenes and carotene oxides in cyclohexanone or toluene/butanol using supercritical CO₂ as a gas anti-solvent. In all of the above studies, the experiments were semi-batch: the liquid solution was charged into the crystallizer, and this was followed by addition of the anti-solvent. In contrast, our work aims at developing GAS crystallization as a continuous process to produce micron-sized protein particles.

Previous work on proteins in supercritical fluids has been in the context of non-aqueous enzymatic reactions (23-26), protein solubilization with reverse micelles (27), and food processing (e.g., 28) in a supercritical fluid medium. In the studies on enzymatic reactions, the enzymes were immobilized onto glass beads and not solubilized in supercritical CO₂. It was found that some enzymes denatured over time while others were unaffected by pressure.

Materials and Experimental Equipment

Materials. The poly(hydroxyacid) used in this study, DL-PLA (Boehringer Ingelheim, R-104, lot no. 93016), had a molecular weight (Mw) of 5300 and a

polydispersity of 1.9. Lovastatin (Merck & Co.) or 2-methylbutanoic acid 1,2,3,7,8,8a-hexahydro-3,7-dimethyl-8-[2-(tetrahydro-4-hydroxy-6-oxo-2H-pyran-2-yl)ethyl]-1naphthalenyl ester, a cholesterol-reducing drug, has a molecular weight of 404. Two model proteins were used in the GAS crystallization study: bovine liver catalase (MW ~ 240,000; Sigma Chemicals) and bovine insulin (Zn, low endotoxin, MW~ 6000; Miles Pentex). Catalase and insulin particles ranged from 150 to 300 μ m, and from 15 to 30 μ m, respectively, when received from the manufacturers. Insulin can be solubilized in a variety of organic solvents (29) while catalase can be solubilized in organic solvents containing low amounts of water. Ethanol (200 proof; Pharmco Products Inc.) was used as received from the manufacturer. Deionized water was obtained by reverse osmosis (Hydro- Picosystem). Hydrochloric acid solution was prepared by diluting 12M HCl (Mallinkrodt; analytical grade, 37%) with DI water. The supercritical solvent was carbon dioxide of bone dry grade (>99.8%; MG Industries).

Rapid Expansion of Supercritical Solutions. In the rapid expansion of supercritical solutions, the poly(hydroxyacid) and/or lovastatin are dissolved in CO₂ above its critical point, and rapidly precipitated by expanding the supercritical solution across an orifice (~30 μ m diameter) to slightly above atmospheric pressure. The experimental apparatus is shown schematically in Figure 1, and has been described in detail elsewhere (10,19). It can be separated into three units: extraction, sampling and precipitation. In the extraction unit, the solvent is pumped to desired pressure and preheated to extraction temperature. For the coprecipitation studies, the apparatus has been modified so as to have two extraction column operating in parallel. The solvent enters either or both extraction columns. Coprecipitation experiments can be done either by packing the two solutes in one column, or with one solute in each column. The solution then enters the sampling section via a six-port injection valve. It leaves the sampling section and flows to the crystallizer, where the solution is expanded through a laser-drilled orifice of diameter 25-30 μ m. A cable heater wrapped around the tube leading to the orifice is used to heat the solution to a desired pre-expansion temperature. Adequate pre-expansion temperatures are needed to prevent phase changes in the solvent upon expansion (condensation) and plugging due to premature precipitation. In addition, the preexpansion temperature affects particle morphology (19). If both extraction columns are in operation, one of the streams will bypass the sampling section. Streams from each of the columns are mixed at the point where cable heating begins. The particles are collected on a glass slide inside a glass beaker in the crystallizer. The supercritical solvent, now a gas, is passed through a rotameter and vented. Typical gas flow rates are 1-2 standard liters per minute (SLPM).

Gas Anti-Solvent Crystallization. In the gas anti-solvent experiments, the protein solution and supercritical solvent are pumped into a crystallizer simultaneously. The liquid solution enters through an orifice (20-70 μ m), and the resulting small droplets are contacted with a large excess of supercritical solvent. This gives rise to both expansion and evaporation of the liquid solution, causing protein precipitation. In these experiments, catalase or insulin was dissolved in a 90% ethanol/10% DI water mixture (typical protein concentration was 0.1 mg/ml). The solution was adjusted to

a pH of 3.0 to 3.5 with 1N HCL. Filtration (0.2 μm nylon filters) removed undissolved protein particles.

A schematic of the experimental apparatus is shown in Figure 2. This solution is pumped (LDC minipump) into the crystallizer (Jerguson Gage; Model 19T40) via an orifice (Ted Pella; 20-70 μm diameter x 0.24 mm thickness; platinum). The use of such nozzles allows introduction of the protein solution into the crystallizer as small liquid droplets. The large surface area associated with the small droplets enhances the GAS expansion, and also the evaporation rate of the liquid into the supercritical fluid. CO_2 is compressed by a high pressure pump (American Lewa Plunger Metering Pump; EL-1) and conveyed into the crystallizer, into which it can flow either cocurrently or countercurrently to the protein stream. The crystallizer, associated valves, and tubing are situated in an insulated air chamber where the temperature is controlled using a PID temperature controller (Omega Engineering CN900), two finned strip heaters (McMaster-Carr, 500 watts) and circulating fans. The pressure of the crystallizer, CO_2 inlet flow, and protein solution inlet flow are controlled by back-pressure regulators (Tescom; 54-2100, 26-1700). Upon expansion, protein particles are precipitated and a fluid mixture of CO_2 , ethanol, and water leaves the crystallizer. Protein particles are collected on a glass slide placed in the crystallizer and on filters (Mott Metallurgical; stainless steel, 0.5-2 μm) at the CO_2 /ethanol/water exit. This fluid mixture is depressurized and expanded to atmospheric pressure as it passes through a depressurizing tank (Swagelok 316L-50DF4-150; 150ml). The instantaneous and total flow rates of CO_2 gas are measured with a rotameter and a dry-test meter (American Meter; DTM200A), respectively. Typical flow rates of CO_2 and protein solution are 17-18 (SLPM) and 0.35 ml/min, respectively.

Analytical Equipment. Particles from both types of experiments were examined by scanning electron microscopy (SEM, JEOL JSM 840A, samples sputter-coated with gold-palladium). The fraction of lovastatin and poly(hydroxyacid) in the RESS precipitate was determined by nuclear magnetic resonance (NMR, GE QE-300, deuterated chloroform). The x-ray diffraction patterns of unprocessed and precipitated lovastatin were compared to verify the drug's crystallinity (Philips-Norelco Goniometer with focusing monochromator). Polymer molecular weights and polydispersities were determined by gel permeation chromatography (GPC). GPC samples were passed through a polystyrene/divinyl-benzene column (Polymer Laboratories PLgel 5 μm , 500 \AA , 30-cm length) with chloroform (HLPC grade; Aldrich Chemicals) as the mobile phase (1 ml/min) and monitored with a refractive index detector (Knauer, Type 198). The peaks were recorded and integrated automatically (Hewlett-Packard, Model 3396-II). The GPC system was calibrated with dilactide and commercial DL-PLA.

Results and Discussion

Rapid Expansion of Supercritical Solution. RESS of L-PLA with supercritical CO_2 has been shown to produce microspheres and microparticles at extraction conditions of 200-250 bar and 55°C (19). RESS of lovastatin in CO_2 at similar extraction conditions and pre-expansion temperatures of 100-110°C resulted in needles of ~40-80 μm length and aspect ratios of 15-25 (Figure 3). X-ray diffraction

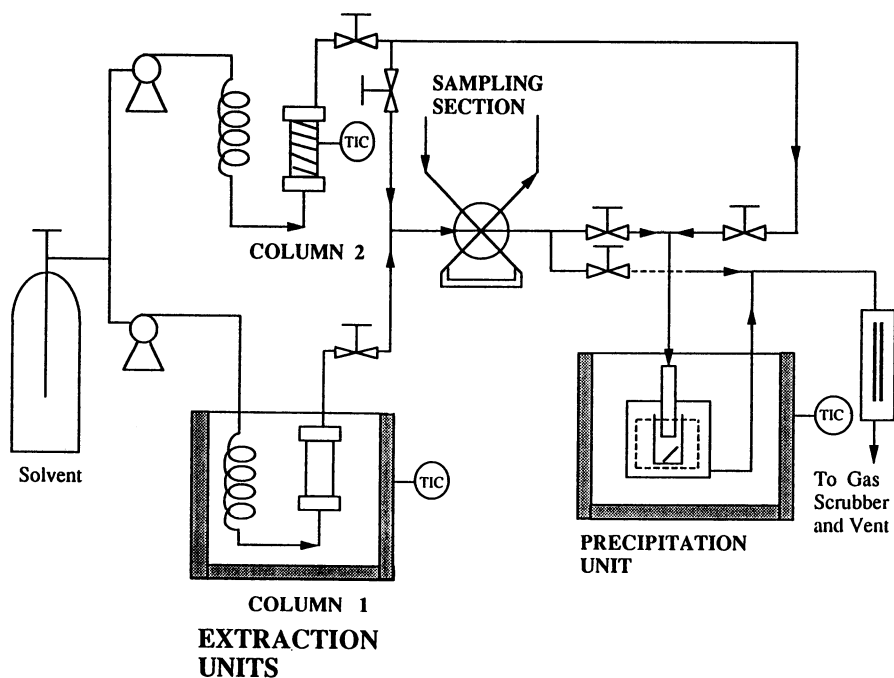


Figure 1. Schematic of experimental apparatus for rapid expansion of supercritical solutions

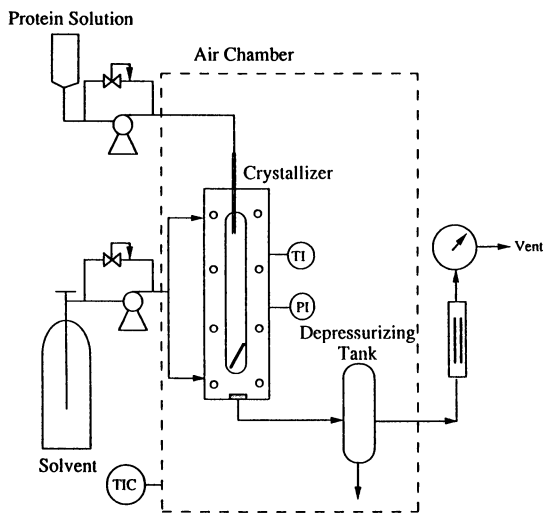


Figure 2. Schematic of experimental apparatus for gas anti-solvent crystallization.

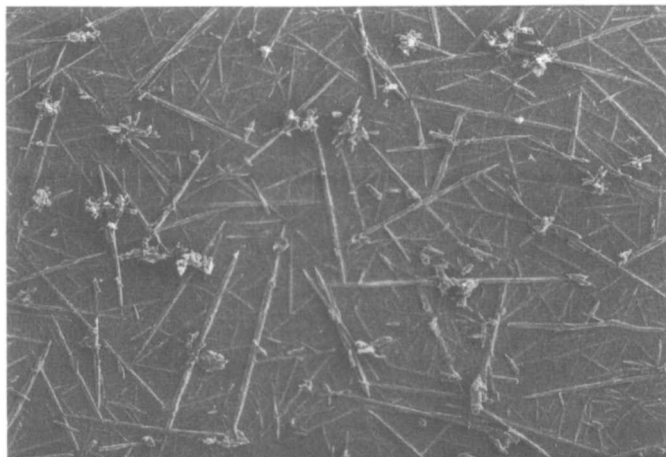


Figure 3. SEM photomicrograph of lovastatin needles precipitated by RESS with supercritical CO_2 .

of lovastatin before and after precipitation showed the same peaks. At higher concentrations of lovastatin (extraction conditions of 379 bar and 55-75°C) and pre-expansion temperatures of 105-135°C, the lovastatin precipitated as aggregates of small particles (0.1-1 μm) (10). In the coprecipitation experiments, extraction conditions of 200-250 bars and 55°C were used.

The three coprecipitation experiments described here illustrate the variation in the precipitate's morphology and composition that can result from slight changes in the relative amounts of drug and polymer initially loaded into the extraction unit. 13.5 grams of polymer (DL-PLA) and 0.5 grams of drug (lovastatin) were intimately mixed in column 1 while column 2 was packed with 15 grams of lovastatin. After passing ~200 TSLPG of supercritical CO_2 at 200-250 bars and 55°C through column 1 to extract the low-molecular-weight oligomers and dilactides, solid particles were produced. As in the case of L-PLA, the polydispersity of the polymer leads to preferential extraction of low-molecular-weight material early in the processing. The low-molecular-weight polymer forms either needles or a viscous, low-Tg precipitate (19).

One coprecipitation experiment was then performed by flowing CO_2 at 200 bar and 55°C through column 1, with column 2 inactive. With preexpansion temperatures of 75-80°C, a range of particles was obtained. Microspheres containing single lovastatin needles (Figure 4), as well as, egg-shaped polymer particles enveloping lovastatin needles (Figure 5), microspheres without protruding needles, and needles without a polymeric enclosure were produced. Proton NMR of the precipitate showed the presence of lovastatin and DL-PLA exclusively, with the lovastatin concentration estimated at 20 wt%.

In a second experiment, both columns were used. Extraction conditions of 190-220 bar and 55°C for column 1, and 35°C for column 2 were used, with preexpansion temperatures of 75-85°C. Large microparticles containing multiple needles of

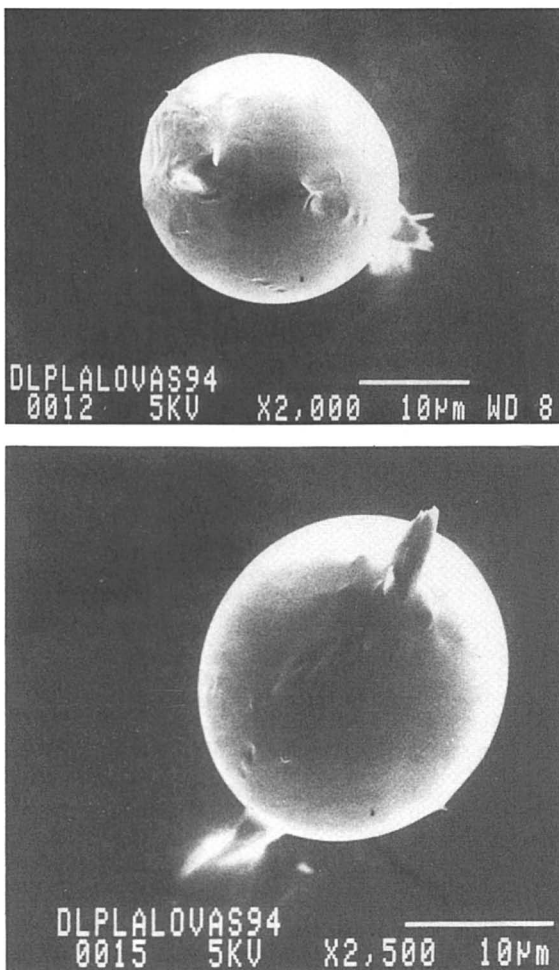


Figure 4. SEM photomicrographs of DL-PLA microspheres with embedded lovastatin needles formed in experiment 1.

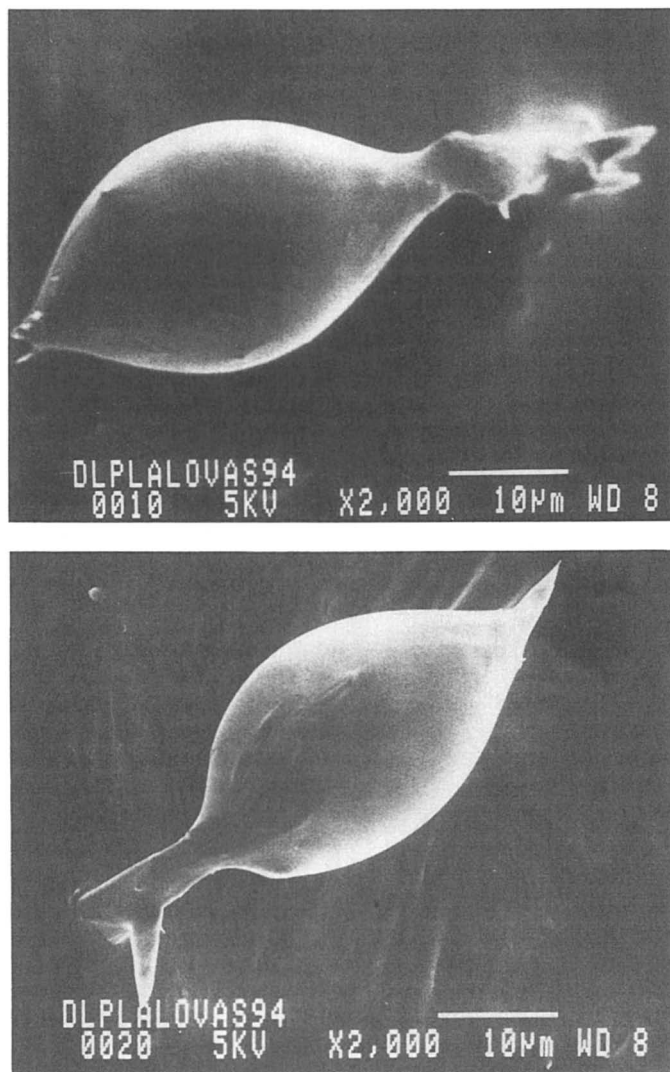


Figure 5. SEM photomicrographs of DL-PLA microparticles with embedded lovastatin needles formed in experiment 1.

lovastatin were obtained (Figure 6). Proton NMR of this precipitate revealed the presence of ca. 27 wt% lovastatin.

In a third experiment, column 1 was packed with 3.6 grams of a reprecipitated DL-PLA/lovastatin mixture. The material remaining in column 1 after the first two experiments was reprecipitated using acetone and water to produce polymer of higher molecular weight and lower polydispersity. GPC showed the polymer to have a Mw of ca. 10,000. RESS coprecipitation of material in column 1 at CO₂ extraction conditions of 200 bar and 55°C and preexpansion temperature of 80°C resulted in a solid network consisting of intertwining fibers of 2-5 μm width (Figure 7). Proton NMR of the solids showed approximately 36 wt% lovastatin. There is a preferential extraction of the lovastatin over the DL-PLA due to the polymer's increased molecular weight. The network morphology is similar to that obtained by RESS of polystyrene in supercritical pentane (5).

In these experiments, the extraction and pre-expansion conditions were similar. However, the relative amounts of polymer and drug packed into the columns were different. This variation, along with the preferential extraction of lovastatin over polymer, and the changing polymer solubility (due to changing molecular weight as extraction continues), resulted in precipitates of different composition. With both solutes in a single column, consistent results over long processing times were difficult to achieve since the polymer's solubility changes as the experiment progresses. Segregation of the polymer and drug in separate columns allows the adjustment of the drug's concentration (via bypass valves) to compensate for changes in the polymer's concentration.

While a quantitative understanding of events leading to the type of particles shown in Figures 4 and 5 remains a distant goal, it seems reasonable to assume that nucleation and growth of drug crystals occurred first, and that these particles subsequently acted as nucleating sites for the polymer. Thus, the joint evolution of the respective supersaturations of drug and polymer along the expansion path appears to be very important. It is influenced by the relative amounts of drug and polymer

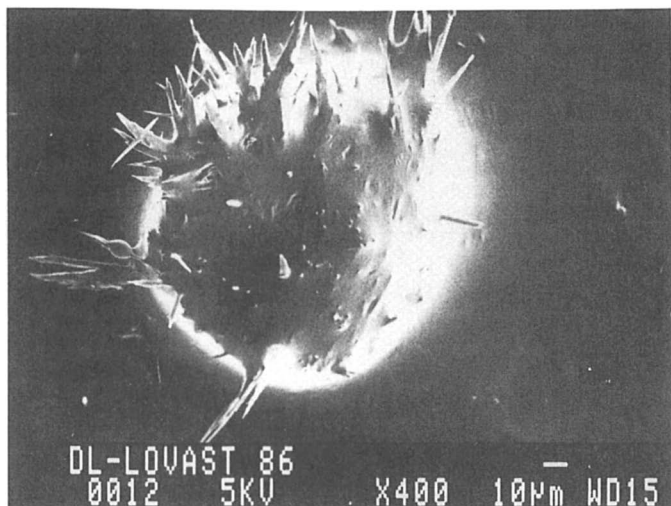


Figure 6. SEM photomicrograph of DL-PLA microparticle with multiple lovastatin needles formed in experiment 2.

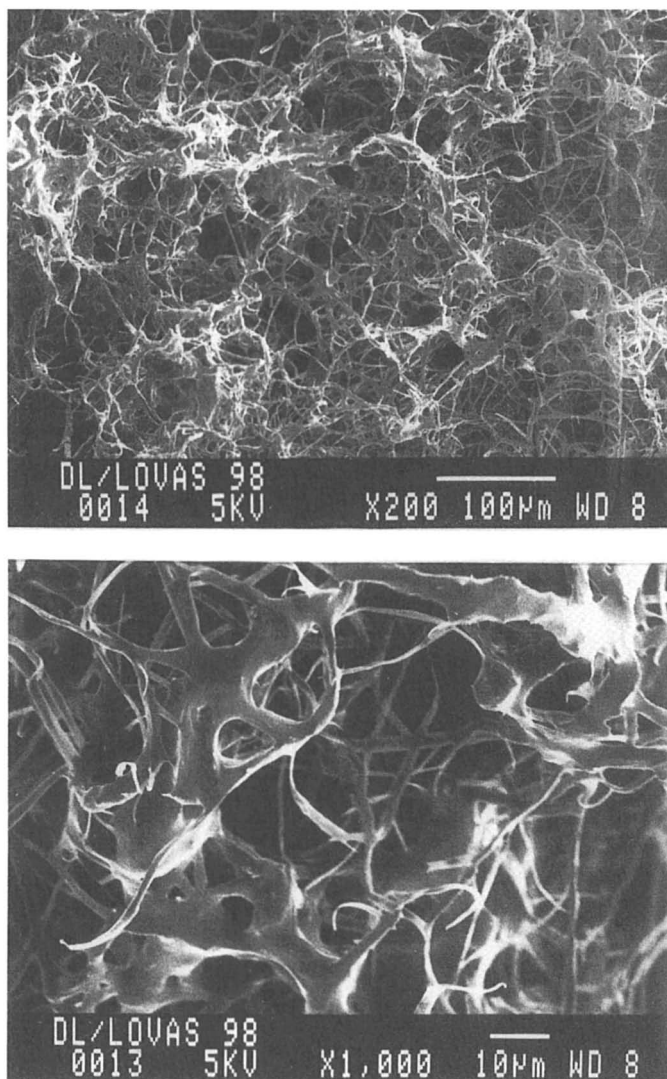


Figure 7. SEM photomicrographs of DL-PLA/lovastatin network formed in experiment 3.

initially in solution, and hence by such variables as initial column loadings, polymer molecular weight, and extraction conditions.

These exploratory experiments shows the feasibility of using RESS to coprecipitate a polymer and a drug. The results are part of ongoing investigations in our laboratory aimed at developing optimal process conditions for RESS coprecipitation of polymer-drug microspheres with consistent composition and desirable drug distribution. Various morphologies have been obtained under different polymer and drug loadings in the columns. The most important result to date is the formation of microparticle consisting of lovastatin crystals coated with polymer. The ideal polymer-drug particles for controlled drug delivery would be microspheres containing many small, uniformly dispersed drug particles, rather than single needles. This requires that the polymer precipitate before the drug particles are allowed to grow into large crystals. Work is in progress to find optimum process conditions that will lead to this desired morphology. Variables under study include extraction conditions, as well as use of capillary tubes of varying length as expansion devices. Segregation of solutes into two columns should afford better control over the coprecipitation.

Gas Anti-Solvent Crystallization. To measure the expansivity of 90% ethanol/10% DI water, the crystallizer was loaded with 20 ml of liquid solution. The liquid volume increased as CO₂ was introduced into the crystallizer under pressure, indicating dissolution of CO₂ in the ethanol/water phase. The expansivity is defined as the difference between the post and pre-pressurization liquid phase volumes (the latter at a particular pressure), divided by the initial volume (at the same temperature and atmospheric pressure) (29). The expansivity was found to increase with pressure, and to decrease with increasing temperature (Figure 8). The GAS crystallization experiments were done at 35°C, a condition that combines high expansivity with the low temperatures that are desirable for protein processing. In these experiments, the protein solution and supercritical CO₂ were pumped cocurrently into the crystallizer, which was held at 90 bar. At 35°C and above 80 bar, significant evaporation of ethanol into the supercritical phase occurs. Expansivity is only a property of the liquid phase as long as no vaporization into the gas phase occurs. When evaporation takes place, it is more appropriate to talk about the equilibrium mole fractions of solvent in the gas, and of the gas in the solvent. These quantities were not measured in our experiments. However, operation under conditions where substantial evaporation occurred was chosen so as to facilitate as complete as possible a removal of the liquid phase from the process.

In the catalase experiment, the protein solution (0.1 mg/ml) and CO₂ flow rates were 0.35 ml/min and 16.9 SLPM, respectively. The protein solution was introduced through a 20µm nozzle of 0.24 mm length. Catalase particles collected on the glass slide were either spherical or rectangular, and approximately one micron in size (Figure 9). The regular shape strongly suggests crystallinity in the precipitated protein. In the insulin experiment, the protein solution (0.1 mg/ml) was introduced through the same nozzle at 0.39 ml/min and CO₂ was charged at a rate of 18.2 SLPM. The insulin particles were collected on a filter at the exit of the CO₂/ethanol/water mixture. Two type of insulin particles were obtained (Figure 10): microspheres (≤ 1µm) and thick needles of ~5 µm length and 1µm in width. The two types of particles were found in separate areas of the filter, although some

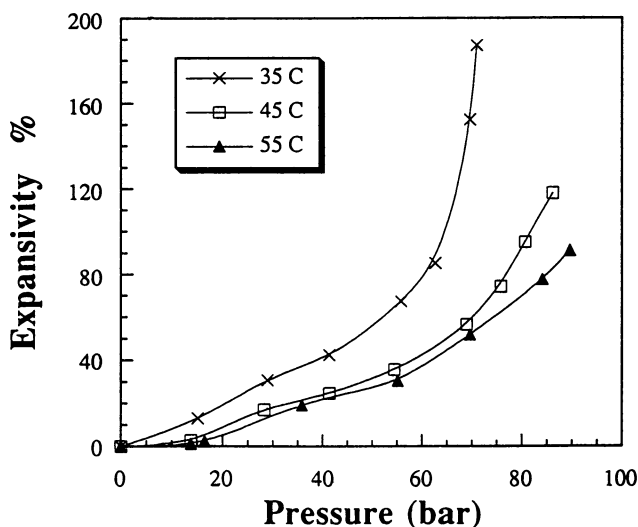


Figure 8. Expansivity of 90% ethanol/ 10% DI water with CO_2 as a function of pressure and temperature.

microspheres were found interspersed with the needles. Both catalase and insulin particles show little variation in size within a given type of particle (microspheres, needles, rectangular particles).

The ability of GAS crystallization to produce micron-sized protein particles is clear from these experiments. Given a solvent system which can be expanded with a supercritical fluid, precipitation of small, uniform protein particles is feasible. The presence of multiple morphologies was most likely the result of particles depositing on the slide or filter at different times. Samples were collected over a period of ~ 4 h in each experiment. This suggests that small variations in process conditions may be occurring and affecting the precipitate's morphology.

The use of water as a component in the protein solution is not desirable in a GAS process. This is because the residual water can not be expanded by supercritical CO_2 . Catalase and insulin were concentrated in the residual aqueous environment making it impossible to collect enough material to conduct protein activity assays. Thus, we do not know at present whether the product retained enzymatic activity. While previous work has shown supercritical conditions to have a minimal effect on enzyme activity, the specific cases of catalase and insulin with CO_2 have not been documented. Alternate liquid solvents such as dimethyl sulfoxide and formamide have been shown to solubilize proteins (30) and are currently being investigated in our laboratory as possible routes for elimination of water from the process. In general, a good GAS solvent should have high solvent power toward the protein of interest, and exhibit large expansivity toward a supercritical fluid at temperatures not exceeding 35°C.

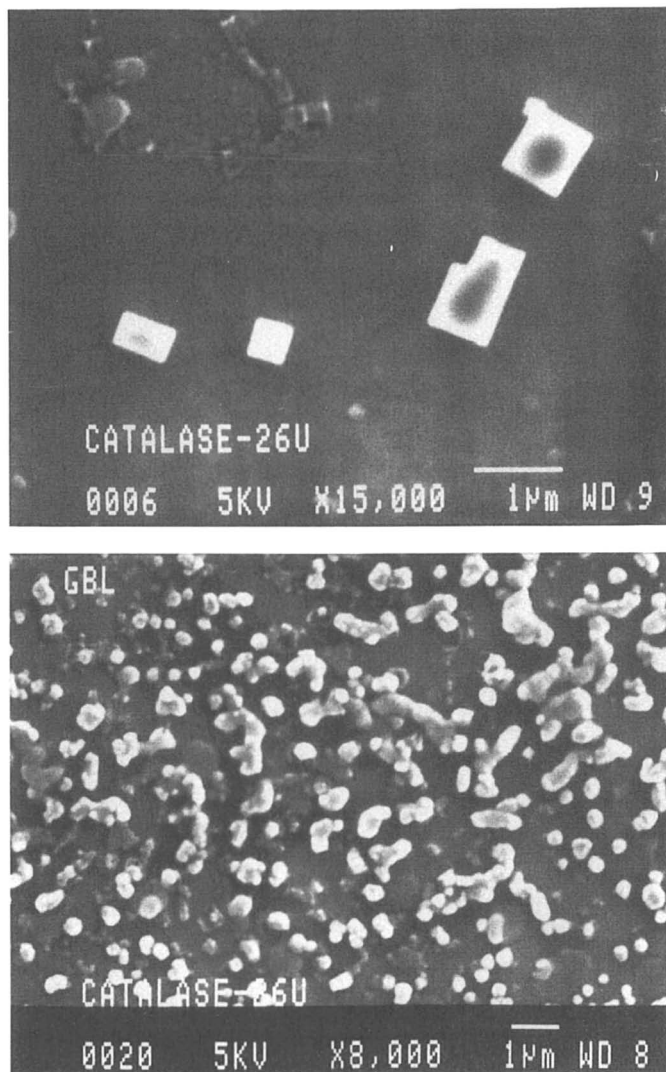


Figure 9. SEM photomicrographs of catalase particles formed by GAS crystallization.

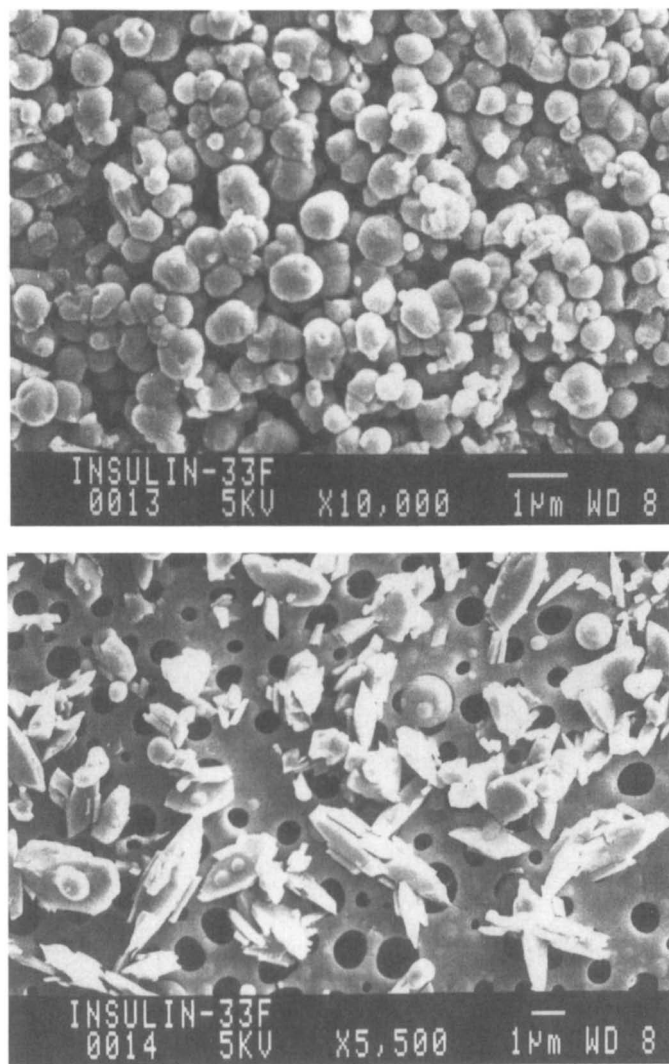


Figure 10. SEM photomicrographs of insulin particles formed by GAS crystallization.

Conclusions

Supercritical fluids have great potential in the area of controlled delivery of drugs. We have chosen two preliminary examples from ongoing work to illustrate this point. One, involving the use of rapid expansion of supercritical solutions as a method for the fabrication of polymer-drug microspheres and microparticles; the other involves the application of gas anti-solvent crystallization to process proteins into micron-sized particles for subsequent incorporation into microcarriers. The advantages of RESS as a method for producing polymer-drug microcarriers are the elimination of surfactants and organic solvents, low-temperature operation (with CO₂), and single-step processing. GAS crystallization shows considerable promise as a process for comminution of proteins down to micron-sized particles.

Rapid expansion of supercritical solutions containing DL-PLA and lovastatin extracted from a column packed with both solutes produced particles exhibiting a range of morphology and composition. Precipitates with high lovastatin concentration (>30%) showed a network morphology while those with lower lovastatin concentration (< 30 wt%) showed microparticle and microsphere morphology. The network consisted of intertwining strands of polymer with the drug incorporated in the strands. The particles consisted of drug needles coated with polymer. The reduction in lovastatin concentration, as well as more effective control over the relative amounts of both components present in the final product, can be more effectively achieved by separating the solutes in different columns.

GAS crystallization using a continuous apparatus produced small catalase and insulin particles ($\leq 5\mu\text{m}$). A range of morphologies was obtained: microspheres, rectangular-shaped particles and needles with low aspect ratios. The use of water in the liquid solvent makes it impossible to collect a sufficient amount of protein powders to assay its enzymatic activity. Use of organic solvents such as DMSO is currently being investigated in our laboratory.

Acknowledgements

PGD gratefully acknowledges the support of the National Science Foundation (Grant CTS-9000614), Enzytech Inc. (Cambridge, MA), the John Simon Guggenheim Memorial Foundation (1991 Fellowship), and the Camille and Henry Dreyfus Foundation (1989 Teacher-Scholar Award). JWT acknowledges the National Science Foundation for a Pre-Doctoral Fellowship. Lovastatin was generously donated by Merck Research Laboratories.

Literature Cited

1. Li, V.H.K.; Robinson, J.R.; Lee, V.H.L. In *Controlled Drug Delivery, Fundamentals and Applications*. Robinson, J.R. and Lee, V.H.L., Eds.; Marcel Dekker: New York, 1987; Chapter 1.

2. Heller, J. In *Medical Applications of Controlled Release*. Langer, R.S. and Wise, D.L., Eds.; CRC Press: Boca Raton, FL, 1984.
3. Juni, K.; Nakano, M. *CRC Crit. Rev. Ther. Drug Carrier Syst.* **1987**, *3*, 209.
4. Spenlehauer, G.; Spenlehauer-Bonthonneau, F.; Thies, C. *Prog. Clin. Biol. Res.(Biol. Synth. Membr.)* **1989**, *292*, 283.
5. Matson, D.W.; Fulton, J.L.; Petersen, R.C.; Smith, R.D. *Ind. Eng. Chem. Res.* **1987**, *26*, 2298.
6. Gallagher, P.M.; Coffey, M.P.; Krukonis, V.J.; Klasutis, N. In *Supercritical Fluid Science and Technology*; Johnston, K.P., Penninger, J.M.L., Eds.; ACS Symposium Series 406; American Chemical Society: Washington, DC, 1989; Chapter 22.
7. Krukonis, V.J. "Supercritical Fluid Nucleation of Difficult to Comminute Solids," presented at the AIChE Annual Meeting, San Francisco, November (1984).
8. Larson, K.A.; King, M.L. *Biotechnol. Prog.* **1986**, *2*, 73.
9. Loth, H.; Hemgesberg, E. *Int. J. Pharm.* **1986**, *32*, 265.
10. Mohamed, R.S.; Halverson, D.S.; Debenedetti, P.G.; Prud'homme, R.L. In *Supercritical Fluid Science and Technology*; Johnston, K.P., Penninger, J.M.L., Eds.; ACS Symposium Series 406; American Chemical Society: Washington, DC, 1989, Chapter 23.
11. Tom, J.W.; Debenedetti, P.G. *J. Aerosol Sci.* **1991**, *22*, 555.
12. Kumar, S.K.; Johnston, K.P. *J. Supercrit. Fluids* **1988**, *1*, 15.
13. Debenedetti, P. G. *AIChE J.* **1990**, *36*, 1289.
14. Dixon, D.J.; Johnston, K.P. *AIChE J.* **1991**, *37*, 1441.
15. Chang, C.J.; Randolph, A.D.; Craft, N.E. *Biotechnol. Prog.* **1991**, *7*, 275.
16. Otsuka, M.; Kaneniwa, N. *Int. J. Pharm.* **1990**, *62*, 65.
17. Rosen, H.B.; Kohn, J.; Leong, K.; Langer, R. In *Controlled Release Systems: Fabrication Technology*; Hsieh, D., Ed.; CRC Press: Boca Raton, FL, 1988; Vol. 2, pp 83-111.
18. Gombotz, W.R.; Healy, M.S.; Brown, L.R.; Auer, H.E. International Patent WO 90/13285, November 15, 1990.
19. Tom, J.W.; Debenedetti, P.G. *Biotechnol. Prog.* **1991**, *7*, 403.
20. Mueller, B.W.; Fischer, W. West Germany Patent 3,744,329, July 6, 1989.
21. Matson, D.W.; Petersen, R.C.; Smith, R.D. *Adv. Ceram. Mater.* **1986**, *1*, 242.
22. Gallagher, P.M.; Krukonis, V.J.; VandeKieft, L.J. *Proc. 2nd Int. Symp. Supercrit. Fluids.* 1991, Boston, MA. p.45.
23. Randolph, T.W.; Blanch, H.W.; Prausnitz, J.M. *AIChE J.* **1988**, *34*, 1354.
24. Randolph, T.W.; Clark, D.S.; Blanch, H.W.; Prausnitz, J.M. *Sci.* **1988**, *239*, 387.
25. Randolph, T.W.; Clark, D.S.; Blanch, H.W.; Prausnitz, J.M. *Proc. Nat'l. Acad. Sci. USA*, **1988**, *85*, 2979.
26. Hammond, D.A.; Karel, M.; Klivanov, A.M.; Krukonis, V.J. *Appl. Biochem. Biotech.* **1985**, *11*, 393.
27. Gale, R.W.; Fulton, J.L.; Smith, R.D. *J. Am. Chem. Soc.* **1987**, *109*, 920.
28. Weder, J. *Food Chemistry* **1984**, *15*, 175.

29. Chang, C.J.; Randolph, A.D. *AICHE J.* **1990**, *36*, 939.

30. Rees, E.D.; Singer, S.J. *Arch. Biochem. Biophys.* **1956**, *63*, 144.

RECEIVED April 27, 1992

Chapter 20

Dynamic Fluorescence Quenching in Reverse Microemulsions in Propane

Thomas S. Zemanian, John L. Fulton, and Richard D. Smith

Chemical Methods and Separations Group, Chemical Sciences Department,
Pacific Northwest Laboratory, P.O. Box 999, Richland, WA 99352

Measurements have been made of micelle size and core exchange rates of reverse (water-in-oil) micellar systems of sodium bis-(2-ethylhexyl) sulfosuccinate (AOT) or didodecyl dimethyl ammonium bromide (DDAB) and water in propane at various pressures and temperatures. Ruthenium tris(bipyridyl) dichloride, soluble in the aqueous phase, was used as a fluorescent probe to determine surfactant aggregation numbers, and hence water core radii. Potassium ferricyanide was used as the water-soluble quencher in these experiments. Pressure and temperature effects are discussed as they pertain to bulk oil phase and surfactant properties.

Microemulsions are thermodynamically stable, optically clear fluid systems consisting of a nonpolar ("oil") phase and a polar, generally aqueous, phase separated by a monolayer of an amphiphilic compound (surfactant). These systems are of broad practical significance (from cosmetics to enhanced oil recovery), and are of scientific interest due to their structure and dynamic nature.

Such systems can order themselves in various fashions, depending on the system temperature, pressure, and the molar ratios between the polar, nonpolar, and amphiphilic components. Three general structures may be identified. A stable microemulsion may contain (i) a continuous aqueous phase with interspersed microdroplets of oil surrounded by surfactant (micellar), (ii) a continuous oil phase containing microdroplets of water surrounded by surfactant (reverse micellar, or water-in-oil (w/o)), or (iii) a bicontinuous structure, in which both phases are continuous and intertwined.

For this paper we shall focus on reverse micellar systems of water, iso-octane, liquid and supercritical propane, and didodecyl dimethyl ammonium bromide (DDAB) or sodium bis-(2-ethylhexyl) sulfosuccinate (AOT) as the surfactant. The use of compressed propane as the oil phase allows tuning of the system characteristics with pressure. Tingey *et al.* (1) have shown, from measurements of the system electrical conductivity, a transition from a bicontinuous system to a reverse micellar system over a narrow range of pressure for the DDAB/propane/water system.

0097-6156/93/0514-0258\$06.00/0
© 1993 American Chemical Society

Although microemulsions are thermodynamically stable, they are by no means static. The micelles and bicontinuous structures are constantly changing and reforming. Infelta (2) developed a method to measure the micelle size using a fluorescent probe molecule and a quencher at sufficiently low concentration to ensure no more than one probe molecule per micelle. This technique may also be used in a time-resolved mode by monitoring the fluorescence decay after excitation by a sharp pulse of light. Such measurements allow determination of the rate at which the micelles coalesce and separate, and in particular the rate of mixing of the contents of their cores. (3,4)

Atik and Thomas (3) give the canonical equation for the decay of fluorescence from such systems as

$$\ln(I/I_0) = -A_2t - A_3(1 - \exp(-A_4t))$$

where I is the fluorescence intensity at time t after the laser pulse, I_0 is the fluorescence at time $t=0$, and A_2 , A_3 , and A_4 are constants derived from kinetic arguments (5). If the assumption can be made that the rate of quenching is much greater than the rate of micelle core exchange, and that the quencher resides almost entirely in the micelle core, then

$$A_2 = k_1 + k_e [Q_t]$$

$$A_3 = [Q_t]/[M] \quad \text{and}$$

$$A_4 = k_q.$$

In the preceding equations, k_1 is the inverse of the unquenched fluorescence lifetime (t), k_e is the bimolecular exchange rate constant, $[Q_t]$ is the molar concentration of the quencher in the microemulsion, $[M]$ is the concentration of micelles, and k_q is the rate of quenching within the micelle water core. From $[M]$ and the known water and surfactant concentrations, one may deduce the water core radius and the surfactant aggregation number for the system. Taking the volume occupied by one molecule of water to be 30 \AA^3 (corresponding to 1.0 g/ml) and assuming the micelle core to be a sphere,

$$R = 1.928 \{[H_2O]/[M]\}^{(1/3)} = 1.928 \{[H_2O] A_3/[Q_t]\}^{(1/3)}$$

where $[H_2O]$ is the concentration of water in the microemulsion and R is the micelle water core radius, given in Angstroms.

Use of this technique for the DDAB/propane/water reverse micellar system requires selection of a fluorescent probe that is water soluble and has a fluorescent lifetime significantly greater than the time scale on which the micelles mix. The ruthenium tris-bipyridyl dication ($\text{Ru}(\text{bipy})_3^{2+}$) is such a probe, and may be quenched using potassium ferricyanide ($\text{K}_3\text{Fe}(\text{CN})_6$). Unfortunately, the fluorescent lifetime of $\text{Ru}(\text{bipy})_3^{2+}$ drops dramatically with increasing temperature.(6) This places an upper limit of approximately 100°C on the use of this probe for dynamic fluorescence quenching experiments. At higher temperatures the lifetime of the probe is insufficient to experience transfer in the excited state from one micelle to another, and hence one cannot probe the rate of micelle core exchange. Some short time data may be recovered in such situations, thereby yielding water core radius information.

Experiment

The fluorescent probe, ruthenium tris-bipyridyl dichloride hexahydrate ($\text{Ru}(\text{bipy})_3\text{Cl}_2 \cdot 6\text{H}_2\text{O}$), was purchased from Chemical Probes, Inc., and was recrystallized from methylene chloride. A 5.35 mM aqueous solution was prepared using the purified probe and distilled, deionized water. This solution was then deoxygenated with nitrogen and sealed in a septum vial. The potassium ferricyanide ($\text{K}_3\text{Fe}(\text{CN})_6$) was obtained from Alfa Products, Inc. and used as received. A 107 mM aqueous solution was prepared, deoxygenated, and sealed in a septum vial. The propane was obtained from Scott Specialty Gases (CP grade) and passed through an oxygen trap (Alltech, Oxy-Purge-N) prior to use. The DDAB was purchased from Eastman Kodak and was recrystallized prior to use. The AOT was purchased from Fluka and purified by the method of Kotlarchyk *et al.* (7) The iso-octane was from Aldrich, and was deoxygenated by bubbling with purified propane just prior to use.

The apparatus used to measure the fluorescence quenching rates is shown in schematic diagram in Figure 1. An 8 ns pulse from a neodymium YAG laser was used to excite the probe using the 532 nm wavelength. The beam was attenuated by using the reflection off the front face of a quartz wedge. This was further attenuated with a divide-by-ten neutral density filter, after which the beam was directed into the pressure cell. This cell was a stainless steel monoblock with an internal volume of 13 ml and was fitted with sapphire windows at right angles to each other. Laser light entered the cell through one of the windows and the subsequent fluorescence of the probe in the micelle water cores was measured through the other window at 90 degrees to the excitation beam. A bandpass filter (600 nm to 630 nm) was used at the exit window to pass the $\text{Ru}(\text{bipy})_3^{2+}$ fluorescence signal (centered at 614 nm) and attenuate stray laser light (532 nm) and fluorescence from the sapphire windows (691 nm). No attempt was made to use magic angle polarization, as the sapphire windows are not isotropic to polarized light.

The fluorescence signal was measured using a side-on photomultiplier tube (PMT, type 948, Hamamatsu) driven at -480 V. The PMT was designed for pulsed/fast response and was terminated with a 50 ohm load. The signal from the PMT was recorded and stored on a LeCroy 7200 storage oscilloscope with a 7242 plug-in interface. The cell and PMT were housed in a black lined box to reduce room light leakage. The temperature of the cell was controlled electrically and measured using a platinum resistance temperature device (Omega). The cell was stirred magnetically. Pressure in the cell was regulated using a hand operated syringe pump (HIP) and was measured using a pressure transducer (Precise Sensors, Inc.).

The spreading of the data due to the PMT response was measured by operating with an AOT/iso-octane/water microemulsion without probe or quencher in the cell. A point-successive deconvolution routine was used to remove this instrument function spreading from the data, and the canonical equation was then fit to the resulting traces using the Marquart nonlinear least-squares technique. A smoothing filter was used during the deconvolution routine to quell high frequency noise that otherwise crept in at the trace edges during iteration. This filter was triangular symmetric and ten nanoseconds in width to prevent significant distortion of the object function. Some slight ringing was noted in some of the short time data, but the fitting routine was able to converge to an acceptable fit despite the deviations.

The unquenched fluorescence lifetime (τ) of the probe is required to extract exchange rate data from measurements of A_2 . This lifetime is temperature dependent and hence τ was first measured in a dilute aqueous solution at temperatures ranging

from 25°C to 135°C. These data were fitted to the equation given by Caspar and Meyer (6):

$$1/\tau = k_1 = k' + k^{\circ} \exp(-\Delta E'/k_B T)$$

where: k_1 is the unquenched fluorescence rate, k' and k° are equation constants, T is absolute temperature, k_B is Boltzmann's constant, and $\Delta E'$ is an effective activation energy.

As shown in Figure 2, this equation fits the data well. However, the fitted constants k' , k° , and $\Delta E'$ differ significantly from those given by Caspar and Meyer, due to differences in the temperature regimes addressed (see Table I).

Table I. Probe lifetime parameters

	Temperature [° C]	k' [s ⁻¹]	k° [s ⁻¹]	$\Delta E'$ [cm ⁻¹]
Caspar & Meyer	-12 to 21	4.1×10^5	4.5×10^{13}	3560
This work	25 to 135	1.5×10^6	1.6×10^{14}	4222

Moreover, the unquenched fluorescence rate of the probe will differ in the micelle core from that in aqueous solution. However, this will introduce an additive systematic error in the exchange rate data at any given temperature; the trends along each isotherm will be preserved.

The fluorescence quenching method and the apparatus were first tested by filling the cell with a reverse (w/o) microemulsion of AOT/iso-octane/water at a water to surfactant ratio of $W=15$ and at a surfactant concentration of $[AOT] = 125$ mM. A small quantity (25 μ l) of the 5.35 mM probe solution was added to bring $[P]$ to 10.3 μ M, and the cell contents were deoxygenated by bubbling with purified propane for 15 minutes. The fluorescence decay was then measured and found to be purely exponential decay with a lifetime of 355 ns at 25°C (see Figure 3a).

That this figure is lower than that in pure water confirms that the probe behaves slightly differently in the micelle core than in aqueous solution, as discussed above. However, this results in a k_1 63% larger than that given by the fitted equation. Since k_1 in our study was significantly smaller (15% at the lower temperatures, rising to 50 % at the highest temperatures) than the measured values of A_2 (from which k_1 is subtracted), the error is generally under 10% and rises to 30 % at 100°C. This error is a constant additive offset of the k_e data for each isotherm, so the trends with pressure are preserved. This error does not affect the water core radius measurements.

A small amount of the 107 mM quencher solution (25 μ l) was added to bring $[Q]$ to 205.8 μ M, and the fluorescence decay was again measured (see Figure 3b). These data, when plotted on a semilog basis showed the expected exponential decay followed by straight line decay (see Figure 3c).

The cell was emptied and cleaned, and (w/o) microemulsions of AOT/propane/water at $W=15$, $[AOT]=125$ mM and of DDAB/propane/water at $W=23$ and $[DDAB]=325$ mM were examined in the system. The pressure was varied from the cloud point of the systems to approximately 500 bar. For the DDAB/propane/water system the temperature was also varied from room temperature (25°C) to 100°C.

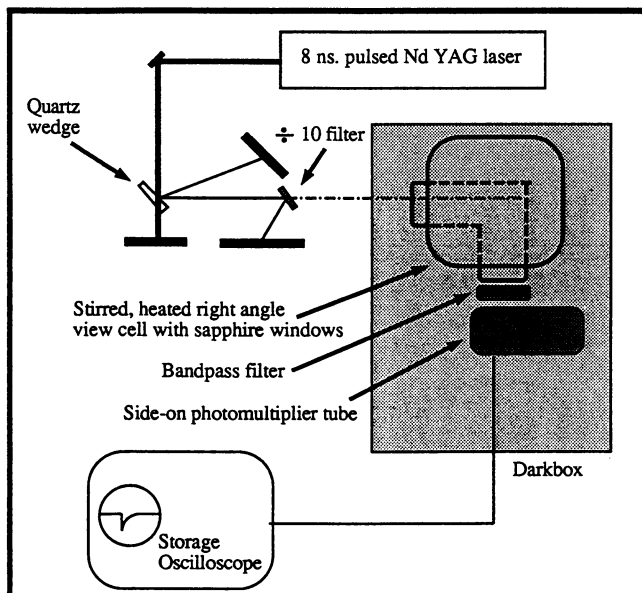


Figure 1: Schematic diagram of the apparatus used to measure quenched fluorescence lifetimes in reverse micelles

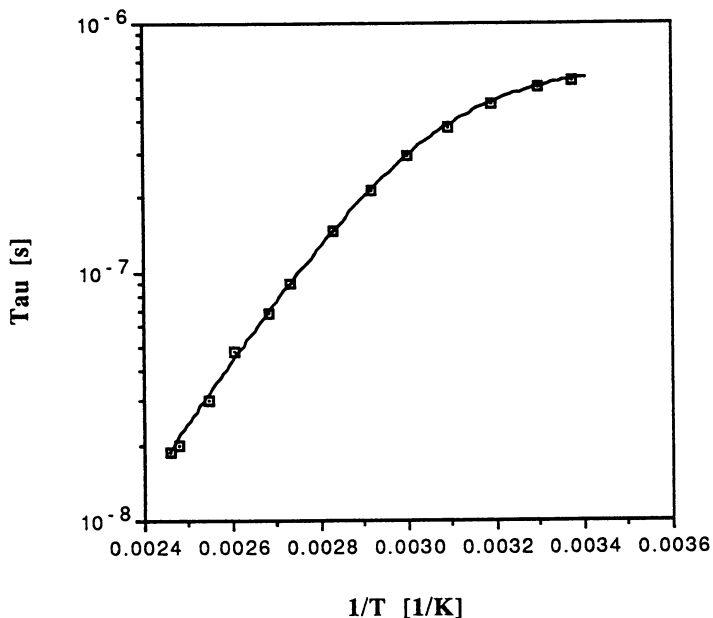


Figure 2: Ru(bipyridyl) $_3^{2+}$ fluorescence lifetime as a function of inverse temperature. Fitted equation is that given by Caspar and Meyer.(5)

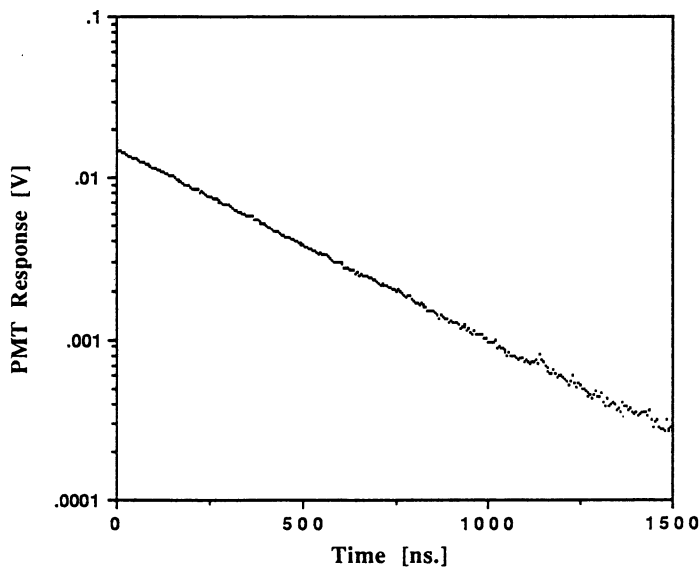


Figure 3a: Unquenched probe fluorescence in the AOT/iso-octane/ water system at 25°C and 1 atm. $W=15$, $[AOT]=125$ mM.

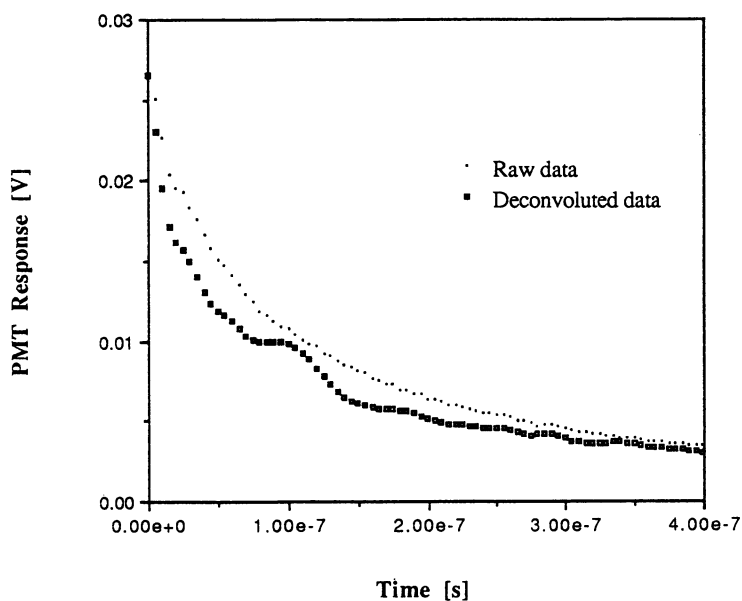


Figure 3b: Fluorescence decay in the AOT/iso-octane/water system at 25°C and 1 atm. $W=15$, $[AOT]=125$ mM.

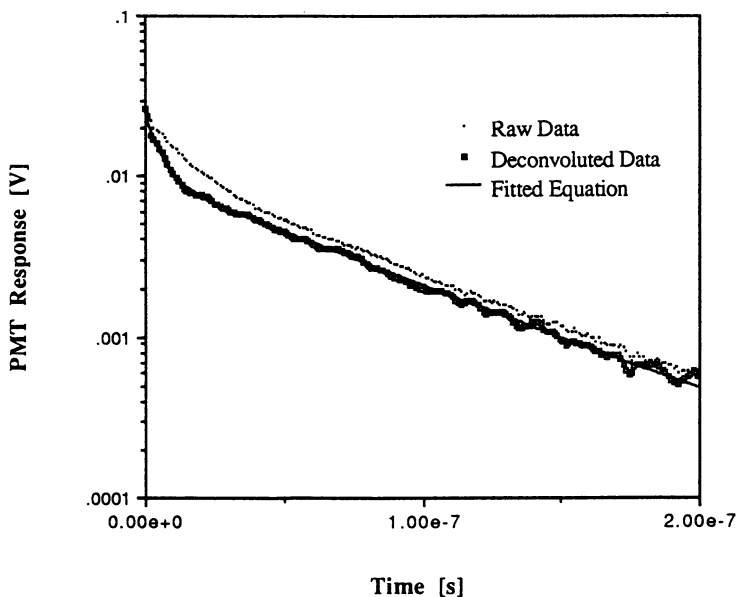


Figure 3c: Fluorescence decay in the AOT/iso-octane/water system at 25°C (semi-log plot) and 1 atm. $W=15$, $[AOT]=125$ mM.

Unfortunately, the 100°C data were of poor quality; at such temperatures the probe lifetime became sufficiently short that very little of the short time decay remained to be fitted, as is evident in Figure 4.

Results and Discussion

Figure 5a shows the pressure dependence of the water core radius as measured for the AOT/propane/water system ($W=15$, $[AOT]=125$ mM). For comparison, the AOT/iso-octane/water system was also run at ambient conditions (25°C and 1 bar) at the same values of W and $[AOT]$. For the iso-octane system the measured water core radius was 2.37 nm.

The micelle size found in iso-octane was similar to that found in propane, confirming other studies of these systems that solvent type has little effect on the size of the micelles. The measured size in iso-octane compares well with what has been reported by other techniques, such as quasi-elastic light scattering (QELS).⁽⁸⁾

Figures 5a and 5b show the pressure dependence of the water core radii for the AOT/propane/water and DDAB/propane/water systems, respectively. The water core radii are independent of pressure over the pressure range studied. This independence reflects the incompressibility of water at these conditions, the insensitivity of the surfactant headgroup surface area to the density of the surrounding nonpolar medium, and the extremely low critical micelle concentrations (cmc) of these systems.

Figure 5c presents the water core radius of the DDAB/propane/water system as a function of temperature. The response to temperature is consistent with the literature^(9,10). A slight decrease in size with increasing temperature is noted. The density of liquid water at these conditions is relatively constant, so the size dependence is

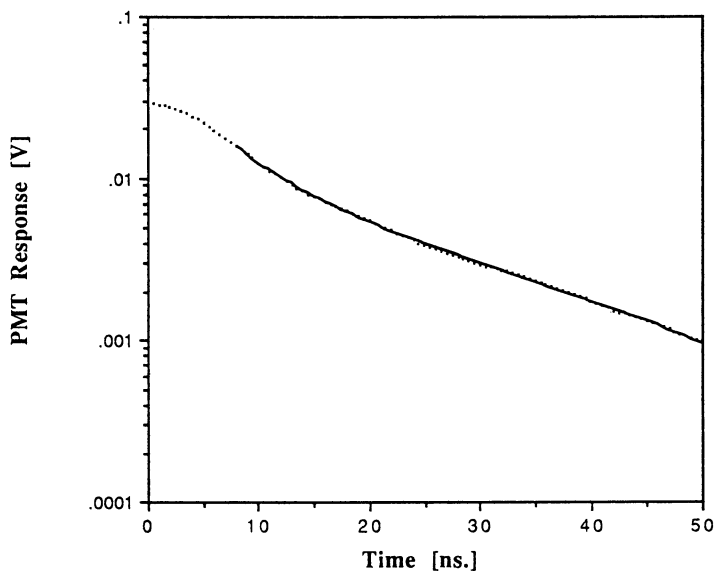


Figure 4: Quenched fluorescence decay in the DDAB/propane/water system at 100°C and 400 bar. W=23, [DDAB]=325 mM.

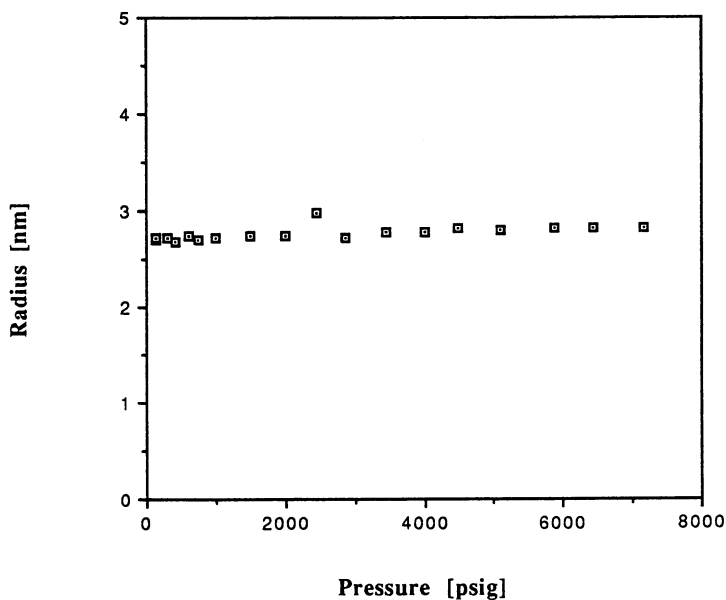


Figure 5a: Water core radius as a function of pressure for the AOT/propane/water system at 25°C. W=15, [AOT]=125 mM.

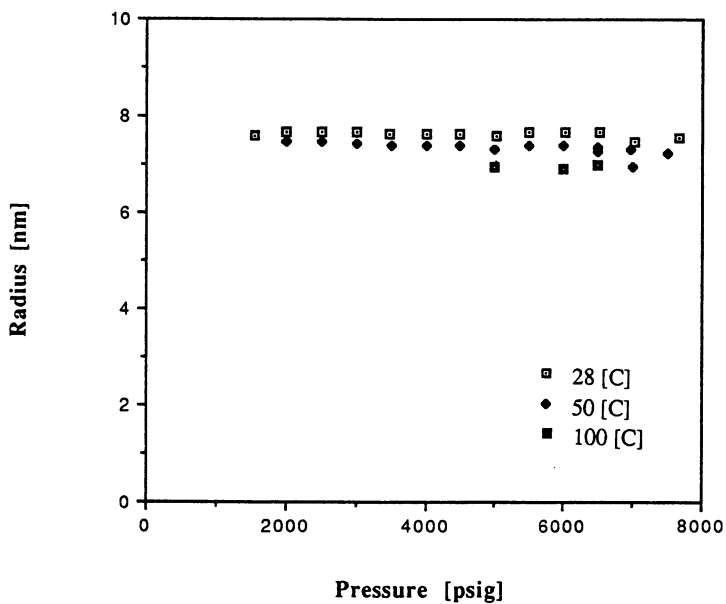


Figure 5b: Water core radius as a function of pressure for the DDAB/propane/water system. $W=23$, $[DDAB]=325$ mM.

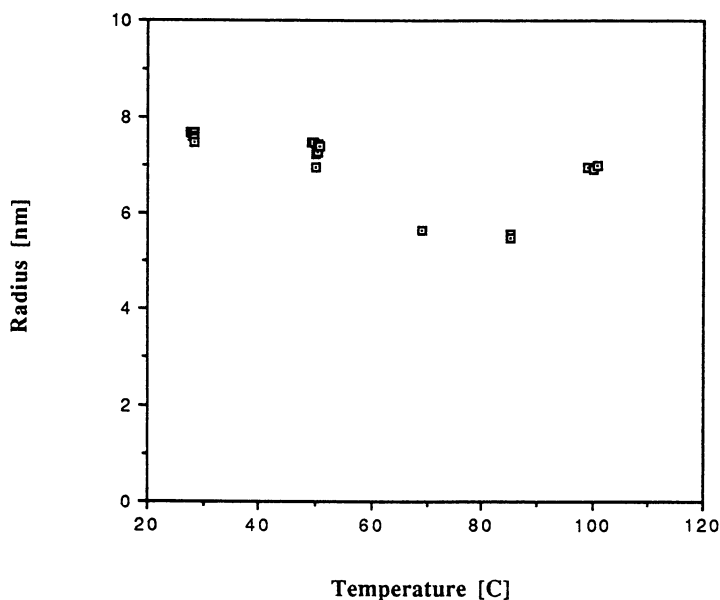


Figure 5c: Water core radius as a function of temperature for the DDAB/propane/water system. $W=23$, $[DDAB]=325$ mM.

probably a result of an increase in the effective surface area of the surfactant molecule headgroups, rather than a result of a change in water volume. (At 28°C the effective headgroup area for DDAB in propane is found to be 23.9 Å², and increases to 24.8 Å² at 50°C and 29.4 Å² at 100°C.) This may be due to greater solvation of the surfactant hydrocarbon tails by the nonpolar bulk fluid at the higher temperatures.

Figures 6a and 6b show the bimicellar water core exchange rate constant (k_e) as a function of pressure in the AOT/propane/water system and the DDAB/propane/water system, respectively. For comparison, k_e for the AOT/iso-octane/water system at 25°C was found to be 1.67×10^9 [l/mol-s]; approximately 6% of that in the propane-based systems. This value agrees well with the values of Lang *et al.* (9) for the DTAB/1-pentanol/chlorobenzene/water system, the tetradecyltrimethyl ammonium bromide/1-butanol/chlorobenzene/water system, and the hexadecyltrimethyl ammonium bromide/1-butanol/chlorobenzene/water systems. They report exchange rate constants between 1×10^9 and 2×10^9 [l/mol-s].

The large differences in exchange rates between the liquid propane and liquid iso-octane systems are not due to differences in micelle size in the two solvents. Numerous studies have shown that the nature of the alkane solvent has little effect on the size of the micelles. The high rates in propane are largely due to lower viscosity of this solvent and the resulting higher micellar diffusivities. The mechanism of core exchange upon micellar collision also plays a role in determining the exchange rate, and may be affected by the nature of the continuous phase solvent.

In both systems the exchange rate is largely independent of pressure, although a weak pressure dependence may be noted in the supercritical propane/DDAB system, although the data are too sparse to conclusively prove this dependence.

In contrast, the exchange rate constant shows a strong increase with temperature (Figure 6c), in agreement with Jada *et al.* (11) This can be attributed to the temperature dependence of viscosity (12) of the bulk phase, resulting in greater diffusion rates of the micelles at higher temperatures.

Conclusions

Reverse micelles of AOT in iso-octane, AOT in propane, and DDAB in propane have been examined using the dynamic fluorescence quenching technique to measure micelle water core radii and bimicellar exchange rate constants. In the propane-based systems several pressures were considered and for the DDAB/propane/water system the temperature was varied between 25°C and 100°C to span the subcritical/supercritical transition of the bulk phase propane.

The water core radii thus obtained agree qualitatively with those obtained by SANS or QELS, and the data show the expected trends with variance of pressure and temperature. Specifically, the water core radii of these systems are independent of pressure (reflecting the incompressibility of water at these conditions and the insensitivity of the surfactant headgroup to the bulk phase conditions), and are largely independent of temperature.

The bimicellar exchange rate constants of these systems are similarly independent of pressure, reflecting the insensitivity of the micellar system to the density of the solvating fluid. The bimicellar exchange rates are strongly temperature dependent, reflecting the sensitivity to temperature of the bulk phase transport properties. More data are required to determine if the micelle mixing is more significant at higher temperatures, *i.e.*, if the increase in micellar core exchange rate is controlled purely by diffusional concerns.

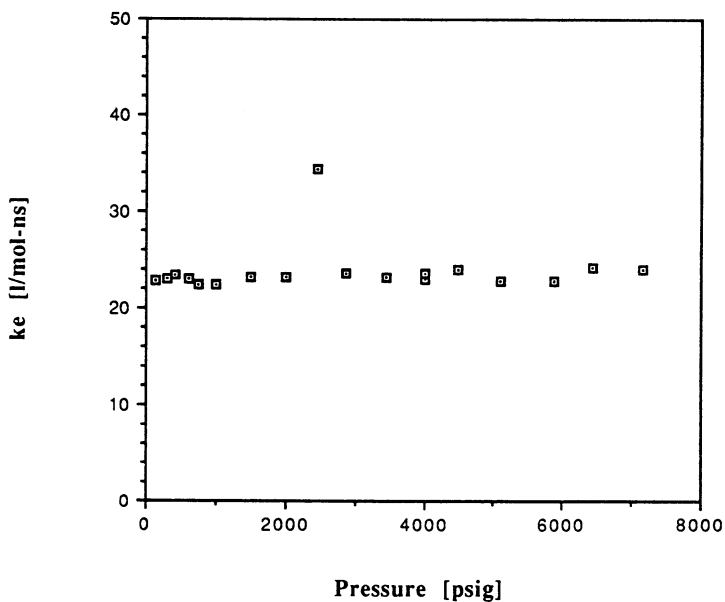


Figure 6a: Bimicellar exchange rate constant as a function of pressure for the AOT/propane/water system at 25°C. W=15, [AOT]=125 mM.

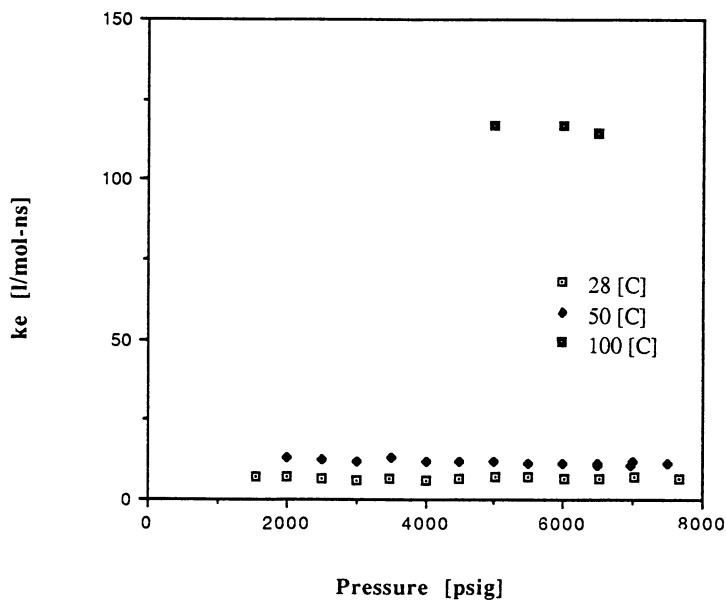


Figure 6b: Bimicellar exchange rate constant as a function of pressure for the DDAB/propane/water system. W=23, [DDAB]=325 mM.

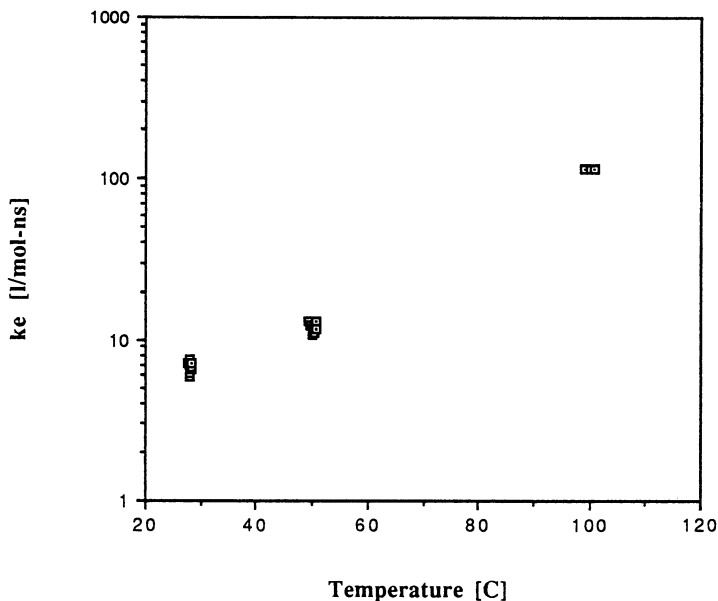


Figure 6c: Bimicellar exchange rate constant as a function of temperature for the DDAB/propane/water system. W=23, [DDAB]=325 mM.

Acknowledgments

The authors wish to thank Don Friedrich and Wayne Hess of the Molecular Science Research Center at Battelle Pacific Northwest Laboratories (Richland, WA) for help with and the use of the laser system. This work was sponsored by the Office of Basic Energy Sciences of the U.S. Department of Energy, contract number DE-AC06-76RLO 1830. T.S. Zemanian is a postdoctoral appointee at PNL through the Northwest College and University Association for Science (Washington State University, Pullman, WA).

Literature Cited

1. Tingey, J.M.; Fulton, J.L.; Matson, D.W.; and Smith, R.D. *J. Phys. Chem.*, **1991**, *95*, 1445-1448
2. Infelta, P.P.; Grätzel, M.; and Thomas, J.K. *J. Phys. Chem.*, **1974**, *78*, 190-195
3. Atik, S.S.; and Thomas, J.K. *J. Am. Chem. Soc.*, **1981**, *103*, 3550-3555
4. Dederen, J.C.; Van der Auweraer, M.; and Schryver, F.C. *Chem. Phys. Lett.*, **1979**, *68*, 451-454
5. Atik, S.S., and Singer, L.A. *Chem. Phys. Lett.*, **1978**, *59*, 519
6. Caspar, J.V., and Meyer, T.J. *Inorg. Chem.*, **1983**, *22*, 2444-2453
7. Kotlarchyk, M.; Chen, S.; Huang, J.S.; and Kim, M.W. *Phys. Rev. A*, **1984**, *29*, 2054-2069

8. Jada, A; Lang, J.; Zana, R.; Makhloufi, R.; Hirsch, E.; and Candau, S.J. *J. Phys. Chem.*, **1990**, *94*, 387-395
9. Lang, J; Jada, A.; and Malliaris, A. *J. Phys. Chem.*, **1988**, *92*, 1946-1953
10. Lang, J.; Lalem, N; and Zana, R. *J. Phys. Chem.*, **1991**, *95*, 9533-9541
11. Jada, A; Lang, J; and Zana, R. *J. Phys. Chem.*, **1989**, *93*, 10-12
12. Younglove, B.A.; and Ely, J.F. *J. Phys. Chem. Ref. Data*, **1987**, *16*, 577-798

RECEIVED April 27, 1992

Chapter 21

Light Scattering Study of Polymer Network Formation in a Supercritical Diluent

J. Richard Elliott, Jr., and H. Michael Cheung

Department of Chemical Engineering, The University of Akron,
Akron, OH 44325-3906

We have undertaken a study of the benefits of using near-critical and supercritical fluids in synthesizing microcellular foams. In this study, we use dynamic light scattering to study the formation of the polymer network directly in near-critical and supercritical freon-22. The polymer system studied is ethylene-glycoldimethacrylate+methylmethacrylate. We have previously obtained microcellular foams by direct polymerization in this system and this study elucidates the gelation process by tracking the correlation length of the inhomogeneities as a function of reaction time from the monomeric state to the gel transition.

A relatively little-known class of materials called aerogels has recently been the focus of several studies. The distinctive feature of these materials is that they combine extremely small pore sizes with remarkably low density, leading to some unique properties. For example, silica aerogel can have a density of 0.05 g/cm^3 while maintaining pore sizes small enough that the bulk material is completely transparent; the pores are too small to refract visible light. Many applications can be envisioned for such materials, including thermally insulating windows, catalyst supports, and membranes (1). However, there are some technical obstacles. Most notably, the silica aerogels are extremely fragile. This has led to attempts to develop organic aerogels (2) also known as microcellular foams (1,3). Organic chemistry offers a broad range of possible molecular designs and polymerization mechanisms which provide alternatives to the silica aerogel process. A systematic approach for developing robust materials with unique and desirable properties may be obtained by combining an understanding of the fundamental processes occurring during the formation of aerogels with the ability to design and synthesize monomers tailored to a specific function.

0097-6156/93/0514-0271\$06.00/0
© 1993 American Chemical Society

In previous studies, we have explored the feasibility of forming aerogels from methacrylates and the roles of polymerization diluent on the morphology of the resulting materials (3,4). We were able to synthesize microcellular foams based on the methacrylate chemistry, but the smallest cell size was about 1 μm with a density of about 0.4 g/cm^3 . In general, we found that a strong solvent system favored smaller cell sizes and lower densities, and that mixed solvents held little advantage for this particular system. We also showed that Freon-22 was a sufficiently strong solvent for this system to substitute for toluene as the polymerization diluent. Since the critical temperature of Freon-22 is 97 C, this finding implies that the polymer network may be formed and supercritically dried directly in the same vessel without exchanging solvents. More recent studies have led to microcellular foams based on epoxy chemistry where we have obtained strong materials with densities of 0.19 g/cm^3 and pore sizes of 0.1 μm (5).

In the present work, we seek to elucidate the mechanism of formation of the microporous structure as it is formed in situ. For instance, scanning electron micrographs (SEM) of our microcellular foams (3,4) as well as those of Pekala and Stone (2) show that they are comprised of tiny beads of polymer from 0.01 to 1.0 μm in diameter. We would like to know whether these beads are formed during the polymerization or during the drying phase. We would also like to know how these beads form and grow so that we can think about ways of making them smaller while maintaining the ability to form a macroscopic material. To study this, we have implemented a high pressure scattering cell for dynamic light scattering. Dynamic light scattering detects the presence and diffusion coefficients of disperse inhomogeneities in a bulk fluid. Typically, diffusion coefficients can be measured for dispersions ranging in size from 1 nm to 10 μm . From the SEM's, we expect our primary particles to eventually grow to about 1 μm for the methacrylate system, so this method provides a useful tool for exploring some of the early stages of the foam formation and the nature of the polymerizing solution.

Experienced readers may note that the mechanism of production of these aerogels is similar to the styrenic procedure for ion exchange resins. Indeed, a comparison of the SEM's of microcellular foams for to those of Swatling et al. (6) shows a strong similarity in the morphology. These similarities probably extend to the mechanism of pore formation as well. A number of theoretical analyses of network formation in ion exchange beads are available (7), however, dynamic light scattering analysis of the reacting system in situ has not been reported. It is difficult to imagine how such an analysis could be performed on the actual reacting system for ion exchange bead production, since this is generally an emulsion polymerization process. If one was to develop a model system which could be used to analyze the mechanisms occurring in ion exchange bead formation, it might look very much like the one we have performed, but the conditions would not need to be near-critical. Therefore, our findings may have some bearing on ion exchange research, but we do not seek to emphasize this relationship at this time.

Materials and Apparatus

Methylmethacrylate (MMA) and ethylglycoldimethacrylate (EGDMA) were used as the comonomers in this study. Freon-22 was used as the diluent. Monomers were washed of their inhibitors and dried using molecular sieves by conventional procedures. Tertbutylperoxypivalate was used as the free radical initiator. To prepare a typical reaction mixture, MMA and EGDMA were added to a 40 ml high pressure "bomb" in the proportions of 12 ml of MMA and 8 ml of EGDMA (Figure 1). 20 μ l of TBPP was then added and the bomb was attached to tubing with an open-shut valve. The bomb and contents were cooled in ice and connected to a supply of Freon-22 kept at room temperature. The Freon valves were opened and Freon allowed to condense into the bomb for 10-20 minutes. The valves were closed, the Freon tank disconnected, and the bomb and contents were refrigerated until ready for use. To charge the high pressure light scattering cell (Figure 1), the bomb was raised to room temperature and the scattering cell was cooled to 5°C. The height of mercury in the cell was adjusted to keep reactive solution out of the cell's mercury reservoir while keeping the mercury well below the light path. The bomb was inverted and connected to the scattering cell and the monomer+diluent solution was allowed to condense into the cell for 10-20 minutes. Valves were sealed and capped and the pressure was adjusted to about 400 psig at room temperature. The temperature in the cell was raised to the designated value by heating tape connected to an Omega temperature controller.

Time-resolved scattering intensities were measured at 90° angle using a Thorn-EMI photomultiplier tube and a Brookhaven Instruments amplifier/discriminator integral with the phototube housing (Figure 2). They were analyzed using a Brookhaven Instruments Corporation BI-2030AT correlator and IBM PC/AT computer using Brookhaven Instruments Non-Negative Least Squares (NNLS) fitting software to estimate the particle size distribution as a function of reaction time. This scattering system has been described previously (8).

Results and Discussion

Results of the study are shown in Table I and Figures 3 and 4. There are at least three possible mechanisms by which the monomer solution may evolve to a macroscopic bulk material. It is helpful in discussing our results to describe these in advance. First, the system may consist of steadily growing primary particles which grow until they fill the entire solution. Then the particle size histograms would show a broad polydisperse population of particles with the peak slowly moving to higher sizes. Second, the system could grow in stages whereby small particles are generated then flocculated into large globules that are eventually too big to grow, then a new population of small particles evolves and begins to flocculate. The particle size distributions in that case would appear as waves of particle size peaks when considered as a function of time. A third possible scenario would be that the primary particles grow to a certain size then stop growing until the concentration of particles becomes so great that the particles percolate at a gelation point and convert from disperse sols to the

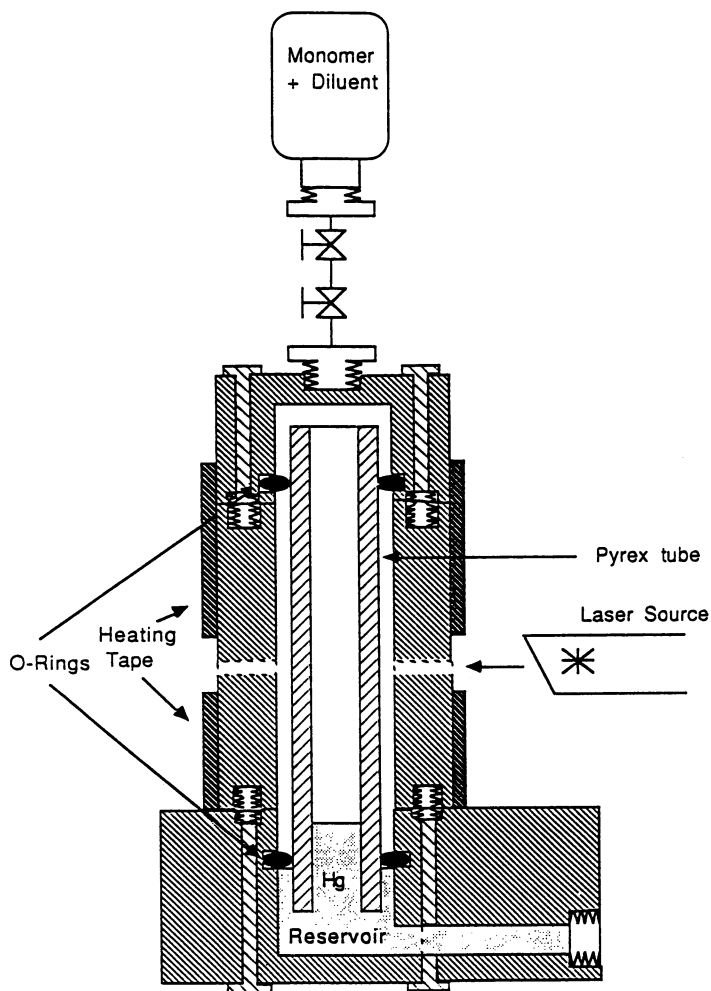


Figure 1. Experimental apparatus for near-critical polymerization.

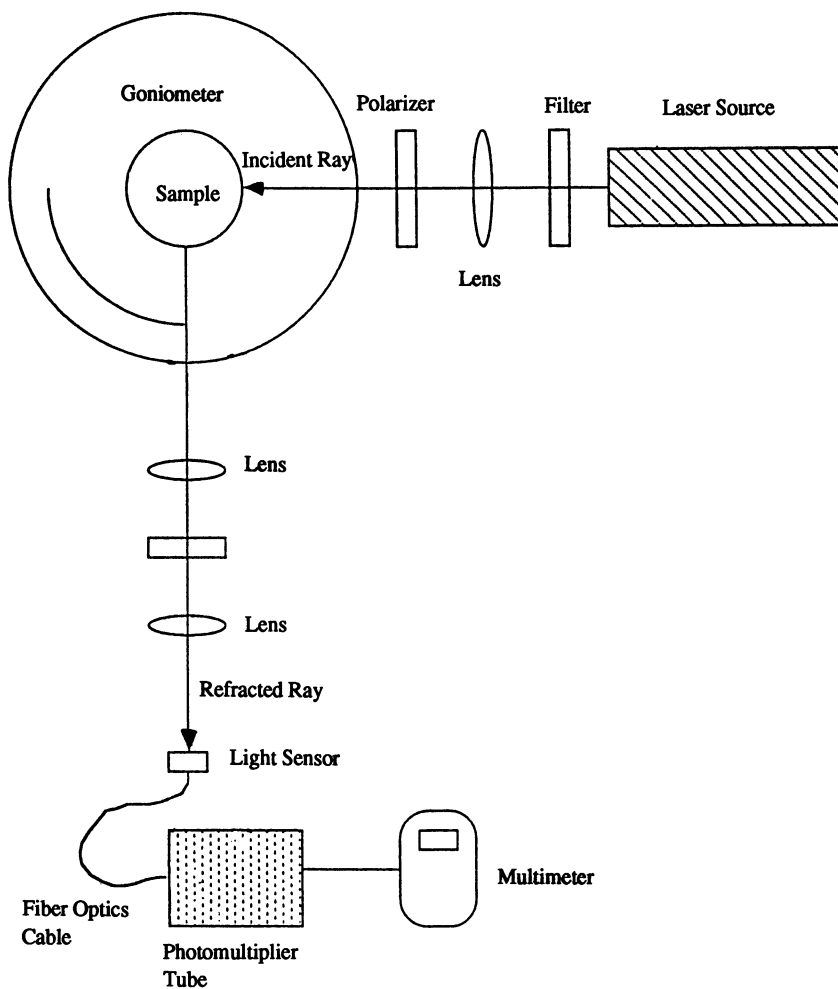


Figure 2. Schematic representation of the arrangement of the light scattering optics.

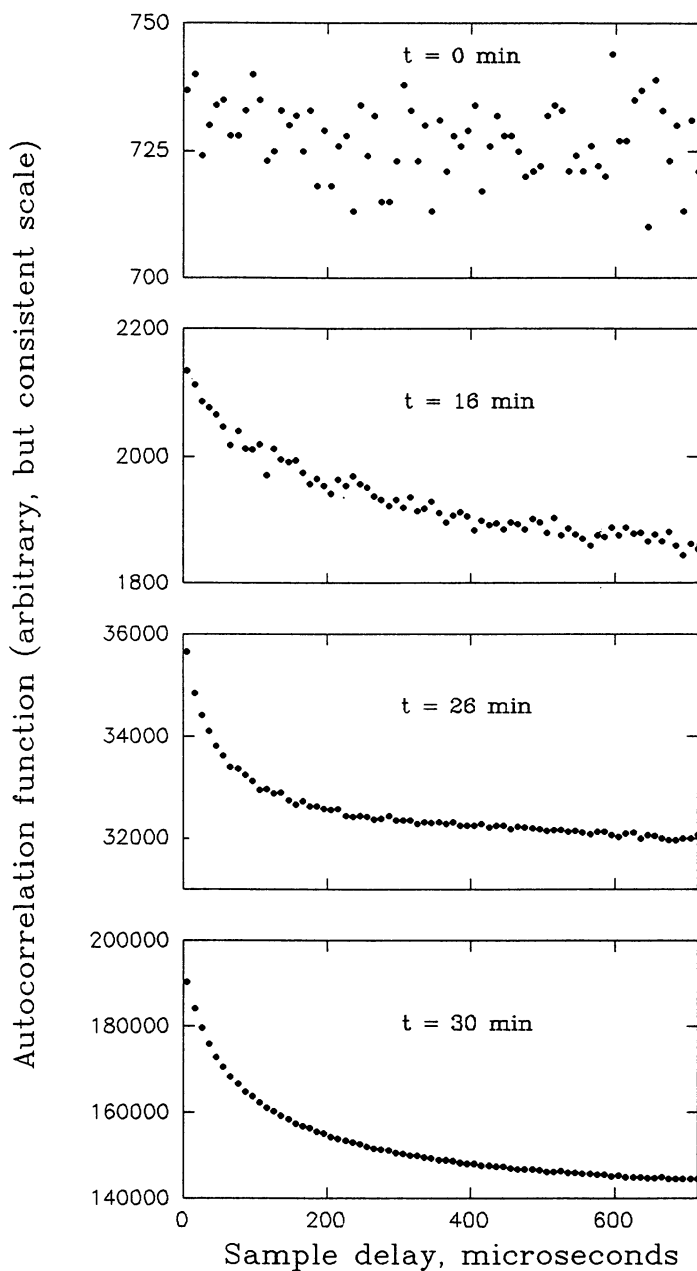


Figure 3. Correlograms for the 10 vol% EGDMA + 40 vol% MMA + 50 vol% Freon-22 systems at 90° angle and conditions given in Table I.

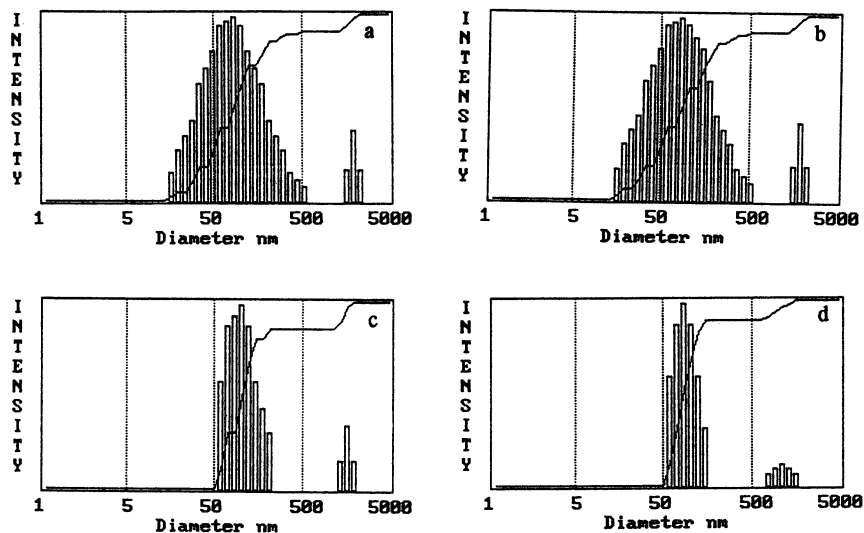


Figure 4. Particle size distributions from dynamic light scattering at the conditions given in Table I.

macroscopic material in a very short time. In that case, we would expect very monodisperse populations that do not change in size but the scattering count changes as more scatterers evolve until the solution gels.

Table I. Results for light scattering studies of 10 vol % EGDMA + 40 vol% MMA + 50 vol% Freon-22 polymerizing solution

LS#	T(°C)	Time(min)	P(psig)	Rate(MHz)	Signal/Noise
Initial	4	0	500	4	0.31
00	55	14	850	4	0.32
02	73	16	1125	4	0.32
06	81	20	1250	4+	0.28
10	89	24	1400	4+	0.25
12	93	26	1410	5	0.28
13	95	28	1450	9	0.10
15	93	30	1460	20	0.14
16	95	31	1460	30	0.25
17	95	32	1460	60	0.26

Figure 3 shows that the most plausible scenario for free radical polymerization is the third scenario described above. The correlograms in Figure 3 show the autocorrelation function vs time for the low EGDMA system as it polymerizes under supercritical conditions. The later correlograms clearly show the characteristic exponential decay which indicates the presence of small particles. Considering

that the sampling time was 10^{-5} seconds for each of these correlograms, it is clear that, qualitatively, small particles dominate the scattering at later times. Following the correlograms back in time, the signal from the small particles becomes progressively weaker. Table I shows that the photon count rate is very low at the early stages and this is because there are no scatterers present. The correlogram at the initial condition shows a flat response as we would expect at 10^{-5} seconds when only dust is present. The correlograms between 14 minutes to 24 minutes are much "noisier" than those earlier and later because the number of scatterers is just enough to give a signal but not enough to give a clear signal. What can be qualitatively observed, however, is that the rate of decay is apparently consistent with what we might expect from a small population of particles of the same size as those in the later correlograms.

It is possible to argue that there might be other particle distributions present, but that we do not observe them because we only observed at a single sampling time. However, previous studies were performed over a series of sampling times from 1 μ sec to 5000 μ sec and the results were always consistent with the description above. Various averaging times were also considered before deciding that a one minute averaging time provided a reasonable compromise between getting good light scattering results for short times and observing the polymerization on a reasonable time scale so that we were not averaging out too much in the way of particle size or number density changes. We also collected extensive data through multiple runs of the same systems to verify the reproducibility of our observations. Figure 3 shows a series of correlograms for a system composed of 10 vol% EGDMA + 40 vol% MMA + 50 vol% Freon-22 where the correlograms were collected at different sampling times. Clearly, one particle distribution can describe all of the observations. The correlograms vs time for the 20 vol% EGDMA solution were basically similar to those of the 10% EGDMA solution for each experimental run.

To make more quantitative arguments with regard to the particle distributions it is necessary to make some approximations about the physical properties of the solution. In particular, the viscosity of the polymerizing solution must be known and the relative refractive indices of the solution and the primary particles must be known to infer particle sizes from what essentially amounts to data on the diffusion coefficient. These physical properties are difficult to measure or estimate with any degree of reliability so we have set these values at a viscosity of 0.28 cp and a refractive index of 1.59:1.33 (particle: solvent). This means that the exact values of the reported particle sizes may be challenged but the relative magnitudes should be consistent throughout our analysis. There are several options that may be considered for transforming the autocorrelation functions into particle distributions. Perhaps the best known is the cumulant expansion technique (9), but it does not provide detailed information about the particle size distribution. For example, it cannot identify multimodal particle size distributions. A commonly used technique which provides more detailed information is the NNLS technique (10). In Figure 4, we used the NNLS technique because we were interested in exploring as much detail as possible. The primary particles appear at about 20 and 30 nm then they grow in

population but not size until, finally, the solution gels when all the particles have grown to about 30 nm. There is also some appearance of 1000 and 10000 nm particles which show up in Figure 4. It seems likely that these particles represent dust initially present in the sample. These results indicate that certain particle sizes are more favored than others and that the polymerization occurs by rapidly populating these favored sizes until three-dimensional connectivity occurs (percolation). This represents a kind of combination between the second and third scenarios described above.

In order to make assertions about the particle sizes, we must also neglect variations in concentration dependent terms that relate to hydrodynamic and thermodynamic interactions. These kinds of interactions can be significant in many cases (11), but we do not seem to see significant effects in our system. The significance of the interactions in an aqueous phase tends to be related to the relatively high dielectric constant of aqueous solutions. Since our continuous phase has a relatively low dielectric constant, one might expect that electrostatic interactions would be small and hard sphere interactions would dominate. Corrections for hard sphere interactions are approximately 15% at a volume fraction of 10%. Since the particles we see are small, their number density can be relatively high before these corrections become significant (11).

Given that the particles seem to appear at a certain size then cease growing, it may be of interest to speculate about the mechanism by which this occurs. First, the appearance of the primary particles at about 20-30 nm but not at smaller sizes with subsequent growth to that size is likely a consequence of the free-radical polymerization. In free-radical polymerization, individual polymer chains grow to their full length all at once until their growth is terminated. Then growth of another chain is initiated. This would mean that relatively few species would exist as medium-sized particles at any given instant. That population would not be large enough to generate a significant scattering signal. The population which does appear is fairly polydisperse and that polydispersity could be explained by variations in the molecular weight that one would expect. But why do these polymer molecules segregate themselves from solution to such an extent that they generate a significant scattering signal? What is the role of crosslinking? These are very difficult questions to answer at this time. Some recent thermodynamic findings suggest that interaction sites on chain molecules show a striking "cooperative attraction" for each other (12). It is possible that long chains in solution could wrap around in a way that this effect is expressed even for sites that are actually on the same chain. Crosslinking could increase the molecular weight in such a way that cooperative attraction effects would be enhanced. Thus it is possible to imagine ways in which these inhomogeneities could be generated, but it may require considerable effort over a number of years to develop a complete understanding of the mechanism for production of these primary particles.

SEM analyses of the final dry products (4) indicate that these same particles are preserved in the macroscopic material even through the supercritical drying process. Thus the drying process seems to have little adverse impact on the morphology of the macroscopic material. This means that research effort should be directed at

understanding the causes of certain particle sizes being favored and toward changing the chemistry such that the favored particle sizes are as small and uniform as possible.

Other factors of interest in future research would include developing non-spherical primary particles and manipulating the aspect ratio. Non-sphericity should have an impact on the percolation behavior. Extensions of the experimental technique would include adding more optical signal processors at multiple angles, using probe particles to obtain viscosity data for the actual solution, eliminating the need for mercury, and adding depolarized scattering capability to measure the rotational diffusion coefficient. These additions would help to provide data which could refine the accuracy of the technique and provide detailed molecular insights into the polymerization/gelation process.

Literature Cited

- [1] Aubert, J.H.; Sylwester, R.P., *CHEMTECH*, 1991, 21,234.
- [2] Pekala, R.E.; Stone, W. *ACS Preprints*, 1988, 29(1),204.
- [3] Elliott, Jr., J.R.; Srinivasan, G.; Akhaury, R. *Polymer Communications*, 1991, 32,10.
- [4] Srinivasan, G.; Elliott, Jr., J.R. *Ind. Eng. Chem. Res.*, 1992, in press.
- [5] Dhanuka, M.S. Thesis, The University of Akron, January (1992).
- [6] Swatling, D.K.; Manson, J.A.; Thomas, D.A.; Sperling, L.H. *J. App. Poly. Sci.*, 1981, 26,591.
- [7] Seidl, J.; Malinsky, J.; Dusek, K.; Heitz, W. *Advances in Poly. Sci.*, 1967, 5,113.
- [8] Sasthav, M. and Cheung, H.M. *Langmuir* 1991, 7,1378.
- [9] Koppel, D.E. *J. Chem. Phys.*, 1972, 57,4814.
- [10] Grabowski, E.F.; Morrison, I.D.; in *Measurement of Suspended Particles by Quasielastic Light Scattering*, B.E. Dahneke, Ed.; Wiley, New York (1983).
- [11] Cheung, H.M.; Qutubuddin, S.; Edwards, R.V.; Mann, Jr., J.A. *Langmuir*, 1987, 1,333.
- [12] Vasudevan, V.J.; Elliott, Jr., J.R. *Mol. Phys.*, 1992,75, 443.

RECEIVED June 12, 1992

Chapter 22

Simulation and Optimization in Supercritical Fluid Chromatography

F. Van Puyvelde¹, E. H. Chimowitz², and P. Van Rompay¹

¹Department of Chemical Engineering, K. U. Leuven De Croylaan 46,
Heverlee 3001, Belgium

²Department of Chemical Engineering, University of Rochester,
Rochester, NY 14627

Gradient programming is an experimentally proven technique for tuning the separating action in supercritical fluid chromatography (SFC). In this study we describe a mathematical framework for simulating and optimizing the process.

Results are given, showing the utility of simulations and how optimization ideas may advance this area of technology.

Chromatographic separations are usually performed under constant operating conditions of pressure and temperature. However, it is also clear that this may not be the optimal manner in which to operate the process. Changing the operating conditions as a function of time (referred to as gradient programming) is an experimentally proven technique, commonly applied in chromatography, to improve the quality of the separation. Temperature programming is very common in gas chromatography, while gradient elution is applied in liquid chromatography. Supercritical fluid chromatography (SFC) however offers a greater range of possibilities to control solute retention since in the near-critical region of the mobile phase, physical properties are extremely sensitive to thermodynamic conditions. Here we provide an analysis for simulating and optimizing SFC under dynamic conditions. The numerical solution of the mathematical model proposed will enable us to run sensitivity studies which can subsequently be used to direct the optimization of the process.

Model Development

In supercritical fluid chromatography, a very small sample of the mixture is injected into the stream of the supercritical solvent; the supercritical fluid is used in excess. This means that the solute species are extremely dilute. In this case the assumption of linear chromatography with the local equilibrium assumption

0097-6156/93/0514-0281\$06.00/0
© 1993 American Chemical Society

is justified. The use of a more elaborate and detailed models is seldom warranted for modeling linear systems (1), (2). For these systems, the precise nature of the mass transfer effects (film resistance, intraparticle mass transfer resistance, etc.) has only a very modest effect on the transient response curves of reasonably long chromatographic columns (2 - 5).

The basic equation used in this analysis is the mass balance. This balance equation states that the difference between the amount of solute flowing into a shell minus the amount of solute flowing out of the shell must equal the rate of accumulation of the solute in the differential shell. Or written mathematically:

$$-\varepsilon \frac{\partial(uc)}{\partial x} + \varepsilon \frac{\partial}{\partial x} \left(D \frac{\partial c}{\partial x} \right) = \frac{\partial}{\partial t} (\varepsilon c + (1 - \varepsilon)q) \quad (1)$$

where c is the concentration of the solute in the mobile phase, q the concentration of the solute on the stationary phase, ε the porosity of the packed bed and D the dispersion coefficient.

Appropriate boundary conditions are:

$$c(x, 0) = 0 \quad (2)$$

$$c(0, t) = \delta(t) \quad (3)$$

$$\frac{\partial c(L, t)}{\partial x} = 0 \quad (4)$$

If the relation between the concentration in the bulk fluid (c) and the concentration in the solid phase (q) is known, for example as a Langmuir isotherm:

$$q = f(c) \quad (5)$$

then equation (1) can be solved readily to give the concentration profiles as a function of the distance in the bed and time. The resulting relation is referred to as the local equilibrium theory model (6).

Adsorption-desorption experiments ofalachlor on activated carbon under supercritical conditions were performed by Modell and coworkers (7). They used the local equilibrium model to verify their results based on the knowledge of the adsorption isotherm. The agreement between the measured and calculated profiles was seen to be very good in both shape and magnitude. This correspondence strongly suggests that the local equilibrium theory is a reasonable representation for interphase behavior here (1). Furthermore, recent experimental data for the desorption of ethyl acetate from activated carbon with supercritical carbon dioxide were also found to fit the local equilibrium model (8). In the case of supercritical fluid chromatography, Van Puyvelde and Chimowitz (9) concluded that many experimental results in the literature confirmed the applicability of the local equilibrium model.

Under the assumption of local equilibrium, the relation between the concentration in the mobile phase and the stationary phase can be written as:

$$q = K_{eq} c \quad (6)$$

where K_{eq} is the equilibrium distribution coefficient.

Combining equations (1) and (6) gives:

$$-\varepsilon \frac{\partial}{\partial x} \left(D \frac{\partial c}{\partial x} \right) + \varepsilon \frac{\partial(uc)}{\partial x} + \frac{\partial}{\partial t} ((\varepsilon + (1 - \varepsilon)K_{eq})c) = 0 \quad (7)$$

Here the distribution coefficient K_{eq} remains unknown. There exists however a relationship in linear chromatography that connects the capacity factor k , which is an experimentally measurable quantity, to the distribution coefficient K_{eq} (10):

$$\left(\frac{\varepsilon}{1 - \varepsilon} \right) k = K_{eq} \quad (8)$$

Thus the model (7) reduces to:

$$-\frac{\partial}{\partial x} \left(D \frac{\partial c}{\partial x} \right) + \frac{\partial(uc)}{\partial x} + \frac{\partial}{\partial t} ((1 + k)c) = 0 \quad (9)$$

with the assumption of a constant diffusivity, equation (9) becomes:

$$-D \frac{\partial^2 c}{\partial x^2} + \frac{\partial(uc)}{\partial x} + \frac{\partial}{\partial t} ((1 + k)c) = 0 \quad (10)$$

It is important to notice that this equation is very general since the velocity is not assumed to be constant and the capacity factor (or the distribution coefficient) is allowed to be time dependent. From this equation it becomes also obvious that the capacity factor will be dependent upon the time dependent gradient profile imposed on the column thermodynamic variables, since this is the term kept inside the time-derivative.

Velocity Profiles. These chromatographic operations are performed with very dilute solute mixtures. The velocity profile can therefore be treated independently of the mass transfer action. The assumption that the velocity is independent of the mass transfer is equivalent to assuming that the coupling is *weak* (11). In the derivation of the equations, a small enough pressure gradient along the column is assumed, so that it actually can be neglected, an assumption consistent with the experimental findings of Kelley and Chimowitz (12).

Density Programming: Velocity Profiles. The density can be programmed by changing the volumetric flow rate of the pump. At the column outlet, a valve is held at a fixed setting, which acts as a fixed resistor (13). The changing volumetric flow rate of the pump induces a changing flow rate and velocity inside the column. This velocity change is a supplementary second order effect that will also affect the retention and the resolution of the species. Since the restrictor is at a fixed setting, there is an accumulation of mobile phase inside the chromatograph, implying higher pressures and consequently higher densities.

Based on a mass balance, an expression for the superficial velocity in the column can be derived (9), (14).

$$u(x, t) = \frac{\varepsilon S(L - x) \frac{d\rho}{dt} + \dot{m}_{outlet}}{\varepsilon S \rho} \quad (11)$$

where ε is the porosity of the packed bed, L the length of the column, S the cross-sectional area of the column, ρ the density and \dot{m}_{outlet} the mass flow rate at the end of the column. The expression (11) provides the velocity profile with density programming action.

Pressure Programming: Velocity Profile. Different pressure control systems have been proposed (15), (16) to produce pressure gradients. An interesting system is the one where a back pressure device regulates the pressure independently of the mass flow rate of the mobile phase. Because of the possibility of controlling the pressure independently of the mass flow rate, the mass flow rate can be kept constant. An expression for the velocity can be derived in a similar way as with density programming and is given by:

$$u(x, t) = \frac{\dot{m}}{\varepsilon S \rho(P)} \quad (12)$$

where the density ρ is a function of the time dependent pressure profile.

Temperature Programming: Velocity Profile. Here the temperature of the oven is changed during the course of the separation. If the mass flow rate is also kept constant, a similar equation for the velocity, as derived with pressure programming is found to be:

$$u(x, t) = \frac{\dot{m}}{\varepsilon S \rho(T)} \quad (13)$$

The density is solely determined by its dependence on temperature, if the pressure is kept constant. Increasing the temperature will decrease the density and thus increase the velocity inside the column.

Modeling the Capacity Factor. A model for the capacity factor will be required to describe column behavior with gradient programming. Capacity factor models in terms of density are most useful for density programming problems, while a different form is required for pressure and/or temperature programming. Both forms are now discussed.

Capacity Factor as a Function of Density and Temperature. The relationship between the capacity factor and the density of the mobile phase can be described by an equation of the form (14), (17):

$$k = a \left(\frac{\rho}{\rho_0} \right)^{-b} \quad (14)$$

where ρ is the density of the mobile phase and ρ_0 a reference density. This relationship holds over a wide range of densities which is useful. The coefficients a and b depend on temperature and may be found from data involving a few isothermal experiments at different densities (pressures) as described by Wilsch (14).

Capacity Factor as a Function of Pressure and Temperature. The model used here is based upon the lattice model described by Kelley and Chimowitz (12). The fluid phase properties are calculated with a perturbed hard sphere equation of state, while the coverage or the adsorption function is based on Langmuirian assumptions. It has been observed that the Langmuirian model can fit the data for supercritical adsorption very well (17). The expression for the capacity factor as a function of pressure and temperature is given by (12):

$$k_j = \frac{\frac{K_0}{\rho_m} \phi_j^\infty P \left(\frac{e^{-D_j/2T}}{1 - e^{-D_j/T}} \right)^3 \frac{\Lambda^3}{kT} e^{-U_j^0/kT}}{1 + \sum_i y_i \phi_i^\infty P \left(\frac{e^{-D_i/2T}}{1 - e^{-D_i/T}} \right)^3 \frac{\Lambda^3}{kT} e^{-U_i^0/kT}} \quad (15)$$

where K_0 is a geometric bed structure parameter, ϕ_j^∞ the infinite dilution fugacity coefficient of component j in the mobile phase, ρ_m the density of the mobile phase, P the pressure, D_j the Debye temperature, T the temperature, Λ the thermal de Broglie wavelength, U_j^0 the potential well depth of species j and k Boltzmann's constant.

Simulation Results: Density Programming. The basic mass balance (10) describing the chromatographic system must be completed by one of the equations describing the velocity profile ((11), (12) or (13)) and an expression for the capacity factor ((14) or (15)). The kind of gradients employed will determine the correct combination of these equations. Van Puyvelde and Chimowitz (9) described a numerical solution procedure which can be used to solve these modeling equations for supercritical fluid chromatography under gradient programming conditions. Here we show how these simulations represent various gradient programming strategies. The inclusion of a diffusional term, provides for the effects of peak broadening.

The first simulations were done for density programming ((10), (11), (14)) on a seven component mixture, using carbon dioxide as the mobile phase. The dimensional and component data are given in Tables I and II. The data were taken from Wilsch and Schneider (14). Figure 1 shows the simulated chromatogram under *constant* conditions of density (690 kg/m^3). Figure 2 shows the effects of a density program. The density is first kept at a value of 680 kg/m^3 , and after 250 s the density is increased at a constant rate of $0.50 \text{ kg/m}^3 \text{ s}$. Comparing Figure 1 and Figure 2 shows the beneficial effects of density programming: the slowest peak is emerges from the column much faster, while peak resolution remains good. The accuracy of these simulations with the experimental data of Wilsch (14) was checked by Van Puyvelde and Chimowitz (9) and found to be quite satisfactory.

Table I. Column Characteristics (14)

L	0.125m
ϵ	0.57
D	1.10^{-7}
diameter	0.005 m
\dot{m}_0	$2.133 * 10^{-5}$ kg/s

Table II. Data on Capacity Factors (14)

Component	number	a	b
Dodecyl phenyl ether	1	0.60	5.36
Tetradecyl phenyl ether	3	0.72	5.74
Hexadecyl phenyl ether	5	0.87	6.13
Octadecyl phenyl ether	7	1.02	6.59
Phenyl myrastate	2	0.55	6.02
Phenyl palmitate	4	0.66	6.41
Phenyl stearate	6	0.79	6.78

System Optimization

Comparing Figures 1 and 2 shows the advantage of using a density gradient programming technique. By employing a gradient, speed of analysis is enhanced while resolution can be kept good. However the question of determining these gradient trajectories in an *a priori* fashion remains an open one. The usual procedure for doing is experimental trial-and-error, a time consuming task.

The second part of this study will focus on the development of a mathematical strategy for the *a priori* determination of density trajectories that optimize system performance.

From experiments (12), (14) as well as from numerical computations it has been observed that resolution and processing speed are coupled: the better the separation, the longer the retention times of the species. The core of the system optimization problem is to *get a desired resolution within a specified amount of time*. The main restriction on this objective is that the regime of maximum resolution coincides with the condition of maximum processing time (19), (20).

Since there is a trade-off between resolution and processing speed, this conflict has to be resolved with the aid of optimal control concepts (21). The optimization problem may be stated as follows: *minimize the value of the objective function by selecting the operating variables as a function of the continuous variable time, subject to the constraints represented by the differential modeling equations*. The objective function must include the conflict between speed and resolution of the

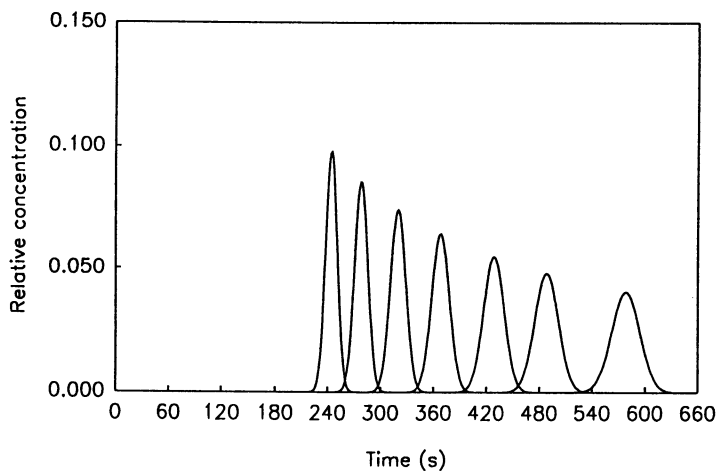


Figure 1. Computed chromatogram: constant density (690 kg/m^3).

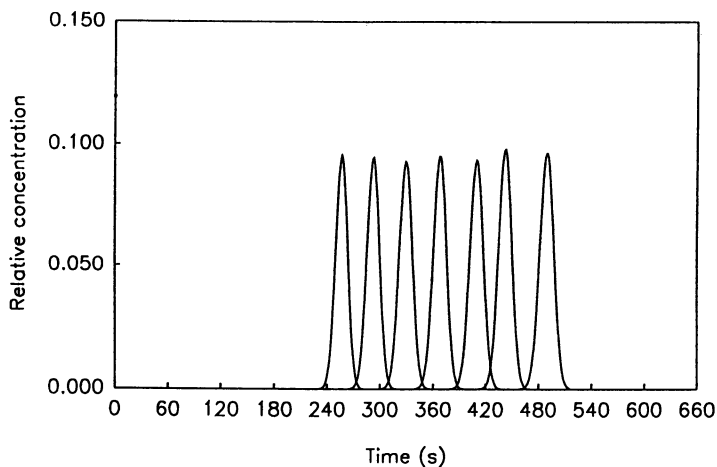


Figure 2. Computed chromatogram: density programming: constant density (680 kg/m^3) during first 250s—constant rate of increase ($0.50 \text{ kg/m}^3\text{s}$).

July 22, 2012 | <http://pubs.acs.org>
 Publication Date: December 17, 1992 | doi: 10.1021/bk-1992-0514.ch022

species. The constraints represent the equations showing the evolution of the various species through the column, i.e. equation (10) for each component.

Transformation Using the Method of Characteristics. The optimization focuses on the determination of the optimal conditions for the chromatographic run. In the approach taken here the duration of the gradient program is not taken as a degree of freedom, but is a priori fixed. The reaction engineering literature is replete with such control problems, but its chromatographic formulation appears to be new (19).

The main issue here is the mathematical formulation of a tractable problem. The starting equation is given by equation (10).

It is important to notice there is the dependence on space (x) as well as on time (t), which gives a *distributed* character to this problem. This distributed aspect complicates the problem, but is not the major drawback of this formulation. The dependent variable in equation (10) is the species concentration, which is not of particular interest here. We are more interested in the retention time behavior of the different components. Retention times and distances are variables that do not appear explicitly in the modeling equation (10). Working with this global expression (10) is thus not convenient and we have to transform the problem into a more suitable form. The details behind this transformation are provided by Van Puyvelde and Chimowitz (20), here we provide the main results. Using the method of characteristics (22) the basic equation (10) can be transformed into a velocity of species form given by:

$$u_j = \frac{dx_j}{dt} = \frac{1}{1 + k_j} u \quad (16)$$

where u_j is the velocity at which component j is moving through the column, x_j is the distance covered by peak mean j , k_j is the capacity factor of component j , and u is the mean velocity of the mobile phase.

Equation (16) is the same equation as the one used in the chromatographic theory describing the velocity of the moving species under the assumption of linear chromatography (23).

Equation (16) provides an expression for the velocity of the peak mean through the chromatographic column. This ordinary differential equation formulation however does not give any information about peak broadening effects. This lack of information is the price we pay for going from the partial differential equation (10) to the ordinary differential equation (16). This allows for a reasonable mathematical treatment and the peak broadening effects must be handled after initial optimization as explained later on.

For the velocity u , the expressions (11), (12) or (13) have to be substituted, depending on the type of programming being investigated. The expression for the capacity factor also depends upon the type of gradient profile strategy used.

The remaining issue is the process objective function. A form logically suited to this problem is given by:

$$W_0(x_N(t_f) - L)^2 + \int_0^{t_f} \sum_{j=1}^{N-1} W_j(x_j(t) - x_{j+1}(t) - \Delta_j)^2 dt \quad (17)$$

W_j are weighting factors, which can be used to express the relative importance of the various terms, x_j is the distance travelled in the column by component j . The components are numbered from fast (=1) to slow (=N). L stands for the length of the column and Δ_j is the distance by which two neighboring peaks have to be separated. The property t_f is the specified time within which the separation has to be completed.

This objective function has to be minimized and it balances the objectives of both speed and resolution. The first term requires the slowest component to emerge from the column at the specified time t_f which can be made as small as desired. This first term will be minimal if $x_N(t_f) = L$, or the distance covered by the slowest component N equals the length of the column L at the specified time t_f . The dynamic part in the expression (within the integral sign) strives to induce the necessary resolution. It requires peak couples to be separated by a distance Δ_j . This term will be minimal if the terms $(x_j - x_{j+1} - \Delta_j)$ are as close to 0 as quickly as possible. Hence both speed and resolution are incorporated into this form of the objective function.

The quantitative advantages of this approach were described in detail by Van Puyvelde and Chimowitz (20). Here we provide some salient results.

Computational Results. The computational results given here are for the case of density programming since it is probably the most useful practical strategy to implement.

The objective function (17) was used to guide the determination of the optimal density profile for the separation system given in Tables I and II. For the first profile as shown in Figure 3, the parameters in the objective function (17) were: $W_0 = 1000$, $W_j = 1$, $t_f = 500$, $\Delta = 0.012m$. This means that the time of analysis is set at 500 s and that the peaks have to be separated by 0.012m. According to the relative value of the weighting function used here, the analysis time is the most important factor. As can be seen from Figure 3, the calculated density program can be split into two phases: a first period where the density is kept at a low value followed by a second period where the density is increased at a nearly constant rate. During the first period the separating capacity of the column is high and the peaks are separated. The increase in density during the second phase serves to accelerate the peaks out of the column such that the requirement of a total time of analysis of 500 s is met. This form of the density program is very similar to the one obtained experimentally by Wilsch (14).

The effect of this density program upon the separation is shown in Figure 4. Figure 4 records the movement of the peak means through the column as a function of time. This type of figure is instructive in demonstrating the effect of the density program. During the first phase, the peaks move through the column, each at their own linear rate. From 240 s on, the gradient effect becomes visible:

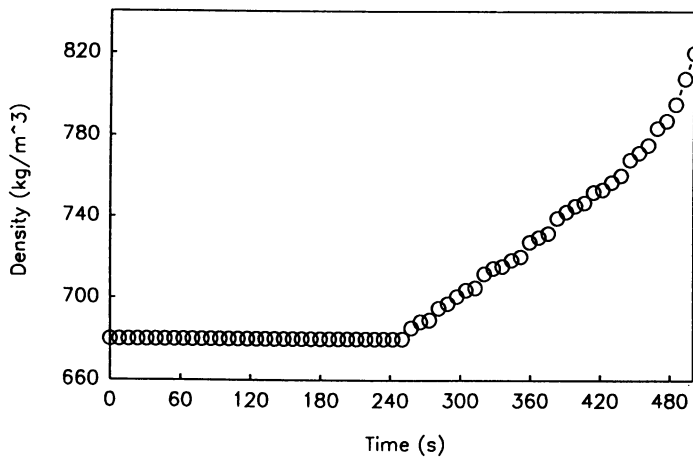


Figure 3. Computed density profile: $W_0 = 1000$, $W_j = 1$, $\Delta = 0.012m$, $t_f = 500s$.

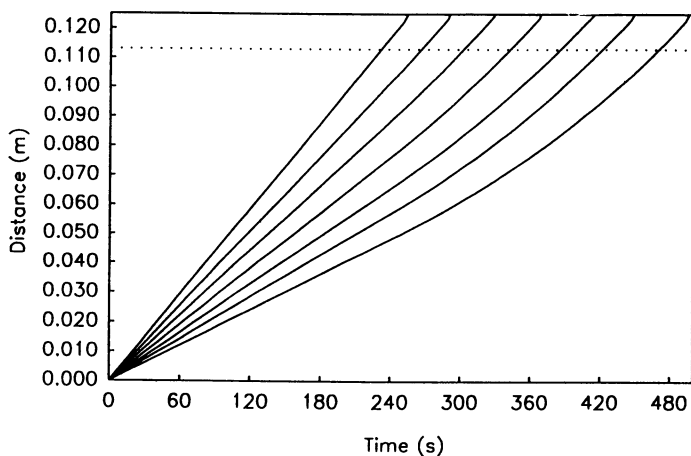


Figure 4. Computed evolution of the peaks using the density profile of Figure 3.

the peaks start to move faster in a nonlinear way. The dotted line on the figure helps to indicate the difference between the peaks. This line is drawn at 0.012 m from the end of the column. The separation between the peak couples is larger than the required 0.012 m. This results from the fact that the total time of analysis t_f was overemphasized. This also indicates that the required resolution can be obtained in less time.

Changing the weighting factors in the objective function (17) will influence the density profile, as will be shown in the next application. It can be inferred from Figure 4 that the required degree of separation can be obtained in less time. Therefore the weights are now changed to: $W_0 = 100$, $W_j = 3$. The total time of analysis is kept the same as before, as well as the required separation distance between the peaks.

The resulting density profile is given in Figure 5. The first period at a low density is shorter than the one in Figure 3. The increase in density during the second period is however much more extreme. It is important to notice that a lower bound (680kg/m^3) and an upper bound (820kg/m^3) for density is placed on the computation. The evolution of the peaks corresponding to the density profile of Figure 5 is pictured in Figure 6. The peaks emerge from the column much faster, while still respecting the requirement of an inter-peak separation distance of 0.012 m. Hence the weighting factors in the objective function enable us to examine trade-offs between speed of processing and resolution.

After the initial optimization study provides an optimal profile like those shown in Figures 3 and 5, we can examine the effects of dispersion in the system, which were previously omitted in order to arrive at the formulation proposed here. Using the optimal density profile a full-scale simulation of the system using equation (10) can be employed which will yield chromatograms analogous to those shown in Figures 1 and 2. Here the peak broadening effects can be visually inspected by the chromatographer to see if the given separation is satisfactory.

Summary

Historically, supercritical fluid chromatography has been used for the separation of homologous or oligomeric series of compounds. There is however a trend for using this technology with more complex samples with non-homologous compounds (24). It is clear that an approach for simulating and optimizing the performance of such systems is desirable.

A theoretical framework is outlined here for these purposes. Results from previously more detailed studies have been used to illustrate the effects of gradient programming and the usefulness of simulation models.

The core of the optimization problem solution requires the use of optimal control ideas. This technique is well suited for these problems, since it attempts to optimize the dynamic behavior of systems. In addition the approach may be generalized to both gas and liquid chromatography.

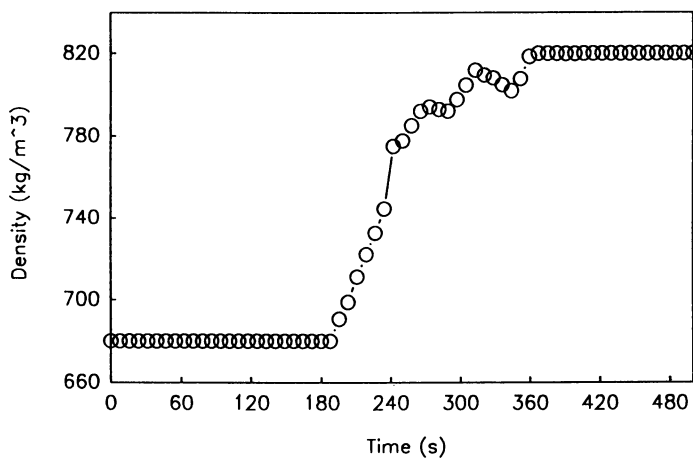


Figure 5. Computed density profile: $W_0 = 100$, $W_j = 3$, $\Delta = 0.012m$, $t_f = 500s$

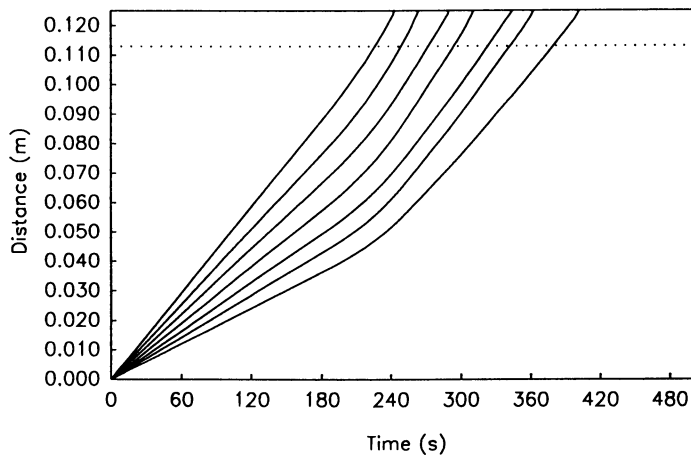


Figure 6. Computed evolution of the peaks using the density profile of Figure 5.

Acknowledgments

The authors would like to acknowledge the National Science Foundation for partial support of this work through Grant No.CTS-8908828.

Literature Cited

- (1) McHugh, M.; Krukoni, V. *Supercritical Fluid Extraction*; Butterworths: Boston, MA, 1986.
- (2) Carta, G. *Chem. Eng. Sci.* **1988**, 43, 2877.
- (3) Lightfoot, E. N.; Sanchez-Palma, R. J.; Edwards D. O. In *New Chemical Engineering Separation Techniques*; Schoen, H., ed.; Interscience Publishers: New York, NY, 1962.
- (4) Ruthven, D. M. *Principles of Adsorption and Adsorption Processes*; John Wiley, New York, NY, 1984.
- (5) Raghavan, N. S.; Ruthven, D. M. *Chem. Eng. Sci.* **1985**, 40, 699.
- (6) Sherwood, T. K.; Pigford, R. L.; Wilke C. R. *Mass Transfer*; McGraw-Hill, New York, NY, 1975.
- (7) Modell, M.; Robey, R. J.; Krukoni, V.; de Fillipi, R. D.; Oestereich, D. Paper presented at the national AIChE meeting, Boston, MA, 1979.
- (8) Tan, C.-S.; Liou, D.-C. *Ind. Eng. Chem. Res.* **1988**, 27, 988.
- (9) Van Puyvelde, F.; Chimowitz, E. H. *J. Supercrit. Fluids* **1990**, 3, 127.
- (10) Plicka, J.; Svoboda, V.; Kleinmann, I.; Uhlirova, A. *J. Chromatogr.* **1989**, 469, 29.
- (11) Kikuchi, N., *Finite Element Methods in Mechanics*, Cambridge University Press, Cambridge, 1986.
- (12) Kelley, F. D.; Chimowitz, E. H. *AIChEJ* **1990**, 36, 1163.
- (13) Klesper, E.; Schmitz, F. P. *J. Supercrit. Fluids*, **1988**, 1, 45.
- (14) Wilsch, A.; Schneider, G. M. *J. Chromatogr.* **1986**, 357, 239.
- (15) Gere, D. R.; Board R.; McManigill, D. *Anal. Chem.* **1982**, 54, 736.
- (16) Hirata, Y.; Nakata, F. *Chromatographia* **1986**, 21, 627.
- (17) Chimowitz, E. H.; Kelley, F. D. *J. Supercrit. Fluids* **1989**, 2, 106.
- (18) Yang, R. T. *Gas Separation by Adsorption Processes*; Butterworths: Boston, MA, 1987.
- (19) Grover, V.; Van Puyvelde, F.; Chimowitz E. H. Submitted to *Comp. Chem. Eng.* **1991**.
- (20) Van Puyvelde, F.; Chimowitz, E. H.; Van Rompay, P. Accepted for publication in *J. Supercrit. Fluids* **1992**.
- (21) Ray, W. H. *Advanced Process Control*; McGraw-Hill: New York, NY, 1981.
- (22) Zwillinger, D. A. *Handbook of Differential Equations*; Academic Press: Boston, MA, 1989.
- (23) Jonsson, J. A. In *Chromatographic Theory and Basic Principles*; Jonsson, J. A., Ed.; Marcel Dekker: New York, NY, 1987.
- (24) Crow, J. A.; Foley, J. P. *Anal. Chem.* **1990**, 62, 378.

RECEIVED June 10, 1992

Chapter 23

Supercritical Extraction of Organic Components from Aqueous Slurries

Aydin Akgerman and Sang-Do Yeo¹

Chemical Engineering Department, Texas A&M University,
College Station, TX 77843

Continuous operation of an extractor for solids extraction by supercritical fluids is hindered by the difficulty of feeding the solids to the extractor at high pressures. Supercritical extraction of organic compounds from solid matrices is performed by slurrying the solid with water. This introduces a three phase, supercritical fluid - water - solid, equilibrium. Activated carbon, alumina and soil are used as the solid phases with carbon dioxide as the supercritical phase. Equilibrium distribution of naphthalene and phenol between the three phases is determined employing a single stage extractor as a function of pressure at different temperatures. A thermodynamic model, which uses two two-phase equilibrium partitioning to predict the three-phase equilibrium, is also developed.

The interest in applications of supercritical extraction in environmental remediation is increasing rapidly (1). Contaminated soil, river and lake sediments, and industry sludges are all solid matrices of major environmental concern and supercritical extraction may be a feasible alternative for remediation of these matrices.

In continuous operation of an extractor to handle solid materials, the solids have to be introduced to the vessel continuously and extracted with the solvent. Since supercritical extraction is a moderately high pressure process, feeding of solids continuously from ambient pressure to the extractor is not a trivial task. Therefore, most supercritical extractors for solids are operated in the semi-batch mode where the solids are loaded to the extractor, the extraction vessel pressurized, the supercritical fluid circulated over the solid bed continuously until the extraction is completed, the vessel de-pressurized, and the solids removed from the extractor. This mode of operation is both expensive and not suitable for high capacity processes. One approach

¹Current address: Princeton University, Chemical Engineering Department, Princeton, NJ 08544

to solve the materials handling problem is to slurry the solid with a liquid phase, such as water, and use slurry pumps for delivery. For environmental applications water may have an additional advantage of replacing selectively the organic contaminant on the solid phase, and enhancing the extraction extent and rates. Extraction of an aqueous - slurry introduces a three phase (solid-water-supercritical fluid) equilibrium where the fourth component is distributed between these three phases. To the best of our knowledge, no data has been reported on equilibrium behavior of such a system.

The objective of this study was to determine the equilibrium distribution of an organic compound in the three phase system and develop the thermodynamics for prediction of this distribution. Four different systems were studied; phenol distribution in activated carbon/water/supercritical CO₂ and soil/water/supercritical CO₂ systems, and naphthalene distribution in alumina/water/supercritical CO₂ and soil/water/supercritical CO₂ systems. The solid phase was loaded with the organic component (phenol or naphthalene), slurried with water, brought to equilibrium with supercritical CO₂ in a single equilibrium stage extractor, and the distribution of the organic in the three phases determined.

For the three phase system consisting of the supercritical phase (F), the water phase (L), and the solid phase (S), the criteria for equilibrium dictates that

$$\hat{f}_{iF} = \hat{f}_{iL} = \hat{f}_{iS} \quad (1)$$

where \hat{f}_{ij} 's are the fugacity of component i in phase j . The objective of the thermodynamic modeling was to predict the loading of the organic component on the solid phase in this three phase system from equilibrium information on two two-phase systems, i.e. supercritical fluid-water equilibrium partitioning and liquid-solid equilibrium partitioning (adsorption equilibrium) of the organic component. In Equation 1, the first two terms can be obtained from a supercritical fluid/water equilibrium for which

$$\hat{f}_{iF} = \hat{\phi}_{iF} y_i P \quad (2)$$

$$\hat{f}_{iL} = \hat{\phi}_{iL} x_i P \quad (3)$$

where the mole fraction of component i in the water and supercritical phases are x_i and y_i , respectively. The mole fractions and the fugacity coefficients in the two phase system can be calculated by using the model proposed by Yeo and Akgerman (2). This model uses a flash calculation procedure combined with the Peng-Robinson equation of state and composition dependent mixing rules. It enables calculation of the fugacity coefficient and the distribution coefficient of each component in a multicomponent system.

The right two terms in Equation 1 can be obtained from equilibrium data on a liquid-solid system, i.e. the adsorption equilibrium. It is not easy to obtain adsorption equilibrium data when the liquid phase is water and the adsorbate (the organic solute)

is a hydrophobic organic compound only scarcely soluble in water (such as naphthalene, solubility ~20 ppm), because it is very difficult, if not impossible, to control the concentration of the hydrophobic adsorbate in water at different concentration levels to obtain reliable data for the adsorption isotherm. Therefore, it is assumed that the fugacity of the solute in the solid phase is independent of the solvent it is adsorbed from (3, 4). Thus

$$\hat{f}_{iS}(x_i, T)|_{aq.} \approx \hat{f}_{iS}(y_i, T, P)|_{SCF} \quad (4)$$

this assumption also implies that the fugacity of the adsorbed species is independent of the system pressure since liquids are incompressible compared to supercritical fluids.

Employing this assumption, in order to determine the fugacity of naphthalene on the solid phase, naphthalene was dissolved in cyclohexane at different concentration levels and the amount adsorbed on the solid phase was determined at these levels to construct the adsorption isotherm. The fugacity of the adsorbate on the adsorbent can then be calculated from

$$\hat{f}_{iS} = x_i \gamma_i(x_i, T) P_i^{sat}(T) \quad (5)$$

In this equation, the activity coefficient γ_i can be calculated by the UNIFAC group contribution method (5) as a function of mole fraction and temperature. The vapor pressure of the component can be calculated by available correlations (6). The liquid phase mole fraction x_i of the adsorbate in the liquid-solid system is related to the solid phase concentration, or the solids loading, through the adsorption isotherm. For most dilute systems, the Freundlich isotherm gives a reasonable fit to the data, although other model equations for adsorption isotherms can also be used.

$$S = F C^N \quad (6)$$

where S is the loading on the solid phase (mol/g), C is the liquid phase concentration (mol/l), and F and N are empirical constants. After the fugacity of the component in the supercritical fluid-liquid system is calculated as a function of temperature and pressure through Equations 2 and 3, and the relationship between the fugacity of the component in the liquid phase and the solid phase loading is established using Equations 5 and 6, the solid phase loading can be predicted as a function of temperature and pressure of the extraction system.

EXPERIMENTAL METHODS. In this study radiolabeled compounds were used because of accuracy in analysis. Radioactively labeled ^{14}C phenol and ^{14}C naphthalene were purchased from Sigma Chemical Co., activated carbon (Darco G-60, -100 mesh powder, lot no. 00429TV) and activated alumina (neutral, Brockmann I, -150 mesh, lot no. 01820DX) were purchased from Aldrich Chemical Co., and EPA Standard Soil was obtained from EnviResponse Co.

Phenol was loaded on activated carbon and soil by preparing 150 ml of 5.18 wt% radiolabeled phenol solution and contacting it with 10 g of activated carbon or soil

to form a slurry. The slurry was agitated in a constant temperature bath for 7 days until it reached equilibrium. It was observed that about 95% of the equilibrium adsorption was established in one day, yet about a week was necessary to reach equilibrium. The equilibrium concentration of the water phase was measured in a Beckman Liquid Scintillation Counter (model 3801) and the solid loading determined from material balance closure. The slurry was then placed in the extractor for extraction with supercritical CO₂. Thus in these cases we started with a slurry already at equilibrium in terms of solute partitioning between the two phases, solid and water.

In order to load naphthalene on alumina or soil, it was precipitated from methanol. 0.03 g of radiolabeled naphthalene was dissolved in 40 ml of methanol and 30 g of solid phase (alumina or soil) was added to the solution. Methanol was evaporated from the mixture by agitating in a fume hood. After all the methanol evaporated, a solid sample was taken and directly added into scintillation cocktail, sonicated, and counted for naphthalene using a direct solids analysis technique we developed (7). It was observed that naphthalene loss due to sublimation during methanol evaporation was less than 2%. This 30 g solid phase was then slurried with 150 ml water and immediately loaded into the extractor.

In both cases, the amount of total adsorbed phenol or naphthalene, that was placed in the extractor, was less than the minimum amount of these species needed to saturate the supercritical phase at the experimental conditions (8, 9).

The experimental assembly consisted of a single stage extractor where the slurry was pressurized with CO₂ to the desired pressure, agitated for 24 hours followed by a phase separation period of minimum 2 hours, the aqueous and the supercritical phases were sampled under pressure, the samples were expanded into scintillation cocktail, and the amount of organic in these phases were determined. Details of the experimental set-up and procedure are given elsewhere (10, 11). Thus only two phases, the supercritical phase and the water phase were analyzed, and the amount of organic on the solid phase was determined by difference from material balance closure. We have shown that under these conditions an organic rich fourth phase does not form (10, 11).

RESULTS AND DISCUSSION. Phenol partitioning between supercritical CO₂/water/activated carbon at 295 K and 320 K as a function of pressure are presented in Figures 1 and 2. Although the experimental temperature of 295 K is in reality subcritical for CO₂, nevertheless it is called the supercritical phase from a practical point of view, i.e. conditions for supercritical extraction are more or less optimized at $0.9 < T_r < 1.2$ and $P > 1.0$. Mole fraction of phenol in the supercritical phase increases with pressure, the aqueous phase concentration does not vary significantly, and phenol loading on the solid phase decreases with pressure. Same trend is observed at both temperatures. Thus as phenol is extracted from the water phase by supercritical CO₂, some phenol desorbs from activated carbon into the aqueous phase in order to keep equilibrium intact. One aspect of this system is the strong affinity of phenol to both water and activated carbon. Therefore it is not easy to extract phenol

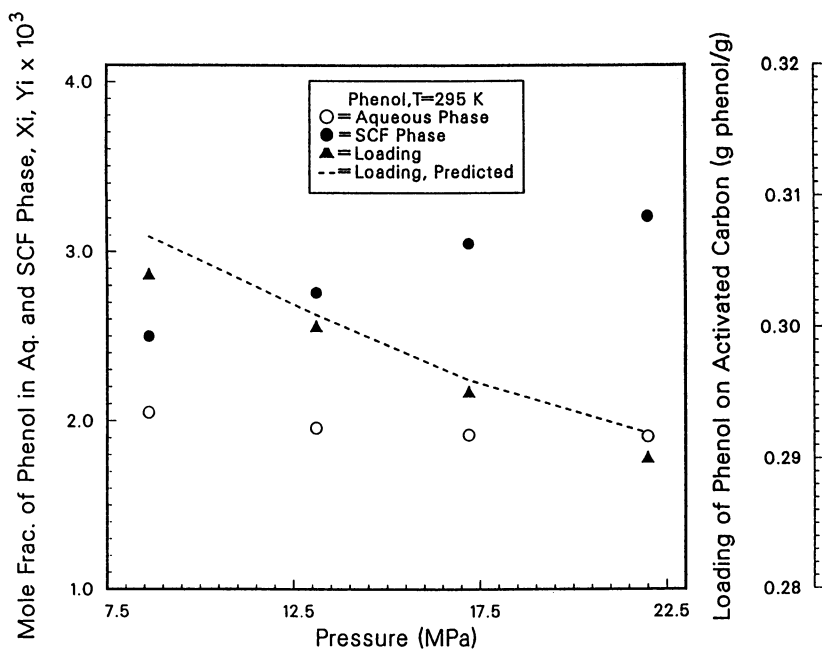


Figure 1. Equilibrium distribution of phenol in supercritical CO₂-water-activated carbon system at 295 K.

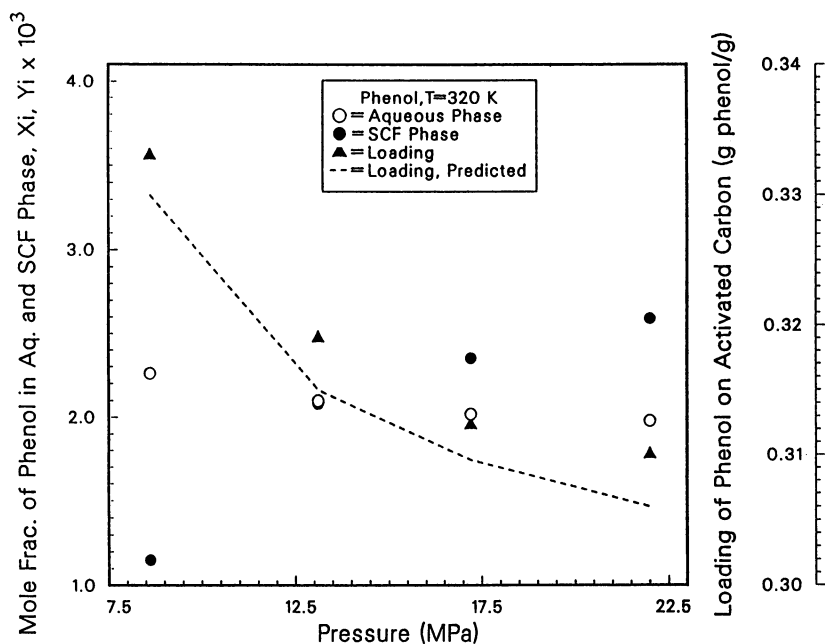


Figure 2. Equilibrium distribution of phenol in supercritical CO₂-water-activated carbon system at 320 K.

into the supercritical phase and hence extraction percentages are low (Figure 3). In this system the only factor that controls the extraction efficiency is the supercritical density. This is also observed from Figure 3, as temperature increases extraction percentage decreases due to decrease in CO₂ density. Phenol extraction from soil behaves the same way (Figure 4), however in this case there also is a significant decrease in water concentration with pressure and the extraction percentages are much higher (Figure 9) due to weakness of phenol affinity to soil; as phenol is extracted into the supercritical phase from water it is easily desorbed from the solid phase to maintain equilibrium. It is interesting to note that the distribution coefficients of phenol between the CO₂ and water phases in the three-phase system (y_i/x_i in presence of the solid phase) are higher than those reported for the two-phase system (10). At present the only explanation to the discrepancy is the presence of the third (solid) phase.

Figures 5 and 6 show naphthalene partitioning between supercritical CO₂, water and alumina as a function of pressure at 320 and 340 K. The mole fraction of naphthalene in the supercritical phase and the water phase decreases with pressure with a corresponding increase in loading on activated alumina. The amount of naphthalene in the aqueous phase is very low, due to solubility limitations and the hydrophobic nature of naphthalene, so that the water phase concentration has little effect on calculation of naphthalene loading from overall material balance. This system exhibits a different trend compared to the phenol systems, i.e. decrease in loading with pressure. This can be explained in terms of solute-solid interactions. Phenol dissociates in water to form an ionic species which forms an acceptor-donor type complex with a charged surface site. On the other hand naphthalene interaction with alumina is weaker, yet gets stronger with pressure. Water has high affinity to alumina so it easily replaces naphthalene on the surface and due to solubility limitations (naphthalene in water) and hydrophobic nature of naphthalene, it is easily extracted into the supercritical phase. However, as pressure increases, naphthalene adsorption increases, thus the maximum extraction is achieved at low pressures. Figure 7 shows the percentage extraction of naphthalene as a function of pressure at two temperatures. Finally, the results of the naphthalene soil system are inconclusive showing very low extraction percentages and no significant changes with pressure (Figure 8, 9). The presence of water phase and ternary interactions determine the thermodynamic equilibrium, yet a better understanding of the chemistry of the systems is needed to explain different behavior.

The prediction of phenol distribution between supercritical CO₂-water- activated carbon is also presented in Figures 1 and 2. The two 2-phase systems are; phenol distribution between water and supercritical CO₂ and phenol distribution between water and activated carbon. The K values for the former are obtained from the data in the literature (10), from the measured y_i value x_i is then calculated, and using this x_i together with Equation 5 and the adsorption isotherm (determined as explained above), the corresponding phenol loading on soil is predicted. The predictions of naphthalene loading on alumina are also presented in Figures 5 and 6. Fugacity of naphthalene in supercritical CO₂-water system is calculated from available data (2). Naphthalene adsorbed on alumina from cyclohexane solution is used to calculate

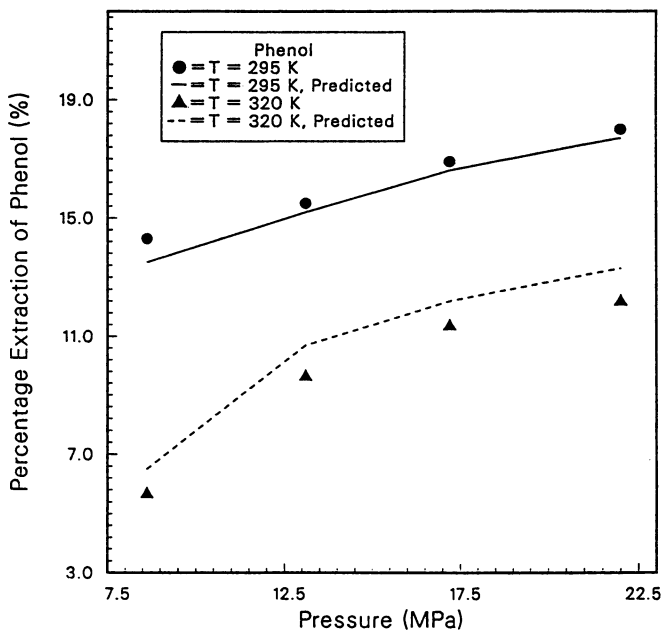


Figure 3. Percentage extraction of phenol from activated carbon, slurried with water, by supercritical CO_2 .

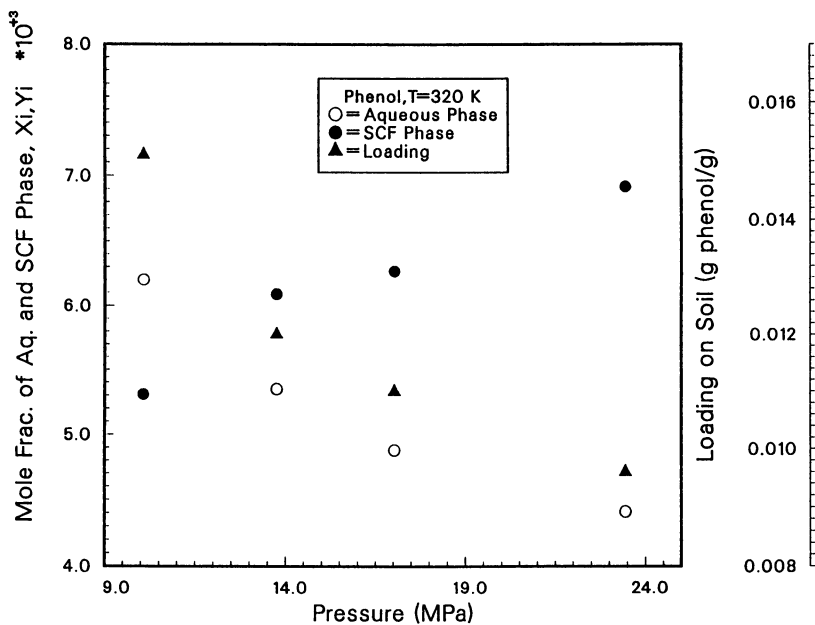


Figure 4. Equilibrium distribution of phenol in supercritical CO_2 -water-soil system at 320 K.

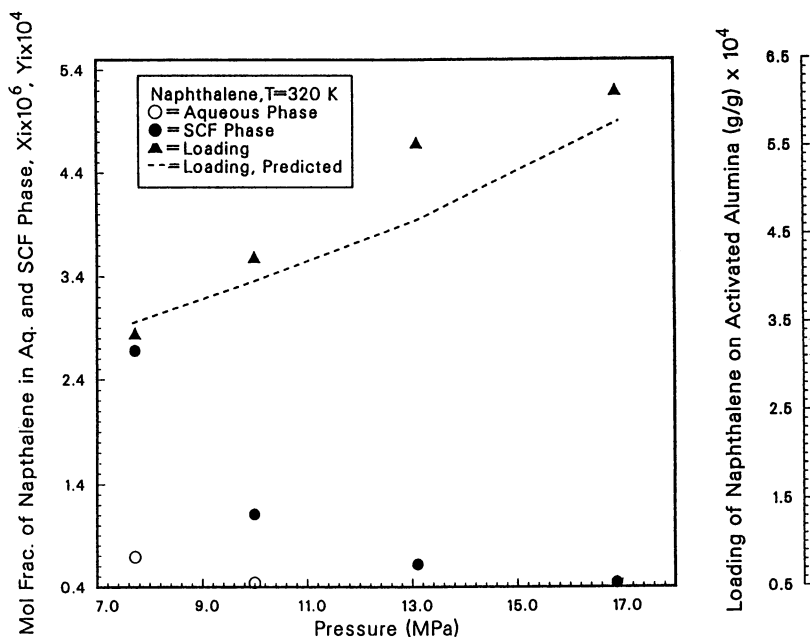


Figure 5. Equilibrium distribution of naphthalene in supercritical CO₂-water-activated alumina system at 320 K.

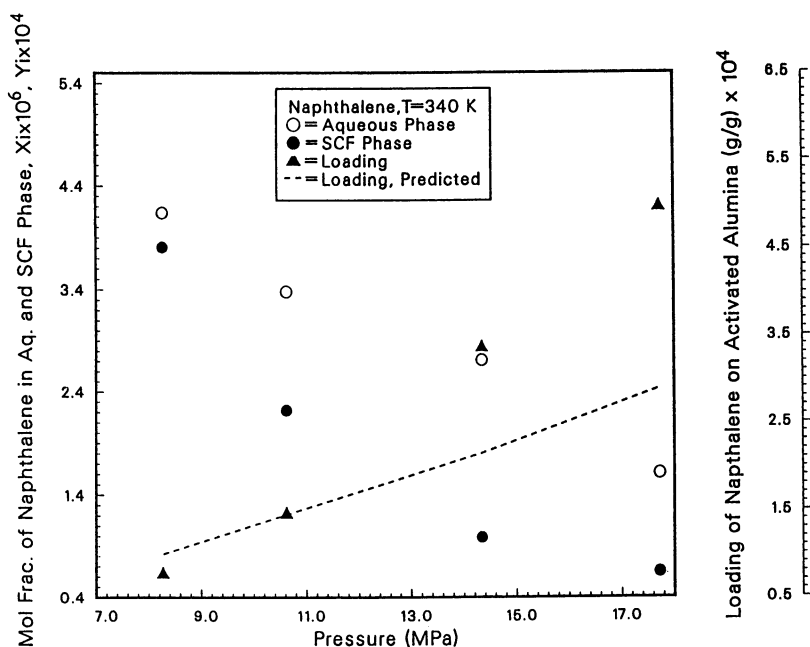


Figure 6. Equilibrium distribution of naphthalene in supercritical CO₂-water-activated alumina system at 340 K.

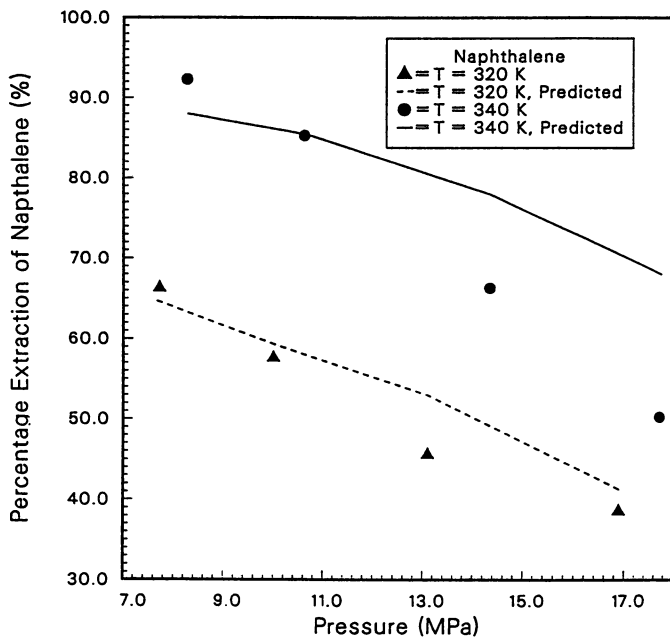


Figure 7. Percentage extraction of naphthalene from activated alumina, slurried with water, by supercritical CO₂

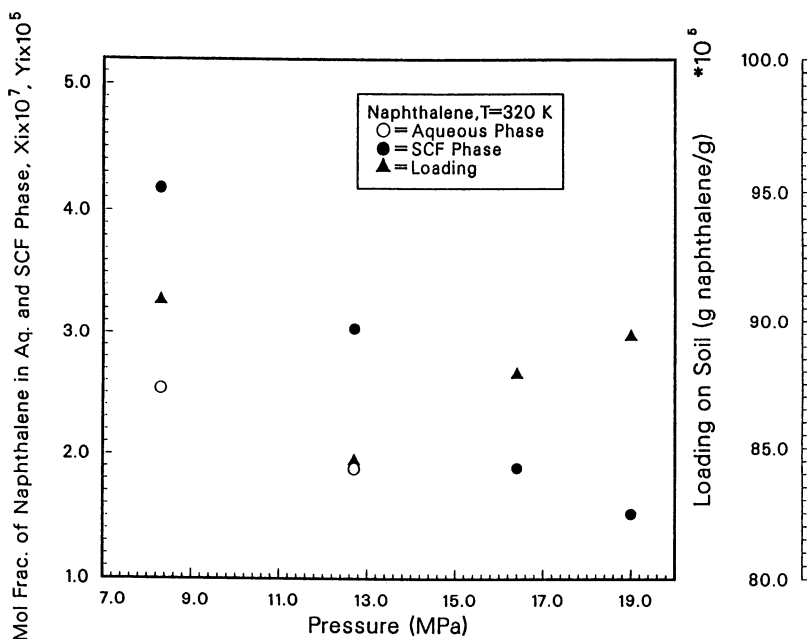


Figure 8. Equilibrium distribution of naphthalene in supercritical CO₂-water-soil system at 320 K.

naphthalene fugacity on alumina (Equations 5 and 6). The parameters used in Equations 5 and 6 are given in Table 1. Since the concentration of naphthalene in the adsorption system was very low, the calculated activity coefficient by the UNIFAC method was concentration independent, thus the activity coefficient in Equation 5 is replaced by activity coefficient at infinite dilution. The fugacity of naphthalene was then calculated as a function of pressure and the loading was determined from the adsorption data. The results indicate that the predictions are quite successful and the proposed approach works at least qualitatively for the two systems considered. Since soil is a complex solid mixture a better understanding of its chemistry is needed before attempting predictive techniques.

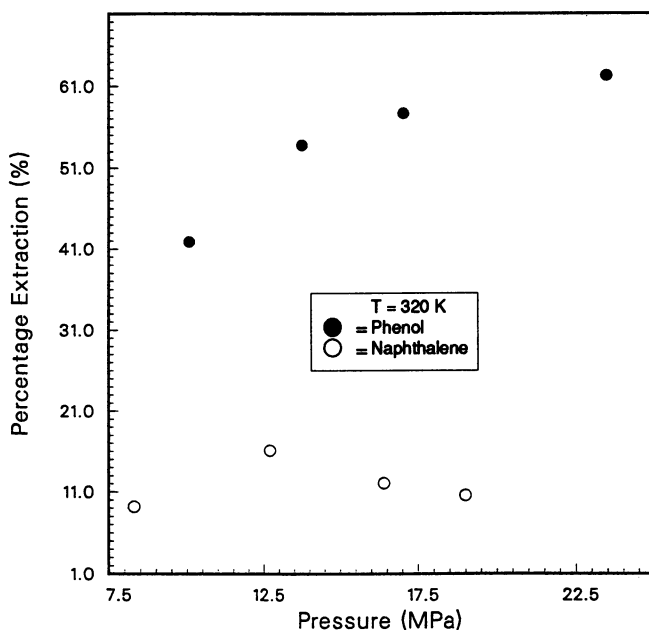


Figure 9. Percentage extraction of phenol and naphthalene from soil, slurried with water, by supercritical CO_2 .

Table 1. Calculated Parameters Used in Eqs. 5 and 6

Parameters	T = 320 K	T = 340 K
γ_i	1.713	1.661
P_i^{sat} (MPa)	0.000135	0.000449
F	0.0354	0.0271
N	0.9465	0.9937

LITERATURE CITED

1. Akgerman, A.; Roop, R. K.; Hess, R. K.; Yeo, S.-D. Yeo, *Supercritical Fluid Technology - Reviews in Modern Theory and Applications*; Editors, Bruno, T. J. and Ely, J. F., CRC Press, 1991, pp. 479 - 509.
2. Yeo, S.-D.; Akgerman, A., *AIChEJ*, 1990, 36, 1743.
3. Kander, R. G.; Paulaitis, M. E., *Chemical Engineering at Supercritical Conditions*; Editors, Paulaitis, M. E.; Penninger, J. M. L.; Gray, Jr., R. D.; Davidson, P., Ann Arbor Science, Ann Arbor, Michigan, 1983, p.461.
4. Akman, U.; Sunol, A., *AIChEJ*, 1991, 37, 215.
5. Sandler, S. I., *Chemical Engineering Thermodynamics*, 2nd Ed., John Wiley & Sons, New York, 1989, p. 373.
6. Reid, R. C.; Prausnitz, J. M.; Poling, B. E., *The Properties of Gases and Liquids*, 4th Ed., McGraw Hill, New York, 1987, p. 657.
7. Hess, R. K.; Erkey, C., Akgerman, A., *J. Supercrit. Fluids*, 1991, 4, 47.
8. Van Leer, R. A.; Paulaitis, M. E., *J. Chem. Eng. Data*, 1980, 25, 258.
9. Tsekhanskaya, Y. V.; Iomtev, M. B.; Mushkina, E. V., *Russ. J. Phys. Chem.*, 1964, 38, 1173.
10. Roop, R. K.; Akgerman, A., *Ind. Eng. Chem. Res.*, 1989, 28, 1542.
11. Yeo, Sang-Do, Ph.D. Dissertation, Texas A&M University, 1991.

RECEIVED April 27, 1992

Chapter 24

Kinetic Model for Wet Oxidation of Organic Compounds in Subcritical and Supercritical Water

Lixiong Li¹, Peishi Chen^{1,3}, and Earnest F. Gloyna²

¹Separations Research Program, Center for Energy Studies, The University of Texas at Austin, Austin, TX 78758

²Environmental and Water Resources Engineering, The University of Texas at Austin, Austin, TX 78712

The methodology of developing a global kinetic model for wet oxidation (WO) of organic compounds is described. Simplified reaction schemes considering rate-controlling intermediates are used in the model development. The selectivity of product vs. intermediate formations is defined as a key model parameter to simplify model calculations and characterize the "strength" of the feed stream. This model has been previously validated for hydrocarbons and oxygenated hydrocarbons using reported WO kinetic data in the temperature and pressure ranges, respectively, from 150°C to 550°C and from 20 bar to 440 bar. The model formulation and kinetic parameters for nitrogen- and chlorine-containing organic compounds are further discussed to demonstrate the model adaptability for WO of a variety of organic compounds, wastewaters and sludges in both subcritical and supercritical water.

Wet oxidation (WO), such as, the Zimpro wet air oxidation (WAO) process (1-2), has been commercially used in the treatment of wastewaters and sludges for at least three decades. Early WO processes have been typically operated in a temperature range of 150°C to 350°C and pressure range of 20 to 200 bar. The operating pressures have been maintained well above the saturation pressures corresponding to the operating temperatures, so that the reactions have occurred in the liquid phase. Residence times have ranged from 15 min to 120 min, and the chemical oxygen demand (COD) removal typically have been about 75% to 90%. Volatile acids and alcohols have constituted a substantial portion of the remaining COD (3-11). Unfortunately, incomplete (partial) WO of some wastewaters has resulted in colored and toxic effluents (12-13).

Supercritical water oxidation (SCWO) can overcome the shortcomings of WAO. The complete miscibility of oxygen and organic compounds in supercritical water creates a single-phase fluid and favorable reaction environment. In supercritical water, high destruction efficiency (> 99.99%) of many complex organic compounds and EPA priority pollutants can be achieved with a short residence time (< 5 min) and

³Current address: Phillip Morris R&D, P.O. Box 26583, Richmond, VA 23261

0097-6156/93/0514-0305\$06.00/0
© 1993 American Chemical Society

the reaction can be accomplished in a totally enclosed facility (14-23). Therefore, SCWO provides a technically viable and environmentally attractive option to managing the growing organic sludge and toxic wastewater treatment problems.

However, WO reaction mechanisms detailing elementary reactions of complex organic compounds and organic mixtures (such as wastewaters and sludges) appear to be tedious. Data describing these mechanisms are only available for a few simple compounds. Furthermore, the values of the reported kinetic parameters may differ considerably. Therefore, general and reliable kinetic models are needed for the development of WO processes. Such a generalized kinetic model has been developed for WO of hydrocarbons and oxygenated hydrocarbons (24). The model has been validated using reported WO kinetic data in the temperature and pressure ranges, respectively, from 150°C to 550°C and from 20 bar to 440 bar. This generalized kinetic model can be used to describe WO of nitrogen- and chlorine-containing organic compounds. It is the objective of this paper to discuss the methodology of this model development.

Existing Global Kinetic Models

Global kinetic models have been widely reported and successfully used within the stated experimental conditions to describe WO of organic model compounds, wastewaters, and sludges. A kinetic database has been initiated (24). Additional references have been summarized in Table I.

Most subcritical WO of organic compounds and mixtures can be described by a first-order reaction with respect to the organic reactants and first-order reaction with respect to oxygen. An oxygen mass-transfer factor can be used in global rate equations to account for the nonzero-order oxygen dependency (9,31-33). For supercritical WO, the oxidation rates appear to be first-order and zero-order with respect to the reactant and oxygen concentrations, respectively. In most WO experiments there is no effort made to differentiate the effect of side reactions. Depending upon reaction conditions and reactants involved, the rate of side reactions, such as hydrolysis (34-36), pyrolysis (35), dehydration (36-37), and liquefaction (38) varies considerably. The kinetic models discussed in this paper, unless otherwise specified, describe the overall reaction which may include oxidation, hydrolysis, pyrolysis and dehydration steps.

Pressure is another factor which can affect the oxidation rate in supercritical water. At a given temperature, pressure variation directly affects water density, and in turn changes the reactant concentration. Furthermore, the properties of water are strong functions of temperature and pressure near its critical point. Due to limited information, the effect of pressure is not included in this paper.

A generalized WO kinetic model is available (24). The model is derived from a simplified reaction scheme involving the formation and destruction of rate-controlling intermediates. The assumption is made that as WO reactions proceed, the initial compounds are converted to (a) oxidation end products, (b) unstable intermediates, and (c) relatively stable intermediates. Conversion of all intermediates to the oxidation end products requires a number of parallel and consecutive reactions. Quantification of the WO reaction mixtures requires the treatment similar to that used in the kinetic lumping technique (39-41).

Since the global WO rate depends on the end product formation rate, as well as the formation and destruction rate of stable intermediates, it is necessary to identify key rate-controlling reaction intermediates. Comparison of kinetic parameters for different organic compounds can assist in identifying rate-controlling components. For example, the activation energies for subcritical WO of volatile acids are higher as compared to those found for organic compounds possessing a lower oxygen content. Acetic acid exhibits the highest activation energy, 167.7 kJ/mol (3). When the same data are fitted using a pseudo-first-order model, the activation energy increases to 182

Table I. Global Kinetic Models for Wet Oxidation of Organic Compounds

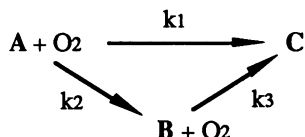
Compounds	Oxidant	Reactor Type	Kinetic Parameters*			Temperature (K)	Pressure (atm)	[C] ₀ (g/L)	References	
			k°	E _a	m					n
Acetic Acid	O ₂	batch	4.40x10 ¹²	182	1	0	543-593	20-200	~30	(3)
Alcoh. Dist. Waste (COD)	O ₂	batch	3x10 ³	45.3	1.5	0.3-0.6	423-483	2-20	33-35	(25)
2,4-Dichlorophenol	O ₂	batch	9.0x10 ¹	28.5	1	0	673-773	240-350	0.3-1	(23)
Methane	O ₂	flow	2.51x10 ¹¹	178.9	0.99	0.66	833-903	245	-	(26)
Methane	O ₂	flow	2.04x10 ⁷	141.7	1	0	833-903	245	-	(26)
m-Xylene (COD)	O ₂	batch	-	89.5	1	0.5	300-500	70-140	0.128	(27)
Phenol	O ₂	batch	-	112	1	0.5	300-500	70-140	0.128	(27)
Phenol	O ₂	flow	1.98x10 ⁷	56.6	1	1	418-453	26-48	0.1	(28)
Phenol	O ₂	batch	-	93	1	0.5	423-468	4-15	0.2	(29)
Phenol (COD)	O ₂	batch	-	48	1	1	413-453	4-15	0.5	(29)
Phenol (Total phenolics)	O ₂	batch	-	57.5	0.5	1.5	353-383	1.5-4.5	0.01-0.05	(30)
Pyridine	O ₂	batch	1.59x10 ⁴	91.5	1	0	673-773	240-350	0.3-1	(23)

*, Kinetic parameters are defined by $-d[C]/dt = k[C]^m[O_2]^n$ and $k = k^0 \exp(-E_a/RT)$, where [C] and [O] are concentrations of organic reactants and oxidant, respectively; E_a is in kJ/mol; T is in K; R = 8.314 J/mol-K; and k° = 1/sec (first-order), liter/mol-sec (second-order), etc., Not reported. [C]₀ = feed concentration. The concentration of compounds labeled with COD is quantified by chemical oxygen demand method; and the concentration of other compounds is quantified by chromatographic techniques. The excess oxidants are used in all tests. Kinetic parameters are reported for the overall reaction in water.

kJ/mol, Table I. The refractory nature of acetic acid and its validity as a key WO intermediate are elaborated elsewhere (24).

Simplified WO Reaction Schemes

The previously proposed reaction scheme for WO of organic compounds can be illustrated as follows:



where

C = [Oxidation end products];

B = [Rate-controlling intermediate]; and

A = [Initial and intermediate organic compounds other than B].

Application of this generalized reaction scheme requires the definition of Group A and identification of Group B. Three classifications of organic compounds which are characteristic of many organic waste streams, are defined as follows:

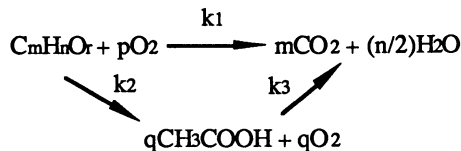
Category I - hydrocarbons and oxygenated hydrocarbons;

Category II - nitrogen-containing organic compounds; and

Category III - chlorinated organic compounds.

Both categories II and III may or may not contain oxygen.

For category I organic compounds, acetic acid is considered to be the key rate-controlling intermediate (24). In this case, the reaction scheme becomes,

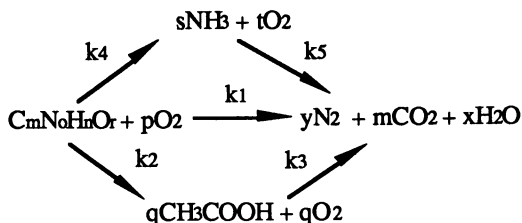


where $C_m H_n O_r$ is a collective term including the initial compounds and unstable reaction intermediates.

Using the same notations given in the generalized reaction scheme, three groups of organic substances can be further specified. Group A includes the initial organic compounds and all unstable intermediates except acetic acid, Group B contains the refractory intermediates represented by acetic acid, and Group C is designated as the oxidation end products (carbon dioxide and water). The concentrations of Groups A and B may be expressed in terms of total organic carbon (TOC), chemical oxygen demand (COD), total oxygen demand (TOD), or biochemical oxygen demand (BOD). The concentration units for these measurements are usually expressed in mass per unit volume. The mass concentration measurements are particularly useful and convenient for quantifying organic contents in wastewaters and sludges.

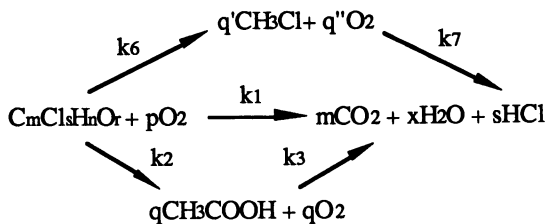
For nitrogen-containing organic compounds (category II), nitrogen gas is confirmed to be the predominant SCWO end product, regardless of the oxidation state of nitrogen in the starting material (42-44). This observation agrees with thermodynamic and kinetic calculations. The formation of ammonia and nitrous oxide has been reported in SCWO of various nitrogen-containing organic compounds and wastewaters (17,42-43,45). Ammonia is usually a hydrolysis product of nitrogen-containing organic compounds (17,36), and nitrous oxide is a partial oxidation product

of ammonia. At higher temperatures, 560°C to 670°C, the formation of nitrous oxide is more favorable than the formation of ammonia (43-44). At low temperatures near 400°C, nitrogen remains in solution as ammonia or ammonium ion (10,44,46). The activation energy for SCWO of ammonia has been reported as 156.8 kJ/mol (47), but the activation energy for nitrous oxide is not known. For low temperature applications, about 400°C, nitrogen conversion rate may depend on ammonia formation and destruction rates. Therefore, a simplified WO reaction scheme for nitrogen-containing organic compounds can be written as,



where $\text{C}_m\text{N}_o\text{H}_n\text{O}_r$ is a collective term including the initial organic compounds and unstable intermediates with or without nitrogen-containing functional groups. If Group A represents the compounds containing primarily the trinegative state nitrogen, then organic nitrogen concentrations can be monitored using the Kjeldahl nitrogen and ammonia nitrogen methods.

A similar reaction scheme can be shown for chlorinated (category III) organic compounds.



Methyl chloride is a representative reaction intermediate among short-chain chlorinated hydrocarbons which are likely to be produced. The abundance of water in the WO environment enhances fast hydrolysis of these intermediates to methanol and ethanol. Therefore, in addition to acetic acid, methanol and ethanol may be used as rate-controlling intermediates for WO of chlorinated organic compounds. Finally, the key rate-controlling intermediates identified for use in the generalized model and the reported kinetic parameters for these compounds are summarized in Table II.

Results and Discussion

The discussed kinetic model is generally suitable to describe WO of various organic compounds under isothermal, well-stirred batch reactor or constant volumetric flow rate plug-flow reactor conditions. As an example, the model expression is given for supercritical WO of category I organic compounds. The reaction rate may be assumed to be first-order with respect to the reactants, and zero-order with respect to oxygen. The concentrations of A and B can be expressed as,

$$[\text{A}] = [\text{A}]_0 e^{-(k_1+k_2)t} \quad (1)$$

Table II. Kinetic Parameters for Key Rate-Controlling Intermediates

Organic Compound Category	Key Intermediate (Alternative)	Oxidation End Product	Kinetic Parameters*			Reference
			Condition (Water)	k (1/sec)	E _a (kJ/mol)	
I	CH ₃ COOH	CO ₂ , H ₂ O	Subcritical	4.40x10 ¹²	182	(3)
			Supercritical	2.55x10 ¹¹	172.7 [^]	(14)
			Supercritical [#]	2.63x10 ¹⁰	167.1	(34)
II	NH ₃ (N ₂ O)	N ₂ , H ₂ O	Supercritical	3.16x10 ⁶	157	(48)
			Not available	-	-	
III	CH ₃ Cl (CH ₃ OH)	HCl, H ₂ O	Not available	-	-	
			Supercritical	2.51x10 ²⁴	395	(49)

* Pseudo-first-order reaction model using oxygen.

[^] Obtained from treating the reported 7 data points.

[#] Using hydrogen peroxide (obtained from treating 57 data points).

$$[B] = [B]_0 e^{-k_3 t} + \frac{k_2 [A]_0}{k_1 + k_2 - k_3} (e^{-k_3 t} - e^{-(k_1 + k_2)t}) \quad (2)$$

where [A]₀ and [B]₀ are the concentrations of A and B at time = 0, respectively. Combining equations 1 and 2 produces equation 3:

$$\frac{[A + B]}{[A + B]_0} = \frac{[A]_0}{[A]_0 + [B]_0} \left(\frac{k_2}{k_1 + k_2 - k_3} e^{-k_3 t} + \frac{(k_1 - k_3)}{k_1 + k_2 - k_3} e^{-(k_1 + k_2)t} \right) + \frac{[B]_0}{[A]_0 + [B]_0} e^{-k_3 t} \quad (3)$$

If [B]₀ = 0, equation 3 can be further simplified to equation 4.

$$\frac{[A + B]}{[A + B]_0} = \frac{k_2}{k_1 + k_2 - k_3} e^{-k_3 t} + \frac{(k_1 - k_3)}{k_1 + k_2 - k_3} e^{-(k_1 + k_2)t} \quad (4)$$

The three rate constants, k_1 , k_2 and k_3 , require further description. If k_2 is much smaller than k_1 , the organic compounds may be oxidized more easily to the end products. If k_2 becomes larger, more acetic acid will be formed. Values of k_1 may be determined from the initial reaction rate data based on lumped parameters, such as, COD and TOC; because Group A is a collective term encompassing the initial compounds as well as unstable intermediates. Conversion of Group A to acetic acid does not change effluent COD or TOC concentration significantly. Therefore the kinetic parameters based on COD or TOC are directly related to k_1 . The kinetic parameters for acetic acid given in Table II can be used for k_3 . Values of k_2 may be derived from further treatment of equation 4.

Since the WO of Group A can be considered as a parallel reaction system, the point selectivity, α_I , is defined as the formation rate of acetic acid to that of carbon dioxide from Group A. If first-order reactions are assumed, the following relation may be obtained for α_I ,

$$\alpha_1 = \frac{r_2}{r_1} = \frac{k_2[A]}{k_1[A]} = \frac{k_2}{k_1} = \frac{k_2^0}{k_1^0} e^{-\frac{(E_2-E_1)}{RT}} \quad (5)$$

The global reaction rate depends on activation energy levels for the three step reactions. Since acetic acid is a refractory intermediate, E_{a3} is greater than either E_{a1} or E_{a2} . For most organic wastes, E_{a2} should approximately be equal to E_{a1} ; because Groups B and C represent series degradation products all derived from similar reactions. For this reason, α_1 should be a weak function of temperature, and merely become a ratio of the frequency factors of the two parallel reactions. The value of α_1 for a feed stream matching the above assumptions falls in between 0 and 1 (24). If the concentration of short-chain organic compounds, including those with two carbon atoms, other than acetic acid, such as ethanol, is high in a wastewater, the value of α_1 may be large. Therefore, α_1 can be used to characterize the "strength" of the waste stream in a WO process.

Two approaches can be used to apply this model for nitrogen- and chlorine-containing organic compounds. The first approach is to express the concentrations of Groups A and B in terms of COD. The concentrations of ammonia and methyl chloride can be expressed by equation 2 when k_2 and k_3 are substituted by k_4 and k_5 , and k_6 and k_7 , respectively. A general expression may then be obtained for $[A + B_I + B_{II} + B_{III}]$, where the subscripts I, II, and III indicate the organic compound category as previously defined. Similarly, typical values of α may be obtained from experimental data for categories II and III. The second approach is to monitor the concentrations of total carbon, total nitrogen, and total chlorine. It can be assumed that the oxidation kinetics for each species of C, N, or Cl is independent of those of other species. Equation 3 can be used for each species with proper substitution of reaction rate constants. The values of k_1 , k_2 , k_4 , and k_6 can be determined from experimental data. If experimental results are not available, an approximation may be established by selecting a waste from the existing kinetic database. It is recommended that the parameters shown in Table II be utilized as k_3 , k_5 , and k_7 .

Conclusions

A previously described global kinetic model can accommodate the WO of nitrogen- and chlorine-containing organic compounds. A similar approach may be used to describe the WO of organic compounds containing other heteroatoms. Such a model may be derived from a simplified reaction scheme based on parallel reaction pathways involving the formation of key intermediates and oxidation end products. This selectivity factor, quantified by the ratio of the parallel reaction rates, can be used to characterize the "strength" of the feed stream in WO processes. A high point selectivity value indicates that feed is more difficult to treat because a large fraction of the feed is converted to the rate-controlling intermediate. This work extends the validity of the previously proposed kinetic model for WO of organic compounds associated with wastewaters and sludges.

Acknowledgments

Appreciation for financial support is extended to Separations Research Program, The University of Texas (Austin, TX) and RPC Energy Services, Inc.. Also, this material is based in part upon work supported by the Texas Governor's Energy Research in Applications Program under Contract No. 5127.

Literature Cited

1. Zimmerman, E. J. *Chem. Eng.* **1958**, *65*, 117.
2. Teletzke, G. H. *Chem. Eng. Progress*, **1964**, *60*, 33.
3. Foussard, J.-N.; Debellefontaine, H.; Besombes-Vailhe, J. *J. Environ. Eng.*, **1989**, *115*, 367.
4. Keen, R.; Baillo, C. R. *Water Res.*, **1985**, *19*, 767.
5. Baillo, C. R.; Faith, B. M.; Masi, O. *Environ. Prog.*, **1982**, *1*, 217.
6. Baillo, C. R.; Lamparter, R. A.; Leddy, D. C. *Proceedings 34th Industrial Waste Conference*, Ann Arbor Science Publ: Ann Arbor, MI, 1980; 206-213.
7. Friedman, A. A.; Smith, J. E.; DeSantis, J.; Ptak, T.; Ganley, R. C. *J. WPCF* **1988**, *60*, 1971.
8. Wu, Y. C.; Hao, O. J.; Olmstead, D. G. *J. WPCF* **1987**, *59*, 39.
9. Ploos van Amstel, J. J. A.; Rietema, K. *Chem. Ing. Tech.*, **1973**, *45*, 1205.
10. Fisher, W. J. *Water Res.* **1971**, *5*, 187.
11. Teletzke, G. H.; Gitchel, W. B.; Diddams, D. G.; Hoffman, C. A. *J. WPCF* **1967**, *39*, 994.
12. Sheppard, J. D. *Can. J. Chem. Eng.* **1985**, *63*, 645.
13. Larson, R. A.; Ju, H.-L.; Snoeyink, V. L.; Recktenwalt, M. A.; Dowd, R. A. *Wat. Res.* **1988**, *22*, 337.
14. Wightman, T. J. *M.S. Thesis*; Univ. of Cal.: Berkeley, CA, 1981.
15. Price, C. M. *M.S. Thesis*, MIT: Cambridge, MA, 1981.
16. Modell, M.; Gaudet, G. G.; Simson, M.; Hong, G. T.; Biemann, K. "Supercritical Water Testing Reveals New Process Holds Promise," *Solid Wastes Manag.*, **1982**, *25*, 26.
17. Timberlake, S. H.; Hong, G. T.; Simson, M.; Modell, M. *S.A.E. Tech. Paper Ser.*, No. 82872, 1982.
18. Thomason, T. B.; Modell, M. *Hazardous Waste*, **1984**, *1*, 453.
19. Helling, R. K. *Ph.D. Dissertation*, MIT: Cambridge, MA, 1986.
20. Staszak, C. N.; Malinowski, K. C.; Killilea, W. R. *Envir. Progress*, **1987**, *6*, 39.
21. Li, L.; Eller, J. M.; Gloyna, E. F. presented at AIChE Summer Meeting, San Diego, CA, 1990.
22. Lee, D. S.; Gloyna, E. F.; Li, L. *J. Supercrit. Fluid*, **1990**, *3*, 249.
23. Lee, D. S.; Kanthasamy, A.; Gloyna, E. F. presented at AIChE Annual Meeting, Los Angeles, CA, 1991.
24. Li, L.; Chen, P. S.; Gloyna, E. F. *AIChE J*, **1991**, *37*, 1687.
25. Daga, N. S.; Prasad, C. V. S.; Joshi, J. B. *Ind. Chem. Eng.*, **1986**, *28*, 22.
26. Webley, P. A.; Tester, J. W. *Energy and Fuels* (in press).
27. Willms, R. S.; Balinsky, A. M.; Reible, D. D.; Wetzell, D. M.; Harrison, D. P. *Ind. Eng. Chem. Res.* **1987**, *26*, 148.
28. Jaulin, L.; Chornet, E. *Can. J. Chem. Eng.*, **1987**, *65*, 64.
29. Mundale, V. D.; Joglekar, H. S.; Kalam, A.; Joshi, J. B. *Can. J. Chem. Eng.*, **1991**, *69*, 1149.
30. Kulkarni, U. S.; Dixit, S. G. *Ind. Eng. Chem. Res.*, **1991**, *30*, 1916.
31. Charest, F.; Chornet, E. *Can. J. Chem. Eng.*, **1976**, *54*, 190.
32. Pruden, B. B.; Le, H. *Can. J. Chem. Eng.*, **1976**, *54*, 319.
33. Joglekar, H. S.; Samant, S.D.; Joshi, J.B. *Wat. Res.* **1991**, *25*, 135.
34. Lee, D. S. *Ph.D. Dissertation*, The Univ. of Texas: Austin, TX, 1990.
35. Huppert, G. L.; Wu, B.C.; Townsend, S.H.; Klein, M.T.; Paspeck, S.C. *Ind. Eng. Chem. Res.* **1989**, *28*, 161.
36. Tiffany, D. M.; Houser, T.J.; McCarville, M.E.; Houghton, M.E. *Am. Chem. Soc., Div. Fuel Chem.*, **1984**, *29*, 56.
37. Xu, X.; De Almeida, C. P.; Antal, Jr. M. J. *Ind. Eng. Chem. Res.* **1991**, *30*, 1478.

38. Mikita, M. A.; Fish, H. T. *ACS Div. Fuel Chem. Prep.* **1986**, *31*(4), 56.
39. Hutchinson, P.; Luss, D. *Chem. Eng. J.* **1970**, *1*, 129.
40. Astarita, G. *AIChE J.* **1989**, *35*, 529.
41. Aris, R. *AIChE J.* **1989**, *35*, 539.
42. Killilea, W. R.; Swallow, K. C.; Hong, G. T. *J. Supercritical Fluids* (in press).
43. Hong, G. T.; Fowler, P. K.; Killilea, W. R.; Swallow, K. C. *SAE Technical Paper Series* No. 871444, 1987.
44. Takahashi, Y.; Wydeven, T.; Koo, C. *NASA Conf. Publ.* #10040, 95-106, 1989.
45. Shanableh, A. M. *Ph.D. Dissertation*, The Univ. of Texas: Austin, TX, 1990.
46. Gamer, C. R. *Iron and Steel Engineer*, **1986**, 55.
47. Webley, P. A.; Tester, J. W.; Holgate, H. R. *Ind. Eng. Chem. Res.* **1991**, *30*, 1745.
48. Webley, P. A.; Holgate, H. R.; Stevenson, D. M.; Tester, J. W. *SAE Technical Paper Series* No. 901333, 1990.
49. Rofer, C. K.; Streit, G. E. *Oxidation of Hydrocarbons and Oxygenates in Supercritical Water*; Phase II Final Report, LA-11700-MS, DOE/HWP-90, Los Alamos National Laboratory, 1989.

RECEIVED April 27, 1992

Chapter 25

Oxidation Processes in the Separation of Solids from Supercritical Water

P. C. Dell'Orco¹, Earnest F. Gloyna¹, and S. Buelow²

¹Environmental and Water Resources Engineering, The University of Texas at Austin, Austin, TX 78712

²Chemical and Laser Sciences Division, Los Alamos National Laboratory, MS J567, Los Alamos, NM 87545

Salt precipitation and removal from supercritical water solutions were studied with a salt separator operating between 400°C and 511°C at 29.8 MPa. Nitrate, chloride, sulfate, and bicarbonate salts of sodium were studied. The behavior of cesium was investigated, and the fate and behavior of corrosion products were assessed. Above 500°C, sulfate and chloride salts were separated near their solubility limits, while sodium nitrate was removed with efficiencies greater than 96%.

Supercritical water oxidation (SCWO) is an innovative treatment technology for wastewaters and biological sludges. This process involves oxidation above the critical temperature (374.2°C) and pressure (22.1 MPa) of water. Advantages of SCWO relative to other waste treatment technologies include high destruction efficiencies of organic matter (1,2), energy savings (3), and the ability to provide a totally enclosed reactor facility.

Several laboratory-scale SCWO reactors have been constructed and operated (4,5). Most of the research conducted with these reactors has focused on kinetic parameters. Little experimental work has been directed to by-product management. Inorganic particulates and salts are produced when wastes are oxidized. Many of these components are undesirable in the final effluent, and must be removed prior to ultimate and safe disposal.

In the supercritical state, changes in water physical properties dramatically alter solvent properties of water relative to ambient conditions (20°C, 0.1 MPa). At temperatures and pressures of interest in SCWO processes (400-700°C, 24.1-35.0 MPa), density and viscosity assume gas-like values (6), while the dielectric constant drops to values similar to non-polar organic solvents at ambient conditions (7). The ion product of water decreases below 10^{-20} mol/kg (8), and hydrogen bonding becomes considerably less extensive (9).

These changes in physical properties ultimately affect the solvent character of water. Diatomic gases, such as nitrogen and oxygen, which are relatively insoluble at low temperatures and pressures, become miscible with supercritical water (10,11). Hydrocarbons also exhibit miscibility (12). Conversely, salts which are soluble in subcritical water become virtually insoluble at supercritical conditions. Studies of distribution coefficients in supercritical steam boilers have provided information on

0097-6156/93/0514-0314\$06.00/0
© 1993 American Chemical Society

salt solubilities (13,14). Additionally, conductance measurements have been used to determine dissociation constants of electrolytes at supercritical conditions (10,15). These insoluble salts, along with metal oxides and hydroxides formed in hydrolysis reactions, constitute the solid matter present in the SCWO process.

An experimental apparatus has been proposed for the study of salt formation in supercritical water (16). This apparatus has been used to confirm phase diagrams for the NaCl-water system, as well as to provide information about precipitation mechanisms and crystal formation sizes (17). Several types of solids separators have been examined for use at supercritical water conditions. Impingement/filtration separators and a hydrocyclone with a deadleg were proposed for use in microgravity separations applications (18). A modified hydrocyclone apparatus with an underflow receiver was assessed for operation in high-flow systems (19). MODAR, Inc. (Natick, MA) has developed an innovative salt separator/reactor, which is being researched for potential use in commercial-scale SCWO processes (20).

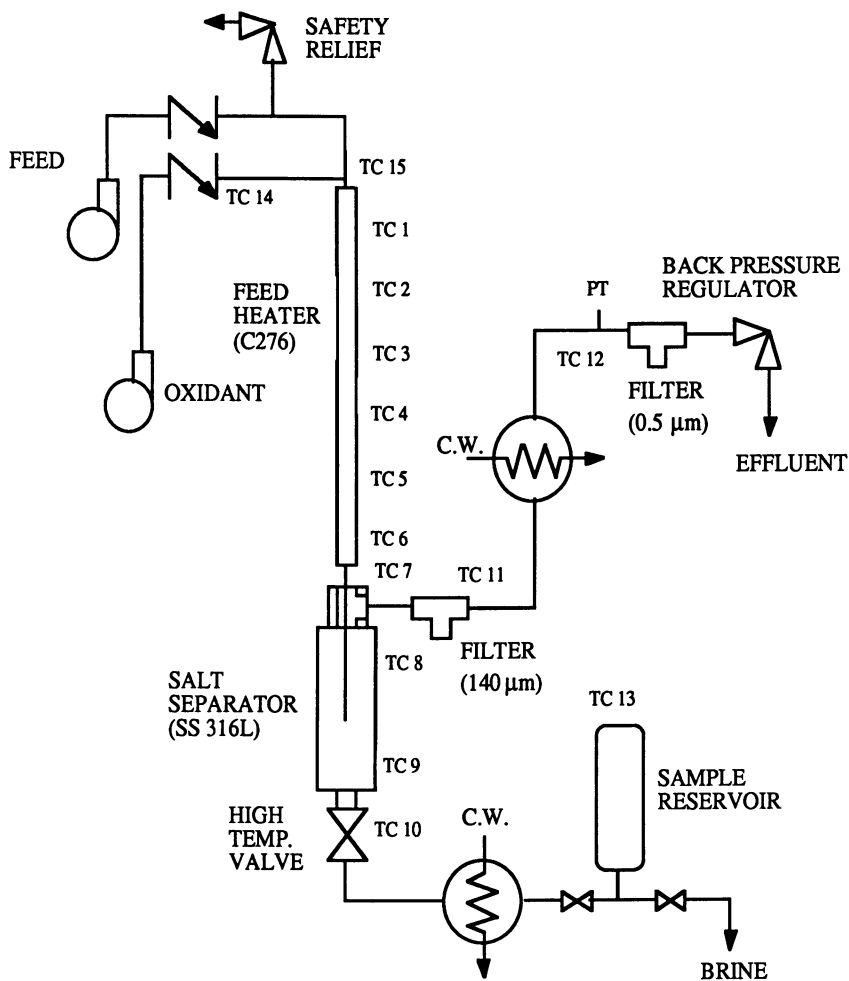
Little quantitative data has been presented on solids separation and formation, and the data that has been collected is inconclusive for engineering design purposes. The objective of this research was to expand the existing database on solids formation and separation in supercritical water, while providing information useful for the design of SCWO systems. Specifically, precipitation reactions of inorganic species pertinent to Department of Energy waste streams were studied in a laboratory-scale reactor equipped with a salt separator. An example of such waste streams are tank wastes at the Hanford Reservation, where high inorganic content and the presence of radionuclides present difficulties for conventional treatment technologies. The salt separator was designed so that low fluid viscosities and velocities in the separator, combined with high hold-up times, would result in the efficient removal of species insoluble at experimental conditions.

Experimental

Figure 1 shows the apparatus used for salt separation experiments. The apparatus consisted of a vertically heated tube which emptied into a pressure vessel that served as a salt separator and reactor. Tubing (3.17 mm OD) led from the vertically heated tube through a tee into the salt separator, and ended 7.62 mm from the bottom of the separator. The tee served as the exit from the salt separator. A screen (140 mesh) was placed at the tee exit, immediately followed by a heat exchanger, which served to cool the effluent to room temperature. The total heated volume of the apparatus was 60 cm³. The volume of the salt separator (including the exit tee) was 57 cm³. Salt removal was achieved through two mechanisms. Homogeneously formed crystals could settle in the separator, or impinge and subsequently stick on the walls of the salt separator and heater. Also, heterogeneously formed crystals could form and adhere to the apparatus walls.

Solutions were fed with low pulse, high performance liquid chromatography (HPLC) pumps. Maximum flow rates achieved by the pumps were 0.17 g/s at 29.8 MPa. Heat was supplied by conduction through brass sheaths surrounding the vertically heated tube. Heat was conveyed to the brass sheaths through resistively heated wire. Salt separator and tee temperatures were maintained with heating tape. All heaters and tapes were controlled with variable transformers. Surface temperatures were monitored with chromel-alumel (type K) thermocouples. Previous experience with similar reactors had shown that surface temperatures were within 1°C of fluid temperatures. Pressure was measured with a transducer (0.5% accuracy, 0-7500 psi) at the outlet of the salt separator. The apparatus was designed to operate at temperatures up to 550°C at 34.4 MPa.

Experiments consisted of pumping salt solutions through the reactor at constant temperature and pressure. The effluent was collected continuously. At 30



Notes:

1. TC denotes thermocouple location. PT denotes pressure transducer location.
2. Feed heater: 6.35 mm OD X 2.10 mm ID. X 60 cm long.
3. Salt separator volume (with exit tee): 57 mL
4. All remaining tubing: 3.17 mm OD X 0.89 mm ID. (SS 316L)
5. Feed heater tubing heated by conduction; salt separator and tee heated with heating tape.

Figure 1. Salt separation apparatus.

minute intervals, the volume and pH of the accumulated effluent were measured, and a sample was collected for ion analyses. After approximately two hours, the flow to the apparatus was stopped, and the high temperature valve at the bottom of the salt separator was opened. This step resulted in the rapid expansion of the apparatus contents through a cooling heat exchanger and into a collection vessel. As a result, the solids accumulated in the apparatus during the course of the experiment could be collected. Salts which precipitated in the separator resolubilized with the reduction of temperature and pressure, forming a concentrated brine.

After the reactor was allowed to cool, rinse water was continuously recycled through the system for a minimum of ten reactor volumes, and subsequently collected. This rinse served to collect those salts which adhered to apparatus walls during the experiment. Rinse acid (1.0 N HNO₃ or 1.0 N H₂SO₄) was also recycled for a minimum of ten reactor volumes and collected. All streams were measured for volume and pH, and samples were preserved for metal ion analyses. Analysis of anions was accomplished with ion chromatography. All metal ions (except cesium) were analyzed by ion-coupled plasma. Atomic absorption was used for cesium ion analysis. Carbonate and bicarbonate concentrations were determined through alkalinity and total inorganic carbon (TIC) analyses. When solids (insoluble at ambient conditions) were collected in experiments, these were dried and weighed, digested in strong acids, and the digestate analyzed. These measurements allowed the performance of a total mass balance of system constituents.

Experimental Results and Discussion

Salt separation studies examined dilute sodium salts of chloride, sulfate, and carbonate/bicarbonate. Concentrated sodium nitrate solutions were also processed. Salts were processed alone and in the presence of organic matter (acetate) undergoing oxidation. Temperatures ranged from 400°C to 511°C. Pressure was constant at 29.8 MPa. Feed flow rates of 0.12 to 0.13 g/s resulted in residence times of 50 to 125 seconds in the heated section of the apparatus, for experiments conducted near 500°C and 400°C, respectively. Residence time in the salt separator was greater than 90% of the total residence time in the heated portion of the apparatus. Five sets of samples were collected for each experiment. These represented feed, effluent, brine (solution consisting of salts accumulated in the salt separator during the experiment), and apparatus water and acid rinses. Mass recoveries for most constituents were between 90 and 110%. An exception to this occurred for the processing of sodium carbonate and bicarbonate streams, for which carbonate and bicarbonate were not completely recovered. These poor recoveries were presumably due to volatilization losses.

During most experiments, 800 to 1000 mL of solution was processed, and 15-30 mL of brine solution was collected. The brine volume was consistent with the calculated water volume in the apparatus prior to pressure reduction. This brine, which would constitute the concentrated waste if such an apparatus was used for the processing of an inorganic waste stream, constituted only 2-3% of the total volume of solution processed. Water and acid rinse volumes were approximately 200 mL. These rinses were necessary to complete mass balances on constituents, and to provide information on the solubility and stickiness of precipitated salts.

Table I summarizes experimental conditions and removal efficiencies for selected experiments. Temperatures shown are those measured for the salt separator, using the average measurements of TC 8 and TC 9 (Figure 1). These were generally within 1-2°C of each other. Above 500°C, removal efficiencies were greater than 90% for all salts except sodium bicarbonate. Near 400°C, the separation of chloride and sulfate were increased by increased sodium concentrations and the presence of an organic constituent undergoing oxidation. Trace cesium was separated with efficiencies greater than 98% when processed with concentrated sodium nitrate solutions. In the processing of concentrated sodium nitrate solutions (Hanford waste

Table I. Results from Salt Separation Studies

Salt in Feed Solution	Temp.* (°C)	Residence Time** (s)	Feed Conc. (mg/L)	Effluent Conc. (mg/L)	% Removed (%)
5 wt% NaNO ₃	507	54			
Na ⁺			14000	206	98.5
NO ₃ ⁻			34600	454	98.7
Cs ⁺			23.1	0.2	99.1
2 wt% NaNO ₃	507	52			
Na ⁺			5690	183	96.8
NO ₃ ⁻			14000	452	96.8
Cs ⁺			24.7	0.5	98.0
NaCl	408	112			
Na ⁺			343	340	0.9
Cl ⁻			496	484	2.4
Cs ⁺			22.5	22.5	0.0
NaCl w/org.	409	118			
Na ⁺			2890	1430	50.5
Cl ⁻			530	383	27.7
Cs ⁺			23.4	17.6	24.8
CH ₃ COO ⁻			6180	3220	53.2
NaCl	509	52			
Na ⁺			380	119	68.7
Cl ⁻			615	180	70.7
Na ₂ SO ₄	407	118			
Na ⁺			216	49	77.3
SO ₄ ⁼			395	92	76.7
Cs ⁺			22.5	22.2	1.3
Na ₂ SO ₄ w/org.	411	122			
Na ⁺			2500	1000	60.0
SO ₄ ⁼			459	2.6	99.4
Cs ⁺			24.7	20.5	17.0
CH ₃ COO ⁻			6050	2380	61.0
Na ₂ SO ₄	509	118			
Na ⁺			217	6.0	97.2
SO ₄ ⁼			391	2.6	99.3
Cs ⁺			22.7	11.0	51.5
NaHCO ₃	509	50.0			
Na ⁺			191	17	91.1
HCO ₃ ⁻			537	68.7	87.2
Cs ⁺			23.3	21.3	8.6

* Temperature of salt separator. All experiments conducted at 29.8 MPa.

** Residence time in heated section of apparatus.

matrices), nearly all sodium nitrate was precipitated. The behavior of three salt systems, sodium sulfate, sodium chloride, and sodium nitrate, is described in detail below.

Sodium Sulfate. Figure 2 shows results of three experiments conducted with sodium sulfate. Average concentrations of feed, effluent, brine, and rinse water samples are shown. No appreciable amounts of sodium or sulfate were recovered in acid rinse samples. Sulfate (4-500 mg/L), fed with stoichiometric sodium and a trace amount of cesium, was precipitated at 407°C and 509°C. Additionally, 2.5 g/L of TOC (total organic carbon), added as sodium acetate, was reacted with sodium sulfate, trace cesium, and an oxidant (30 wt% H₂O₂, 150% excess) at 411°C.

At 407°C for the salt-only system, effluent sulfate concentrations (92 mg/L) and sodium concentrations (50 mg/L) indicated the presence of 136 mg/L (sulfate limiting concentration) of sodium sulfate in the effluent. Effluent pH values and concentrations varied little with time. Near 410°C, the solubility of sodium sulfate at 30 MPa was determined by interpolation of Martynova's data to be near 1 mg/L (21). The data of Morey and Hesselgesser (22), however, suggest a higher solubility. Due to discrepancies in reported sodium sulfate solubilities and the scarcity of solubility data, it was difficult to ascertain the percentage of insoluble sodium sulfate which was separated.

High sodium and sulfate concentrations were found in both the brine and rinse water. The majority of the recovered sulfate (63.4%) was found in the rinse water. Effluent cesium concentrations were similar to feed concentrations, indicating little precipitation. The pH of brine (2.9) and rinse water (2.4) samples indicated the accumulation of an acid at experimental conditions. These low observed pH values likely resulted from sulfuric acid formation and the precipitation of acid forms of corrosion products. Acid formation, caused by hydrolysis reactions, possibly affected the solvent character of the fluid in the salt separator, influencing the solubility equilibrium for the sodium sulfate-water system.

When reacted at 411°C with 2.5 g/L of TOC (sodium acetate) and hydrogen peroxide, sulfate removals were increased over those of the pure salt system. From a feed concentration of 459 mg/L, only 2.6 mg/L remained in the effluent stream after precipitation. This corresponded to a sodium sulfate concentration of 4 mg/L in the effluent, and a corresponding removal efficiency of 99.4% for sulfate. Of the recovered sulfate, 94.1% was partitioned in the rinse water sample, indicating the tendency of sodium sulfate to strongly stick on the apparatus walls. Sodium, which could also precipitate with bicarbonate and acetate, had a concentration of 1000 mg/L in the effluent, corresponding to a 60.0% removal efficiency. Over 42% of the recovered sodium was partitioned in the rinse water. Alkalinity concentrations (as bicarbonate) of 6550 mg/L and 5650 mg/L were determined for the brine and rinse water samples, compared with an average effluent value of 2290 mg/L. The high concentrations of sodium, sulfate, and alkalinity in the rinse water sample indicated that sodium sulfate and bicarbonate were either heterogeneously precipitated, or removed through impingement and subsequent sticking on the walls of the salt separator and the heater. The stickiness of these salts was also manifested by the actual plugging of equipment. Plugging occurred at 77 minutes of a planned 120 minute experiment in the vertically heated tubing, approximately between thermocouples 4 and 5 (Figure 1). Upon apparatus cooling, the plug was readily dissolved by the rinse water.

Differences between this experiment and the pure salt separation experiment were the neutral pH's of the effluent samples (~ 6.3), and the basic pH's of the brine (9.4) and rinse water (10.5) samples. Sodium was also present in higher concentrations. The higher sodium concentrations caused increased sulfate precipitation. Additionally, in this highly buffered system with neutral to basic pH values, sodium sulfate solubility equilibrium was likely different from the pure salt

experiment. Sodium precipitation as sodium bicarbonate and possibly sodium acetate was extensive, as indicated by pH values, sodium concentrations, and alkalinity data. Cesium, which was scarcely removed in the pure salt experiment, was removed with a relatively high efficiency (51%) when processed with sodium acetate, indicating a cesium acetate or cesium bicarbonate precipitate.

At 509°C, high separations of sodium sulfate were observed when the pure salt solution was processed. At this temperature greater than 98% of the influent sodium sulfate was recovered in either brine or rinse water samples. The largest fractions of sulfate were recovered in the rinse water (75.8%) and brine (19.6%) samples. Sodium behaved similarly. The observed effluent concentration of sodium sulfate was less than 4 mg/L. This compared with an observed solubility near 0.04 mg/L (21). The pH values of the effluent (6.2-6.6) were neutral, while the pH of brine (2.2) and rinse water (3.3) samples was acidic. As observed at 407°C, acid accumulation seemed to occur, possibly as sulfuric acid and acid forms of corrosion products. A lower fraction sodium and sulfate were recovered in the rinse water at this temperature than at 407°C. This implies that sodium sulfate may be less "sticky" at the elevated temperature, possibly resulting from reduced waters of hydration due to a lower water density.

Sodium Chloride. Figure 3 shows results of analogous experiments conducted with sodium chloride. At 408°C, little sodium chloride was separated. In the experiment conducted without organic matter, effluent concentrations of sodium and chloride were similar to feed concentrations. Over 96% of sodium chloride fed was recovered in effluent. The balance was recovered primarily in brine (1.4%) and rinse water (2.3%) samples. Constituent concentrations in the effluent increased with pH through the course of the experiment. Effluent pH values ranged from 4.0 to 5.1, while effluent chloride concentrations varied from 434 mg/L at 30 minutes to 488 mg/L at two hours. The feed concentration of chloride was 487 mg/L. Solubility of sodium chloride at 25.5 MPa and 409°C has been reported near 400 mg/L (21). At 29.8 MPa, this solubility is elevated, due to greater degrees of solvation from higher concentrations of water.

One possible explanation for low sodium chloride removals at 408°C (relative to the removal expected from solubility data) is that the precipitate remained entrained in the effluent stream. This was considered doubtful, because low fluid viscosities ($\sim 10^{-5}$ kg/m*s) and flow velocities (< 1 cm/s) encountered in the separator could probably entrain little solid matter. Instead, the unsteady-state nature of this experiment indicated equilibrium effects on the separation. The solubility of the sodium chloride is likely affected by hydrolysis reactions of corrosion products, which resulted in acid formation. In an unbuffered system, such hydrolysis and association reactions will affect the hydrogen ion concentration in the supercritical fluid and the amount of unbound chloride and sodium available for precipitation. Both of these factors will affect the solubility equilibrium of the electrolyte.

When precipitated concurrently with acetate oxidation at 409°C, most sodium was recovered in the brine and rinse water samples. From pH values of the brine (9.5) and rinse water (10.5), it appeared that sodium precipitated to a great extent as a bicarbonate, which was created as a result of acetate oxidation. The amount of recovered sodium partitioned in the brine (16.1%) and rinse water (23.5%) indicated that sodium bicarbonate precipitates were removed primarily by heterogeneous precipitation or impingement on separator walls, as was observed in the analogous sodium sulfate experiment. This was confirmed by alkalinity concentrations of 23,460 mg/L and 7880 mg/L in the brine and rinse water, respectively. Chloride concentrations in the effluent (382 mg/L) indicated approximately 630 mg/L of soluble sodium chloride. In this experiment, the pH of the effluent (6.0) did not vary over time, due to buffering provided by acetate and carbonate/bicarbonate equilibria.

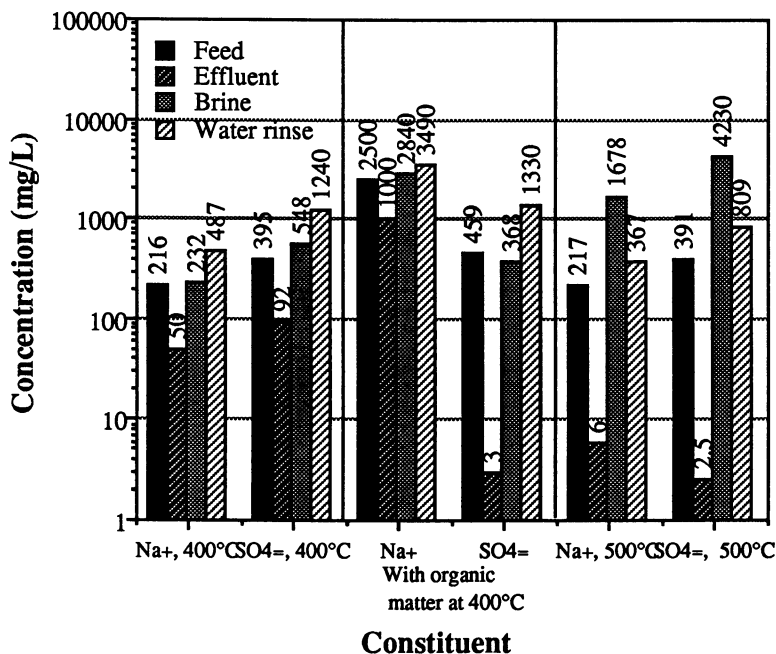


Figure 2. Summary of salt separation experiments with sodium sulfate.

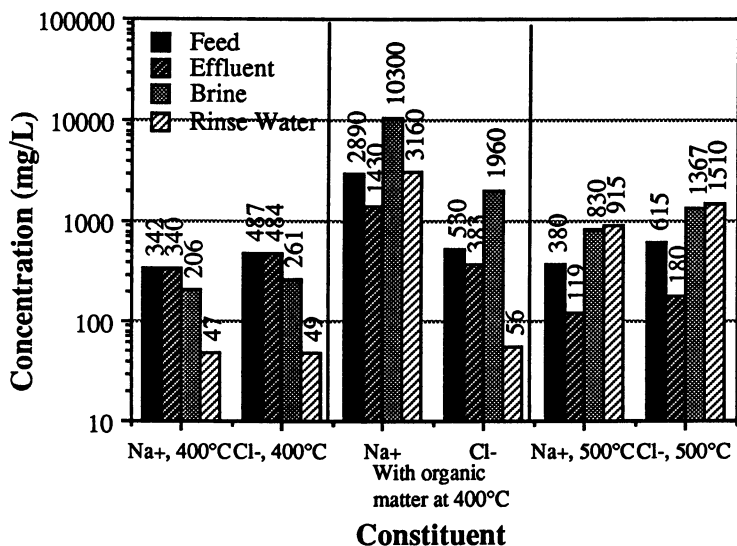


Figure 3. Summary of salt separation experiments with sodium chloride.

This buffering possibly caused the increased removal efficiency of sodium chloride relative to that observed in the unbuffered experiment. Unlike the analogous sodium sulfate/organic experiment, reactor plugging was not observed while processing sodium chloride with sodium acetate. In both experiments near 400°C, cesium effluent concentrations were similar to feed concentrations, indicating little precipitation.

A greater extent of sodium chloride precipitation was observed when the pure salt was processed at 509°C. Effluent concentrations of sodium (119 mg/L) and chloride (180 mg/L) indicated the presence of 298 mg/L of soluble sodium chloride, near the observed solubility of 300 mg/L at experimental conditions (21). Brine and rinse water samples had pH's in the neutral range (5.6 and 7.7), indicating little acid accumulation in the separator. Effluent pH's were slightly basic, varying from 7.9 to 8.1. These compare to a feed pH of 7.3. Effluent basicity may have been caused by some accumulation of hydrochloric acid in the separator, as also indicated by the slight acidity of the brine sample. Chloride was also found to be in slight stoichiometric excess in the brine solution. Sodium chloride was recovered primarily in the rinse water (63.6%). Relative concentrations and partitioning of sodium and chloride indicated that sodium chloride, like sodium sulfate, was a sticky salt near 500°C and 29.8 MPa. Unlike sodium sulfate solutions, however, reactor plugging was not observed while processing sodium chloride.

A particularly interesting aspect of the sodium chloride system at dilute concentrations is the possible existence of one phase vapor solution, a two phase vapor-liquid or vapor-solid solution, or a three phase vapor-liquid-solid solution (16). For the sodium chloride experiment conducted at 409°C, a vapor-liquid system is expected to exist, while above 500°C, a vapor-solid system occurs (23). Unlike sodium chloride, supersaturated sodium sulfate solutions exhibit only a two-phase, vapor-solid system at the temperature-pressure-composition conditions of these experiments (24). Knowledge of these phase boundaries can help to describe observed experimental behavior.

The processing of salt solutions in these experiments resembled a semi-batch process. While precipitated salts were allowed to accumulate in the salt separator, a fresh feed stream was constantly introduced to the separator. Because the system is semi-batch, non-steady state conditions could exist in the separator, if the precipitated phase has an appreciable equilibrium vapor pressure of the electrolyte. This would result in some maximum amount of salt accumulation, after which the precipitated phase and the feed solution would have equal fugacities of the salt, causing precipitation to cease. This could explain why, at 408°C, sodium chloride concentrations and effluent pH values increased over the course of the experiment to feed solution values. Parisod and Plattner (25) determined an equilibrium sodium chloride distribution coefficient (K_D , wt% NaCl vapor/wt% NaCl liquid) of $5.4E-03$, with a vapor concentration of 0.14 wt% NaCl at 420°C and 292 bars. While the vapor concentration of 0.083% in this experiment was lower, the presence of trace constituents (cesium acetate, corrosion products) could lower the value of K_D observed in pure systems, possibly through the acidification of the liquid phase. This would result in the development of an equilibrium between the precipitated phase and the feed solution, and result in decreased extents of precipitation over the course of the experiment. The latter behavior was observed experimentally at 408°C for sodium chloride.

Increasing effluent concentrations were not observed in any sodium sulfate experiments or in sodium chloride experiments at 509°C, and at 409°C with acetate oxidation. Above 500°C, both salts exist as solids in the precipitated phase, with vapor pressures that were insufficient to affect precipitation reactions over experimental time scales. Additionally, the presence of high sodium acetate/sodium bicarbonate concentrations in the vapor and precipitated phases at 409°C could

substantially alter the phase behavior of sodium chloride, resulting in constant effluent concentrations with time.

Sodium Nitrate. Solutions of 2 and 5 wt% sodium nitrate were processed to simulate Hanford tank waste matrices. These matrices represent the primary constituents of tank wastes after some dilution and neutralization. These were processed at 409°C and 507°C. Figure 4 shows results from an experiment conducted at 507°C for the 2 wt% solution. The 5 wt% solution, although not shown graphically, exhibited identical trends in constituent concentrations and pH values of samples. At 409°C, effluent pH's and sodium nitrate concentrations increased with time, until feed values were reached in the last effluent sample. Sodium concentrations increased from an initial effluent concentration of 2860 mg/L to a final value of 5670 mg/L, while corresponding nitrate concentrations ranged from 6840 mg/L to 14800 mg/L. Similar to trends observed for sodium chloride experiments, this increase may have resulted from solubility equilibria changes in the salt separator with time. Unlike sodium chloride, sodium nitrate phase behavior at these conditions is not reported in the literature.

Above 500°C, this pattern was not observed. For both 2 and 5 wt% solutions, effluent concentrations and pH's (near 3) were relatively constant over time. For the 2 wt% solution, effluent concentrations of sodium and nitrate were 183 mg/L and 452 mg/L, respectively. For the 5 wt% solution, effluent concentrations were similar, with values of 206 mg/L for sodium and 454 mg/L for nitrate. Large amounts of sodium nitrate were precipitated in both experiments, resulting in a heavily concentrated brine (> 600,000 mg/L sodium nitrate), as shown in Figure 4. Greater than 80% of all recovered sodium and nitrate were recovered in the brine sample. Cesium was also removed extensively (removal efficiency = 98.0%), and was primarily recovered in the brine (84.3%). A comparison of pH values of effluent streams (near 3) and brine and rinse water streams (> 12) indicated some hydrolysis of sodium ion and subsequent precipitation of sodium hydroxide. This resulted in a reduction of effluent pH through the generation of nitric acid, while causing high pH values in brine and rinse water samples, due to the presence of the hydroxide.

Although the decomposition temperature of sodium nitrate (in air) has been measured at 380°C (26), nitrate decomposition was scarcely observed in these experiments. Table II shows some balances for sodium nitrate, as well as for sodium chloride, which does not decompose over experimental temperature ranges. The table shows that nitrate undergoes little decomposition near 400°C, and only slight conversion (< 3%) to nitrite near 500°C. Mass balances achieved for nitrate are similar to those achieved by chloride.

Despite the large amount of precipitated salts observed during sodium nitrate experiments near 500°C, the apparatus did not plug. The proportion of sodium nitrate recovered in brine samples relative to rinse water samples indicated that sodium nitrate did not stick to reactor walls, like chloride and sulfate salts. The melting point of anhydrous sodium nitrate (306.8°C) (26) indicates that any precipitate will be in an ionic liquid form. Perhaps the lack of stickiness occurred because the dense ionic liquid was able to flow down the walls of the separator and collect in a pool near the bottom. The fact that sodium and nitrate effluent concentrations were nearly the same for the processing of 2 and 5 wt% solutions at 507°C indicated that the insoluble fraction of sodium nitrate was removed from the feed stream with a high efficiency. From observation of effluent concentrations from the processing of 2 and 5 wt% sodium nitrate solutions, a solubility of 620 mg/L was estimated at 509°C and 29.8 MPa.

Corrosion Products. The occurrence and separation of corrosion products were also investigated. The corrosion products analyzed were iron, chromium, and nickel, the primary components of the C276 alloy heating tube and the SS 316L salt separator.

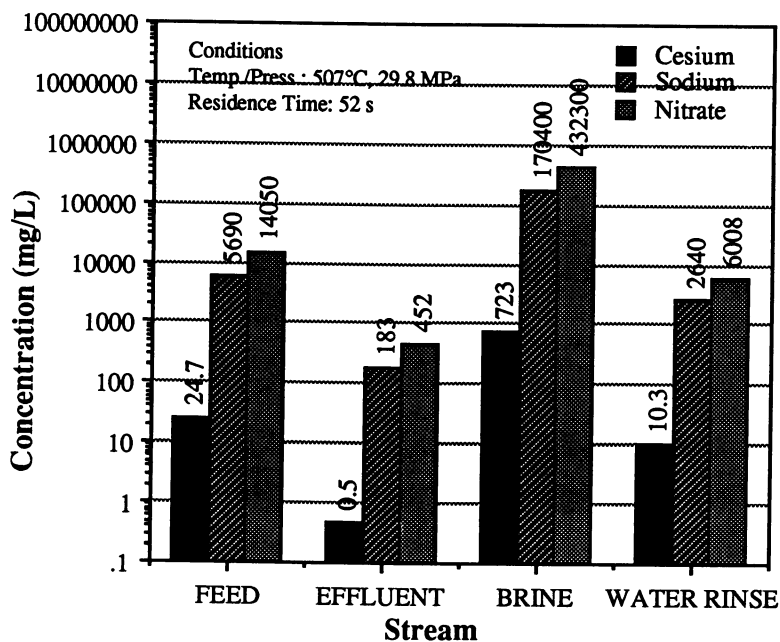


Figure 4. Results of 2 wt% sodium nitrate solution processing.

Table II. Mass Balances For Sodium Nitrate and Sodium Chloride*

Feed/ Species	Mass Fed (mg)	Mass Recovered				% Rec. (%)
		Effluent (mg)	Brine (mg)	Rinse Water (mg)	Rinse Acid (mg)	
<i>409°C, 5% NaNO₃</i>						
Na ⁺	12380	11100	857	376	32.2	100.9
NO ₃ ⁻	31068	27770	2270	864	68.6	100.4
NO ₂ ⁻	BDL	69.9	BDL	BDL	BDL	---
<i>507°C, 5% NaNO₃</i>						
Na ⁺	12300	178	7860	2720	793	93.6
NO ₃ ⁻	34600	396	22800	7100	2180	106.7
NO ₂ ⁻	BDL	8.42	615	55.0	4.27	---
<i>408°C, NaCl</i>						
Na ⁺	303	287	4.74	9.64	1.63	101.7
Cl ⁻	431	415	6.00	10.1	0.20	100.5
<i>509°C, NaCl</i>						
Na ⁺	320	107	19.1	194	---	97.8
Cl ⁻	518	167	31.4	320	---	97.0

* See Table I for experimental conditions.

Corrosion in all experiments involving an oxidant (nitrate, hydrogen peroxide) was chromium selective, while in all experiments without an oxidant, corrosion appeared non-selective. Over all experiments, corrosion products were recovered as 55.1% chromium, 19.1% nickel, and 25.8% iron. Iron and nickel were primarily recovered in acid rinse samples, indicating their precipitation as water insoluble species. For the processing of the 2 wt% sodium nitrate solution, 85.4% of the recovered iron and 69.5% of the nickel were recovered in the rinse acid. Neither of these constituents were detected in any effluent samples. It is likely that these constituents underwent hydrolysis reactions at the walls of the apparatus, forming oxides which were insoluble in water at both supercritical and ambient conditions. Because of the relative insolubility of these oxides, it is possible that corrosion products were not completely recovered. Whether corrosion rates were acceptable from a design point of view was difficult to ascertain, because of the variety of feed streams and the relatively small time (< 60 hours) that the apparatus was exposed.

Contrary to nickel and iron, most chromium was recovered as a water soluble species. Near 500°C, chromium was partitioned primarily in brine and rinse water samples. For example, when the 2 wt% sodium nitrate solution was processed at 507°C, effluent chromium concentrations were 0.8 to 0.9 mg/L, while brine and rinse water concentrations were 102 and 6.3 mg/L. Brine and rinse water samples contained 77.6% of all recovered chromium. This indicated the precipitation removal of a chromium species, probably the sodium salt of the chromate ion. The presence of chromate was also manifested by the strong yellow coloration of the brine. At 409°C for the same feed solution, effluent chromium concentrations were 1.1 to 6.7 mg/L, while brine and rinse water concentrations were only 15.5 and 1.4 mg/L. At the lower temperature, only 25.4% of the recovered chromium was recovered in the brine and rinse water. Nearly 70% was recovered in effluent samples. The accumulation of chromium in the separator was observed in most experiments above 500°C, while most chromium appeared in the effluent at salt separator temperatures near 400°C.

Conclusions

A pressure vessel acting as a salt separator accomplished separations near the solubility limits of sodium chloride and sodium sulfate near 500°C and 29.8 MPa. Sodium bicarbonate was also precipitated in experiments conducted with organic matter and sodium. Concentrated sodium nitrate salts, simulating Hanford waste matrices, were processed successfully, and were effectively removed from the feed stream. A heavily concentrated brine (> 600,000 mg/L) was collected from the processing of a 2 wt% solution. Greater than 96% of the influent sodium nitrate was precipitated. Greater than 98% of influent cesium was also collected as a precipitate. A solubility for sodium nitrate of 620 mg/L was estimated at 510°C and 29.8 MPa.

Different mechanisms for salt removal were observed. Sodium sulfate, chloride, and bicarbonate appeared to be sticky salts, removed primarily by heterogeneous precipitation or impingement and subsequent sticking on separator walls. Sodium nitrate was relatively non-sticky, and was recovered primarily in brine solutions. Finally, analyses for corrosion products indicated that iron and nickel formed oxides which were insoluble at experimental conditions. Chromium formed species that were water soluble in water at 20°C, but which were accumulated in the salt separator at 500°C.

Acknowledgements

This research was performed under appointment to the Environmental Restoration and Waste Management Graduate Fellowship Program, administered by Oak Ridge Associated Universities for the U.S. Department of Energy. Most of this

work was performed at Los Alamos National Laboratory and supported by the Office of Technology Development of the Department of Energy. This project was a cooperative endeavor between the SCWO Research Laboratories at The University of Texas at Austin and LANL. The authors would like to thank Pat Trujillo and Dale Counce for performing the analytical measurements, and Jerry Atencio, for his help in assembling the apparatus.

Literature Cited

1. Lee, D. S. and Gloyna, E. F., "Supercritical Water Oxidation-A Microreactor System," Presented at Water Pollution Control Federation Specialty Conference, New Orleans, LA, April 17-19, 1988.
2. Modell, M., "Supercritical Fluid Technology in Hazardous Waste Treatment," Presented at the International Conference on Recent Advances in the Management of Hazardous and Toxic Wastes in the Process Industries, Vienna, Austria, March, 1987.
3. Modell, M., "Treatment of Pulp Mill Sludges by Supercritical Water Oxidation - Final Report," DOE/CE/40914-T1, July, 1990.
4. Lee, D. S., "Supercritical Water Oxidation of Acetamide and Acetic Acid," Ph.D. Dissertation, The University of Texas at Austin, 1990.
5. Helling, R. K.; Tester, J. W. *Env. Sci. and Tech.*, **1988**, *22*, 1319.
6. Gallagher, J. S.; Haar, L., "Thermophysical Properties of Water (Steam)", National Institute of Standards and Technology Standards (formerly National Bureau of Standards) Reference Database 10,1988.
7. Quist, A. S. *J. Phys. Chem.*, **1970**, *74* (18), 3396 (1970).
8. Marshall, W. L.; Franck, E. U. *J. Phys. Chem. Ref. Data*, **1981**, *10*, 295.
9. Franck, E. U. *Pure and Appl. Chem.*, **1970**, *24*, 13.
10. Japas, M. L.; Franck, E. U. *Ber. Buns. Phys. Chem.*, **1985**, *89*, 1268.
11. Japas, M. L.; Franck, E. U. *Ber. Buns. Phys. Chem.*, **1985**, *89*, 793.
12. Connolly, J. F. *AIChE Journal*, **1966**, *11*(1), 13.
13. Martynova, O. I.; Smirnov, O. K. *Teploenergetika*, **1964**, *9*(2), 145.
14. Styrikovich, M. A.; Martynova, O. I.; Kurtova, I. S. *Teploenergetika*, **1966**, *13*(7), 45.
15. Marshall, W. L. *High Temperature, High Pressure Electrochemistry in Aqueous Solutions*, **1976**, (NACE-4), 109.
16. Armellini, F. J.; Tester, J. W. *Proceedings of the 2nd International Conference on Supercritical Fluids*, **1991**, 21.
17. Armellini, F. J.; Tester, J. W. *SAE Tech. Paper Ser.*, **1990**, No. 901313.
18. Killilea, W.R.; Hong, G. T.; Swallow, K. C.; Thomason, T. B. *SAE Tech. Paper Ser.*, **1988**, No. 881038.
19. Dell'Orco, P. C.; Gloyna, E. F., "The Separation of Particulates from Supercritical Water Oxidation Effluents," M.S. Thesis, The University of Texas at Austin, 1991.
20. Barner, H. E.; Huang, C. Y.; Johnson, T.; Martch, M. A., "Supercritical Water Oxidation: An Emerging Technology," Presented at CHEMA - '91, International Meeting on Chemical Engineering and Biotechnology, June 9, 1991.
21. Martynova, O. I. *High Temperature, High Pressure Electrochemistry in Aqueous Solutions*, **1976**, (NACE-4), 131.
22. Morey, G. W.; Hesselgesser, J. M. *Econ. Geol.*, **1951**, *46*, 821.
23. Pitzer, K. S.; Pabalan, R. T. *Geochim. Cos. Acta*, **1986**, *50*, 1445.
24. Ravich, M. I.; Borovaya, F. E. *Russ. Jour. Inorg. Chem.*, **1964**, *9*(4), 520.
25. Parisod, C. J.; Plattner, E. *J. Chem. Eng. Data*, **1981**, *26*, 16.
26. *CRC Handbook of Chemistry and Physics*; Wheat, R. C. Ed.; 66th Edition; CRC Press: Boca Raton, FL, 1986.

RECEIVED April 27, 1992

Chapter 26

Removal of Heteroatoms from Organic Compounds by Supercritical Water

Thomas J. Houser, Ying Zhou, Chun-Cheng Tsao¹, and Xu Liu

Department of Chemistry, Western Michigan University,
Kalamazoo, MI 49008

Interest in the reactions of supercritical water (SW) with organic compounds containing N, S, and O atoms was initiated by the potential use of SW as a solvent in the conversion of coal. Thus, through the removal of heteroatoms, the resulting product would lead to cleaner burning fuels. Up to this time the studies have been limited to organic compounds containing only N, O, or Cl. The results of the reaction of benzaldehyde with SW have been included to illustrate the types of reactions and products that may be obtained from the removal of amino groups from organic reactants since benzaldehyde was observed as an intermediate in the benzylamine-SW reaction. The compounds which are of current interest are those that model certain hazardous materials which may in the future require large scale destruction or conversion to innocuous products. These are: (a) 1-chlorohexane, (b) ethyl benzilate, (c) trihexylamine, (d) quinuclidine, (e) phenylpiperidine, and (f) phenylpyridine. The reactivities of these compounds and the product distributions from their pyrolyses and reactions with SW will be discussed.

The possible use of supercritical fluid extraction (SFE) of coal to obtain cleaner, more versatile fluid products has been of significant interest. Some fluids have the opportunity to participate as reactants at process conditions, which may yield extracts of very different compositions than those obtained from other treatments and which will be dependent on the fluid used. Thermodynamic consideration of SFE leads to the prediction that the

¹Current address: Chemistry Department, University of Maryland, College Park, MD 20742

0097-6156/93/0514-0327\$06.00/0
© 1993 American Chemical Society

enhanced solubility (volatility) of the solute may be several orders of magnitude (1-3). Thus, this method combines many of the advantages of distillation with those of extraction. Because of this interest in SFE and the related potential use of supercritical water (SW) as a medium for the efficient oxidation and destruction of environmentally hazardous materials there has been an increase in the number of reports on the basic chemistry that may be taking place in the presence of SW (4-15).

The results which are being reported are primarily concerned with the reactions of organic model compounds thought to be representative of hazardous materials which, at some future time, may require large scale destruction. Because of the difficulty of removing heterocyclic nitrogen, previous experiments were initiated by extensively examining the reactivities of quinoline and isoquinoline, as well as brief examinations of the reactivities of other compounds (4). The selection of water as the fluid was based on its physical and chemical properties (16) and on the observation that a few studies of SFE of coal using water as the fluid have given encouraging results (17,18). Zinc chloride was chosen as a catalyst in the previous studies because of its reported catalytic activity for hydrocracking aromatic structures (19). This paper discusses the results of a study of the reactions of supercritical water (SW) with benzaldehyde, which is postulated to be similar to an intermediate in the isoquinoline reaction (4), as well as 1-chlorohexane, ethyl benzilate, trihexylamine, quinuclidine, phenylpiperidine, and phenylpyridine. Several of the compounds have functional groups which are found in nitrogen mustards and BZ(3-quinuclidinyl benzilate) or their reaction intermediates.

Experimental

Most experiments were carried out in small (47 or 29 cm³) stainless steel, batch reactors, which were not equipped for the collection of gaseous products for analysis. The larger reactor was loaded with about 1.00 or 2.00 g of the organic compound, depending on availability. Water (10 mL) was added for the SW experiments to produce the desired pressure at reaction temperature, catalysts were added as needed, then the reactor was purged with argon and bolted closed using a copper gasket. Similar procedures were used with the smaller reactor with correspondingly smaller amounts of reactants. The reactor was placed in a fluidized sand bath furnace for the required reaction time, about 15 minutes was required to reach 375C. Following reaction, the vessel was air cooled, opened, the reaction mixture removed and the water and organic layers separated. Portions of solvent, usually methylene chloride, carbon tetrachloride or benzene, were used to rinse the reactor and extract the water layer. These portions were combined with the organic layer and additional solvent added to a standard volume for quantitative determinations made gas chromatographically using peak area calibrations from known solutions. The components for these solutions were identified mass spectrometrically. Ammonia analyses were run on the water layer from some experiments using an Orion ion selective electrode. In a few trihexylamine

experiments it was evident that significant amounts of gaseous hydrocarbon products were being formed, thus a mL of toluene was added to the reaction mixture to attempt to dissolve some of these products for qualitative identification. The addition of toluene had no apparent effect on the results but did allow better detection of C₄ and C₅ hydrocarbons.

There were certain limitations on the GC-MS determinations: Some components could not be separated completely and these are reported as a total yield of mixture using an average calibration factor. Some products are reported as an isomer of a probable structure as deduced from the molecular weight and MS fragmentation pattern. Finally, many of the higher molecular weight minor products could be measured only with a low degree of precision by GC and calibration factors were estimated.

Results and Discussion

It should be noted that the catalyst, ZnCl₂, was added only to the quinuclidine (QN) and phenylpyridine (PPY) reactants, since these were less reactive than phenylpiperidine (PPI), and to ethyl benzilate to see its influence on the product distribution. The catalyst amounts are reported in grams since it is assumed that the liquid ZnCl₂ (m.p. 283C) is acting as a heterogeneous catalyst. This assumption is based the solubilities of similar salts in SW. The lowest concentration used in the current study is about 1 wt%, whereas the solubilities at 400C and 250 bar were reported to be 0.1 wt% for NaCl (20) and 0.002 wt% for CaCl₂ (21), both of which decrease at higher temperatures.

Benzaldehyde. The previous study of the isoquinoline-SW reaction (4) indicated that following the rupture of the CN bond in the 1-2 or 2-3 position, the nitrogen portion would undergo hydrolysis and decarboxylation (similar to that observed for benzonitrile to yield benzene) while the carbon end was either capped directly, or shortened and capped by hydrogen, thus producing toluene, ethylbenzene or o-xylene, the major volatile products. To further investigate the reactions leading to these products the benzylamine-SW reaction was studied (5). At 450C and longer reaction times the major products were toluene, benzene, biphenyl and a methylbiphenyl isomer. However, at milder conditions benzaldehyde as well as benzyldenebenzylamine (C₆H₅CH₂N=CHC₆H₅) and small amounts of benzyl alcohol were observed as intermediates, with a reduction in benzene yield. The results of the benzyldenebenzylamine-SW reaction confirmed that CN single bonds were the source of the toluene, whereas C=N reacted to form benzene and those products obtained from the phenyl group. (Tsao, C.C.; Zhou, Y.; Liu, X.; Houser, T.J. *J. Supercritical Fluids*, in press.)

The results of the benzaldehyde-SW reaction have been included to illustrate the types of reactions that can occur after nitrogen atoms have been removed from organic molecules. The data in Table I show that SW appears to have little effect on the extents of the pyrolysis reaction or, (except for benzene at one hour, which may be spurious) on its product distribution.

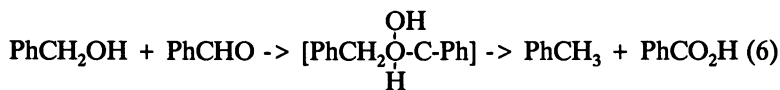
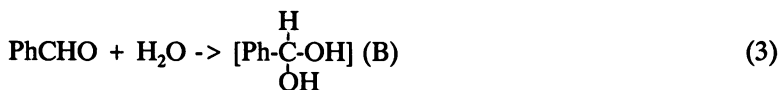
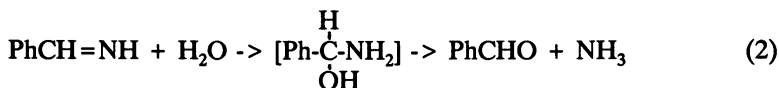
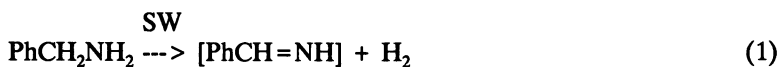
Table I. Benzaldehyde-SW Reaction at 400C

	1	6	1	3	6	1	3	6	1	3	6	1	3	9
Time (hr)	0	0	267	267	267	267	267	267	267	267	267	267	267	267
Water Pressure (Bar)	0	0	0	0	0	2M	2M	2M	6M	2M	2M	0	2M	2M
NH ₃ Added (M)	0	0	0	0	0	0	0	0	0	0	0	0	2	2
DHA (g)	0	0	0	0	0	0	0	0	0	0	0	0	2	2
% Reaction	29	76	25	53	71	73	85	93	94	89	89	94	89	99
<i>Volatile Product Yields (moles product/mole reacted)</i>														
Benzene	.70	.54	.36	.49	.50	.32	.41	.44	.28	.16	.44	.28	.16	.18
Toluene	.067	.073	.059	.083	.064	.11	.17	.21	.12	.39	.21	.12	.39	.38
Benzyl Alcohol	.017	0	.068	.012	.009	.021	.028	.025	.034	-	.028	.034	-	-
Benzoic Acid	.10	.069	.14	.075	.047	0	0	0	0	-	0	0	-	-
Benzamide	-	-	-	-	-	.012	.01	.007	.026	-	.012	.026	-	-
Biphenyl	.055	.07	.017	.031	.041	.048	.046	.06	.017	-	.046	.017	-	-
168 Isomers ^a	.03	.045	.01	.015	.02	.01	.02	.03	.015	-	.02	.015	-	-
166,180-196 Mixture ^a	.10	.04	.05	.04	.025	.03	.035	.025	.025	-	.035	.025	-	-
Benzylidenebenzylamine	-	-	-	-	-	.01	.022	.02	.031	-	.022	.02	-	-
Above 200 ^a	.005	.015	<.005	.01	.02	.10	.04	.03	.07	-	.04	.03	-	-

^aThe numbers represent molecular weights, e.g. 168-isomers of diphenyl methane, 166-fluorene, 180-stilbene, 196-phenyl benzyl ketone.

However, it should be noted that (a) with the addition of ammonia, which would be present as a product during nitrogen removal, the reaction rates are increased as well as the toluene yields, and (b) the presence of benzaldehyde during nitrogen removal was due to SW. The most important observation is that the major product is benzene, indicating an oxidation/decarboxylation sequence is predominant. Clearly the presence of a source of hydrogen, dihydroanthracene (DHA), promotes the reactions which form toluene at the expense of benzene.

In order to explain the observed product distribution, the following sequence of reactions is believed to be that which lead to the formation and destruction of benzaldehyde (Ph = C₆H₅):



If only reaction 5 is operating, which is a Cannizzaro-type disproportionation, then approximately equal yields of benzene and toluene would be expected from benzoic acid and benzyl alcohol respectively. However, the reaction sequence of 3, 5, 6 and 7 (or a combination of 4 and 5) would lead to benzene vs. toluene (and their related products) being formed in a two to one ratio, similar to that which was observed. Reaction 7 was confirmed by an examination of the benzoic acid-SW reaction.

1-Chlorohexane (CH). The results of the CH-SW reaction at 400C were disappointing, although not entirely unexpected. The CH was 100% reacted at the shortest time, 0.5 hr., and on opening the reactor, gases were evolved rapidly and had a pleasant odor. Titration of the water layer revealed all the

chlorine as water soluble chloride and ICP metals analysis showed an equivalent metal ion concentration, mostly iron with progressively smaller amounts of nickel, manganese and a few others. A shift to an Inconel-600 reactor from the stainless steel reactor only changed the relative amounts of nickel and iron with chromium in place of manganese, still all the HCl presumed formed had reacted with the wall. Thus, the wall reactions were distorting the organic products. The major product was hexane, with small but significant amounts of butane, pentane and a C₃ benzene being formed; the more volatile gases could not be observed. One pyrolytic experiment produced a gas that was quite irritating (HCl had not reacted completely) and the major product was hexene, with some o-xylene along with the other products similar to those from the SW reaction. Thus it was concluded that our system, or any metal system (other than possibly platinum), would not be suitable for the study of the organic chlorides without distorting the products.

Ethyl Benzilate (EB). The data for the EB-SW reaction are shown in Tables II and III (EB = Ph₂COHCO₂C₂H₅). From Table II it appears that EB quickly hydrolyses to ethyl alcohol and benzylic acid, which initially decarboxylates to primarily diphenylmethane, benzophenone and diphenyl carbinol. At 400C the pyrolysis does not yield diphenyl carbinol or phenol, both of which were formed in the water reaction. Otherwise the products were similar. Diphenyl methane yields are relatively constant or increase slightly with time but decrease with rising temperatures. The total yield of one ring products increases with time and with temperature primarily at the expense of benzophenone and diphenyl carbinol.

An examination of Table III shows that ZnCl₂ can change the product distribution at all conditions increasing the yields of one ring products at the expense of those with two or more rings. If it is assumed that a desirable objective would be to convert some of these stockpiled materials to chemicals useful to industry, rather than their complete destruction to CO₂ and water, the approach using SW may be of value.

Trihexylamine (THA) and Quinuclidine [QN = CH(CH₂CH₂)₃N]. The results of the THA-SW reaction are summarized in Table IV. THA was used as an aliphatic tertiary amine replacement for QN which was expensive and difficult to obtain. The material balances are not very good, probably due to the highly volatile, low molecular weight gases that were lost when the reactor was opened. It can be seen that there are significant amounts of amines remaining at the shorter times when water was used, and it appears that pyrolysis is more effective for removing detectable amines. The ZnCl₂ catalyst increased the overall hydrocarbon yields and reduced the amines significantly, indicating the need for a catalyst for complete organic nitrogen removal if SW is used.

However, a comparison of THA results with those from QN-SW reaction indicates that THA may have been a poor substitute due to the nature of products found, i.e. no pyridines. The results for the QN-SW reaction are shown in Table V, only the extents of reaction are presented since the material balances are very poor, partly due to gaseous products but also to

Table II. Ethyl Benzilate-SW Reaction - Uncatalyzed^a

Time (hr)	0.5	6.0	0.5	1.0	2.0	6.0	10.0	3.0	1.0	2.0	4.0	1.0	2.0	4.0	1.0	2.0
Temp (°C)	400	400	400	400	400	400	400	425	450	450	450	500	450	450	500	500
Water Pressure (Bar)	0	0	267	267	267	267	267	287	359	359	359	390	359	359	390	390
<i>Volatiles Product Yields (moles product/mole reacted)</i>																
Benzene	0	0	.005	0	0	0	0	.035	.019	.020	.025	.067	.082			
Toluene	.009	.003	.007	.018	.033	.050	.086	.065	.095	.176	.172	.132	.134			
Ethyl Benzene	.010	.023	0	.012	.008	.009	.012	0	0	.019	.023	.023	.022			
Phenol	0	0	.011	.020	.023	.040	.038	0	.060	.109	.098	.067	.064			
Diphenyl Methane	.378	.366	.371	.363	.371	.404	.423	.36	.374	.367	.430	.331	.305			
Benzophenone	.398	.283	.287	.282	.205	.144	.126	.19	.186	.135	.115	.147	.110			
Diphenyl Carbinol	0	0	.107	.115	.146	.106	.081	.097	.040	.008	.004	0	0			
Heavy Products (MW. 200-350)	.03	.03	.10	.09	.07	.11	.07	.02	.05	.04	.04	.03	.03			

^aThe extents of reaction were all 100%.

Table III. Ethyl Benzilate-SW Reaction - Catalyzed^a

Time (hr)	1.0	4.0	1.0	3.0	6.0	4.0	1.0	2.0
Temp (°C)	400	400	425	425	425	450	500	500
Water Pressure (Bar)	267	267	287	287	287	359	390	390
ZnCl ₂ (g)	.201	.101	.201	.101	.101	.101	.101	.101

Volatile Product Yields (moles product/mole reacted)

Benzene	.007	.091	.029	.10	.093	.23	.47	.49
Toluene	.050	.078	.062	.11	.12	.23	.37	.41
Ethyl Benzene	.022	.033	.033	.063	.037	.037	.045	.033
Phenol	.047	.016	.038	.041	.051	.062	.007	.05
Diphenyl Methane	.36	.39	.39	.38	.38	.32	.10	.11
Benzophenone	.21	.20	.18	.13	.13	.052	.006	0
Diphenyl Carbinol	.043	0	.038	0	0	0	0	0
Heavy Products (MW. 200-350)	.05	.03	.05	.05	.04	.03	.004	.002

^aThe extents of reaction were all 100%. These experiments were in the smaller reactor (29 mL).

Table IV. Trihexylamine-SW Reaction

Time (hr)	1	0.5	1	2	6.5	1
Temp (°C)	400	400	400	400	400	400
Water Pressure (Bar)	0	267	267	267	267	267
ZnCl ₂ (g)	0	0	0	0	0	0.183
% Reaction	97	56	77	99	100	100

Volatile Product Yields (moles product/mole reacted)

Butane	.038	0.0078	0.0096	0.0057	0.043	0
Pentane	0.097	0.064	0.090	0.079	0.28	0.14
Hexane	0.44	0.26	0.30	0.26	0.33	0.76
Octane	0	0	0	0	0.044	0
Nonane	0.18	0.12	0.13	0.31	.20	0.078
C ₁₁ & C ₁₂ Alkanes	.13	0.19	0.083	0.066	0.10	0.22
(C ₆ H ₁₃) ₂ NH	0.063	0.43	0.32	0.11	.021	0.0080
C ₁₂ H ₂₄	0	0	.0032	0.010	0.017	0.0040
C ₁₅ H ₃₀	0.064	0	0	0	0	0
C ₁₈ H ₃₅ N	0	0.086	0.075	0.056	0.018	0.0045
Heavy Products	0.10	0.01	0.02	0.04	0.2	0.06
NH ₃	-	-	.71	.98	-	.93

Table V. Quinuclidine-SW Reaction

Time (hr)	8	1	3	1	1	2
Temp (°C)	400	400	425	425	450	450
Water Pressure (Bar)	251	251	287	287	323	323
% Reacted	7	100	26	95	30	91
ZnCl ₂ (g)	0	0.106	0	0.110	0	0

reactant and product solubility in water, making analyses very difficult and highly uncertain. In addition, the specific ion NH₃ electrode was not stable in the presence of QN or its products. However, it can be seen that it is very much less reactive than THA. ZnCl₂ does promote the reaction of QN effectively but the major observable products were alkyipyridines. Thus work was initiated on phenylpyridine and phenylpiperidine which have much lower solubilities in water, as do their expected products.

Phenylpiperidine and Phenylpyridine. Since PPI (PhC₅H₁₀N) is a non-aromatic cycloamine it should be similar to QN. The data in Table VI show that it is somewhat more reactive than QN and the material balances are somewhat low, but better than those of QN and THA. It can be seen that at the longer times or a higher temperature the hydrocarbon yields are increased, but there still remains significant amounts of pyridine products, which also were found in the QN products and appear to be the least reactive nitrogen species. Some solids and tar (non-volatile product remaining in the solution) are formed.

Thus, experiments were initiated with PPY. It can be seen from the data in Table VII that PPY is much less reactive than any of the other amines studied and also a large amount of tar is formed. Since the addition of dihydroanthracene (DHA) did not speed the reaction, the PPI reacts more rapidly due to the saturated heteroatom ring already present. This observation is quite different than the results previously reported (5) for quinoline and 1,2,3,4-tetrahydroquinoline (THQ). The addition of DHA to quinoline did increase its rate of reaction. However, since THQ was more reactive than quinoline but its initial product and, by far, most abundant product up to 89% reaction of THQ was quinoline, the reaction pathways of quinoline/THQ and PPY/PPI heterocyclic systems appear significantly different. Although the studies with these compounds have not been completed it can be concluded that once the pyridines are formed from the QN reaction, extreme conditions and/or catalysts are necessary to remove the nitrogen they contain.

Table VI. Phenylpiperidine-SW Reaction

Time (hr)	1	2	4	6	1
Temp (°C)	400	400	400	400	450
Water Pressure (Bar)	251	251	251	251	323
% Reaction	32%	60%	73%	100%	98%

Product Yields (moles of volatile products/mole reacted)

Toluene	0.005	0.015	0.055	0.108	0.124
Ethyl Benzene	0.012	0.033	0.059	0.103	0.152
Propyl Benzene	0.021	0.038	0.054	0.055	0.074
C ₄ Benzene	0	0.027	0.055	0.073	0.092
C ₅ & C ₆ Benzenes	0	0	0.010	0.046	0.039
4-Phenyl Pyridine	0.111	0.058	0.064	0.088	0.057
Diphenyl Methane	0.058	0.027	0.032	0.026	0.016
Methylphenyl Pyridine	0	0	0.027	0.028	0.010
Heavy Products	0.027	0.023	0.042	0.025	0.007
NH ₃	0.46	0.73	0.79	0.78	0.95
Solids (wt%)	7.8	8.8	5.9	0	0
Tar (wt%)	19.5	8.7	7.4	15.8	6.6

Table VII. 3-Phenylpyridine-SW Reaction

Time (hr)	6	6	3	1	3	6	6
Temp (°C)	450	450	425	450	450	450	450
Water Pressure (Bar)	323	323	287	323	323	323	323
% Reaction	0	0	0	36%	57%	71%	42%
Additive (g)	0	0.501	0.1124	0.226	0.221	0.221	0.121
		DHA	ZnCl ₂	ZnCl ₂	ZnCl ₂	ZnCl ₂	ZnCl ₂

Product Yields (moles produced/mole reacted)

Toluene	0.010	0.027	0.047	0.050
Ethyl Benzene	0	0.013	0.025	0.032
C ₃ to C ₅ Benzenes	0.016	0.020	0.031	0.044
Naphthalene	0.018	0.028	0.041	0.069
Heavy Products	0	0.012	0.014	0.015
NH ₃	1.12	0.95	1.02	1.02
Tar (wt%)	-	-	-	53

Acknowledgements

Supported by, or in-part by, the U.S. Army Research Office.

Literature Cited

1. Gangoli, N.; Thodos, G. *Ind. Eng. Chem., Prod. Res. Dev.* **1977**, *16*, 208.
2. Williams, D.F. *Chem. Eng. Science* **1981**, *36*, 1769.
3. Whitehead, J.C.; Williams, D.F. *J. Inst. Fuel* **1975**, 182.
4. Houser, T.J.; Tiffany, D.M.; Li, Z.; McCarville, M.E.; Houghton, M.E. *Fuel* **1986**, *65*, 827.
5. Houser, T.J.; Tsao, C.C.; Dyla, J.E.; VanAtten, M.K.; McCarville, M.E. *Fuel* **1989**, *68*, 323.
6. Abraham, M.A.; Klein, M.T. *Ind. Eng. Chem. Prod. Res. Dev.* **1985**, *24*, 300.
7. Townsend, S.H.; Klein, M.T. *Fuel* **1985**, *64*, 635.
8. Lawson, J.R.; Klein, M.T. *Ind. Eng. Chem. Fund.* **1985**, *24*, 203.
9. Helling, R.K.; Tester, J.W. *J. Energy & Fuels* **1987**, *1*, 417.
10. Helling, R.K.; Tester, J.W. *Environ. Sci. Technol.* **1988**, *22*, 1319.
11. Webley, P.A.; Tester, J.W. *Fundamental Kinetics and Mechanistic Pathways for Oxidation Reactions in Supercritical Water* SAE Technical Paper Series #881039; 18th Intersociety Conference on Environmental Systems: San Francisco, CA, **1988**.
12. Webley, P.A.; Holgate, H.R.; Stevenson, D.M.; Tester, J.W. *Oxidation Kinetics of Model Compounds of Metabolic Waste in Supercritical Water* SAE Technical Paper Series #901333; 20th Intersociety Conference on Environmental Systems: Williamsburg, VA, **1990**.
13. Jin, L.; Shah, Y.T.; Abraham, M.A. *J. Supercritical Fluids* **1990**, *3*, 233.
14. Thornton, T.D.; Savage, P.E. *J. Supercritical Fluids* **1990**, *3*, 240.
15. Lee, D.S.; Gloyna, E.F.; Li, L. *J. Supercritical Fluids* **1990**, *3*, 249.
16. Frank, E.U. *Endeavour* **1968**, *27*, 55.
17. Deshpande, G.V.; Holder, G.D.; Bishop, A.A.; Gopal, J.; Wender, I. *Fuel* **1984**, *63*, 956.
18. Stenberg, V.I.; Hei, R.D.; Sweeny, P.G.; Nowak, J. *Preprints, Div. Fuel Chem., Am. Chem. Soc.* **1984**, *29(5)*, 63.
19. Salim, S.S.; Bell, A.T. *Fuel* **1984**, *63*, 469.
20. Bischoff, J.L.; Pitzer, K.S. *Amer. J. Sci.* **1989**, *289*, 217.
21. Martynova, O.I. *High Temperature, High Pressure Electrochemistry in Aqueous Solutions*; Jones, D.de G.; Stachle, R.W., Eds.; National Association of Corrosion Engineers: Houston, TX, **1976**, pp 131-138.

RECEIVED April 27, 1992

Chapter 27

Effect of Gas Density on Holdup in a Supercritical Fluid Bubble Column

Brenda J. Rush, Y. T. Shah¹, and Martin A. Abraham

College of Engineering and Applied Sciences, The University of Tulsa,
Tulsa, OK 74104

Supercritical CO₂ has been used as a dispersed phase in a high pressure bubble column as a means of determining the effect of density on the holdup. The density of the dispersed phase in the near critical region was found to be substantially more important than for traditional gas-liquid bubble columns but similar to that obtained in liquid-liquid systems. A traditional correlation for holdup in gas-liquid systems was modified to incorporate this large density dependence and to adequately model the experimental data.

The holdup of a gas in a liquid is of fundamental importance in gas-liquid operations, such as multiphase reactions and mass transfer processes. The holdup, defined as volume fraction of the indicated phase, has been correlated with gas flow rate, surface tension, viscosity, and liquid density, however, the flow rate of the gas is frequently the most significant variable. Although early work suggested that holdup was independent of pressure (1), several investigators have recently shown an effect of density on the gas holdup (2-4). Wilkinson and Dierendonck (3) studied various gases (such as He, N₂, Ar, CO₂ and SF₆) dispersed in water and determined that gas holdup increased significantly with gas density, particularly at higher gas velocity. This effect was explained on the basis of bubble break-up, which increases with increasing gas density, causing the formation of smaller bubbles and hence increased holdup. Clark (4) obtained similar results for H₂ and N₂ in methanol and attributed the increase in gas holdup to a reduced tendency of bubbles to coalesce at higher pressures. Neither of these investigators found that increased gas density reduced bubble size at formation and concluded that high pressure columns will give higher gas holdup particularly at higher gas velocity.

Idogawa *et al.* (2) considered He, H₂, and air and determined that bubble size was essentially independent of surface tension at higher pressures. The effect of fluid properties on the holdup was determined, and correlated as

¹Current address: LeBow College of Engineering, Drexel University, 32nd & Chestnut Streets, Philadelphia, PA 19104

$$\frac{\varepsilon}{1-\varepsilon} = 0.059 u_g^{0.8} \rho_g^{0.17} (\sigma/72)^{-0.22} \exp(-P) \quad (1)$$

for superficial gas velocity of 3 cm/sec. Earlier results for low pressure bubble columns revealed that the gas holdup was only weakly dependent upon the gas density, as given by the appropriate correlation (5)

$$\varepsilon = 0.672 \left[\frac{u_g \mu_L}{\sigma} \right]^{0.578} \left[\frac{\mu_L^4 g}{\rho_L \sigma^3} \right]^{-0.131} \left[\frac{\rho_g}{\rho_L} \right]^{0.062} \quad (2)$$

in dimensionless form. These correlations give similar dependence on flow rate and surface tension, however, show a dramatic difference in the dependence of holdup on gas density.

The correlation of Idogawa *et al.* (2), is based on experiments over a pressure range to approximately 15 MPa, and thus a maximum gas density of approximately 120 kg/m³, and also involves only one gas flow rate, 3 cm/sec. The earlier correlation of Hikita *et al.* (5) was derived for many systems, but with gas densities in the range of 1 kg/m³. In the current work, a dense gas near its critical point is used to provide dispersed phase densities approaching that of the continuous phase. Thus, the current work extends the results of previous investigators into a range of high pressure (or high gas density) concurrently with high gas flow rates.

In previous work, significant changes in dispersed phase density were obtained through the use of different gases. However, near the critical point of the fluid, a large change in density occurs over a small pressure change (6). As an example, a pressure increase of approximately a factor of 2 yields an increase in the CO₂ density of approximately an order of magnitude, in the range of the critical temperature. For gases far away from their critical point, the change in density is proportional to the change in pressure. The current work takes advantage of the critical region phenomena by using pressure rather than gas composition to control the density of the dispersed phase.

Within this chapter, we present the gas holdup results obtained from our experiments with dense CO₂ dispersed in water. The use of CO₂ near its critical point provided a high density dispersed phase at experimentally feasible pressures and temperatures. The holdup is described in terms of superficial gas velocity and the estimated density of the CO₂ rich phase and compared with literature data. Within the current chapter, no attempt is made to explain the increased holdup in terms of increased bubble breakup or decreased coalescence. However, the results are correlated with flow rate, density, viscosity, and surface tension using conventional bubble column parameters.

Experimental

A schematic diagram of the experimental system is shown in Figure 1. CO₂ was supplied as a pressurized liquid and fed through a high pressure gas-to-gas boost pump (Haskel) which provided the required CO₂ flowrate; a de-surger was installed in the CO₂ feed line downstream of the pump to eliminate pressure pulsations associated with the pump. The CO₂ then flowed into the base of the bubble column, which had been previously filled with tap water. Temperature was maintained with

a length of beaded heating wire (Cole-Parmer) and a power controller and monitored by three thermocouples inserted into the centerline of the column. A needle valve was located after the column through which the CO₂ was flashed to release the pressure. The low pressure gas then passed into a gas-liquid separator to remove entrained water. Finally, a portion of the CO₂ stream was vented and the remainder mixed with fresh feed and recycled to the pump. The water obtained in the separator was discarded.

The pressure inside the column was controlled by the needle valve downstream of the column, and the flow rate was maintained by the upstream pump and the use of make-up CO₂. The column consisted of a 2.5 m tall, 9 cm inside diameter steel tube. The gas passed through a distributor plate comprised of a series of 4 mm diameter holes arranged in a star pattern; there were 69 holes in the perforated plate distributor. The column was initially filled with tap water to a predetermined height. Experiments were accomplished at three superficial gas velocities; 3 cm/sec, 8 cm/sec, and 12 cm/sec and at a constant temperature of 30 °C.

Pressure taps were fitted to the side of the column at 30 cm intervals. A Validyne DP15-32-V-1-W-5-A differential pressure transducer was connected to the pressure taps and the pressure generated by 30 cm of fluid was converted to the average fluid density. Within the column, the density was essentially independent of the distance above the distributor plate, as long as it was sufficiently far above the distributor plate. The pressure taps used within the experiments were both approximately 1 m above the distributor, and were identical for all experiments. The gas holdup could be related to the average fluid density

$$\bar{\rho} = \epsilon\rho_L + (1-\epsilon)\rho_g \quad (3)$$

where ϵ is the gas holdup.

The CO₂ flow rate was determined through measurement of the pressure drop resulting from pressurized flow within a small length of 1/8 inch diameter tubing. In separate experiments, the pressure drop in the exit tubing was calibrated with the CO₂ flow rate, measured as the CO₂ was vented to atmosphere through a flow rotameter.

In the calculations that follow, several physical properties are required. These have been estimated as follows. The density of CO₂ was estimated using the Peng-Robinson equation of state, and the water density was assumed to be constant with a value of 998 kg/m³. The surface tension was estimated from published literature data (7). Liquid viscosity was assumed to be constant at 1 cp, implicitly assuming that CO₂ dissolution in water was small, even at pressures as high as 75 bar. The latter assumption was justified by literature reports (8) and confirmed using estimated values for the Henry's Law constant obtained from the Peng-Robinson equation of state.

Results and Discussion

CO₂ holdup is illustrated as a function of CO₂ density in Figure 2, for superficial velocities of 3 and 12 cm/sec. The current results are compared with literature data.

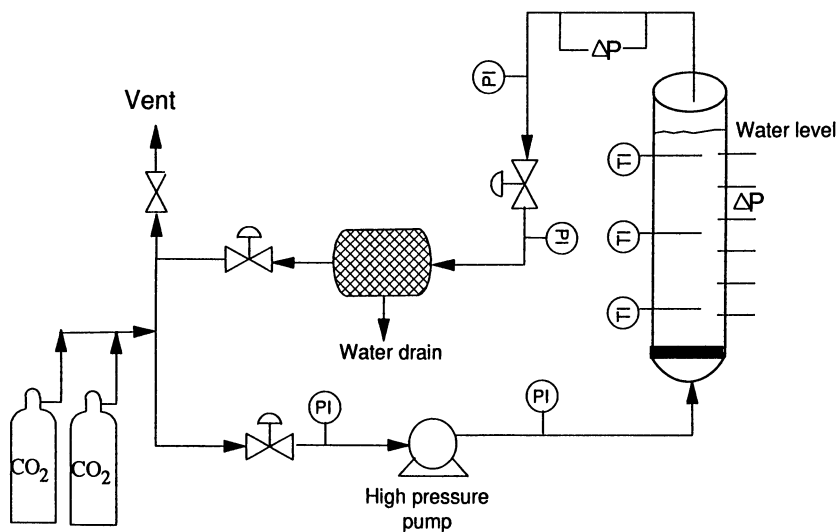


Figure 1: Schematic diagram of experimental system for measurement of supercritical fluid holdup in a bubble column.

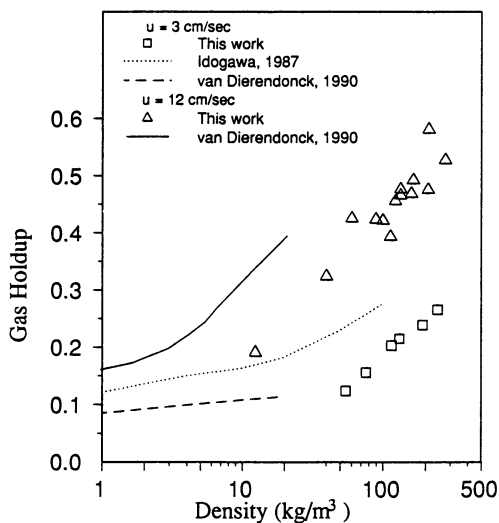


Figure 2: Comparison of the experimental data with results available in literature (2,3).

Note that at 3 cm/sec, the gas holdup obtained by Idogawa (2) in the low density regime (20 kg/m³ and less) is approximately 30% greater than that obtained by van Dierendonck (3). Our experimental data obtained at 3 cm/sec compares well with the data of van Dierendonck (3) and approaches the high density data of Idogawa (2). Idogawa does not report gas holdup for velocity other than 3 cm/sec, thus the data obtained at 12 cm/sec can only be compared with the van Dierendonck results. Although our data approximate the literature values, the current results give somewhat lower CO₂ holdup than would be expected from the results of van Dierendonck (3), particularly at gas density below 50 kg/m³.

Correlations are available which would allow more direct comparison of the experimental results with previous data. One correlation which was developed for bubble column operation at low pressure is that of Hikita, *et al.* (5), which is given in equation 2. The current results are compared with the prediction of the correlation in Figure 3. If the correlation correctly modeled the current data, one would expect all the data points to fall on the straight line with a slope of 1, indicated in Figure 3. Note that the data fall approximately on the 45° line, but the slope at each velocity is substantially different than 1. This suggests that a key parameter in the operation of a high pressure bubble column has not been properly identified.

Figure 4 depicts our experimental data based in the prediction from the correlation of Idogawa (2), given by equation 1. This correlation was developed from experiments at pressures up to 15 MPa and should better represent the experimental data. Again, the data are fairly well represented by the prediction, however, at each velocity considered, the slope was different than 1. This suggests that this correlation also fails to account for the effect of a key parameter under the high density conditions considered in the current work.

As described previously, there is a substantial density change which occurs over a small pressure change in the current system. However, the available correlations indicate that density of the dispersed phase has only a minor role on the holdup. In the correlation of Hikita, the holdup was almost independent of density; the correlation of Idogawa provides a density dependence of 0.17. Since the dispersed phase density was greater in the current experiments than for the previous correlations, it is logical to conclude that the density effect may not have been properly accounted for in previous work.

Figure 5 indicates the effect of CO₂ density on the holdup for the three superficial velocities considered in the current experiments. In each case, the data are fairly well represented by a power-law fit,

$$\epsilon = a \rho^b \quad (4)$$

as indicated by the straight lines on the log-log plot of Figure 5. The slopes of the lines vary with CO₂ velocity, but range from 0.501 at 3 cm/sec to 0.321 at 12 cm/sec. Taking a weighted average (based on the number of data points at each superficial velocity), the best overall value for *b* is 0.405. This value is nearly an order of magnitude greater than that obtained by Hikita (5), and substantially higher than that more recently reported by Idogawa (2). However, previous correlations for

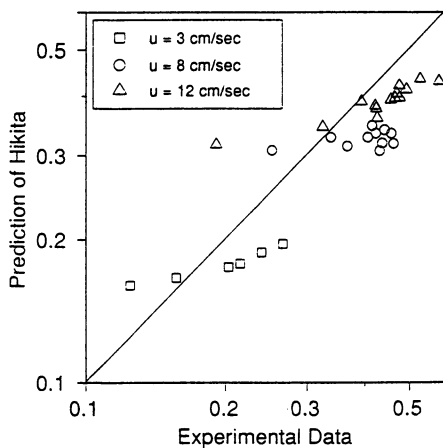


Figure 3: Quality of correlation presented by Hikita *et al.*(5) in the prediction of high density CO₂ holdup.

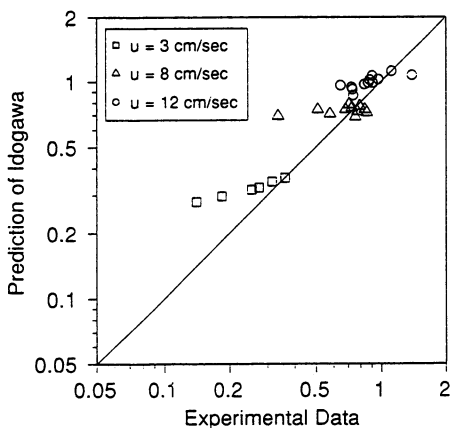


Figure 4: Quality of correlation presented by Idogawa *et al.*(2) in the prediction of high density CO₂ holdup.

liquid-liquid systems suggest that the exponent on the dispersed phase density should be approximately 1/3 (9), only slightly different than that obtained in the current work. Thus, it is possible that density of the dispersed phase is an important parameter not fully considered for bubble column operation with a dense gas as the dispersed phase.

The correlation of Hikita (5), presented in equation 2, was modified to account for the dispersed phase density, without change in the exponent on either of the other dimensionless groups. Thus, the proposed correlation becomes

$$\varepsilon = 1.554 \left(\frac{u_g \mu_L}{\sigma} \right)^{0.578} \left(\frac{\mu_L 4g}{\rho_L \sigma^3} \right)^{-0.131} \left(\frac{\rho_g}{\rho_L} \right)^{0.405} \quad (5)$$

where the leading multiplier has also been modified to compensate for the increased dependency on density. The quality of fit for the experimental data is indicated as Figure 6, where the dotted lines represent a 20% deviation from the 45° line. Substantially all of the data fits the correlation within the 20% limit, and the experimental scatter is distributed evenly across the 45° line.

Conclusions

The current experimental data extends the range of available bubble column data into regions of high density, particularly those in which the density of the dispersed phase is of the same order of magnitude as the continuous phase. Use of supercritical CO₂ allowed the density to be adjusted by changing the system pressure, rather than changes in the gas composition. Experiments revealed that high supercritical CO₂ holdup could be obtained at high superficial velocity and densities approaching liquid-like values. The data were adequately correlated using the form suggested by the low pressure literature, modified to account for the increased density effect.

Nomenclature

a	Constant in power law fit for gas holdup with density, see equation 4
b	Exponent in power law fit for gas holdup with density, see equation 4
g	Acceleration due to gravity, 9.8 m/s ²
h	Height of the column of liquid, m
P	Pressure, bar
u	Superficial velocity, m/sec
ε	Gas holdup, volume fraction
μ	Viscosity, N s/m ²
ρ	Density, kg/m ³
ρ̄	Average fluid density in the column, kg/m ³
σ	Surface tension of the system, N/m

Subscripts

g	gas or dispersed phase
L	liquid phase

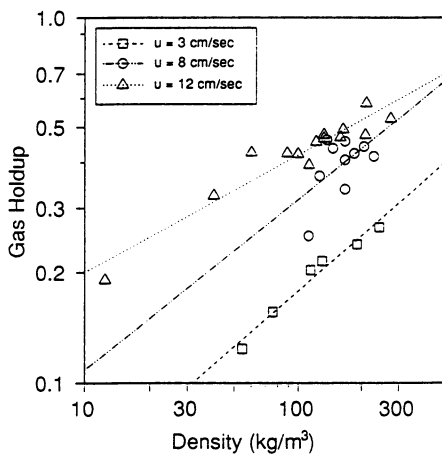


Figure 5: Effect of CO₂ density on holdup at superficial velocity of 3, 8, and 12 cm/sec. Lines represent best fit, power-law regression.

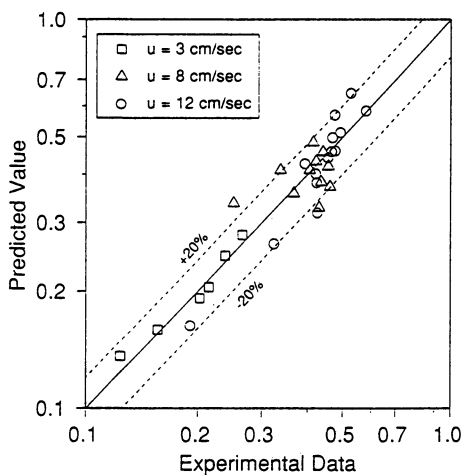


Figure 6: Comparison of experimental data with predictions from correlation modified from that of Hikita *et al*(5), and presented in equation 5. Error bars indicate $\pm 20\%$ of the predicted value.

Acknowledgment

This research was sponsored, in part, by the National Science Foundation under Grant number CTS-8909940-01. Their support is gratefully appreciated.

References

1. Shah, Y.T., B. G. Kelkar, S.P. Godbole, and W.D. Deckwer, *AIChE J.*, **1982**, *28*, 353.
2. Idogawa, K., K. Ikeda, T. Fukuda, S. Morooka, *Int. Chem. Eng.*, **1987**, *27*, 93.
3. Wilkinson, P. M. and L. L. v. Dierendonck, *Chem. Eng. Sci.*, **1990**, *45*, 2309.
4. Clark, K. N., *Chem. Eng. Sci.*, **1990**, *45*, 2301 .
5. Hikita, H., S. Asai, K. Tanigawa, K. Segawa, M. Kitao, *Chem. Eng. J.*, **1980**, *12*, 59.
6. Paulaitis, M.E., V. J. Krukonis, R.T. Kurnik, and R.C. Reid, *Reviews in Chemical Engineering*, **1983**, *1*, 179.
7. Massoudi R. and A. D. King, Jr., *J. Phys. Chem.*, **1974**, *78*, 2262.
8. Coan, C.R. and A.D. King, Jr., *J. ACS*, **1971**, *93*, 1857.
9. Steiner, L. and S. Hartland, In *Handbook of Fluids in Motion*, Cheremisinoff, N. P. and Gupta, R. , eds, Ann Arbor Science, Ann Arbor, Michigan, 1983, p. 1069.

RECEIVED June 19, 1992

Chapter 28

Production of Mesophase Pitch by Supercritical Fluid Extraction

T. Hochgeschurtz, K. W. Hutchenson¹, J. R. Roebers², G.-Z. Liu,
J. C. Mullins, and M. C. Thies

Department of Chemical Engineering, Center for Advanced Engineering
Fibers, Clemson University, Clemson, SC 29634

Supercritical fluid extraction is being investigated for the production of the mesophase pitch used to make high-performance carbon fibers. A heat-soaked, isotropic petroleum pitch has been fractionated with supercritical toluene in a region of liquid-liquid equilibrium at temperatures and pressures to 656 K and 140 bar, respectively. Since both phases are black and opaque at the conditions of interest, an AC impedance bridge technique was used to detect the liquid-liquid interface level in the equilibrium cell. For all tested experimental conditions, the bottom-phase fraction contained a high percentage of the mesophase necessary for producing anisotropic carbon fibers. Generalized correlations have been developed for the characteristic constants of the Peng-Robinson equation applicable to high molecular weight, aromatic hydrocarbons.

Petroleum pitch is a high molecular weight, carbonaceous material which can be produced from the by-products of the thermal and catalytic cracking of crude oil distillates. These by-products are generally considered to be waste materials by refiners because upgrading into a more useful form, such as lubricating oil, is relatively expensive. Thus, the isotropic pitch which can be produced is relatively inexpensive and readily available.

Isotropic pitch has considerable potential as a raw material for the production of economical high-performance carbon fibers, which are used in the manufacture of advanced composites (1). However, the current methods for treating isotropic pitch to produce the fiber precursor, or mesophase, have deficiencies that result in high production costs and less than ideal properties (2).

¹Current address: E. I. du Pont de Nemours and Company, P.O. Box 80304,
Wilmington, DE 19898

²Current address: Bayer AG, Ingenieurbereich Anlagenplanung, D-5090 Leverkusen,
Bayerwerk, Germany

American Chemical Society
© 1993 American Chemical Society
Library

1155 16th St., N.W.

In Supercritical Fluid Engineering Science; Kiran, E., et al.;
ACS Symposium Series; American Chemical Society: Washington, DC, 1992.

Washington, D.C. 20036

Supercritical fluid (SCF) extraction is being investigated by our group for the production of mesophase pitch fractions from isotropic petroleum pitch. Previous work (3,4) focused on the fractionation of isotropic pitch with supercritical toluene in a region of vapor-liquid equilibrium at temperatures and pressures to 673 K and 76 bar, respectively. Although the isotropic pitch was successfully separated into narrow molecular weight fractions in this region, no more than 20% of the pitch could be extracted into the vapor phase. Since a significant fraction of the low molecular weight species in isotropic pitch must be removed before mesophase can form (5), no pitch fractions containing mesophase were isolated.

In this study we report on the fractionation of a heat-soaked, isotropic pitch with supercritical toluene in a region of liquid-liquid equilibrium, which was found to exist at high pressures.

Experimental Apparatus and Procedure

A continuous-flow apparatus has been constructed that can be used to measure both vapor-liquid and liquid-liquid equilibrium compositions at temperatures to 673 K and pressures to 350 bar. The apparatus is conceptually similar to that reported by previous workers (6,7), but is capable of operating with materials which have melting points as high as 573 K. A flow apparatus is necessary for our work to produce large enough samples of pitch fractions for subsequent analysis and for spinning into carbon fibers. Such an apparatus is also needed to eliminate thermal polymerization reactions of the pitch by reducing residence times at elevated temperatures to only a few minutes. Several hours at 673 K are known to be required before any appreciable extent of polymerization can occur (8). Figure 1 shows a simplified schematic of the experimental apparatus, and a brief description is given below. Most of the details of the experimental apparatus and procedure have been described elsewhere (6,9,10). However, several important modifications have been made since our last paper, and these are discussed in detail.

The isotropic pitch is pumped indirectly using a high-pressure cylinder equipped with an internal floating piston; the piston is displaced by the regulated flow of a working fluid (toluene, in this case). In previous work, the pitch was pumped in the molten state by maintaining the cylinder at 423 K. In this study, a 50/50 mixture by weight of pitch and toluene is charged to the high pressure cylinder. This mixture is a viscous, homogeneous liquid at ambient temperatures, so no heating of the cylinder is required. The solvent and working fluid are delivered at flow rates of approximately 290 and 250 mL/h, respectively, using LDC/Milton Roy Model 396 metering pumps. The weight ratio of solvent to pitch for this study was maintained constant at 3:1. The two streams are preheated, combined in a impingement mixer, and then further preheated before passing through a Kenics-type static mixer into the equilibrium cell, which functions as a phase separator.

The pitch/solvent mixture enters the cell in the middle of the inner chamber. At the operating temperatures, pressures, and solvent-to-feed (S/F) ratio investigated in this study the mixture separates into two phases: a solvent-rich, lighter liquid phase and a pitch-rich, heavier liquid phase. Each phase is drawn off independently through top and bottom sample ports in the cell. Micrometering valves (Autoclave Engineers, 60VRMM 4882-GY) are located on both lines exiting the cell. The top-phase valve is used primarily for pressure control and the bottom-phase valve for level control. After expansion to atmospheric pressure, both phases pass through on/off valves (Autoclave Engineers 60VM4071-GY) and are collected.

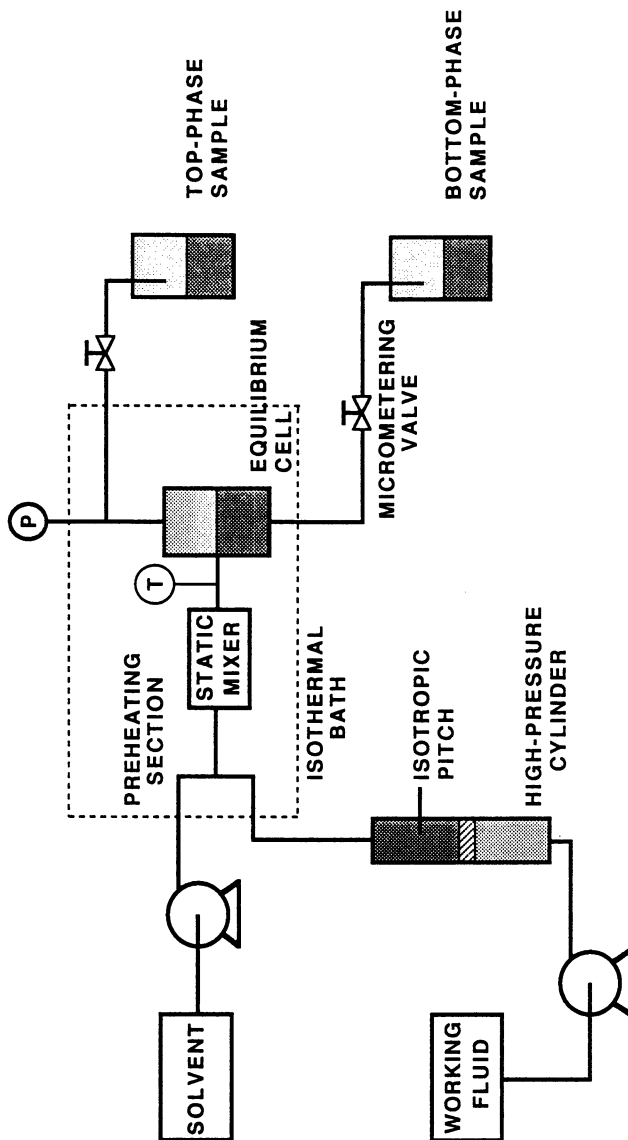


Figure 1. Simplified schematic of the experimental apparatus.

July 22, 2012 | <http://pubs.acs.org>
 Publication Date: December 17, 1992 | doi: 10.1021/bk-1992-0514.ch028

The sample collection scheme has been substantially modified from that previously reported. All sample lines and valves exiting the nitrogen bath are wrapped with electrical heating tape and insulated, and can be maintained at temperatures to 673 K if necessary. In this study, the solvent-rich top phase contained the lower molecular weight components of pitch and was maintained at temperatures from 373-523 K. However, the pitch-rich, bottom liquid phase contained the highest molecular weight components of pitch and had to be maintained above its melting point, i.e., at approximately 600 K.

Several changes have been made to reduce the plugging of lines with high-melting solids: (1) The sample tubing between each micrometering and on/off valve is now larger (6.35 mm o.d. x 2.11 mm i.d.); (2) the sample tubing exiting each on/off valve has an o.d. of 9.5 mm, an i.d. of 3.2 mm, and is made of aluminum to facilitate heat transfer to the tip of the tubing; (3) the aluminum tubing is inserted approximately halfway into insulated Pyrex reaction vessels. As before, samples of each phase are collected in 250-mL sample bottles placed inside the vessels.

The equilibrium cell was originally designed by Roebbers (10,11) for visual determination of the interface level between two fluid phases. However, for our measurements in the liquid-liquid region both phases were found to be black and opaque. After evaluating several possible methods of nonvisual interface detection, we chose an AC impedance bridge technique, which is described below, for the detection of the interface level (see Figure 2).

An electrode made of 304 stainless steel was fabricated and inserted into the slot of the equilibrium cell chamber, and served as one electrode of a parallel-plate capacitor. The body of the cell served as the other electrode. The capacitor, then, consisted of these two electrodes and the two liquid phases between them. The internal electrode was insulated from the cell body with spacers made of a machinable ceramic (Macor; Corning Glass) and was connected to the external circuit with an 18-gauge electrical wire. The wire was insulated from the cell wall and sealed against pressure with a soapstone cone, compression-type electrical connector (Newport Scientific), which is rated for operation to 700 K and 1300 bar. The internal volume of the cell is reduced to approximately 30 ml with the electrode insert.

The cell capacitor serves as one leg of an AC impedance bridge and indicates the differences in dielectric constant and electrical resistivity which exist between these two phases. The basic concept of the technique is that a change in the impedance occurs with a changing interface level and is converted to a voltage output. Details of the bridge design are presented elsewhere (12).

To control the level of the liquid-liquid interface during an experimental run, the system is first brought to steady state at the desired operating conditions of temperature, pressure, and S/F ratio. The bottom-phase micrometering valve is kept sufficiently open so that there is no accumulation of the pitch-rich bottom phase in the cell (i.e., the cell only contains the solvent-rich, top liquid phase). The impedance bridge is then nulled to 0.0 ± 0.1 volts by adjusting the capacitors and resistors on the variable leg of the bridge. After the bridge is nulled, the bottom-phase micrometering valve is closed and the level of bottom phase is allowed to build until an output voltage of 4-10 volts is obtained on the Fluke DMM. This micrometering valve is then controlled throughout an experimental run to maintain a constant voltage output, and thus a constant liquid-liquid interface level. Since the properties of the pitch-rich bottom phase (e.g., the percentage of mesophase) affect the voltage output obtained, the interface level is not precisely known. However, we have experienced little difficulty in operating the apparatus in this manner and have had no problems with cross-contamination of phases.

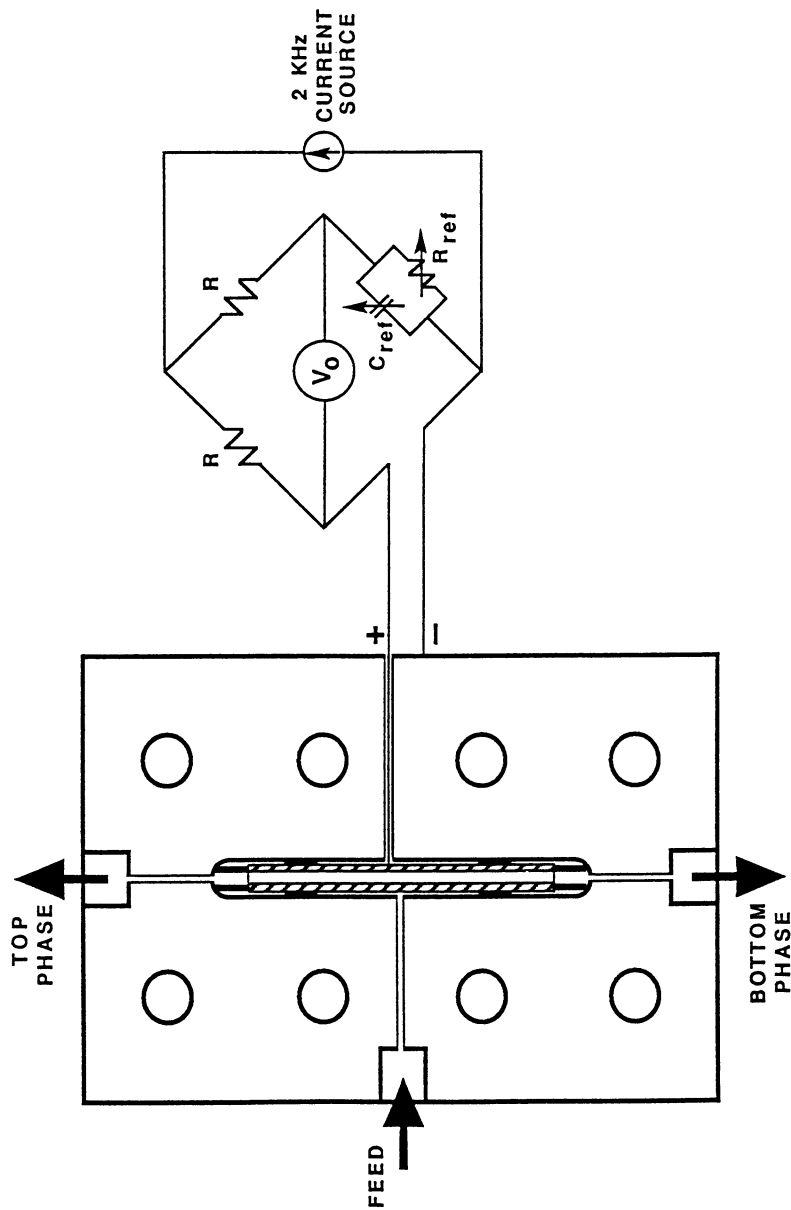


Figure 2. Schematic of the equilibrium cell, internal electrode, and AC impedance bridge.

July 22, 2012 | <http://pubs.acs.org>
 Publication Date: December 17, 1992 | doi: 10.1021/bk-1992-0514.ch028

Although both phases in the cell are black and opaque, their appearances during sample collection are distinctly different. The solvent-rich top phase, which was found to contain only isotropic pitch, is collected at near ambient temperatures and has a viscosity similar to that of liquid toluene. Upon exiting the micrometering valve, the pitch-rich bottom phase flashes, removing most of the toluene, and the pitch is collected as a porous solid at approximately 473 K.

A number of safety features were incorporated into the design of the apparatus and are required for working with flammable supercritical solvents. An inert atmosphere of less than 1 mol % oxygen is maintained inside the isothermal bath to prevent a deflagration should a solvent leak occur. A polycarbonate shield is mounted over the observation window of the bath. An independent temperature controller serves as a high-temperature shutoff. Rupture disks are used to protect both the equilibrium cell and the high-pressure cylinder from overpressure. Finally, power to the bath heaters is automatically shut off if the system pressure drops below some preset value.

Experimental Measurements

The cell pressure was measured with a Heise Bourdon-tube gauge (0-2500 psi range) which had been calibrated with a Budenberg dead weight pressure gauge tester to 0.05% of the indicated pressure. The system pressure in the liquid-liquid region was controlled to within ± 50 psi, giving an experimental uncertainty of ± 50 psi.

The equilibrium temperature of the combined feed stream entering the cell and of the top and bottom phases in the cell were measured with Type K thermocouples referenced to an aluminum block located in the isothermal bath. The temperature of the reference block was measured with a secondary standard RTD (Burns Engineering). Both the thermocouple voltages and RTD resistance were measured with a Keithley Model 191 DMM. The RTD and DMM were previously calibrated as a unit to ± 0.05 K using a Rosemount 162CE primary temperature standard and a Mueller resistance bridge. The reported values present average temperatures measured during the course of an experiment and are believed to be accurate to ± 0.5 K.

Multiple samples of each phase were collected in 250-mL glass jars for a time period of 20-30 min each. The weight percent of toluene in the top phase was determined by drying the collected samples in a vacuum oven (National Appliance, Model 5851) for 12-14 h at approximately 450 K. Subsequent analysis of the dried samples by gel permeation chromatography (GPC) confirmed that no residual toluene was present. Since the top-phase samples were collected at near ambient temperatures, no correction for toluene losses was necessary.

Determining the weight percent toluene in the bottom-phase samples was more difficult. Since the bottom-phase sampling lines had to be maintained at temperatures of approximately 600 K, most toluene in the phase flashed after passing through the micrometering valve. Compositions were therefore calculated by subtracting the top-phase flow rates of pitch and toluene from the corresponding feed flow rates. Since the bottom-phase flow rate is relatively small, this calculational method produced highly variable results for the bottom-phase compositions.

To calculate extraction yields, the weight of pitch collected in each phase had to be determined. The top-phase samples were dried to remove all toluene in the manner described above. The bottom-phase samples were dried in a similar fashion. The residual samples were then dissolved in 1,2,4-trichlorobenzene and analyzed by gel permeation chromatography to correct for residual toluene (if any) that was still present.

Gel permeation chromatography was performed with a Waters 150-C ALC/GPC chromatograph equipped with a refractive index detector. HPLC-grade 1,2,4-trichlorobenzene was used as the mobile phase at a flow rate of 1 mL/min. Details of the GPC techniques used are presented elsewhere (3,10).

Since the purpose of this study is to produce mesophase pitch by SCF extraction, bottom-phase samples were analyzed to determine the percentage of mesophase present. First, the samples were dried under vacuum at 630 K for 30 min. with a Vacuum/Atmospheres Co. TS-4000 Dri-Lab system. Using this system, samples were exposed to elevated temperatures for a maximum of two hours, and the elevated-temperature environment was maintained at <1 ppm oxygen and water to prevent pitch oxidation. Following this solvent devolatilization step, the samples were mounted in a self-setting resin (Quickmount; Fulton Metallurgical Products) and polished with a Buehler Ecomet grinder-polisher. Samples were then analyzed for percent mesophase by polarized light microscopy with a Zeiss microscope (Model ICM 405). The microscope is interfaced to an image analysis system (Georgia Instruments), which is used to calculate the percentage of mesophase present.

Selected bottom-phase fractions were melt-spun into carbon fibers on our bench-scale spinning apparatus. This apparatus was designed and constructed at Clemson University (12) and has been extensively used by researchers for testing small batches of experimental mesophases. A 12-hole spinnerette with a 18 μm screen filter was used. The spinning temperature and pressure were 633 K and 40 bar, respectively, and the quench temperature was 300 K. Fibers were spun at a mass flow rate of 0.04 g/s with a winder speed of 9.8 m/s. Details of the design and operation of the spinning apparatus are presented elsewhere (13,14).

The spun "green" fibers were subsequently stabilized at a final holding temperature of 553 K in an oxidation oven designed and constructed at Clemson University. After stabilization, the fibers were carbonized with an Astro carbon resistive element furnace. A heating rate of 20 K/min up to a final temperature of 2673 K was used. Details of the oxidation and carbonization procedures are presented elsewhere (15).

The final fiber properties, i.e., the tensile strength and modulus, were determined by single-filament testing on an Instron universal testing machine. Microstructural analysis of these fibers was also performed with a JEOL 848 scanning electron microscope. Details of the fiber-testing and SEM procedures are given elsewhere (16).

Materials

A heat-soaked petroleum pitch was obtained from Conoco Inc. This pitch is similar in its physical properties to Ashland A-240 petroleum pitch (CAS No. 68187-58-6), but was filtered by Conoco to remove particulate matter which could affect the properties of any fibers spun from our extracted pitch fractions. ACS-grade toluene (CAS No. 108-88-3) was obtained from Fisher Scientific and HPLC-grade 1,2,4-trichlorobenzene (CAS No. 120-82-1) was purchased from Baxter Healthcare. These chemicals were all used as received without further purification.

Experimental Results

Liquid-liquid equilibrium compositions have been measured for mixtures of toluene and a heat-soaked petroleum pitch at 578.6, 614.5, and 655.5 K. These results are presented in Figure 3 as a pseudobinary pressure-vs.-composition diagram which, for illustrative purposes, treats the pitch as a single component. Compositions were

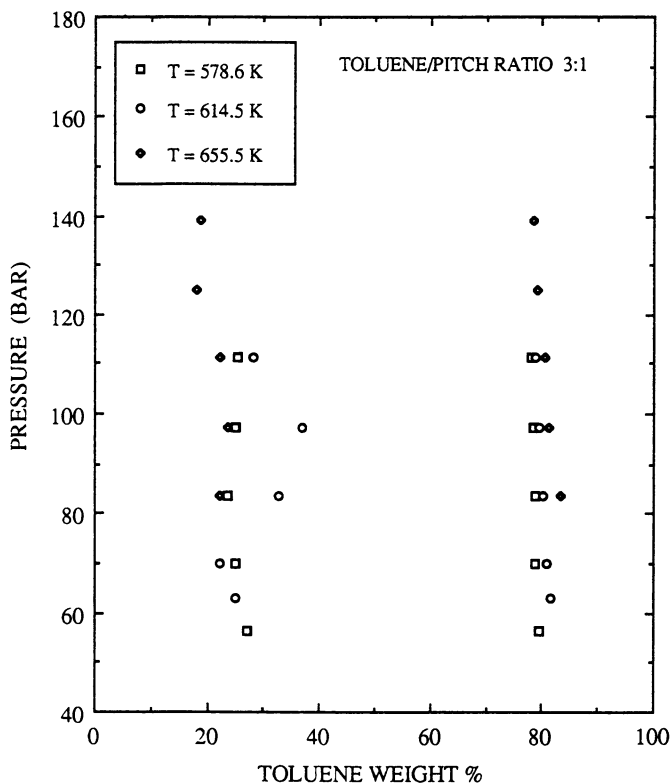


Figure 3. Liquid-liquid equilibrium compositions for the toluene/pitch system at 578.6, 614.5, and 655.5 K.

obtained at pressures from the onset of liquid-liquid equilibrium to approximately 140 bar at a S/F ratio of 3:1. Data on the right-hand side of the figure represent compositions of the toluene-rich top phase and on the left-hand side represent the compositions of the pitch-rich, mesophase-containing bottom phase. Each data point represents the cumulative average of at least two and as many as seven collected samples. Top-phase samples were reproducible to within ± 0.01 -0.2 wt % for a given experimental run and are believed to be accurate to better than ± 0.5 wt % in all cases. The slight but gradual increase in the solubility of pitch in the top phase with pressure for a given temperature is consistent with our knowledge of liquid-liquid phase behavior and provides a further indication of the data's reliability. As previously discussed, bottom-phase compositions are less accurate. Since we would expect the phase boundary curve to be nearly vertical over the measured pressure range, we estimate the experimental uncertainty in these results to be ± 10 wt %.

Extraction yields are presented in Figure 4. Here, the extraction yield is defined as the weight percent of the feed pitch which is extracted into the solvent-rich top phase. Reported values are believed to be accurate to at least ± 2 wt %. Note that in all cases more than 50% of the feed pitch was extracted. These results are in marked contrast to our results from the vapor-liquid region which exists at lower pressures, in which a maximum extraction yield of 20% was obtained (4,9,10).

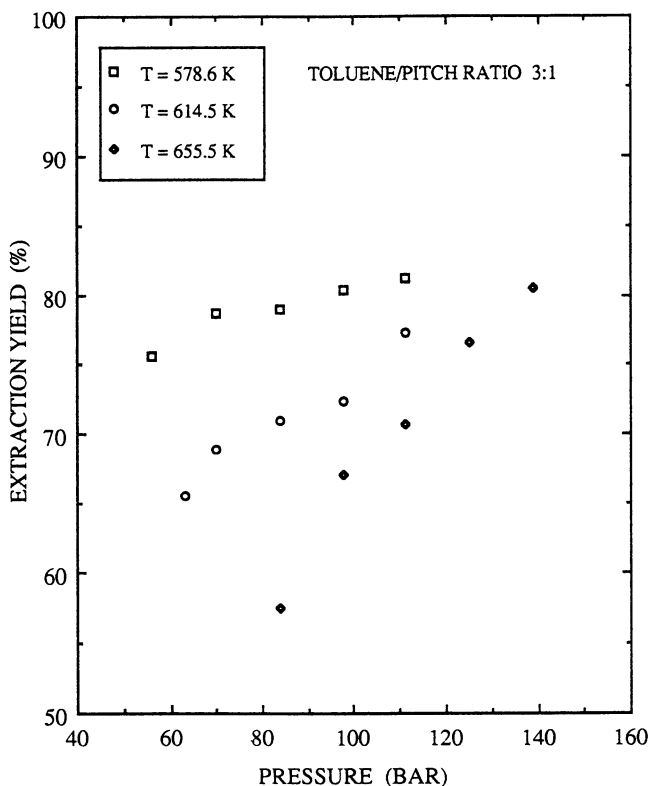


Figure 4. Extraction yields for the toluene/pitch system at 578.6, 614.5, and 655.5 K.

The trends exhibited in Figures 3 and 4 are consistent with our knowledge of the behavior of supercritical fluids, but also contain unexpected results. As would be expected, Figure 3 shows that the effect of pressure on phase compositions in a liquid-liquid region is minimal. However, Figure 4 shows that the effect of pressure on the yield becomes significant above the critical temperature of pure toluene ($T_c = 592$ K).

The collected pitch samples were analyzed for percent mesophase by polarized light microscopy as previously described. Top-phase pitch samples were, as expected, isotropic in all cases. However, after solvent devolatilization bottom-phase pitch samples were found to contain from 50 to 100% mesophase. (Samples always contained some mesophase before devolatilization, but the percentage always increased after complete removal of the "disordering" solvent molecules.) This mesophase is the desired precursor for carbon fibers, provided that its softening point is low enough to spin (2).

A bottom-phase pitch fraction produced at 614.5 K and 70 bar (which consisted of a 100% continuous bulk mesophase after solvent devolatilization) was melt-spun,

stabilized, and carbonized to produce carbon fibers. The final mechanical properties of these fibers, as determined by single-filament testing, are shown in the Table below.

Table I. Properties of Carbon Fibers Spun From SCF-Extracted Mesophase

<i>Fiber Diameter</i> (μm)	<i>Tensile Strength</i> (GPa)	<i>Tensile Modulus</i> (GPa)	<i>Elongation to Failure</i> (%)
9.0	3.3	820	0.58

Gauge length = 10.0 mm
40 filaments were tested

Although our SCF extraction process has not been optimized, these results indicate its potential, since the measured tensile strength and modulus are comparable to those present in the highest quality, commercially available pitch-based fibers (2).

Thermodynamic Modeling

One goal of this study is to use measured phase equilibrium data to develop a thermodynamic model for mixtures of petroleum pitch and supercritical toluene. A pseudocomponent model using the Peng-Robinson equation (17) was chosen for this initial effort. In a manner analogous to the work of Alexander et al. (18), the basic approach employed was to develop generalized correlations for the equation-of-state (EOS) constants a_c , b , and κ in terms of average molecular structure parameters.

For this initial modeling effort, the three pitch fractions of Ashland A-240 petroleum pitch reported by Dickinson (19) were treated as pseudocomponents representing the feed pitch. Dickinson used ^1H and ^{13}C NMR spectroscopy, vapor pressure osmometry, gel permeation chromatography, and elemental analysis in conjunction with Knight's method (20) to generate average molecular structure parameters for each of the fractions. Figure 5 shows average molecular structures proposed for the pitch fractions based on these parameters. Dickinson actually isolated four fractions, but the heaviest fraction, which was 12 wt % of the total, was insoluble in the solvents used for the analytical characterization work. Disregarding the insoluble fraction, the feed composition of the three pitch fractions at the experimental toluene/pitch ratio of 1.9 were 5.2, 3.5, and 0.9 mol %, respectively.

A database of 43 model aromatic hydrocarbons was compiled from the literature to correlate the EOS constants a_c , b , and κ with average molecular structure parameters. The database was restricted to aromatic compounds to ensure a chemical nature similar to pitch. Compounds were selected based on the availability of vapor pressure data. All available compounds having two or more aromatic rings were included in the database; however, the number of one-ring compounds was restricted to prevent skewing of the correlated parameters. The group contribution method of Somayajulu (21) was used to estimate critical constants, T_c and P_c , for compounds with no available experimental values. Using these critical constants, the acentric factor of each of the 43 aromatic compounds was optimized to obtain the best fit of the Peng-Robinson equation to the

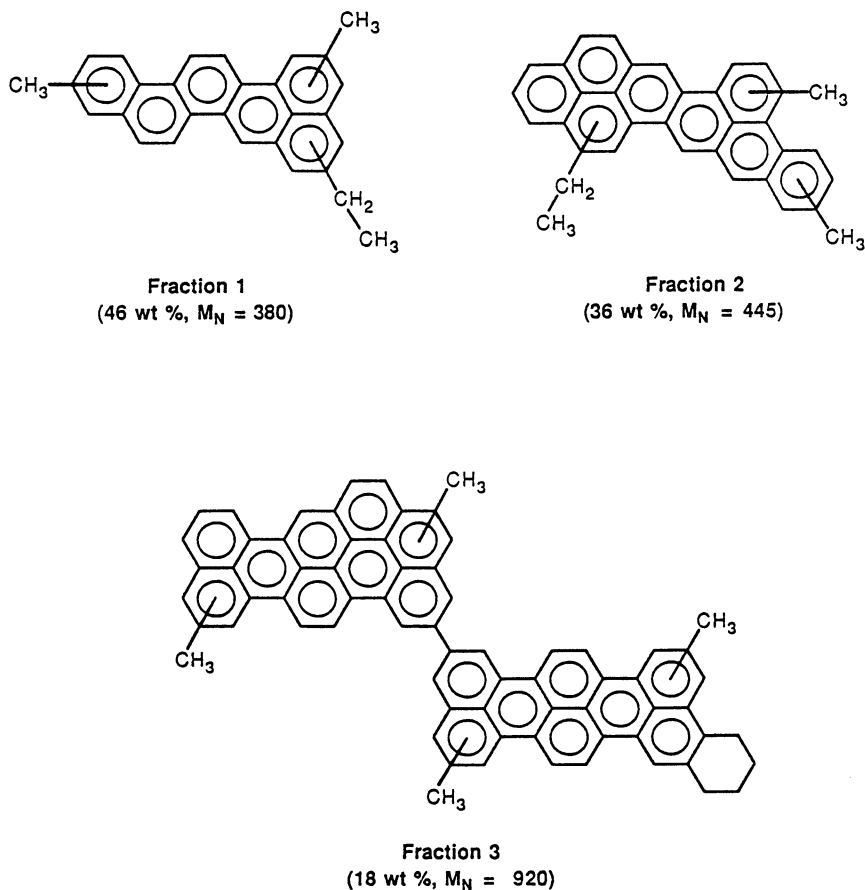


Figure 5. Pseudocomponents of Ashland A-240 pitch.

available vapor pressure data. In most cases, the optimization resulted in relatively small corrections to literature values. Additional details of the fitting technique used and the results for the acentric factor and κ are presented elsewhere (9).

Modeling Results. After obtaining the characteristic constants of the Peng-Robinson equation of state (a_c , b , and κ) for each of the model compounds, the constants were correlated with molecular structure parameters. The general form of the correlation is given by

$$\Psi_i = A_{i,0} + \sum_{j=1}^p A_{i,j} \Phi_{i,j}(\pi_j)$$

where

- Ψ_i = an EOS characteristic constant (a_c , b , or κ),
- p = an arbitrary number of average molecular structure parameters used in the correlation,
- $A_{i,j}$ = a coefficient obtained from data regression,
- $\Phi_{i,j}$ = a functional form of the characterization variable π_j ,
- π_j = an average molecular structure parameter characterizing component i .

For the model compounds, the molecular structure parameters were determined by definition rather than by the estimating equations of Knight (20). The problem, simply stated, is how to select the best subset of the molecular structure parameters, and how to choose the best functional forms of these parameters for use in the correlation.

The parameter M_N , or the number average molecular weight, proved to be a key characterizing parameter. Based on the known molecular weight dependence of thermodynamic properties such as viscosity (22), several functional forms were considered, including M_N , M_N^2 , $M_N^{1/2}$, and $\ln(M_N)$.

A number of statistical criteria and procedures were used to evaluate possible models to correlate the three EOS constants. The statistical package SYSTAT (23), which was used to perform multiple linear regressions, was used to examine these various models. The most promising models were further screened by determining how reasonably they predicted the pure-component vapor pressures for the pitch pseudocomponents shown in Figure 5. For example, one model predicted an increase in vapor pressure with increasing molecular weight; another model predicted unreasonably low vapor pressures.

The eight remaining models were then evaluated by determining how well they correlated experimental vapor-liquid equilibrium (VLE) data for mixtures of Ashland A-240 pitch and toluene, which have previously been reported (4). An isothermal flash algorithm was used to calculate the phase compositions. In all cases, the EOS constants for toluene were calculated by the conventional correlations of Peng and Robinson (17) using selected values of T_c , P_c , and the acentric factor, and the model of interest was used to calculate the EOS constants for the three pitch pseudocomponents. For each model evaluated, the binary interaction parameter k_{12} was optimized by minimizing the sum-of-squared deviations between the observed and calculated VLE data. For these calculations, the interaction between toluene and each of the pitch fractions was assumed to be the same, and a single value of k_{12} was assumed for the interaction coefficient. The interaction coefficient between the pitch fractions was assumed to be zero.

The correlating structure parameters and the coefficients for the best model are shown below in Table II, and the experimental and calculated vapor-liquid equilibria for this model are given in Figure 6. C_{aro} is the number (no.) of aromatic carbon (C) atoms per average (avg) molecule, C_1 is the no. of aromatic nonbridge C atoms per avg molecule, R_s is the no. of alkyl substituent groups per avg molecule, and $\%c_A$ is the percent aromatic C.

Table II. Generalized Correlations for the Characteristic Constants of the Peng-Robinson Equation

Molecular Structure Parameter $\Phi_{i,j}(\pi_j)$	Coefficients ($A_{i,j}$) for PR Equation-of-State Constants		
	$a \times 10^{-6}$ ($\text{bar}(\text{cm}^3/\text{mol})^2$)	b (cm^3/mol)	κ
intercept	19.236	11.934	0.1470
M_N	0.20714	1.1464	0.005560
C_{aro}	6.5752	-0.99583	-0.04484
C_1	-0.95602	0.048953	0.007808
R_s	1.7284	1.2851	0.002826
$\%c_A$	-0.66496	-0.32175	0.005755

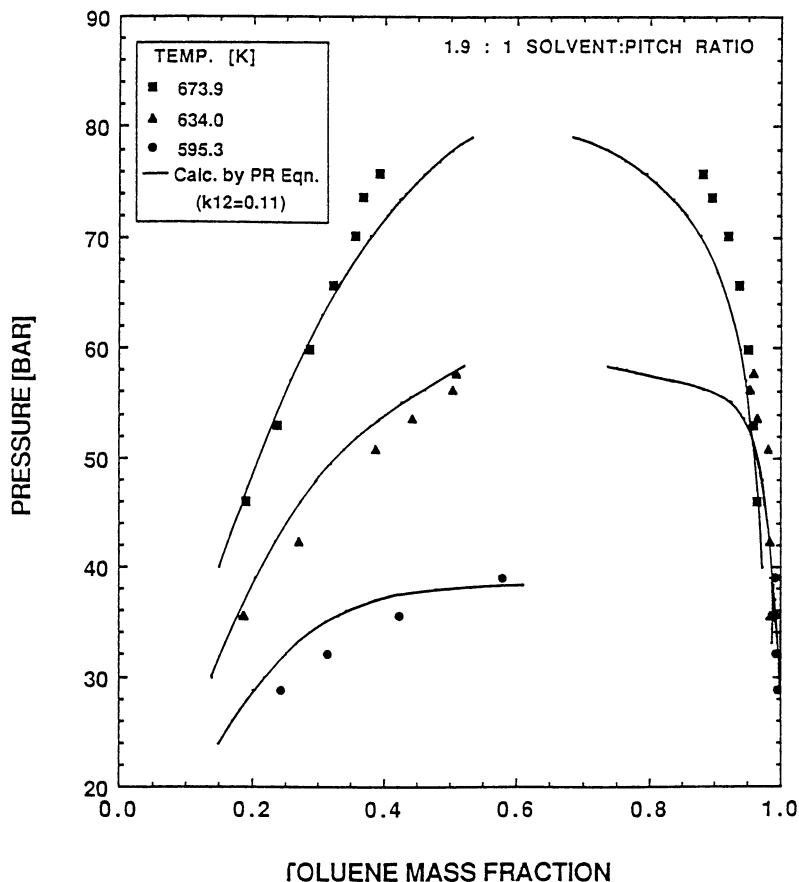


Figure 6. Comparison of experimental and calculated vapor-liquid equilibria for the A-240 pitch/toluene system.

The generalized correlations in Table II were then used to calculate vapor pressures for each model compound at each temperature given in our database. The overall average absolute percent error was found to be 21%. For comparison, Alexander et al. (18) reported a 50% error in calculated vapor pressures for aromatic compounds with their model.

As a final illustration, the selected model was used to correlate experimental VLE data for the phenanthrene/toluene system, which had been previously measured (6). The generalized correlations in Table II were used for phenanthrene; for toluene, the EOS constants were calculated from the conventional correlations of Peng and Robinson using selected values of T_c , P_c , and the acentric factor. As can be seen in Figure 7, the calculated results are in excellent agreement with the experimental data.

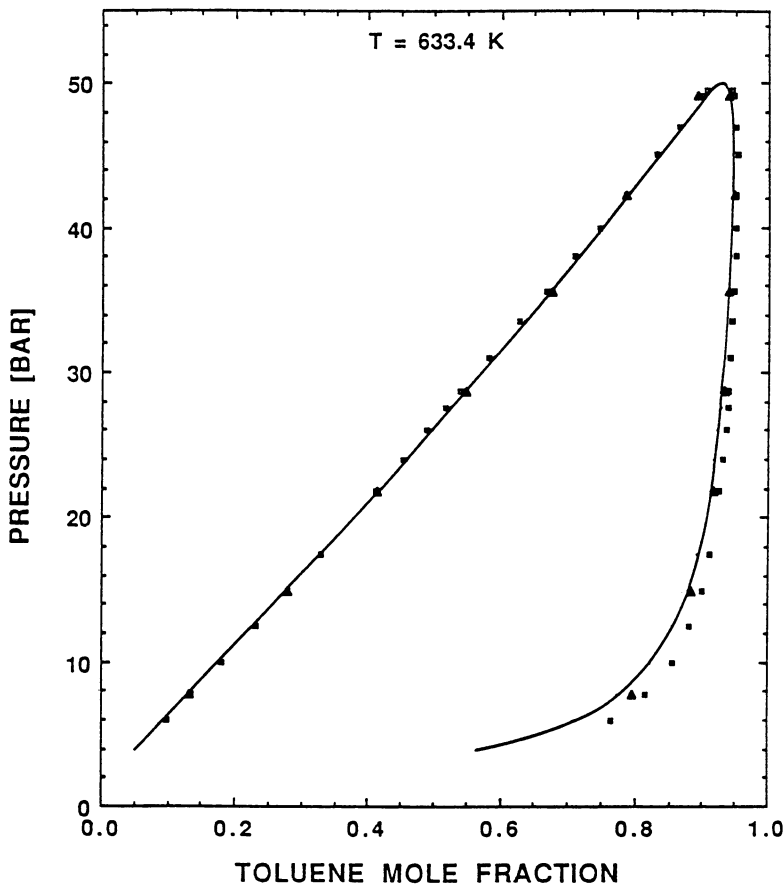


Figure 7. Comparison of experimental and calculated vapor-liquid equilibria for the phenanthrene/toluene system.

Conclusions

A continuous-flow apparatus has been used to fractionate a heat-soaked, isotropic petroleum pitch with supercritical toluene in a region of liquid-liquid equilibrium at 578.6, 614.5, and 655.5 K. Since both phases are black and opaque, an AC impedance bridge technique was used to detect the liquid-liquid interface level in the equilibrium cell. A properly devolatilized, bottom-phase fraction collected at 614.5 K and 70 bar has been spun into carbon fibers whose final mechanical properties are comparable to the best commercially available products. Since our investigation of the effects of the operating temperature, pressure, and S/F ratio on the properties of the produced pitch fractions has only recently begun, the above results indicate that SCF extraction is a promising alternative for producing mesophase pitch.

An initial effort towards developing a thermodynamic model for the phase equilibria of mixtures of petroleum pitch and supercritical toluene has been made. Only a fair prediction of previously measured experimental data in a region of vapor-liquid equilibrium was obtained. The shortcomings of the proposed model may result from

several factors, including 1) an insufficient number of pseudocomponents for characterizing the pitch and 2) an inherent weakness of a cubic equation of state for modeling such complex systems. Future improvements to the model development must address these concerns.

Acknowledgments

Financial support of the Defense Advanced Research Projects Agency and the U.S. Army Research Office (Contract No. DAAL03-89-K-0067) is gratefully acknowledged. In addition, the authors wish to thank Bill Willis of the College of Engineering's Engineering Services for the design and construction of the impedance bridge, and Kerry Robinson for analyzing the fibers by SEM. Finally, we wish to thank Professor Jim Holste of Texas A&M University for encouraging us to try the capacitance bridge technique.

Literature Cited

- (1) Edie, D. D.; Dunham, M. G. *Carbon* **1989**, *27*, 647-655.
- (2) Edie, D. D. In *Carbon Fibers and Filaments*; Figueiredo, J. L., Ed.; Kluwer Academic: Boston, 1990; pp. 43-72.
- (3) Hutchenson, K. W.; Roebbers, J. R.; Thies, M. C. *J. Supercrit. Fluids* **1991**, *4*, 7-14.
- (4) Hutchenson, K. W.; Roebbers, J. R.; Thies, M. C. *Carbon* **1991**, *29*, 215-223.
- (5) Diefendorf, R. J.; Riggs, D. M. U.S. Patent 4 208 267, 1980.
- (6) Hutchenson, K. W.; Roebbers, J. R.; Thies, M. C. *Fluid Phase Equilib.* **1990**, *60*, 309-317.
- (7) Yu, J. M.; Huang, S. H.; Radosz, M. *Fluid Phase Equilib.* **1989**, *53*, 429-438.
- (8) Riggs, D. M.; Shuford, R. J.; Lewis, R. W. In *Handbook of Composites*; Lubin, G., Ed.; Van Nostrand Reinhold: New York, 1982; pp. 196-266.
- (9) Hutchenson, K. W. Ph.D. Dissertation, Clemson University, 1990.
- (10) Roebbers, J. R. Ph.D. Dissertation, Clemson University, 1991.
- (11) Roebbers, J. R.; Thies, M. C., *Ind. Eng. Chem. Res.* **1990**, *29*, 1568-1570.
- (12) Hochgeschurtz, T. Diplomarbeit, RWTH Aachen, Germany, 1991.
- (13) Edie, D. D.; Fox, N. K.; Barnett, B. C.; Fain, C. C. *Carbon* **1986**, *24*, 477-482.
- (14) Hayes, G. J. M.S. Thesis, Clemson University, 1989.
- (15) Edie, D. D.; Hayes, G. J.; Rast, H. E.; Fain, C. C. *High Temperatures-High Pressures* **1990**, *22*, 289-298.
- (16) Stoner, E. G. Ph.D. Dissertation, Clemson University, 1991.
- (17) Peng, D.-Y.; Robinson, D. B. *Ind. Eng. Chem. Fundam.* **1976**, *15*, 59-64.
- (18) Alexander, G. L.; Schwarz, B. J.; Prausnitz, J. M. *Ind. Eng. Chem. Fundam.* **1985**, *24*, 311-315.
- (19) Dickinson, E. M. *Fuel* **1985**, *64*, 704-706.

- (20) Knight, S. A. *Chem. Ind.* **1967**, *45*, 1920-1923.
- (21) Somayajulu, G. R. *J. Chem. Eng. Data*, **1989**, *34*, 106-120.
- (22) Reid, R. C.; Prausnitz, J. M.; Poling, B. E. *The Properties of Gases and Liquids*; 4th ed.; McGraw-Hill: New York, 1987.
- (23) Wilkinson, L. *SYSTAT: The System for Statistics*; Version 3, SYSTAT Inc.: Evanston, IL, 1987.

RECEIVED April 27, 1992

Chapter 29

Kinetics of Supercritical Fluid Extraction of Coal

Physical and Chemical Processes

Chunjie Zhang, J. M. Smith, and B. J. McCoy

Department of Chemical Engineering, University of California—Davis,
Davis, CA 95616

This paper presents a simplified kinetics study of supercritical tert-butanol extraction of Illinois No. 6 bituminous coal. Extraction rates were estimated by continuously measuring the spectrophotometric absorbance (at 235 nm) of the effluent from a fixed-bed flow reactor. The experiments were conducted in the temperature range of 553–633 K and at 6.8 MPa constant pressure by programmed-temperature techniques. A model for which the extractable compounds in the coal are represented by two groups of components, undergoing parallel first-order reactions, satisfactorily describes the experimental data. The kinetics data indicate that the first group is extracted by a physical process, which occurs below 573 K. The second group is extracted via a thermal decomposition reaction (with an apparent average activation energy of 54 kJ/gmol), which is dominant above 573 K.

Much research has been performed over the last 25 years on producing liquid chemicals and fuels from coal by a variety of processes. Supercritical fluid extraction of coal (1–3) has received attention because of the greater dissolution power of the supercritical fluid compared to gases in conventional pyrolysis. Supercritical liquefaction typically involves the thermal breakdown of coal and subsequent dissolution of the pyrolysis products in the solvent. Depending on the solvent, supercritical extraction can be successfully performed at relatively low temperatures (593–673 K), moderate to high pressures (6–30 MPa), and in batch or continuous modes. The method shows potential for commercial application, although most studies have been limited to research on thermodynamics, chemical mechanisms, and the structure of the coal and extract. An important feature of supercritical coal extraction that has received limited attention in the literature concerns the kinetics of the dissolution process, especially quantitative interpretation of experimental data.

The research directed specifically to the kinetics of supercritical coal extraction (4,5) is based on the non-polar solvent, toluene. To our knowledge, there is little published information on supercritical extraction with polar or hydrogen-donor solvents, although some research on alcohol extraction of coal (6–8) has been reported. Higher conversions were reported with low molecular weight alcohols than with hydrocarbons under equivalent conditions (9,10), possibly due to hydrogen-donor action. Hydrogen-donor solvents may exert a stronger dissociating or depolymerizing

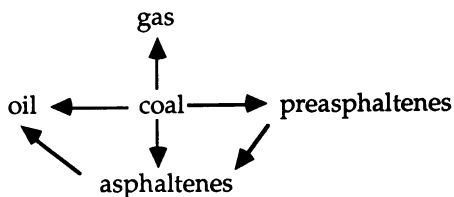
0097–6156/93/0514–0363\$06.00/0
© 1993 American Chemical Society

action on coal than non-donor solvents, thus increasing the yield of extractable coal material (10,11). We found in our earlier work (12) that with Illinois No. 6 coal extraction in supercritical tert-butanol ($P_c=3.97$ MPa, $T_c=506.2$ K), there was some chemical interaction between the coal and the solvent, even at the comparatively low temperature of 573 - 623 K. Similar results were reported by Makabe and Ouchi (8) and by Kuznetsov et al. (11). The chemical reaction kinetics and mechanism for the extraction of coal with alcohols, however, are still unclear, and further research is needed.

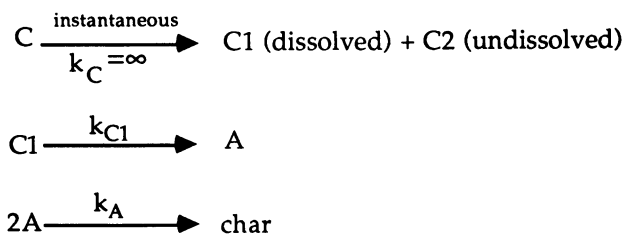
A dynamic method using UV spectrophotometry to monitor continuously the extraction processes in a continuous-flow reactor has been successfully used to study kerogen extraction from shale with toluene (13), and lignin and cellulose extractions from wood with tert-butanol (14-16). From such data mathematical models were developed to describe chemical reactions and transport processes during these supercritical processes. The results suggested that the dynamic method may be suitable to investigate quantitatively the kinetics processes for extraction of coal. In this work our objective was to develop a simple, quantitative kinetics model to describe such experimental data.

Theory

Most general models for coal liquefaction are of the lumped-parameter type, where the products are combined into groups characterized by their solubility in different solvents. The most common groups are oil, asphaltenes, preasphaltenes, and insoluble coal. The concentration of these fractions in the liquefaction products can be used to establish reaction networks and estimate rate constants. The typical mechanistic model for coal liquefaction with a donor-solvent is (17):



Deshpande et al. (5) proposed a model of supercritical extraction of bituminous coal with toluene. It was hypothesized that only part of the coal, including volatiles and non-volatiles, dissolve in the fluid and undergo a liquefaction reaction, forming oils, asphaltenes, gases, and char as products. The following is the reaction scheme in terms of rate constants k_C , k_{C1} and k_A :



Conversion versus time data from a continuous-flow reactor with coal injection was used to estimate the kinetics parameters and the fraction extracted.

Slomka and Rutkowski (4) proposed a second-order reaction model to describe supercritical toluene extraction of bituminous coal. The second-order rate equation, with respect to undissolved but potentially extractable coal, closely fits the conversion of a long-time run in a batch system.

It has been proposed (18) that coal is composed of two molecular groups, or phases. The mobile phase comprises smaller molecules attached to or held within the network by physical and weak chemical bonds. The insoluble phase of coal is primarily a three-dimensional, cross-linked, macromolecular network or matrix. From the calibration procedure described later, the extract from supercritical tert-butanol extraction of Illinois No. 6 coal in the temperature range of 553 to 633 K likewise can be divided approximately into two groups of components. At low temperature (below 573 K) the absorbance of the effluent versus time exhibited one peak; at higher temperature (above 573 K) two peaks appeared in the absorbance history. In our earlier work of GC-MS analyses for the same system (12), it was found that at low temperature a mixture of aliphatic and aromatic compounds was produced, and as temperature increased, the mixture contained more aromatic components. Presumably, at higher temperature more aromatic materials are produced by thermal decomposition of the macromolecular network. Based on these results a parallel-reaction model is proposed. The first reaction is a physical extraction process to release weakly-bound compounds. The second reaction represents the degradation of the macromolecular network to produce more aromatic compounds.

We assume that the extractable compound concentration is uniform in the coal particle, and each kind of extractable compound follows first-order, irreversible kinetics. Then the reaction scheme may be represented simply as



and the rate equations are

$$-dc_1/dt = k_1c_1 \quad (3)$$

$$-dc_2/dt = k_2c_2 \quad (4)$$

where c_i represents the concentration of solid reactant per gram of coal. The reaction constants, k_i , are expressed in terms of energies of activation, E_{ai} ,

$$k_i = k_{0i} \exp(-E_{ai}/R_g T) \quad (i=1, 2) \quad (5)$$

Then, the total reaction rate, R , is represented by

$$R = k_1c_1 + k_2c_2 \quad (6)$$

Since a very thin coal bed was used and the conversion through the whole fixed-bed was extremely low, the reactor can be assumed to approximate a differential reactor (19). Internal and external particle mass transfer resistance were shown to be negligible, and both fluid and particles are assumed to have uniform concentrations. A dynamic mass balance on the reactor is represented in terms of outlet concentration of extract, $q = q_1 + q_2$, by the expression

$$\alpha V dq/dt + Qq = mR \quad (7)$$

where α is the bed void fraction, V is the volume of reactor bed, Q is the flow rate of solvent, and m is coal mass. Initial conditions are:

$$C_1 = C_{01}, \quad C_2 = C_{02}, \quad q_1 = q_2 = 0, \quad \text{when } t = 0. \quad (8)$$

where C_{01} and C_{02} are the total concentrations of extractable compounds in coal for the first and second reactions. These values are expected to be dependent on reaction conditions, e.g., temperature and pressure.

The uniform temperature of the bed of coal and the nature of the solid-reactant-based rate equations enable the integration of equations (3) and (4) to the form:

$$C_1 = C_{01} \exp(-k_1 t) \quad (9)$$

$$C_2 = C_{02} \exp(-k_2 t) \quad (10)$$

Equations (9) and (10) can be substituted into equation (6) to express the total reaction rate in terms of time:

$$R = k_1 C_{01} \exp(-k_1 t) + k_2 C_{02} \exp(-k_2 t) \quad (11)$$

With constant temperature and initial conditions, equation (7) combined with equation (11) is a first-order differential equation whose solution is

$$q = \{mk_1 C_{01} / [Q(1 - \alpha\tau k_1)]\} \{ \exp(-k_1 t) - \exp[-t/(\alpha\tau)] \} + \{mk_2 C_{02} / [Q(1 - \alpha\tau k_2)]\} \{ \exp(-k_2 t) - \exp[-t/(\alpha\tau)] \} \quad (12)$$

where the residence time, $\tau = V/Q$, is in the range of 0.01-0.02 min for our experiments (Table I).

The first reaction rate was observed to be faster than the second. At temperatures above 573 K the first reaction is rapidly completed, and the second reaction becomes dominant. Thus, at long times and high temperatures the first reaction term, $\{mk_1 C_{01} / [Q(1 - \alpha\tau k_1)]\} \{ \exp(-k_1 t) - \exp[-t/(\alpha\tau)] \}$, can be ignored. Then equation (12) can be written as

$$q = \{mk_2 C_{02} / [Q(1 - \alpha\tau k_2)]\} \{ \exp(-k_2 t) - \exp[-t/(\alpha\tau)] \} \quad (13)$$

In equation (13), $[1/(\alpha\tau)] \gg k_2$, or $\exp(-k_2 t) \gg \exp[-t/(\alpha\tau)]$, and $\exp[-t/(\alpha\tau)]$ is negligible. Also, $1 \gg \alpha\tau k_2$, and $(1 - \alpha\tau k_2)$ is nearly equal to 1. Thus, for $t > 0$ the equation (13) is reduced to

$$q = [mk_2 C_{02} / Q] \exp(-k_2 t) \quad (14)$$

Equation (14) can be used only in the case that the characteristic time for extraction (i.e., the residence time) is much smaller than the characteristic time for reaction (i.e., $1/k_2$). A plot of $\ln(q)$ vs. time based on equation (14) is linear. The intercept of the line is $\ln[mk_2 C_{02} / Q]$, and the slope is $(-k_2)$. From the slope and intercept of experimental data, k_2 and C_{02} can be obtained. For the first reaction, $1 \gg \alpha\tau k_1$ and $1/\alpha\tau \gg k_1$, are likewise true.

Since there is a heating period at the beginning of a run, the first reaction occurs in a non-constant temperature range. The parameters k_{01} , C_{01} and E_{a1} can be estimated by minimizing the sum of the squares of the difference between the experimental and calculated extraction concentrations during the heating-up period for low temperature runs ($T < 573$ K). For such runs the extract from the second reaction is negligible.

Experiments

Experimental method. The extraction was conducted in a fixed-bed reactor where the solvent flowed continuously through the coal bed. The apparatus, shown in Figure 1, consists of four sections: (1) feed and pressurizing section, (2) extraction section, (3) temperature-control section, (4) flow-rate-control and sample-collection section. Experimental programmed-temperature runs were conducted in two ways: continuous heating up to a constant temperature, and two-step heating. In the continuous heating method the temperature of the reactor including the coal bed is increased at the rate of 8.4 K/min to the desired temperature, which is maintained until the end of a run. During all runs, flow rate and pressure were held constant. In this study a flow rate, 1.4×10^{-5} m³/min (under the conditions of 298 K and 0.1 MPa), was used, and pressure in the reactor was 6.8 MPa (1000 psi). The temperature was in the range of 553–633 K. During the run the cooled liquid extract was directed into a flow-through cuvette of the spectrophotometer, and the absorbance was continuously monitored at 235 nm. Since there is an 8 minute time delay between the reactor and the UV detector in our apparatus, the time of the measured absorbance was corrected for the flow from the point of reactor exit to the absorbance measurement. For an apparatus essentially identical to ours it was found (13) that the effect of dispersion between reactor exit and the spectrophotometer is very small and can be ignored.

Experimental runs were conducted at different flow rates, 1.0×10^{-5} and 1.4×10^{-5} m³/min, while the other conditions were unchanged. It was found that the same conversions were obtained with the same extraction time. This indicated that external mass transfer resistance can be ignored when a flow rate of 1.4×10^{-5} m³/min is used.

The Illinois No. 6 coal used in this work, DECS-2 (PSOC-1539), was prepared by sieving to a particle size range of $5.89\text{--}8.33 \times 10^{-4}$ m (20–28 mesh). Whitehead (20) found that particle sizes smaller than 2.36×10^{-3} m did not significantly affect the experimental results. Kershaw (2) reported that for coal particle size below 1.6×10^{-3} m, there was little relation between the conversion and particle size, and there was no tendency to agglomerate if particle size was larger than 2.0×10^{-4} m. Based on these data we are confident that for our particle size there is no internal mass transfer resistance.

The coal samples were stored under water to prevent oxidation, and before extraction were vacuum-dried at 343 K to constant weight. An amount of pure tert-butanol, 1.0×10^{-2} m³/kgcoal, was added to the dried coal samples, and after shaking the mixture of the coal and solvent for 40 minutes at 313 K, the solvent was poured out and fresh tert-butanol was added. This procedure, which removes some highly soluble compounds from the coal, was repeated until the absorbance of the solvent that was contacted with coal was below 0.1. The coal samples were vacuum-dried again at 343 K and weighed. After this pretreatment procedure, which was necessary to achieve reproducible results, the coal samples were ready for extraction.

During the high-temperature experimental run (633 K) it was observed that there was a small amount of gas produced. Based on GC-MS analysis, Zhang et al. (12) found that the gas product is composed mainly of butene from the decomposition of the solvent. At the experimental conditions, gas formation is negligible compared to the liquid product.

In equation (12) the concentration, q , of coal extract in the solvent at the exit of the reactor is at supercritical conditions, while the measured concentration, q_a , in the

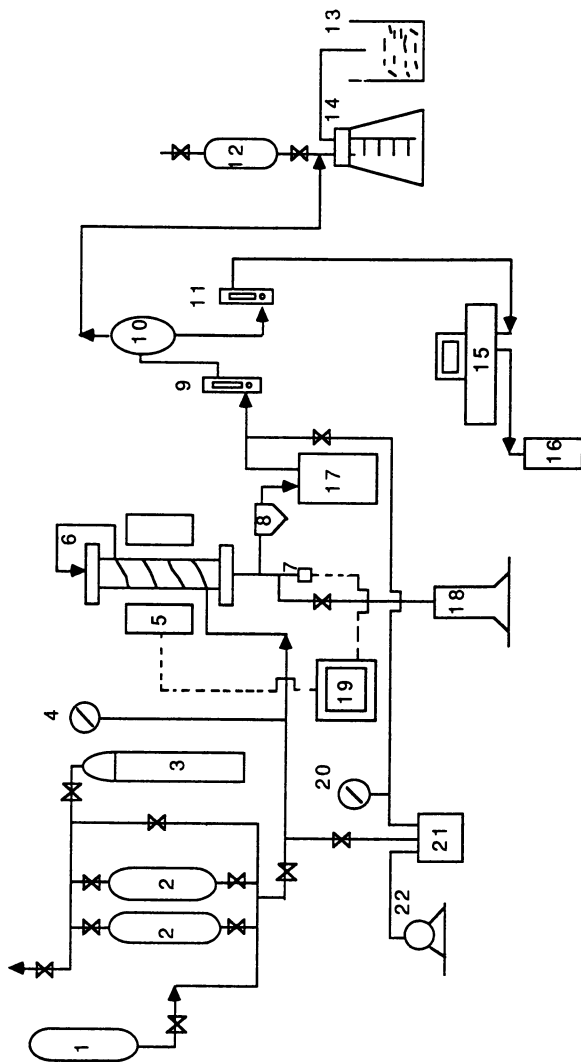


Figure 1. Schematic diagram of the apparatus: 1, solvent supply tank; 2, two pressure feed tanks; 3, nitrogen cylinder; 4, pressure gauge; 5, electric furnace; 6, extraction reactor; 7, thermocouple connection; 8, filter; 9, first flow meter; 10, gas-liquid separator; 11, second flow meter; 12, gas sampling tube; 13, water collector; 14, gas burette; 15, spectrophotometer; 16, collection vessel for effluent; 17, water-cooling heat exchanger; 18, collection vessel for pressure relief; 19, temperature controller; 20, vacuum gauge; 21, surge tank; 22, vacuum pump.

cuvette is at 298 K and 0.1 MPa. The measured concentration was converted to supercritical conditions by the expression

$$q = (\rho/\rho_a) q_a \quad (14)$$

The flow rate in the reactor was corrected in the same way:

$$Q = (\rho_a/\rho) Q_a \quad (15)$$

where ρ_a is the density of the solvent at ambient conditions, equal to 787 kg/m³. The density of the solvent at supercritical conditions is ρ , which was estimated from the generalized correlation of Lee and Kesler (21). Extract concentrations were always very low in our experiments so that solubility limitations were never an issue.

For comparison, the supercritical extraction runs were performed at 633 K and 6.8 MPa with toluene as the solvent instead of tert-butanol. The other experimental conditions for toluene runs are same as those for tert-butanol runs.

Monitoring the extract. The composition of coal is so complex that it is impossible to determine the time-dependent concentration of each component in the coal extract. Our method is to measure the total coal extract concentration with time by continuously monitoring the absorbance of the effluent at the wavelength of 235 nm in a flow-through spectrophotometer. Because the total weight loss of coal, and hence the extract concentration, is related to the absorbance of the extract, it is not essential that all extract components have the same absorbance. We scanned the effluents from blank runs (i.e., when coal is absent) and coal runs. For a blank run scan it was found that the absorption of the solvent effluent at 235 nm was the lowest in the wavelength range of 200-400 nm. On the other hand, the scan of the coal effluent indicated that at 235 nm the coal extract, whether from a low or high temperature run, had an absorbance sufficiently large to monitor the concentration history. The absorption of the solvent effluent was effectively negligible compared with that of the coal extract. Also, by dilution the absorption of the coal extract was found to be proportional to the extract concentration. So, we chose 235 nm as the monitoring wavelength during the supercritical runs.

To convert absorbance to extract concentration, calibration based on the total weight loss of coal samples is necessary. The calibration runs were made with a large-size coal sample (6 g) at five different temperatures and constant pressure (6.8 MPa). Before a run the coal samples were pretreated as described previously. After extraction the coal was treated with the same procedure. The fraction extracted is obtained from the coal sample weight before and after extraction. Based on the absorbance of coal extract in the effluent at 235 nm and the weight loss of the coal samples, a calibration curve for diluted samples of the collected effluent was constructed for each temperature run. The results are shown in Figure 2.

For different temperature runs the calibration curves are all straight lines with different slopes. The slope of the calibration curve (concentration versus absorbance) increases with increasing temperature of extraction. A plot of this slope versus temperature (Figure 3) is consistent with the concept that two groups of components are mixed together in the liquid extract. Lower temperatures produce more physically-extracted compounds, and higher temperatures produce more chemically-extracted compounds. As extraction temperature increases, the contribution of physically-extracted compounds to the absorbance diminishes. A third-order polynomial curve is drawn through the data in Figure 3 to illustrate how these two groups of compounds can mix to provide the resultant absorbance. The physically-extracted group gives a larger absorbance at 235 nm although the total weight loss of coal sample in lower

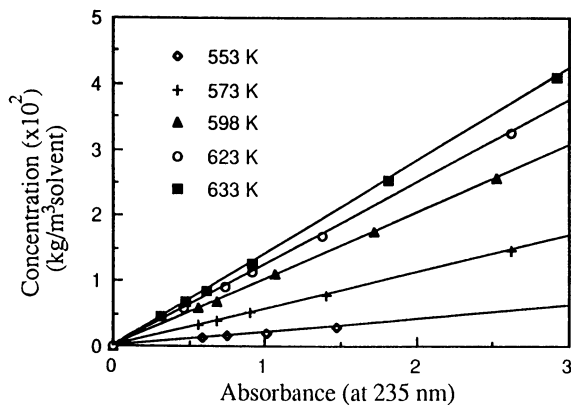


Figure 2. Calibration curves at different temperatures (pressure=6.8 MPa).

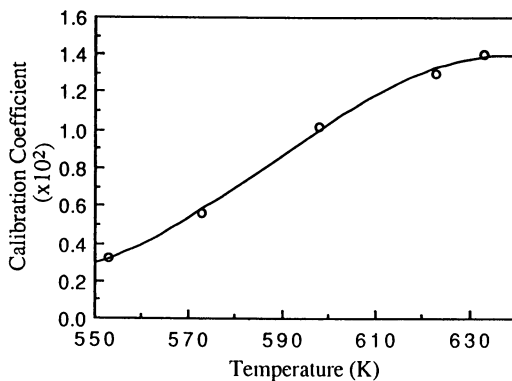


Figure 3. Effect of temperature on the slope of the concentration versus absorbance lines (Figure 2).

temperature runs is small. The low-temperature extract must consist, therefore, of molecules with chromophoric groups that absorb strongly (22,23). For the chemically-extracted group, more aromatic compounds are obtained because of the breakdown of the coal macromolecular network. Aromatic compounds have a prominent absorption band at 235 nm (23). Bartle et al. (24) also noted that the extract of supercritical fluid extraction of bituminous coal has a maximum absorption around 235 nm. These facts support the concentration measurement method using the absorption of coal extract at 235 nm with the aid of calibration curves.

Results

Experimental runs. Table I summarizes the experimental conditions and extraction conversion for the runs when the reactor is heated to one constant temperature. The conversion is defined as the fractional weight loss of the coal sample. The conversion is very low at 573 K and increases to 8.0% at 633 K.

Table I. Summary of Experimental Conditions and Conversion

Temperature (K)	T_R	Pressure (MPa)	P_R	Solvent Density (kg/m ³)	τ (min)	Conversion (%)
553	1.09	6.8	1.71	231	0.02	0.4
563	1.11	6.8	1.71	203	0.02	-
573	1.13	6.8	1.71	182	0.02	1.7
598	1.18	6.8	1.71	148	0.02	4.3
623	1.23	6.8	1.71	129	0.01	6.1
633	1.25	6.8	1.71	124	0.01	8.0

Figures 4-6 show the extraction curves and temperature profiles for different temperatures in the temperature range of 598-633 K at a constant pressure of 6.8 MPa. The plotted points were selected from the continuous data at intervals of 2 minutes at the beginning of the run and 5 minutes at the long time run. During the heating period some components were extracted rapidly from the coal, so that the extraction rate reached a peak. When temperature went through a certain value of temperature (above 593 K) the extraction rate increased again. At a high temperature (Figure 6) two peaks appear: one occurs before temperature reaches the maximum and the second as temperature reaches the maximum. These results are evidence that two kinds of components, which undergo different chemical reactions, exist inside the coal particles. Also, the reaction rates for these two processes are different.

Figure 7 shows a temperature-programmed experimental run at a constant pressure of 6.8 MPa. In this experiment, the reactor was first heated to 553 K and held at that temperature until the extraction was nearly complete. Then the temperature was increased from 553 K to 623 K and kept constant to the end of the run. A peak appears corresponding to each temperature step. After the first peak the extraction rate diminishes nearly to zero, suggesting that the first reactant group is depleted. A long tail exists after the second peak, indicating that the second reaction is slower than the first.

A two-step programmed-temperature experiment was conducted at two different temperatures, 563 K and 598 K (Figure 8). Because the second-step temperature is lower in Figure 8 than in Figure 7, the area under the second peak in Figure 8 is smaller than that in Figure 7. This result indicates that as temperature increases, the extractable

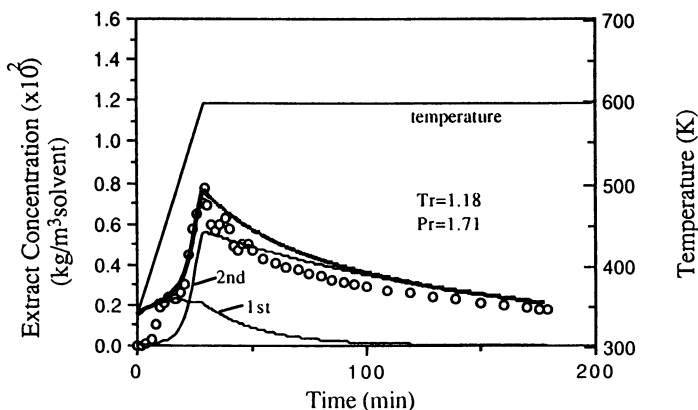


Figure 4. Experimental data and calculated extraction curve at 598 K and 6.8 MPa. Extract concentration is based upon kg of initial coal sample mass (— calculated, \circ experimental, — calculated by first or second reaction).

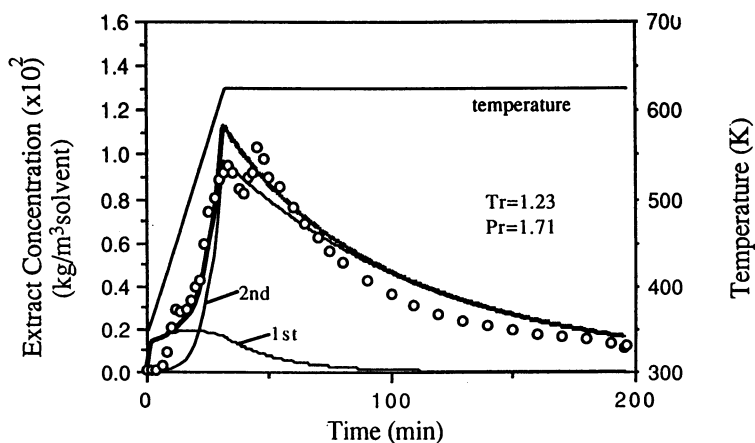


Figure 5. Experimental data and calculated extraction curve at 623 K and 6.8 MPa. Extract concentration is based upon kg of initial coal sample mass (— calculated, \circ experimental, — calculated by first or second reaction).

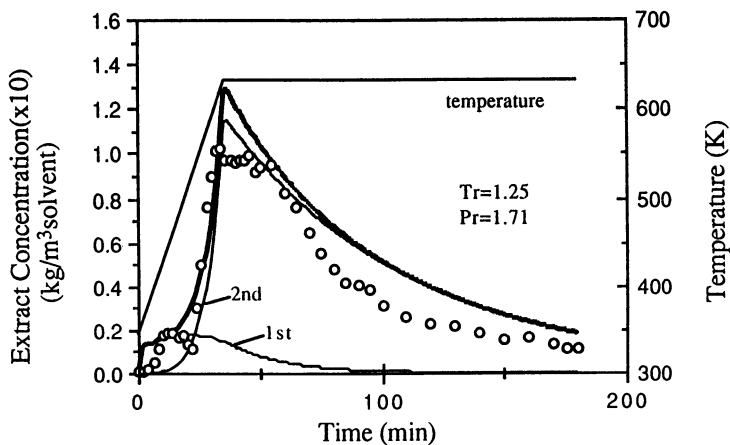


Figure 6. Experimental data and calculated extraction curve at 633 K and 6.8 MPa. Extract concentration is based upon kg of initial coal sample mass (— calculated, \circ experimental, — calculated by first or second reaction).

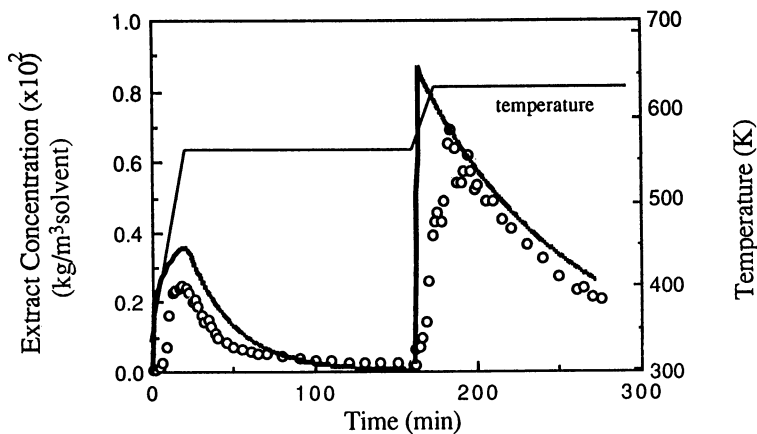


Figure 7. Comparison between calculated extraction curve and temperature-programmed experimental data. Extract concentration is based upon kg of initial coal sample mass (— calculated, \circ experimental, $P_r=1.71$, $T_r=1.09$ and 1.23).

concentration, C_{02} , from the second reaction increases. There is little difference in the areas under the first peaks in Figure 7 and Figure 8. Thus temperature has little effect on the extractable amount, C_{01} , for the first reaction. These experimental results suggest qualitatively that the first reaction has a higher rate constant than the second, and that the total extractable concentration for the first reaction is less than that of the second, which is temperature dependent. Slomka and Rutkowski (4) and Deshpande et al. (5), in their mathematical models, also allowed the concentration of extractable compounds to vary with temperature.

Kinetics parameters and model predictions. The kinetic parameters were determined according to the estimation methods described earlier. The data at long times for the continuous heating runs (Figures 4-6) were used to determine the second rate constant and extractable concentration, C_{02} . Table II gives the parameter values for this second group of reactants, which were produced at the higher temperatures. The data of the higher temperature region in the two-step temperature-programmed runs gave k_2 values that agreed within 5% of the values in Table II. The values of k_2 at 553 K and 563 K in Table II are estimated by means of the Arrhenius equation. The activation energy, E_{a2} , is an average value representing a group of reactants. Since C_{02} is temperature dependent, different components are reacting at different temperatures. Thus, it is an additional simplification to use a single Arrhenius equation. The resultant E_{a2} is therefore an apparent average value.

Table II. Kinetics Data

1. Relations between temperature and k and c_0				
Temperature (K)	c_{02} (kg/kgcoal)	k_2 (min ⁻¹)	c_{01} (kg/kgcoal)	k_1 (min ⁻¹)
553	-	0.0029*	0.008	0.035
563	-	0.0036*	0.008	0.036
573	0.024	0.0045	0.008	0.037
598	0.065	0.0068	-	0.040*
623	0.081	0.0110	-	0.043*
633	0.087	0.0129	-	0.044*

2. Activation energy and pre-exponential factor	
Activation energy (kJ/gmol)	Pre-exponential factor (min ⁻¹)
$E_{a1}=8.0$	$k_{01}=2.0 \times 10^{-1}$
$E_{a2}=54$	$k_{02}=3.5 \times 10^2$

* estimated by Arrhenius equation.

For the first group of reactants, k_1 and C_{01} were determined by numerically solving the equations (3)-(8) and minimizing the sum of the squares of the differences between the experimental and calculated concentrations for the low temperature runs. It was found that the total extractable amount, C_{01} , changed little with temperature. The data from 553, 563 and 573 K runs were used to estimate C_{01} , k_{01} and E_{a1} , and the

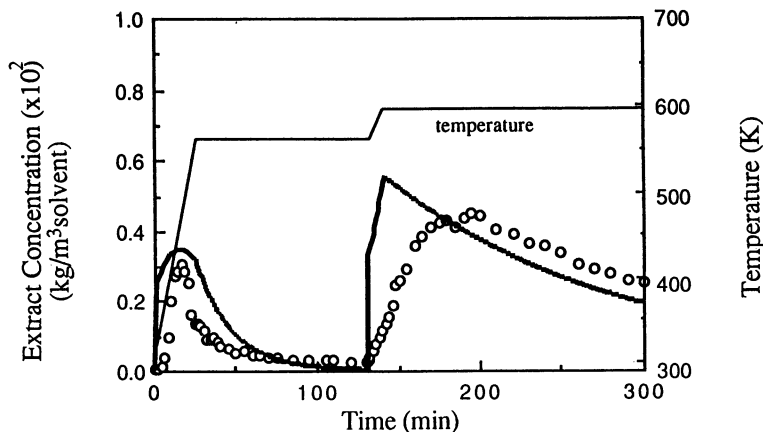


Figure 8. Comparison between calculated extraction curve and temperature-programmed experimental data. Extract concentration is based upon kg of initial coal sample mass (— calculated, \circ experimental, $P_1=1.71$, $T_1=1.11$ and 1.18).

results are also given in Table II. Predicted concentration versus time curves are shown as solid curves in Figures 4-8.

Discussion

Temperature effect on reaction rates. For the second group of reactants the apparent average activation energy of the second reaction, E_{a2} , is 54 kJ/gmol; for the first reaction, E_{a1} is 8.0 kJ/gmol. At the same low temperature (<573 K) the rate for the second group of reactants, for example, is about 10 times less than the rate for the first group. As temperature increases, the second reaction becomes more important.

An activation energy in the range of 0-40 kJ/gmol is usually regarded as a physical process, and above 40 kJ/gmol as a chemical process (4). The value of 8.0 kJ/gmol for E_{a1} indicates that the first reaction is a physical process and is dominant at the low temperature. In this low temperature range (553-573 K) the extraction seems mainly to be physical dissolution of interstitial substances from the coal matrix by the solvent tert-butanol. The activation energy for the second reaction, 54 kJ/gmol, indicates that chemical reactions are responsible for the formation of the extract products that are soluble in supercritical tert-butanol solvent (Figure 9).

Relations between extractable compound concentration and temperature.

Extractable compound concentration is defined as the total extractable amount per gram coal at a certain temperature and pressure. Figure 10 shows the relation between extractable concentration, C_{O2} , and temperature. Extrapolation to low temperatures shows that the second reaction will be negligible for temperatures below 563 K, as observed in the two-step temperature experiments. The concentration, C_{O2} , increases strongly with temperature, implying that more compounds can be extracted when temperature increases. This supports the concept that the second chemical reaction is caused by the thermolytic cleavage of the bonds of the coal macromolecular network.

For the first group of components we assumed that C_{O1} is independent of temperature. This assumption was confirmed by the good agreement between the experimental data and predicted results for low temperature runs. It seems reasonable

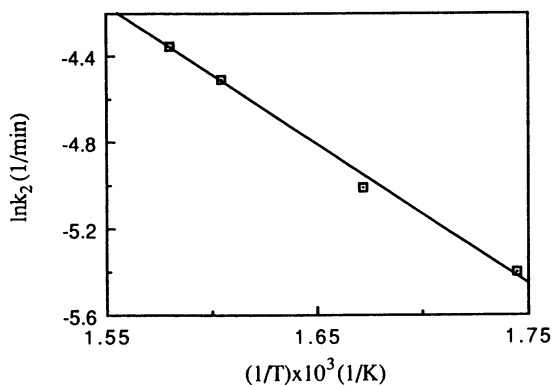


Figure 9. Arrhenius plot for second rate constant.

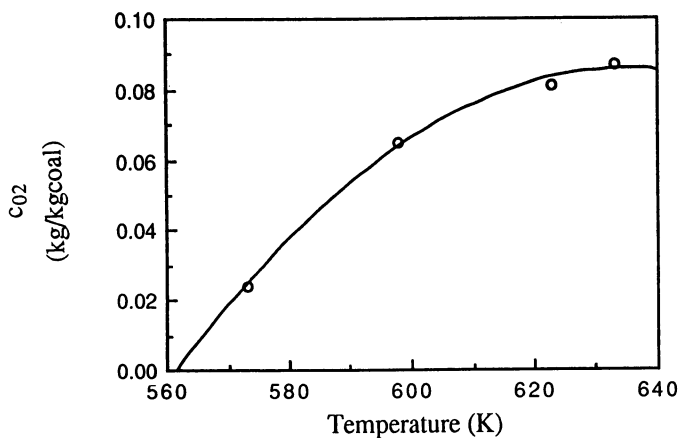


Figure 10. Concentration of extractable compounds for the second group of reactants versus temperature (6.8 MPa).

to conclude that these compounds are physically attached or sequestered within the coal matrix, and are easily extracted.

The fractional conversion of coal obtained from experimental runs (Table I) is slightly lower than the value predicted by the model. The reason is that the experimental runs were not taken to total depletion. Our experience is that near the end of extraction, the final 1-2% conversion requires several hours to be completed.

Comparison of kinetics data between tert-butanol and toluene extraction of coal. Slomka and Rutkowski (4) proposed a second-order reaction with respect to extractable compound concentration to describe the supercritical toluene extraction of bituminous coal. A first-order liquefaction reaction and a second-order reaction to form char were suggested by Deshpande et al. (5). The activation energies and pre-exponential factors resulting from these two studies are based on mechanisms different from the present work. In the temperature range of 646-698 K and 9-23 MPa pressure Deshpande et al. determined an activation energy of 79.8 kJ/gmol for the liquefaction reaction forming oils, asphaltenes and gases. Slomka and Rutkowski (4) obtained an activation energy of 101 kJ/gmol in the temperature range of 627-683 K and 9.8 MPa. In our work the activation energy of the chemical extraction is of the same order of magnitude, 54 kJ/gmol at 6.8 MPa.

The thermolysis of coal is thought to involve the thermal cracking of coal molecules by rupture of chemical bonds within the coal macromolecular network. The cracking or depolymerization reactions produce free radicals (coal fragments) that must be stabilized, or capped, to prevent retrograde, repolymerization reactions. Zhang et al. (12) found evidence, in the form of branched extract molecules detected by GC-MS, that some tert-butanol reacts with the coal extract. This raises the question of whether the chemical interaction of the tert-butanol increases the extraction. Deshpande et al. (5) calculated an extractable fraction of 4% for toluene extraction at 647 K and 9.0 MPa by fitting the experimental data with the model. For supercritical tert-butanol extraction of coal the total extractable fraction at 633 K and 6.8 MPa from our work is higher, 8%. However, the extraction processes can be compared only for the same coal under similar conditions. For our system when toluene was used as the solvent instead of tert-butanol, the extraction fraction was 10% at 633K and 6.8 MPa. We conclude that the chemical interaction of tert-butanol with the coal does not strongly affect the extraction process compared with the toluene as the solvent.

Conclusions

The principal conclusions from this investigation are:

- (1) The experimental approach of dynamic monitoring with a UV spectrophotometer at 235 nm can be used to investigate the physical-chemical process associated with supercritical tert-butanol extraction of bituminous coal.
- (2) For Illinois No. 6 coal at a constant pressure of 6.8 MPa two extractable fractions can be identified. Below 573 K, a physical extraction process dominates. Above 623 K, the rate of extraction is determined by the thermal degradation of the macromolecular network of coal.
- (3) At our operating conditions a simplified kinetics model, based on a set of two parallel, first-order reactions, can describe the physical-chemical process of supercritical extraction of coal.
- (4) The extractable compound concentration in the coal is an increasing function of temperature. At the temperature and pressure employed, total fractions extracted were low (≤ 8 wt%), but comparable to the extraction with toluene as the solvent.

Nomenclature

c	concentration of extractable compounds in coal, kg/kgcoal
E_{ai}	activation energy, kJ/gmol
k	reaction rate constant, min^{-1}
k_{0i}	pre-exponential factor, min^{-1}
m	mass of initial coal sample, kg
P	pressure, MPa
P_C	critical pressure, MPa
P_r	reduced pressure, P/P_C
q	extract concentration in the effluent in the exit of reactor, $\text{kg}/\text{m}^3\text{solvent}$
Q	flow rate of solvent, m^3/min
R	reaction rate, $\text{kg}/(\text{kgcoal}\cdot\text{min})$
R_g	gas constant, $\text{kJ}/(\text{gmol}\cdot\text{K})$
t	time, min
T	temperature, K
T_C	critical temperature, K
T_r	reduced temperature, T/T_C
V	volume of reactor bed, m^3
Greek letters	
α	bed void fraction
τ	residence time, min
ρ	density of solvent, kg/m^3

Acknowledgment

The financial support of Pittsburgh Energy Technology Center Grant No. DOE DE-FG22-90PC90288 is gratefully acknowledged.

Literature Cited

- 1 Sunol, A. K.; Beyer, G. H. *Ind. Eng. Chem. Res.* **1990**, *29*, 842.
- 2 Kershaw, J. R. *J. Supercrit. Fluid* **1989**, *2*, 35.
- 3 Wilhelm, A.; Hedden K. *Supercritical Fluid Technology*; Penninger, J. M. L. et al. Ed.; Process Technology Proceedings, Vol. 3; Elsevier, 1985, pp 357-375.
- 4 Slomka, B.; Rutkowski, A. *Fuel Process. Technol.* **1982**, *5*, 247.
- 5 Deshpande, G. V.; Holder, G. D.; Shah, Y. T. *Ind. Eng. Chem. Process Des. Dev.* **1986**, *25*, 705.
- 6 Ross, D. S.; Blessing, J. E. *Fuel* **1979**, *58*, 433.
- 7 Ross, D. S.; Blessing, J. E. *Fuel* **1979**, *58*, 438.
- 8 Makabe, M.; Ouchi, K. *Fuel* **1981**, *60*, 327.
- 9 Amestica, L. A.; Wolf, E. E. *Fuel* **1984**, *63*, 227.
- 10 Vasilakos, N. P.; Dobbs, J. M.; Parisi, A. S. *Ind. Eng. Chem. Process Des. Dev.* **1985**, *24*, 121.
- 11 Kuznetsov, P. N.; Sharypov, V. I.; Beregovtsova, N. G.; Rubaylo, A. I.; Korniyets, E. D. *Fuel* **1990**, *69*, 911.
- 12 Zhang, C. J.; Wang, M.; McCoy, B. J. *2nd International Conference on Supercritical Fluids*; Boston, Massachusetts, May 1991, pp 332-335.
- 13 Triday, J.; Smith, J. M. *AIChE J.* **1988**, *34*, 658.
- 14 Goto, M.; Hortacsu, O.; McCoy, B. J. *Ind. Eng. Chem. Res.* **1990**, *29*, 1091.
- 15 Goto, M.; Smith, J. M.; McCoy, B. J. *Ind. Eng. Chem. Res.* **1990**, *29*, 282.
- 16 Reyes, T.; Bandyopadhyay, S. S.; McCoy, B. J. *J. Supercrit. Fluid* **1989**, *2*, 80.

- 17 Angelova, G.; Kamenski, D.; Dimova, N. *Fuel* **1989**, *68*, 1434.
- 18 Williams, J. M.; Vanderborgh, N. E.; Walker, R. D. *Coal Science and Chemistry*; Volborth, A. Ed.; Elsevier, **1987**, pp 461-471.
- 19 Levenspiel, O. *Chemical Reaction Engineering*; John Wiley & Sons, Inc., 1972, pp 483-484.
- 20 Whitehead, J. C. *The 89th National Meeting of the American Institute of Chemical Engineering*, Philadelphia, June 1980.
- 21 Lee, B. I.; Kesler, M. G. *AIChE J.* **1975**, *21*, 510.
- 22 Sommer, L. *Analytical Absorption Spectrophotometry in the Visible and Ultraviolet*. Elsevier, 1989, Chapter 6.
- 23 Bauman, R. P. *Absorption Spectroscopy*. John Wiley & Sons, Inc., 1962, Chapter VIII.
- 24 Bartle, K. D.; Mills, D. G.; Mulligan, M. J.; Amaechina, I. O.; Taylor, N. *Anal. Chem.* **1986**, *58*, 2403.

RECEIVED April 27, 1992

Chapter 30

Depolymerization Reactions of *cis*-Polyisoprene and Scrap Rubber in Supercritical Toluene

Jagdish C. Dhawan¹, Aladar F. Bencsath², and Richard C. Legendre³

¹Department of Chemical Engineering, ²Department of Biochemistry, and ³Department of Chemistry, University of South Alabama, Mobile, AL 36688

cis-Polyisoprene was thermolysed in supercritical toluene at 349°C and 13.8 MPa in a 1-liter batch autoclave. The reaction products were examined by gas chromatography-mass spectrometry. A total of 171 components including isomers were identified. The extensive cracking of the polymer results in low molecular weight aromatics mainly consisting of xylenes, alkylbenzenes, and diphenylalkanes. Similar results were observed when scrap rubber from an aircraft tire is processed in toluene under identical operating conditions.

The problem of disposing of used tires has become acute in recent years simply because the discard rate of scrap tires in the United States approaches one per person per year. Obviously, scrap tires pose an important challenge from the material and energy conservation standpoint. Pyrolysis of scrap tires continues to be an area of intense investigation(1,2,3) However, the unfavorable economics of pyrolysis has dampened prospects for commercialization.

In this chapter, we report on the GC-MS experimental results of the depolymerization of *cis*-polyisoprene in supercritical toluene. We will also discuss the results of our experiments with scrap rubber from an aircraft tire which is predominantly made of polyisoprene. These results show that depolymerization reactions under supercritical conditions indeed offer some advantages over conventional pyrolysis of scrap rubber.

Pyrolysis of *cis*-Polyisoprene

Pyrolysis of polyisoprene(4) in a high vacuum ($\sim 10^{-6}$ mmHg) begins at 300°C and is almost complete at 400°C. About 85 wt% of the resulting material is a non-volatile residue of 577 avg. molecular weight. The volatile material (~ 12 wt%

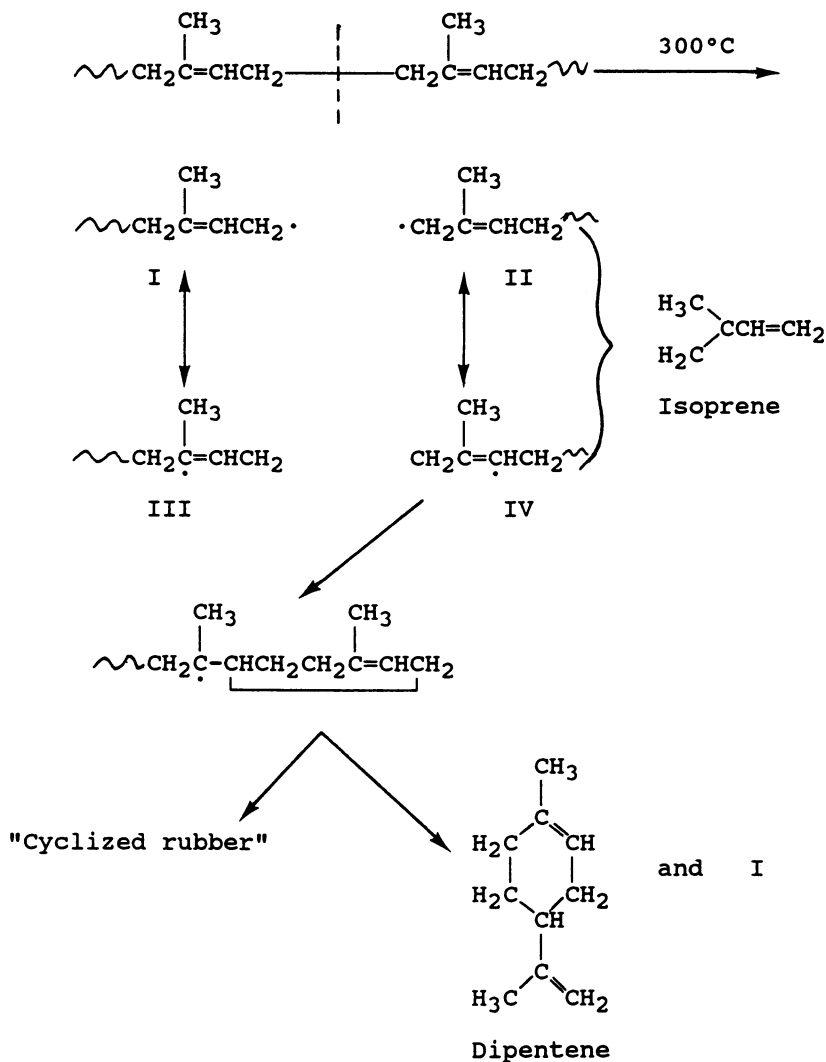
0097-6156/93/0514-0380\$06.00/0
© 1993 American Chemical Society

yield) consists of butanes, cyclopentadienes, isoprene monomer, pentenes, cyclohexadienes, hexadienes, hexenes, cycloheptadienes, heptenes, and dipentene. When natural rubber (cis-polyisoprene) is heated at 220-270°C, isoprene and its dimer, dipentene, are the main volatile products(5). During the formation of these volatile products, the molten polymer becomes more viscous and finally sets to an insoluble solid.

Sarfare et al.(6) studied thermal degradation of natural rubber in Tetralin solution at 140°C. These investigators also concluded that degradation proceeds through a random chain scission process. However, the process of degradation was followed only viscometrically to follow the decrease in the molecular weight of the starting polymer; the resulting material was not otherwise characterized. Golub (7) examined the microstructural changes produced during the thermal degradation of 1,4-polyisoprene based on infrared and NMR-spectral measurements of the residues after about 60% weight loss in the temperature range 325-400°C, and reported thermal cyclization associated with the reaction of pendant vinyl groups by Scheme A as shown below:

The use of a supercritical fluid (SCF) as a reaction medium can provide an alternative approach to lower the operating temperature of pyrolysis reactions. The lower operating temperature can minimize the formation of undesirable hydrocarbon gases and char. Improved yields and selectivities have been reported(8) in an SCF reaction medium when compared with the results obtained under pyrolysis. Koll and Metzger(9) used supercritical acetone as the reaction medium for the thermal degradation of cellulose and found higher extraction yields at temperatures lower than those used for conventional pyrolysis. Metzger et al.(10) studied thermal intermolecular organic reactions in supercritical fluid media at pressures of up to 50.7 MPa and temperatures of up to 500°C and found that alkanes were coupled to alkenes, to 1,3-dienes, and to alkynes (acetylene). Blyumber et al.(11) studied the oxidation of n-butane in both the liquid phase and an SCF-phase. The liquid-phase reaction products were predominantly acetic acid and methyl ethyl ketone, whereas the SCF-phase oxidation products were remarkably different and included formaldehyde, acetaldehyde, methyl-, ethyl-, and propyl alcohols, and formic acid. It is suggested(8) that the difference in these two product groups is related to the types of free radicals that are formed under two different reaction conditions, indicating that in the SCF-phase the butane-derived free radicals have a higher probability to further decompose into methyl radicals rather than terminating the reaction by recombining.

Pyrolysis reactions of hydrocarbon polymers can be divided into degradation (or primary) reactions and synthesis (or secondary) reactions. All degradation reactions are characterized by the cracking and dehydrogenation phenomena. In cracking reactions, paraffins decompose to one paraffin and one olefin. In dehydrogenation reactions, hydrogen is split off, causing the formation of a double bond without changing the chain length of the original paraffin. The pyrolytic cracking of a C-C or a C-H bond can take place by way of free-radical formations via homolytic decomposition or ion formation via heterolytic decomposition. It should be noted



SCHEME A

Reproduced with permission from reference 7. Copyright 1972 John Wiley & Sons.

that homolytic decomposition (free-radical formation) is energetically favored over in heterolytic decomposition, due mainly to the threefold higher bond dissociation energy.

Experimental

A schematic diagram of the equipment used is shown in Figure 1. It consists of a 1-liter capacity (1 dm^3) batch autoclave with a magnetically driven agitator (Autoclave Engineers, Inc.). The reactor is equipped with an electrical heater with temperature control, pressure gauge and product recovery system. The latter consists of a pressure let-down valve which allows release of part of the solvent from the pressurized reactor to a container at atmospheric pressure. A condenser is provided to ensure liquid recovery and gas separation.

Materials. The polymer used was cis-polyisoprene as supplied by Aldrich Chemical Co. The aircraft tire rubber was obtained from a used Goodyear tire (Flight Special II, part No. 156E 6 1-3, TSOC62b; 15 x 6.00-6). Analytical grade toluene was obtained from Fisher Scientific Co. and was 99.9% pure as determined by the vendor's GC analysis.

Procedure and Safety. The reactor was charged with 24.4 g of polymer (or 36.4 g tire rubber) and filled with toluene (~ 980 ml) at room temperature. Details of the experimental procedure have been discussed elsewhere⁽¹²⁾. For the safe operation of the reactor, polymer and liquid solvent were loaded and then compressed to the desired operating pressure of 13.8 MPa at room temperature. The compression energy stored in a liquid is several fold less than that in gases. Any air entrapped was released using bleed and vent valves before heating. During heating solvent volume was adjusted by discharging the solvent through the bleed valve so that the static pressure in the reactor could be maintained at 13.8 MPa during the entire operation. The components eluted from the chromatograph were identified by submitting the corresponding mass spectra to a library search.

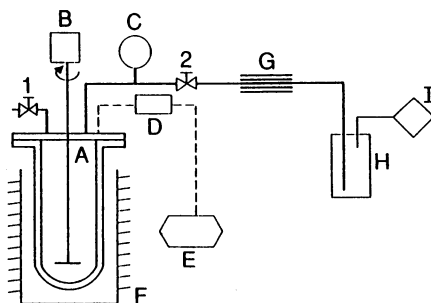


Figure 1. Schematic diagram of the experimental apparatus. (A) autoclave; (B) agitator; (C) pressure gauge; (D) temperature indicator; (E) temperature controller; (F) electric furnace; (G) cooler; (H) sample collector; (I) gas chromatograph; (1-2) high-pressure valves.
(Reprinted with permission from ref. 12. Copyright 1991 Polymer Research Associates, Inc.)

Results and Discussion

Thermolysis of Toluene Under Supercritical Conditions. We conducted the thermolysis of supercritical toluene at 343°C and 13.8 MPa for 1-h. The total ion current chromatogram displaying separated compounds is shown in Figure 2. The results of the qualitative and semi-quantitative analyses are listed in Table I. We found that about 2% of the toluene reacts and forms various products with molecular weights ranging from 78 to 182. Diphenyl, diphenylmethane, diphenylethane and their methylated analogs are the major high molecular weight compounds. The low molecular weight products include benzene, ethylbenzene and xylenes. The thermolytic reaction products of supercritical toluene at 350°C and 17 MPa for 1-h conducted in a 1-liter rocking autoclave has been reported by Kershaw(13). The yield of high boiling material was only about 0.03% in his experiment and diphenylethane was the major product. All of the compounds identified were the same as those in our work although the relative yields were different. We believe that the quantitative differences are owing to the difference in the experimental setup, method of solvent loading and the different reactor pressure (17 MPa vs 13.8 MPa).

Thermolysis of cis-Polyisoprene in Supercritical Toluene. The GC-MS chromatogram of the reaction products from cis-polyisoprene in the presence of supercritical toluene is shown in Figure 3. 171 peaks were distinguished in the chromatogram and 26 of these were found in higher abundances than 0.5% (toluene-free basis). These major components (some of them include several isomers) are shown in Table II. The minor compounds including unidentified ones represent around 12% of the mixture and are listed in Table III. As can be seen, the compounds in Table II consist of arylalkyl or diarylalkyl products. Besides a few low molecular weight (C3 to C9) aliphatics, arylalkyl and diarylalkyl are the major compounds. Diphenylmethane, methyl diphenyl and dimethyl diphenyl constitute 36% of the total products. Interestingly, about half of these diaryl compounds were also formed in the pyrolysis of pure supercritical toluene under identical experimental conditions. The amounts of benzene in both cases were comparable (7% vs 11% from pure toluene). However, there were significant differences in the concentrations of alkylated benzenes between the two experiments. Ethylbenzenes and xylenes were twice as abundant in the pure toluene experiment, and there were no detectable traces of higher alkylated benzenes. In the case of the polyisoprene experiment, the total concentration of higher alkylated benzene compounds was 23.3%. This is obviously due to the participation of the fragmented radicals from the polymer which is further supported by the insignificant amount of nonvolatile dry residue found in the reactor products (~0.6 g from the 24.4 g polymer charged). The presence of meaningful amounts of diphenyl alkanes having more than two methylene units and their alkyl-substituted analogs is additional evidence of polymer participation in the formation of these products. Further comparison of the diarylalkyl compounds reveals that the production of diphenylmethane was nearly the same in both experiments (12.3% vs 14.0% without polymer) which indicates that the dimerization of toluene is unaffected by the presence of the polymer. In contrast, tetrahydronaphthalene, dihydroindenes and their dehydrogenated derivatives

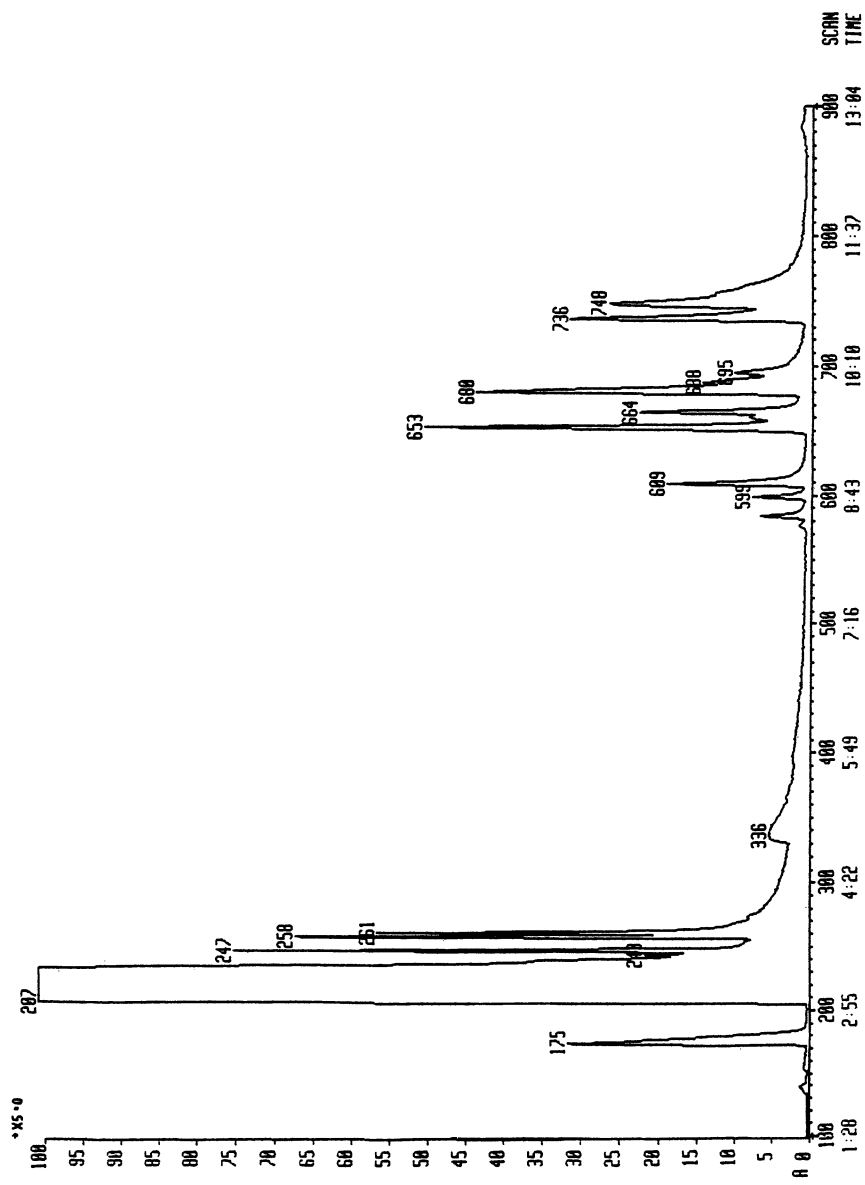


Figure 2. Total ion chromatogram of supercritical toluene reaction products at 349°C and 13.8 MPa

July 22, 2012 | <http://pubs.acs.org>
 Publication Date: December 17, 1992 | doi: 10.1021/bk-1992-0514.ch030

Table I. GC-Mass Spectral Analysis of Supercritical Toluene

Compound	Scan*	M.W. (%)**	(%)***
1 Benzene	175	78	10.9
2 Ethylcyclohexane	247	112	6.3
3 Ethylbenzene	258	106	8.0
4 Xylene	261	106	7.4
5 Diphenyl	576	154	0.2
6 2-Methyldiphenyl	584	168	1.1 0.3
7 3-Methyldiphenyl	168	1.3	
8 4-Methyldiphenyl	168	0.5	
9 2,4-Dimethyldiphenyl	599	182	1.1
10 Diphenylmethane	609	168	5.0 2.4
11 2,2-Dimethyldiphenyl	653	182	11.4
12 2,3-Dimethyldiphenyl	664	182	4.4
13 Diphenylethane	680	182	14.0 71.9
14 4-Methyldiphenylmethane	182	1.1	
15 1-Methyl-2-phenylmethylbenzene	688	182	1.6
16 1-Methyl-4-phenylmethylbenzene	695	182	1.0
17 3,3-Dimethyldiphenyl	736	182	10.3 4.8
18 4,4-Dimethyldiphenyl	748	182	17.3 1.6
Unidentified compounds	14.8		
Total		100	98.7

*(Spectrum number corresponding to the chromatographic peak of the eluting compound)

** (Toluene-free basis)

*** (Reference 13)

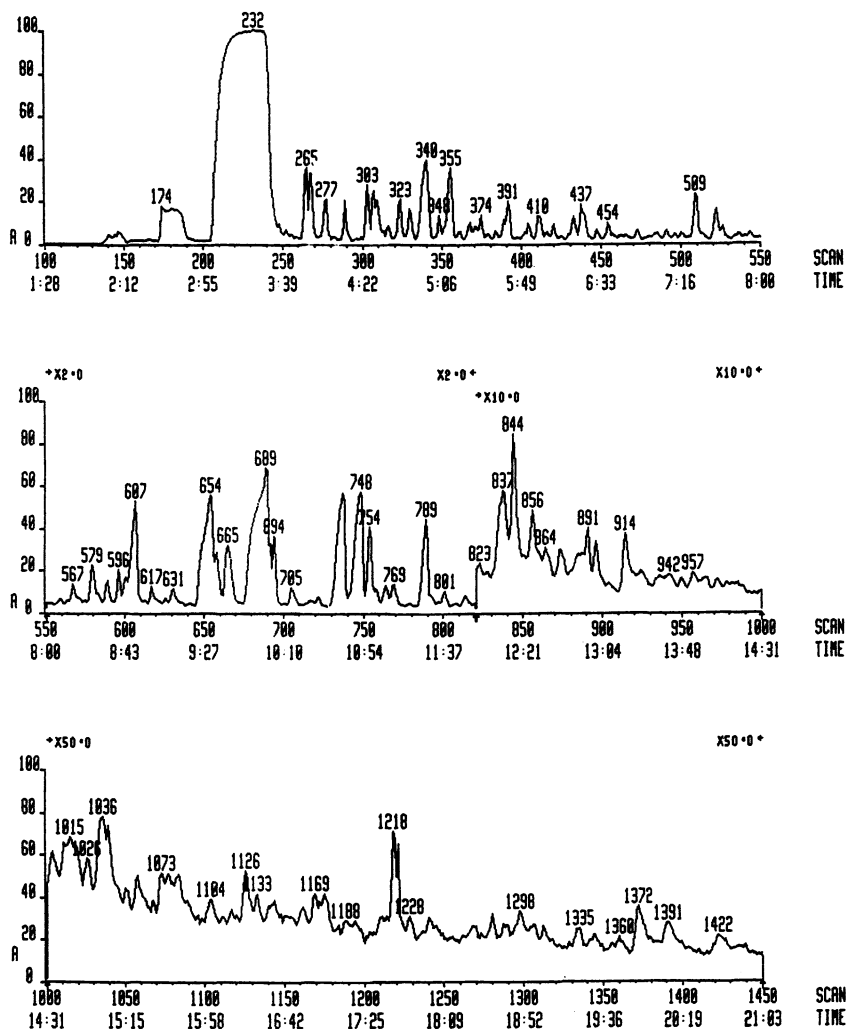


Figure 3. Total ion chromatogram of supercritical toluene-cis-Polyisoprene reaction products at 349°C and 13.8 MPa

Table II. GC-Mass Spectral Analysis of Supercritical Toluene-*cis*-Polyisoprene Reaction Products Above 0.5% Abundances

COMPOUND	Scan**	M.W.	(%)
1 Methylpropane(#137,#140,#146)*	140	58	1.5
2 Benzene	174	78	7.0
3 Xylene(#265,#267)*	267	106	5.4
4 1-Ethenyl-3-methylene-cyclopentene	277	106	1.5
5 Propylbenzene(#289,#303)*	303	120	3.3
6 Ethylmethylbenzene(#307,#313,#316)*	316	120	2.5
7 Trimethylbenzene(#309,#323)*	323	120	1.7
8 1-Methyl-4-1-methylethylbenzene (#337,#340)*	340	134	6.8
9 2-Methylstyrene(#299,#348)*	348	118	0.5
10 1,2-Diethylbenzene(#355,#361)*	361	134	3.4
11 2-Ethyl-1,4-dimethylbenzene (#367,#371,#391)*	391	134	2.6
12 2,3-Dihydro-5-methylindene(#374,#404)*	404	132	0.7
13 2,2-Dimethylpropylbenzene(#378,#410)*	410	148	1.3
14 Naphthalene	437	128	1.0
15 Dihydrodimethylindene (#424,429,432,439,482,496)*	439	146	2.3
16 3-Methylpentylbenzene(#447,#454)*	454	162	0.8
17 2-Methylnaphthalene(#509,#522)*	522	142	3.2
18 1-(2-Propenyl)naphthalene	579	168	0.8
19 Dimethylnaphthalene (#583,#589,#617,#621,#631)*	631	156	1.2
20 Diphenylethane(#681,#689)*	689	182	12.3
21 1-Methyl-2-phenylmethylbenzene	692	182	0.9
22 2-Ethylidiphenyl	694	182	0.8
23 Methylidiphenyl(#648,658)*	764	168	5.5
24 Diphenylpropane	789	196	2.3
25 Dimethyldiphenyl(#596,601,654, 665,722,737,748,#754,769,801)*	801	180	17.6
26 1-Methylfluorene(#837,#844)*	844	180	1.3
	Total		88.2

*(Includes isomers at the scan numbers shown)

** (Spectrum number corresponding to the chromatographic peak of the eluting compound)

Table III. GC-Mass Spectral Analysis of Supercritical Toluene-cis-Polyisoprene Reaction Products Below 0.5% Abundances

COMPOUND	Scan**	M.W.	(%)
1 Pentane(#154,#159)*	159	72	0.3
2 Hexane	166	84	0.3
3 Methylpentene(#162,#172)*	172	84	0.2
4 2,4-Hexadiene	192	82	0.1
5 1,2-Dimethylcyclohexene	252	106	0.1
6 Ethylcyclohexane	255	112	0.1
7 Propylcyclohexane	282	126	0.1
8 Methylstyrene	299	118	~0
9 Butylbenzene	329	134	0.1
10 1-Methyl-2-propylbenzene	351	134	0.3
11 2-Methylbutylbenzene	388	148	0.4
12 1,3-Dimethyl-5-1-methylethylbenzene	397	148	0.1
13 Diethylmethylbenzene(#383,#402)*	402	148	0.5
14 1,2,3,4-Tetrahydronaphthalene	420	132	0.4
15 1,2-Diethyl-3,4-dimethylbenzene	443	162	~0
16 Cyclopentylbenzene	457	146	0.2
17 1,3-Dimethyl-2-butenylbenzene	462	160	0.1
18 Methylphenylpentene	472	162	0.3
19 1,2,3,4-Tetrahydro-5-methylnaphthalene	485	146	0.3
20 3-Methylcyclopentylbenzene	491	160	0.3
21 Dihydro-1,1,5-trimethylindene (#465,#480,#500)*	500	160	0.4
22 1-2-Butenyl-2,3-dimethylbenzene	526	160	0.4
23 Tetrahydro-2,7-dimethylnaphthalene (#534,#540)*	540	160	0.2
24 Cyclohexylmethylbenzene(#537,#543)*	543	174	0.4
25 2,4-Dimethylcyclopentylbenzene (#559,#564)*	564	174	0.2
26 Diphenyl	567	154	0.3
27 Diphenylmethane	607	168	0.3
28 1,2,3,4-Tetrahydro-2,5,8-trimethyl naphthalene	613	174	0.1
29 1,4,6-Trimethylnaphthalene	626	170	0.1
30 1,2-Dihydro-1,1,6-trimethylnaphthalene	636	172	~0
31 2,3,6-Trimethylnaphthalene	705	170	0.4
32 1-Methyl-7(1-methylethyl)naphthalene	717	184	0.1
33 1,2-Dimethyl-4-(phenylmethyl)-benzene	827	196	~0
34 1-Methyldiphenylethane	856	194	0.2

Continued on next page

Table III. *Continued*

COMPOUND	Scan**	M.W.	(%)
35 Diphenylbutane (#814,#873)*	873	210	0.4
36 1-Methyl-3-(4-methylphenyl)-methylbenzene	884	196	0.1
37 2-Ethylidiphenyl	887	182	0.1
38 Phenylmethylphenylbutane	891	224	0.2
39 Phenylbutylphenylmethane	896	224	0.1
40 Phenanthrene	914	178	0.4
41 1-Methyl-3-(2-methylphenyl)-methylbenzene	936	194	0.1
42 2,3-Dihydro-1-methyl-3-phenylindene	942	208	0.1
43 1,1'-(3-Methyl-1-propene-1,3-diyl)bisbenzene	950	208	~0
44 2-Phenylnaphthalene	972	204	0.1
45 2-Methylphenanthrene(#1036,#1039)*	1039	192	0.2
46 Dimethylphenanthrene (#1077,1126,1133,1144)*	1144	206	0.1
47 2-Phenylmethylnaphthalene	1169	218	~0
Unidentified compounds			2.6
Total			11.8

* (Includes isomers at the scan numbers shown)

** (Spectrum number corresponding to the chromatographic peak of the eluting compound)

are only found when polymer was present in the reactor. Naphthalene can be produced by the pyrolytic dehydrogenation of butylbenzene(14). Similar dehydrogenation mechanisms of butyl- or higher substituted alkylbenzenes can be considered behind the formation of Tetralin and methylindenes.

Figure 4 shows the GC-MS chromatogram obtained from an experiment with scrap rubber of an aircraft tire in supercritical toluene. The elution pattern of the products is remarkably similar to those obtained in the model experiment with *cis*-polyisoprene. The products corresponding to the chromatographic peaks were identical in these two chromatograms. The weight of filtered and dried carbon residue from extraction of 36.4g scrap aircraft tire rubber was 13.2g (36.3%). It should be noted that the similarities in the results (Figure 2 and 3) exist in spite of the fact that in the scrap rubber the polyisoprene is present in a vulcanized (cross-linked) state.

In conclusion, our results demonstrate that under supercritical conditions, the reaction of toluene with *cis*-polyisoprene results in an extensive cracking of polymer. The pool of free-radicals thus generated undergo several types of radical combination reactions with the radicals from toluene such that the stabilized products are low molecular weight aromatic compounds. Secondary reactions leading to

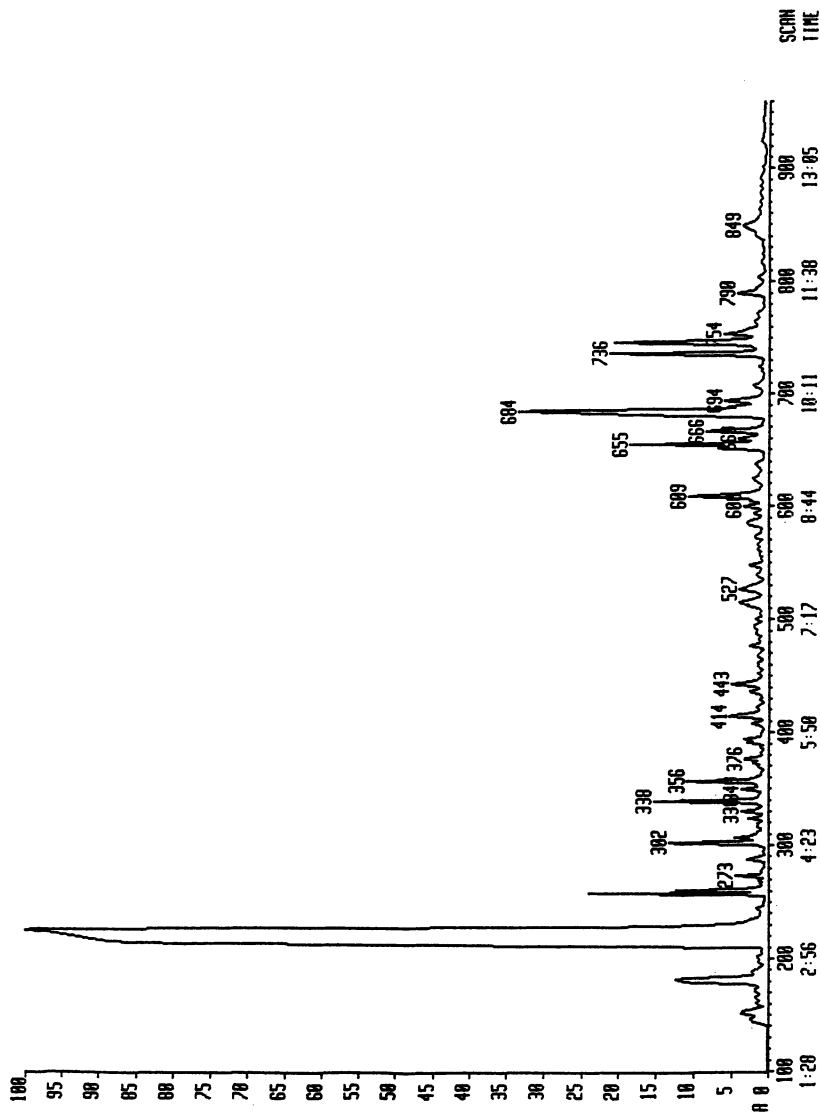
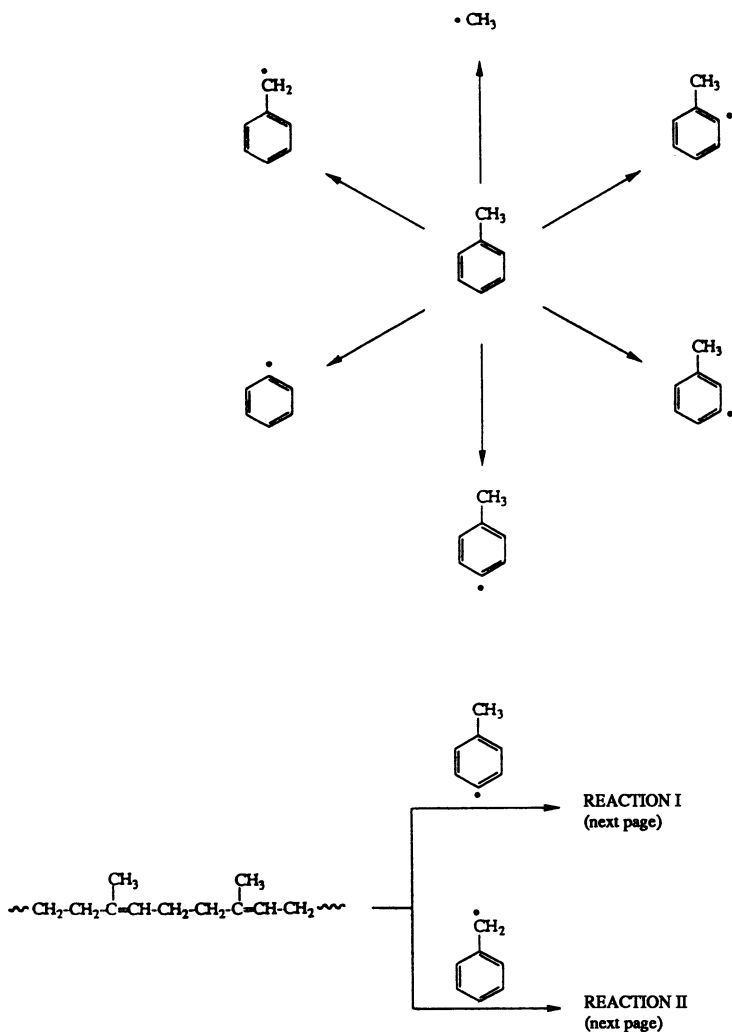
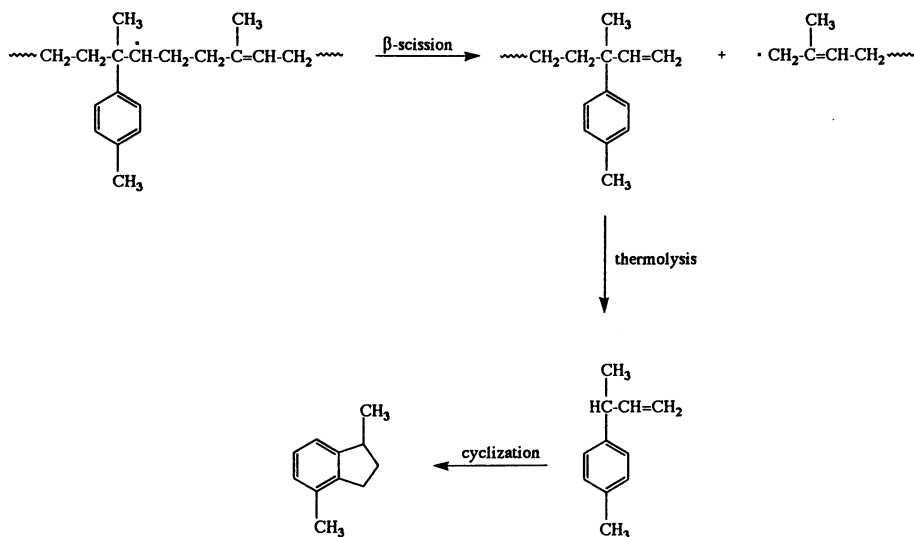


Figure 4. Total ion chromatogram of supercritical toluene-aircraft tire rubber reaction products at 349°C and 13.8 MPa

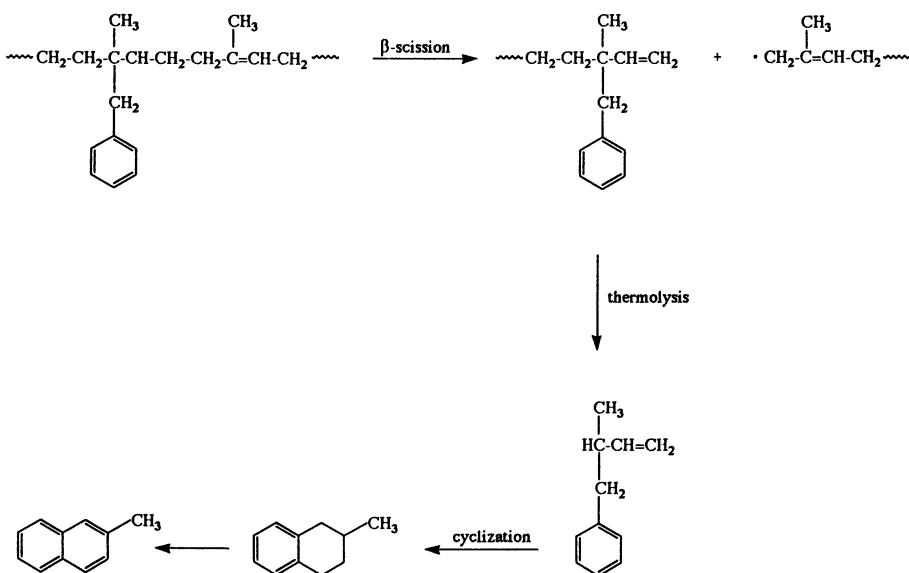
oligo- and polycondensates are remarkably suppressed under the experimental conditions of 343°C temperature and 13.8 MPa pressure. As a result, less than 1% of the product consists of three-ring fused aromatics such as phenanthrene and its alkylated derivatives. It is recognized that the polymer in the supercritical phase apparently undergoes several types of free-radical rearrangement reactions such as chain-initiation, hydrogen abstraction, free-radical decomposition and concerted-molecular reactions. Some pathways likely to result in the type of reaction products involving the radicals from toluene and from the polymer are postulated below. In these examples, a toluene radical attacks a double bond in the isoprene chain forming a C-C bond (Markovnikov's rule). A subsequent β -scission, thermolysis and cyclization results in the formation of: (I) dihydromethylindene isomers and (II) methylnaphthalene isomers.



REACTION I



REACTION II



ACKNOWLEDGMENT

The authors gratefully acknowledge the assistance of Mr. L.E. McCormick of the College of Engineering for the building of the experimental apparatus.

Literature Cited

1. Williams, P. T.; Besler, S.; Taylor, D. T. *FUEL*, **1990**, *2*, pp 1474-1479
2. Lucchesi, A.; Maschio, G.; *Conservation & Recycling*, **1983**, *6*, pp 85-90
3. Kawakami, S.; Inoue, K.; Tanaka, H.; Sakai, T. *ACS Symp. Ser.*, **1980**, *130*, pp 557-572
4. Madorsky, S. L.; Straus, S.; Thompson, D.; Williamson, L. *J. Research NBS*, **1949**, *42*, pp 499-514
5. Grassie, N. *Chemistry of High Polymer Degradation Processes*; Butterworths Scientific Publications, London, **1956**, p 83
6. Sarfare, P. S.; Bhatnagar, H. L.; Biswas, A.B. *J. Appl. Polym. Sci.*, **1963**, *7*, p 2199
7. Golub, M. A.; Gargiulo, R. J.; *Polymer Letters*, **1972**, *10*, pp 41-49
8. McHugh, M.; Krukoni, V. *Supercritical Fluid Extraction-Principles and Practice*, Butterworths, Stoneham, Massachusetts, **1986**, pp 199-215
9. Koll, P.; Metzger, J. *Angew. Chem. Int. Ed. Engl.*, **1978**, *17*, p 754
10. Metzger, J. O.; Hartmans, H.; Malwitz, D.; Koll, P. *In Thermal Organic Reactions in Supercritical Fluids*; Chemical Engineering at Supercritical Conditions, p 515 Paulaitis, M. E.; Penninger, J. M. L.; Gray, R. D.; Davidson, P., Eds.; Ann Arbor Science, Ann Arbor, Michigan, **1983**
11. *The Oxidation of Hydrocarbons in the Liquid Phase*; Emanuel, N. M.; McMillan, New York, **1985**
12. Dhawan, J. C.; Legendre, R. C.; Bencsath, A. F.; Davis, R. M. *J. Supercrit. Fluids*, **1991**, *4*, pp 160-165
13. Kershaw, J. R. *So. Af. J. of Chem.*, **1978**, *31*, pp 15-18

RECEIVED June 12, 1992

Author Index

- Abraham, Martin A., 338
Akgerman, Aydin, 294
Bencsath, Aladar F., 380
Bennett, Karen L., 228
Brennecke, Joan F., xi,1,201
Buelow, S., 314
Carleson, Thomas E., 66
Chandra, Sirish, 66
Chen, Peishi, 305
Cheung, H. Michael, 271
Chimowitz, E. H., 134,281
Cochran, Henry D., 149,188
Colgate, S. O., 121
Coppom, Joseph M., 220
Debenedetti, Pablo G., 238
de Fernandez, M. E. Pozo, 74
Dell'Orco, P. C., 314
de Roo, J. L., 46
de Swaan Arons, J., 46
Dhawan, Jagdish C., 380
Eckert, Charles A., 220,228
Ekart, Michael P., 228
Elliott, J. Richard, Jr., 271
Foster, Neil R., 34
Fulton, John L., 158,175,258
Gloyna, Earnest F., 305,314
Gude, Michael T., 10
Gurdial, Gurdev S., 34
Hamilton, B. L., 92
Hochgeschurtz, T., 347
Houser, Thomas J., 327
Huang, Shawn S., 66
Hutchenson, K. W., 347
Jennings, David W., 10
Kao, C.-P. Chai, 74
Kiran, Erdogan, xi,1,104
Kisler, S. H., 55
Knutson, Barbara L., 220
Lee, L. L., 188
Legendre, Richard C., 380
Li, Lixiong, 305
Lim, Gio-Bin, 238
Liu, G.-Z., 347
Liu, Xu, 327
Luks, K. D., 55
Matthews, M. A., 92
McCoy, B. J., 363
Mullins, J. C., 347
Munoz, F., 134
Patton, C. L., 55
Paulaitis, M. E., 74
Peters, C. J., 46
Pfund, David M., 149,158
Prud'homme, Robert K., 238
Puyvelde, F. Van, 281
Roebbers, J. R., 347
Rush, Brenda J., 338
Sen, Yasar L., 104
Shah, Y. T., 338
Shenai, V. M., 92
Sivaraman, A., 121
Smith, J. M., 363
Smith, Richard D., 158,175,258
Straver, E. J. M., 46
Teja, Aryn S., 10
Thies, M. C., 347
Tilly, Kevin D., 34
Tom, Jean W., 238
Tomasko, David L., 220
Tsao, Chun-Cheng, 327
Van Rompay, P., 281
Wai, Chien, 66
Wai, Larry, 66
West, Barry, 220
Windsor, Wendy, 220
Yee, Geary G., 175
Yeo, Sang-Do, 294
Yun, S. L. Jimmy, 34
Zemanian, Thomas S., 258
Zhang, Chunjie, 363
Zhou, Ying, 327

Affiliation Index

- Clemson University, 347
 Delft University of Technology, 46
 Georgia Institute of Technology, 10,220,228
 K. U. Leuven, 281
 Los Alamos National Laboratory, 314
 Oak Ridge National Laboratory, 149,188
 Pacific Northwest Laboratory,
 149,158,175,258
 Princeton University, 238
 Texas A&M University, 294
 The University of Akron, 271
 University of California—Davis, 363
 University of Delaware, 74
 University of Florida, 121
 University of Idaho, 66
 University of Illinois, 220
 University of Illinois at Urbana–
 Champaign, 228
 University of Maine, xi,1,104
 University of New South Wales, 34
 University of Notre Dame, xi,1,201
 University of Oklahoma, 188
 University of Rochester, 134,281
 University of South Alabama, 380
 The University of Texas at Austin, 305,314
 The University of Tulsa, 338,55
 University of Wyoming, 92
 Western Michigan University, 327

Subject Index

A

- Acetone–carbon dioxide systems, *See*
 Phase behavior of supercritical fluid–
 entrainer systems
 Acoustic cavity measurements, thermophysical
 properties of natural gas mixtures from
 speeds of sound, 121–132
 Adsorption from supercritical fluids
 Boltzmann factor for wall–particle
 interactions, 192,193*f*
 calculations for inhomogeneous
 density–correlation function
 relationship determination, 189–191
 competitive adsorption between wall and
 repulsive or attractive solute,
 196,197–198*f*
 distance from wall vs. radial
 distribution, 198,199*f*
 examples, 188
 experimental objective, 188
 hard wall, 194–195*f*
 Henderson–Plischke–Sokolowski theory,
 188–189
 Lennard–Jones wall, 194,195–199*f*
 parameters of interaction potentials,
 191,193,194*t*
 range vs. wall–particle pair correlation
 function, 192–193*f*
 Adsorption from supercritical fluids—
Continued
 temperature vs. density near hard wall,
 194–195*f*
 test calculations for correlation
 functions, 191,192–193*f*
 wall strength vs. density near
 Lennard–Jones wall, 194,195–196*f*
 Aerogels, 271
 Aggregation of methanol in supercritical
 fluids
 average increment in binding energy for
n-mer formation, 170,172*f*
 calculated vs. experimental monomer
 concentrations, 165,167*t*
 carbon dioxide model, 161
 case descriptions, 162–163
 distribution of methanol polymer sizes
 in supercritical CO₂ and ethane, 165,167*f*
 experimental description, 159,162
 hydrogens with methanol oxygens, 163,164*f*
 interaction site models, 159–160
 intermolecular site–site pair correlation
 functions for methanol
 parameter estimation using geometric
 combining rules, 161
 potential models, 160–161
 pressure vs. methanol polymer size
 distribution in supercritical CO₂, 170,172*f*

Affiliation Index

- Clemson University, 347
 Delft University of Technology, 46
 Georgia Institute of Technology, 10,220,228
 K. U. Leuven, 281
 Los Alamos National Laboratory, 314
 Oak Ridge National Laboratory, 149,188
 Pacific Northwest Laboratory,
 149,158,175,258
 Princeton University, 238
 Texas A&M University, 294
 The University of Akron, 271
 University of California—Davis, 363
 University of Delaware, 74
 University of Florida, 121
 University of Idaho, 66
 University of Illinois, 220
 University of Illinois at Urbana–
 Champaign, 228
 University of Maine, xi,1,104
 University of New South Wales, 34
 University of Notre Dame, xi,1,201
 University of Oklahoma, 188
 University of Rochester, 134,281
 University of South Alabama, 380
 The University of Texas at Austin, 305,314
 The University of Tulsa, 338,55
 University of Wyoming, 92
 Western Michigan University, 327

Subject Index

A

- Acetone–carbon dioxide systems, *See*
 Phase behavior of supercritical fluid–
 entrainer systems
 Acoustic cavity measurements, thermophysical
 properties of natural gas mixtures from
 speeds of sound, 121–132
 Adsorption from supercritical fluids
 Boltzmann factor for wall–particle
 interactions, 192,193*f*
 calculations for inhomogeneous
 density–correlation function
 relationship determination, 189–191
 competitive adsorption between wall and
 repulsive or attractive solute,
 196,197–198*f*
 distance from wall vs. radial
 distribution, 198,199*f*
 examples, 188
 experimental objective, 188
 hard wall, 194–195*f*
 Henderson–Plischke–Sokolowski theory,
 188–189
 Lennard–Jones wall, 194,195–199*f*
 parameters of interaction potentials,
 191,193,194*t*
 range vs. wall–particle pair correlation
 function, 192–193*f*
 Adsorption from supercritical fluids—
Continued
 temperature vs. density near hard wall,
 194–195*f*
 test calculations for correlation
 functions, 191,192–193*f*
 wall strength vs. density near
 Lennard–Jones wall, 194,195–196*f*
 Aerogels, 271
 Aggregation of methanol in supercritical
 fluids
 average increment in binding energy for
n-mer formation, 170,172*f*
 calculated vs. experimental monomer
 concentrations, 165,167*t*
 carbon dioxide model, 161
 case descriptions, 162–163
 distribution of methanol polymer sizes
 in supercritical CO₂ and ethane, 165,167*f*
 experimental description, 159,162
 hydrogens with methanol oxygens, 163,164*f*
 interaction site models, 159–160
 intermolecular site–site pair correlation
 functions for methanol
 parameter estimation using geometric
 combining rules, 161
 potential models, 160–161
 pressure vs. methanol polymer size
 distribution in supercritical CO₂, 170,172*f*

- Aggregation of methanol in supercritical fluids—*Continued*
 simulation method, 161–162
 site–site potential definition, 160
 solute–solute aggregation numbers, 163,164f
 solute–solute neighbor numbers, 163,165,166f
 solvent neighbor numbers/bulk solvent density vs. distance from hydrogen/solvent end group hydrogen size parameter, 165,166f
 transferable intermolecular potential model, 160–161
 typical oligomers in CO₂ and ethane, 168–171
 use of molecular simulations, 159
- Aircraft tire, thermolysis in supercritical toluene, 390,391f
- Alcohol–carbon dioxide systems, *See* Phase behavior of supercritical fluid–entrainer systems
- Alcohol–solute interactions in supercritical carbon dioxide, fluorescence spectroscopy double proton transfer between alcohol and 7-azaindole to form tautomer, 222,223f
 exciplex formation mechanism, 222,223f,224
 exciplex to monomer intensity ratio vs. cosolvent concentration, 224,225f
 experimental procedure, 220
 fluorescence emission vs. cosolvent concentration, 222,223f
 fluorescence shift dependence on cosolvent concentration vs. solvent, 224,225f
 lack of cage effects, 226
 use of 7-azaindole as probe, 220
- Alcohols, simple, hydrogen bonding in supercritical fluids, 175–184
- Alkane–carbon dioxide systems, *See* Phase behavior of supercritical fluid–entrainer systems
- Alkanol–carbon dioxide mixtures, *See* High-pressure vapor–liquid equilibria in carbon dioxide–1-alkanol mixtures
- Anthracene, cosolvent effect, 232,233f
- Aqueous slurries, supercritical extraction of organic components, 294–304
- Attractive mixtures, definition, 160
- Average fluid density, definition, 340
- 7-Azaindole, use as sensitive probe of solvent structure, 221
- B**
- Balance entropy of solute molecule environment, definition, 145
- Benzaldehyde, heteroatom removal by supercritical water, 329–331
- Binary interaction coefficients, calculation, 32
- Binary mixtures of near-critical propane and triglycerides, three-phase liquid–liquid–vapor behavior, 47–53
- n*-Butane, viscosity of polymer solutions, 104–119
- 1-Butanol–carbon dioxide mixtures, *See* High-pressure vapor–liquid equilibria in carbon dioxide–1-alkanol mixtures
- C**
- Capacity factor definition, 229
 density, temperature, and pressure relationships, 284–285
 modeling, 284
- Carbon dioxide aggregation of methanol, 158–172
 supercritical, alcohol–solute interaction studies, fluorescence spectroscopy, 220–226
 use as near-critical solvents, 47
- Carbon dioxide–1-decanol–*n*-tetradecane mixture, multiphase equilibrium behavior, 55–64
- Carbon dioxide model of Murthy, Singer, and McDonald, description, 161
- Catalyst life, supercritical fluid effect, 203
- Chemical potential of ternary supercritical fluid mixtures cosolvent effect, 153–154,156f
 density effect, 153–154
 pair correlation functions of solvent and cosolvent molecules with solute, 154,155f
 parameters, 153
 pressure effect, 153–154
 previous research, 149
 theoretical methods for calculation, 149–150
 theory, 150–153,155f

- Chemical potential of ternary system, definition, 144
- Chemical transformations, description, 104
- 1-Chlorohexane, heteroatom removal by supercritical water, 331–332
- Chromatographic applications, example, 8
- Chromatographic separations, optimum operating conditions, 281
- Chromatographic technique to study specific interaction effects in supercritical fluid solutions
- advantages, 228,230
 - capacity factor, 229
 - cosolvent effects, 231–234
 - experimental procedure, 231–232
 - fugacity coefficients, 229–231,233f
 - importance of cosolvent effect measurement, 232,235
 - previous research, 228–229
 - solvent effect for 2-naphthol in ethane relative to that in CO₂, 232,234f
 - theory, 229–231,233f
- Clustering
- description, 135
 - diffusion effect, 92–102
- Coal
- phases, 365
 - supercritical fluid extraction, *See* Supercritical fluid extraction of coal
- Coal liquefaction, mechanistic model, 364
- Coal-processing applications, example, 8
- Competitive energetic and entropic effects
- describing solvation in near-critical solutions
 - competition between energetic and entropic effects, 142–144
 - development of local properties to describe solvation, 135–142
 - experimental description, 135
 - local density enhancements, 139,140f
 - local entropy definition, 139,141–142
 - local properties for ternary and higher order systems at finite compositions, 144–145
 - radial evolution of chemical potential function, 138t,140f
- Composition, critical, behavior of supercritical fluid–entrainer systems, 36
- Compressibility, determination, 68
- Concentration, viscosity effect for polymer solutions in near- and supercritical fluids, 113,116–118
- Controlled release of drugs, applications of supercritical fluids, 239–255
- Corrosion products, separation from supercritical water oxidation processes, 323,325
- Cosolvent, chemical potential effect, 153–154,156f
- Cosolvent effect, chromatographic measurement technique, 228–235
- Critical composition, behavior of supercritical fluid–entrainer systems, 36
- Critical point of pure substances and mixtures of defined composition, use to construct phase diagrams, 35–36
- Critical pressure
- behavior of supercritical fluid–entrainer systems, 36
 - estimation, 68
- Critical properties of mixtures, importance, 36
- Critical temperature
- behavior of supercritical fluid–entrainer systems, 36
 - estimation, 68
- Critical volume, estimation, 68
- Current state of supercritical fluid science and technology
- application areas, 7–9
 - determination and correlation of transport properties, 5–6
 - expanding interest, 2
 - increase in applications, 2–3
 - investigation and modeling of molecular interactions and local fluid structure, 6–7
 - measurement and prediction of phase behavior, 3–5
 - reasons for using binary and multicomponent fluids, 3
 - shift from single-processing fluids to binary and multicomponent fluids, 2
- D
- 1-Decanol–*n*-tetradecane–carbon dioxide mixture, multiphase equilibrium behavior, 55–64
- Decay of fluorescence, equation, 259
- Degradation reactions of hydrocarbon polymers, characteristics, 381

Density

- chemical potential effect, 153–154
- viscosity effect for polymer solutions in near- and supercritical fluids, 111,113–116

Density programming

- simulation for supercritical fluid chromatography, 285–287*f*
- velocity profiles for supercritical fluid chromatography, 283–284

Depolymerization reactions of

- cis*-polyisoprene and scrap rubber in supercritical toluene apparatus, 383*f*
- experimental procedure, 383
- pathways, 392–394
- thermolysis of aircraft tire in supercritical toluene, 384,391*f*
- thermolysis of *cis*-polyisoprene in supercritical toluene, 384,387*f*,388–390*t*
- thermolysis of toluene under supercritical conditions, 384–386*t*

Diffusion, examples of effect on reactions in supercritical fluids, 208–209**Diffusion coefficients, determination and correlation, 5****Diffusion in liquid and supercritical fluid mixtures**

- accuracy of data, 96–97
 - clustering effect on phase equilibria, 94
 - diffusion coefficients for benzoic acid, 98–102
 - diffusion coefficients for phenanthrene, 98,100–102
 - diffusion coefficients in acetone and acetone–methanol, 95,97*t*
 - diffusion coefficients in supercritical CO₂ and CO₂–methanol, 95,96*t*
 - entrainer effect on phase equilibria, 92
 - experimental description, 92–93,95
 - methanol effect, 97–98
 - methods for correlating diffusivities, 93–95
 - molecular weight effect, 97
 - precision of data, 95
 - sources of experimental error, 95–96
 - standard deviations for data, 95
 - suitability of hard-sphere theory for correlating diffusivities, 98
- Diffusion rates, supercritical fluid effect, 202–203,204*f***

Diverging part of residual partial molar enthalpy, definition, 136–137**Diverging part of residual partial molar entropy, definition, 136–137****Drugs, applications of supercritical fluids in controlled release, 239–255****Dynamic fluorescence quenching in reverse**

- microemulsions in propane apparatus, 260,262*f*
- bimicellar water core exchange rate constant, 267–269
- data fitting procedure, 261
- experimental procedure, 258,260–265,267
- fluorescence decay, 261,263–264*f*
- fluorescence decay equation, 259
- fluorescent probe selection, 259
- micelle water core radius, 259
- probe fluorescence lifetime vs. inverse temperature, 261,262*f*
- probe lifetime parameters, 261*t*
- temperature effect, 261,265*f*,267
- unquenched probe fluorescence, 261,263*f*
- water core radius, 265–267

E**Effective dispersion coefficient, definition, 97****Enskog–Thorne diffusion coefficient, definition, 94****Entrainer(s)**

- definition, 36
- diffusion effect, 92–102
- function, 36

Entrainer–supercritical fluid systems, phase behavior, 35–45**Environmental remediation applications, examples, 8–9****Equation of state, Peng–Robinson, 67****Equation of state analysis of phase behavior**

- for water–surfactant–supercritical fluid mixtures
- data reduction, 77–88
- experimental description, 74
- key element, 75–76
- liquid density for surfactant, 77,78*t*
- measured and calculated closed loop liquid–liquid miscibility gap for water–surfactant binary mixtures, 86,87*f*

- Equation of state analysis of phase behavior
for water–surfactant–supercritical fluid
mixtures—*Continued*
measured and calculated phase compositions
for H₂O–CO₂ binary mixtures, 79,80f
measured and calculated pressure–
composition diagrams for vapor– and
liquid–liquid equilibrium for CO₂–
surfactant binary mixtures, 79,85f,86
measured and calculated vapor–liquid
equilibrium pressure–composition
diagrams for CO₂–surfactant
binary mixtures, 79,83–84f
measured vapor–liquid equilibrium
pressures and liquid compositions for
CO₂–surfactant mixtures, 79,81t,82f
measured vapor–liquid equilibrium
pressures and liquid compositions for
surfactant–water mixtures, 79,81t
predicted phase diagrams, 86,89–90f
pressure effect, 75
regressed parameters for CO₂ binary
mixtures, 78t,79
temperature dependence of KB₁₂ parameter
for water–surfactant binary mixtures, 86,88f
thermodynamic model, 76–77
vapor pressures for surfactant, 77,78t
Ethane, aggregation of methanol, 158–172
Ethanol–carbon dioxide mixtures, *See* High-
pressure vapor–liquid equilibria in carbon
dioxide–1-alkanol mixtures
Ethyl benzilate, heteroatom removal by
supercritical water, 332,333–334t
Excess number of solvent molecules that
surround a solute, definition, 160
Expansivity, definition, 251
Extraction applications, examples, 8
- F**
- Fluid density, average, definition, 340
Fluorescence quenching in reverse
microemulsions in propane, dynamic,
See Dynamic fluorescence quenching in
reverse microemulsions in propane
Fluorescence spectroscopy, alcohol–solute
interactions in supercritical CO₂, 220–226
Fourier transform IR spectroscopy,
measurement of hydrogen bonding of
simple alcohols in supercritical fluids, 175
- Fugacity
calculation, 296
definition, 295–296
Fugacity coefficient, determination, 67–68
Fugacity coefficient of solute, 229
- G**
- Gas antisolvent crystallization
advantages, 241
applications, 242
description, 240
difficulties with water, 252
production of micron-sized protein
particles, 251–252,253–254f
Gas chromatography, temperature
programming, 281
Gas density effect on holdup in
supercritical fluid bubble column
CO₂ density effect on CO₂ holdup vs.
superficial velocity, 342,344,345f
CO₂ holdup vs. CO₂ density, 340,341f,342
experimental system, 339–340,341f
previous research, 339
quality of correlation in prediction of
high-density CO₂ holdup, 342–345
relationship to fluid density, 340
Gas mixtures
natural, thermophysical properties from
speeds of sound derived from
acoustic cavity measurements, 121–132
need for property prediction, 121
Global kinetic models for wet oxidation of
organic compounds in subcritical and
supercritical water
examples, 306,307t
generalized model, 306
rate-controlling reaction intermediates,
306,308–309,310t
Gradient programming, chromatographic
applications, 281
Group contribution method for solubility
estimation of hydrocarbon solutes in
supercritical carbon dioxide
comparison of estimated interaction
parameter values to literature values,
69,70t
group contribution to interaction
parameter, 68,69t
importance, 66–67

Group contribution method for solubility estimation of hydrocarbon solutes in supercritical carbon dioxide—*Continued*
 interaction parameter vs. cholesterol solubility, 70,72f
 interaction parameter vs. phenanthrene solubility, 70,71f
 pressure vs. cholesterol solubility, 70,72f
 pressure vs. phenanthrene solubility, 68,71f
 theory, 67–68

H

Hard-sphere theory for correlating diffusivities, representation, 94
 Hard wall, adsorption from supercritical fluids, 194–195f
 Henderson–Abraham–Barker integral equation theory, description, 188–189
 Henderson–Plischke–Sokolowski integral equation theory, description, 189
 Heteroatom removal from organic compounds by supercritical water
 benzaldehyde, 329,330t,331
 catalyst concentrations, 329
 1-chlorohexane, 331,332
 ethyl benzilate, 332,333–334t
 experimental procedure, 328–329
 phenylpiperidine, 335,336t
 phenylpyridine, 335,336t
 quinuclidine, 332,335t
 trihexylamine, 333–335
 High-pressure vapor–liquid equilibria in carbon dioxide–1-alkanol mixtures
 apparatus, 15,16f
 applications, 12
 CO₂–1-alkanol liquid-phase compositions, 22,23–24f
 CO₂–1-alkanol vapor-phase compositions, 22,24,26f
 CO₂–1-butanol system critical locus–phase envelope, 27,28f
 CO₂–1-butanol system vapor–liquid equilibria, 20,21f
 CO₂–1-butanol system vapor–liquid equilibrium correlation, 31f,32
 CO₂–ethanol system critical locus–phase envelope, 27,28f
 CO₂–ethanol system vapor–liquid equilibria, 17,18–19f

High-pressure vapor–liquid equilibria in carbon dioxide–1-alkanol mixtures—*Continued*
 CO₂–ethanol system vapor–liquid equilibrium correlation, 30f,32
 CO₂–higher 1-alkanol system vapor–liquid equilibria, 20,22
 CO₂–methanol system vapor–liquid equilibria, 17
 CO₂–1-pentanol system critical locus–phase envelope, 27,30f
 CO₂–1-pentanol system vapor–liquid equilibria, 20,23f
 CO₂–1-pentanol system vapor–liquid equilibrium correlation, 31f,32
 CO₂–1-propanol system, vapor–liquid equilibria, 17,20,21f
 CO₂ solubility measurements, 12,14t,15
 CO₂–water liquid-phase measurements, 15,16f
 CO₂–water vapor-phase measurements, 15,17f
 critical behavior, 25,27t,28f,30f
 equation of state modeling, 27,29t,32
 experimental procedure, 15
 modeling, 27,29–32
 objective, 15
 slopes of critical lines at infinite dilution, 25,27t
 vapor–liquid equilibria measurements, 12,13t,15
 Holdup in supercritical fluid bubble column, gas density effect, 338–345
 Holdup of gas in liquid, fluid property and gas density effects, 338–339
 Hydrocarbon solutes in supercritical carbon dioxide, solubility estimation using group contribution method, *See* Group contribution method for solubility estimation of hydrocarbon solutes in supercritical carbon dioxide
 Hydrodynamic theory for correlating diffusivities
 Stokes–Einstein equation, 93
 Wilke–Chang equation, 93–94
 Hydrogen-bonded aggregate, formation in supercritical fluids, 175
 Hydrogen-bonded clusters, studies, 158
 Hydrogen-bonding compounds
 aggregate formation in supercritical fluids, 158
 importance of solvent effects on aggregation, 159

Hydrogen bonding of alcohols in apolar liquid solvents, spectroscopic studies, 176

Hydrogen bonding of simple alcohols in supercritical fluids

aggregation number determination, 183,185*t*,186*f*

alkanol properties, 181,182*t*,183

experimental procedure, 176–178

factors affecting hydrogen-bonding equilibrium, 183–184

fraction of total monomeric alcohol in ethane and CO₂, 180–181,182*f*

methanol dipole moment vs. aggregation, 181,183

mole fraction of methanol-*d* vs. amount of hydrogen bonding in solution, 178,179*f*

monomer concentration vs. total mole fraction of alcohol in CO₂, 179,180*f*

monomer concentration vs. total mole fraction of alcohol in ethane, 179–180,181*f*

multiple equilibria model of aggression, 183–184

phase behavior of methanol-*d* in CO₂, 183,185*f*

size of aggregate, 176

I

Interaction parameter

definition, 69

group contributions, 69*t*

measurement, 68–69

Interaction site models, pair potential, 159

Isopropyl alcohol–CO₂ systems, *See* Phase behavior of supercritical fluid–entrainer systems

Isotropic pitch

potential application, 347

problems with production of mesophase pitch, 347

K

Kinetics model for wet oxidation of organic compounds in subcritical and supercritical water

example for category I organic compounds, 309–311

example for chlorine-containing organic compounds, 311

Kinetics model for wet oxidation of organic compounds in subcritical and supercritical water—*Continued*

example for nitrogen-containing organic compounds, 311

existing models, 306–308

kinetic parameters for rate-controlling intermediates, 309,310*t*

simplified reaction schemes, 308–309

Kinetics of supercritical extraction of coal apparatus, 367,368*f*

calibration curves at different

temperatures, 369,370*f*

comparison of kinetics data for *tert*-butanol and toluene extraction, 377

experimental conditions and extraction conversions, 371*t*

experimental procedure, 367,369

experimental runs, 371–375

extractable compound concentration vs. temperature, 375–377

extraction curves vs. temperature, 371,372–373*f*

kinetics parameters, 374*t*,375

model predictions, 374–375

monitoring of extract, 369–371

previous research, 363–364

reaction rate determination, 365–367

temperature effect on concentration vs. absorbance plots, 369–371

temperature-programmed experimental run, 371,373*f*

temperature vs. reaction rates, 375

theory, 364–367

two-step temperature-programmed experimental run, 371,374,375*f*

L

Large-scale cosolvent separations, lack of applications, 228

Lennard–Jones wall, adsorption from supercritical fluids, 194,195–199*f*

Light scattering, study of polymer network formation in supercritical fluids, 271–280

Liquid chromatography, gradient elution, 281

Liquid diffusion, 92–102

- Liquid–liquid–vapor three-phase behavior in binary mixtures of near-critical propane and triglycerides, *See* Three-phase liquid–liquid–vapor behavior in binary mixtures of near-critical propanes and triglycerides
- Local composition, supercritical fluid effect, 207
- Local composition of cosolvent, evidence for enhancement, 220
- Local density, supercritical fluid effect, 205–207
- Local density buildup function, definition, 139
- Local density enhancements in near-critical fluids, experimental evidence, 135
- Local density of solvent, comparison to bulk density, 220
- Local entropy, definition, 139,141–142
- Local equilibrium theory model of supercritical fluid chromatography equation, example and theory, 282–283
- Local fluid structure, investigation and modeling, 6–7
- Local structure changes about solute, macroscopic thermodynamic property effect, 135
- M**
- Mass-transfer resistances, supercritical fluid effect, 203
- Mesophase pitch production by supercritical fluid extraction
ac impedance bridge, 350,351f
apparatus, 348,349f
carbon-fiber product properties, 355,356f
equation of state correlation, 357,358f
experimental procedure, 348,350,352–353
experimental vs. calculated vapor–liquid equilibria, 358,359–360f
extraction yields for toluene–pitch system vs. temperature, 354,355f
liquid–liquid compositions for toluene–pitch system vs. temperature, 353,354f,355
previous studies, 348
pseudocomponents of pitch, 356,357f
thermodynamic modeling, 356–357
- Methanol, aggregation in supercritical fluids, 158–172
- Methanol–carbon dioxide mixtures, *See* High-pressure vapor–liquid equilibria in carbon dioxide–1-alkanol mixtures
- Micelle water core radius, definition, 259
- Microcellular foams, development, 271
- Microemulsions
description, 258
general structures, 258
phase behavior, 74
reverse, dynamic fluorescence quenching in propane, 258–269
structure–phase behavior relationship, 74
- Model development for simulation and optimization in supercritical fluid chromatography
boundary conditions, 282
capacity factor, 284–285
Langmuir isotherm, 282
local equilibrium theory model, 282–283
mass balance equation, 282
velocity profiles, 283–284
- Modeling, vapor–liquid equilibria, 27,29–32
- Modifiers, definition and function, 36
- Molecular fluid structure in near-critical region, study approaches and techniques, 134
- Molecular interactions, investigation and modeling, 6–7
- Molecular simulations, function, 159
- Molecular weight, viscosity effect for polymer solutions in near- and supercritical fluids, 113,116–118
- Multiphase equilibria, supercritical fluid mixtures, 4
- Multiphase equilibrium behavior of carbon dioxide–1-decanol–*n*-tetradecane mixture
barotropic inversion points, 57–59
experimental procedure, 55–57
liquid–liquid–gas domain for solute molecular size vs. reduced temperature, 61–63,64f
objectives, 56
pressure–temperature projection, 57,58f,t
pressure vs. CO₂ mole fraction, 59,61f
pressure vs. molar volume, 59,62f
pressure vs. *n*-tetradecane mole fraction, 59,63f
previous studies, 55
temperature vs. *n*-tetradecane mole fraction, 57,59f

Multiple equilibria model of aggregation,
hydrogen bonding of simple alcohols in
supercritical fluids, 183–184

N

Naphthalene, supercritical extraction from
aqueous slurries, 294–304

2-Naphthol, cosolvent effect, 232,234f

Natural gas mixtures, thermophysical
properties from speeds of sound derived
from acoustic cavity measurements, 121–132

Near-critical solutions, competitive
energetic and entropic effects
describing solvation, 134–145

Near-critical solvents, advantages, 47

Near-critical triglycerides, liquid–liquid–
vapor phase behavior in binary mixtures,
47–53

Near-supercritical fluids
importance in polymer industry, 105
use as tunable process solvents or
tunable reaction media, 104
viscosity of polymer solutions, 104–119

Number of solvent nearest neighbors
surrounding a solute, definitions, 160

O

Optimization for supercritical fluid
chromatography
computational results, 289–292f
objective, 286,288
statement of problem, 288
transformation of model equation using
method of characteristics, 288–289

Organic aerogels, 271

Organic components, supercritical extraction
from aqueous slurries, 294–304

Organic compounds
heteroatom removal by supercritical
water, 327–336
kinetic model for wet oxidation in
subcritical and critical water, 305–311

P

Pair potential, definition, 159

Peng-Robinson equation of state,
expression, 67

1-Pentanol–CO₂ mixtures, *See*
High-pressure vapor–liquid equilibria
in carbon dioxide–1-alkanol mixtures

Petroleum pitch, production, 347

Petroleum processing applications,
example, 8

Pharmaceutical applications, example, 7–8
Phase behavior, measurement and prediction
using supercritical fluids, 3–5

Phase behavior of supercritical
fluid–entrainer systems
apparatus, 36–37,38f
chemical nature of components vs.
temperature and pressure, 39,45
experimental materials, 36,38f
experimental pressure–temperature–
composition results, 39,40–41t,42f
experimental procedure, 37
measurement procedure, 37,39
mixture preparation, 37
objective, 35

pressure vs. composition for CO₂–alcohol
mixtures, 39,44f

pressure vs. composition for CO₂–alkane
mixtures, 39,44f

structure of compounds vs. temperature
and pressure, 45

temperature vs. composition for
CO₂–alcohol mixtures, 39,43f

temperature vs. composition for
CO₂–alkane mixtures, 39,43f

Phenol, supercritical extraction from
aqueous slurries, 294–304

Phenylpiperidine, heteroatom removal by
supercritical water, 335,336f

Phenylpyridine, heteroatom removal by
supercritical water, 335,336f

Physical transformations, description, 104

Poly(hydroxy acids), use in controlled
drug release systems, 239

cis-Polyisoprene
pyrolysis, 380–382
thermolysis in supercritical toluene,
384,387f,388–390f

Polymer applications, example, 8

Polymer network formation in supercritical
fluids using light scattering
apparatus, 273,274f
autocorrelation function vs. time,
273,276f,277–278

Polymer network formation in supercritical fluids using light scattering—*Continued*
 comparison to styrenic production for ion-exchange resins, 272
 experimental procedure, 273
 future research, 280
 light scattering optics, 273,275f
 mechanism for particle growth, 279–280
 objectives, 272
 particle size distributions, 273,277f,278–280
 possible mechanisms, 273,277–278
 previous research, 272
 results, 273,277t,279

Polymer processing, importance of supercritical and near-supercritical fluids, 105

Polymer solutions, viscosity in near- and supercritical fluids, 104–119

Polystyrene, viscosity in near- and supercritical fluids, 104–119

Potential energy of solute, definition, 138

Potential energy of ternary system, definition, 144

Pressure
 chemical potential effect, 153–154
 critical, behavior of supercritical fluid–entrainer systems, 36
 viscosity effect for polymer solutions in near- and supercritical fluids, 108–112

Pressure programming, velocity profiles for supercritical fluid chromatography, 284

Propane
 dynamic fluorescence quenching in reverse microemulsions, 258–259
 interest as solvent, 47–48
 near-critical, liquid–liquid–vapor in binary mixtures, 47–53
 use as near-critical solvent, 47

Property prediction for gas mixtures, importance, 121

Pyrolysis of *cis*-polyisoprene
 process description, 380–382
 use of supercritical fluids, 381

Pyrolysis of scrap rubber, problems, 380

Pyrolysis reactions of hydrocarbon polymers, types, 381

Q

Quinuclidine, heteroatom removal by supercritical water, 332,335t

R

Rapid expansion of supercritical solutions
 advantages, 240–242
 applications, 239,242
 description, 239–240

Rate constant, pressure effect in supercritical fluid, 203,205

Reactant solubilities, supercritical fluid effect, 203

Reactions in supercritical fluids, spectroscopy
 catalyst life effect, 203
 diffusion rate effect, 202–203,204f
 examples of diffusion effect, 208–209
 examples of solute–cosolvent clustering, 214,215f
 examples of solute–solute interactions, 215–216
 examples of solute–solvent clustering, 212–214
 examples of thermodynamic pressure effect on rate constant, 209–212
 experimental description, 202
 local composition effect, 207
 local density effect, 205–207
 mass-transfer resistance effect, 203
 pressure effect on rate constant, 203,205
 reactant solubility effect, 203
 selectivity effect, 205
 separation effect, 203,204f

Reference state heat capacities, calculation, 126

Repulsive mixtures, definition, 160

Residual chemical potential, definition, 135–137

Residual entropy of solute molecule, definition, 145

Residual partial molar enthalpy, definition, 136–137

Residual partial molar entropy, definition, 136–137

Reverse microemulsions, dynamic fluorescence quenching in propane, 258–269

Roughness factor, definition, 94

S

Second virial coefficient, calculation, 129,131t,132f

- Selectivities
 cosolvent effect, 228
 supercritical fluid effect, 205
- Separability, definition, 62–63
- Separation, supercritical fluid effect, 203,204*f*
- Separation of solids from supercritical water oxidation process, *See* Solids separation from supercritical water oxidation processes
- Simple alcohols
 hydrogen bonding in supercritical fluids, 175–184
 use as modifiers, 175
- Simulation for supercritical fluid chromatography, density programming, 285,286*t*,287*f*
- Site–site pair correlation functions, description of structures in molecular fluids, 159–160
- Sodium chloride, separation from supercritical water oxidation processes, 320–324
- Sodium nitrate, separation from supercritical water oxidation processes, 323,324*f,t*
- Sodium sulfate, separation from supercritical water oxidation processes, 319–320,321*f*
- Solids separation from supercritical water oxidation processes
 corrosion product separation, 323,325
 experimental conditions, 317,318*f*
 experimental procedure, 315,317
 objective, 315
 salt removal efficiencies, 317–319
 salt separation apparatus, 315,316*f*
 sodium chloride separation, 320–324
 sodium nitrate, 323,324*f,t*
 sodium sulfate separation, 319–320,321*f*
 water physical property effect on solvent properties of water, 314
- Solubility, estimation in supercritical fluids, 4–5
- Solubility estimation of hydrocarbon solutes in supercritical carbon dioxide using group contribution method, *See* Group contribution method for solubility estimation of hydrocarbon solutes in supercritical carbon dioxide
- Solute–alcohol interactions in supercritical carbon dioxide, fluorescence spectroscopy, *See* Alcohol–solute interactions in supercritical carbon dioxide, fluorescence spectroscopy
- Solute–cosolvent clustering, examples, 214,215*f*
- Solute–solute interactions, examples, 215–216
- Solute–solvent clustering, examples, 212–214
- Solvation
 competitive energetic and entropic effects in near-critical solutions, 134–145
 development of local properties for description, 135–142
- Solvent cage formation, examples, 212–214
- Sonic speed
 calculation, 123
 determination of thermophysical properties of natural gas mixtures, 121–132
- Spectroscopic investigations of reactions in supercritical fluids, *See* Reactions in supercritical fluids, spectroscopy
- Stokes–Einstein equation, expression, 93
- Structures in molecular fluids, use of interaction site models of intermolecular pair potential, 159
- Supercritical carbon dioxide
 alcohol–solute interaction studies, fluorescence spectroscopy, 220–226
 solubility estimation of hydrocarbon solutes using group contribution method, *See* Group contribution method for solubility estimation of hydrocarbon solutes in supercritical carbon dioxide
- Supercritical extraction, examples, 66
- Supercritical extraction in environmental remediation, interest in applications, 294
- Supercritical extraction of coal
 model, 364
 reaction rate, 365–366
- Supercritical extraction of organic components from aqueous slurries
 calculated parameters for fugacity determination, 299,303*t*
 equilibrium distribution of naphthalene in activated alumina vs. pressure, 299,301*f*
 equilibrium distribution of naphthalene in activated alumina vs. temperature, 299,301*f*

- Supercritical extraction of organic components from aqueous slurries—**
Continued
- equilibrium distribution of naphthalene in soil, 299,302f
 - equilibrium distribution of phenol in activated carbon vs. pressure, 297,298f
 - equilibrium distribution of phenol in activated carbon vs. temperature, 297,298f
 - equilibrium distribution of phenol in soil vs. pressure, 299,300f
 - experimental procedure, 295–297
 - extraction percentage of naphthalene from activated alumina, 299,302f
 - extraction percentage of phenol and naphthalene in soil, 299,303f
 - extraction percentage of phenol from activated carbon, 297,299,300f
 - fugacity calculation, 296
 - fugacity definition, 295–296
 - systems studied, 295
- Supercritical extractors for solids**
- problems with continuous feed, 294
 - use of aqueous slurries, 294–295
- Supercritical fluid(s)**
- adsorption, 188–199
 - advantages, 2
 - aggregation of methanol, 158–172
 - expanding interest, 2
 - importance in polymer industry, 105
 - light scattering study of polymer network formation, 271–280
 - specialty separation and reaction applications, 220
 - spectroscopic investigations of reactions, 201–216
 - use as tunable process solvents or tunable reaction media, 104
 - use in pyrolysis of rubber, 381
 - viscosity of polymer solutions, 104–119
- Supercritical fluid bubble column, gas density effect on holdup, 338–345**
- Supercritical fluid chromatography**
- density programming simulation results, 285–288
 - gradient programming possibilities, 281
 - model development, 281–287
 - system optimization, 286,288–292
- Supercritical fluid–entrainer systems, phase behavior, 35–45**
- Supercritical fluid extraction**
- applications, 36
 - mesophase pitch production, 347–359
- Supercritical fluid extraction of coal**
- advantages, 327–328
 - potential applications, 363
 - process, 363
- Supercritical fluid(s) in controlled release of drugs**
- apparatus for gas antisolvent crystallization, 244,245f
 - apparatus for rapid expansion, 243,245f
 - background, 239–242
 - catalase particles formed by gas antisolvent crystallization, 251–252,253f
 - expansivity vs. pressure and temperature, 251,252f
 - experimental materials, 242–243
 - factors affecting precipitate composition, 249,251
 - gas antisolvent crystallization procedure, 243–244
 - insulin particles formed by gas antisolvent crystallization, 252,254f
 - microparticles with embedded lovastatin needles, 246,248f
 - microparticles with multiple lovastatin needles, 246,249f
 - microspheres with embedded lovastatin needles, 246,247f
 - rapid expansion of lovastatin needles, 244,246,249–251
 - rapid expansion procedure, 243
 - solid network formation, 249,250f
- Supercritical fluid mixtures**
- application, 134
 - application areas, 7–9
 - determination and correlation of transport properties, 5–6
 - diffusion, 92–102
 - estimation in supercritical fluids, 4–5
 - investigation and modeling of molecular interactions and local fluid structure, 6–7
 - measurement and prediction of phase behavior, 3–5
 - multiphase equilibria, 4
 - solubility estimation, 4–5
 - ternary, chemical potentials, 149–156

- Supercritical fluid research and development
 new focus, 201–202
 previous focus, 201
- Supercritical fluid science and technology, current state, 2–9
- Supercritical fluid solutions, chromatographic technique to study cosolvent effects, 228–235
- Supercritical solvents
 advantage of higher diffusion coefficients, 92
 properties, 66
- Supercritical toluene, depolymerization reactions of *cis*-polyisoprene and scrap rubber, 380–394
- Supercritical water, heteroatom removal from organic compounds, 327–336
- Supercritical water oxidation
 advantages, 305–306,314
 applications, 3
 description, 314
 kinetic model of organic compounds, 306–311
 solids separation, 314–325
 water physical property effect on solvent properties of water, 314
- Surfactant clusters, formation, 175–176
- T**
- Taylor dispersion technique
 accuracy of data, 96–97
 experimental and best-fit response curves, 96,99*f*
 experimental data, 95,96–97*t*
 precision, 95
 sources of errors, 95–96
- Temperature
 critical, behavior of supercritical fluid–entrainer systems, 36
 viscosity effect for polymer solutions in near- and supercritical fluids, 111,112*f*
- Temperature programming, velocity profiles for supercritical fluid chromatography, 284
- Ternary and higher order systems at finite compositions, local properties, 144–145
- Ternary supercritical fluid mixtures
 chemical potentials, 149–156
 solvent effects, 149
- n*-Tetradecane–carbon dioxide–1-decanol mixture, multiphase equilibrium behavior, 55–64
- Thermodynamic model, phase behavior for water–surfactant–supercritical fluid mixture, 76–77
- Thermodynamic pressure, examples of effect on rate constant for reactions in supercritical fluids, 209–212
- Thermophysical properties of natural gas mixtures from speeds of sound derived from acoustic cavity measurements
 acoustic resonance parameters for simulated natural gas mixture, 126,127*t*
 apparatus, 122–123
 composition of simulated natural gas mixture, 122*t*
 experimental procedure, 121–122
 reference-state isobaric heat capacity vs. temperature for simulated natural gas mixture, 129,130*f*
 second acoustic virial coefficient vs. temperature for simulated natural gas mixture, 129,130*f*
 sonic speed calculation, 123,125
 sonic speed in *n*-butane, 123,124*t*
 sonic speed in simulated natural gas mixture, 123,125*t*
 sonic speed vs. pressure for *n*-butane, 125–126,127*f*
 square of sonic speed vs. pressure for simulated natural gas mixture, 126,128*f*
- Three-phase liquid–liquid–vapor behavior in binary mixtures of near-critical propane and triglycerides
 experimental procedure, 49
 experimental results, 49,50*t*
 lower and upper critical endpoints vs. temperature, 49–50,51–52*f*
 lower critical endpoints, 49,50*t*
 objective, 47
 power of 2/3 of temperature region vs. carbon number, 50,52–53*f*
 pressure–temperature–composition projection of phase behavior, 48–49,50*f*
 upper critical endpoints, 49,50*t*
- Tires, used, disposal problems, 380
- Toluene, thermolysis under supercritical conditions, 384,385*f*,386*t*

Transferable intermolecular potential model of Jorgensen, description, 160–161
Translational–rotational coupling factor, description, 100
Transport properties, determination and correlation, 5–6
Triglycerides, near-critical, liquid–liquid–vapor in binary mixtures, 47–53
Trihexylamine, heteroatom removal by supercritical water, 333–335

U

Used tires, disposal problems, 380

V

van der Waals driven solvent clusters, formation, 175
Vapor–liquid equilibria, modeling, 27,29–32
Vapor–liquid equilibria in carbon dioxide–1-alkanol mixtures, high pressure, *See* High-pressure vapor–liquid equilibria in carbon dioxide–1-alkanol mixtures
Vapor pressure, estimation, 68
Velocity profiles for supercritical fluid chromatography
density programming, 283–284
pressure programming, 284
temperature programming, 284
Viscosity
determination, 106,108
determination and correlation, 5–6

Viscosity of polymer solutions in near- and supercritical fluids
demixing pressures, 108,109*f*
density effect, 111,113–116
experimental description, 105–106,108
polymer concentration effect, 113,116–117*f*,118
polymer molecular weight effect, 116–117*f*,118
practical importance, 105
pressure effect, 108–112
previous research, 105
temperature effect, 111,112*f*
theoretical importance, 105
viscometer system, 106,107*f*

W

Water, kinetic model for supercritical oxidation of organic compounds, 305–311
Water–amphiphile–liquid alkane mixture, phase behavior, 75
Wet oxidation
early operating conditions, 305
limitations, 305
Wilke–Chang equation, expression 93–94

Z

Zimpro wet air oxidation process, commercial applications, 305